MUSEUM NATIONAL D'HISTOIRE NATURELLE

Ecole Doctorale Sciences de la Nature et de l'Homme – ED 227

Année 2026

N°attribué par la bibliothèque

|_|_|_|_|_|_|_|_|_|_|_|_|_|

THESE

Pour obtenir le grade de

DOCTEUR DU MUSEUM NATIONAL D'HISTOIRE NATURELLE

et

DOTTORE DI RICERCA DELL'UNIVERSITÀ DEGLI STUDI DI FIRENZE

Spécialité : Préhistoire / Earth and Planetary Sciences



Présentée et soutenue publiquement par

Liz Charton

Le 05/02/2026

Environnements glaciaires des sociétés du Paléolithique moyen à supérieur en Méditerranée sud-occidentale depuis 200 000 ans.

Sous la direction de **:**

Nathalie Combourieu-Nebout, Directrice de recherches, CNRS, UMR 7194 « Histoire Naturelle des Humanités Préhistoriques »

Adele Bertini, Professeure**,** Dipartimento di Scienze della Terra, Università degli Studi di Firenze

JURY :

Mme Combourieu-Nebout, Nathalie	**Directrice de Recherche CNRS, Muséum national d'histoire naturelle, Paris (075)**	**Directrice de Thèse**
Mme Bertini, Adele	**Professeure, Università degli Studi di Firenze (Italie)**	**Directrice de Thèse**
M. Fletcher, Will	**Professeur, University of Manchester (Royaume-Uni)**	**Rapporteur**
Mme Magri, Donatella	**Professeure, Sapienza Università di Roma (Italie)**	**Rapportrice**
M. Sierro, Francisco	**Professeur, Universidad de Salamanca (Espagne)**	**Examinateur**
Mme Arzarello, Marta	**Professeure, Università degli Studi di Ferrara (Italie)**	**Examinatrice, présidente**
M. Lebreton, Vincent	**Professeur, Muséum national d'histoire naturelle, Paris (075)**	**Co-encadrant**
Mme Peyron, Odile	**Directrice de recherche CNRS, Institut des Sciences de l'Evolution-Montpellier (034)**	**Co-encadrante**
Mme Moncel, Marie-Hélène	**Directrice de recherche CNRS, Muséum national d'histoire naturelle, Paris (075)**	**Membre invité**


Karine Rouault-Charton

Somos una especie en viaje,

no tenemos pertenencias, sino equipaje.

Vamos con el polen en el viento,

estamos vivos porque estamos

en movimiento

Jorge Drexler, *Movimiento*

Remerciements

Mes premiers remerciements vont à Nathalie Combourieu-Nebout, Adele Bertini et Vincent Lebreton, sans qui cette thèse n'existerait pas. Merci de m'avoir donné goût à la paléoclimatologie et à l'étude du pollen à travers vos cours passionnants à Paris et à Florence, puis d'avoir accepté de m'accompagner tout au long de cette aventure. Pour votre confiance depuis le début, votre soutien sans faille et les innombrables relectures, merci.

Al Dipartimento di Scienze della Terra e al laboratorio di Palinologia dell'Unifi, dove questa avventura è iniziata per me nel 2019 quando ancora studiavo per la laurea triennale, grazie. A Federica, Gabriele, Pierluca, a Houssem, un ringraziamento speciale, così come a Serena Cartei per il suo aiuto nella gestione della cotutela. A Firenze, che mi ha visto crescere come adulta, et che amerò sempre, nel bene e nel male.

A l'ensemble du laboratoire de palynologie du Muséum basé à l'IPH, à Yannick Miras, Maé Catrain, Rafael Cabral, Tiffanie Fourcade, merci pour votre soutien. Un merci tout particulier à Lionel Dubost pour m'avoir formée au traitement des échantillons d'ODP 976 en laboratoire, et pour les manipulations à l'HF.

Un grand merci à Odile Peyron et toute son équipe de Montpellier, en particulier Mary, Léa, Betty et Lucas, pour m'avoir formée aux reconstructions climatiques, et pour l'accueil toujours chaleureux.

A Marie-Hélène Moncel un immense remerciement, pour son aide inestimable, ses relectures et les discussions toujours passionnantes sur Néandertal.

A Manuel Vaquero, Gema Chacón, Laurent Marquer et Dominique Grimaud-Hervé pour leur bienveillance et leurs commentaires toujours précieux lors des Comités de thèse.

Bien évidemment, merci aux post-docs qui m'ont accompagnée pendant ces trois ans, qui m'ont énormément appris, et pour qui j'ai toute l'admiration du monde : Dael Sassoon, Carolina Cucart et Mary Robles.

Aux étudiants de master et de doctorat du Muséum avec qui j'ai partagé le sous-sol de l'IPH ces dernières années, et qui l'ont rendu bien moins sombre et poussiéreux ! A Maé et Rafael (encore), mais aussi Jean-Baptiste, Clarisse, Marta, Jean, Julia, Angela, et Caroline. Aux autres doctorants du Musée de l'Homme que j'ai toujours eu plaisir à retrouver les quelques fois où j'ai pu « passer de l'autre côté » de Paris, en particulier à Pierre, Jérôme, Doria, Lucie, Marina, Marta et Chi-Shan.

Un remerciement tout particulier à Jérôme, sans les conseils de qui je n'aurais pas embarqué dans ce navire fou du master IMQP à Tarragone, puis de la thèse au Muséum… C'est drôle, tout ce que je te dois quand j'y pense, depuis ce stage de licence en Bourgogne, jusqu'à la thèse !

A Clara Letellier que j'ai eu la chance d'encadrer deux mois pendant son stage de L3, pour sa motivation qui a aussi nourri la mienne pendant la (presque) dernière ligne droite de la thèse…

A tous les gens avec qui j'ai pu échanger aux Fêtes de la Science, Journées du Patrimoine, et autres évènements de divulgation scientifique à Paris et à Florence, pour avoir à chaque fois ravivé la passion et m'avoir rappelé que le sens profond de ce que je fais est d'être partagé avec le plus grand nombre.

Merci au club guitare du Muséum pour les pauses musicales du mercredi qui m'ont beaucoup soulagé l'esprit en plus de me délier les doigts.

A Didier, que je suis toujours heureuse de saluer le matin à l'IPH, pour sa gentillesse et les bonnes discussions de guitaristes.

Merci également aux camarades de la CGT Muséum pour m'avoir redonné espoir dans la possibilité d'un autre système, d'une autre recherche, plus éthique et respectueuse de tous et toutes.

A l'Université publique et (presque) gratuite, seule fierté française dont j'ose me vanter à l'étranger (avec la baguette).

J'ai eu la chance de faire partie des élèves qui se sont toujours bien sentis à l'école. Aux professeurs de collège et de lycée qui ont toujours stimulé mon intérêt pour les langues, l'Histoire, l'Archéologie et les sciences

naturelles, et qui m'ont donné envie de poursuivre les études qui m'intéressaient, merci. Je pense particulièrement à Mme Hénicz, qui m'a emmenée en voyage à l'étranger pour la première fois sur les traces des Romains et des Etrusques, à Mr. Guerre qui le premier m'a parlé de paléoclimats et de palynologie, à Mme Dupuis, Mme Srdoc, Mme Giudiccelli, Mme Di Marco, pour m'avoir donné goût à l'Espagnol, à l'Anglais et à l'Italien. Avec tout ce qu'il y a de difficile dans vos métiers de profs, sachez que je me souviens toujours de vous, et que je vous dois beaucoup…

A mes compagnons archéologues et amis de Tarragone et de Ferrare, qui n'ont pas quitté mes pensées malgré l'éloignement. A Irene, Ibi, Miriam, Clara, Ian, Roberta, Giulietta. ¡Cuántas ganas de volver a veros!

A Nicolas, pour les heureux moments et son soutien sans faille.

A Silvia, ma voisine et grand-mère d'adoption à Florence, ainsi qu'à Blanca et Sara, pour leur amitié qui a été comme un baume au cœur.

A la danse, qui m'a permis de surmonter les moments difficiles en me rappelant que le corps a son propre langage et à quel point il me fait du bien. A Mabel, Elyse, et mes camarades des cours de danse de Florence et d'Ivry, vous n'imaginez pas ce que ce travail (et ma santé mentale) vous doit.

A mes amies cergyssoises de toujours qui sont et resteront le rocher auquel me raccrocher dans la tempête. A Sissi, Rania et Charlotte, je vous aime infiniment.

A mes sœurs, Oréline et Kiliane, auprès de qui je retrouve toujours le sens de « la vraie vie ».

A mes arrière-grands-parents, qui ont travaillé les terres bretonnes de leurs mains, à mes grands-parents ouvriers, et à mes parents qui les premiers ont foulé le sol de l'université. Je n'oublie pas d'où je viens. Merci mamie, papi, pour m'offrir toujours un refuge dans les terres natales sans jamais poser de questions sur la thèse (de toute façon, c'est du charabia). Votre jardin, c'est le terreau sur lequel je pousse humblement.

Maman, papa, merci de m'avoir fait confiance et de m'avoir toujours soutenue dans mes études. Pour les allers-retours aux activités, à la gare et à l'aéroport…Merci, pour votre amour, votre patience et votre écoute face à mes crises existentielles et scientifiques.

A ma maman un grand merci pour sa jolie peinture qui est venue illustrer ma thèse et dont je suis très fière.

A Hugo, enfin…. merci d'avoir traversé avec moi ces derniers mois de thèse, et de les avoir rendus moins pénibles par ton amour, ton esprit brillant, et ton soutien, toujours.

Table des matières

RESUME .....

RIASSUNTO .....

ABSTRACT .....

INTRODUCTION GENERALE **1**

1. CADRE DE L'ETUDE **7**

1.1 CADRE NATUREL 7

1.1.1 Végétation et climat du sud-ouest méditerranéen *7*

1.1.2 Processus atmosphériques majeurs *11*

1.1.3 Contexte océanographique et hydrographique *13*

1.1.4 Processus de la sédimentation et implication pour l'origine du pollen *14*

1.2 CADRE PALEOCLIMATIQUE 15

1.2.1 Dynamiques climatiques orbitales *15*

1.2.2 Dynamiques climatiques à échelle millénaire *17*

1.2.3 Réponse de la végétation méditerranéenne aux changements climatiques des derniers 200 000 ans *23*

1.3 CADRE ARCHEOLOGIQUE : POPULATIONS HUMAINES PALEOLITHIQUES EN EUROPE DU SUD-OUEST DEPUIS 200 000 ANS 25

1.3.1 Néandertal en Europe: présentation générale *25*

1.3.2 Le MIS 6 entre tradition Acheuléenne et innovations technologiques, une période en mosaïque .. *30*

1.3.3 Les MIS 5 à 3: le monde Néandertalien classique *31*

1.3.4 Vers la fin de Néandertal et l'arrivée d'Homo sapiens: la transition du Paléolithique moyen à supérieur *32*

1.3.5 Hypothèses sur les causes de l'extinction de Néandertal *37*

1.3.6 Considérations finales sur les dynamiques humaines et environnementales *41*

2. MATÉRIEL ET MÉTHODES **43**

2.1 LA CAROTTE ODP 976: HISTORIQUE DE L'EXPEDITION ET DES ETUDES 43

2.2 METHODES DE LA PALYNOLOGIE 45

2.2.1 Echantillonnage et extraction physico-chimique *45*

2.2.2 Problèmes de lisibilité et taphonomie *47*

2.2.3 Concentrations polliniques *50*

2.2.4 Analyses microscopiques *51*

2.2.5 NPPs *53*

2.3 MODELE D'AGE 53

2.3.1 Principes généraux *53*

2.3.2 Méthodes pour ODP 976 ..... *54*

2.4 ANALYSES STATISTIQUES MULTIVARIEES 59

2.4.1 Analyses de cluster *59*

2.4.2 Analyses de corrélation *59*

2.4.3 Analyses en Composantes Principales (ACP) *60*

2.5 RECONSTRUCTIONS CLIMATIQUES QUANTITATIVES A PARTIR DU POLLEN: UNE APPROCHE MULTIMETHODE 60

2.5.1 Principe et application à la séquence ODP 976 ..... *60*

2.5.2 La méthode des analogues modernes (MAT) *63*

2.5.3 Une approche par régression: Weighted Averaging Partial Least Squares (WA-PLS) *63*

2.5.4 Les approches par réseaux de neurones: Random Forest (RF) et Boosted Regression Trees (BRT) . *63*

2.5.5 Extraction des paramètres climatiques actuels *64*

2.5.6 Base de données d'échantillons actuels *65*

3. VEGETATION AND CLIMATE CHANGES DURING THE MIDDLE TO UPPER PALAEOLITHIC TRANSITION IN THE SOUTHWESTERN MEDITERRANEAN: WHAT HAPPENED TO THE LAST NEANDERTHALS DURING HEINRICH STADIAL 4? 71

3.1 RESUME EN FRANÇAIS 71
3.2 PAPER 1 (QSR): VEGETATION AND CLIMATE CHANGES DURING THE MIDDLE TO UPPER PALAEOLITHIC TRANSITION IN THE SOUTHWESTERN MEDITERRANEAN: WHAT HAPPENED TO THE LAST NEANDERTHALS DURING HEINRICH STADIAL 4? 73
3.2.1 Abstract 73
3.2.2 Introduction 74
3.2.3 Regional settings 77
3.2.4 Methods 79
3.2.4.1 Core sampling and pollen analyses 79
3.2.4.2 Age model 80
3.2.4.3 Multivariate statistical analyses 83
3.2.4.4 Pollen-based climatic reconstructions: a multi-method approach 83
3.2.4.5 Archaeological database 84
3.2.5 Results 86
3.2.5.1 Pollen diagram 86
3.2.5.2 Multivariate statistics 90
3.2.5.3 Climate reconstructions 92
3.2.5.4 Archaeological synthesis 94
3.2.6 Discussion 95
3.2.6.1 The sub-millennial oscillations in the Alboran Sea record between 41–34 ka BP 95
3.2.6.1.1 The three-phased imprint of Greenland Stadial 9 96
3.2.6.1.2 Greenland Interstadial 8 and Greenland Stadial 8 99
3.2.6.2 The HS4 / GI8 vegetation dynamics at a regional scale 100
3.2.6.3 Pollen-based climate reconstructions and climate changes at sub-millennial scale 105
3.2.6.4 Human occupations during the 42–34 ka BP climate instability 108
3.2.7 Conclusion 115
3.2.8 Acknowledgments 116

4. RAPID CLIMATIC VARIABILITY AND DYNAMICS OF MIDDLE PALAEOLITHIC HUMAN POPULATION DURING THE LAST CLIMATIC CYCLE (MIS 5-2) IN THE SOUTHWESTERN MEDITERRANEAN 117

4.1. RÉSUMÉ EN FRANÇAIS 117
4.2. INTRODUCTION 120
4.3. AGE MODEL 123
4.4. RESULTS 128
4.4.1. Pollen analyses 128
4.4.2. Pollen-based climate reconstructions 133
4.4.3. Clay particles analyses 137
4.4.4. Multivariate statistical analyses 138
4.5. DISCUSSION 143
4.5.1. The last glacial (MIS 4-2): rapid dynamics int the ODP 976 record 143
4.5.1.1. Overview 143
4.5.1.2. Climatic significance of the main pollen taxa variability 146
4.5.1.3. Comparison with regional and North-Atlantic records 148
4.5.1.4. Structure of the different extreme events: HS7 to HS1 151
4.5.2. The last interglacial (MIS 5) 156
4.5.2.1. Overview 156
4.5.2.2. Regional comparison 160
4.5.3. Human occupation in the Iberian Peninsula during the last climatic cycle 164
4.5.3.1. Preliminary considerations 164
4.5.3.2. MIS 5 165
4.5.3.3. MIS 4 170
4.5.3.4. MIS 3 and the late Middle Palaeolithic 172
4.6. CONCLUSIONS 176

5. DECODING TERMINATION II AND THE ONSET OF THE LAST INTERGLACIAL IN THE WESTERN MEDITERRANEAN 179

5.1. INTRODUCTION 180
5.2. THE MULTIPROXY RECORD FOR TERMINATION II FROM ODP 976 182
5.2.1. Pollen-inferred vegetation and climate 183
5.2.2. Paleo-dust record and atmospheric configuration 185
5.2.3. Multiproxy land-sea correlation 186
5.3. COMPARISON WITH SPELEOTHEM RECORDS AND OCEAN-ATMOSPHERE DYNAMICS 188
5.4. SIMILARITIES AND DIFFERENCES BETWEEN THE LAST AND THE PENULTIMATE DEGLACIATIONS 190
5.5. RELEVANCE FOR THE DISCUSSION ON PLEISTOCENE SERIES BOUNDARIES 193
5.6. CONCLUSIONS 196

6. THE PENULTIMATE GLACIAL (MIS 6) IN THE SW MEDITERRANEAN: VEGETATION, CLIMATE AND HUMAN DYNAMICS. 199

6.1. RESUME EN FRANÇAIS 199
6.2. PAPER 2 (*CLIMATE OF THE PAST*): HOW UNSTABLE WAS THE ENVIRONMENT DURING THE PENULTIMATE GLACIAL IN THE SOUTH-WESTERN MEDITERRANEAN? VEGETATION, CLIMATE AND HUMAN DYNAMICS DURING MIS 6. 201
6.2.1. Abstract 201
6.2.2. Introduction 202
6.2.3. Study site 204
6.2.4. Methods 206
6.2.4.1. Age Model 206
6.2.4.2. Pollen analyses 208
6.2.4.3. Pollen-inferred climate reconstructions: a multi-method approach 209
6.2.5. Results 210
6.2.5.1. Pollen record 210
6.2.5.2. Pollen-inferred climate reconstructions 215
6.2.6. Discussion 217
6.2.6.1. Paleoenvironment of MIS 6 and Termination II in the western Mediterranean 217
6.2.6.2. Hydroclimate connection with ORLs deposition during MIS 6 218
6.2.6.3. Mediterranean vegetation changes during the penultimate glaciation: a synthesis 219
6.2.6.4. Rapid climate variability during MIS 6: a regional multiproxy comparison 223
6.2.6.5. Comparison of MIS 6 with the last glacial period (MIS 4-2) 231
6.2.6.6. Human occupation during MIS 6 in SW Europe 234
6.2.7. Conclusion 240
6.2.8. Acknowledgments 241

7. DISCUSSION GENERALE 243

7.1. CADRE INTERPRETATIF ET LIMITES METHODOLOGIQUES 243
7.2. DYNAMIQUES DE LA VEGETATION ET DU CLIMAT EN MEDITERRANEE DEPUIS 200 000 ANS: UNE SYNTHESE DE L'ENREGISTREMENT D'ODP 976 246
7.3. DIFFERENCES, SIMILARITES ET MODULATION ORBITALE DES OSCILLATIONS SUB-MILLENAIRES AU COURS DES DERNIERS 200 000 ANS 252
7.4. MISE EN PERSPECTIVE DE L'ENREGISTREMENT PALYNOLOGIQUE D'ODP 976 A ECHELLE GLOBALE AINSI QU'AVEC LES PRINCIPALES LONGUES SEQUENCES MEDITERRANEENNES 256
7.5. NEANDERTAL DANS SON ENVIRONNEMENT INSTABLE DEPUIS 200 000 ANS EN MEDITERRANEE OCCIDENTALE 264

8. CONCLUSIONS ET PERSPECTIVES 269

9. LISTE DES FIGURES 273

10. LISTE DES TABLEAUX 277

11. DECLARATION SUR L'UTILISATION DE L'IA GENERATIVE 278

12. REFERENCES BIBLIOGRAPHIQUES 279

13. SUPPLÉMENTS 353

Résumé

Homo neanderthalensis est présent en Europe occidentale depuis au moins 200 000 ans avant le présent (ka BP), à travers deux cycles glaciaire-interglaciaire, jusqu'à son extinction autour de 40 ka BP, alors que les premières populations d'*Homo sapiens* s'installent sur le continent. Parmi les principales hypothèses expliquant le déclin de Néandertal figurent notamment la compétition directe ou indirecte avec Sapiens, ainsi que les changements climatiques abrupts pendant la dernière période glaciaire, au cours du stade isotopique marin (MIS) 3. Le climat en Europe durant cette période a été marqué par une succession de réchauffements (interstadiaires) et de refroidissements (stadiaires) à échelle sub-millénaire (cycles de Dansgaard-Oeschger), ainsi que par plusieurs évènements froids et arides extrêmes liés à des débâcles massives d'icebergs dans l'Atlantique Nord (les stadiaires de Heinrich, HS). Si le HS4 (~39.9-38.2 ka BP), contemporain des dernières occupations néandertaliennes, est bien connu et documenté grâce aux carottages marins au large de la péninsule Ibérique, les évènements analogues précédents sont moins bien connus, entravant notre compréhension des dynamiques de population néandertaliennes face à un environnement instable sur le long terme. Cette thèse propose donc de retracer l'histoire des changements environnementaux rapides des derniers 200 000 ans (MIS 7-1) afin d'explorer leur potentiel impact sur les populations néandertaliennes jusqu'à leur extinction. L'étude palynologique de la carotte sédimentaire ODP 976 en mer d'Alboran (sud-ouest Méditerranéen) a mis en évidence la dynamique de la végétation dans une région clé souvent présentée comme un refuge climatique pour les populations humaines. Une approche quantitative à partir des assemblages polliniques a été utilisée afin de reconstituer les paramètres climatiques (températures et précipitations) annuels et saisonniers au cours des derniers 200 ka à travers différentes méthodes (MAT, WA-PLS, RF, BRT). Finalement, une synthèse des sites archéologiques associés à Néandertal en Méditerranée occidentale a permis d'évaluer la dynamique des populations néandertaliennes au cours du temps. Les résultats montrent que la région du sud-ouest méditerranéen s'est montrée très sensible aux évènements climatiques froids de l'Atlantique nord depuis 200 000 ans, avec des conditions particulièrement arides et une prédominance de la végétation steppique et semi-désertique pendant les HS. Un climat froid et aride a affecté la région pendant l'avant-dernière période glaciaire (MIS 6, entre ~190-129 ka BP), période marquée par des oscillations climatiques moins intenses par rapport aux MIS 4 et 3 (~70-30 ka BP). Le HS11, pendant la Terminaison glaciaire 2, se démarque par sa durée (~6000 ans), son intensité et sa structure complexe, à un moment clé où les industries lithiques du Paléolithique Inférieur semblent définitivement abandonnées. Plusieurs refroidissements abrupts ont été enregistrés pendant le dernier interglaciaire (MIS 5, 129-71 ka BP), d'une intensité moindre comparé à ceux des MIS 4-3. Les épisodes les plus extrêmes traversés par Néandertal dans la région correspondent aux HS11 (~132 ka BP), HS6 (~61 ka BP), HS5 (~48 ka BP) et HS4 (~39 ka BP). Finalement, l'instabilité climatique croissante caractérisant l'entrée progressive en glaciation a pu influencer la diversification des comportements néandertaliens au cours des MIS 4 et 3, et favoriser une dynamique de replis répétés dans les refuges glaciaires. Malgré des données chronologiques encore limitées, la synthèse met en évidence une potentielle vulnérabilité des populations néandertaliennes face au HS6, au HS5 et au HS4 qui ont pu jouer un rôle dans leur extinction finale. Cette étude contribue à l'obtention d'une séquence paléoenvironnementale de référence décrivant à haute résolution toute la variabilité climatique en Méditerranée occidentale.

Riassunto

Homo neanderthalensis è attestato in Europa occidentale da almeno 200.000 anni prima del presente (ka BP), attraverso due cicli glaciali–interglaciali, fino alla sua estinzione intorno a 40 ka BP, in concomitanza con l'insediamento delle prime popolazioni di *Homo sapiens* nel continente. Tra le principali ipotesi per spiegare il declino dei neandertaliani figurano la competizione diretta o indiretta con Sapiens, nonché i bruschi cambiamenti climatici intervenuti durante l'ultimo periodo glaciale, in particolare nel corso dello stadio isotopico marino (MIS) 3. Il clima europeo di questo periodo è stato caratterizzato da una successione di riscaldamenti (interstadiali) e raffreddamenti (stadiali) su scala sub-millenaria (cicli di Dansgaard-Oeschger), oltre che da diversi raffredamenti estremi connessi a episodi di rafting di iceberg nell'Atlantico settentrionale, noti come stadiali di Heinrich (HS). Sebbene l'HS4 (~39,9–38,2 ka BP), contemporaneo delle ultime occupazioni neandertaliane, sia ampiamente documentato grazie ai carotaggi marini al largo della Penisola Iberica, gli eventi analoghi precedenti risultano meno conosciuti, limitando la nostra comprensione delle dinamiche di populazioni neandertaliane relative all'instabilità ambientale su scala di lungo periodo. La presente tesi si propone pertanto di ricostruire la storia dei rapidi cambiamenti ambientali degli ultimi 200 000 anni (MIS 7–1), al fine di valutarne il potenziale impatto sulle popolazioni neandertaliane fino alla loro estinzione. Lo studio palinologico della carota sedimentaria ODP 976 nel Mare di Alborán (Mediterraneo sud-occidentale) ha consentito di ricostruire la dinamica della vegetazione in una regione chiave, spesso considerata un rifugio climatico per le popolazioni umane. Un approccio quantitativo basato sugli assemblaggi pollinici è stato applicato per ricostruire i parametri climatici (temperature e precipitazioni) annuali e stagionali nel corso degli ultimi 200 000 anni mediante diversi metodi (MAT, WA-PLS, RF, BRT). Infine, una sintesi dei siti archeologici attribuiti a Neandertal nel Mediterraneo occidentale ha permesso di analizzare le dinamiche spaziotemporali delle popolazioni neandertaliane. I risultati indicano che la regione del Mediterraneo sud-occidentale è stata altamente sensibile agli eventi climatici freddi dell'Atlantico settentrionale negli ultimi 200.000 anni, con condizioni particolarmente aride e una prevalenza di vegetazione steppica e semidesertica durante gli HS. Un clima freddo e arido è stato ricostruito nella regione durante il penultimo glaciale (MIS 6, ~190–129 ka BP), periodo caratterizzato da oscillazioni climatiche di minore ampiezza rispetto a quelle dei MIS 4 e 3 (~70–30 ka BP). L'HS11, avvenuto durante la Terminazione glaciale 2, si distingue per la sua notevole durata (~6000 anni) e la sua struttura particolarmente complessa, durante una fase cruciale nella cuale le industrie litiche del Paleolitico inferiore vengono definitivamente abbandonate. Numerosi raffreddamenti bruschi sono stati inoltre registrati nel corso dell'ultimo interglaciale (MIS 5, 129–71 ka BP), sebbene di minore intensità rispetto a quelli documentati nel corso dei MIS 4–3. Gli episodi più estremi vissuti dalle popolazioni neandertaliane nella regione corrispondono agli HS11 (~132 ka BP), HS6 (~61 ka BP), HS5 (~48 ka BP) e HS4 (~39 ka BP). Infine, la maggiore instabilità climatica associata alla progressiva transizione verso condizioni glaciali potrebbe aver influenzato la diversificazione dei comportamenti neandertaliani durante i MIS 4 e 3, favorendo dinamiche di ripetuto ripiegamento nei rifugi glaciali. Nonostante la limitazione dei dati cronologici attualmente disponibili, la sintesi evidenzia una potenziale vulnerabilità delle popolazioni neandertaliane agli eventi HS6, HS5 e HS4, i quali potrebbero aver contribuito al loro declino e al processo della loro estinzione finale. Il presente studio contribuisce inoltre all'ottenimento di una sequenza paleoambientale di riferimento ad alta risoluzione, in grado di descrivere l'intera variabilità climatica del Mediterraneo occidentale.

Abstract

Homo neanderthalensis was present in Western Europe since at least 200,000 years before present (ka BP), across two glacial–interglacial cycles and until its extinction around 40 ka BP, which coincided with the expansion of the first *Homo sapiens* populations on the continent. The main hypotheses proposed to explain Neanderthal decline involve a direct or indirect responsibility of Sapiens, as well as abrupt climatic changes that occurred during the last glacial period, within Marine Isotope Stage (MIS) 3. Climate in Europe during this time experienced a succession of warm (interstadial) and cold (stadial) phases at a sub-millennial scale (Dansgaard–Oeschger cycles), as well as several extremely cold and arid events linked to massive iceberg discharges in the North Atlantic (Heinrich stadials, HS). While HS4 (~39.9–38.2 ka BP), contemporaneous with the last Neanderthal occupations, is well known thanks to several marine archives retrieved off the Iberian margin, earlier analogous events are less well documented, hindering our ability to understand long-term Neanderthal population dynamics in the face of persistent environmental instability. This thesis therefore aims at reconstructing rapid environmental changes during the last 200,000 years (MIS 7–1) in order to explore their potential impact on Neanderthal populations up to their extinction. The palynological study of the marine sediment core ODP 976 in the Alboran Sea (southwestern Mediterranean) revealed the history of vegetation in a key region often described as a climatic refugia for human populations during the Pleistocene. A quantitative approach based on pollen assemblages was used to reconstruct the changes in annual and seasonal climatic parameters (temperature and precipitation) over the last 200 ka BP using multiple methods (MAT, WA-PLS, RF, BRT). Finally, a synthesis of archaeological sites associated with Neanderthals in Western Mediterranean Europe enabled an assessment of the spatial and temporal dynamics of Neanderthal populations through time. The results show that the southwestern Mediterranean region was highly sensitive to North Atlantic cold events over the past 200,000 years, exhibiting particularly arid conditions and a predominance of steppe and semi-desert vegetation during HS events. The penultimate glacial period (MIS 6, ~190–129 ka BP) was characterized by cold and dry climate and subdued climatic oscillations compared to MIS 4-3 (~70-30 ka BP). HS11, occurring during Glacial Termination 2, stands out for its duration (~6000 years), its intensity, and its complex structure, at a key moment when Lower Palaeolithic lithic industries were definitively abandoned. Several abrupt cooling events were recorded during the last interglacial period (MIS 5, 129–71 ka BP), though they were less intense than those of MIS 4–3. The most extreme events experienced by Neanderthals in the region correspond to HS11 (~132 ka BP), HS6 (~61 ka BP), HS5 (~48 ka BP), and HS4 (~39 ka BP). Finally, the increasing climatic instability marking the progressive glaciation inception may have influenced the diversification of Neanderthal behaviours during MIS 4 and 3, and may have favoured repeated population contractions into glacial refugia. Despite limited chronological data, the synthesis supports a potential vulnerability of Neanderthal populations to HS6, HS5, and HS4, which may have played a role in their extinction. This study contributes to establishing a high-resolution paleoenvironmental reference sequence describing environmental variability in the Western Mediterranean.

Introduction générale

L'unité essentielle de la Méditerranée, c'est le climat, un climat très particulier, semblable d'un bout à l'autre de la mer, unificateur des paysages et des genres de vie. Il est, en effet, presque indépendant des conditions physiques locales, construit du dehors par une double respiration, celle de l'océan Atlantique, le voisin de l'ouest, celle du Sahara, le voisin du sud. Chacun de ces monstres sort régulièrement de chez lui pour conquérir la mer, laquelle ne joue qu'un rôle passif : sa masse d'eau tiède (11°C) facilite l'intrusion de l'un, puis de l'autre.

F. Braudel, La Méditerranée*, p. 28*

Les mots de l'historien résonnent particulièrement pour le paléoclimatologue de la Méditerranée, définie ici comme espace incluant la mer et toutes les terres qui la bordent et qui partagent un climat et des paysages semblables (voir section 1.2). L'étude des archives géologiques, incluant les sédiments marins et continentaux ainsi que les spéléothèmes, permet une plongée dans les conditions climatiques et environnementales passées de la Méditerranée, qui ont varié à différentes échelles de temps. Tel un historien du monde physique, le paléoclimatologue déchiffre les indicateurs fossiles afin de documenter les conditions passées et de restituer au mieux les processus impliqués. Il étoffe une compréhension du monde passé qui vise à éclairer les scénarios possibles pour l'avenir. Ainsi, les reconstructions climatiques s'appuyant sur les données fossiles permettent l'ajustement et l'affinement des modèles de prédiction du changement climatique futur.

La Méditerranée abrite des écosystèmes marins et continentaux uniques et particulièrement sensibles à la crise climatique causée par les activités humaines, comme l'a montré le Groupe d'Experts Méditerranéens sur le Changement Climatique et Environnemental (MedCC) (MedECC, 2020). Les évènements climatiques extrêmes, tels que les vagues de chaleur et épisodes de sécheresse (Guion et al., 2022; Pastor et al., 2024; Trigo et al., 2025; Vautard et al., 2007; Zampieri et al., 2009) ainsi que les pluies torrentielles et les inondations (Diodato et al., 2011; Granata et al., 2025) se sont multipliées depuis le début de l'ère industrielle. Ils sont appelés à s'intensifier sous l'effet du dérèglement climatique et de la transformation des paysages produits par les modes de vie des sociétés humaines occidentales modernes (Giorgi & Lionello, 2008). Ainsi, comprendre comment les environnements Méditerranéens ont évolué par le passé, et comment les groupes humains qui l'ont habité depuis la Préhistoire se sont adaptés à ces changements, apparaît d'autant plus crucial aujourd'hui.

L'Homme est présent en Méditerranée occidentale depuis au moins 1 million d'années (Huguet et al., 2025; Martínez Navarro et al., 1997). Depuis au moins 200 000 ans et jusqu'à son extinction autour de 40 000 ans avant le présent, l'Homme de Néandertal (*Homo neanderthalensis*) peuple cette région de manière continue (voir section 2.3). Il y est l'unique représentant du genre *Homo* jusqu'à l'arrivée des premiers *Homo sapiens*, autour de 50 ka BP (milliers d'années avant le présent fixé à 1950)

en Europe occidentale (Hublin et al., 2020; Slimak et al., 2022). La période clé de la disparition des dernières populations néandertaliennes et de l'arrivée des *Homo sapiens* en Europe est appelée transition du Paléolithique moyen à supérieur (Teyssandier, 2024; Zilhão et al., 2024). Si Néandertal a traversé au moins deux cycles climatiques complets en Eurasie occidentale impliquant de longues périodes plus chaudes (interglaciaires) et plus froides (glaciaires) ponctuées de variations plus rapides et intenses (voir section 2.2), les causes de son extinction restent généralement mal comprises. Des visions parfois contradictoires s'opposent, impliquant principalement la responsabilité directe d'*Homo sapiens* (Martínez-Navarro, 2020), la compétition pour les ressources entre les deux espèces (Banks et al., 2008; Timmermann, 2020), ou bien les changements climatiques abrupts de la dernière période glaciaire et en particulier l'un des plus intenses, l'évènement de Heinrich 4 (d'Errico & Sánchez Goñi, 2003; Finlayson & Carrión, 2007; Sepulchre et al., 2007). Cette dernière hypothèse reste difficile à tester, étant donné le registre archéologique fragmentaire et le manque d'archives paléoclimatiques bien datées et à haute résolution pour préciser le contexte paléoenvironnemental des occupations humaines sur le long terme. Ainsi, si les variations rapides du climat sur les derniers 60 000 ans (~MIS 3-1) sont relativement bien connues en Méditerranée, les périodes antérieures sont bien moins documentées, entravant notre compréhension de leur possible impact sur les populations humaines.

Le sud-ouest Méditerranéen, objet de cette thèse, est une région critique pour aborder ces problématiques, et ce pour plusieurs raisons. D'une part, elle est soumise à des influences climatiques d'importance globale et impliquant ses trois domaines bioclimatiques limitrophes : à l'Ouest, l'océan Atlantique, au Sud, le désert du Sahara, et à l'Est, le reste du bassin Méditerranéen. C'est donc une zone d'intérêt majeur pour déchiffrer les mécanismes d'interactions entre ces différentes influences dans le passé et comprendre leur impact sur les écosystèmes méditerranéens. D'autre part, la région a représenté tout au long du Quaternaire une zone refuge pour les espèces végétales et animales, incluant le genre *Homo* (Bennett et al., 1991; Bicho & Carvalho, 2022; Carrión et al., 2003). Ainsi, il est généralement accepté que la péninsule Ibérique et, plus généralement, le sud-ouest méditerranéen, ont constitué une zone continuellement habitée par Néandertal pendant les épisodes climatiques les plus défavorables, et même une région de persistance tardive des derniers groupes néandertaliens avant leur extinction (Finlayson et al., 2006, 2008; Zilhão, 2006, 2021).

Le cadre environnemental et climatique de la région pendant ces périodes est connu à travers plusieurs archives paléoenvironnementales continentales longues et continues comme les carottes sédimentaires lacustres et les spéléothèmes, qui sont cependant peu nombreuses dans la péninsule Ibérique (e.g. Camuera et al., 2018, 2019; Carrión et al., 2024a, 2024b; Hodge et al., 2008). Ainsi, les dynamiques climatiques et environnementales à longue échelle de temps sont actuellement surtout documentées par les séquences marines de la côte atlantique de la péninsule Ibérique, largement

étudiées pour le dernier cycle climatique (les derniers ~130 ka BP) (e.g. d'Errico & Sánchez Goñi, 2003; Fletcher et al., 2010a; Margari et al., 2010; Roucoux et al., 2005; Sánchez Goñi et al., 1999, 2002, 2022; Shackleton et al., 2000; Tzedakis et al., 2018) (voir section 1.2.3). Par ailleurs, les données paléoécologiques provenant des sites archéologiques en association directe avec les occupations humaines (pollen, charbons, isotopes, faune) ont également enrichi la compréhension des interactions Homme-environnement dans la péninsule Ibérique sur ces périodes (e.g. Carrión et al., 1999, 2007; García et al., 2022; Ochando et al., 2020a, 2020b, 2022). Padul représente en Méditerranée occidentale la seule séquence palynologique continue couvrant le dernier cycle climatique dans son entièreté ainsi que l'avant-dernière période glaciaire, avec une résolution variable mais insuffisante dans la section basale pour appréhender les oscillations climatiques rapides (Camuera et al., 2018, 2019, 2022). Ainsi, à l'heure actuelle aucun enregistrement paléoenvironnemental en Méditerranée occidentale ne permet de documenter en continu et à haute résolution la dynamique rapide des environnements sur l'entièreté des deux derniers cycles climatiques. L'étude palynologique de la carotte ODP 976 sur les derniers 200 000 ans entend combler cette lacune.

Cette thèse propose ainsi de reconstituer l'évolution des environnements végétaux et du climat en Méditerranée sud-occidentale au cours des derniers 200 000 ans, ainsi que de mener une réflexion sur les relations entre les groupes humains néandertaliens et leurs environnements pléistocènes instables. Ce travail vise ainsi à évaluer l'hypothèse climatique de l'extinction de Néandertal en caractérisant les variations climatiques sur les deux derniers cycles climatiques. Les questions scientifiques suivantes seront abordées :

- Quel a été l'impact des changements climatiques à haute fréquence sur les environnements continentaux du sud-ouest méditerranéen au cours des derniers 200 000 ans ?

- Des variations abruptes du climat et de l'environnement, telles que celles bien connues pendant le MIS 3, ont-elles affecté le sud-ouest méditerranéen pendant les MIS 6, 5 et 4 ?

- Finalement, quel rôle ont pu jouer les variations environnementales rapides dans les dynamiques du peuplement néandertalien de la Méditerranée occidentale ?

L'archive sédimentaire, la carotte marine du Leg ODP 161 site 976, offre une plongée continue dans le Pléistocène grâce à différents traceurs, témoins indirects des conditions climatiques dominantes sur terre et en mer au cours du temps. Le pollen, indicateur essentiel des environnements végétaux dans la région, est l'objet d'étude principal de ce travail. Les données polliniques seront croisées à celles d'autres indicateurs déjà partiellement publiés dans la séquence, tels que les enregistrements (i) des rapports isotopiques de l'oxygène provenant des tests de foraminifères planctoniques, (ii) des alkénones, et (iii) des rapports élémentaires Mg/Ca dans ces mêmes

foraminifères qui permettent l'estimation des températures de surface de l'eau, ou encore (iv) de la composition minéralogique des argiles composant le sédiment, témoins des courants marins et atmosphériques passés.

Les objectifs de la thèse sont :

- Compléter l'étude palynologique déjà partiellement publiée du dernier cycle climatique de la carotte ODP 976, et l'étendre au MIS 6, de manière à obtenir une série palynologique continue et à haute résolution sur 200 000 ans en Méditerranée sud-occidentale.

- Reconstruire l'évolution des paramètres climatiques annuels et saisonniers dans la région à partir du pollen avec une approche multiméthode (voir section 2.5).

- Restituer ainsi la dynamique rapide de la végétation et du climat en Méditerranée sud-occidentale, et comparer ces résultats avec ceux des principales autres longues séquences palynologiques et paléoclimatiques méditerranéennes.

- Comparer les caractéristiques des oscillations rapides entre les deux périodes glaciaires (MIS 6 et MIS 4-2), et l'interglaciaire du MIS 5, à partir d'un même enregistrement palynologique et utilisant les mêmes méthodologies de reconstructions climatiques.

- Proposer une synthèse des occupations néandertaliennes du sud-ouest Méditerranéen sur les derniers 200 000 ans permettant d'émettre des hypothèses quant à l'impact des variations rapides du climat sur les dynamiques de peuplement humain.

La thèse sera structurée comme détaillé ci-après.

La section 1 vise à présenter les cadres naturel (1.1), paléoclimatique (1.2), et archéologique (1.3) de l'étude. La section 2 commencera par présenter la carotte ODP 976 (2.1), puis les méthodes utilisées pour la palynologie (2.2), l'élaboration du modèle d'âge (2.3), les analyses statistiques (2.4) et les reconstructions climatiques à partir du pollen (2.5).

Les résultats de l'étude seront ensuite présentés et discutés dans quatre sections (3 à 6) qui correspondent à des articles publiés, en cours de publication ou en cours d'écriture.

La première (section 3) est centrée sur la période courte mais cruciale entre 41 et 34 ka BP, comprenant la transition du Paléolithique moyen à supérieur et l'évènement de Heinrich 4. Il s'agira de comprendre la structure interne de cet évènement abrupt en Méditerranée sud-occidentale, et sa place dans le débat archéologique sur la disparition des derniers néandertaliens dans la péninsule Ibérique.

La deuxième (section 4) entend réaliser une synthèse et une comparaison des changements abrupts enregistrés dans la carotte ODP 976 au cours du dernier cycle climatique dans son entièreté, entre 130 000 et 11 000 ans (MIS 5e – MIS 1). Une discussion sur les occupations néandertaliennes dans la péninsule Ibérique au cours du dernier cycle climatique y sera développée à la lumière des dynamiques environnementales reconstruites.

La troisième (section 5) se centrera sur l'analyse de la terminaison glaciaire II (TII, 136-129 ka BP) dans l'enregistrement multi-proxies et à haute résolution de la carotte ODP 976. Ces données permettent d'enrichir une discussion d'ordre à la fois climatique, pour la transition entre l'avant-dernière période glaciaire (MIS 6) et le dernier interglaciaire (MIS 5), et d'ordre stratigraphique pour la transition entre le Pléistocène Moyen et le Pléistocène Supérieur.

La quatrième (section 6), enfin, sera centrée sur l'avant-dernière période glaciaire (MIS 6) et aura pour but d'identifier de possibles analogues d'évènements rapides (type Dansgaard-Oeschger et type Heinrich) dans l'enregistrement de la carotte ODP 976 entre 200 et 129 ka BP. Les occupations néandertaliennes en Méditerranée occidentale contemporaines de cette période seront discutées dans ce contexte paléoenvironnemental.

La section 7 sera consacrée à une discussion générale qui visera à répondre aux problématiques de la thèse. Une première partie analysera le cadre interprétatif et les limitations méthodologiques de l'étude (section 7.1). Par la suite, une synthèse des changements climatiques décrits à partir de la carotte ODP 976 en Méditerranée sud-occidentale sur les derniers 200 000 ans sera présentée (section 7.2). La troisième partie s'intéressera aux différences et aux similarités entre les dynamiques environnementales rapides du dernier cycle climatique (MIS 5e-1) et de l'avant-dernière période glaciaire (MIS 6), en apportant des hypothèses sur les causes impliquées (section 7.3). L'enregistrement palynologique de la carotte ODP 976 sera ensuite mis en perspective à échelle globale ainsi qu'avec les autres longues séquences méditerranéennes disponibles pour les derniers 200 000 ans (section 7.4). Enfin, la dernière partie synthétisera les dynamiques d'occupations humaines en lien avec les changements environnementaux au cours des deux derniers cycles climatiques (section 7.4).

La section 8 sera consacrée aux conclusions générales et perspectives de l'étude.

1. Cadre de l'étude

1.1 Cadre naturel

1.1.1 Végétation et climat du sud-ouest méditerranéen

La mer d'Alboran s'étend entre la côte Ibérique au nord, et celle du Nord de l'Afrique au sud (Fig. 1.1).

La péninsule Ibérique est caractérisée dans sa grande majorité par un climat et une végétation de type méditerranéen, marqué généralement par des hivers doux et humides, et de longues périodes de sécheresse estivale (Lionello et al., 2006; Sánchez-Laulhé et al., 2021) (Fig. 1.1). Le nord du Maroc et de l'Algérie présente également un climat et une végétation de type méditerranéen, limités au sud des montagnes de l'Atlas par le désert du Sahara.

Les nombreux reliefs ainsi que le découpage marqué en golfes et péninsules du pourtour méditerranéen font sa particularité, et sont à l'origine de contrastes climatiques marqués. Les régimes de précipitations annuelles et saisonnières sont très variables géographiquement, avec des zones sèches à semi-désertes, et d'autres plus humides à subtropicales (Deitch et al., 2017; Sumner et al., 2001). Ces contrastes orogéniques, climatiques et pluviométriques déterminent des zones d'étagements de végétation sur tout le pourtour méditerranéen (Fig. 1.1) :

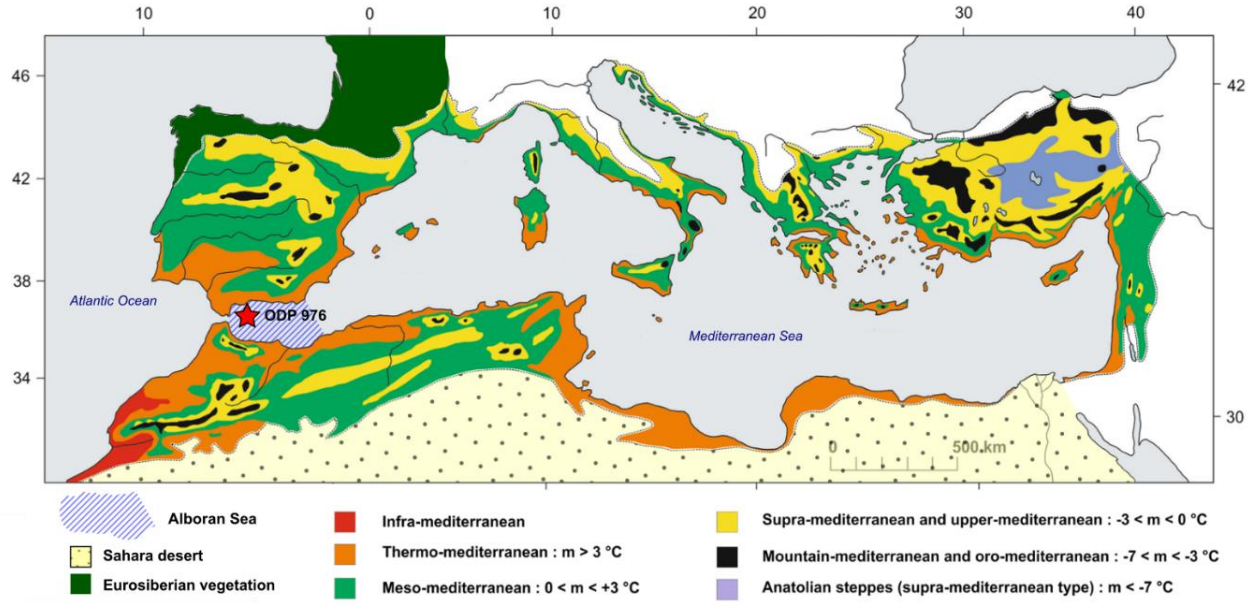


Fig. 1.1. Carte représentant la répartition des aires d'étagement de végétation méditerranéenne, ainsi que la zone d'étude (mer d'Alboran) et le lieu de forage de la carotte ODP 976. m : température moyenne du mois le plus froid. Modifié d'après Médail (2017).

- L'étage infra-méditerranéen : spécifique à la côte atlantique marocaine, il s'étend sur une frange altitudinale comprise entre le niveau de la mer et 700-800 m, et est caractérisé par des climats peu contrastés de type semi-arides, arides et saharien côtiers (Benabid, 1982). Les formations végétales qui lui correspondent incluent principalement des espèces d'arbustes méditerranéens, d'herbacées, et des taxons endémiques de la région comme l'Arganier (*Argania*).

- L'étage thermo-méditerranéen : il correspond à l'étage le plus bas en altitude (jusqu'à 500-700m au-dessus du niveau de la mer), le long du pourtour du littoral méditerranéen, et présente un contraste saisonnier réduit. Les précipitations annuelles y sont généralement très basses, mais avec de forts gradients possibles entre les zones littorales plus humides et les zones plus isolées sèches à semi-arides. Les températures y sont très élevées en été et douces en hivers. La végétation résultante de ces conditions est principalement constituée de ligneux bas (formation végétale de type *Mattoral*, terme incluant la Garrigue). Les arbres et arbustes sclérophylles (résistants à la sécheresse) y sont dominants, tels que l'Olivier (*Olea*), le Pistachier lentisque (*Pistacia*), le Myrte (*Myrtus*), le Genévrier (*Juniperus*), le Romarin (*Rosmarinus*), ou le Ciste (*Cistus*). Les herbacées résistantes à la sécheresse y sont également abondantes, incluant principalement les genres *Artemisia*, *Ephedra*, et les familles Poaceae et Amaranthaceae.

- L'étage méso-méditerranéen : il constitue l'étage le plus étendu (jusqu'à 500 à 800 m d'altitude au-dessus du niveau de la mer), avec une saisonnalité plus importante que l'étage thermo-méditerranéen : les précipitations annuelles peuvent atteindre 1500 mm dans les zones les plus humides, et les températures d'hivers peuvent y descendre jusqu'à 0°C. La végétation dominante est celle de la forêt sclérophylle sempervirente, dont les représentants principaux sont le Chêne vert (*Quercus ilex/coccifera*), le Pin méditerranéen (*Pinus halepensis*/*pinea*) mais inclut dans les parties supérieures des forêts mixtes décidues mésophiles et sempervirentes avec du Chêne décidu (*Quercus pubescens* et autres espèces décidues).

- L'étage supra-méditerranéen : par-dessus l'étage méso-méditerranéen, il se situe entre 500 et 1200 m d'altitude environ et se caractérise par des précipitations plus abondantes (entre 800 et 1500 mm/ans) et des températures plus fraiches, voire négatives en hiver. Il s'agit de l'étage de la forêt tempérée décidue, dont le représentant majoritaire est le *Quercus pubescens*, accompagné d'autres grands arbres tels que l'érable (*Acer*), le Hêtre (*Fagus*) ou l'Orme (*Ulmus*).

- Les étages oro- et alti-méditerranéen : A partir de 1200 m d'altitude environ s'étend l'étage oro-méditerranéen caractérisé par un climat plus humide et froid, accompagné de neiges hivernales. Les forêts de conifères (*Pinus*, *Abies*, *Picea*) dominent cet étage jusqu'à 2000 m environ, altitude à partir de laquelle s'ouvre l'étage alti-méditerranéen dominé par les pelouses herbacées et ligneux bas. Le

Cèdre (*Cedrus atlantica*) en est un élément endémique dans les montagnes marocaines au-delà de ~1500 m : 20% de sa population actuelle dans le nord-ouest africain se trouve dans le Rif, et 80% dans les montagnes de l'Atlas, plus au sud (Cheddadi et al., 2017; Jiménez-Moreno et al., 2020; Xiao et al., 2022). Sa répartition est fortement dépendante de l'intensité des précipitations, et en particulier des paramètres climatiques hivernaux (Xiao et al., 2022).

Dû à sa physiographie, le sud-ouest méditerranéen montre donc des formations végétales représentatives de tous les étagements méditerranéens décrits précédemment (Fig. 1.1). La végétation thermo-méditerranéenne s'étend tout le long des côtes andalouses et marocaines, tout comme celle méso-méditerranéenne qui est cependant plus étendue dans le sud ibérique. Les étages supra et oro-méditerranéens sont également représentés sur les deux versants, liés à la Cordillère bétique et celle du Rif marocain. Les deux chaines montagneuses se font face de part et d'autre de la Mer d'Alboran et représentent la partie plus occidentale du système Alpin périméditerranéen (Fig. 1.2). Leur formation est le résultat de la collision entre plaques Eurasienne et Africaine, avec une tectonique active depuis le Crétacé supérieur. La Sierra Nevada culmine à 3479 m d'altitude (Monte Mulhacen) et représente une barrière biogéographique importante déterminant des domaines climatiques bien précis dans la région. Au sud de celle-ci, sur la côte andalouse, la végétation thermo-méditerranéenne domine, avec un gradient longitudinal fort des précipitations : tandis qu'un régime semi-désertique domine à l'est (Almería), le climat est plus humide à subtropical à l'ouest (Gibraltar) (voir diagrammes ombrothermiques sur la Fig. 1.2). Les sommets montagneux du Rif sont moins hauts que ceux de la Sierra Nevada, et culminent à 2456 m au Djebel Tidirhine. En revanche, les montagnes de l'Atlas marocain, plus au sud, culminent au-delà de 4000 m. Le nord-ouest marocain est caractérisé par un climat méditerranéen plus humide et des précipitations plus intenses (Till & Guiot, 1990), proches des conditions de la pointe de Gibraltar (Fig. 1.2).

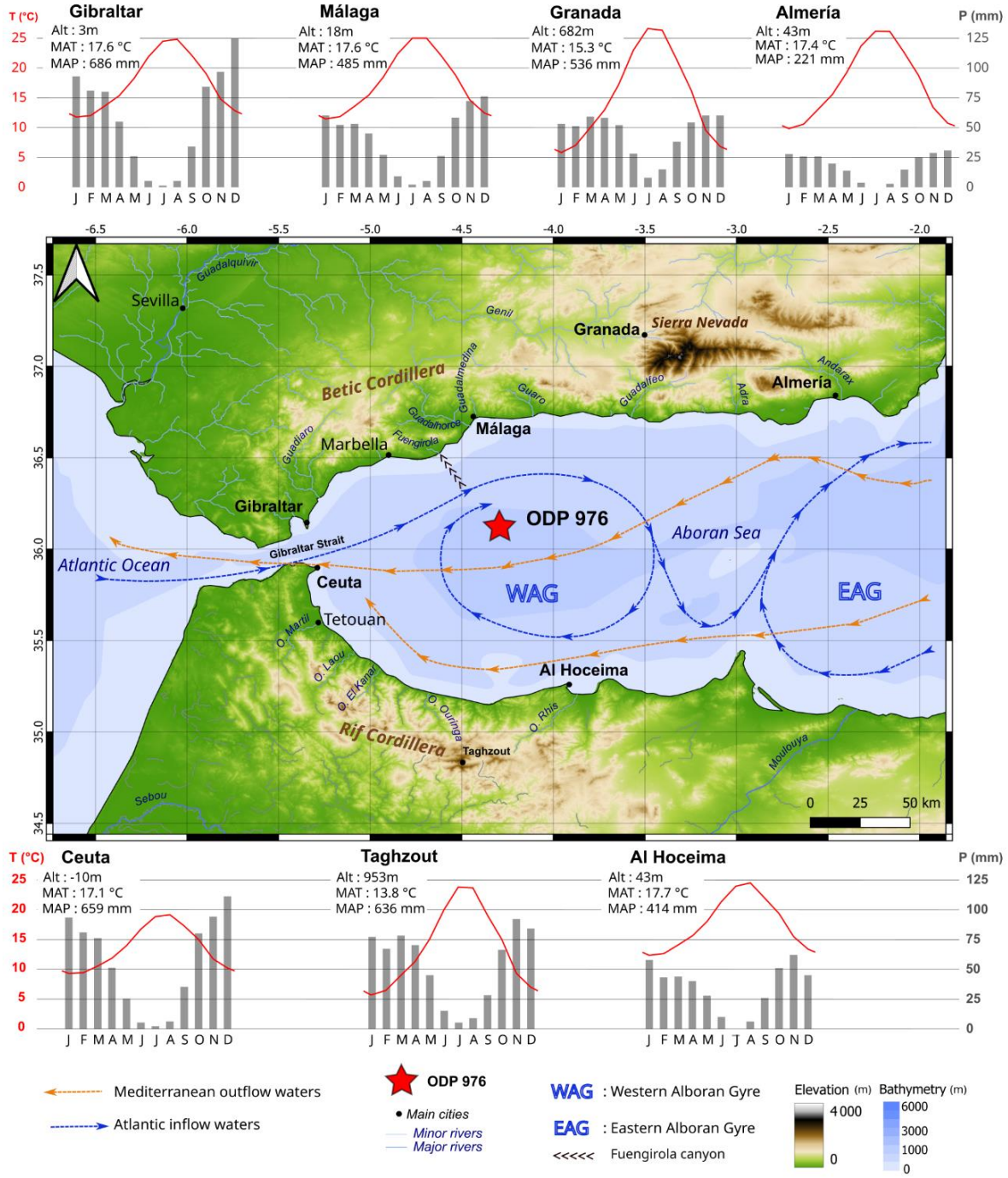


Fig. 1.2. Carte de la région de la Mer d'Alboran représentant les principales caractéristiques géographiques et physiques, ainsi que les principaux courants marins. Les diagrammes ombrométriques (précipitations et températures moyennes par mois) de sept villes du pourtour méditerranéen sont montrés (source : https://fr.climate-data.org/). MAT : température moyenne annuelle. MAP : précipitations annuelles.

En résumé, des climats et formations végétales très similaires se retrouvent sur les deux versants de la Mer d'Alboran : des zones semi-arides où dominent le matorral méditerranéen, les ligneux sclérophylles et les herbacées, pareillement représentées des deux côtés ; des zones plus humides de forêts méditerranéennes et forêts mixtes tempérées, plus étendues sur le versant

ibérique que sur le versant marocain ; et des zones plus en altitude où se succèdent des étagements de forêts mixtes, de conifères, et d'herbacées. Il est important de mentionner que sur la bordure nord de la péninsule Ibérique s'étend une zone biogéographique différente, de type eurosibérien, le long du massif Pyrénéen et jusqu'au nord du Portugal en traversant le Pays basque, la Cantabrie, les Asturies et la Galice. Sous l'influence du climat atlantique et particulièrement de l'humidité océanique, les précipitations y sont abondantes (1000-1800 mm /an). La végétation y est dominée par la forêt décidue tempérée composée en grande majorité du Chêne décidu (*Quercus pubescens* / *robur*), et d'autres caducifoliées comme le Frêne (*Fraxinus*), l'Erable (*Acer*), l'Orme (*Ulmus*) et l'Aulne (*Alnus*). Le long du littoral proche de la côte et sur les sols siliceux se développe une végétation particulière où dominent les landes à bruyères (*Erica* et *Calluna*).

Avec ces caractéristiques, le pourtour de la mer d'Alboran représente un point chaud de biodiversité encore aujourd'hui, avec un taux d'endémisme supérieur à 20% (Médail et al., 2012; Quézel, 1995). Ce réservoir de biodiversité résulte à la fois de la position latitudinale de la pointe andalouse ayant constitué un refuge climatique pour les espèces végétales dans le passé (Carrión & Leroy, 2010), et des reliefs importants sur les deux versants qui abritent un fort endémisme montagnard (Manzano et al., 2017; Médail & Diadema, 2009; Verlaque et al., 1997). Le littoral de la mer d'Alboran a ainsi représenté, ainsi que le reste des aires littorales méditerranéennes de la péninsule Ibérique, un réservoir important de biodiversité tout au long du Quaternaire (Carrión et al., 2003, 2008; Carrión & Leroy, 2010; González-Sampériz et al., 2010; Magri et al., 2017)

1.1.2 Processus atmosphériques majeurs

La direction et l'intensité des vents, ainsi que des précipitations dans la région dépend en grande partie d'un phénomène atmosphérique atlantique bien connu et appelé l'oscillation Nord-Atlantique (NAO). Ce phénomène correspond aux variations du rapport entre les pressions atmosphériques au niveau de l'Islande (dépression / masses d'air à basse pression) et au niveau des Açores (anticyclone / masses d'air à haute pression), appelé indice NAO (https://www.ncei.noaa.gov/access/monitoring/nao/). L'évolution de cet indice définit deux états qui alternent dans le temps , sur une échelle annuelle à pluriannuelle (Hurrell, 1995). En phase positive, les masses d'air à haute pression se déplacent vers les hautes latitudes, provoquant la remontée de la Zone de Convergence Intertropicale (ITCZ) et des vents d'ouest (*westerlies*), donc des conditions plus humides dans le Nord de l'Europe, et des conditions plus sèches dans le sud de l'Europe et particulièrement en Méditerranée (Trigo et al., 2002, 2004). L'impact de la configuration NAO est donc opposé en Europe du Nord et en Europe du Sud (Fig. 1.3). En phase négative, l'inverse se produit : les gradients de pression entre les hautes et basses latitudes atlantiques diminuent, l'ITCZ redescend, et

les vents d'ouest sont déplacés vers les plus basses latitudes amenant des précipitations plus intenses en Méditerranée, particulièrement sur la péninsule Ibérique.

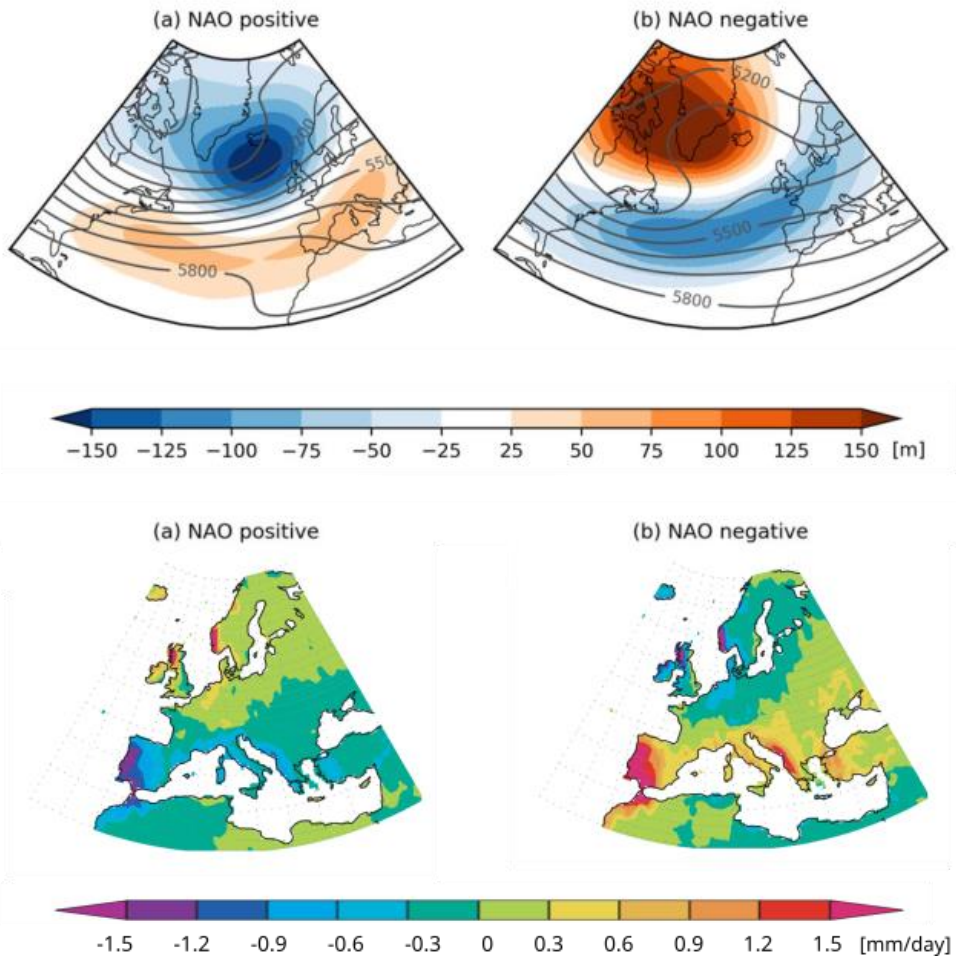


Fig. 1.3. Comparaison des deux configurations de l'Oscillation Nord Atlantique (NAO) et impact sur les anomalies de précipitations en Europe occidentale. Haut : régimes de circulation atmosphérique en phase NAO positive (a) et NAO négative (b), modifié d'après Wiel et al. (2019). Les lignes représentent les isohypses du niveau de pression standard 500 hPa, et les couleurs indiquent l'anomalie d'altitude de cette même pression standard 500 hPa (rouge : anomalie de haute pression, bleu : anomalie de basse pression). Bas : anomalies de précipitations (mm/jour) pour les mois d'hivers pour une configuration NAO positive (a) et négative (b), modifié d'après Trigo et al. (2004).

Les précipitations d'hivers sont les plus affectées par ce phénomène, impactant également la dynamique de végétation (Gouveia et al., 2008), ainsi que le transport éolien de particules du nord de l'Afrique vers l'Europe de l'ouest (Moulin et al., 1997). Cette modulation du régime de circulation atmosphérique et de précipitations par la configuration NAO a également joué un rôle important dans les variations climatiques observées en Méditerranée au cours du Pléistocène (e.g. Bout-Roumazeilles et al., 2007; Cacho et al., 2000; Moreno et al., 2002; Sánchez Goñi et al., 2002). Elle continue d'influencer le débit des cours d'eau et donc la vitesse de sédimentation, particulièrement en

Méditerranée sud-occidentale où les taux de sédimentations diminuent drastiquement lorsque l'index NAO tend vers des valeurs positives (Trigo et al., 2004).

1.1.3 Contexte océanographique et hydrographique

La mer d'Alboran constitue le bassin secondaire le plus occidental de la Méditerranée : elle s'ouvre à l'ouest sur le détroit de Gibraltar, s'étend à l'est sur ~400 km, pour une largeur entre ses deux versants nord et sud d'environ 200 km, et une profondeur maximale inférieure à 2000 m.

La circulation des courants marins est la résultante de l'échange des eaux de la Méditerranée et de l'océan Atlantique à travers le détroit de Gibraltar, lui-même dépendant de l'excès d'évaporation dans la mer Méditerranée par rapport aux précipitations. Ce déficit hydrologique est à l'origine de la circulation thermohaline en Méditerranée, qui permet la sortie de masses d'eaux profondes et très salées méditerranéennes, et l'entrée de masses d'eau peu salées atlantique par les courants de surface (Pérez-Asensio et al., 2020; Vargas-Yáñez et al., 2002). A cause des forts contrastes de salinité, trois niveaux de masses d'eau fortement stratifiés peuvent être décrits (Fig. 1.3). A la surface, les eaux atlantiques, appelées *Atlantic Inflow Water* (AIW) ou *Atlantic Jet* voient graduellement leur niveau de salinité et leur températures augmenter vers l'est, constituant alors la *Modified Atlantic Water* (MAW), qui forme deux gyres antihoraires à la surface de la mer d'Alboran (Fig. 1.2) : la *Western Alboran Gyre* (WAG) et la *Eastern Alboran Gyre* (EAG) (Renault et al., 2012). Les masses d'eau intermédiaires plus chaudes et salées constituent la *Levantine Intermediate Water* (LIW), formées par mouvements de convection en Méditerranée orientale ; enfin les eaux les plus profondes correspondent à la *Western Mediterranean Deep Water* (WMDW) et se forment dans le Golfe du Lion (Fig. 1.3).

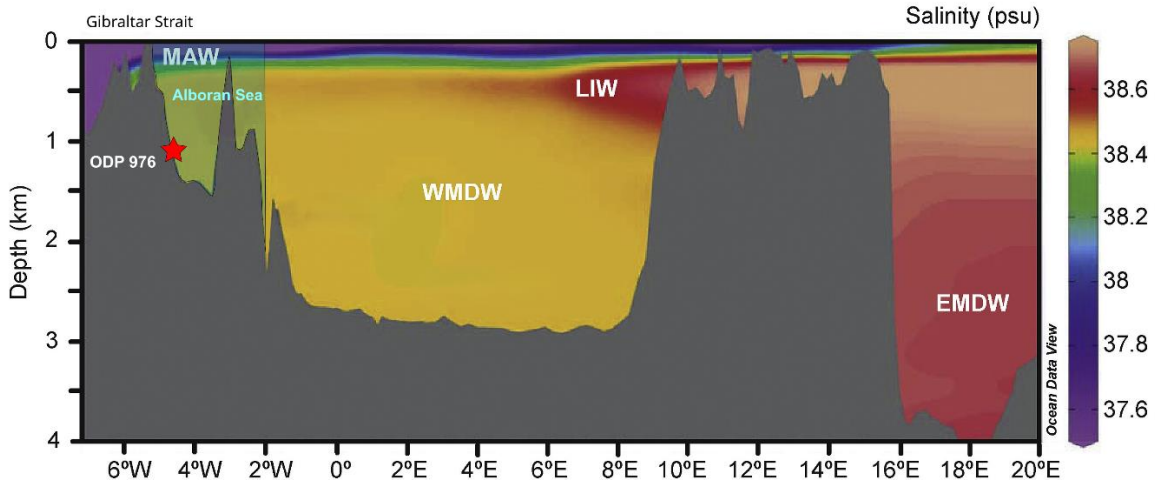


Fig. 1.3. Coupe verticale du bassin Méditerranéen occidental montrant le gradient de salinité et la stratification des masses d'eau (modifié d'après Pérez-Asensio et al. (2020). MAW: *Modified Atlantic Water*; LIW: *Levantine Intermediate Water*; WMDW: *Western Mediterranean Deep Water*; EMDW: *Eastern Mediterranean Deep Water*.

1.1.4 Processus de la sédimentation et implication pour l'origine du pollen

Les sédiments déposés en Mer d'Alboran proviennent en grande partie des processus d'érosion intenses des reliefs montagneux de la Cordillère Bétique en premier, et du Rif Marocain en moindre proportion (Fabres et al., 2002). L'étude de la composition des sédiments détritiques dans la carotte a montré une origine préférentiellement du sud de la péninsule Ibérique et particulièrement de la côte de Gibraltar (Marsaglia et al., 1999). Les courants de surface Atlantiques étant les vecteurs principaux des sédiments déposés, une origine Atlantique significative doit aussi être considérée pour les particules sédimentaires transportées en Mer d'Alboran (Auffret et al., 1974).

Vingt-six systèmes fluviaux en Andalousie débouchent dans la Mer d'Alboran (Liquete et al., 2005). Ces cours d'eau présentent généralement un drainage moyen à faible, mais la sédimentation est alimentée de manière périodique par des évènements climatiques extrêmes. La marge sud-ibérique de la mer d'Alboran présente une physiographie complexe formée par des structures d'effondrement et des failles : plusieurs canyons sous-marins ont été identifiés comme axes majeurs de transport de sédiments vers le site ODP 976, le plus important et le plus long étant le canyon de Fuengirola (Alonso, Ercilla, Martinez-Ruiz, et al., 1999). Du côté marocain, la source détritique principale provient des bassins versants du Rif septentrional, principalement constitués d'*Oueds* et de torrents de petites dimensions et au débit très réduit, voir périodiquement asséchés (Reddad et al., 2016; Zaghloul et al., 2009). Si le fleuve Moulouya représente la seule exception, il est plus éloigné du point de carottage du site ODP 976 et débouche dans la partie la plus à l'Est de la Mer d'Alboran (Fig. 1.2).

Enfin, le transport aérien de particules dans la région ne doit pas être négligé : le pollen est transporté toute l'année par des vents locaux en provenance de la péninsule Ibérique, mais aussi en partie de l'Afrique du Nord. Les poussières sont régulièrement transportées par les masses d'air provenant du Sahara en Méditerranée occidentale, avec des pics d'apports pendant les périodes estivales et à l'automne (Guerzoni et al., 1997; Sánchez-Laulhé et al., 2021). Deux voies principales de transport éolien des particules du Nord de l'Afrique vers la Méditerranée occidentale existent: par l'Atlantique à travers les vents d'ouest (apport estival principalement), et par le nord directement vers la Méditerranée centrale et occidentale (apport automnal principalement) (Israelevich et al., 2012). Si l'apport sédimentaire fluvial et marin est généralement majoritaire sur le transport éolien en mer d'Alboran, celui-ci peut cependant atteindre des pourcentages importants du flux sédimentaire (40-50%) lors de pics d'intensité des vents du sud (Guerzoni et al., 1997). Ces pics d'apports éoliens sont modulés par l'oscillation Nord-Atlantique, et ce phénomène est aussi bien mis en évidence pour le Pléistocène: pendant les évènements climatiques froids (stadiaires), la remontée de l'ITCZ et donc

l'intensification des vents du Sahara a provoqué des apports éolien plus important en Mer d'Alboran (Bout-Roumazeilles et al., 2007; Moreno et al., 2002).

Ainsi, il est généralement admis que la source principale des grains de pollen déposés en mer d'Alboran est la péninsule Ibérique (dans sa moitié méridionale en majorité), et en plus faible proportion, mais très variable, par l'Afrique du Nord.

1.2 Cadre paléoclimatique

D'un point de vue stratigraphique, les derniers 200 000 ans couvrent la fin du Pléistocène moyen (dont la limite inférieure, le *Global Boundary Stratotype Section and Point* « GSSP », est positionné à 774.1 ka BP), suivi du Pléistocène supérieur (pas de GSSP actuellement, limite inférieur approximative à 129 ka BP) et de l'Holocène (GSSP positionné à 11.7 ka BP) (e.g. Head, 2023). La période est caractérisée par des changements climatiques globaux à différentes échelles de temps, incluant des dynamiques liés aux paramètres orbitaux terrestres ainsi que des dynamiques suborbitales.

1.2.1 Dynamiques climatiques orbitales

La théorie de Milankovitch prédit la succession de cycles climatiques à échelle globale selon l'évolution de trois paramètres orbitaux de la Terre, qui contrôlent la quantité d'énergie reçue du Soleil à la surface terrestre (insolation) (Berger, 1980; Milanković, 1941; Ruddiman, 2008):

- l'Excentricité de l'orbite terrestre, qui oscille avec deux périodicités principales d'environ 400 000 ans et 100 000 ans

- L'Obliquité de l'axe de rotation terrestre, qui varie avec une périodicité d'environ 41 000 ans

- La Précession des équinoxes, dont la périodicité varie entre 19 000 et 24 000 ans

La combinaison des variations de ces trois paramètres au cours du temps détermine l'alternance de périodes glaciaires et interglaciaires. Les périodes glaciaires sont marquées par une extension majeure de la couverture glaciaire aux pôles impliquant un niveau marin plus bas, et des températures océaniques plus basses. Les périodes interglaciaires voient, au contraire, la diminution de l'extension des calottes glaciaires, l'augmentation du niveau marin et des températures océaniques globales.

Les oscillations de température des eaux à l'échelle globale sont enregistrées par le rapport isotopique des tests de foraminifères, le $\delta^{18}O$ (Emiliani, 1955). Les variations globales du rapport isotopique marin permettent la définition de stades isotopiques marins (*Marine Isotopic Stages*, MIS),

dont les numéros pairs correspondent aux périodes froides (stades et sous-stades glaciaires), et les numéros impairs correspondent aux périodes chaudes (stades et sous-stades interglaciaires). Ainsi, une stratigraphie isotopique marine très précise a été établie pour la succession des périodes glaciaires et interglaciaires à échelle globale pour tout le Quaternaire (Lisiecki & Raymo, 2005; Railsback et al., 2015).

La Transition du Pléistocène moyen ancien (*The Early Middle Pleistocene Transition*, ~1.4-0.4 ka) a marqué la mise en place des cyclicités climatiques de 100 000 ans contrôlées principalement par l'excentricité, et caractérisées par de longues périodes glaciaires et des réchauffements abrupts suivant les terminaisons glaciaires (Head, 2023; Maslin & Brierley, 2015; Ruddiman et al., 1986).

Les derniers 200 000 ans couvrent ainsi une partie de l'avant-dernier cycle climatique correspondant à la fin de l'avant-dernier interglaciaire (le MIS 7), l'avant-dernière période glaciaire dans son entièreté (le MIS 6), ainsi que le dernier cycle climatique de 100 000 ans dans son entièreté (MIS 5-2), et le début de l'interglaciaire (MIS 1) du cycle climatique actuel (Sánchez Goñi, 2022a, 2022b). Le dernier cycle climatique (MIS 5-2) présente une structure complexe (Fig. 1.4), avec plusieurs variations de températures globales au cours du MIS 5 (constituant la dernière période interglaciaire, divisée en cinq sous-stades du 5e au 5a), ainsi que durant les MIS 4-3-2, constituant la dernière période glaciaire.

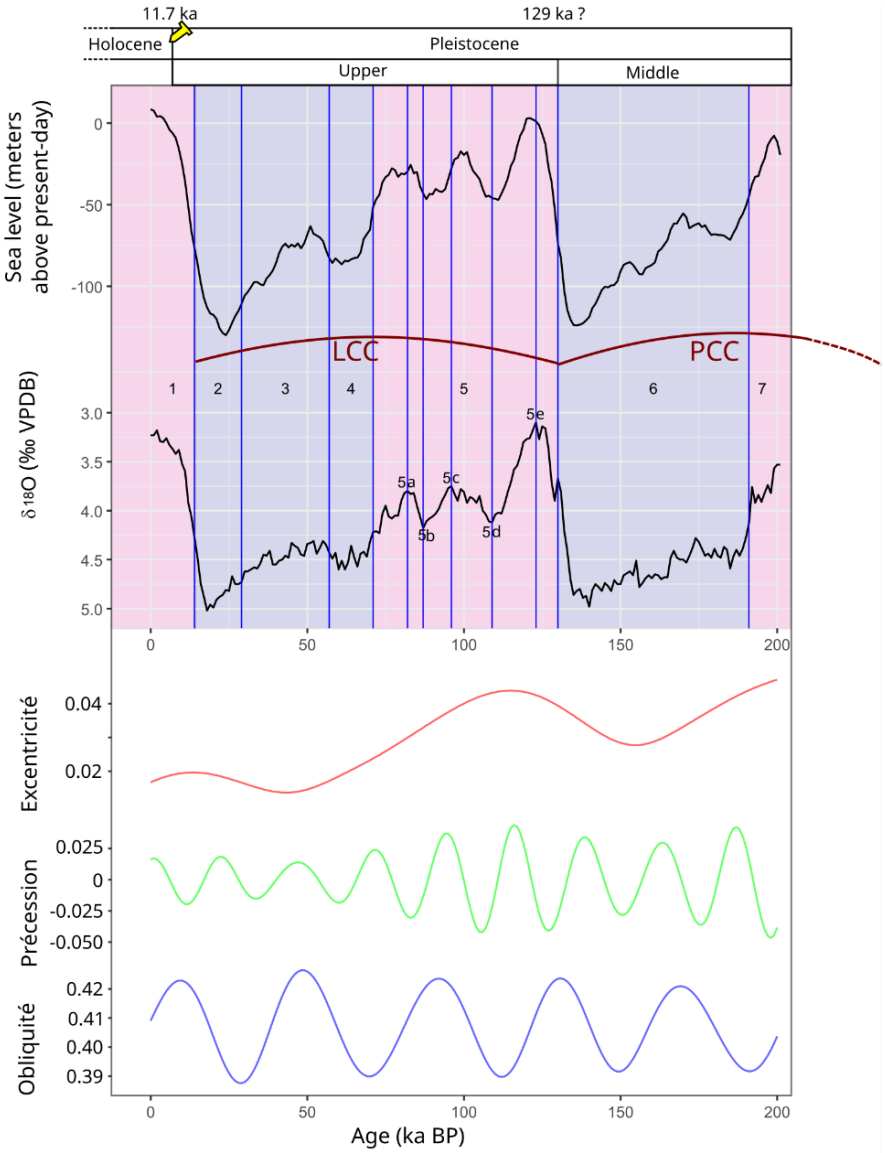


Fig. 1.4. Structure climato-stratigraphique globale et évolution des paramètres orbitaux (Berger & Loutre, 1991) **au cours des derniers 200 000 ans.** L'évolution du niveau marin et le *stack* isotopique global LR04, avec les nombres et les délimitations (lignes verticales bleues) des stades et sous-stades isotopiques (MIS) sont définis par Lisiecki & Raymo (2005) et Railsback et al. (2015). Les subdivisions stratigraphiques sont positionnées en haut, avec les dates des délimitations associées au GSSP (Holocène) ou en cours de définition (Pléistocène supérieur) (e.g. Head, 2023). Les périodes glaciaires sont indiquées en bleu, et les périodes interglaciaires en rose. LCC : *Last Climatic Cycle*. PCC : *Penultimate Climatic Cycle*.

1.2.2 Dynamiques climatiques à échelle millénaire

En parallèle des évolutions climatiques orbitales, une dynamique à plus haute fréquence, dite suborbitale ou millénaire, a affecté le système climatique global tout au long du Pléistocène, que ce soit pendant les périodes glaciaires et interglaciaires. Ces oscillations rapides sont particulièrement bien documentées pendant la dernière période glaciaire, avec de nombreuses archives à haute

résolution. Elles ont été mises en évidence pour la première fois dans les carottes sédimentaires de l'Atlantique Nord, ainsi que dans les carottes de glace au Groënland.

Dans les carottes sédimentaires de l'océan Atlantique Nord, des niveaux de dépôt de sédiments transportés par les icebergs (*Ice-Rafted Debris*, IRDs) provenant majoritairement de la calotte laurentienne, mais aussi en partie des calottes européennes, ont été identifiés dans plusieurs sites situés entre 40 et 65° de latitude, zone appelée la « ceinture de Ruddiman » (Ruddiman, 1977). Ces dépôts d'IRDs particulièrement abondants pendant la dernière période glaciaire indiquent des incursions périodiques de masses d'icebergs dans les eaux subpolaires, reflétant une instabilité de la calotte polaire Arctique dans le passé (Ruddiman, 1977). Pendant la dernière période interglaciaire (MIS 5), les dépôts d'IRD apparaissent moins abondants et plus localisés aux latitudes élevées, indiquant une corrélation entre l'extension de la calotte glaciaire et l'intensité de ces évènements en Atlantique Nord (Ruddiman, 1977). Par la suite, des niveaux bien précis d'IRDs correspondant à des débâcles intensives d'icebergs ont été identifiés comme « évènements de Heinrich » (HE) (Heinrich, 1988), et numérotés de 1 à 6, du plus récent au plus ancien (Bond et al., 1992; Broecker et al., 1992). Des évènements additionnels (HE7 à 11) ont été identifiés dans les nombreux carottages réalisés au large de Terre-Neuve. Contemporains de l'interglaciaire MIS 5, ils sont de moindre intensité par comparaison aux HE1-6, à l'exception du H11 qui se distingue par son amplitude au moment de la transition MIS 6-5 (Rasmussen et al., 2003). Ainsi, un HE est défini par la présence d'un niveau de dépôt important d'IRD en Atlantique Nord. Associés à l'évidence sédimentologique de ces débâcles d'iceberg, d'autres indicateurs comme les isotopes, les assemblages de foraminifères ou le pollen montrent des conditions de froid et d'aridité extrêmes dans l'Atlantique Nord et en Europe occidentale au moment de ces HE, conséquence principale de l'arrêt de la circulation thermohaline dans l'océan Atlantique (*AMOC : Atlantic Meridional Overturning Circulation*) (e.g. Bond et al., 1992; Cacho et al., 1999; Naughton et al., 2009; Sánchez Goñi et al., 2002). Ces intervalles climatiques peu favorables sont appelés « stadiaires de Heinrich » (HS) (Barker et al., 2009; Sánchez Goñi & Harrison, 2010). Dans le Nord de l'Atlantique, la période froide observée dans les proxys marins correspond généralement à l'intervalle de dépôt des IRDs ; les concepts de HE et HS sont alors pratiquement confondus. Cependant, plus au sud, l'intervalle froid et aride mis en évidence par les proxys marins et continentaux en Europe commence généralement avant, et peut s'étendre après le pic de dépôt des IRDs en Atlantique : le HE est alors inclus dans le HS et en représente la phase culminante (Sánchez Goñi & Harrison, 2010). Ce décalage entre HS et HE indique des mécanismes de rétroaction internes complexes : la perturbation de l'AMOC et l'établissement de conditions froides en Europe précède généralement la débâcle d'Iceberg, qui amplifie le refroidissement par la suite. Par ailleurs, les approches par modélisation couplée glace-océan ont montré que le détachement de blocs de banquise

serait liée à la formation de courants de subsurface plus chauds suite à la réduction de l'AMOC, qui favoriseraient la fonte de la banquise à sa base (Alvarez-Solas et al., 2010, 2013; Alvarez-Solas & Ramstein, 2011; Marcott et al., 2011).

En parallèle, plusieurs projets de longs carottages de glace au Groënland ont permis de documenter l'évolution des températures globales depuis le dernier interglaciaire (MIS 5) à travers le $\delta^{18}O$ de la glace : GISP (*Greenland Ice Sheet Projects* 1 et 2, Grootes et al., 1993), GRIP/NGRIP (*North Greenland Ice Core Project members*, 2004), et NEEM (*NEEM community members*, 2013). Ces carottes arctiques, permettant une très haute résolution d'étude, ont démontré la succession d'épisodes climatiques plus chauds (interstadiaires du Groënland, GI) et plus froids (stadiaires du Groënland, GS) à échelle de temps sub-millénaire (Dansgaard et al., 1993; Johnsen et al., 1992). La succession rapide de ces phases suit une cyclicité nommée d'après ses découvreurs : un cycle de Dansgaard-Oeschger (D-O) inclut ainsi un GI caractérisé par un réchauffement très abrupt, et un GS caractérisé généralement par un refroidissement très progressif. Une chronologie très précise des GIs and GSs, et donc des cycles D-O, a pu être établie grâce au taux de sédimentation remarquablement élevé des dépôts de glace au Groënland (Andersen et al., 2006; Rasmussen et al., 2014; Seierstad et al., 2014; Svensson et al., 2008) : la *Greenland Ice Core Chronology* 2005 (GICC05) pour les derniers 60 b2k (années avant l'an 2000), et la GICC05modelext au-delà de 60 b2k et jusqu'à environ 120 b2k (Rasmussen et al. 2014). Une dynamique climatique rapide a également été mise en évidence dans les carottes de glace en Antarctique (Bouchet et al., 2023; Jouzel et al., 2007; Masson-Delmotte et al., 2010). La glace antarctique permet une résolution moins importante que celles du Groënland, mais présente un enregistrement beaucoup plus long, qui s'étend à l'heure actuelle jusqu'à 800 000 ans (projet EPICA-European Project for Ice Coring in Antarctica), et pourrait bientôt s'étendre jusqu'à 1.2 million d'années (projet Beyond EPICA Oldest Ice, https://www.beyondepica.eu/en/). Les rythmes de changements de température enregistrés au Groënland et en Antarctique sont généralement très bien corrélés, mais des différences notoires ont pu être observées (Barbante et al., 2006). En particulier, une relation d'antiphase entre les changements de température enregistrés dans les carottes de glace en Arctique et ceux enregistrés dans les carottes de glace en Antarctique a mis en évidence un phénomène de bascule bipolaire (*bipolar seesaw*) qui permet la redistribution de la chaleur planétaire à travers l'AMOC (Barker et al., 2009; Davtian & Bard, 2023; Stocker, 1998). Ainsi, un réchauffement (interstadiaire) dans les glaces antarctiques est généralement associé à un refroidissement (stadiaire) dans les glaces arctiques, et inversement. De même, contrairement aux phénomènes observés dans les cycles D-O au Groënland, la dynamique des stadiaires et interstadiaires en Antarctique est différente, avec des réchauffements plus lents et moins intenses comparés aux GIs (Barbante et al., 2006).

A partir de ces observations parallèles dans les carottes de glaces et dans les carottes de l'Atlantique, nait une théorie unificatrice qui corrèle les cycles de D-O et l'occurrence d'évènements de Heinrich au sein de cycles dits « de Bond » (Alley, 1998; Bond et al., 1993). Plusieurs cycles D-O se succèdent au sein d'un cycle de Bond, caractérisé par un long refroidissement progressif (i.e. des GIs de moins en moins chauds, et des GSs de plus en plus froids), culminant avec une débâcle d'icebergs, et donc un évènement de Heinrich pendant l'ultime GS du cycle (Fig. 1.5). Alors qu'un cycle D-O dure entre 1.5 et 4.5 ka, un cycle de Bond inclut plusieurs cycles D-O et dure entre 7 et 11 ka. Cette superposition de cyclicités à échelle millénaire témoigne d'une imbrication de dynamiques complexes liées principalement aux calottes polaires et à la circulation thermohaline dans l'océan Atlantique.

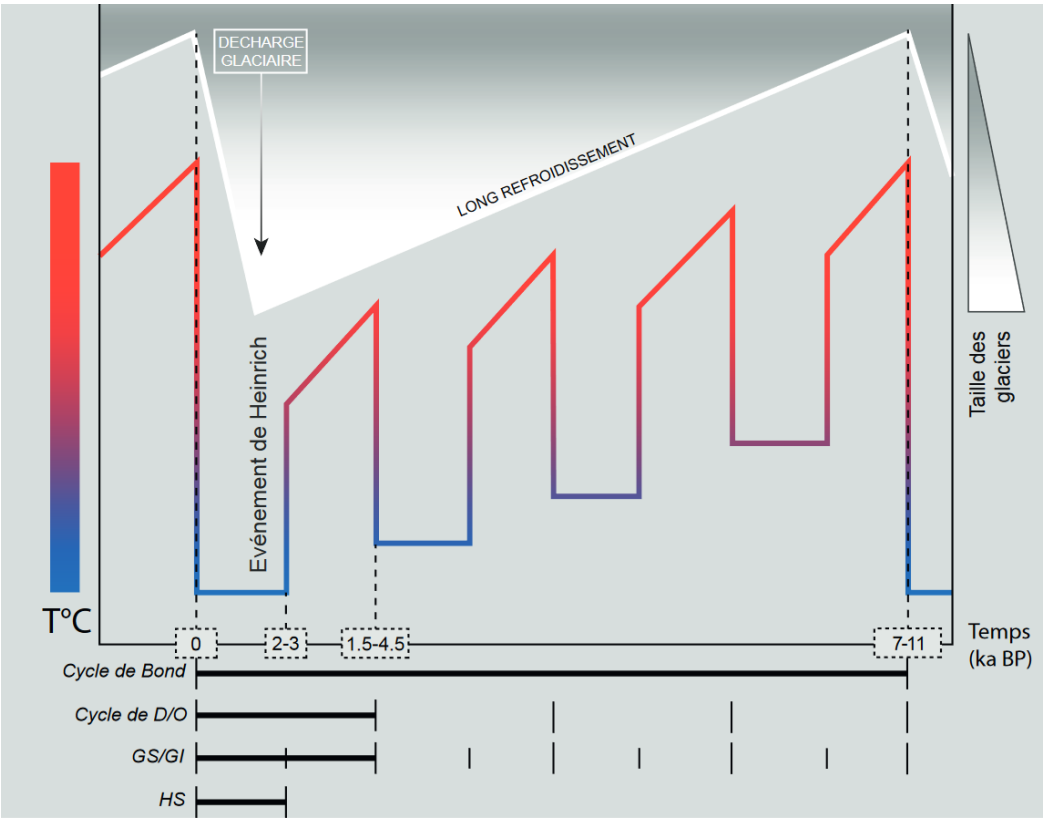


Fig. 1.5. Structure théorique des cycles D-O et d'un cycle de Bond, d'après Alley (1998), modifié par Duprat-Oualid (2019).

Les causes de cette variabilité rapide du climat, et en particulier des évènements de Heinrich, restent encore mal comprises et ont fait l'objet d'une importante littérature scientifique (voir synthèses par Henry et al., 2016; Kageyama et al., 2013; Toucanne et al., 2022) Les premiers modèles expliquant l'occurrence de tels évènements se basaient avant tout sur des hypothèses orbitales, impliquant une cyclicité d'environ 11 000 ans (la moitié d'un cycle de précession) pour une déstabilisation de la calotte laurentidienne, provoquant la débâcle d'icebergs et successivement l'arrêt de l'AMOC (Heinrich, 1988). Les études successives à haute résolution de nombreuses carottes

atlantiques, ainsi que les datations au radiocarbone (pour les derniers 40 000 ans), ont démontré que la fréquence de cette cyclicité n'était pas vérifiée, et qu'elle n'était donc pas une conséquence directe des cyclicités orbitales, donnant lieu au terme de « dynamique suborbitale ». De plus, les données à haute résolution ainsi que les simulations climatiques ont montré une désynchronisation entre l'arrêt de l'AMOC et le timing de la débâcle d'iceberg, indiquant que cette dernière pouvait être la conséquence, et non pas la cause du premier (Alvarez-Solas et al., 2010; Alvarez-Solas & Ramstein, 2011; Barker et al., 2015). La cause première de l'affaiblissement de l'AMOC reste ainsi non élucidée, et des dynamiques climatiques complexes ont été mises en évidence à l'intérieur mêmes des HS dans les archives marines et glaciaires à haute résolution, impliquant plusieurs phases successivement plus sèches et plus humides, et des processus atmosphériques globaux déterminant impliquant les basses latitudes (Guillevic et al., 2014; Toucanne et al., 2022; Wary et al., 2018; Wendt et al., 2019).

Il est maintenant accepté que les oscillations D-O et HE ont eu une signature globale, et non pas restreinte à l'Atlantique Nord. Cependant, l'un des éléments compliquant l'élaboration d'un modèle explicatif global robuste reste la synchronisation dans le temps des évènements identifiés dans les différentes régions du globe. Récemment, l'étude de nouvelles archives paléoclimatiques aux basses latitudes, notamment en zone tropicale (Brésil, Chine principalement) a apporté de nouveaux éléments de compréhension de ces phénomènes climatiques suborbitaux, en montrant un rôle important des migrations latitudinales de l'ITCZ et de l'intensité des moussons tropicales asiatiques dans les oscillations D-O et les HS (Cheng et al., 2016; Liang et al., 2022; Wang et al., 2018; Wang et al., 2008; Wang et al., 2001; Wendt et al., 2019). Les évènements froids (GSs et HSs) sont généralement associés à une migration au sud de l'ITCZ, et des épisodes de faibles moussons asiatiques (Barker et al., 2011). Une compilation globale des enregistrements de spéléothèmes datés indépendamment a récemment démontré la synchronicité des interstadiaires identifiés en Europe occidentale, en Amérique du Sud et en Asie orientale, et validé en grande partie la chronologie GICC05 établie au Groënland (Corrick et al., 2020)

Ainsi, nous disposons d'une description particulièrement précise et robuste des changements climatiques rapides au cours du dernier cycle climatique (MIS 5-1), incluant les cycles D-O au Groënland, leur contrepartie dans les rapports isotopiques des carottes marines, et les évènements de Heinrich (Fig. 1.6). Au total, 26 cycles D-O et 12 évènements de Heinrich ont été identifiés sur les derniers 120 ka BP.

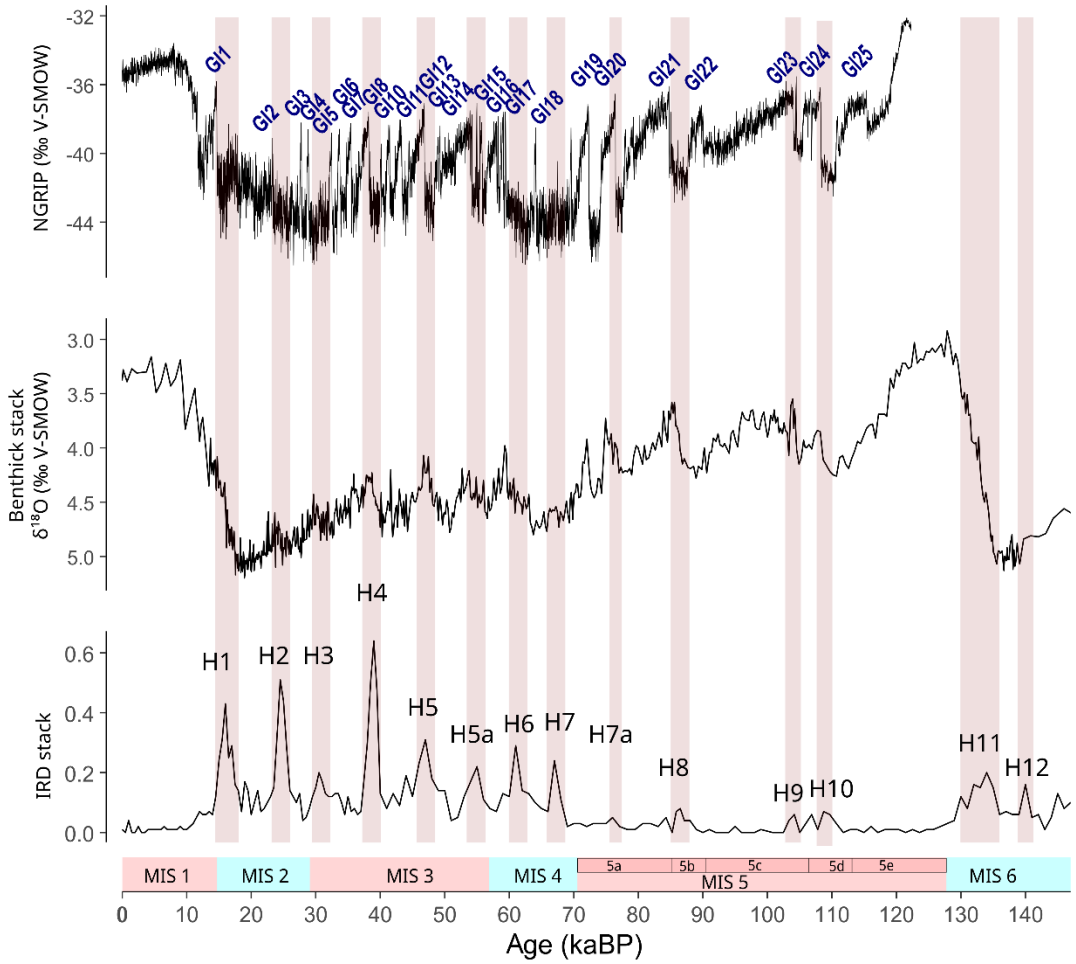


Fig. 1.6. Courbes de références pour les changements suborbitaux au cours du dernier cycle climatique, de haut en bas : le rapport isotopique des glaces du Groenland (carotte NGRIP sur l'échelle chronologique GICC05 et GICC05modelext) avec les la stratigraphie des interstadiaires (*Greenland Interstadials*, GI) numérotés selon Rasmussen et al. (2014) ; la courbe du rapport isotopique benthique de la carotte MD95-2042 (Lisiecki et al., 2022; Shackleton et al., 2000) ; le stack LS16 des *Ice-Rafted Debris* (IRD) de (Lisiecki & Stern, 2016).

Une telle climato-stratigraphie de référence dans l'Atlantique Nord n'existe pas pour l'avant-dernière période glaciaire, qui reste bien moins documentée. Notre connaissance des dynamiques climatiques rapides pendant le MIS 6 repose donc avant tout sur les carottes en Antarctique (Jouzel et al., 2007), quelques carottes marines du Nord de l'Atlantique (Margari et al., 2010, 2014; Sierro & Andersen, 2022), et des enregistrements continentaux en Eurasie tels que les spéléothèmes (Ayalon et al., 2002; Hodge et al., 2008; Nehme et al., 2018; Wainer et al., 2011, 2013; Wang et al., 2018; Wang et al., 2001), les dépôts de loess (Rousseau et al., 2020) ou les carottes continentales (Roucoux et al., 2011; Sadori et al., 2016; Sinopoli et al., 2019; Tzedakis et al., 2006).

1.2.3 Réponse de la végétation méditerranéenne aux changements climatiques des derniers 200 000 ans

La réponse de la végétation méditerranéenne aux changements du dernier cycle climatique est documentée depuis longtemps grâce aux longues séquences palynologiques continentales européennes en France, en Italie et en Espagne (e.g. Allen et al., 2000; de Beaulieu & Reille, 1992, 2007; Follieri et al., 1988; Guiot et al., 1989; Magri, 1999; Pons & Reille, 1988; Reille et al., 1992, 1998; Watts, 1996). Les séquences de la Méditerranée orientale (Grèce, Macédoine du Nord, Turquie) ont ensuite été largement étudiées et offrent aujourd'hui une très haute résolution d'étude (e.g. Milner et al., 2016; Roucoux et al., 2011; Sadori et al., 2016; Tzedakis, 1999, 2003, 2006, 2005; Wagner et al., 2019). Ces longues séquences ont permis de mettre en évidence les changements profonds de paysages végétaux au cours des derniers 130 000 ans, suivant les changements climatiques globaux et l'évolution des calottes glaciaires liés aux dynamiques orbitales. Ces dynamiques orbitales du climat ont influencé les écosystèmes végétaux en favorisant largement l'expansion de la couverture forestière pendant les interglaciaires (MIS 5, MIS 1, et dans une moindre mesure le MIS 3), et sa contraction pendant la longue période glaciaire initialement appelée glaciation Würmienne en Europe (MIS 4-2). Ainsi, les paysages glaciaires en Europe méditerranéenne, sont caractérisés par une large prédominance des herbacées (*Artemisia*, Poaceae, Amaranthaceae, Asteraceae…) ainsi que le retrait des taxons arborés tempérés (*Quercus* type décidu, *Fagus*, *Alnus*…), et des taxons méditerranéens (*Olea*, *Quercus ilex*, *Pistacia*…) dans des zones refuges restreintes spatialement.

L'augmentation de la résolution d'étude des carottes continentales, ainsi que l'étude des carottes marines au large de la péninsule Ibérique, ont permis de mettre en évidence également la réponse de la végétation méditerranéenne aux dynamiques suborbitales du climat. Les séquences marines offrent l'avantage de pouvoir observer dans un même échantillon les changements dans les océans (assemblages de foraminifères, dinoflagellés, rapports isotopiques, alkénones…) et sur les continents (assemblages pollinique), aidant ainsi à la compréhension des mécanismes impliqués dans les changements suborbitaux (e.g. Naughton et al., 2007; Sánchez Goñi, et al., 2002, 2010, 2018). Ainsi, les périodes stadiaires en Méditerranée sont associées généralement à des pics de végétation herbacées, voire steppique et semi-désertique pendant les HSs, contemporaines de conditions plus froides dans les océans. A l'inverse, les interstadiaires sont marqués par un réchauffement des eaux, et une reconquête de la végétation tempérée et méditerranéenne, qui peut-être plus ou moins importante selon les épisodes et selon les régions observées (Sánchez Goñi et al., 2008, 2009). En particulier, une réponse différente de la végétation peut être reconstruite entre l'ouest de l'Europe, la Méditerranée occidentale et la Méditerranée orientale pendant les cycles D-O du dernier cycle climatique (Fletcher et al., 2010a; Sánchez Goñi, 2022b; Sánchez Goñi et al., 2008).

Ainsi, les séquences palynologiques disponibles pour la dernière période glaciaire se sont multipliées, bien que beaucoup ne couvrent pas l'intégralité de la période mais des fenêtres spécifiques (voir synthèse de Fletcher et al., 2010a). La multiplication de l'étude de ces enregistrements palynologiques a permis de bien calibrer chronologiquement et corréler les changements de végétation à échelle suborbitale en Europe sur les derniers 70 000 ans (Sánchez Goñi et al., 2017).

La figure 1.7 montre les principales longues séquences palynologiques disponibles sur les derniers 200 000 ans en Méditerranée qui permettront une comparaison avec l'enregistrement de ODP 976 dans cette étude : les séquences les plus longues et continues ont été sélectionnées.

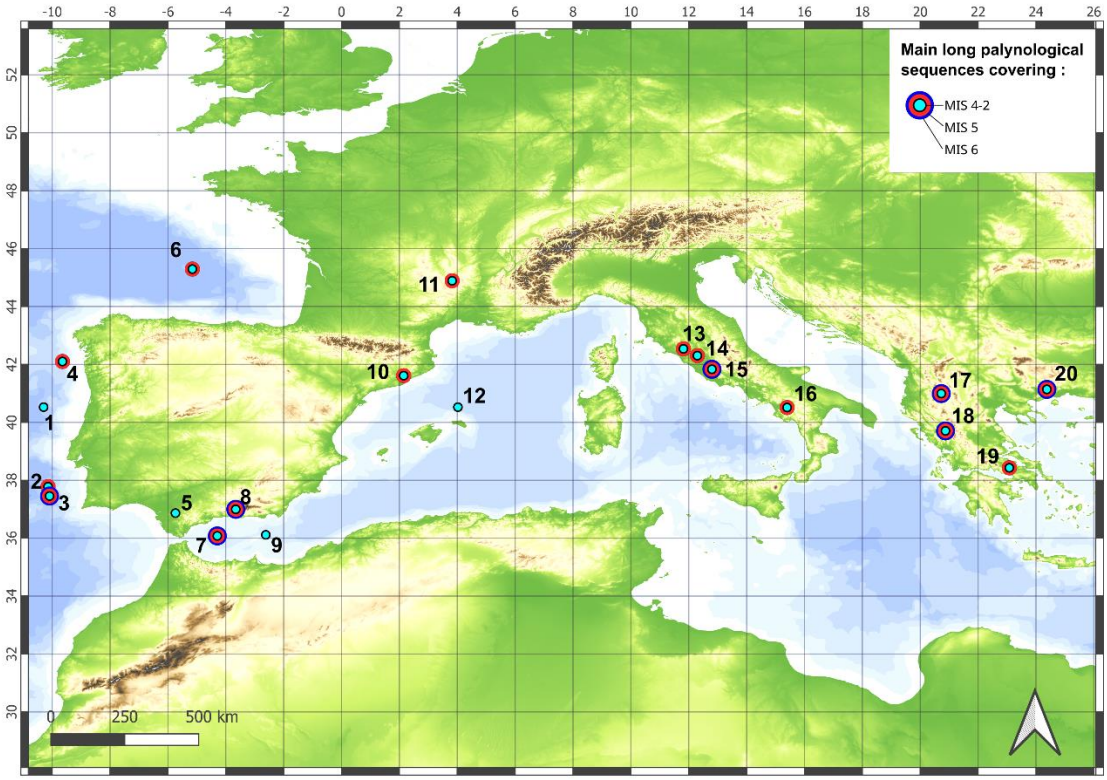


Fig. 1.7. Principales séquences palynologiques longues et continues disponibles pour les derniers 200 000 ans en Méditerranée et sur la côte Atlantique. Par longitude croissante : **1**: MD95-2039; **2**: MD95-2042; **3**: MD01-2444; **4**: MD99-2331; **5**: Los Tollos; **6**: MD04-2845; **7**: ODP 976; **8**: Padul; **9**: MD95-2043; **10**: Abric Romani; **11**: Lac du Bouchet; **12**: MD99-2343; **13**: Lagaccione; **14**: Lago di Vico; **15**: Valle di Castiglione; **16**: Lago Grande di Monticchio; **17**: Ohrid; **18**: Ioannina; **19**: Kopais; **20**: Tenaghi Philippon.

L'absence de longue séquence de référence sur le versant sud-méditerranéen est frappante, et limite grandement notre vision des processus impliquant l'Afrique du Nord dans les changements climatiques passés. Les principales séquences longues et continues sont situées dans les Balkans et en Méditerranée orientale (e.g. Fletcher et al., 2013; Litt et al., 2014; Roucoux et al., 2011; Tzedakis, 1993,

1999, 2002, 2003, 2005, 2006, 2018; Wagner et al., 2019), en Italie (Allen et al., 2000; Allen & Huntley, 2009; Follieri et al., 1988, 1989; Magri, 1999; Martín-Puertas et al., 2014; Watts, 1996), en France (e.g. de Beaulieu & Reille, 1992, 2007, 2008; Guiot et al., 1989; Reille et al., 1998), ainsi que dans les carottages marins de la côté ibérique atlantique (e.g. Donders et al., 2021; Margari et al., 2010; Roucoux et al., 2005, 2006, 2011; Sánchez Goñi et al., 1999, 2002, 2012; Shackleton et al., 2000). Il est également à souligner que de nombreux autres sites continentaux ayant fait l'objet d'analyses palynologiques existent, notamment dans la péninsule Ibérique, et ont fourni des information précieuses sur les environnements continentaux contemporains des groupes humains dans le passé (Biltekin et al., 2019; Burjachs & Julià, 1994; Carrión et al., 1995, 1995, 1999, 2018, 2019a, 2019b, 2024; Ochando et al., 2019, 2020a, 2020b, 2020c, 2022). Cependant, il s'agit généralement d'enregistrements discontinus, présentant des difficultés d'attribution chronologiques, et il reste donc difficile à l'heure actuelle d'établir des corrélations entre ces enregistrements et les longues séquences marines du pourtour ibérique. Nous avons ainsi fait le choix de restreindre les comparaisons régionales aux longues séquences méditerranéennes.

1.3 Cadre archéologique : populations humaines paléolithiques en Europe du sud-ouest depuis 200 000 ans

Les paragraphes suivants visent à établir un état de l'art de nos connaissances sur les populations humaines présentes en Eurasie occidentale entre 200 000 et 30 000 ans (*Homo neanderthalensis* et *Homo sapiens*).

1.3.1 Néandertal en Europe : présentation générale

L'évolution des populations humaines en Eurasie au Pléistocène moyen (774-130 ka BP) est une histoire complexe, où les relations de parenté entre les différentes espèces fossiles identifiées (*H. erectus*, *H. heidelbergensis*, *H. neanderthalensis,* « Dénisoviens ») sont encore non résolues (e.g. Hautavoine et al., 2024). Des restes fossiles d'*Homo neanderthalensis* (King, 1864) sont connus depuis le début du 19e siècle en Europe occidentale, et il est désormais admis que l'origine de cette espèce est le résultat d'un processus évolutif long et complexe spécifique à l'Eurasie occidentale (Hublin, 2009; Rosas et al., 2022, 2025). L'ancêtre commun le plus récent entre Sapiens et Néandertal a probablement vécu en Afrique entre 765 et 550 ka BP (Prüfer et al., 2014). Une origine dès 400 ka BP est admise pour Néandertal selon le modèle le plus accepté, et soutenu par la paléogénétique (Meyer et al., 2016). A partir d'environ 250 ka le phénotype néandertalien est bien établi en Eurasie occidentale, avec des fossiles partageant tous des caractères dérivés bien identifiés (Rosas et al., 2025). Deux principaux modèles évolutionnaires existent pour expliquer l'apparition puis la fixation des traits néandertaliens

en Europe: alors que le modèle en « deux phases » implique un différentiation claire d'*H. neanderthalensis* des populations ancestrales d'*H. heidelbergensis* (Rosas et al., 2022), le modèle « par accrétion » présente une accumulation progressive de caractères dérivés néandertaliens (Di Vincenzo & Manzi, 2023; Hublin, 2002, 2009). Ces caractères incluent notamment un volume crânien très important, un neurocrâne allongé avec la présence d'un chignon occipital, la présence d'un torus sus-orbitaire, la projection médio-faciale vers l'avant, une stature plus basse mais plus robuste qu'*H. sapiens* (Rosas et al., 2022). La succession des phases glaciaires et interglaciaires en Europe au cours du Pléistocène moyen aurait joué un rôle important dans l'apparition progressive des traits dérivés néandertaliens en favorisant des évènements appelés « goulots d'étranglement » (*bottleneck events*). Au cours de ces évènements, la contractions des populations et la survie de groupes isolés dans des zones refuges aurait favorisé l'apparition de traits dérivés qui se seraient ensuite généralisés durant les phases d'expansion (Di Vincenzo & Manzi, 2023). Les études paléogénétiques récentes soutiennent ces modèles de populations complexes au Pléistocène moyen, avec des phénomènes d'isolement et des évènements d'introgression génétique de populations d'Afrique en Europe (Petr et al., 2020; Posth et al., 2017).

Néandertal en Europe est connu à partir des nombreux restes fossiles identifiés. Les principaux sites ayant livré des restes humains attribués à Néandertal sur les derniers 200 000 ans en Europe occidentale sont représentés sur la figure 1.8. L'inventaire s'est appuyé d'une part sur le catalogue de Janković et al. (2024), ainsi que sur une revue bibliographique extensive (voir Tableau S1 dans les suppléments). Il s'agit en grande majorité de dents et fragments crâniens isolés, tandis que les sites ayant livré des restes postcrâniens et crâniens plus complets sont peu nombreux. Par ailleurs, leur datation représente un défi permanent. Pour les restes les plus jeunes (jusqu'à 50 000 ans environ), la méthode du radiocarbone permet généralement une datation très précise et fiable, lorsque le taux de collagène est suffisant, et qu'un pré-traitement spécifique a été réalisé pour éviter les contaminations (Bird et al., 1999; Douka & Higham, 2017; Higham et al., 2006, 2009; Wood et al., 2012). Les restes fossiles plus anciens peuvent être datés directement ou indirectement grâce à d'autres méthodes comme le rapport Uranium/Thorium (U/Th), la racémisation des amino-acides (AAR), les méthodes par luminescence (OSL / TL / IRSL), ou encore par *Electron Spin Resonance* (ESR), des méthodes qui ont cependant une plus grande incertitude temporelle associée. Dans la plupart des cas, lorsque des datations absolues ne sont pas disponibles, une attribution chronologique relative et peu précise peut être estimée sur des considérations d'ordre stratigraphique et paléoenvironnementales.

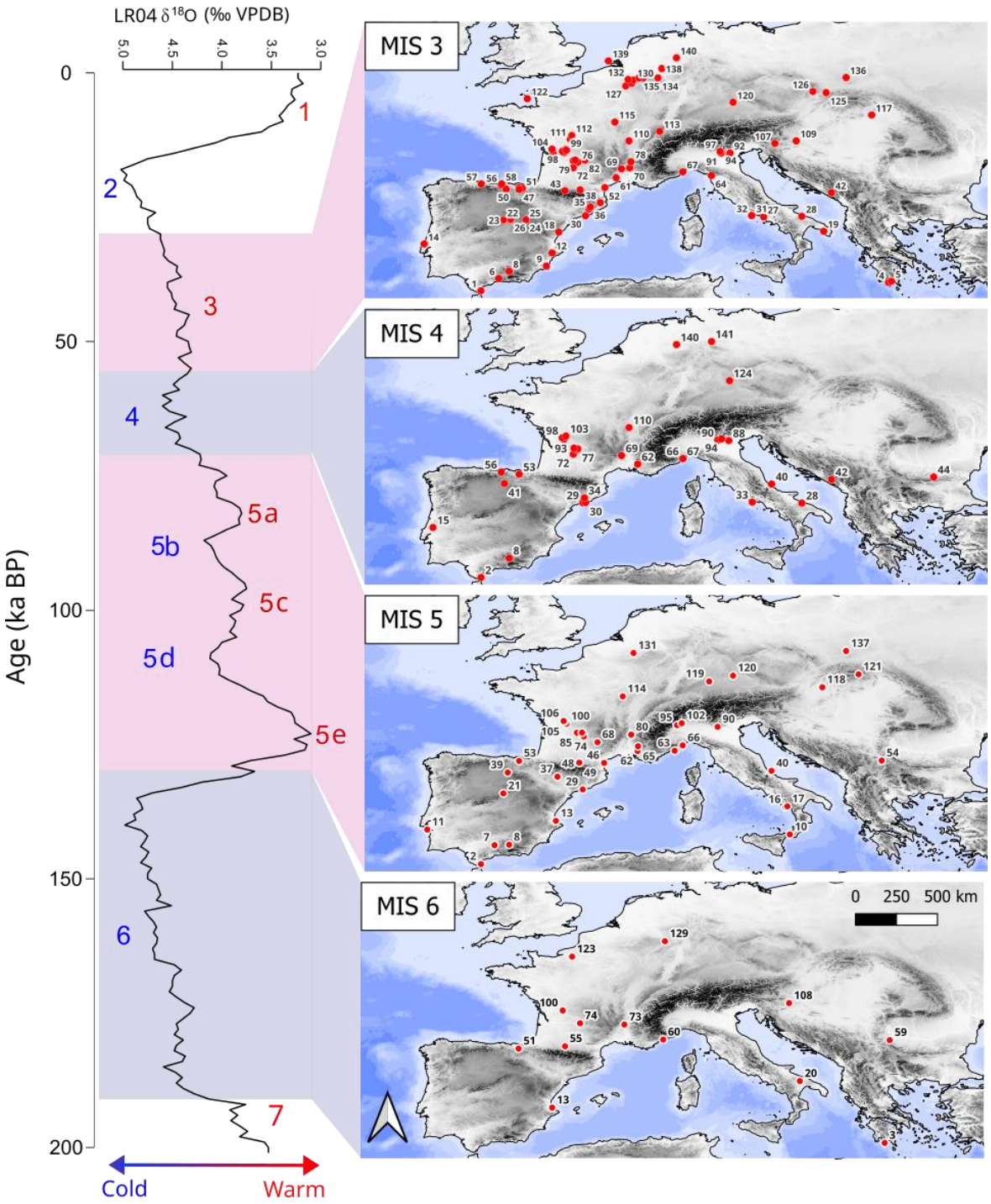


Fig. 1.8. Cartes des principaux sites ayant livré des restes humains attribués à Néandertal en Eurasie occidentale, selon leur attribution chronologique (basée sur les datations radiométriques lorsque disponibles, ou à défaut sur l'interprétation stratigraphique), du MIS 6 au MIS 3. Les sites sont numérotés par latitude croissante. **1**: Gibraltar (Devil's Tower) ; **2**: Gibraltar (Forbes' Quarry) ; **3**: Apidima ; **4**: Kalamakia ; **5**: Lakonis cave ; **6**: Zafarraya ; **7**: Cueva del Ángel ; **8**: Carihuela ; **9**: Sima de las Palomas ; **10**: Archi ; **11**: Figueira Brava ; **12**: El Salt ; **13**: Bolomor ; **14**: Gruta Nova da Columbeira ; **15**: Gruta da Oliveira ; **16**: Taddeo ; **17**: Riparo del Molare ; **18**: Tossal de la Font ; **19**: Grotta del Cavallo ; **20**: Altamura ; **21**: Pinilla del Valle (Camino) ; **22**: Pinilla del Valle (Des-cubierta) ; **23**: Pinilla del Valle (Buena Pinta) ; **24**: Los Casares ; **25**: Los Casares ; **26**: Jarama VI ; **27**: Roccia di San Sebastiano ; **28**: Bisceglie (Grotta Santa Croce) ; **29**: Cueva Foradada ; **30**: Cova del Gegant ; **31**: Grotta del Fossellone ; **32**: Grotta Breuil ; **33** : Grota Guattari ; **34**: Abric Romani ; **35**: Cova Simanya ; **36**:

Teixoneres ; **37**: Cueva de los Moros de Gabasa ; **38**: Banyoles ; **39**: Atapuerca (Galeria de las Estatuas) ; **40**: Grottoni di Calascio ; **41**: Valdegoba ; **42**: Crvena Stijena ; **43**: Le Noisetier ; **44**: Bacho Kiro ; **45**: Grotte du Portel-Ouest ; **46**: Ramandils ; **47**: Arrillor ; **48**: Soulabe-las-Maretas ; **49**: Malarnaud ; **50**: Prado Vargas ; **51**: Lezetxiki ; **52**: La Crouzade ; **53**: Axlor ; **54**: Pešturina cave ; **55**: Grotte du Coupe-Gorge ; **56**: El Castillo ; **57**: El Sidron ; **58**: Covalejos ; **59**: Kozarnika ; **60**: Grotte du Lazaret ; **61**: Grotte de l'Hortus ; **62**: Baume des Peyrards ; **63**: Madonna dell'Arma ; **64**: Buca del Tasso ; **65**: Bau de l'Aubesier ; **66**: Caverna delle Fate ; **67**: Arma delle Manie ; **68** : Rescoundudou ; **69**: Abri des Pêcheurs ; **70**: Grotte Mandrin ; **71**: Sous-les Vignes ; **72**: Las Pélénos ; **73**: Payre ; **74**: Grotte Sirogne ; **75**: Grotte Vaufrey ; **76**: Pech de l'Aze I ; **77**: Combe-Grenal ; **78**: Baume Néron ; **79**: Roc-de-Marsal ; **80**: Baume Moula-Guerçy ; **81**: La Ferrassie ; **82**: Chapelle-aux-Saints ; **83**: Le Moustier ; **84**: Kiik-Koba ; 85: Regourdou ; **86**: Jaurens ; **87**: Grotta di San Bernardino ; **88**: Grotta de Nadale ; **89**: Jonzac (Chez Pinaud) ; **90**: Ca' Verde ; **91**: Mezzena ; **92**: Riparo Broion ; **93**: La Quina ; **94**: Riparo Tagliente ; **95**: Contrada Ianni ; **96**: Grotte Castaigne ; **97**: Grotta di Fumane ; **98**: Petit-Puymoyen ; **99**: Fontechevade ; **100**: Abri Suard Bourgeois-Delaunay ; **101**: Grotte de la Tour ; **102**: Ciota Ciara ; **103**: Les Pradelles ; **104**: Saint-Césaire ; **105**: Artenac ; **106**: Rochelot ; **107**: Partizanska Jama ; **108**: Krapina ; **109**: Vindija ; **110**: Vergisson ; **111**: Les Rochers-de-Villeneuve ; **112**: Les Cottés ; **113**: Cotencher ; **114**: Genay ; **115**: Grotte du Bison ; **116**: Grotte du Renne ; **117**: Subalyuk cave ; **118** : Šaľa ; **119**: Hohlenstein-Stadel ; **120**: Sesselfelsgrotte ; **121**: Gánovce-Hrádo ; **122**: La Cotte de St Brélade ; **123**: Tourville-la-rivière ; **124**: Hunas cave ; **125**: Šipka cave ; **126**: Kůlna ; **127**: Trou de l'Abîme ; **128**:Trou Magrite ; **129**: Ochtendung ; **130**: Goyet ; **131**: Scladina ; **132**: Spy ; **133**: Bay Bonnet (Fonds-de-Forêt) ; **134**: Walou Cave ; **135**: Engis (Schmerling cave) ; **136**: Stajnia cave ; **137**: Stajnia ; **138**: Feldhofer cave ; **139**: Zeeland Ridges ; **140**: Warendorf ; **141**: Salzgitter-Lebenstedt. Voir tableau des Suppléments 11.2 pour les références.

La connaissance de Néandertal ne se limite pas aux sites contenant des restes fossiles, mais repose aussi sur un nombre plus important de sites archéologiques où des traces de sa présence ont été identifiées, incluant des industries lithiques (outils en pierre taillée), des restes de foyers (identifiés par la sédimentologie et l'étude des charbons), et des restes fauniques (grande faune et micromammifères, herpétofaune, malacofaune…). Alors que ces derniers offrent des informations cruciales à la fois paléoenvironnementales et sur les stratégies de subsistance des groupes néandertaliens, l'étude des industries lithiques permet également d'établir une chronologie culturelle basée sur les modes de taille employés et la typologie des outils produits. Des transitions techno-culturelles sont ainsi définies lorsque des changements majeurs et généralisés dans les modes de taille sont observés.

Au cours des derniers 200 000 ans, deux grandes transitions techno-culturelles ont été identifiées en Eurasie occidentale : celle du Paléolithique inférieur au Paléolithique moyen (*Early-to-Middle Palaeolithic Transition*, EMPT), très longue et progressive entre le MIS 11-9 et le MIS 5 (~400-130 ka BP) (Adler et al., 2014; Villa, 2009), et celle du Paléolithique moyen au Paléolithique supérieur (*Middle-to-Upper Palaeolithic Transition*, MUPT), plus rapide, au cours du MIS 3 (~50-30 ka BP) (Carvalho & Bicho, 2022; Zilhão, 2006). Toutes les deux présentent des problématiques très différentes. La première implique certainement plusieurs populations d'espèces du genre *Homo*

présentes en Europe à cette période (*H. erectus*, *H. heidelbergensis*, *H. neanderthalensis*), et sa dynamique, très lente et en mosaïque, est encore mal comprise. La deuxième, mieux documentée, est clairement associée à la disparition des populations néandertaliennes et à la colonisation du continent par *Homo sapiens*. Dans chacune de ces deux transitions technoculturelles et biologiques, le rôle des facteurs environnementaux est encore mal établi. Entre ces deux transitions s'est développé le monde Néandertalien dit « classique » (MIS 5-3).

La Figure 1.9 synthétise les principales caractéristiques climatiques, humaines et culturelles de la période d'étude qui seront développées dans les paragraphes suivant.

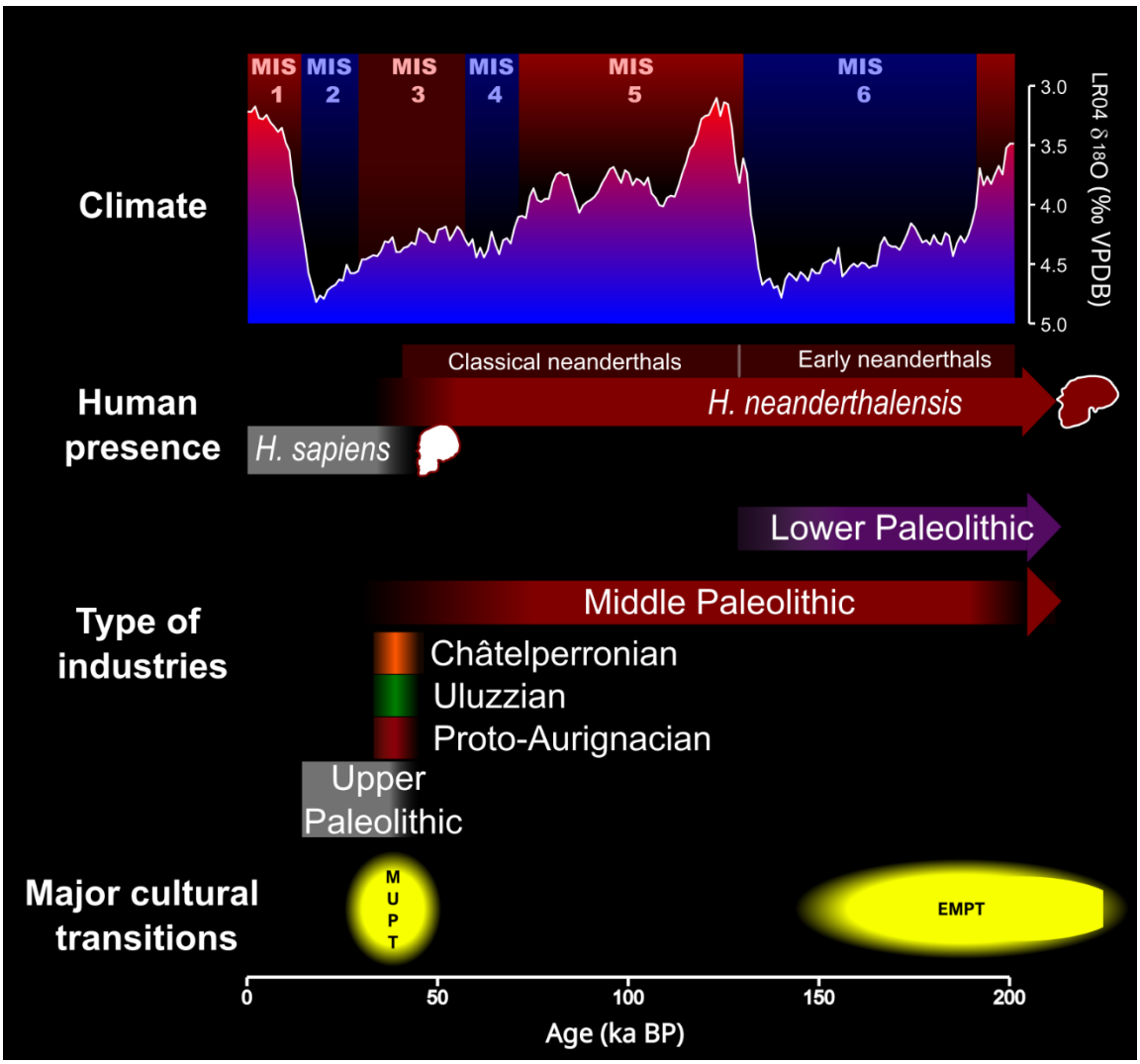


Fig. 1.9. Synthèse des principales trajectoires climatiques, humaines et culturelles en Europe occidentale au cours des derniers 200 000 ans. EMPT: Early-to-Middle Palaeolithic Transition; MUPT: Middle-to-Upper Palaeolithic Transition.

1.3.2 Le MIS 6 entre tradition Acheuléenne et innovations technologiques, une période en mosaïque

Très peu de fossiles attribués à Néandertal ont été répertoriés pendant l'avant-dernière période glaciaire. Ils sont généralement considérés comme appartenant au groupe des « Néandertaliens anciens », « Pré-Néandertaliens », ou « groupe Saalien » (Di Vincenzo & Manzi, 2023; Hublin, 2002) partageant encore des caractéristiques morphologiques avec des taxons ancestraux (*H. erectus*, *H. heidelbergensis*). Le plus remarquable est le spécimen d'Altamura dans le sud de l'Italie (daté entre 170 et 130 ka BP), retrouvé « emprisonné » dans des concrétions calciques qui ont permis un état de conservation exceptionnel, et même l'extraction d'ADN ancien (Lari et al., 2015).

Les sites archéologiques attribués au MIS 6 sont très peu nombreux en Europe, et il est généralement admis que le nord de l'Europe était quasiment dépeuplé pendant cette période glaciaire (Ashton & Scott, 2016; Hérisson et al., 2016; Richter, 2016). Au contraire, l'Europe Méditerranéenne semble avoir été continuellement habitée par Néandertal (Aureli & Ronchitelli, 2018; de Lumley, 2018; Garcia-Ibaibarriaga et al., 2018; Ochando et al., 2019). D'un point de vue techno-culturel, les productions lithiques retrouvées pendant cette période sont caractérisées par une grande diversité, et les sites archéologiques témoignent d'une mosaïque d'industries généralement classées en deux groupes (Carmignani et al., 2017; Mathias & Moncel, 2020). D'une part, les industries traditionnelles du Paléolithique inférieur, dites Acheuléennes (ou de Mode 2), et incluant principalement le façonnage de grands outils bifaciaux (bifaces) (Moncel & Schreve, 2016). D'autre part, de nouvelles formes de débitage plus complexes d'éclats, et en particulier de type Levallois, se généralisent progressivement et sont regroupées sous le nom d'industries du Paléolithique moyen ancien (*Early Middle Palaeolithic*, Mode 3) (Moncel et al., 2020, 2021). Cette longue période qui voit la coexistence d'industries traditionnelles acheuléennes (Mode 2) qui persistent et de technologies innovantes (Mode 3), est désignée comme la « transition du Paléolithique inférieur au Paléolithique moyen » (*Early-to-Middle Palaeolithic transition*) (Baena et al., 2017; Malinsky-Buller, 2016; Villa, 2009). Cette transition reste relativement moins étudiée que celle du Paléolithique moyen à supérieur (voir section 1.3.4). Si les industries de type Paléolithique moyen trouvent leurs origines dès le MIS 9-8 comme sur les sites d'Orgnac en France (Moncel et al., 2012), ou Ambrona et Gran Dolina de Atapuerca dans la péninsule Ibérique (de Lombera-Hermida et al., 2020; Santonja et al., 2018), elles se généralisent graduellement jusqu'à devenir dominantes dans le registre archéologique du MIS 5, au même moment où disparaissent les industries acheuléennes (Baena et al., 2021; Carmignani et al., 2017; Michel et al., 2022; Rubio-Jara et al., 2016; Rubio-Jara & Panera, 2019).

1.3.3 Les MIS 5 à 3 : le monde Néandertalien classique

A partir du MIS 5, les restes fossiles Néandertaliens sont dits « classiques », c'est-à-dire qu'ils possèdent généralement tous les caractères dérivés typiques de Néandertal, bien exprimés dans l'ensemble des fossiles de cette période (Di Vincenzo & Manzi, 2023; Hublin, 2002; Rosas et al., 2022, 2025).

Il est généralement admis que l'amélioration des conditions climatiques au début du MIS 5, favorise l'expansion de l'aire de répartition de Néandertal, se traduisant par l'augmentation du nombre de sites de manière générale et plus particulièrement au nord de l'Europe, où le retrait des masses glaciaires permet la recolonisation des espaces (Hérisson et al., 2016; Lewis et al., 2011; Scott, 2011; Shaw et al., 2025; White & Pettitt, 2011). Il faut attendre le MIS 4 pour voir une véritable recolonisation des îles britanniques (Ashton & Scott, 2016). Des visions contradictoires existent, considérant le MIS 5e comme une période très peu favorable à Néandertal car trop forestière (Defleur et al., 2020; Defleur & Desclaux, 2019). De manière générale, pendant l'interglaciaire du MIS 5 il reste difficile de placer les occupations dans un sous-stade isotopique précis, surtout dans les dépôts karstiques, en raison de l'incertitude sur les âges inhérents aux méthodes de datation utilisées.

D'un point de vue des technologies lithiques, cette période est caractérisée par la généralisation du Paléolithique moyen (anciennement appelé Moustérien), en particulier le débitage Levallois, la production laminaire et le débitage discoïde, accompagnée par une plus grande standardisation des outils et une régionalisation plus importante des traditions (Carrión & Walker, 2019; Delagnes & Meignen, 2007). La multiplication des sites sur cette période, mais aussi la grande disparité spatiale de ces données, rend complexe l'interprétation des tendances régionales et chronologiques, et des causes derrières ces mosaïques culturelles (Romagnoli et al., 2022). Les espaces méditerranéens, incluant les trois péninsules Ibérique, Italienne et Balkanique, et le sud de la France, ont été continuellement habités pendant cette période, et présentent un répertoire très diversifié d'occupations néandertaliennes et de comportements technologiques où il est difficile d'identifier des tendances (de la Torre et al., 2013; Eixea, 2018). En France, où un nombre important de sites existe, une tendance chronologique plus claire peut être identifiée avec la prévalence des technologies Levallois et laminaires jusqu'au MIS 5, en particulier dans le nord-ouest, puis celle des technologies Quina, MTA (Moustérien de Tradition Acheuléenne), et discoïde/denticulé à partir du MIS 4 dans le sud-ouest (Delagnes & Rendu, 2011). Cette tendance peut être expliquée par une évolution des stratégies de subsistances liées au mode de chasse, dans un contexte de refroidissement global du climat : la fin du MIS 5, et le MIS 4 représentent une phase de refroidissement progressif lié à l'entrée en période glaciaire. De fait, un nombre de sites moins important est observé au MIS 4 (González

Molina et al., 2024; Mallol et al., 2019; Richter, 2016; Rios-Garaizar, 2017). Il ainsi été suggéré que l'émergence des technologies de type « Quina » dans le sud-ouest de la France pendant le MIS 4 a pu constituer une réponse adaptative face à la détérioration progressive des conditions climatiques (Banks et al., 2021).

Au MIS 3, une augmentation du nombre de sites, ainsi qu'une diversification encore plus vaste des comportements est observée : dans le sud-ouest de la France, et en Cantabrie, deux régions particulièrement bien étudiées, la coexistence d'industries Levallois, laminaires, Discoïdes, Quina, est bien mise en évidence sur un nombre important de sites (Baena et al., 2017; Fourcade, 2022; Guibert et al., 2008; Romagnoli et al., 2022). Par ailleurs, des industries du Paléolithique moyen à caractère plus local ont été mises en évidence, comme le Vasconien dans le nord-ouest de la péninsule Ibérique (Deschamps, 2017, 2019, mais voir González-Molina et al., 2024), ou le Néronien dans la vallée du Rhône (Slimak, 2008).

1.3.4 Vers la fin de Néandertal et l'arrivée d'*Homo sapiens* : la transition du Paléolithique moyen à supérieur

La fin du MIS 3 voit en Europe une phase de changements profonds à la fois culturels et biologiques, représentés par la transition du Paléolithique moyen au Paléolithique supérieur, l'arrivée d'*Homo sapiens* en Europe occidentale, et l'extinction de Néandertal (Hoffecker, 2009). Si les sites ayant livrés des restes fossiles néandertaliens sur cette période apparaissent plus nombreux (Fig. 1.7), il s'agit en très grande majorité de fragments crâniens et de dents isolées.

H. Sapiens est déjà présent au Levant depuis au moins 177 ka BP (Hershkovitz et al., 2018), et certaines études évoquent également des incursions très anciennes en Grèce (Harvati et al., 2019). Cependant, la principale vague de migration aboutissant à la colonisation totale du continent eurasiatique a débuté il y a environ 70-60 ka BP (Groucutt et al., 2015; Mellars, 2006). Les généticiens ont montré par ailleurs que plusieurs vagues de migration successives ont pu exister après la sortie d'Afrique (*Out of Africa*), avec un foyer de population source sur le plateau persique capable de permettre la colonisation du continent (Vallini et al., 2022, 2024). A la suite de cette vague de sortie d'Afrique, le processus de colonisation se développe de manière relativement très rapide (voir Fig.1.10) : *H. sapiens* est présent en Europe occidentale à partir de 47 ka BP au moins dans les Balkans (Hublin et al., 2020), avec des propositions remontant même à 54 ka BP dans la vallée du Rhône (Slimak et al., 2022). Ainsi, en l'espace d'environ 15-20 000 ans depuis les premières incursions en Europe occidentale, Sapiens est l'unique représentant du genre *Homo* en Eurasie.

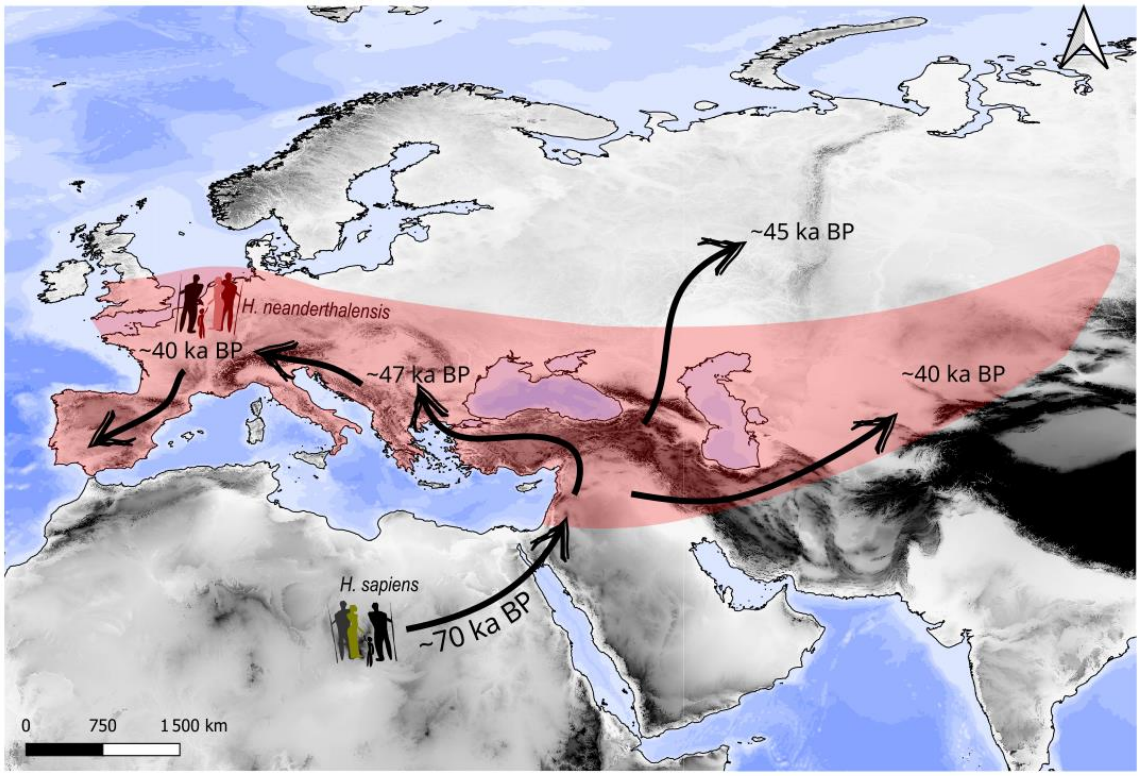


Fig. 1.10. Aire de répartition d'*Homo neanderthalensis* (rose), avec les voies principales de migration ayant amené à la colonisation de l'Eurasie par *Homo sapiens*.

La présence des premiers *Homo sapiens* sur les sites archéologiques est donc attestée de manière certaine uniquement à travers les restes fossiles (très peu nombreux, voir Fig. 1.11), ou à travers les industries du Paléolithique supérieur initial, correspondant aux cultures Proto-aurignacienne et Aurignacienne ancienne, datées d'environ 42 à 38 ka BP (Benazzi et al., 2015; Higham et al., 2014; Marín-Arroyo et al., 2023; Picin et al., 2022). Ces cultures sont en rupture totale avec celles du Paléolithique moyen, et sont caractérisées par la production de lames et lamelles, et la présence d'éléments de parures (coquillages perforés) (Banks et al., 2013; Bon, 2002; Bordes, 2006; Vanhaeren & d'Errico, 2006).

En parallèle de la persistance des industries du Paléolithique moyen associées à Néandertal, et de l'arrivée des industries du Paléolithique supérieur initial associées à *Sapiens*, plusieurs industries dites « de transition » ont été identifiées, dont les principales en Europe méditerranéenne occidentale sont le Châtelperronien (présent en France et dans le nord de la péninsule Ibérique) et l'Uluzzien (dans la péninsule Italienne et la côte ouest-balkanique) (Fig. 1.11). L'identité biologique de leurs auteurs reste mal établie, ou sujette à débat, puisqu'elles correspondent à une période de cohabitation entre Néandertal et *Sapiens*, entre ~50 et 38 ka BP (Hublin, 2015; Moncel & Voisin, 2006; Zilhão et al., 2024).

Le Châtelperronien a été défini en France dans la Grotte des Fées à Châtelperron (Bordes et al., 2009; Roussel et al., 2016), et son extension chronologique est estimée entre 44 et 38 ka BP environ (Mora et al., 2018; Morales et al., 2019; Talamo et al., 2020). Il est généralement proposé que son origine est néandertalienne, plusieurs sites ayant délivré des restes humains attribués à Néandertal dans les niveaux châtelperroniens comme les grottes d'Arcy-sur-Cure (Henrion et al., 2023), Saint-Césaire (ou La Ferrassie (Balzeau et al., 2020; Talamo et al., 2020). Cependant, l'intégrité des niveaux stratigraphiques de ces sites est débattue (Gravina et al., 2018), et certaines études proposent que des restes attribués à *H. sapiens* sont également présents dans les mêmes niveaux d'occupation châtelperroniens (Gicqueau et al., 2023). L'Uluzzien a été défini en Italie sur le site de la Grotte d'Uluzzo (Silvestrini et al., 2022; Spinapolice et al., 2022). Plusieurs dents humaines associées à ces niveaux d'occupation ont été attribuées à *H. sapiens* (Benazzi et al., 2011; Oxilia et al., 2022), bien que cette attribution soit contestée par certains auteurs (Zilhão et al., 2015, 2024). D'un point de vue chronologique, les occupations uluzziennes les plus anciennes sont datées autour de 45 ka BP, et semblent être « scellées » sous l'éruption Ignimbrite de Campanie, bien datée à 39 280 ± 110 et mise en évidence par le niveau tephra Y-5 sur de nombreux sites en Italie et dans les Balkans, le principal étant la Grotta del Cavallo en Italie du Sud (Badino et al., 2020; Douka et al., 2014; Falcucci et al., 2024; Giaccio et al., 2017; Higham et al., 2024; Koumouzelis et al., 2001; Marín-Arroyo et al., 2023; Picin et al., 2022; Zanchetta et al., 2018).

Cette diversité d'industries de transition et du début du Paléolithique supérieur à la fin du MIS 3 témoigne de l'hétérogénéité culturelle des premiers groupes *Sapiens* arrivés en Europe occidentale ainsi que d'une grande complexité de scénario pour la transition du Paléolithique moyen au Paléolithique supérieur, impliquant potentiellement plusieurs vagues de migrations, différents groupes culturels pour les *Homo sapiens*, et des processus locaux de métissage et d'acculturation (Marín-Arroyo et al., 2023; Zilhão et al., 2024).

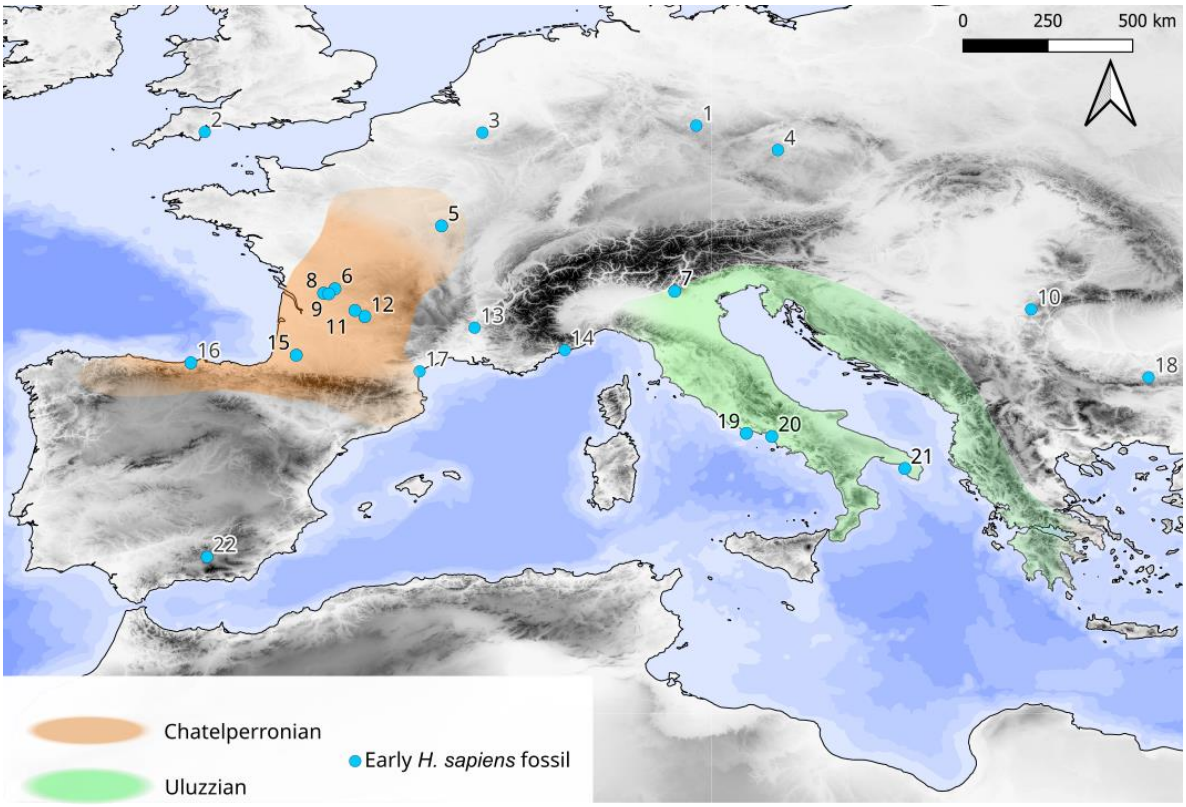


Fig. 1.11. Principaux sites du MIS 3 présentant des restes humains attribués à *H. sapiens*, datés d'avant 30 ka BP, avec les aires de répartition des principales cultures dites « de transition ». Les sites sont numérotés par latitude décroissante : **1**: Ilsenhöhle ; **2**: Kent's Cavern ; 3**:** Goyet ; **4**: Zlatý kůň ; **5**: Grotte du Renne ; **6**: Fontechevade ; **7**: Grotta di Fumane ; **8**: Les Rois ; **9**: La Quina ; **10**: Oase ; **11**: Abri Castanet ; **12**: Le Piage ; **13**: Grotte Mandrin ; **14**: Riparo Bombrini ; **15**: Brassempouy ; **16**: Covalejos ; **17**: La Crouzade ; **18**: Bacho Kiro ; **19**: Fossellone ; **20**: Roccia di San Sebastiano ; **21**: Grotta del Cavallo ; **22**: Carihuela. La plupart sont associés aux cultures du Paléolithique supérieur initial (Uluzzien, Protoaurignacien et Aurignacien). Pour les références, voir Tableau S2 dans les suppléments.

Dans le débat sur la Transition du Paléolithique moyen à supérieur et sur l'extinction de Néandertal, la question de la spatialisation revêt un intérêt particulier. Les études génétiques sur les spécimens néandertaliens tardifs ont montré une fragmentation des populations de Néandertal pendant le MIS 3, antérieure à l'arrivée des *Homo sapiens*, menant des petits groupes de Néandertal à l'isolement génétique avant l'extinction (Dalén et al., 2012; Hajdinjak et al., 2018; Slimak et al., 2023, 2024). Les *Homo sapiens* ont donc potentiellement rencontré, à leur arrivée en Europe occidentale, des groupes déjà très réduits et isolés de Néandertaliens. La péninsule Ibérique a été perçue depuis longtemps comme un lieu de persistance tardive de ces derniers groupes néandertaliens, avec des sites aux chronologies apparemment « jeunes », proposées jusqu'à 28 ka BP (Finlayson et al., 2006, 2008). Le modèle de la « Frontière de l'Ebre » a proposé qu'une frontière biogéographique, représentée par le tracé de l'Ebre, a séparé les dernières populations néandertaliennes au sud et les premiers groupes d'*Homo sapiens* au nord, expliquant ainsi la persistance tardive des groupes du

Paléolithique moyen et l'absence d'occupations du Paléolithique supérieur initial dans le sud de la péninsule Ibérique (Zilhão, 2000). Ce modèle a été critiqué (Vaquero, 2006; Vaquero et al., 2006), puis démenti par plusieurs éléments, incluant (i) la remise en cause des datations de sites associés à Néandertal considérés comme jeunes et leur re-datation par les méthodes d'ultrafiltrations (e.g. Galván et al., 2014; Higham et al., 2014; Wood et al., 2013, 2014) et (ii) la mise en évidence d'industries du Paléolithique supérieur initial dans le centre et dans le sud de la péninsule, comme sur le site de Bajondillo (Cortés-Sánchez et al., 2019 mais voir Anderson et al., 2019 et Zilhão, 2021a), de Lapa do Picareiro (Haws et al., 2020, 2021 mais voir aussi Zilhão, 2022), ou plus récemment de l'Abrigo de la Malia (Sala et al., 2024). Ainsi, malgré les arguments avancés contre le modèle de la frontière de l'Ebre, la question reste ouverte et un certain nombre d'auteurs continue de défendre une vision où les industries aurignaciennes au sud de la frontière de l'Ebre serait différentes et plus tardives que celles du reste de l'Europe occidentale (Villaverde et al., 2017, 2021; Zilhão, 2021b; Zilhão et al., 2017). De même, les chronologies exactes des dernières occupations néandertaliennes sont encore mal établies. Dans le nord de la péninsule, les travaux récents supportent une disparition précoce des industries du Paléolithique moyen autour de 45 ka BP, puis un chevauchement des occupations châtelperroniennes et aurignaciennes entre 43 et 41 ka BP (Marín-Arroyo et al., 2018). Dans le sud de la péninsule Ibérique, les chronologies sont encore sujettes à débat, avec d'une part les partisans d'une extinction néandertalienne « précoce », juste avant ou contemporaine de l'évènement de Heinrich 4 (39.9 ka BP) (Galván et al., 2014; Higham et al., 2014; Wood et al., 2013), et d'autre part les partisans d'une persistance plus tardive jusqu'à 37 ka BP au moins sur les sites du sud de la péninsule (Carrión et al., 2019b; Zilhão, 2021b; Zilhão et al., 2017). Il apparaît donc que la péninsule Ibérique est une région clé où la chronologie et le scénario de la transition du Paléolithique moyen à supérieur reste encore à déchiffrer, afin d'éclairer les processus à l'origine de l'extinction des derniers Néandertaliens.

La compréhension des scénarios de cette transition fait face à des difficultés liées principalement (i) au faible nombre de restes humains disponibles sur cette période et associés aux différentes industries, et (ii) à la limite d'applicabilité de la méthode du radiocarbone, qui complique l'établissement d'une chronologie précise et fiable pour la succession des cultures (Paléolithique moyen, Châtelperronien, Uluzzien, Protoaurignacien…). Cette deuxième problématique est fondamentale, et a grandement bénéficié récemment des approches chronologiques par modélisation Bayésienne (voir par exemple Fourcade et al., 2022; Higham et al., 2014, 2024; Marín-Arroyo et al., 2018; Marín-Arroyo & Mihailović, 2017; Price et al., 2021). Malgré les questions encore ouvertes sur la chronologie du Paléolithique moyen final, et sur l'attribution biologique des industries de transition, les études génétiques confirment que Néandertal et Sapiens ont cohabité en Europe occidentale pendant une période longue d'au moins 5 000 ans dans certaines régions (Iasi et al., 2024; Sümer et

al., 2025). Des évènements d'hybridation entre les deux espèces ont bien été mis en évidence : les *Homo sapiens* aurignaciens en Europe ont hérité d'environ 3% de génome de Néandertal (Fu et al., 2015, 2016; Hajdinjak et al., 2021; Harvati & Roksandic, 2016; Prüfer et al., 2021). En revanche, l'absence de génome Sapiens chez Néandertal montre que le transfert de gênes a eu lieu à sens unique (Hajdinjak et al., 2018, 2021). Ainsi, le modèle par assimilation, impliquant l'hybridation des deux espèces et l'incorporation partielle du génome néandertalien dans le génome Sapiens, est largement soutenu par les données génétiques, et de plus en plus par les données archéologiques (Smith et al., 2005, 2017; Zilhão et al., 2024). Des chercheurs vont même jusqu'à proposer une absorption totale des dernières populations néandertaliennes, déjà très réduites, dans les groupes Sapiens (Stringer & Crété, 2022).

Pour résumer, la période de la fin du MIS 3 en Europe occidentale est caractérisée par une mosaïque de populations humaines (Higham et al., 2014, 2024; Zilhão et al., 2024), incluant des Néandertaliens tardifs produisant des industries du Paléolithique moyen final et peut-être des industries de transition, différents groupes de Sapiens produisant des industries du Paléolithique supérieur initial, et peut être des groupes « mixtes », résultats d'hybridation entre différentes groupes biologiques et culturels. Le résultat final de ce processus est la disparition de Néandertal, et la survie de populations d'*Homo sapiens* en partie hybridées avec Néandertal.

1.3.5 Hypothèses sur les causes de l'extinction de Néandertal

Les causes du déclin puis de l'extinction de Néandertal eu Europe restent encore très discutées, et le débat a été alimenté depuis longtemps par de nombreuses hypothèses impliquant plusieurs causes, parmi lesquelles peuvent être citées :

- l'éruption volcanique des Champs Phlégréens en Italie autour de 39 ka BP (Fitzsimmons et al., 2013; Golovanova et al., 2010)

- l'excursion magnétique de Laschamp autour de 42 ka BP (Cooper et al., 2021a; Valet & Valladas, 2010, mais voir les critiques de Hawks, 2021, et la réponse de Cooper et al., 2021b) ;

- la transmission de maladies chez Néandertal et sa plus grande vulnérabilité face aux pathogènes (Greenbaum et al., 2019; Houldcroft & Underdown, 2016; Pagano et al., 2019; Trájer, 2023) ;

- des processus démographiques internes aux populations néandertaliennes impliquant le taux de reproduction et la mobilité des groupes (Cucart-Mora et al., 2018; Degioanni et al., 2019; Sørensen, 2011; Vaesen et al., 2021), la consanguinité (Ríos et al., 2019), ou encore les comportements de

subsistence (Vidal-Cordasco & Marín-Arroyo, 2025) et le cannibalisme (Agustí & Rubio-Campillo, 2017) ;

- des tueries de masse perpétrées par Sapiens, responsables des extinctions massives de grands mammifères à la fin du Pléistocène et dont Néandertal serait l'une des victimes (Hortolà & Martínez-Navarro, 2013; Martínez-Navarro, 2020) ;

La cause climatique a été défendue depuis le début par de nombreux auteurs, qui mettaient en évidence la synchronie entre les dernières occupations néandertaliennes dans la péninsule Ibérique et les conditions climatiques rudes pendant le MIS 3, tout particulièrement pendant l'évènement de Heinrich 4 (Finlayson & Carrión, 2007; Jiménez-Espejo et al., 2007; Mellars, 2004; Stewart, 2004; Stringer et al., 2004). Une vision différente a été proposée par l'étude de d'Errico & Sánchez Goñi, 2003, qui a ouvert d'importants débats sur l'impact des variations climatiques du MIS 3 sur Néandertal et Sapiens. A partir de l'enregistrement paléoclimatique des carottes marines au large de la péninsule Ibérique, les auteurs ont proposé (i) que les changements climatiques rapides et répétés du MIS 3 ont fragilisé, réduit, et poussé les populations néandertaliennes de la péninsule Ibérique à se replier dans des refuges le long des côtes, (ii) qu'*Homo sapiens* a pris l'avantage dans la forte compétition pour les ressources qui l'a opposé à Néandertal à son arrivée dans la péninsule, et (iii) que l'évènement de Heinrich 4, caractérisé par un paysage ouvert et un climat aride dans l'intérieur de la péninsule, a retardé l'avancée de Sapiens et ainsi permis la survie plus tardive des derniers groupes néandertaliens dans les derniers refuges du sud (Sepulchre et al., 2007). Ce modèle repose donc sur l'influence combinée du climat et de la compétition entre les deux espèces, le deuxième facteur étant le plus déterminant pour les auteurs. Cette vision a été très critiquée, notamment par les chercheurs travaillant sur les enregistrements paléoécologiques des sites néandertaliens, affirmant que (i) l'usage des carottes marines pour reconstruire l'environnement de Néandertal est limité, puisque incapable de rendre compte de la mosaïque des environnements continentaux dans lesquels évoluait Néandertal, et (ii) rien ne prouve qu'une compétition ait existé entre les deux espèces, et qu'elle se soit déroulée à l'avantage de Sapiens, vue la faible densité des populations (Carrión, 2004; Finlayson, 2008; Finlayson et al., 2004, 2008).

En effet, il reste difficile de démontrer l'existence de la compétition entre les deux espèces, qui reste contestée par de nombreuses études plus partisanes de la cause climatique (Klein et al., 2023; Timmermann, 2020; Villa & Roebroeks, 2014; Wolf et al., 2018). L'hypothèse de la compétition repose sur une vision où Sapiens aurait une supériorité technologique et comportementale sur Néandertal, en particulier dans sa capacité d'adaptation face aux changements environnementaux, c'est-à-dire une plus grande plasticité écologique. Une vision traditionnelle tend à opposer Sapiens, espèce généraliste,

dotée d'innovations technologiques déterminantes, capable d'une grande mobilité, et avec un taux de reproduction élevé, à Néandertal, espèce aux comportements de subsistance plus spécialisés, vivant en petits groupes dans des habitats plus réduits et fragmentés (Melchionna, 2018; Timmermann, 2020). Aucun consensus n'existe quant au facteur déterminant qui aurait causé un déficit de compétition de Néandertal par rapport à Sapiens. Les études évoquent la supériorité cognitive, symbolique et linguistique de Sapiens (Gilpin et al., 2016; Mellars, 2005; Pearce et al., 2013), ses innovations technologiques incluant la production de microlithes et de projectiles (Brown et al., 2012; Shea & Sisk, 2010; Wynn, 2009), l'exploitation d'un plus vaste panel de ressources (Hockett & Haws, 2005; Marean, 2005), une meilleure organisation économique (Horan et al., 2005), la division sexuée du travail (Kuhn & Stiner, 2006), ou une population plus nombreuse (Cucart-Mora et al., 2018; Mellars & French, 2011). Cependant, notre vision de Néandertal a grandement évolué ces vingt dernières années (Romagnoli et al., 2022). Des comportements complexes ont été mis en évidence par des découvertes archéologiques très récentes, incluant une grande mobilité et des connexions inter-groupes sur de longues distances (Herrero-Alonso et al., 2025; Pigott et al., 2025), une très grande diversité de stratégie de subsistance impliquant les petits mammifères, les ressources marines et les plantes (Carvalho et al., 2018; Fa et al., 2013; Hardy, 2022; Nabais et al., 2023; Stringer et al., 2008; Villa et al., 2020), des comportements sociaux complexes incluant du soin médical et des pratiques funéraires (Balzeau et al., 2020; Been & Barzilai, 2024; Rendu et al., 2016; Sala et al., 2025; Spikins et al., 2019) et des comportements symboliques (García-Diez & Ochoa, 2013; Hoffmann et al., 2018; Jaubert et al., 2016, 2022; Marquet et al., 2014; Peresani et al., 2011; Pitarch Martí et al., 2021; Rodríguez-Hidalgo et al., 2019; Zilhão, 2012). Par ailleurs, la supériorité cognitive de Sapiens et son exclusivité des comportements dits « modernes » sont également remis en cause (Amorós & Carrión, 2026). La mise en évidence de l'hybridation entre les deux espèces, ainsi que l'assimilation biologique et peut-être culturelle de Néandertal par Sapiens, est par ailleurs en contradiction avec l'hypothèse de la compétition entre les deux espèces (Stringer & Crété, 2022). L'estimation démographique reste elle aussi très débattue : si des études génétiques récentes ont argumenté en faveur d'une plus large métapopulation néandertalienne (Rogers et al., 2017), la plupart des chercheurs se montrent favorables à un désavantage démographique de Néandertal par rapport à Sapiens, impliquant une plus petite métapopulation et une division en petit groupes de Néandertal (Bocquet-Appel & Degioanni, 2013; Cucart-Mora et al., 2018; Mafessoni & Prüfer, 2017; Skov et al., 2022)

Plusieurs paradigmes se sont donc succédés dans le débat sur les causes de l'extinction de Néandertal, avec une prévalence des hypothèses climatiques, puis des processus impliquant la compétition entre les deux espèces et la démographie, bien que toutes ces hypothèses soient fortement interconnectées. Aujourd'hui, l'intérêt pour la cause climatique a repris de l'importance,

notamment grâce à la multiplication des enregistrements climatiques à très haute résolution permettant une meilleure corrélation entre les changements environnementaux et les dynamiques de peuplement (Badino et al., 2020; Cartapanis, 2025; Fourcade et al., 2022; Staubwasser et al., 2018; Tzedakis et al., 2007; Wolf et al., 2018). Par ailleurs, les approches par modélisation de niche (*niche modelling*, ou *species distribution modelling*) ont redonné du poids à l'hypothèse combinant les changements climatiques à la compétition entre les deux espèces : Néandertal et Sapiens entrant en compétition pour la même niche écologique, la réduction de celle-ci de manière répétée et abrupte au cours des changements rapides du Pléistocène récent aurait induit la contraction des populations néandertaliennes et accentué la compétition entre les deux espèces pour les mêmes ressources au détriment de Néandertal (Albouy et al., 2024; Banks et al., 2008; Melchionna, 2018; Melchionna et al., 2018; Sánchez Goñi, 2022b; Timmermann, 2020). En calculant l'évolution de la Productivité Première Nette (NPP) entre 55 et 30 ka BP dans la péninsule Ibérique, Vidal-Cordasco et al., (2022) propose qu'une réduction significative de celle-ci, et donc des ressources disponibles pour Néandertal, a eu lieu et a représenté une des causes potentielles du repli des populations néandertaliennes dans les refuges thermoméditerranéens, sur la côte sud-ibérique. Cependant, il existe encore peu d'études de modélisation sur une plus grande échelle de temps capable de donner une profondeur temporelle à ces modèles, et celles-ci proposent souvent des conclusions différentes. Trájer (2023) soutient que les populations pré-néandertaliennes et néandertaliennes en Europe se sont progressivement adaptées à l'expansion des biomes froids au cours du Pléistocène, montrant une grande capacité d'adaptation à des environnements différents. L'étude de Benito et al. (2017) sur le MIS 5 conclut que les régions du littoral méditerranéen étaient particulièrement favorables à Néandertal pendant cette période, contrairement à l'Europe centrale continentale. La modélisation à échelle planétaire de Raia et al. (2020) soutient que les changements climatiques sont les principaux facteurs responsables des extinctions d'espèces passées du genre *Homo*, incluant *H. neanderthalensis*. Banks et al. (2021) reconstruit l'évolution de la niche écologique de Néandertal entre 82 et 60 ka BP et conclut qu'une contraction importante de l'habitat de Néandertal a eu lieu à la fin du MIS 5 autour de 70 ka BP, tandis que l'étude de Degioanni et al. (2025) centrée sur la période entre 90 et 50 ka BP affirme que l'habitat de Néandertal n'a pas subi de contraction majeure à la fin du MIS 3, écartant la cause climatique pour son extinction.

Pour conclure, malgré la plus grande importance donnée à l'hypothèse climatique ainsi qu'à celle de la compétition dans le débat sur l'extinction de Neandertal, il est très probable que des processus multifactoriels et potentiellement interactifs soient impliqués. Slimak (2019) propose une réflexion épistémologique sur notre manière d'appréhender les causes de l'extinction de Néandertal : étudier la contingence des facteurs naturels et culturels n'est plus suffisant pour comprendre le

scénario de la Transition du Paléolithique moyen à supérieur et il est nécessaire dans les futurs travaux de faire appel aux méthodes de l'anthropologie culturelle afin de changer notre vision des comportements humains pendant cette période cruciale de l'évolution humaine.

Les sciences naturelles peuvent cependant encore largement contribuer au débat. Particulièrement cruciales sont les nouvelles études proposant (i) de nouvelles datations ou re-datations de sites archéologiques bien étudiés et présentant un registre archéologique et paléoécologique varié (ii) des modélisations et simulations permettant de tester l'importance des différents facteurs écologiques et humains impliqués et (iii) de nouveaux enregistrements paléoenvironnementaux longs et à haute résolution, comme ODP 976.

1.3.6 Considérations finales sur les dynamiques humaines et environnementales

Il est encore difficile, à l'heure actuelle, d'établir des relations entre dynamiques de populations humaines et changements environnementaux. Preuve en est que des interprétations tout à fait contradictoires existent quant aux réponses des populations humaines face aux dynamiques du climat. Néandertal est perçu traditionnellement comme une espèce à affinité plutôt « froide » de par sa morphologie robuste (règles écologiques de Bergmann et de Allen) et sa persistance au cours de longues glaciations (Churchill, 2006; Depaepe, 2022; Holliday, 1997; Hublin, 2002; Ocobock et al., 2021; Steegmann et al., 2002; Wroe et al., 2018). Des auteurs ont même proposé que le réchauffement climatique du MIS 5e les aurait déstabilisés et poussé les néandertaliens au cannibalisme pour survivre (Defleur et al., 2020; Defleur & Desclaux, 2019), une vision fortement critiquée par Slimak & Nicholson (2020). Les interprétations écologiques basées uniquement sur des traits morphologiques doivent être considérées avec précaution (Rae et al., 2011b, 2011a). A l'opposé de cette image de Néandertal comme une espèce « froide », plusieurs études le montrent plutôt comme une espèce ubiquiste (Stewart, 2005), ou plus adaptée aux milieux fermés avec une végétation arborée, comme celle du MIS 5 et des interstadiaires du MIS 3 (Carrión et al., 2019a; Stewart et al., 2019; Trájer, 2023). Ces auteurs montrent une contraction des populations néandertaliennes pendant les épisodes les plus froids, et leur survie dans des refuges climatiques le long des côtes méditerranéennes (Carrión et al., 2018, 2019a; Finlayson, 2008; Finlayson et al., 2006; Ochando et al., 2019).

Dans les sources d'interprétations contradictoires peut également être cité l'évènement de Heinrich 4, présenté comme un évènement aux conséquences « catastrophiques » pour Néandertal (Finlayson & Carrión, 2007), ou comme un « dernier jardin d'Eden » avant leur extinction finale (d'Errico & Sánchez Goñi, 2003, 2004, opposés à Carrión, 2004). Plus globalement, le rôle du climat dans l'expansion des populations d'*Homo sapiens* est encore mal cerné : certains ont montré que

l'avancée de Sapiens était favorisée par les épisodes climatique plus tempérés (Müller et al., 2011; Paquin et al., 2024), d'autres par des épisodes plus froids (Pederzani et al., 2021).

Les dynamiques de peuplement humain au Pléistocène sont traditionnellement reconstruites sous le prisme du modèle « *source and sink* » (Dennell et al., 2011; Sánchez-Yustos & Diez-Martín, 2015). Ce modèle implique l'existence de populations humaines *sink*, vouées à l'extinction localement, et de populations humaines *sources* persistantes dans des régions climatiquement favorables et aptes à recoloniser d'autres territoires par la suite. Ainsi, les peuplements humains au Pléistocène pourraient s'expliquer par des processus d' « *ebb and flow* », impliquant des épisodes de recolonisation répétée de territoires successivement défavorables puis favorables (Hublin & Roebroeks, 2009). Ce modèle, construit pour analyser les dynamiques de peuplement au Pléistocène moyen, a par la suite été largement appliqué pour expliquer la colonisation de l'Europe de l'ouest par les populations humaines du Pléistocène inférieur (Bermúdez de Castro & Martinón-Torres, 2013; MacDonald et al., 2012). Cependant, il convient de ne pas tomber dans une vision déterministe de l'évolution humaine. Il paraitrait simpliste d'envisager que les groupes humains ne feraient que « danser au rythme du Pléistocène » (Gamble, 1999, p. 125), subissant des contractions et expansions répétées au rythme des glaciaires /stadiaires et interglaciaires/interstadiaires. Cette idée résulterait d'une vision limitée des trajectoires sociales et culturelles humaines, qui loin d'être complètement soumises aux forçages climatiques et environnementaux, dépendent aussi de facteurs internes aux groupes humains, même pour des groupes caractérisés par des modes de vies nomades et de chasseurs-cueilleurs. Ces derniers font preuve de résilience et d'une grande capacité d'adaptation, qui peut s'exprimer par des innovations technologiques, ou une réorganisation des groupes sociaux, des stratégies de subsistance, et de la gestion de leur territoire.

Ainsi, avant de s'appuyer sur une longue séquence marine pour reconstruire l'environnement des groupes humains au Paléolithique, il est important de considérer le potentiel ainsi que les limitations d'une telle étude. La possibilité d'accès à un enregistrement continu, sur des centaines de milliers d'années et avec une résolution très fine, des variations climatiques régionales est précieuse et permet une contextualisation exceptionnelle du registre archéologique régional, sous réserve d'une chronologie robuste. Cette thèse entend exploiter ce grand potentiel dans le sud de la péninsule Ibérique, une région clé pour la question des derniers néandertaliens. Cependant, son utilisation ne doit pas se faire sans précautions, loin de toute vision déterministe, et les limitations de l'approche et des méthodologies seront discutées dans la partie 7.1.

2. Matériel et méthodes

2.1 La carotte ODP 976 : historique de l'expédition et des études

L'expédition 161 du programme international de forage océanique ODP (aujourd'hui IODP-*International Ocean Drilling Program*) s'est déroulée en 1995 en Mer d'Alboran, sur le navire océanographique *Joides Resolution* (Comas et al., 1996). Plusieurs sites de forages ont été déterminés, avec pour objectif principal d'obtenir une séquence stratigraphique du bassin sud-ouest méditerranéen remontant à la crise de salinité méssinienne, afin de comprendre l'histoire des connections entre Atlantique et bassin méditerranéen (Zahn et al., 1999). Sur le site 976, cinq points différents ont été forés (*Holes* A-E) à une profondeur de 1108 m. Le *Hole* B a atteint une profondeur de forage de 650 m (mesurée en mbsf : *meters below sea-floor*). A partir des cinq forages, une séquence sédimentaire composite de 350 m de long a été construite. Cette séquence composite sert de base à toutes les études paléoenvironnementales menées sur ODP 976 et sa profondeur est exprimée en *meters composite depth* (mcd). Les sédiments qui constituent la séquence tout au long du Pléistocène sont remarquablement homogènes: il s'agit principalement d'argiles et d'argiles limoneuses composées de nanofossiles calcaires, de particules argileuses et de foraminifères (Skilbeck & Tribble, 1999).

Aujourd'hui, la carotte ODP 976 est conservée à l'IODP *core repository* localisé au centre des sciences environnementales marines Marum de Brême (Allemagne) (https://www.marum.de/en/Bremen-Core-Repository.html). Des échantillons sédimentaires (ainsi que des piluliers palynologiques et de foraminifères) issus d'études précédentes sont conservés au laboratoire de palynologie de l'UMR 7194 « HNHP », basé à l'Institut de Paléontologie Humaine à Paris.

Des études antérieures entreprises sur la séquence d'ODP 976 concernent des indicateurs paléoenvironnementaux au Pléistocène, parmi lesquelles :

- l'analyse sédimentologique (Skilbeck & Tribble, 1999) et des faciès sédimentaires (Alonso et al., 1999) ;

- les analyses de la composante organique du sédiment (Organic-Rich Layers, ORL) (Murat, 1999) ;

- les analyses palynologiques préliminaires (pollen et kystes de dinoflagellés) (Combourieu-Nebout et al., 1999) ;

- les analyses isotopiques préliminaires sur les foraminifères planctoniques (von Grafenstein et al., 1999), qui ont permis d'établir le modèle d'âge préliminaire de la carotte ;

- les analyses isotopiques sur les foraminifères planctoniques à plus haute résolution, ainsi que des reconstructions de températures de surface (SST) sur les deux dernières terminaisons glaciaires, TI et TII (Jiménez-Amat & Zahn, 2015; Martrat et al., 2014) ;

- les analyses palynologiques à plus haute résolution sur les derniers 50 000 ans (Combourieu-Nebout, et al., 2009a, 2009b; Combourieu-Nebout et al., 2002), sur les MIS 12-10 (Sassoon et al., 2023), ainsi que sur les MIS 20-18 (Toti et al., 2020). Des analyses palynologiques sur le dernier cycle climatique ont été publiées en partie dans des articles de synthèse (Fletcher et al., 2010a; Genty et al., 2005; Masson-Delmotte et al., 2005) ;

- les analyses de composition minéralogique d'argiles pour les derniers 50 000 ans (Bout-Roumazeilles et al., 2007) ;

- les reconstructions climatiques basée sur le pollen pour les derniers 50 000 ans (Bout-Roumazeilles et al., 2007; Combourieu-Nebout et al., 2009), ainsi qu'une comparaison des MIS 19, 5 et 1 (Sassoon et al., 2025) ;

Des études palynologiques, isotopiques et de composition minéralogique d'argiles à haute résolution sont également en cours sur les parties plus anciennes de la carotte, afin de couvrir les derniers 1.2 millions d'années en continu : analyses de Rafael Cabral pour les MIS 9-7, thèse et articles en cours par Maé Catrain pour les MIS 37-15 (Catrain et al., 2025), articles en cours par Gabriele Niccolini et al. sur les MSI 20-18, et par Tiffanie Fourcade et al. pour les MIS 15-12.



Fig. 2.1. Mission d'échantillonnage à Brême (Avril 2023). A: L'entrepôt de carottes de Brême (*Bremen Core Repository*) du programme IODP, situé dans les locaux du *Marum Center for Marine Environmental Sciences*, conserve environ 200 km de carottes marines. B: Echantillonnage pour analyses palynologiques à très haute résolution d'une section de la carotte ODP 976. C: l'équipe d'échantillonnage, de gauche à droite : Maé Catrain, Liz Charton, Nathalie Combourieu, Odile Peyron.

2.2 Méthodes de la palynologie

La palynologie s'intéresse à l'étude des palynomorphes (Reille, 1990), groupe de microfossiles incluant principalement les grains de pollen, et les palynomorphes non-polliniques (*non-pollen palynomorphs*, NPPs). Ces derniers embrassent une très large diversité d'êtres vivants (van Geel, 1998, 2001), mais sont principalement représentés dans les échantillons de carottes marines par les spores de fougères, d'algues et de champignons, ainsi que les kystes de Dinoflagellés. Les méthodes utilisées pour le traitement physico-chimique du sédiment, le calcul des concentrations polliniques, ainsi que les analyses microscopiques, seront détaillées dans les paragraphes suivants.

2.2.1 Echantillonnage et extraction physico-chimique

La thèse s'est appuyée sur un ensemble d'échantillons sédimentaires qui avaient préalablement été traités par Nathalie Combourieu-Nebout au laboratoire de palynologie de l'UMR EPOC à Bordeaux et au Laboratoire des Sciences du Climat et de l'Environnement à Saclay (LSCE). Un

échantillonnage supplémentaire a été réalisé en avril 2023 à la carothèque de l'IODP à Brême, afin de compléter la séquence palynologique avec une résolution tous les 10 cm pour le MIS 6 d'une part, et d'obtenir une résolution plus fine pour les MIS 3-5 d'autre part.

Au total, 130 échantillons supplémentaires ont été traités au cours de la thèse au laboratoire de palynologie de l'UMR HNHP au Muséum National d'Histoire Naturelle basé à l'Institut de Paléontologie Humaine à Paris, dont 120 ont été comptés (voir Tableau S3 dans les suppléments).

Le traitement a suivi la méthode d'extraction utilisée pour les précédentes études palynologiques de la carotte ODP 976 (Combourieu-Nebout et al., 1999, 2002; Combourieu-Nebout, Peyron, et al., 2009; Sassoon et al., 2023), d'après le protocole traditionnel de Faegri & Iversen (1964). Il repose sur une série d'attaques successives à l'acide chlorhydrique (HCl) qui permet de dissoudre la phase calcique du sédiment, ainsi qu'à l'acide fluorhydrique (HF) qui dissout la phase siliceuse. Les étapes du protocole sont détaillées ci-après :

1) Pesée du sédiment : entre 2 et 7 g, puis dissolution dans l'eau distillée et mesure volumétrique dans une éprouvette graduée.

2) Tamisage à 150 µm. Les refus de tamis sont ensuite séchés et conservés dans des piluliers. Ils sont généralement constitués de quelques restes détritiques minéraux (cailloux > 150 µm), et tests calciques de foraminifères. Dans un échantillon du MIS 6, trois spécimens de coquilles de gastéropodes planctoniques appartenant à l'espèce *Limacina retroversa* (Fig. 2.2) ont été récupérés, indicateurs d'eaux froides subarctique (Jeanne Rampal, communication personnelle, 2023).

3) Centrifugation du filtrat 5 min à 3000 r/min et transfert dans un tube à essai de 50 mL.

4) Ajout de deux pastilles de lycopodes de concentration connue (lot : 13761 grains de *Lycopodium* par pastille).

5) Attaque des culots à l'acide chlorhydrique (HCl 37%) à froid, pendant une à deux heures : ajout d'environ environ 25 mL d'HCl progressivement afin de contrôler l'effervescence.

6) Centrifugation, puis rinçage des culots à l'eau distillée (50 mL).

7) Attaque des culots à l'acide fluorhydrique (HF 40%) à froid, pendant 24h.

8) Centrifugation, puis rinçage des culots à l'eau distillée (50 mL).

9) Deux rinçages des culots par HCl 37% afin d'éliminer les fluorosilicates néoformés lors de l'attaque par HF. Laisser le deuxième rinçage agir une trentaine de minutes.

10) Centrifugation, puis trois rinçages successifs des culots à l'eau distillée (50 mL).

11) Filtration sur tamis de 10 µm. Récupération du filtrat, puis ajout de glycérol.

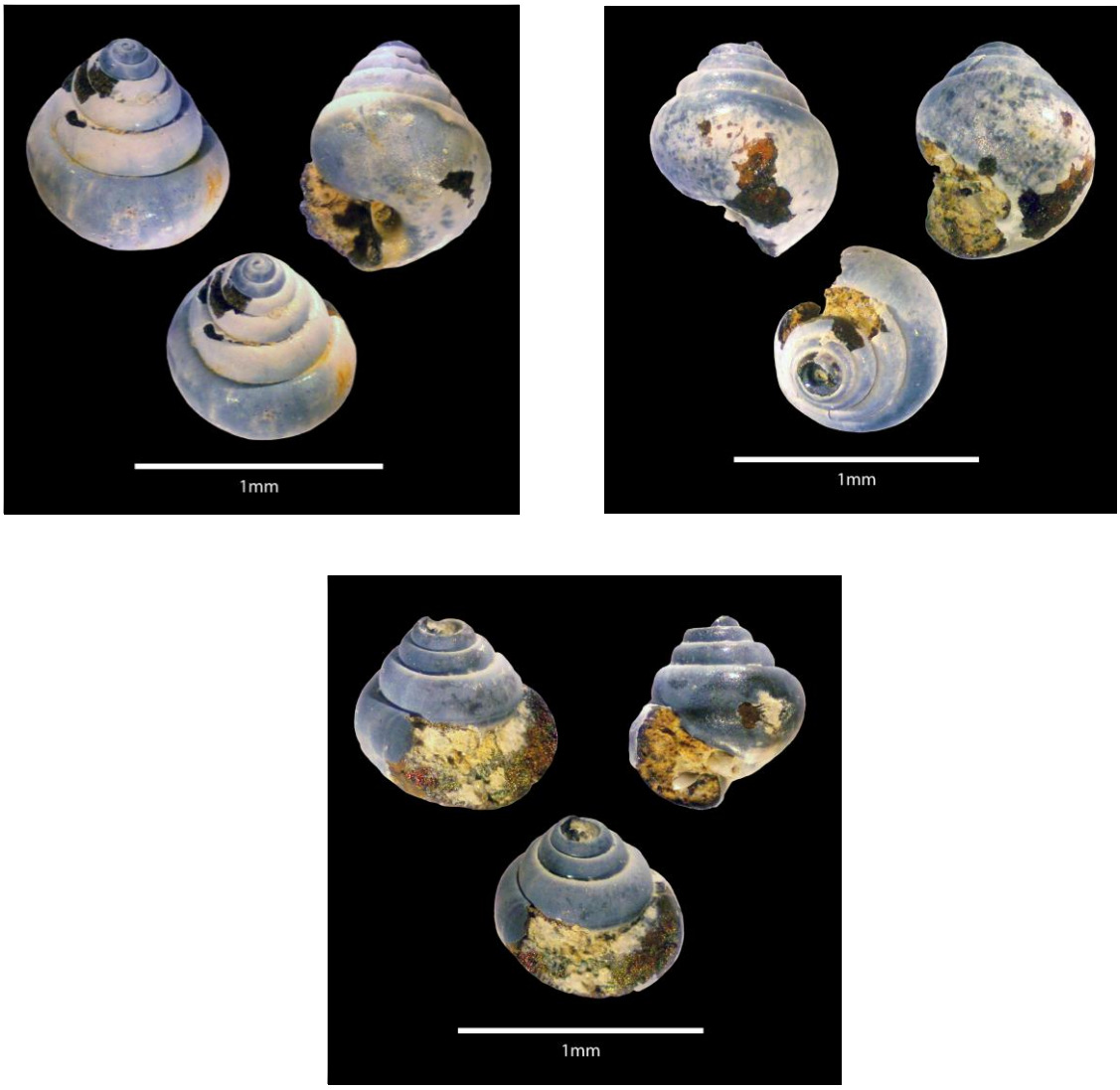
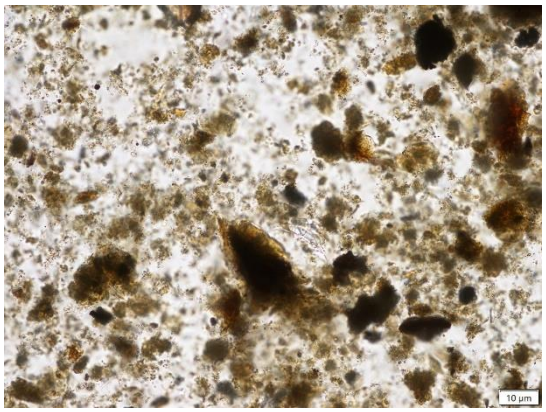


Fig. 2.2. Trois spécimens de *Limacina retroversa* identifiés dans le refus de tamis de l'échantillon B6H4 130-132 (profondeur: 47.40 m), correspondant au MIS 6. Détermination taxonomique : Jeanne Rampal, communication personnelle (2023). Photos : Dael Sassoon.

2.2.2 Problèmes de lisibilité et taphonomie

Suite aux premières séries de traitement, la lecture des lames était difficile en raison de la présence abondante de microparticules et de matière amorphe. La comparaison avec les échantillons traités précédemment par N. C.-N. (Fig. 2.3) et traités à l'HF 70% a montré une meilleure clarté des lames minces qui avaient subi un traitement à l'HF plus concentré.

C2H6 97-99 (traité à l'IPH en 2023, HF 40%)



C2H6 99-101 (traité à Bordeaux en 1998, HF 70%)

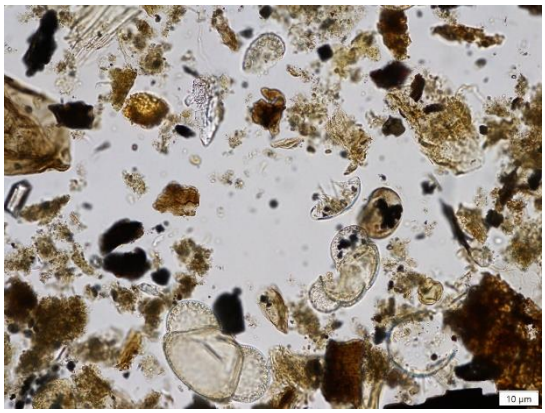
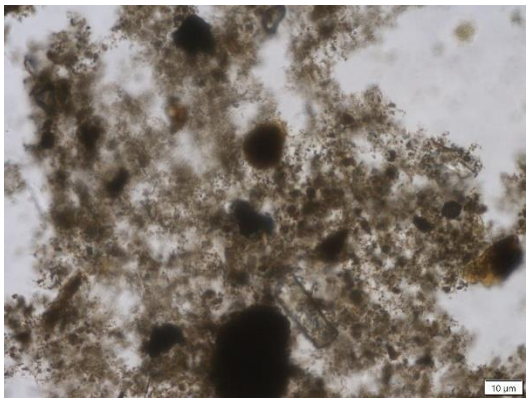


Fig. 2.3. Comparaison du facies de deux échantillons proches. A gauche échantillon traité à l'IPH au cours de la thèse (avec passage à HF 40%) et à droite échantillon traité lors des premières analyses palynologiques de la carotte ODP 976 en 1998 (avec passage à HF 70%).

Le traitement physico-chimique a alors été reconsidéré afin d'inclure un lavage à l'HF plus long et à plus haute concentration ainsi qu'une filtration accompagnée d'un passage aux ultrasons afin de mieux séparer les microéléments agglutinés pour améliorer la qualité du filtrage final. Le faciès résultant de cette modification ayant été jugé plus satisfaisant (Fig. 2.4), les 129 échantillons déjà traités ont été soumis à nouveau au lavage à l'HF (70%), ainsi qu'au filtrage à ultrasons.

Après HF 40%



Après HF 70%

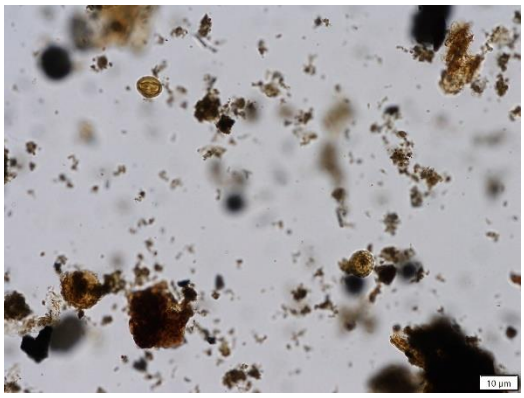


Fig. 2.4. Comparaison du facies d'un même échantillon traité durant la thèse à l'HF 40% (à gauche) et à 70% (à droite).

Un problème taphonomique récurrent dans les échantillons d'ODP 976 est posé par la présence de pyrite. En contexte littoral marin, la pyrite (FeS_2) peut être interprétée comme indicatrice

d'environnement anoxique riche en sulfures (Ejarque et al., 2022). L'acide nitrique permettrait d'éliminer la pyrite (Riding, 2021), mais sa précipitation dans les cavités des palynomorphes (Planche 1) rend impossible son élimination sans détruire le palynomorphe hôte. Il n'a donc pas été possible d'éliminer la pyrite, toutefois les déterminations des grains de pollen contenant de la pyrite ont généralement pu être faites avec fiabilité (Fig. 2.5).

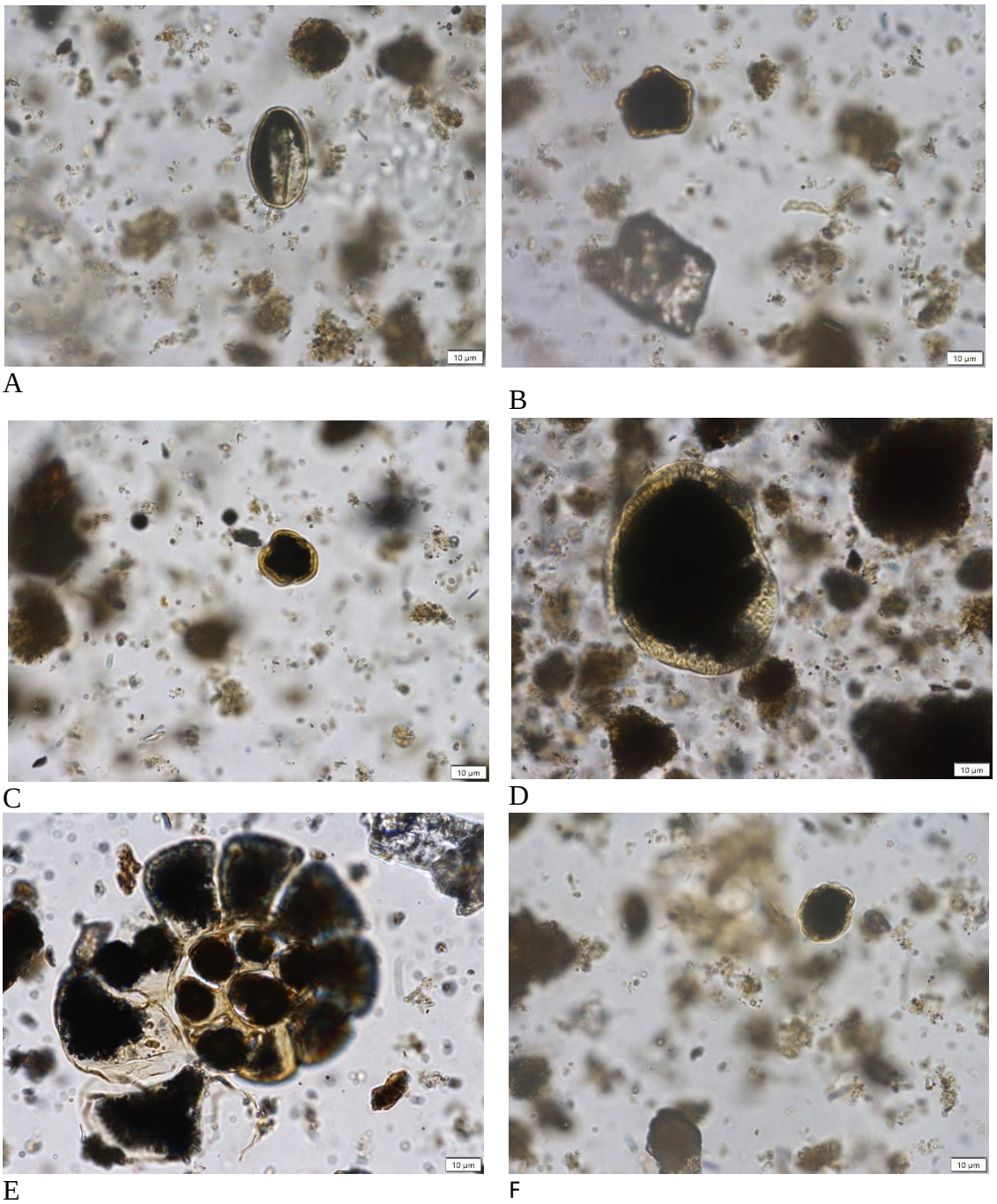


Fig. 2.5. Exemples de palynomorphes pyritisés. A : *Quercus* ; B : *Alnus*, C : *Artemisia* ; D : *Cedrus* ; E: Foraminifère; F: tricolpé (?) indéterminable.

2.2.3 Concentrations polliniques

L'usage d'un traceur externe de concentration connue est la méthode la plus largement utilisée pour le calcul des concentrations polliniques dans le sédiment traité. Des pastilles de spores de *Lycopodium* de concentration connue ont été utilisées dans ce travail. La concentration pollinique des échantillons est donnée par la formule :

$$Cp = \frac{S_p \times L_c}{N_L \times m}$$

Avec :

Cp : la concentration pollinique (en grains/grammes de sédiment)

S_p : la somme de tous les grains de pollen comptés

L_c : la somme des grains de *Lycopodium* comptés

N_L : la somme totale des grains de *Lycopodium* incorporés lors du traitement.

m : la masse de sédiment traitée en grammes (peut être remplacée par le volume V en cm^3)

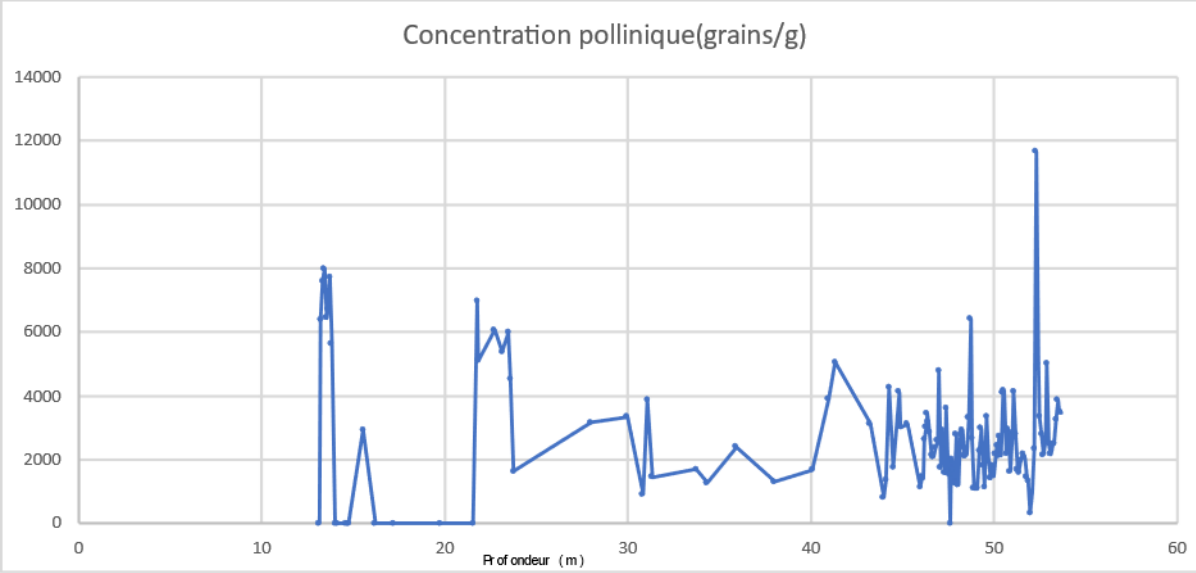


Fig. 2.6. Concentration pollinique calculée pour les 120 échantillons traités et analysés au cours de la thèse.

La lisibilité des lames suite au protocole ajusté est jugée bonne. La concentration pollinique des échantillons traités et analysés varie entre 337 et 11651 grains/grammes de sédiment (voir Fig. 2.6 et Tableau S3 dans les suppléments). Ces concentrations ne seront pas exploitées dans cette étude, et sont données à titre indicatif.

2.2.4 Analyses microscopiques

Un total de 213 échantillons complets a été compté au cours de la thèse. Les comptages de 16 autres échantillons ont été complétés afin de renforcer la somme pollinique qui était inférieure à 100 grains. Au final, 229 échantillons ont donc été apportés à la séquence, qui comprend maintenant 752 échantillons entre 0 et 54.76 m, correspondants à la période de la fin du MIS 7 au MIS 1.

Les comptages ont suivi la méthode généralement appliquée en contexte sédimentaire marin, et au cours des précédentes études sur la carotte ODP 976 (Combourieu-Nebout et al., 1999, 2002; Combourieu-Nebout, Peyron, et al., 2009; Sassoon et al., 2023). Une somme pollinique de 150 grains doit être atteinte, *Pinus* exclu. Ce dernier est généralement surreprésenté en contexte marin du fait (i) de son mode de transport anémogame qui lui permet une dispersion sur des distances très larges, et (ii) de la nature de l'enregistrement sédimentaire captant des grains de pollen provenant de distances à échelle régionale et subrégionale (Chmura et al., 1999; Heusser & Balsam, 1977; Mudie, 2011; Prentice, 1985).

L'identification des taxons polliniques a été effectuée d'après la collection de référence actuelle du laboratoire de palynologie du Muséum national d'Histoire naturelle, ainsi qu'en consultant les atlas de référence (Beug, 2004; Reille, 1992). 182 types polliniques ont été identifiés et classés par affinités écologiques (Tableau 2.1) suivant les classifications utilisées dans les études palynologiques précédentes de la séquence (Combourieu-Nebout, Peyron, et al., 2009; Sassoon et al., 2023).

Les planches 1 à 11 présentent des photographies microscopiques des principaux taxons polliniques identifiés au cours de ce travail (voir Suppléments). Des grains plus altérés ont également été inclus dans ces planches afin de donner un aperçu de la conservation différentielle des grains de pollen sous l'effet de divers processus taphonomiques.

Groupé écologique	Taxons polliniques identifiés
Pinus	*Pinus*
Forêt décidue tempérée	*Quercus* décidu, *Alnus*, *Betula*, *Fraxinus*, *Fagus*, *Ilex*, *Platanus*, *Populus*, *Pterocarya*, *Salix*, *Ribes*, *Sambucus*, *Taxus*, *Acer*, *Aesculus*, *Buxus*, *Carpinus*, *Ostrya*, *Castanea*, *Corylus*, *Cornus sanguinea*, *Hedera*, *Juglans*, Taxaceae, *Tilia*, *Ulmus*, *Viburnum*, *Zelkova*, *Syringa*
Autres arbres	Sapotaceae, *Carya*, Arecaceae, *Sterculia*, *Cuscuta*, *Arcethobium*
Forêt d'altitude	*Cedrus*, *Abies*, *Picea*
Ericaceae	Ericaceae, *Calluna vulgaris*, type *Arbutus*
Végétation pionnière	Cupressoideae (incluant *Cupressus*, *Juniperus*, Cupressoideae undiff)
Végétation méditerranéenne	*Quercus ilex*, *Olea*, *Phillyrea*, *Pistacia*, Cistaceae (including *Cistus*, *Helianthemum*, Cistaceae undiff), *Cistus ladaniferus*, Other Mediterranean: *Fraxinus ornus*, *Quercus suber*, *Tuberaria*, *Halimum*, *Jasminum*, *Ligustrum*, Oleaceae undiff, *Rhamnus*, Rhamnaceae, *Rhus*, *Ruta*, *Tamarix*, *Vitis*, *Myrtus*
Steppe et semi-désert	*Artemisia*, Amaranthaceae, *Ephedra* (including *Ephedra fragilis*-type, *Ephedra distachya*-type, *Ephedra altissima*-type, *Ephedra* undiff). Other semi-desertic: *Calligonum*, *Erodium*, *Hippophae*, *Eleagnus*, *Lygeum.*
Végétation herbacée	Asteroideae, Cichorioideae, Poaceae, Brassicaceae, Apiaceae, Convolvulaceae, *Calystegia*, Lamiaceae, Lamiaceae tricolpe-type, *Lamium*, *Phlomis*, *Rosmarinus*, *Stachys*, Liliaceae, *Allium*, *Scilla*, *Asphodelus*, Plantaginaceae undiff, *Plantago*, *Plantago lanceolata*, *Centaurea*, *Centaurea scabiosa*, *Centaurea jacea*, *Centaurea cyanus*, *Aristolochia*, *Asparagaceae*, *Boraginaceae*, *Echium*, *Heliotropium*, Campanulaceae, Cannabaceae, Caryophyllaceae, *Spergularia*, *Paronychia* / *Hernaria*, Celastraceae, *Euonymus*, Crassulaceae, *Sedum*-type, Dipsacaceae, *Knautia*, *Scabiosa*, *Cephalaria*, Euphorbiaceae, *Euphorbia*, *Mercurialis*, Fabaceae, *Lotus*, Papilionaceae, *Vicia*, Gentianaceae, Geraniaceae, *Geranium*, *Hypecoum*, *Hypericum*, *Impatiens*, Iridaceae, *Linum*, *Lonicera*, Malvaceae, Papaveraceae, Plumbaginaceae, *Limonium*, *Armeria*, Polygonaceae, *Polygonum*, *Rumex*, Primulaceae, Rannunculaceae, *Adonis*, *Helleborus*, *Reseda*, *Thalictrum*, *Rosaceae*, *Filipendula*, *Potentilla*, *Sanguisorba minor*-type, *Verbena officinalis*, Rubiaceae, *Galium*, Saxifragaceae, Scrophullariaceae, *Pedicularis*, *Verbascum*, *Euphrasia*, *Odontides*, Solanaceae, Thymelleaceae, Urticaceae, *Urtica*, Valerianaceae, *Valeriana*, *Valerianella*, *Centrenthus*, *Viola*
Herbacées aquatiques	Cyperaceae, *Polygala*, *Alisma*, *Butomus*, *Ceratophyllum*, *Lythrum*, *Hydrocharis*, *Potamogeton*, *Ruppia*, *Typha-Sparganium*, *Nuphar*, *Nymphaea*, *Miryophyllum*

Tableau 2.1. Principaux groupes écologiques et groupes de taxons végétaux utilisés pour l'interprétation des données palynologiques d'OPD 976.

2.2.5 NPPs

L'étude paléoécologique des NPPs est encore très récente, et se généralise de plus en plus en contexte lacustre et archéologique (e.g. Cugny et al., 2010; Gelorini et al., 2011; Miras, 2021; Miras et al., 2010, 2023; Revelles, 2017, 2019; Revelles et al., 2017; Shumilovskikh et al., 2016; Shumilovskikh et al., 2015). A l'exception des kystes de dinoflagellés, la signification écologique des NPPs en contexte marin reste très peu explorée (e.g. Bandarupalli et al., 2021; Coussin, 2021; Jones et al., 2019). Il est généralement admis que les spores de fougères, d'algues et de champignons reflètent l'environnement continental local, mais peuvent être transportées sur de plus grandes distances par les cours d'eau. Par ailleurs, de nombreuses espèces de champignons marins existent (Jones et al., 2019), et l'identification des spores reste encore difficile dû au manque de référentiel bien établi.

De nombreux NPPs sont présents dans les échantillons d'ODP 976, incluant principalement des kystes de dinoflagellés, des restes organiques de foraminifères, et une grande diversité de spores de champignon (les plus abondantes étant les Coniochaetaceae et Sordariaceae). Des identifications préliminaires de NPPs ont été réalisées au cours des analyses palynologiques sur le MIS 6 (voir planches microscopiques 12 à 17 dans les Supléments), mais ne seront pas exploitées dans ce travail. L'exploration plus systématique du potentiel des NPPs en contexte marin sera entrepris dans de futures recherches en systématisant leur comptage et en harmonisant l'identification taxonomique des types.

2.3 Modèle d'âge

2.3.1 Principes généraux

La construction d'un modèle d'âge pour les longues séquences marines est un point crucial d'une grande complexité, qui nécessite une bonne compréhension de la signification des différents proxys et de leur relation avec les phénomènes climatiques régionaux et globaux (Lisiecki et al., 2022). En l'absence de datations absolues, l'approche la plus utilisée est celle de la corrélation graphique entre une courbe de la séquence d'étude jugée comme reflétant des changements à échelle globale, et une courbe de référence globale.

Le rapport isotopique des tests de foraminifères est le proxy le plus utilisé afin de réaliser ces corrélations entre longues séquences, puisque considéré comme un indicateur fiable des conditions de températures océaniques globales, qui ont fluctué au cours des différents stades isotopiques marins (MIS) et des oscillations plus rapides type Dansgaard-Oeschger (D-O) (Lisiecki et al., 2022; Lisiecki & Stern, 2016; Lisiecki & Raymo, 2005). Le rapport isotopique des foraminifères benthiques et planctoniques est globalement similaire, mais diffère en ce qu'ils représentent respectivement une

signature de la température océanique globale plus proche de celle enregistrée dans les carottes de glace antarctique pour le premier, et des carottes de glace arctique pour le second (Shackleton et al., 2000).

Plusieurs courbes de référence globales peuvent être utilisées selon la résolution et les caractéristiques du signal à calibrer. La courbe isotopique de l'oxygène marin de référence est la plus utilisée pour les derniers 5.3 millions d'années car elle correspond à la compilation des enregistrements isotopiques de 57 séquences marines réparties à la surface du globe (le « *stack* LR04 »), à partir de laquelle sont définies les limites des MIS (Lisiecki & Raymo, 2005).

Pour une calibration chronologique plus fine dans l'Hémisphère nord, les courbes isotopiques des carottes de glace arctiques (NGRIP, GRIP, GISP2 and NEEM) sont les plus généralement utilisées, offrant une stratigraphie fine et bien définie des oscillations rapides (GI et GS) du dernier cycle climatique (Rasmussen et al., 2014). L'échelle chronostratigraphique de ces évènements rapides est appelée « GICC05 » pour les âges inférieurs à 60.2 ka BP (Andersen et al., 2006; Blockley et al., 2012; Svensson et al., 2008), et « GICC05modelext » pour les âges plus anciens, basés sur une chronologie étendue par une approche de modélisation (Rasmussen et al., 2014). Ainsi, pour l'Atlantique Nord, l'approche la plus généralement appliquée est celle de la calibration des enregistrements à travers la corrélation des courbes isotopiques planctoniques avec celles des carottes du Groënland (par exemple: Margari et al., 2020; Sanchez Goñi et al., 2012; Sánchez Goñi et al., 2017).

Les courbes isotopiques de l'Antarctique, en particulier celle d'EPICA Dome C offrent une résolution moins bonne que celles de l'hémisphère Nord, mais couvrent les oscillations climatiques rapides à échelle globale des derniers 800 000 ans (Bazin et al., 2013; Bouchet et al., 2023; Jouzel et al., 2007; Masson-Delmotte et al., 2010). Plus récemment, les courbes isotopiques de l'oxygène des spéléothèmes asiatiques, en particulier provenant des grottes de Hulu, Sanbao et Dongge, sont également utilisées comme courbes de référence dans la construction des modèles d'âge, puisqu'elles reflétent les cycles de moussons asiatiques connectés aux grandes variations des cycles climatiques, ainsi qu'aux cyclicités plus rapides type D-O (e.g. Cheng et al., 2016; Liang et al., 2022; Wang et al., 2018; Wang et al., 2001).

2.3.2 Méthodes pour ODP 976

La construction d'un modèle d'âge pour la carotte ODP 976 sur les derniers 200 000 ans a représenté une partie importante de ce travail et s'est appuyée sur différentes approches qui seront par la suite détaillées dans chacune des parties de discussion.

En premier lieu, 15 datations radiométriques au ^{14}C des tests de foraminifères planctoniques ont été publiées précédemment pour la section supérieure de la carotte (Combourieu-Nebout et al., 2002; Combourieu-Nebout, Peyron, et al., 2009). Ces datations ont été recalibrées avec la courbe de référence la plus récente pour le milieu marin, en appliquant une correction ΔR = 175 ± 35 pour l'effet réservoir en Mer d'Alboran (Charton, 2025, Table 1; Heaton et al., 2020; Siani et al., 2000). Une approche de modélisation de ces datations radiométriques sur l'interface Oxcal 4.4 (Ramsey, 1995) a mis en évidence une tendance au vieillissement des dates au-delà de 10 m de profondeur (~30 ka BP), par rapport à un modèle d'âge basé sur l'alignement de la courbe des taxons polliniques tempérés avec la courbe NGRIP sur l'échelle GICC05 (voir Fig. 2.7) Ainsi, quatre des datations au-delà de 10 m de profondeur ont été écartées du modèle d'âge final. Seule la datation de l'échantillon C2H5 45-47 a été retenue valide car très proche du point de calage utilisé pour le GI6 et cohérente avec le modèle d'âge final.

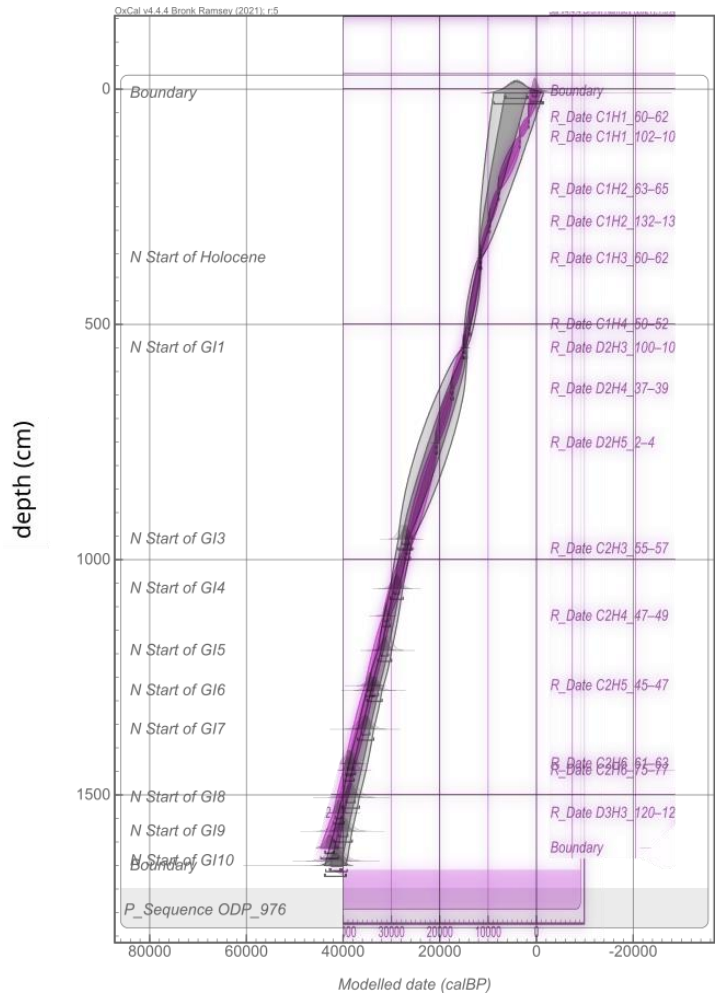


Fig. 2.7. Comparaison entre les deux modèles d'âge basés sur les datations au radiocarbone uniquement (rose) et sur les points de calage avec la stratigraphie des interstadiaires du Groënland (gris). Modèles d'âge générés sur Oxcal 4.4. (Ramsey, 1995). En dessous de 1000 cm de profondeur, un vieillissement des dates radiocarbones est observé par rapport au modèle d'âge basé sur la corrélation des interstadiaires.

Pour le reste de la séquence, le modèle d'âge précédent établi par von Grafenstein et al. (1999) reposait principalement sur la calibration de la courbe des isotopes planctoniques avec la stratigraphie des MIS, ainsi que sur quelques évènements biostratigraphiques (De Kaenel et al., 1999). Il convenait de mettre à jour ce modèle d'âge afin d'intégrer les analyses isotopiques à plus hautes résolution disponible depuis, et d'appliquer les nouvelles méthodes de calibration chronologique avec la stratigraphie isotopique du Groënland.

Dans un premier temps, pour la partie du MIS 3 étudiée à très haute résolution, un modèle d'âge provisoire a été construit afin de compléter les datations au radiocarbone en corrélant les interstadiaires du Groënland avec la courbe pollinique des taxons tempérés (forêt décidue tempérée). Le choix de s'appuyer sur une courbe pollinique plutôt que sur la courbe isotopique a été motivé par la très haute résolution offerte par la première sur cet intervalle, enrichie par nos nouvelles analyses palynologiques. Ce modèle d'âge est celui adopté pour le premier chapitre de discussion de la thèse (section 4) et qui a fait l'objet d'une publication scientifique (Charton et al., 2025).

Par la suite, il a été fait le choix d'établir un modèle d'âge plus général avec une méthodologie homogène pour la carotte jusqu'à 110 ka BP, qui s'appuie plutôt sur l'enregistrement isotopique des foraminifères planctoniques. Une corrélation graphique entre la courbe des isotopes planctoniques d'ODP 976 d'une part (données publiées et données inédites de R. Zahn) et la stratigraphie isotopique des interstades du Groënland d'autre part a été entreprise, en choisissant comme point de contrôle le point intermédiaire entre les deux valeurs isotopiques extrêmes (voir section 4.3). Le positionnement des points de contrôle a représenté une tâche complexe, certainement dû à l'atténuation du signal des cycles D-O dans l'enregistrement isotopique en Méditerranée (Combourieu-Nebout et al., 2002).

Pour l'intervalle entre 115 et 145 ka BP, nous avons utilisés les sept points de contrôle chronostratigraphiques définis par Jiménez-Amat et Zahn (2015), basés sur la calibration de la courbe de température des eaux de surface (SST) à partir du rapport élémentaire Mg/Ca avec les courbes isotopiques de deux spéléothèmes de référence des grottes de Corchia et Dongge (Drysdale et al., 2009; Kelly et al., 2006).

Enfin, pour l'intervalle du MIS 6 antérieur à 146 ka BP, aucune courbe isotopique ou de températures à haute résolution pour ODP 976 n'était disponible. La courbe pollinique des taxons tempérés à haute résolution produite dans cette étude a alors été utilisée, afin d'établir une corrélation avec la courbe palynologique de référence de la carotte atlantique MD01-2444 (Margari et al., 2010, 2014). Le modèle d'âge de la carotte MD01-2444 repose sur la corrélation stratigraphique de la courbe des isotopes benthiques avec la courbe isotopique de l'Antarctique, sur l'échelle chronologique AICC2012 (Bazin et al., 2013; Fletcher, Sánchez Goñi, et al., 2010; Shin, Nehrbass-Ahles,

Grilli, Beeman, et al., 2020). Cinq points ont été sélectionnés, correspondant à des pics de forêt tempérée dans la carotte Atlantique, et à des pics du total de taxons tempérés dans ODP 976 (incluant donc aussi les Ericaceae et les taxons méditerranéens, voir méthodes dans la section 7 pour plus de détails).

Au total, le modèle d'âge d'ODP 976 pour les derniers 200 000 ans repose donc sur une interpolation linéaire entre 44 points, qui correspondent à des datations radiocarbones et des points de calage chronostratigraphiques des courbes isotopiques et pollinique d'ODP 976 par rapport au carottes de glace du Groënland, aux spéléothèmes de Corchia et Dongge, et à la carotte MD01-2444 (Tableau 2.2, Fig. 2.8).

Sample name / event name	Type of control point	depth_m	Age (yrs calBP, B2k et BP)	Error (yrs)	References
Core top	core top	0	0	_	_
C 1H 1 60–62	R_date	0.61	1 280	-170 / +168	1
C 1H 1 102–104	R_date	1.03	3 100	-187 / + 203	1
C 1H 2 63–65	R_date	2.14	7 481	-166 / + 162	1
C 1H 2 132–134	R_date	2.83	9 409	-224 / +190	1
C 1H 3 60–62	R_date	2.61	11 213	-201 / + 251	1
C 1H 4 50–52	R_date	5.01	13 466	-230 / + 261	1
D 2H 3 100–102	R_date	5.51	14 549	-391 / + 373	1
D 2H 4 37–39	R_date	6.38	16 733	-333 / + 304	1
D 2H 5 2–4	R_date	7.53	20 107	-385 / + 372	1
C 2H 3 55–57	R_date	9.78	25 986	-665 / + 780	1
Start of GI4	GICC05	10.58	28 900	900	2
Start of GI5	GICC05	12.08	32 500	1 130	2
C 2H 5 45–47	R_date	12.69	33 737	-1667 / + 1 482	1
Start of GI6	GICC05	12.78	32 740	1 210	2
Start of GI7	GICC05	12.68	35 480	1 320	2
Start of GI8	GICC05	15.05	38 220	1 450	2
Start of GI9	GICC05	15.89	40160	1 580	2
Start of GI10	GICC05	16.59	41 460	1 630	2
Start of GI11	GICC05	17.39	42 340	1 740	2
Start of GI12	GICC05	18.08	46 860	1 910	2
Start of GI13	GICC05	18.5	49 280	2 031	2
Start of GI14	GICC05	19.8	54 220	2 301	2
Start of GI15	GICC05	21.79	55 800	2 392	2
Start of GI16	GICC05	22.83	58 280	2 511	2
Start of GI17	GICC05	23.09	59 440	2 573	2
Start of GI18	GICC05modelext	24.85	64 000	_	2
Start of GI19	GICC05modelext	26.6	72 340	_	2
Start of GI20	GICC05modelext	27.8	76 440	_	2
Start of GI21	GICC05modelext	30.78	85 060	_	2
Start of GI22	GICC05modelext	32.25	90 040	_	2

Start of GI23	GICC05modelext	34.43	104 520	_	2
Start of GI24	GICC05modelext	36.11	108 280	_	2
Dongge Cave D5	Speleothème	36.88	117 430	_	3
Dongge Cave D4	Speleothème	37.8	121 430	_	3
Corchia Cave C2	Speleothème	38.92	122 660	_	3
Corchia Cave C1	Speleothème	39.78	126 540	_	3
Dongge Cave D3	Speleothème	40.25	128 730	_	3
Dongge Cave D2	Speleothème	42.61	135 570	_	3
Dongge Cave D1	Speleothème	44.14	142 090	_	3
Temperate pollen peak	MD01-2444	46.4	149 430	_	4
Temperate pollen peak	MD01-2444	48.5	160 000	_	4
Temperate pollen peak	MD01-2444	49.3	170 070	_	4
Temperate pollen peak	MD01-2444	50.48	178 420	_	4
Temperate pollen peak	MD01-2444	53.2	192 760	_	4

Tableau 2.2. Liste des datations et points de contrôle utilisés pour construire le modèle d'âge d'ODP 976 sur 200 000 ans. Les datations radiocarbones provenant de Combourieu-Nebout et al. (2002) ont été recalibrées sur Oxcal en appliquant la courbe Marine20 et une correction de l'effet réservoir ΔR=-175 ± 35 (voir méthodes). La date calibrée indiquée correspond à la médiane à 95.4%

Ref. 1: Combourieu-Nebout et al., 2002 (dates recalibrées)

Ref. 2: Rasmussen et al., 2014 ; von Grafenstein et al., 1999 et données isotopiques inédites de la carotte ODP 976 pour les MIS 5-3 présentées dans cette étude.

Ref. 3: Jiménez-Amat and Zahn, 2015 ; Kelly et al., 2006 ; Drysdale et al., 2009

Ref 4: Margari et al., 2010

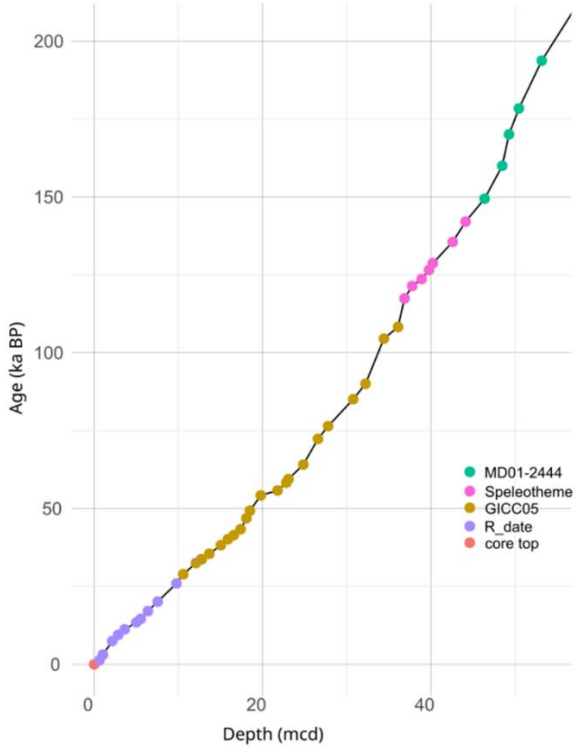


Fig. 2.8. Modèle d'Age pour ODP 976 construit dans cette étude couvrant les derniers 200 000 ans. R_date : datations ^{14}C sur tests de foraminifères planctoniques ; GICC05 : points de contrôles chronostratigraphiques sur la courbe isotopique des foraminifères planctoniques par rapport à la

stratigraphie des interstadiaires du Groënland GICC05 et GICC05modelext ; *Speleotheme* : points de contrôle chronostratigraphiques établis par Jiménez-Amat et Zahn (2015) sur la courbe des températures de surfaces (ratio élémentaire Mg/Ca) par rapport aux courbes isotopiques des spéléothèmes de Corchia (Drysdale et al., 2009) et Dongge Cave (Kelly et al., 2006) ; MD01-2444 : points de contrôle chronostratigraphiques établis par corrélation entre la courbe pollinique de la forêt tempérée de la carotte MD01-2444 (Margari et al., 2010), et celle de la carotte ODP 976 (cette étude), sur l'échelle chronologique AICC2012. Voir texte pour les détails.

2.4 Analyses statistiques multivariées

Plusieurs analyses statistiques multivariées ont été appliquées aux données palynologiques afin d'aider à leur interprétation. Celles-ci incluent des analyses de cluster, de corrélation, et des analyses en composantes principales.

2.4.1 Analyses de cluster

L'analyse de cluster est réalisée en même temps que le diagramme pollinique, sur l'environnement R avec le package *rioja* (Juggins, 2024). La méthode de clustering CONISS est utilisée afin d'aider à définir des *clusters*, ou zones polliniques, basées sur la ressemblance de l'assemblage pollinique d'échantillons proches. Le clustering est basé sur le calcul d'une matrice de dissimilarité à partir des assemblages polliniques, à laquelle une contrainte sur l'ordre des échantillons est appliquée. On parle de *clustering* sous contrainte hiérarchique ou stratigraphique (Grimm, 1987). Afin de choisir le nombre de clusters à retenir, et donc le nombre de zones polliniques significatives, l'approche par *brocken stick* est utilisée (Bennett, 1996).

Si cette approche est très utile et permet l'affichage d'un arbre de clusters très visuel, sa principale limitation réside dans sa grande sensibilité aux différences de résolution temporelle dans la séquence. En effet, les zones analysées à plus haute résolution tendent à être divisée en plus de clusters / zones polliniques, tandis que les zones étudiées à plus faibles résolution ne donneront qu'un nombre moindre de clusters. Pour cette raison, l'expertise du palynologue reste fondamentale et doit souvent accompagner l'analyse de cluster afin de séparer des zones du diagramme pollinique visuellement très différentes dans leur assemblage pollinique, mais qui n'aurait pas été identifié à travers l'analyse CONISS à cause de la résolution plus faible.

2.4.2 Analyses de corrélation

La corrélation positive, négative ou nulle entre différentes variables, en l'occurrence des taxons polliniques et autres indicateurs paléoclimatiques (minéraux argileux, isotopes…), est établie à partir d'un indice de corrélation. L'indice de corrélation de Pearson a été utilisé (Bolar, 2019), et la visualisation de la matrice a été obtenue avec le package *corrplot* (Wei et al., 2024).

2.4.3 Analyses en Composantes Principales (ACP)

L'analyse en composantes principales (ACP) est largement utilisée en support de l'interprétation des données palynologiques basées sur le diagramme pollinique (par exemple: Fourcade et al., 2022; Sassoon et al., 2023). Elles permettent d'étudier les relations de corrélation dans un jeu de données comportant un nombre important de variables et d'individus à partir d'une matrice de covariance, en projetant la variance des différences variables dans un repère en *n* dimensions (composantes principales - CP). Les variables sont ici représentées par les taxons polliniques, et les individus par les échantillons analysés. Les CP portent le pourcentage d'explication de la variance totale du jeu de données, avec un pourcentage de variance croissant plus le nombre de CP sélectionnées est grand : l'axe 1 (première CP) porte le plus grand pourcentage d'explication de la variance, et ainsi de suite. Plus le pourcentage d'explication des deux premières CP sélectionnées est grand, plus l'ACP est considérée comme robuste puisque reflétant une part importante de la variance totale du jeu de données. Chaque variable est caractérisée par sa corrélation aux deux axes. Plus une variable est éloignée de l'origine du repère, plus son poids est important, et plus elle proche d'un axe du repère, plus elle est corrélée à cet axe.

L'analyse en composantes principales est une méthode de simplification, qui entraine également une perte d'information importante liée à la déformation de données complexes projetées dans un repère en 2D. Des précautions doivent donc être prises lors de l'interprétation des résultats, en considérant le pourcentage de représentation des axes, et la répartition des variables dans l'espace bidimensionnel. Les packages *ade4* (Dray et al., 2025) et *factoextra* (Kassambara & Mundt, 2020) ont été utilisées pour réaliser les ACP.

2.5 Reconstructions climatiques quantitatives à partir du pollen : une approche multiméthode

2.5.1 Principe et application à la séquence ODP 976

La reconstruction des conditions climatiques passées représente un enjeu fondamental pour éclairer notre compréhension des mécanismes complexes derrière le changement climatique actuel, ainsi que la réponse possible des écosystèmes méditerranéens. En particulier, reconstruire l'évolution des précipitations et des dynamiques saisonnières dans le passé semble crucial pour mieux comprendre le développement et l'impact de la sécheresse et du dérèglement du régime saisonnier des précipitations en Méditerranée (Combourieu-Nebout et al., 2009; Donders et al., 2021; Luterbacher et al., 2012). En appliquant cette approche à notre étude de la séquence ODP 976, les questions scientifiques suivantes se posent : comment ont varié les précipitations annuelles et saisonnières au cours du Pléistocène moyen récent et du Pléistocène supérieur ? Comment ont-elles

évolué dans le cadre des cyclicités climatiques orbitales ainsi que des oscillations à plus courte échelle de temps ?

Depuis la fin du XXe siècle, différentes méthodes de reconstruction quantitative des paramètres climatiques à partir de données polliniques ont été développées (Chevalier et al., 2020). Appliquées à de longues séries temporelles européennes, elles permettent d'estimer l'évolution passée des températures et précipitations annuelles et saisonnières à partir des données palynologiques fossiles d'un site donné. Si ces méthodes ont été largement appliquées en région méditerranéenne pour la période holocène (les derniers ~11 700 ans) (Cheddadi et al., 1998; D'Oliveira et al., 2023; Dugerdil et al., 2021; Herzschuh et al., 2023; Joannin et al., 2012; Luterbacher et al., 2012; Mauri et al., 2015; Peyron et al., 1998, 2011, 2013, 2017; Robles, 2024), un nombre plus limité d'applications existe pour les périodes plus anciennes du Pléistocène (Combourieu-Nebout et al., 2009; Davis et al., 2022; Guiot, 1987, 1990; Guiot et al., 1989, 1993; Joannin et al., 2011; Robles et al., 2025; Sánchez Goñi et al., 2021).

Chevalier et al. (2020) dresse une synthèse de l'historique et des principes écologiques et mathématiques des différentes méthodes existantes. Cinq assomptions fondamentales supportent ces approches de quantification climatique à partir du pollen :

1) L'assemblage pollinique d'échantillons actuels est fortement relié aux conditions climatiques de la région où ils ont été prélevés.

2) La relation climat / végétation et donc climat / pollen est restée stable dans le temps (principe d'actualisme)

3) Les variables climatiques reconstruites sont les plus déterminantes pour la composition de la végétation reflétée par l'assemblage pollinique, alors que d'autres variables ne seraient que d'importance mineure.

4) Les taxons polliniques identifiés dans la base de données actuelles et fossiles correspondent aux mêmes entités biologiques (principe d'actualisme)

5) Le modèle mathématique appliqué dans la méthode représente fidèlement la complexité des relations entre variables climatiques et réponse écologique de la végétation.

Le principe d'actualisme est à la base de toute méthode de quantification des paramètres climatiques à partir du pollen. Le principe peut être résumé ainsi : deux assemblages polliniques actuels et fossiles proches reflètent une végétation semblable dans le passé et dans le présent, et sont donc le résultat de conditions climatiques similaires. Ainsi, reconstruire les conditions climatiques d'un échantillon fossile revient à trouver un ou plusieurs assemblages polliniques actuels proches afin de lui associer leurs valeurs de paramètres climatiques (selon un algorithme qui dépend de la méthode

appliquée) : c'est le principe de la « substitution du temps par l'espace » («*space-for-time Substitution* », Fig. 2.9).

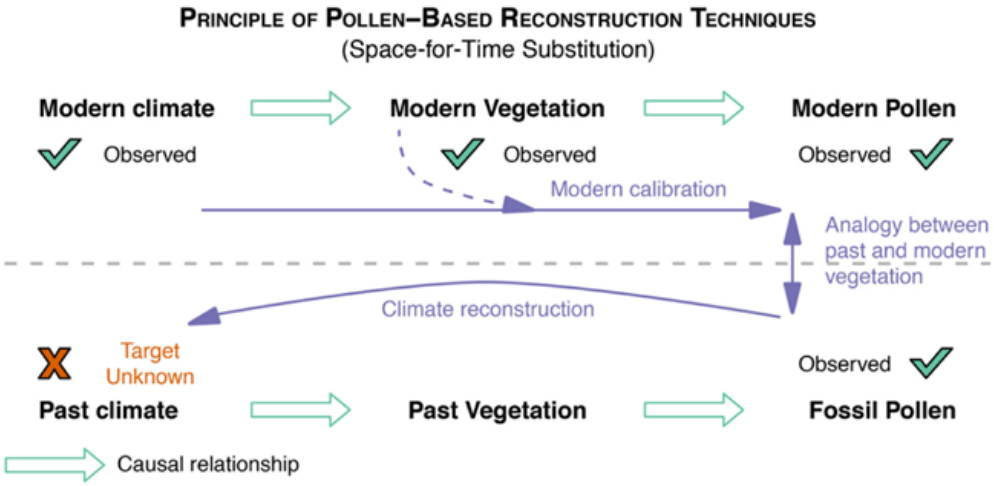


Fig. 2.9. Schéma du principe sur lequel reposent les méthodes de reconstructions climatiques à partir du pollen (Chevalier et al., 2020).

Différentes méthodes existent afin de reconstruire les paramètres climatiques à partir des assemblages polliniques, basées sur des approches mathématiques différentes. Il a été montré qu'utiliser une approche multiméthode augmente la robustesse des paramètres climatiques reconstruits (Brewer et al., 2008; D'Oliveira et al., 2023; Dugerdil et al., 2021; Peyron et al., 2013; Robles et al., 2023, 2025; Salonen et al., 2019). Les quatre méthodes sélectionnées dans cette étude seront décrites dans les paragraphes suivants : la méthode des analogues modernes (*Modern Analogues Technique* - MAT), une méthode de régression par les moindres carrés partiels (*Weighted Averaging Partial Least Squares* - WA-PLS), ainsi que deux approches par réseaux de neurones, *Random Forest* (RF) et *Boosted Regression Trees* (BRT). Six paramètres ont été reconstruits : PANN (précipitations annuelles), MAAT (températures annuelles), SUMMERPR (précipitations d'été), WINTERPR (précipitations d'hivers), MTWA (température du mois le plus chaud) and MTCO (température du mois le plus froid).

L'application des quatre méthodes a été réalisée sur l'environnement R à l'aide des packages *rioja* pour MAT et WA-PLS (Juggins, 2024), *dismo* pour BRT (Hijmans et al., 2024) et *randomForest* pour RF (Breiman et al., 2024). Le script a été écrit par L. Dugerdil en collaboration avec O. Peyron, M. Robles et L. d'Oliveira, et adapté à la séquence d'ODP 976 au cours de cette thèse avec O. Peyron et M. Robles.

2.5.2 La méthode des analogues modernes (MAT)

La méthode des analogues modernes (*Modern Analogue Technique*) est la méthode la plus couramment utilisée et la première développée pour reconstruire les paramètres climatiques à partir du pollen (Guiot, 1990). Il s'agit d'une méthode basée sur la comparaison directe des assemblages polliniques actuels et fossiles. Elle repose sur la sélection d'un nombre défini d'échantillons modernes dont l'assemblage pollinique est proche de l'échantillon fossile, et qui sont alors considérés comme analogues. La sélection des analogues est basée sur le calcul d'un index de dissimilarité (*squared-chord distance*) entre l'échantillon fossile et les échantillons actuels. Une moyenne pondérée des valeurs des paramètres climatiques des analogues sélectionnés est ensuite réalisée afin d'obtenir la valeur reconstruite pour l'échantillon fossile. Cette méthode a été largement appliquée aux séquences palynologiques européennes et montre de bons résultats, proches de ceux obtenus avec d'autres proxys indépendants comme les biomarqueurs lipidiques (brGDGTs) (Cheddadi et al., 1998; Davis et al., 2003; D'Oliveira et al., 2023; Dormoy et al., 2009; Dugerdil et al., 2021; Guiot et al., 1993; Mauri et al., 2015; Peyron et al., 2011, 2013; Robles et al., 2023; Sassoon et al., 2025; Sinopoli et al., 2019).

2.5.3 Une approche par régression : *Weighted Averaging Partial Least Squares* (WA-PLS)

La méthode WA-PLS est une approche par régression, ou fonction de transfert. Elle est basée sur la modélisation de la relation non-linéaire et unimodale entre les paramètres climatiques et l'abondance relative des taxons polliniques (ter Braak & Juggins, 1993). Elle repose sur l'assomption que les espèces végétales sont plus abondantes dans des conditions climatiques proches des valeurs optimales, auxquelles elles sont le mieux adaptées. Après calibration à partir du jeu de données actuelles, ces fonctions sont ensuite appliquées aux échantillons fossiles afin de calculer les paramètres climatiques pour chaque échantillon par rapport à son assemblage pollinique. Avec la MAT, la WA-PLS est considérée parmi les méthodes les plus robustes et les plus appliquées (Camuera et al., 2022; Herzschuh et al., 2023; Joannin et al., 2011, 2012; Sánchez Goñi et al., 2021; Sassoon et al., 2025).

2.5.4 Les approches par réseaux de neurones : *Random Forest* (RF) et *Boosted Regression Trees* (BRT)

Contrairement aux deux méthodes précédentes, la RF et la BRT sont basées sur une approche par *machine learning*. Les deux méthodes estiment les paramètres climatiques des échantillons modernes en construisant un grand nombre d'arbres de régression multiple qui génèrent des jeux de données polliniques par *bootstapping* (c'est-à-dire par rééchantillonnage multiple aléatoire) (Chevalier et al., 2020). Les valeurs des paramètres climatiques à reconstruire sont ensuite moyennées sur tous les arbres de régression établis. Tandis que la RF sélectionne les échantillons de manière

complètement aléatoire pour construire les arbres de régression, la BRT assigne une plus haute probabilité d'être sélectionnés aux échantillons n'ayant pas été sélectionnés précédemment.

Ces méthodes ont été appliquées aux séquences palynologiques récemment, avec des résultats prometteurs (D'Oliveira et al., 2023; Robles et al., 2023; Salonen et al., 2014, 2019; Sassoon et al., 2025).

2.5.5 Extraction des paramètres climatiques actuels

Les paramètres climatiques actuels correspondant à la localisation d'ODP 976 ont été extraits à partir des données de ERA 5, produit de la réanalyse climatique mondiale du Centre européen pour les prévisions météorologiques à moyen terme (CEPMMT), qui intègre les observations météorologiques connues depuis 1950 à des approches de modélisation climatiques (voir Hersbach et al., 2020 et références).

Ces valeurs des six paramètres climatiques actuels ayant pour but d'être comparées aux valeurs reconstruites pour le passé à partir de la carotte ODP 976, une moyenne à la fois spatiale et temporelle a été réalisée afin de rendre compte du caractère régional et pluriannuel des paramètres climatiques reconstruits à partir d'un carottage marin. Les six valeurs extraites correspondent donc à la moyenne des paramètres climatiques de 1960 à 2022, sur un rayon de 400 km autour du point de carottage d'ODP 976 (Fig. 2.10)

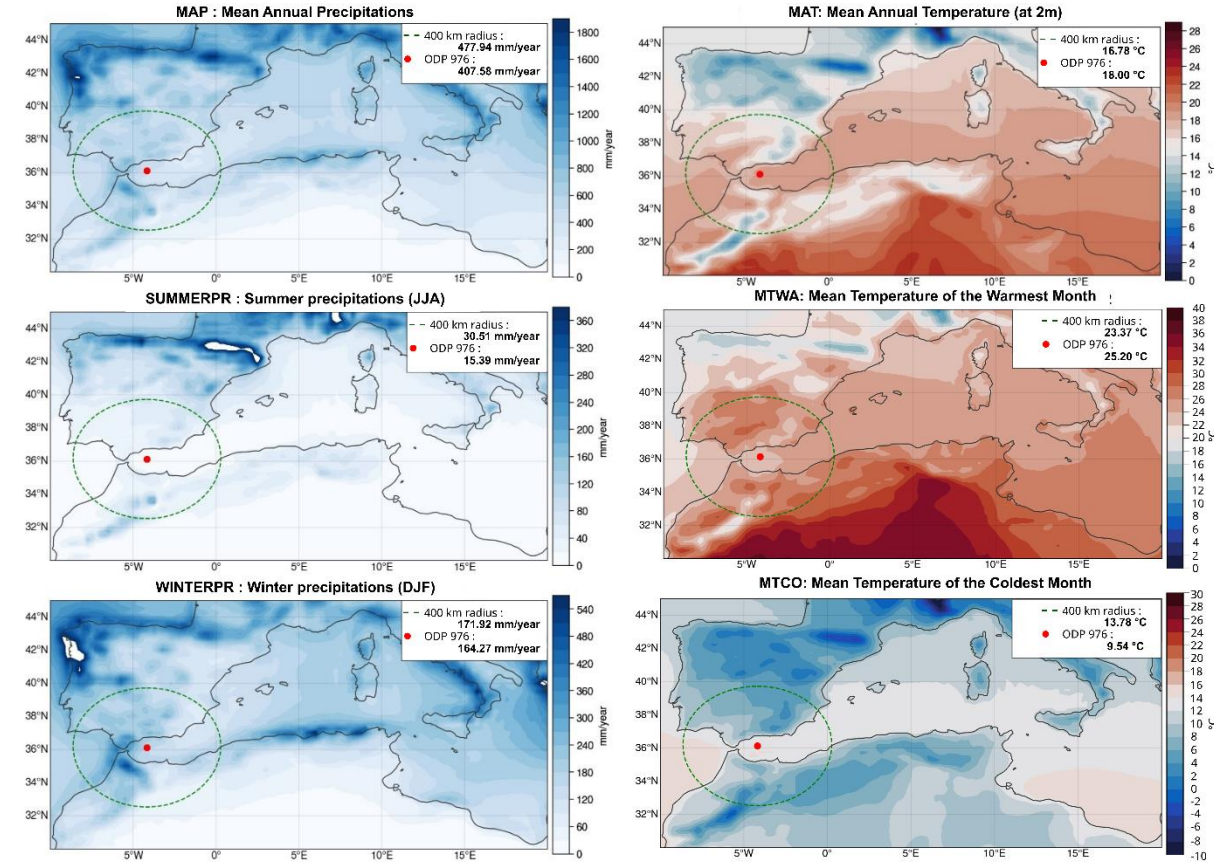


Fig. 2.10. Cartes des valeurs modernes des six paramètres climatiques en Méditerranée occidentale à partir du modèle ERA 5 1960-2022 du ECMRWF (*European Centre for Medium-Range Weather Forecasts*) (Hersbach et al., 2020). Le point rouge indique la valeur à la localisation précise d'ODP 976 ; la valeur retenue pour les comparaisons avec les reconstructions passées est celle de la moyenne du radius de 400 km autour de la carotte. Extraction des valeurs : Nicolas Michalezyk.

2.5.6 Base de données d'échantillons actuels

La base de données d'échantillons actuels utilisée pour calibrer les méthodes de reconstructions climatiques a été assemblée par Peyron et al. (2013, 2017), Dugerdil et al. (2021), et Robles (2024). Elle comprend 3373 échantillons répartis sur l'ensemble de l'Eurasie et une partie du Maroc (Fig. 2.11). Une procédure de biomisation a été suivie pour attribuer un Biome de référence à chaque échantillon, basé sur son assemblage pollinique et les types fonctionnels de plantes (*Plant Functional Types* - PFTs) (Guiot et al., 1993; Peyron et al., 1998; Prentice et al., 1992, 1996).

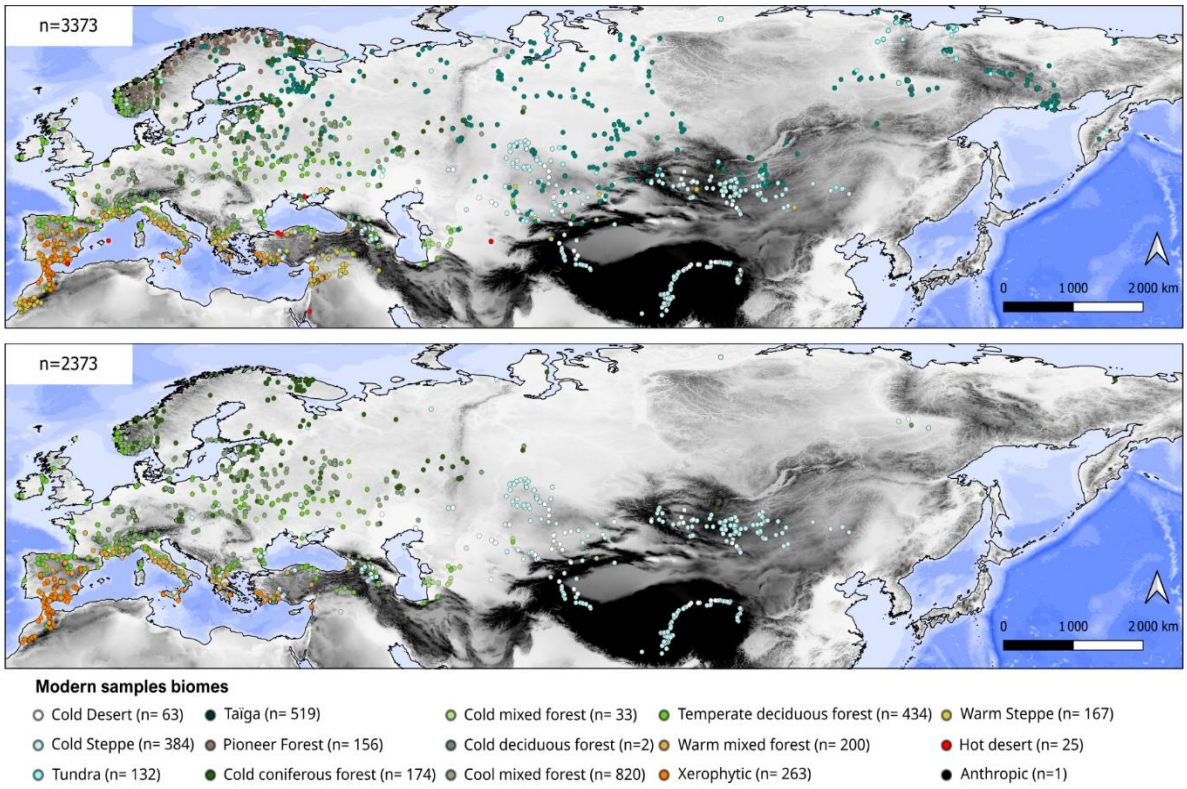


Fig. 2.11. Distribution des échantillons actuels constituant la base de données eurasiatique de référence (en haut, n=3373 échantillons), et celle utilisée pour les reconstructions climatiques dans cette étude (en bas, n=2273 échantillons), colorés en fonction de leur biome.

Pinus a été exclu des bases de données actuelle et fossile, car il est surreprésenté dans l'assemblage pollinique en contexte marin et minimise les abondances des autres taxons tout en masquant leur influence sur les paramètres climatiques (Sassoon et al., 2025; Sinopoli et al., 2019). Par ailleurs, il a été montré que les méthodes de reconstructions climatiques à partir du pollen peinent à estimer correctement les températures des environnements arides, entrainant une mauvaise différenciation entre les steppes chaudes et les steppes froides (Tarasov et al., 1998). Dugerdil et al. (2021) a montré que réduire la base de données moderne aux biomes présents localement autours du site, ou jugés pertinents, améliore la robustesse des reconstructions. Pour cette étude, il a donc été décidé d'écarter les échantillons actuels appartenant aux biomes Taïga, Toundra et Forêt Pionnière, biomes dont le taxon majoritaire est *Pinus*, ainsi que les biomes des steppes chaudes et déserts chauds. Ce dernier choix permet de mieux reconstituer les températures associées aux stadiaires et aux évènements de Heinrich de la dernière période glaciaire, dont le caractère froid a été largement démontré à travers les proxys marins et les spéléothèmes (e.g. Cacho et al., 1999; Darfeuil et al., 2016; Genty et al., 2005; Martrat et al., 2004, 2007; Wainer et al., 2011). La base de données finale utilisée comporte 2373 échantillons (Fig. 2.11). Six paramètres climatiques ont été reconstruits : les précipitations annuelles (MAP - *mean annual precipitation*), les températures moyennes annuelles (MAAT - *mean annual temperature*), le précipitations d'été (Juin, Juillet, Août) (SUMMERPR - *summer*

precipitation), les précipitations d'hiver (Décembre, Janvier, Février) (WINTERPR - *winter precipitation*), les températures moyennes du mois le plus chaud (MTWA - *mean temperature of the warmest month*), et les températures moyennes du mois le plus froid (MTCO - *mean temperature of the coldest month*).

Afin de comprendre les relations attendues entre taxons polliniques et variable climatique reconstruite, la tolérance climatique des taxons polliniques les plus abondants dans la carotte ODP 976 a été calculée à partir de la base de données actuelles (Fig. 2.12). De manière frappante, les différences les plus importantes entre les taxons sont observées pour les paramètres climatiques annuels et d'hiver, tandis qu'une plus faible dispersion entre taxons caractérise les paramètres d'été. Cette observation soutient que les paramètres climatiques d'hiver sont cruciaux dans la différenciation de la végétation et du climat des différents biomes. Les taxons caractérisés par une tolérance aux plus hautes températures annuelles et saisonnières sont représentés par les taxons méditerranéens (*Quercus* type *ilex*, *Olea*). Les taxons de steppe et semi-désert (*Artemisia*, *Ephedra*, Amaranthaceae), bien que présentant une dispersion élevée, montrent la plus grande tolérance aux basses températures ainsi qu'aux faibles précipitations, avec *Pinus*. Les taxons tolérants aux plus hautes précipitations annuelles incluent *Cedrus*, *Quercus* type décidu, les Cichorioideae, ainsi que les taxons méditerranéens, avec des différences majeures dans la répartition saisonnière des précipitations entre ces différentes taxons.

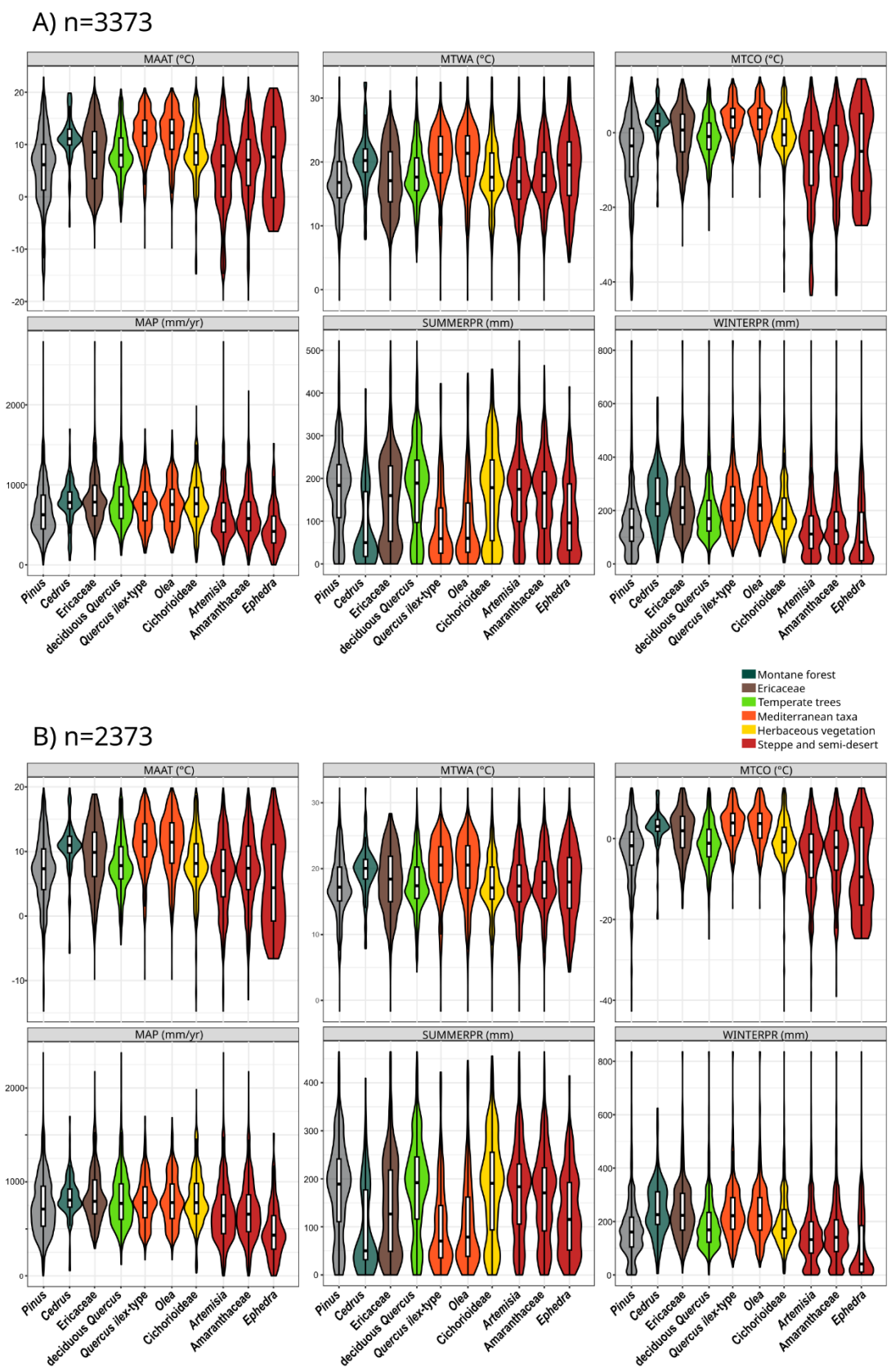


Fig. 2.12. Spectres de tolérance des principaux taxons identifiés dans la carotte ODP 976 aux six paramètres climatiques reconstruits à partir de la base de données eurasiatiques de référence complète (A), et de la base de données réduite utilisée pour les reconstructions (B). Les

diagrammes en violon montrent la distribution des données modernes (densité de probabilité du taxon pollinique par paramètre climatique, pondérée par l'abondance pollinique). Les diagrammes « moustache » mettent en évidence des statistiques globales (médiane, quartiles, *outliers*). MAP: mean annual precipitation; MAAT: mean annual temperature; SUMMERPR: summer precipitation; WINTERPR: winter precipitation, MTWA: mean temperature of the warmest month; MTCO: mean temperature of the coldest month.

Alors que *Cedrus* et les taxons méditerranéens tolèrent de très faibles précipitations d'été (donc une saisonnalité marquée), les Ericaceae, *Quercus* type décidu ainsi que les Cichorioideae montrent une préférence pour des précipitations d'été plus importantes, donc une saisonnalité réduite avec des précipitations plus également distribuées dans l'année. Il est intéressant de remarquer que les Ericaceae montrent une très large distribution de leur tolérance aux précipitations d'été, avec une partie des données indiquant une tolérance à la sécheresse estivale (compatible avec un régime méditerranéen). Enfin, la suppression des échantillons appartenant aux biomes Taïga, Toundra, forêt pionnière, steppe chaude et désert chaud dans la base de données moderne servant aux reconstructions ne modifie pas drastiquement la distribution de la tolérance climatique des principaux taxons (Fig. 2.12 A et B). Elle permet en revanche de limiter la dispersion des températures annuelles, et d'abaisser la médiane des températures du mois le plus froid pour les taxons de steppe et semi-désert (*Artemisia*, Amaranthaceae et *Ephedra*), et favorisera donc une meilleure reconstruction des biomes de steppe froide.

3. Vegetation and climate changes during the Middle to Upper Palaeolithic transition in the southwestern Mediterranean: what happened to the last Neanderthals during Heinrich Stadial 4?

3.1 Résumé en français

Ce premier chapitre de résultats et discussion a fait l'objet d'une publication dans la revue *Quaternary Science Reviews*, parue en avril 2025 (DOI : 10.1016/j.quascirev.2025.109345). L'étude propose une focalisation sur un intervalle chronologique de 7 000 ans, entre 41 et 34 ka BP. Cette période est centrale dans le débat sur la transition du Paléolithique moyen au Paléolithique supérieur en Europe, associée à l'extinction de Néandertal et à l'arrivée d'*Homo sapiens*. Dans la péninsule Ibérique, de nombreux sites archéologiques datés de cette chronologie ont été présentés comme des refuges climatiques pour les dernières populations néandertaliennes, tandis que le débat persiste sur l'arrivée plus tardive de Sapiens au sud de la péninsule et l'existence d'une frontière biogéographique séparant les populations des deux espèces, représentée par le tracé du fleuve Ebre. Le rôle potentiel des changements climatiques rapides dans le scénario de cette transition, et en particulier dans la persistance puis l'extinction des dernières populations néandertaliennes dans la région, est largement débattu.

Cet intervalle chronologique est caractérisé par des variations climatiques rapides majeures, incluant deux cycles complets de Dansgaard-Oeschger : l'interstadiaire du Groënland (GI) 9, le stadiaire du Groënland (GS) 9, le GI8 et le GS8. Le GS9 est associé à un évènement stadiaire de Heinrich considéré parmi les plus intenses, le HS4, qui représente la phase culminante de froid et d'aridité en Europe pendant l'épisode stadiaire autour de 39 ka BP. Si des archives glaciaires et des spéléothèmes à très haute résolution existent pour documenter cet intervalle et ont montré une succession en trois phases climatiques pour le GS9, la résolution des enregistrements palynologiques disponibles en Europe est généralement trop faible pour capter les variations internes à échelle sub-centennale du GS9 / HS4, à l'exception de quelques carottages dans l'Atlantique.

La carotte ODP 976 située en Mer d'Alboran représente une archive paléoclimatique de référence pour déchiffrer les changements abrupts de la dernière période glaciaire en Méditerranée sud-occidentale. Localisée à 50 km de la côte sud-ibérique, elle permet d'accéder en continu aux changements des environnements régionaux contemporains des populations humaines paléolithiques. Cette étude présente les résultats de comptages palynologiques à très haute résolution, incluant 76 échantillons sur une section de 3m de carottage. Une résolution chronologique maximale d'environ 25 ans est atteinte pendant le HS4 tandis que la résolution moyenne sur l'intervalle

est d'environ 100 ans. Pour la première fois, une approche multiméthode de reconstructions climatiques à partir du pollen a été appliquée à cet intervalle, incluant la méthode des analogues modernes (MAT), une approche de régression, *Weighted Averaging Partial Least Squares* (WA-PLS), et deux approches par réseaux de neurones, *Boosted regression trees* (BRT) et *Random Forest* (RF). Une synthèse des sites archéologiques datés entre 42 et 34 ka BP en Méditerranée occidentale (incluant la péninsule Ibérique, le sud de la France, l'Italie, et les Balkans) est établie afin d'enrichir la discussion sur le scénario de la transition du Paléolithique moyen à supérieur et l'extinction de Néandertal dans le bassin méditerranéen occidental.

Les résultats montrent :

(i) Une succession en trois phases pour le GS9 (Fig. 4.6), bien connectée au phasage établi au Groënland et aux latitudes subtropicales. L'impact principale du HS4 sur la végétation Méditerranéenne est représentée par la deuxième phase, où les plantes semi-désertiques sont majoritaires et les reconstructions climatiques indiquent des conditions de froid et de sécheresse intense.

(ii) L'impact majeur du HS4 dans le sud-ouest méditerranéen par rapport à l'Atlantique et au reste de la Méditerranée (Fig. 4.8). Les comparaisons régionales des enregistrements palynologiques et paléoclimatiques indiquent que des conditions plus arides et une végétation régionale plus ouverte ont caractérisé le sud-ouest de la péninsule Ibérique.

(iii) Une forte instabilité environnementale lors de la troisième phase du GS9 et à la transition avec le GI8, qui montre le caractère progressif du réchauffement et de la recolonisation des forêts tempérées et méditerranéennes successivement. Cette instabilité à la fin du HS4 ressemble, sur une échelle de temps plus réduite, à celle bien connue pendant la fin de la dernière période glaciaire et l'entrée dans l'Holocène (Fig. 4.9).

(iv) Une contraction des occupations néandertaliennes dans la Méditerranée pendant le GS9/HS4, qui s'inscrit cependant dans une dynamique de déclin à plus long terme. Il reste par ailleurs compliqué de replacer les chronologies des occupations humaines dans un cadre paléoclimatique à échelle sub-millénaire, en raison des incertitudes et de la fiabilité parfois limitée des datations absolues ^{14}C sur cet intervalle chronologique autours de 40 ka BP (Fig.4.11 et 4.12).

3.2 Paper 1 (QSR): Vegetation and climate changes during the Middle to Upper Palaeolithic transition in the southwestern Mediterranean: what happened to the last Neanderthals during Heinrich Stadial 4?

Liz Charton*[1,2], Nathalie Combourieu-Nebout[1], Adele Bertini[2], Vincent Lebreton[1], Odile Peyron[3], Mary Robles[3], Dael Sassoon[4], Marie-Hélène Moncel[1]

**corresponding author: Liz Charton (liz.charton@mnhn.fr)*

Affiliations:

1: UMR 7194, Histoire Naturelle de l´Homme Préhistorique, CNRS-MNHN, Institut de Paléontologie Humaine, Paris, France

2: Dipartimento di Scienze della Terra, Universita di Firenze, Italy

3: Institut des Sciences de l'Evolution de Montpellier, UMR CNRS 5554 ISEM, Université de Montpellier, France

4 : Geosciences Barcelona (GEO3BCN), CSIC, Lluìs Solè i Sabarìs s/n, 08028 Barcelona, Spain

3.2.1 Abstract

During the last glacial period, and particularly Marine Isotope Stage 3 (MIS 3, dated 60–27 ka), various abrupt and arid climate episodes impacted the northern hemisphere. These are known as Heinrich Stadials and are linked with major iceberg discharged in the North Atlantic. Heinrich Stadial 4 (HS4), one of the strongest of these events occurring around 39 ka BP, has raised numerous debates regarding its potential impact on the Middle to Upper Palaeolithic transition (MUPT) and Neanderthal extinction, especially in the Iberian Peninsula where late persistence of Neanderthals has been claimed beyond 40 ka BP. Although palynological studies from the Iberian margins have previously highlighted vegetation changes during this period, these have generally been of low resolution and thus, the environmental conditions during HS4 and the possible impact of this event on the last Neandertal populations are still poorly understood.

This study uses the marine core from Ocean Drilling Program (ODP) Site 976, located in the Alboran Sea, to provide new ultra-high-resolution analyses for the interval between 41–34 ka BP, including the Greenland Stadial 9 (GS9) / HS4 and the Greenland Interstadial 8 (GI8). The aim is to reconstruct vegetation and climate changes in southern Mediterranean with a resolution never achieved before and to discuss human occupation in the frame of these changes. Vegetation, climate changes and human occupation are discussed on the basis of 1) pollen analysis, 2) quantitative climate reconstructions based on a multi-method approach, and 3) maps of human occupation based on a synthesis of archaeological sites for western Mediterranean Europe in the 42–34 ka BP time interval. Results show a fast spread at centennial scale of steppe and semi-desert vegetation, with a typical three-phased pattern for the GS9 (HS4). This pattern is compatible with the results of various records

from Greenland, southwestern Europe and Brazil. The description of these phases with an unpreceded resolution for the SW Mediterranean region supports the connection between the hydroclimatic changes in Greenland and lower latitudes, while the transition to the following GI8 climate amelioration displays a major vegetation instability that mimics the pattern of the last deglaciation at sub-millennial scale. The climate reconstruction shows cold conditions during HS4 and enhanced aridity mostly linked to the winter rainfall deficit caused by the abrupt disturbance of the Mediterranean seasonal regime of precipitations. The regional comparison with available palynological and paleoclimatic records from the western Mediterranean and the Atlantic sheds light on the spatial expression of the arid event, highlighting a south-westward trend in aridification in the Iberian Peninsula. The Alboran Sea appears as a critical area at the interface of the Atlantic and Mediterranean influences, recording the particular expression of fast climate oscillations in the westernmost part of the Mediterranean. The possible impact of such extreme climate event on the MUPT is discussed based on an updated dataset of archaeological sites and dates for western Mediterranean Europe in the 42–34 ka BP time interval. Maps of human occupation show that Neanderthals may have undergone population contraction during the arid conditions of HS4, but it is still challenging to place the MUPT in a sub-millennial chronological framework due to the uncertainty and limitations of archaeological data.

Keywords: Palynology, Last Glacial Period, sub-millennial climate variability, climate reconstruction, MIS 3, Dangsaard/Oeschger cycles, Heinrich Events, climate-human links, Neanderthals to Sapiens transition, western Mediterranean Human occupations, Alboran Sea

3.2.2 Introduction

The spread of aridity under the effect of anthropogenic climate change is a global challenge for human societies (Park et al., 2018; Zaitchik et al., 2023). This is especially true in the Mediterranean region, which is particularly sensitive to current and future climate changes, as it was to past climate variability (Guion et al., 2022; Hidalgo-Triana et al., 2023; Lionello and Scarascia, 2018; Médail and Quézel, 2003; MedECC, 2020; Vautard et al., 2007; Zampieri et al., 2009). A better understanding of extreme climate events in the past is crucial, particularly during the last glacial period (Marine Isotope Stages “MIS” 4-2). This time interval was characterized by important climate oscillations at a global scale, evidenced for the first time in Greenland and North Atlantic records, and referred to as Dansgaard-Oeschger (DO) events and cycles (Bond et al., 1999; Dansgaard et al., 1993; Johnsen et al., 1992). The ice core record enabled the establishment of a precise stratigraphy and chronology for the fast succession of cold (Greenland Stadials, hereafter GS) and warm (Greenland Interstadials, hereafter GI) events at millennial scale was established (Rasmussen et al., 2006; 2014; Seierstad et al., 2014). In

addition to these millennial oscillations, other abrupt climate events occurring during some GSs and named Heinrich Events (HEs) were identified for the first time through the deposition of Ice-Rafted Debris (IRD) layers in the North Atlantic cores (Heinrich, 1988; Hemming, 2004; Rasmussen et al., 2003). The cold climate phases associated with these events are known as "Heinrich Stadials" (hereafter HS), marked in the North Atlantic and Europe by enhanced cold and dry climate conditions (Sánchez Goñi, 2022a; Sánchez Goñi and Harrison, 2010; Toucanne et al., 2022). MIS 3 (~57–29 ka BP) was marked by some of the strongest oscillations, including nineteen DO cycles (Rasmussen et al., 2014) and three HSs associated with three GSs (HS3 to GS5, HS4 to GS9 and HS5 to GS13). HS4, associated to GS9 between 39.9 and 38.22 ka BP, is commonly considered the most intense (Heinrich, 1988; Hemming, 2004; Rasmussen et al., 2014).

Mediterranean ecosystems have also been strongly impacted by these climate oscillations (M. Liu et al., 2024), and a huge number of paleoenvironmental records in Mediterranean Europe evidenced the response of marine and terrestrial environments to the alternance of GI, GS, and HS during the Last Glacial (Fletcher et al., 2010a and references therein). The GS and HS "cold" episodes were associated with low Sea Surface Temperatures (SSTs) (Cacho et al., 1999; Martrat et al., 2004; Penaud et al., 2016) and the expansion of open herbaceous and semi-desert landscapes on the land (Sánchez Goñi et al., 2002; Sánchez Goñi and d'Errico, 2005; Sánchez Goñi and Harrison, 2010).

MIS 3 Heinrich Stadials drew particular attention in the past decades for their potential impact on human societies present in Europe at that time, as Palaeolithic societies are believed to be strongly affected by fast-changing environments (Bradtmöller et al., 2012; Raia et al., 2020; Willis et al., 2004). Specifically, the interval between 50 and 35 ka BP saw one of the major events in European Prehistory, the Transition from the Middle to the Upper Palaeolithic (MUPT hereafter). Populations of *Homo neanderthalensis* producing Middle Palaeolithic industries (Mousterian) progressively went extinct and were replaced by pioneer populations of *Homo sapiens*, producers of Upper Palaeolithic industries (Aurignacian), and perhaps "industries of transition" such as the Uluzzian or the Châtelperronian, whose authorship remains largely debated (Teyssandier, 2024; Zilhão, 2006). A great number of studies addressed the striking correlation between the timing of Neanderthal demise and the particularly harsh climate conditions during the HS4 (Daura et al., 2017; D'Errico and Sánchez Goñi, 2003; Finlayson and Carrión, 2007; Fourcade et al., 2022; Jiménez-Espejo et al., 2007; Sepulchre et al., 2007). However, the current paradigm rejects the idea of a single homogeneous driver for Neanderthal extinction and defends a more complex model with a transitional mosaic pattern (Straus, 2022). The exact causes and processes behind the MUPT remain strongly debated, with the environmental drivers and exclusive competition with *Homo sapiens* as the main factors in the explanatory models. The biggest issue in understanding the pattern of the MUPT resides in the difficult attribution of a precise

chronological framework for archaeological layers situated at the limit of extension of the radiocarbon method (Douka and Higham, 2017; Higham et al., 2009; Wood et al., 2013), and many erroneously dated sites have to be readdressed with correct pre-treatment for radiocarbon dating or with other dating methodologies (Douka et al., 2014; Higham et al., 2011, 2014; Richard et al., 2015, 2021; Wood et al., 2014). Still, the resolution and uncertainty of radiometric dating in archaeological sites for this period complicate the precise correlation with the sub-millennial chrono-climatic record.

The southern Iberian Peninsula is a central area in the debate on the MUPT due to the apparent late persistence of Neanderthals in key sites in the region and the late arrival of *Homo sapiens* groups (D'Errico and Sánchez Goñi, 2003; Finlayson, 2008; Finlayson et al., 2006; Zilhão, 2006). It has been argued for a long time that the MUPT occurred with a strong spatio-temporal gradient toward the south, leading to the "Ebro frontier model" (Zilhão, 2000), which has been largely contested (Cortés-Sánchez et al., 2019; Vaquero, 2006; Vaquero et al., 2006). However, some late chronologies of Middle Palaeolithic sites are still considered valid, and evidence of the presence of *Homo sapiens* before 30 ka BP is scarce (Anderson et al., 2019; Zilhão, 2021a, 2021b; Zilhão et al., 2017).

Various palynological sequences, especially from marine cores, have already provided important insights into the regional environmental conditions during the extreme events of MIS 3 (Fig. 3.1) (Combourieu-Nebout et al., 2002; D'Errico and Sánchez Goñi, 2003; Fletcher and Sánchez Goñi, 2008, 2010a, 2010b; Fourcade et al., 2024; Roucoux et al., 2005; Sánchez Goñi et al., 2002, 2010, 2020), although their direct use to address the scenario of the MUPT has been challenged (Carrión, 2004; d'Errico and Sánchez Goñi, 2004; Finlayson and Carrión, 2007). As a reaction to these criticisms, recent research has focused on the use of archaeological archives to reconstruct local environmental conditions associated with human occupations, especially in Spain. The main results point towards the persistence of favourable warm and temperate environments (refugia) locally around Neanderthal sites all along the Last Glacial Cycle (Carrión et al., 2018, 2019a; Carvalho and Bicho 2022; Ochando et al., 2019, 2020a, 2020b, 2020c). These studies offer precious insights into the ecological conditions directly associated with human presence, but they present many limitations inherent to the archaeological record. Indeed, prehistoric settlements often present disturbed, non-continuous records with bad preservation of the ecological indicators (Lebreton et al., 2010; Sánchez Goñi, 1993, 1996). Therefore, despite the longstanding debate regarding the contextualization of human settlements, the use of marine sequences remains the most reliable way to draw a regional picture of environmental changes with continuous undisturbed records (Heusser, 1973; Sánchez Goñi, 2006). Recently, new palynological sequences with a robust chronological approach were used to address the cultural changes in SW France, leading to the conclusion that no synchronicities could be observed between environmental and cultural changes during the MUPT (Fourcade et al., 2022). However, while

Heinrich Stadials are well documented in the Greenland records where internal three-phase dynamics at sub-centennial scale could be described for the GS9, allowing to place the main fingerprint of HS4 during phase 2 (Guillevic et al., 2014), the resolution of the European palynological sequences remains often insufficient to reconstruct the variability inside each HS, with the exception of Margari et al. (2020).

ODP 976 marine core is situated in the Alboran Sea, at a key location to reconstruct the environment of the late Middle Palaeolithic populations in the south-westernmost part of Europe. The core has allowed the documentation of the last glacial with different proxies, including pollen, oxygen isotopes, planktonic foraminifera, dinocysts, and dust particles (Bout-Roumazeilles et al., 2007; Combourieu-Nebout et al., 1999, 2002, 2009; Genty et al., 2010; Kageyama et al., 2005; Martrat et al., 2014). Its position at the gateway between Mediterranean and Atlantic influences makes it an ideal archive to study the response of Mediterranean ecosystems to the North-Atlantic climate oscillations during two important events, GS9 /HS4 and the later GI8, that are considered relevant in the debate on the MUTP. The study period spans from 41 to 34 ka BP and therefore chronologically includes the upper GS10 (41.46–40.16 ka BP), the very short GI9 (40.16–39.9 ka BP), the HS4 associated to the GS9 (39.9–38.22 ka BP), the GI8 (38.22–36.58 ka BP), the GS8 (36.58–35.48 ka BP), the GI7 (35.48–33.74 ka BP) and the lower GS7 (33.74–33.74 ka BP) (Rasmussen et al., 2014).

The objectives of this study are i) to provide a very detailed record of the vegetation and climate dynamics at a regional scale, to describe the precise structure and expression of the GS9 /HS4 and the GI8 in the southwestern Mediterranean, ii) to compare these results with other palynological records to explore the spatial variability of the climate event in the Iberian Peninsula and iii) to produce maps of human occupation during the 42–34 ka BP interval to discuss the spatio-temporal pattern of the MUPT in Western Mediterranean Europe in the light of this precise regional chrono-environmental frame.

3.2.3 Regional settings

Ocean Drilling Program (ODP) Site 976 (36°12 N, 4°18W, 1108 m depth) is located in the Alboran Sea about 110 km east of the Gibraltar Strait, 70 km south of the Spanish coast, and 100 km North of Morocco. The Alboran Sea is a narrow extensional basin in the westernmost part of the Mediterranean Sea. It is bordered to the north by the Betic Cordillera and to the south by the Moroccan Rif mountainsf and Atlas chains (Fig 1), The Alboran Sea is characterized by strong currents resulting from the water exchanges with the Atlantic Ocean through the Gibraltar Strait. Surface currents are controlled by Atlantic inflow (Atlantic Jet) of low-salinity waters, while the intermediate depth currents result from the outflow of Mediterranean high-salinity waters. The surface water currents result in two

anticyclonic gyres named Western and Eastern Alboran Gyres (WAG and EAG) (Renault et al., 2012). Sedimentation in the Alboran Sea originates mainly from the strong erosion processes of the south of the Iberian Peninsula but also includes dust aerial inputs from North Africa with important variability during the past glacial/interglacial periods (Bout-Roumazeilles et al., 2007; López-González et al., 2019; Sánchez Goñi et al., 2009). Major river basins in Andalusia contribute to sedimentation in the ODP 976 area, among which the Verde and Guadalfeo rivers are the most important, and through major submarine basins like the Fengirola canyon (Alonso et al., 1999, Liquete et al., 2005; Lobo et al., 2006). Thus, and although Moroccan river systems have been poorly studied, we assume that most of the terrestrial sedimentary input at ODP site 976 comes from the southern Iberian Peninsula.

The modern climate in the Alboran Sea region displays a typical Mediterranean seasonality defined by long, hot and dry summers and mild and cool winters (Lionello et al., 2006; Pons and Quézel, 1998). Winter moisture input is a consequence of the dominant westerlies from the Atlantic, while summer drought is generally linked to the subtropical input of high-pressure masses (Sumner et al., 2001). The current vegetation distribution on the Alboran borderlands follows this climatic gradient (Fig. 3.1): dry steppe elements as *Artemisia* and *Lygeum* grow on the most arid lowlands along the cost, sclerophyllous evergreen taxa, including *Quercus ilex*, *Olea* and *Pistacia* are the main representants of the thermo- to meso-Mediterranean belts, while temperate vegetation with deciduous trees constitutes the overlying supra-Mediterranean belt (Quézel, 2000). Finally, coniferous forests of *Abies*, *Pinus* and *Picea* grow in the oro-Mediterranean belt (over 1200 m approximately), with the presence of *Cedrus* in the Moroccan Rif mountains altitudinal vegetation.

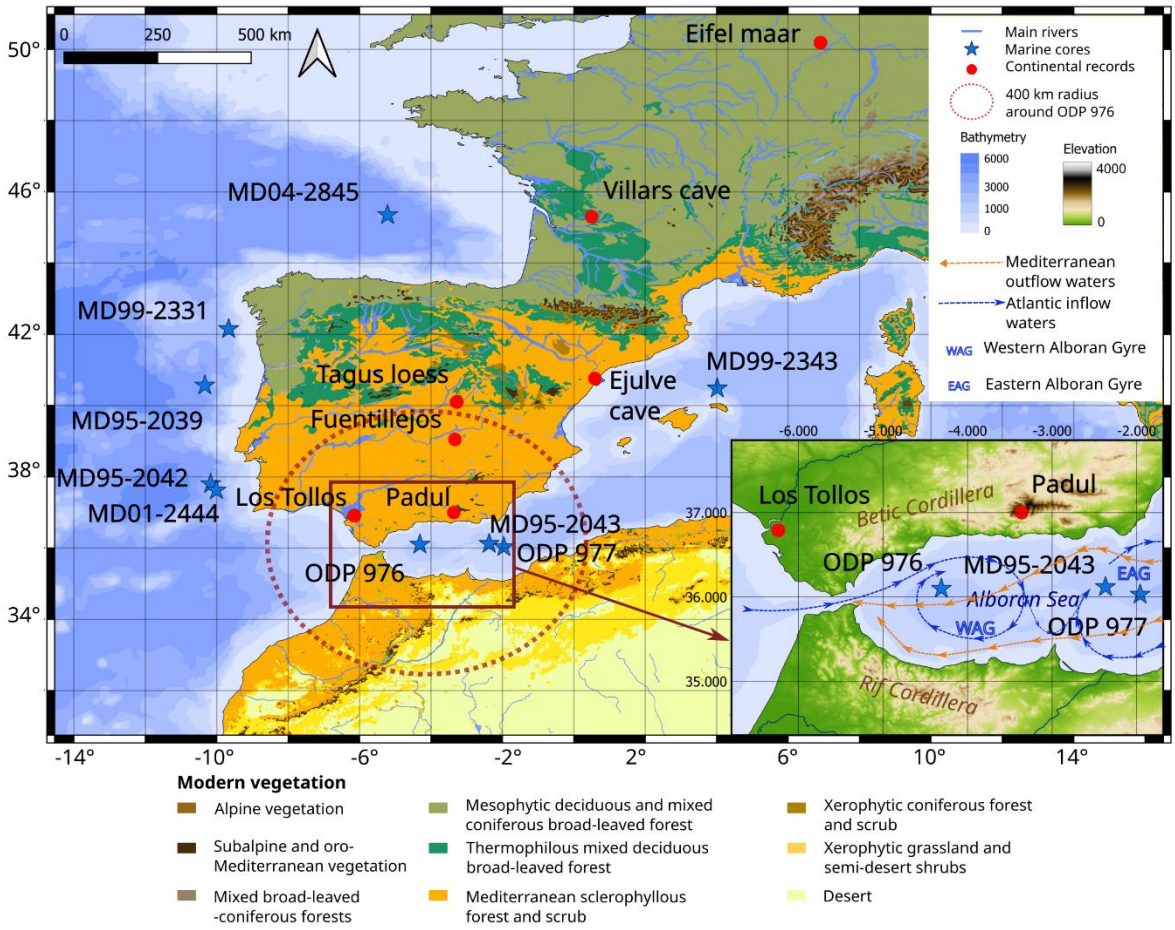


Fig. 3.1. Vegetation distribution and position of the marine and terrestrial sites discussed in the text (source :Map of the Natural vegetation of Europe (Bohn et al., 2007) and the U.S. Geological Survey's (USGS) Global Land Cover Characteristics data base 2.0) for North Africa). Bottom right: Map of the Alboran Sea with oceanographic features (EAG: Eastern Alboran Gyre, WAG: Western Alboran Gyre) and location of the marine core ODP 976.

3.2.4 Methods

3.2.4.1 Core sampling and pollen analyses

A high-resolution sampling of the ODP 976 core was carried out at the Bremen IODP core repository. This study includes 76 samples corresponding to depths between 13.08 and 16.04 meters. The resolution spans from 10 to 1 cm, with an average of 4 cm.

Between 5 and 10 g of sediments were collected and processed for palynological analyses following the protocol defined by Faegri and Iversen (1964) and used in previous palynological studies of the ODP 976 core (Combourieu-Nebout et al., 2002; 2009; Sassoon et al., 2023). The protocol includes the following steps: 150 µm sieving (for the retrieving of macrofossils and macroparticles),

10% HCl, 40% HF, 20% HCl and final 10 µm sieving. Acetolysis was avoided to preserve dinoflagellate cysts.

A minimum of 150 pollen grains excluding *Pinus* and 15 pollen taxa were counted per sample. *Pinus* was excluded from the pollen sum as it is wind-transported through long distances, generally resulting in its overrepresentation offshore in marine palynological sequences (e.g. Combourieu-Nebout et al., 2002; Fletcher et al., 2010b; Mudie, 2011). An average of 609 pollen grains (177 excluding *Pinus*) was counted per sample, resulting in a total of 46,204 grains counted for the interval.

The interpretation of vegetation changes is based on the main assumption that the pollen assemblages in the Alboran Sea sediments represent the vegetation of the Western Mediterranean borderlands (Combourieu-Nebout et al., 2002; 2009; Sassoon et al., 2023). The abundance of *Cedrus* pollen in Alboran Sea records indicates that a significant but unknown proportion of the other pollen types may also originate from North Africa, and thus the pollen assemblage represents a source area which combines the southern Iberian Peninsula and Northern Africa borderlands (Fletcher and Sánchez Goñi, 2008). Despite the regional nature of the signal, similarities observed between the pollen record from MD95-2043 with the Sierra Nevada peatland record from Padul (Fig. 3.1) indicate that marine records from the Alboran Sea are valid archives to describe the history of southern Iberian Peninsula terrestrial environments (Fletcher and Sánchez Goñi, 2008).

3.2.4.2 Age model

Previous age models published for the upper section of ODP 976 core were essentially based on AMS 14C dates on *Neogloboquadrina pachyderma* and *Globigerina bulloides* foraminifera shells (Combourieu-Nebout et al., 2002, 2009b) and additional tie points derived from the NorthGRIP $\delta^{18}O$ (Bout-Roumazeilles et al., 2007). For this study, the same approach was adopted, and a mixed-age model was elaborated using the OxCal 3.4 interface (Ramsey, 1995). The radiocarbon dates were recalibrated (Table 3.1) with the Marine20 curve applying a ΔR = -175 ± 35 for the reservoir age correction in the Alboran Sea (Heaton et al., 2020; Siani et al., 2000) taken from the Marine20 database (Reimer and Reimer, 2001).

Below 10 m depth, a tendency towards ageing dates and increasing uncertainty was noticed, probably due to the vicinity to the limit of the radiocarbon method. Therefore, below 10 m depth the radiocarbon dates were excluded and seven tie points derived from the GICC05 timescale were used instead, based first on the planktonic isotopic curve, and then on higher-resolution curve of temperate pollen taxa, including deciduous forest taxa, Ericaceae, and Mediterranean forest taxa (Table 3.2). This approach is often used for the age control of long pollen sequences, based on the observation that Mediterranean paleoclimatic records are well connected to changes observed in the North Atlantic

and Greenland archives (Fletcher et al., 2010b; Sánchez Goñi and Harrison, 2010, Shackleton et al., 2000), although it does not allow the estimation of time gaps between changes observed in Greenland and in the Alboran Sea. Tie-points were placed following the conventional method, at the midpoint of the first temperate taxa increase (Fletcher et al., 20010a; Shackleton et al., 2000). However, the ultra-high-resolution pollen analysis revealed a more complex transition to the GI8 interstadial conditions, with a first moderate increase of temperate vegetation contemporaneous to still "cold" planktonic isotopic values and preceding the true interstadial amelioration. Therefore, the GI8 tie-point was placed on the second increase of the temperate curve, coherent with the isotopic curve. The implications of this on the structure of the GS9 and the GI8 will be discussed in section 5.1. According to the age model (Fig. 3.2), the sequence spans from 40.927 to 34.095 ka BP, and the maximal temporal resolution reached for the analysis is 23 years, with an average of ~93 years for the entire interval.

The same methodology was applied to update the age model of core MD95-2043, recalibrating the radiocarbon dates with the Marine20 curve and using additional tie points based on the temperate pollen curve on the GICC05 timescale (Fletcher, personal communication).

Sample	Depth (mcd)	Sample taxon	^{14}C age (year BP)	error	min 95.4%	max 95.4%	Median probability
C 1H 1 60–62	0.61	*G. bulloides*	1710	40	1110	1448	1280
C 1H 1 102–104	1.03	*G. bulloides*	3235	30	2913	3303	3100
C 1H 2 63–65	2.14	*G. bulloides*	7010	50	7315	7643	7481
C 1H 2 132–134	2.83	*G. bulloides*	8730	60	9185	9599	9409
C 1H 3 60–62	3.61	*N. pachyderma*	10075	50	11012	11464	11213
C 1H 4 50–52	5.01	*G. bulloides*	11960	80	13236	13727	13466
D 2H 3 100–102	5.51	*G. bulloides*	12720	80	14158	14922	14549
D 2H 4 37–39	6.38	*N. pachyderma*	14330	90	16399	17037	16733
D 2H 5 2–4	7.53	*G. bulloides*	17220	120	19722	20479	20107
C 2H 3 55–57	9.78	*G. bulloides*	22420	315	25321	26766	25986
C 2H 4 47–49	11.21	*N. pachyderma*	27140	460	29826	31552	30635
C 2H 5 45–47	12.69	*N. pachyderma*	29930	670	32070	35219	33737
C 2H 6 61–63	13.35	*G. bulloides*	33750	635	36410	39387	37938
C 2H 6 75–77	13.49	*N. pachyderma*	34230	1130	36140	40855	38464
D 3H 3 120–122	15.4	*G. bulloides*	35700	785	38617	41438	40025

Table 3.1. Recalibrated 14C dates for ODP 976 (OxCal 3.4), using the marine20 calibration curve and ΔR = -175 ± 35 correction for the Alboran Sea reservoir.

Event	Depth (m)	GICC05 Age (ka BP)	GICC05 Error (ka)
Start of GI4	10.61	28.9	0.898
Start of GI5	11.93	32.5	1.132
Start of GI6	12.78	33.74	1.212
Start of GI7	13.605	35.48	1.321
Start of GI8	15.05	38.22	1.449
Start of GI9	15.77	40.16	1.58
Start of GI10	16.4	41.46	1.633

Table 3.2. Tie points of ODP 976 core temperate pollen curve to Greenland GICC05 stratigraphy (Rasmussen et al., 2014) used to build the age model for the core.

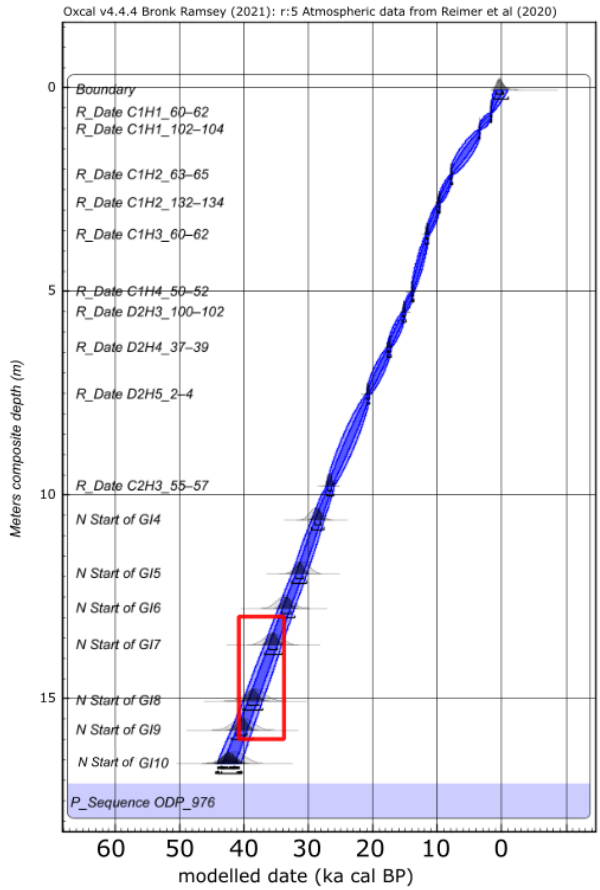


Fig. 3.2. Age model for ODP 976 based on radiocarbon dates (upper 10 m) and correlation with Greenland interstadials chronology (Rasmussen et al., 2014). The model was built with Oxcal 3.4 interface (Ramsey, 1995, see methods) using a Poisson process model "P_sequence" (Ramsey, 2008), setting k parameter at 1 (for the rigidity), interpolation rate at 1, and the variability interval for k parameter at [-2,2], as described by C. B. Ramsey and Lee (2013) to build a robust model for any sedimentary sequence. The red rectangle represents the study period.

3.2.4.3 Multivariate statistical analyses

A CONISS cluster analysis was performed for pollen zonation using the *vegan* package on R (Oksanen et al., 2024). A Principal Component Analysis (PCA) was applied to the dataset to further explore the relationship between pollen taxa and pollen zones using the *ade4* R package (Dray and Dufour, 2007). The PCA was restricted to 59 samples between 13.19 and 16.04 m depth, corresponding to the GI9, GS9 /HS4 and GI8 to analyse the vegetation succession during these precise events, through an interstadial-stadial-interstadial time interval.

3.2.4.4 Pollen-based climatic reconstructions: a multi-method approach

A multi-method approach was applied to the ODP 976 pollen assemblages to provide more reliable climate estimates than the classic approaches based on a single method (Chevalier et al., 2020; Peyron et al., 2011, 2013; Salonen et al., 2019). Here, four methods based on various ecological concepts and mathematical algorithms have been selected: the Modern Analogue Technique (MAT), the Weighted Averaging Partial Least Squares (WA-PLS) and two machine-learning approaches based on regression trees, Random Forest (RF) and Boosted Regression Trees (BRT).

The MAT method (Guiot, 1990) is the most widely applied methodology for pollen-based climate reconstructions and is based on the measurement of a degree of dissimilarity between the fossil samples and a set of modern samples (the modern pollen dataset). The climate parameters associated with the most similar modern samples (the closest analogues) are averaged to reconstruct the values of each fossil sample. WA-PLS (ter Braak and Juggins, 1993) is a regression approach and consists of an improved version of Partial Least Square regression, accounting for the non-linearity and complexity of the relationship between climate and vegetation composition. Assuming that taxa are most abundant the closest they are to their optimum climatic conditions, WA-PLS models the plant/climate relationships from a modern calibration dataset. A weighing of the climatic values based on the pollen taxa percentage is operated. These functions are then transferred to the fossil dataset to reconstruct climate parameters. Contrary to the two former methods, RF and BRT (Elith et al., 2008; Salonen et al., 2012) rely on machine learning and generate a large set of regression trees based on a randomised pollen dataset by bootstrapping (with pollen taxa selected randomly). Both methods differ in their way of selecting samples from one decision tree to the next: RF operates completely randomly, while BRT assigns a higher probability to select samples that have not been selected before (boosting), increasing the performance of the model for elements that are less well predicted (Chevalier et al., 2020). The application of these machine learning methodologies is very promising in palaeoclimatology, particularly for the BRT. Those methods have been successfully tested with European and Mediterranean pollen records to reconstruct climate changes for different time periods

(D'Oliveira et al., 2023; Robles et al., 2023; Salonen et al., 2019) and were applied for the first time to the marine pollen samples of ODP 976 core by Sassoon et al. (2025). Here, 15 iterations were run for both methods, and the results were averaged to obtain the most reliable reconstructions.

The four methods were run on R using packages *Rioja* for MAT and WA-PLS (Juggins, 2024), *dismo* for BRT (Hijmans et al., 2023) and *randomForest* for RF (Liaw and Wiener, 2022). The modern pollen dataset used here includes 2721 modern samples scattered across Eurasia and the Mediterranean region, including north-western Africa.

Six climate variables have been estimated: PANN (annual precipitations), MAAT (annual temperatures), SUMMERPR (summer precipitations), WINTERPR (winter precipitations), MTWA (mean temperature of the warmest month) and MTCO (mean temperature of the coldest month). To calculate the anomalies, the modern values were extracted from ERA 5 reanalysis of the ECMWF (European Centre for Medium-Range Weather Forecasts), based on data assimilation into meteorologic modelling from 1960 to 2022 (Hersbach et al., 2020). An averaged value of the climate parameters on a 400 km radius around the ODP 976 site was extracted, giving MAP = 478 mm, SUMMERPR = 30.5 mm, WINTERPR = 172 mm, MAT = 16.78°C, MTWA = 23.37 °C and MTCO = 13.78°C. These values for modern climate, averaged temporally and spatially, provide a better basis for understanding the nature of the climate signal extracted from a marine palynological sequence at a regional pluri-annual scale.

It is important to underline that the climatic inferences derived from a marine palynological signal have to be interpreted at a regional scale, as none of the fossil pollen grains comes from the local area (Chevalier et al., 2020). Therefore, the absolute values obtained for reconstructed climate parameters have to be considered with caution, whereas the general trends are considered as reliable as they follow climate changes derived from other proxies such as speleothems isotopes or molecular biomarkers (Genty et al., 2011; Sánchez Goñi et al., 2002; Rodrigo-Gámiz et al., 2022; Sassoon et al., 2025).

3.2.4.5 Archaeological database

In order to compare our results with the human records and discuss the MUPT pattern in southwestern Europe, a dataset was built to gather the multimethod dating (AMS radiocarbon, luminescence, U/Th, ESR, AAR) of archaeological sites in the Iberian Peninsula, Italy, and the South of France (up to N 47°, stopping at the latitude of Arcy-sur Cure sites) falling in the MIS 3 interval (57–29 ka BP), with their cultural attribution (Middle Palaeolithic including types when available / Châtelperronian / Uluzzian / Aurignacian *sensus lato*) and biological attribution based on eventual human remains. When no human remains are present, the Middle Palaeolithic industries are interpreted as Neanderthal production, while the Uluzzian and the Aurignacian industries are

considered *Homo sapiens* production (Benazzi et al., 2015; Peresani, 2022; Peresani et al., 2019; Silvestrini et al., 2022). The biological attribution of the Châtelperronian remains largely debated (Gravina et al., 2018; Teyssandier, 2024).

The dataset was built using previous revised datasets and literature (Vermeersch, 2024; Albouy et al., 2024; Guibert et al., 2008; Melchionna et al., 2018; Raia et al., 2020). Only sites with radiometric measurements were selected, while sites with relative chronological attribution were not considered to maintain accuracy, to enable comparison with the high-resolution ODP 976 environmental record. It is known that dating archaeological sites between 50–30 ka BP is challenging due to the temporal limitation of the radiocarbon method. This has led to considerable revisions of the chronology of late Neanderthals and early Modern Human occupations in Europe (Higham et al., 2009, 2014, 2024; Wood et al., 2013, 2014). In some sites, another usual challenge might come from the lack of integrity of the stratigraphic sequence, resulting in potential mixing and contamination of recent materials in older layers, hindering the association between cultural content and chronological information. Many sites have been subject to stratigraphic revisions or debates regarding their integrity (e.g. Gravina et al., 2018). To assess these challenges and account for the debates present in the literature regarding the chronology of the transition in numerous archaeological sites, a confidence gradient from 0 (minimum confidence) to 2 (maximum confidence) was used following the methodology of previous datasets (Fourcade et al., 2022; Guibert et al., 2008). Index 0 refers to dates that are generally regarded as not reliable in the literature, and completely excluded from the chronological models. Index 1 usually refers to dates that have been considered as probable outliers in the site's age models, or bear low collagen content, or come from old studies with questionable stratigraphy and not revised since then, and are therefore doubtful but not completely excluded. Finally, index 2 is given to dates that have not been considered invalid until now and seem robust in the literature chronological models. The radiocarbon dates were all recalibrated using the latest calibration curve Intcal20 (Reimer, 2020) and *Bchron* R package (Haslett and Parnell, 2008). This approach does not use geochronological Bayesian modelling, but only non-modelled dates available in the sites and calibrated with their 95% interval. The implications and limitations of this approach will be taken into account in the discussion.

To produce maps of human occupations during the interval of study, sites with calibrated dates falling in the 42–34 ca ka BP interval were selected. The occupations were mapped using QGIS version 3.32.3 (QGIS.org, 2023). QGIS Geographic Information System. Open-Source Geospatial Foundation Project. http://qgis.org°).

3.2.5 Results

3.2.5.1 Pollen diagram

A total of 120 terrestrial pollen taxa were identified and classed in 9 ecological groups based on their present vegetation distribution and ecological requirements to facilitate the interpretation of vegetation changes: *Pinus*, montane forest, temperate deciduous forest, other trees, Ericaceae, Cupressoideae, Mediterranean sclerophyllous forest, semi-desert and steppe vegetation, terrestrial herbaceous plants, and aquatic herbaceous (Table 3). Pollen data illustrate a continuous high-resolution record of vegetation changes between 41 and 34 ka BP (Fig. 3.3). Based on the CONISS cluster analysis, the record has been divided into 4 main pollen zones with 9 subzones, describing the fast succession of vegetation changes associated to the stadial/interstadial oscillations (Table 4). The semi-desert and steppe vegetation group, mainly *Artemisia*, *Ephedra* and Amaranthaceae displays its maximum abundance in zones 2 and 4b corresponding to the two stadials GS9 and GS8, while the temperate deciduous forest mainly represented by deciduous *Quercus* is most abundant in zones 1, 3c and 4c, corresponding to the three interstadials GI9, GI8 and GI7.

Ecological group	**Pollen taxa**
Pinus	*Pinus*
Montane forest	*Cedrus, Abies*, *Picea*, *Betula*, *Fagus*
Temperate deciduous forest	Deciduous *Quercus, Acer, Carpinus, Alnus, Alnus incata*-type*, Fraxinus, Salix*, *Ilex, Platanus, Populus, Sambucus,* Taxaceae*, Taxus, Buxus, Castanea, Corylus, Ulmus, Viburnum,* Syringa, *Juglans*
Other trees	*Argania*
Ericaceae	Ericaceae, *Calluna vulgaris*
Cupressoideae	Cupressoideae, *Juniperus*
Mediterranean sclerophyllous forest	*Quercus ilex, Quercus suber,* Cistaceae*, Cistus, Cistus ladaniferus, Olea, Phillyrea, Ligustrum, Pistacea, Rhamnus, Rhus, Ruta, Vitis*
Steppe and semi-desert vegetation	*Artemisia*, Amaranthaceae, *Ephedra distachya, Ephedra fragilis, Ephedra altissima, Ephedra* sp*, Erodium, Hippophae, Lygeum*
Terrestrial herbaceous plants	Apiaceae, Asteroideae, *Antemis*-type, *Ambrosia*-type, *Carduus*-type, *Xanthium*-type, Cichorioideae, *Centaurea* sp, *Centaurea jacea*, *Centaurea cyanus*, *Hedera*, *Asphodelus*, Lamiaceae, *Lamium*, *Phlomis*, Liliaceae, *Scilla*, *Plantago*, *Plantago lanceolata*, *Helianthemum*, *Jasminum*, Poaceae, Brassicaceae, *Matthiola*, Caryophyllaceae, *Paronychia*, Convolvulaceae, *Calystegia*, *Calligonum*, Boraginaceae, *Echium*, Campanulaceae, Cannabaceae, Crassulaceae, *Sedum*-type, Dipsacaceae, *Knautia*, *Scabiosa*, Euphorbiaceae, *Euphorbia*-type, *Mercurialis*, Fabaceae, Gentianaceae, Geraniaceae, *Linum*, *Limonium*, *Armeria*, *Rumex*, Primulaceae, Ranunculaceae, *Helleborus*, *Pedicularis*, *Thalictrum,* Rosaceae, *Potentilla*, *Verbena officinalis*, *Galium*, Scrofulariaceae, Thymeleaceae, Urticaceae, *Urtica*-type, Valerianaceae, *Centranthus*, *Arceuthobium*
Aquatic herbaceous	*Alisma*, Cyperaceae, *Lotus, Potamogeton*, *Typha-Sparganium*, *Nymphaea*

Table 3.3. List of taxa identified in the ODP 976 record and their ecological group attribution. *Argania* has been separated as it is endemic from Morocco and therefore indicates African input.

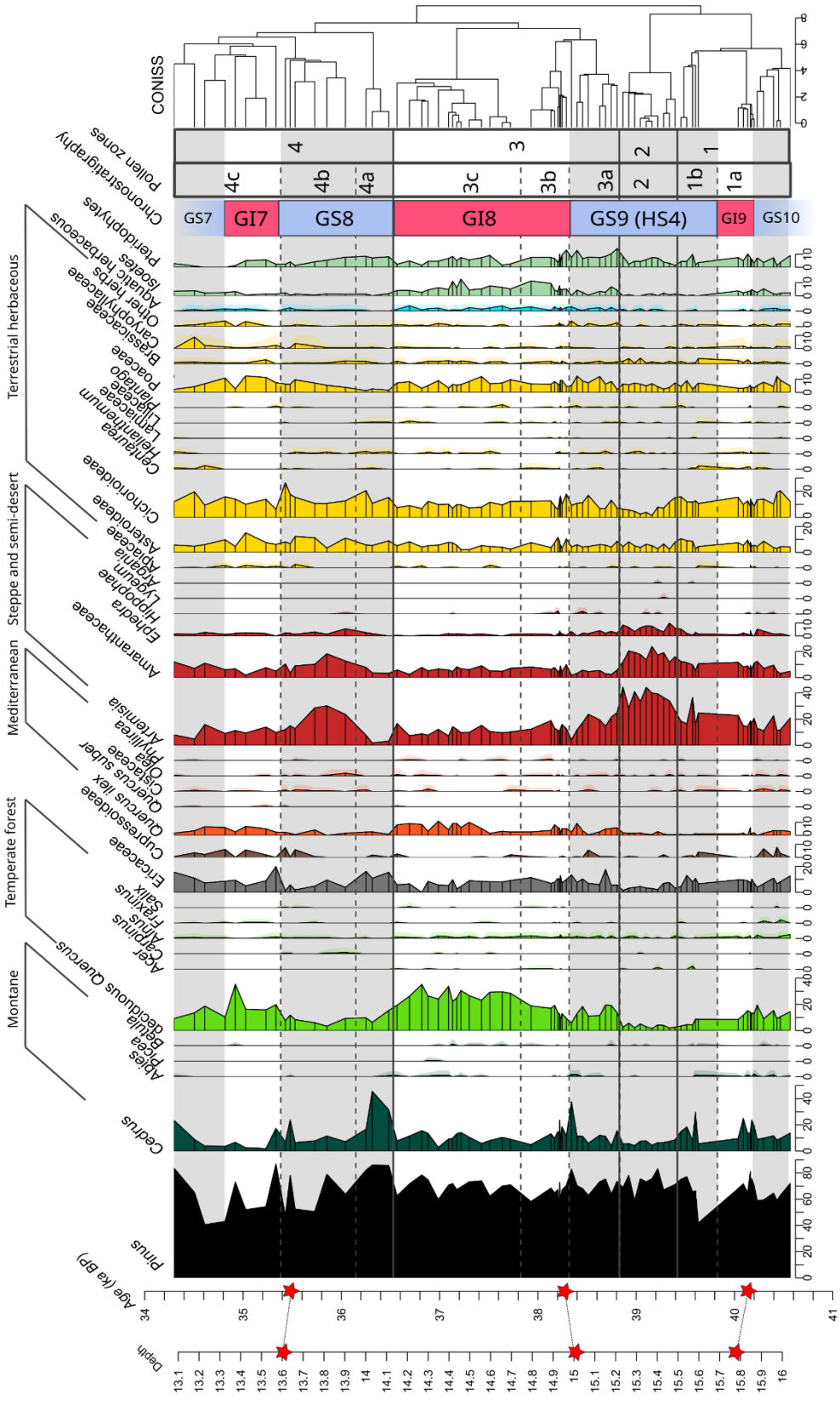


Fig. 3.3. Synthetic pollen diagram representing the main pollen taxa identified in the sequence across the time. The red stars indicate the fixpoints used to build the age model (see method). For detailed diagram, see supplementary figures S2, S3. Grey bars represent the stadial intervals.

Pollen zone	Pollen subzone	Description of the pollen assemblage: most abundant taxa range (%) and most significative trends	Interpretation of the vegetation and climate	Greenland events
4 **Depth: 13.19–13.8 m** **Age: 36.483–33.298 ka BP**	4c	Increase of deciduous *Quercus* (19–35%) Contraction of Artemisia (15–4%)	Expansion of the temperate forest. Mild-humid climate.	GI7 / GS7
	4b	Rapid increase of *Artemisia* (23–29%), Amaranthaceae (10-18%) and *Ephedra* (1–6%) Decrease of deciduous *Quercus* (3–10%) and *Quercus ilex* (1–4%)	Cold steppe (stadial vegetation). Cold and dry climate	GS8
	4a	*Cedrus* 16–45% Increase of Ericaceae (10–16%) and Cichorioideae (10–20%) Decrease of deciduous *Quercus* (15–6%) Strong fall of *Quercus ilex (*1–3%) Minimum of *Artemisia* (1–7%)	Altitudinal forest and heathland Still humid and colder climate.	
3 **Depth: 15.28–13.23m** **Age: 38.806–36.567 ka BP**	3c	Expansion of deciduous *Quercus* (19–30%) *Artemisia* stable (9–15%) Cichorioideae (9–12%) Ericaceae (8–11%) *Q. ilex* (2.6–11%) Increase of *Isoetes* (5–11%)	Major expansion of the temperate deciduous forest and Mediterranean vegetation, optimum of the GI8 Mild-humid climate.	GI8
	3b	Generally still abundant *Artemisia* (10–19%), but decreasing trend Progressive increase of deciduous *Quercus* (9–19%) *Quercus ilex* (2–8%) Ericaceae (7–13%) Decrease of *Cedrus* (18–4%)	Clear expansion of the temperate forest, and Mediterranean vegetation stable. Presence and instability of steppe and herbaceous vegetation still. Retreat of montane vegetation.	
	3a	First decrease of *Artemisia* (14%), then second peak (23%), and finally large decrease at the top (4%). Same pattern for the other semi-desert taxa (*Ephedra*, Amaranthaceae) First peak of *Cedrus* (15.7%) at the bottom, and second large peak at the top of the zone (37.5%)	Unstable retreat of the cold steppe, and recovery of temperate and Mediterranean vegetation. Altitudinal forest and heathland expansion. Slightly cooler and more humid climate.	GS9 /HS4

		Rapid increase of deciduous *Quercus* (2–20%) in 200 years Progressive increase of herbaceous taxa such as Cichorioideae (6–17%) Peak of Ericaceae (1–17%) following the retreat of the steppe Increase of *Q. ilex* (1–10%) Increase of Pteridophytes (8–14%) and *Isoetes* (0–7%)		
2 **Depth: 15.48–15.3 m** **Age: 39.396–38.865 ka BP**	2	*Artemisia* (26–45%) Amaranthaceae (11–20%) *Ephedra* (3–10%) Presence of *Hippophae, Lygeum* and *Argania* Major decrease of Cedrus (4–8%), deciduous Quercus (1–6%), Ericaceae (2–7%), and Cichorioideae (7–11%) *Q. ilex* (0.6–2 %)	**Heinrich stadial 4**: Fast expansion of the cold steppe. Cold and dry climate. Minimum extension of temperate and Mediterranean taxa. Input of pollen grains from North Africa.	
1 **Depth: 16.04–15.5 m** **Age: 40.569–39.456 ka BP**	1b	*Cedrus* (8–30%) *Artemisia* (15–37%) Presence of *Argania* Dramatic decrease of Mediterranean taxa: *Q. ilex* (0.5–0.87 %)	Expansion of the altitudinal forest and steppe in lower lands. Retreat of temperate and Mediterranean vegetation. Input of pollen grains from North Africa. Temperature decrease.	
	1a	*Cedrus* (9–23%) *Artemisia* (10–22%) Deciduous *Quercus* (8–19%) Ericaceae (4–12%) *Q. ilex* (0–6%) Cichorioideae (8–19%) *Isoetes* (1–5%)	Altitudinal forest + mixed temperate forest, presence of Mediterranean taxa. Climate rather humid and cool.	GI9 / GS10

Table 3.4. Description of the main pollen zone with the main characteristics of the pollen assemblage, the vegetation and climate interpretation, and the associated Greenland Chronology.

3.2.5.2 Multivariate statistics

The first axis of the PCA analysis (Fig. 3.4) accounts for 31.7 % of the total variance and shows the opposition between the steppe and semi-desert groups in the negative values and the Mediterranean, temperate and aquatic groups in the positive values. Axis 1 seems to reflect a gradient of humidity between dry pollen assemblage in the negative values, and more humid vegetation in the

positive values. Axis 2 explains 17.6% of the total variance and is characterized by the Montane group and Ericaceae in the positive values, as opposed to Mediterranean, temperate and steppe groups in the negative values. A gradient of temperature may be represented by this axis, separating cold taxa in the positive values and warmer groups in the negative values. These patterns of humidity and temperature variations recall the pollen indexes defined by Fletcher et al., (2010b) in the nearby core MD95-2043, where the ratio of temperate forest pollen versus montane forest was used as a temperature index, and the ratio of temperate forest versus steppe and semi-desert taxa expressed a humidity index.

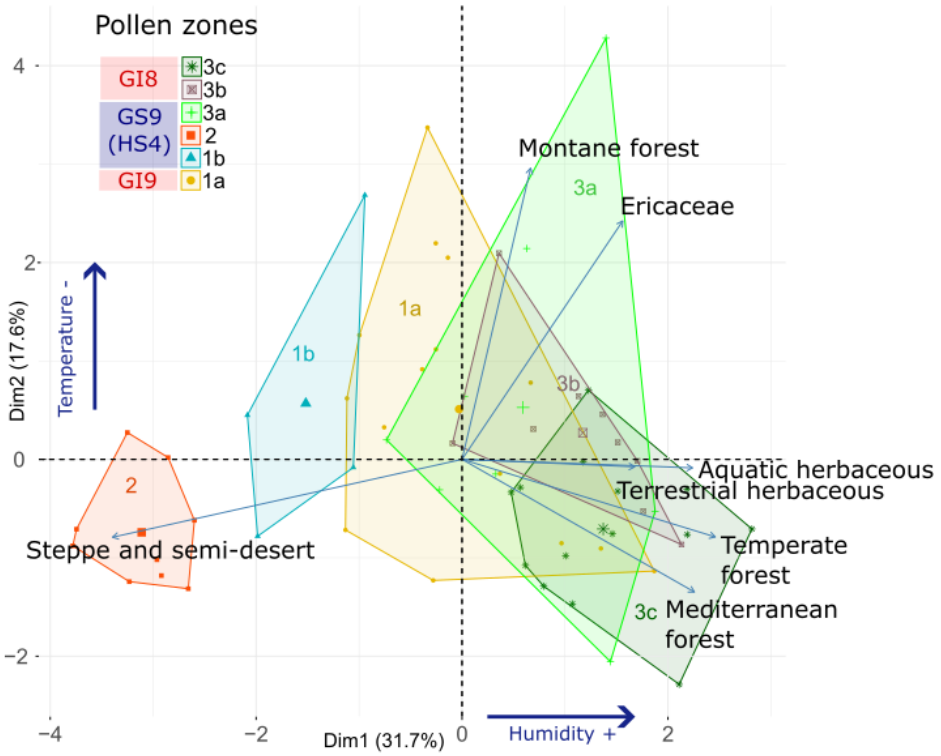


Figure 3.4. PCA biplot of variables (ecological groups of taxa) and samples. Samples are grouped in polygons representing the different pollen zones defined by CONISS cluster analysis.

The PCA also shows a strong Guttman effect (Camiz, 2005), the ordination of the ecological groups and samples displays a typical arch shape. This peculiar distribution is very indicative in ecological studies, and is generally linked to the presence of a strong ecological gradient in the variables. This supports our interpretation that two great factors (humidity and temperature) influence the distribution of the data, and that there is a non-linear interconnection between them. As a consequence, there might be a strong seasonality gradient in the PCA controlling the variation of humidity and temperature, and therefore the distribution of taxa and samples.

The first phase of GS9 (pollen zone 1b) has a significant score in axis 2 (up to 2.5), dominated by Ericaceae and Montane taxa and indicating cool but still humid conditions. The main phase of GS9

(pollen zone 2) has the minimum score of PCA axis 1 (between -2.5 and -3.5) and is clearly characterized by the dominance of semi-desert vegetation, indicator of cold and arid conditions characteristic of HS4. Thus, according to these results during GS9 temperatures decrease first, followed by a decrease in humidity. Finally, the last phase of GS9 (pollen zone 3a) has intermediate scores in axis 1 indicating a humidity increase, and a broad range in axis 2 (between -2 and 4) showing significant temperature variations.

The pattern during the following GI8 shows two phases, the first one (zone 3b) with intermediate values (between -1 and 2) in axis 2 (temperatures) and slightly higher scores1 (between 0 and 2) in axis 1 (humidity). The second GI8 phase (pollen zone 3c) has minimum scores of axis 2 (temperatures) down to -2, and maximum scores on axis 1 (precipitations) up to 2.5, reflecting the maximum influence of temperate and Mediterranean vegetation, and the temperature and humidity optima. Thus, according to these results, during the transition to the GI8 in the Alboran Sea, humidity increases first, and temperatures increase in a second time.

In summary, the PCA represents the strongest opposition between dry and rather cold vegetation associated with HS4 as the main phase of the GS9, and mild warm vegetation associated with the optimum phase of the GI8. It describes thus well the transition from stadial to interstadial configuration, governed by a combination of both temperature and humidity and with a strong influence of seasonality.

3.2.5.3 Climate reconstructions

Results of the multi-method approach are presented in Fig. 3.5. MTCO and MAAT are the best reconstructed parameters according to the Pearson correlation coefficient (R^2 values, Table 5) for all methods, while Root Mean Square Error (RMSE) values indicate MTWA and MAAT as the most accurately reconstructed parameters. Precipitations are generally reconstructed with a lower accuracy than temperatures according to both metrics. The four methods are generally in good agreement. MAT and BRT appear as the most accurate methods (R^2 and RMSE values, Table 5) and also as the most sensible methods with major shifts observed, while the RF and WA-PLS curves appear more flattened. In the whole sequence, reconstructed temperatures are generally lower than the present, while precipitations were higher than today except during the cold phases depicted for the HS4 or GS8 (Fig. 3.5). Very cold and dry conditions during HS4, the main phase of the GS9 (38.8–39.4 ka BP), are well evidenced during the winter season. Winter climate parameters show the most important amplitude of variations through the sequence, while summer parameters are generally more stable. WINTERPR, MAP and MTCO reach their minimum during HS4 (pollen zone 2), and MAP and SUMMERPR reach their maximum during the GI8.

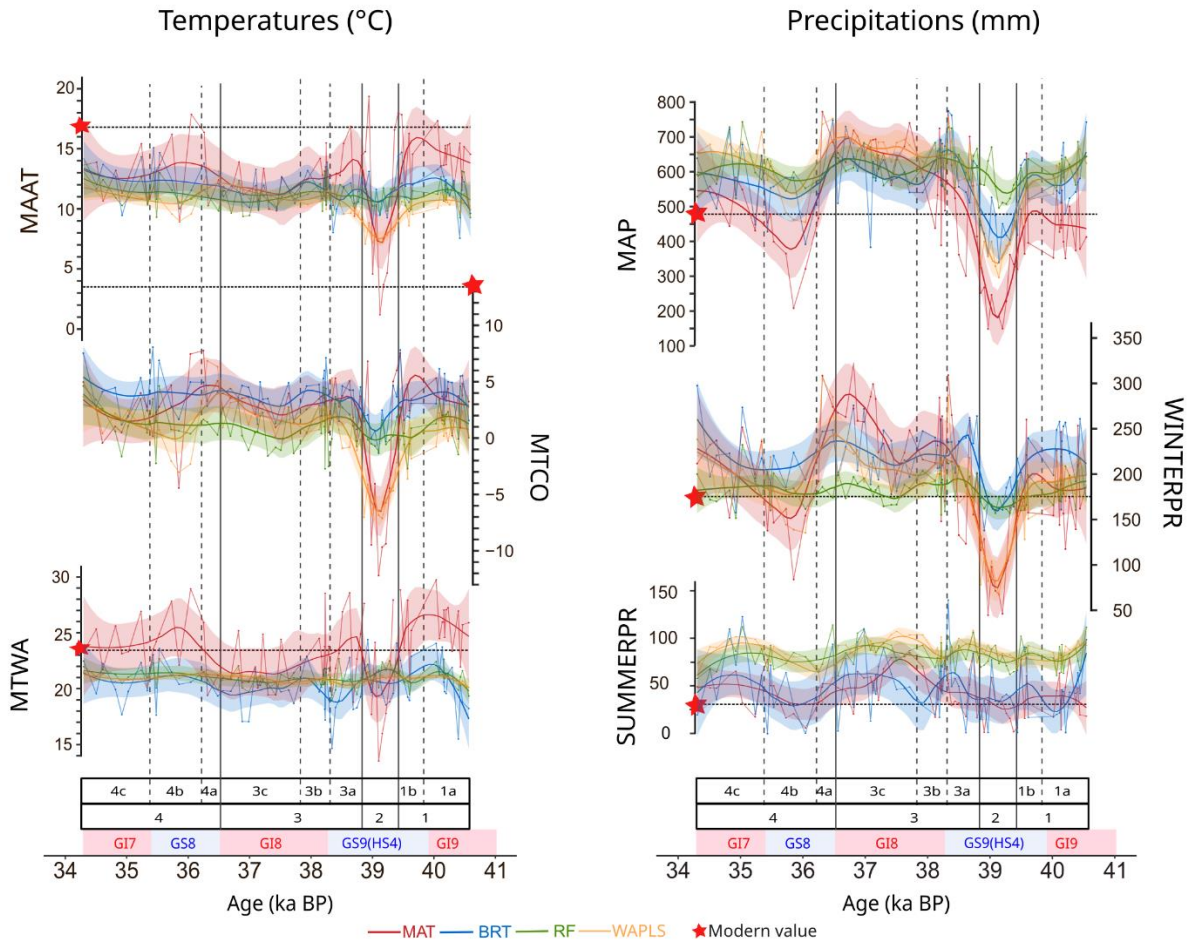


Figure 3.5. Pollen-based climate reconstructions. MAAT (Mean Annual Temperature), MTWA (Mean Temperature of the Warmest month), MTCO (Mean Temperature of the Coldest month), MAP (Mean Annual Precipitations), SUMMERPR (Summer Precipitations), and WINTERPR (Winter Precipitations) for the four methods applied: MAT (Modern Analogue Technique), WA-PLS (Weighted-Averaging Partial Least Squares), BRT (Boosted Regression Trees) and RF (Random Forest). The light-coloured interval represents the 95% confidence window, and the bold curves are the loess smoothed values. The horizontal dashed line represents the modern value (see methods), and the vertical lines represent the pollen zones defined by CONISS cluster analysis, associated to the Greenland climate episode.

A three-phase sequence is evidenced during the Heinrich Stadial 4 (Fig. 3.5) in the Alboran Sea. The first phase of the GS9 (zone 1b) is characterized by a decrease in temperatures associated with relatively high precipitations. This supports the PCA analyses interpretation of temperatures decreasing before humidity, and therefore a colder but still humid first phase during GS9. The second phase, corresponding to the main HS4 fingerprint (zone 2), is characterized by a marked fall in temperatures and precipitations. The last phase (zone 3a) and the successive transitional phase to the GI8 (zones 3a and 3b) are characterized by generally higher temperatures and precipitations, but significant climate instability during the transition. All four methods show a major change in annual and winter precipitation parameters during HS4, although with different intensities. For the three

temperature parameters, however, the machine learning-based methods RF and BRT display very smooth curves contrary to the MAT and WA-PLS curves, indicating that the temperature change is less clear than the precipitation change during the HS4.

R^2	RF	MAT	WA-PLS	BRT
MTCO	0.77	0.87	0.68	0.93
MAAT	0.72	0.85	0.67	0.91
SUMMERPR	0.68	0.82	0.56	0.89
MTWA	0.64	0.81	0.58	0.88
MAP	0.61	0.75	0.47	0.85
WINTERPR	0.54	0.68	0.39	0.80
RMSE				
MTCO	4.00	3.39	3.79	3.04
MAAT	3.06	2.55	3.41	2.36
SUMMERPR	55.91	48.58	66.04	43.83
MTWA	2.93	2.47	3.21	2.30
MAP	201.19	182.94	237.11	171.95
WINTERPR	75.28	72.90	87.01	66.39

Table 3.5. R2 (Pearson correlation coefficient) and RMSE (Root Mean Square Error) values for the climate parameters reconstructed and the four methods. The higher the R2, and the lower the RMSE, the more accurate the reconstructions are.

3.2.5.4 Archaeological synthesis

The dataset includes a total of 1610 dates from 182 archaeological sites (Table 6-A, Supplementary Table S4). The uncertain technocomplex category refers to layers bearing non-discriminating assemblages, referred to as "transitional" without further precision, or mixed layers containing both Middle and Upper Palaeolithic artefacts (e.g. El Castillo layer 18, Teixoneres chamber X unit II, Saint-Césaire EJOP sup). Reducing the dataset to the 42–34 ka cal BP interval, 947 dates from 134 sites were obtained (Table 6-B), among which 28 dates with confidence index 0 were eliminated, resulting in 919 dates from 132 sites with confidence index 1 and 2 (Table 6-C, Supplementary Fig. S1). The dataset was further elaborated, selecting only the radiocarbon dates (747 dates from 102 sites; Table 6-D), and finally only the radiocarbon dates with confidence index 2 (636 dates from 78 sites; Table 6-E). These two former sub-datasets also include four tephra layer dates corresponding to the Cambrian Ignimbrite (CI) eruption at 39.850 ± 140 calendar years BP, found in Klisoura and Grotta del Cavallo, where it represents a *terminus ante quem* for the Uluzzian end (Ntinou, 2021; Zanchetta et

al., 2018), in Grotta di Castelcività where it represents a *terminus ante quem* for the end of the Aurignacian (Falcucci et al., 2024; Higham et al., 2024), and in Bioče where it represents a *terminus post quem* for Middle Palaeolithic (Vishnevskiy et al., 2019).

		Middle Palaeolithic		Châtelperronian		Uluzzian		Aurignacian SL		Uncertain		None		Total	
		Sites	Dates	Sites	Dates	Sites	Dates	Sites	Dates	Sites	Dates	Sites	Dates	Sites	Dates
A) All radiometric methods and confidence index (50-30 ca ka)	Before GS9 / HS4	156	735	14	89	9	75	41	260	6	43	1	1	175	1204
	During GS9 / HS4	55	118	9	35	6	26	47	282	4	17	0	0	98	478
	After GS9 / HS4	46	124	8	19	5	17	55	437	4	9	0	0	93	606
	Total	158	791	14	94	9	81	58	595	7	48	1	1	182	1610

		Middle Palaeolithic		Châtelperronian		Uluzzian		Aurignacian SL		Uncertain		None		Total	
		Sites	Dates	Sites	Dates	Sites	Dates	Sites	Dates	Sites	Dates	Sites	Dates	Sites	Dates
B) All radiometric methods and confidence index (42-34 ca ka BP)	Before GS9 / HS4	93	240	13	67	8	61	41	185	6	27	1	1	124	581
	During GS9 / HS4	54	118	9	35	6	26	47	282	4	17	0	0	97	478
	After GS9 / HS4	45	100	8	19	5	17	55	421	4	9	0	0	92	566
	Total	97	272	13	72	8	67	58	504	6	31	1	1	134	947

		Middle Palaeolithic		Châtelperronian		Uluzzian		Aurignacian SL		Uncertain		None		Total	
		Sites	Dates	Sites	Dates	Sites	Dates	Sites	Dates	Sites	Dates	Sites	Dates	Sites	Dates
C) All radiometric methods with confidence index 1 and 2 (42-34 ca ka BP)	Before GS9 / HS4	91	222	13	67	6	61	41	184	6	27	1	1	122	562
	During GS9 / HS4	52	106	9	35	6	26	46	282	4	17	0	0	95	466
	After GS9 / HS4	42	87	8	18	4	15	55	420	4	9	0	0	90	549
	Total	95	249	14	71	8	65	57	502	6	31	1	1	132	919

		Middle Palaeolithic		Châtelperronian		Uluzzian		Aurignacian SL		Uncertain		None		Total	
		Sites	Dates	Sites	Dates	Sites	Dates	Sites	Dates	Sites	Dates	Sites	Dates	Sites	Dates
D) Radiocarbon dates with confidence index 1 and 2 (42-34 ca ka BP)	Before GS9 / HS4	64	117	12	60	5	51	37	165	6	25	0	0	94	418
	During GS9 / HS4	26	37	6	29	3	16	44	259	4	14	0	0	67	355
	After GS9 / HS4	17	28	6	15	4	10	49	394	4	6	0	0	67	453
	Total	67	132	11	64	6	55	52	468	6	28	0	0	102	747

		Middle Palaeolithic		Châtelperronian		Uluzzian		Aurignacian SL		Uncertain		None		Total	
		Sites	Dates	Sites	Dates	Sites	Dates	Sites	Dates	Sites	Dates	Sites	Dates	Sites	Dates
E) Radiocarbon dates with confidence index 2 (42-34 ca ka BP)	Before GS9 / HS4	44	82	9	48	4	38	35	154	5	21	0	0	72	343
	During GS9 / HS4	10	11	4	13	3	12	42	245	4	11	0	0	53	292
	After GS9 / HS4	1	1	0	0	1	5	46	376	3	3	0	0	48	385
	Total	44	82	9	48	4	38	50	446	5	22	0	0	78	636

Table 3.6. Synthesis of the dataset with a number of dates and sites included for each time range and confidence index. The two tables C and E describe the data used to produce the two sets of maps in discussion.

3.2.6 Discussion

3.2.6.1 The sub-millennial oscillations in the Alboran Sea record between 41–34 ka BP

While the vegetation changes are slight during the GS10 / GI9 at the base of the diagram (Fig. 3.3), and the GI7/GS7 at the top, the most significant vegetation and climate variations are expressed during the GS9/HS4, the GI8 and the successive GS8.

3.2.6.1.1 The three-phased imprint of Greenland Stadial 9

In the ODP 976 record, the marine indicators and the steppe/semi-desert taxa show synchronous changes in marine and terrestrial ecosystems during GS9 / HS4 (Fig. 3.6). The cooling of sea surface waters is recorded through the isotope signal together with alkenone-derived SSTs, foraminifera and dinocysts associations (Fig. 3.7) while on land, *Artemisia* and other semi-desert pollen indicators reflect an expansion of the steppe (e.g. Allen et al., 1999; Combourieu-Nebout et al., 2002; Fourcade et al., 2022, 2024; Sanchez Goñi and Harrison, 2010). The peak abundance of the foraminifera *N. pachyderma* is contemporaneous to the drastic decrease of SSTs linked to the massive iceberg's freshwater discharge in North Atlantic, while the peak abundance of the dinoflagellate cyst *Bitectatodinium tepikiense* indicates enhanced temperature contrasts in Mediterranean sea surface waters (e.g. Bond et al., 1992; 1999; Cacho et al., 1999; Cortijo et al., 1997; Penaud et al., 2011; Ruddiman, 1977), in agreement with other marine cores from the Mediterranean region, where IRD layers are lacking (Fig. 3.7). Nevertheless, in the Alboran sea the typical drop in *G. bulloides* $\delta^{18}O$ ratio is attenuated (Fig. 3.7), probably due to the Atlantic low saline waters entrance which offsets SST's cooling (e.g. Combourieu-Nebout et al., 2002). The disturbance of marine conditions is connected to the widespread iceberg discharge into the North Atlantic, which coincides with particularly fresh North Atlantic surface waters, weak North Atlantic deep-water (NADW) formation, and Atlantic meridional overturning circulation (AMOC) (Menviel et al., 2020).

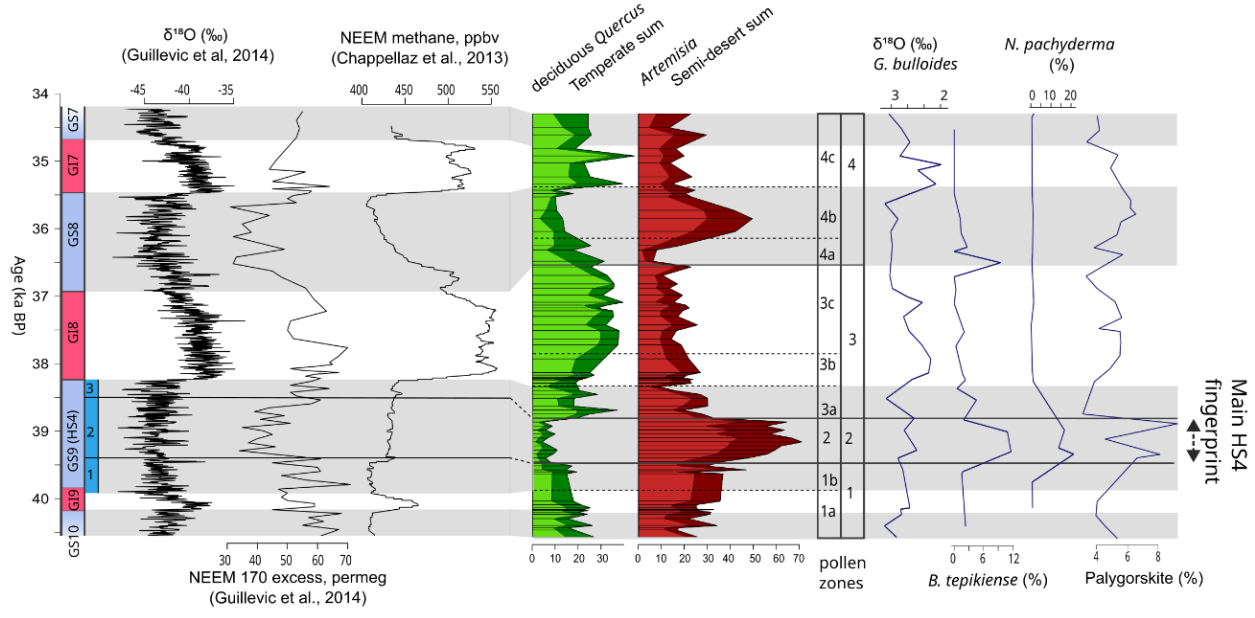


Figure 3.6. Correlation of the Greenland NEEM record with the main proxy available for ODP 976 core.

Until now, most Mediterranean paleoclimatic sequences evidenced the Heinrich cold episodes with a lower temporal resolution (Figs. 7, 8) (e.g. Sánchez Goñi and Harrison 2010 and references therein), with the exception of Margari et al. (2020) which provided a high-resolution record of marine proxies for core MD01-2444. ODP 976 record allows the description for the first time of the fast vegetation dynamics during GS9, with a mean temporal resolution of the pollen of about 58 years (between 10 and 116 years). Three pollen phases were identified during the GS9, and supported by the CONISS cluster analysis (pollen zones 1b, 2 and 3a) (Fig. 3.6). The first phase (pollen zone 1b) is marked by a large peak abundance of *Cedrus*, an increase of *Artemisia* and Ericaceae, and a brutal decrease of the temperate forest (Fig. 3.3). Considering the lower limit of 39.9 ka BP for the GS9 (Rasmussen et al., 2014), this first phase would last ~500 years until 39.4 ka, according to the ODP 976 age model. The main phase of the GS9 (pollen zone 2) exhibits the maximum abundance of semi-desert and steppe vegetation (55-71%) and the deciduous temperate forest minimum (1-5%) (Figs 3, 6). This phase of intense aridity lasts ~600 years, between 39.4 and 38.8 ka BP, according to the age model, and corresponds to the main fingerprint of HS4 (Fig. 3.6). The final phase (pollen zone 3a) displays a fast but short spread of the temperate deciduous forest and Ericaceae, followed by a slight development of semi-desert taxa (30%) and then a large expansion of *Cedrus,* indicating a general climate instability at the end of GS9 (Fig. 3.3). This last phase lasts between 38.8 and 38.3 ka BP, implying a duration of ~500 years in ODP 976 record. In total, the imprint of GS9 in the Alboran Sea lasted around 1.6 ka, between around 39.9 and 38.3 ka BP, with the main HS4 cold and arid phase lasting around 600 years.

Special consideration must be made about the significance of *Cedrus* pollen abundance for the evaluation of the pollen source area. The *Cedrus* increase observed in the first and third phases of the GS9 in the Alboran Sea is likely to result from two processes (Fig. 3.8). First, the cool and humid conditions before and after HS4 favouring the expansion of montane vegetation at the north in the Betic Cordillera and at the south in the Rif Cordillera. This interpretation is supported by the PCA results where *Cedrus* appears, together with Ericaceae, as a humidity indicator. In addition, the high percentages of *Cedrus* likely indicate an increased aerial input from North Africa in the Mediterranean resulting from the atmospheric circulation rearrangement, also evidenced by the increased palygorskite input and the presence of *Argania* pollen, an endemic Moroccan plant, in the first and second phases of the GS9 in ODP 976 record (Fig. 3.3) (Bout-Roumazeilles et al., 2007). This interpretation is supported by a recent study in the Sierra Nevada records, showing *Cedrus* as a North-African indicator mainly, and which variations in the last glacial period followed the climate millennial oscillations (Jiménez-Moreno et al., 2020). Unfortunately, no Moroccan record is currently available for this time period to further investigate the proportion of pollen that may be incoming from Africa.

The ODP 976 phasing record is in agreement with the three-phases pattern identified during the GS9 in the NEEM ice-core record, using methane concentration and ^{17}O-excess as main proxies (Guillevic et al., 2014) (Fig. 3.6), with a duration of 390, 740, and 550 years respectively and a total duration of 1,680 yr. The Greenland pattern seems linked with changes in the hydroclimatic configuration of lower latitudes and likely connected to the position of the ITCZ, as indicated by the variability of methane concentration and ^{17}O-excess proxies. Such pattern was not observed previously on the Greenland $\delta^{18}O$ curve, as traditional $\delta^{18}O$ only reflects the ice temperature changes at the local scale (Chappellaz et al., 2013; Dahl-Jensen et al., 2013; Gkinis et al., 2021).

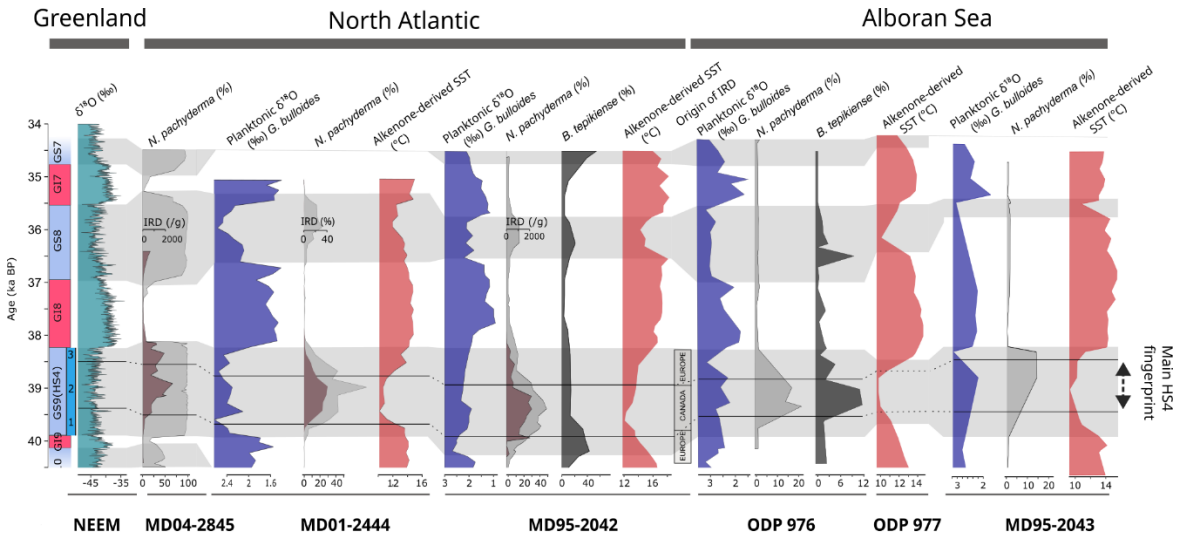


Fig. 3.7. Correlation between Greenland NEEM record (Guillevic et al., 2014), IRD deposition (brown curve for the Atlantic records) and the main marine proxies available for the six marine cores MD04-2845 (Sánchez Goñi et al., 2013) MD01-2444 (Margari et al., 2020), MD95-2042 (Sánchez Goñi et al., 2000, 2013; Davtian and Bard, 2022), ODP 976 (von Grafenstein et al., 1999; Combourieu-Nebout et al., 2002), ODP 977 (Martrat et al., 2004), and MD95-2043 (Cacho et al., 1999 ; Pérez-Folgado et al., 2003). Each core is plotted according to its own age model. MD95-2042 age model was taken from the latest data published by Davtian and Bard (2022), based on recalibrated radiocabron dates. MD01-2444 and ODP 977 age model are based on correlation tunning between planktonic 18O and Greenland isotopic events. ODP 976 and MD95-2043 age models are based on AMS dates and some additional tiepoints of the temperate pollen curve on GICC05 timescale. The three phases of GS9 and the main HS4 fingerprint, were tentatively placed on each core following Guillevic et al. (2014) and this study.

Phase 1 is characterized in Greenland NEEM record by a decrease in CH4 concentrations reflecting the beginning of the drying in the northern hemisphere subtropical zones, including the ODP 976 area, resulting from the first southward shift of the ITCZ (Guillevic et al., 2014; Rhodes et al., 2015). The first increase of semi-desert vegetation pollen in the ODP 976 record could correspond to this first drying episode (Fig. 3.6). The transition to phase 2 in Greenland was linked to the maximum southward shift of the ITCZ causing changes in low latitude water cycles, and this interpretation is supported by

lower latitude records, like Brazil stalagmites (Wendt et al., 2019) and African margin sediments (Jullien et al., 2007). During the main phase of the GS9 , the ITCZ's southernmost position causes intense drought in the northern hemisphere and intense rainfalls in the southern latitudes. ODP 976 record supports such enhanced drought phase through the development of the semi-desert vegetation and the contemporaneous inputs of palygorskite clay particles from North Africa (Bout-Roumazeilles et al., 2007) (Fig. 3.6). This arid phase seems to be contemporaneous with the iceberg discharge in the North Atlantic, happening after the onset of stadial conditions as evidenced by the delay in IRD deposition compared to the SST drop in Iberian Margin sedimentary cores (Barker et al., 2015; Martrat et al., 2007) (Fig. 3.7). In the Bay of Biscay core MD04-2845, and the Iberian Margin cores MD01-2444 and MD95-2042, the IRD deposition occurs in a second time after the abrupt peak increase in *N. pachyderma* (Fig. 3.7), supporting the hypothesis of ice-rafting events being the consequence of the onset of stadial conditions, rather than the primary cause (Barker et al., 2015). Therefore, and as suggested by Guillevic et al. (2014), this most arid second phase could illustrate the main fingerprint of the HS4 during the GS9, but the precise chronological relationship between HSs and GSs still needs to be clarified. The transition to Greenland NEEM phase 3 was interpreted as a progressive northward shift of the ITCZ and the gradual reestablishment of the Atlantic meridional overturning circulation (AMOC) at the end of the iceberg discharge (Guillevic et al., 2014; Wendt et al., 2019).

These three-phases were already described in core MD01-2444 based on the high-resolution marine proxies (Margari et al., 2020), and in cores MD95-2042 and MD95-2043 based on pollen and marine proxies (Fletcher and Sánchez Goñi, 2008; Sánchez Goñi et al., 2000). The progressive amelioration at the end of HS4 was identified in core MD01-2444, and the temperate tree reversal at the HS4/GI8 transition is consistent with ODP 976 pollen zone 3a. For the first time, ODP 976 provides ultra-high resolution palynological evidence for the climate amelioration and instability characteristic of the final phase of GS9.

3.2.6.1.2 Greenland Interstadial 8 and Greenland Stadial 8

The GI8 warming in ODP 976 is illustrated by the increase in SSTs shown in the *G. bulloides* $\delta^{18}O$ values and the development of temperate and Mediterranean forest pollen taxa as observed in other Mediterranean records (e.g. Allen et al., 1999; Combourieu-Nebout et al., 2002; Fletcher et al., 2010b; Fourcade et al., 2024). Strikingly, the deciduous temperate forest curve follows the trend of methane concentration in the Greenland NEEM ice core record (Chappellaz et al., 2013) (Fig. 3.6), as previously noticed by Margari et al. (2020), indicating that the vegetation signal in the Alboran Sea is well correlated to global atmospheric methane concentrations, and therefore to southern latitudes wetlands activity (Rhodes et al., 2017). While the warming of the GI8 indicated by the $\delta^{18}O$ increase is abrupt in Greenland, the shift back to interstadial conditions in the Alboran Sea pollen record appears

progressive, as indicated by the two-phase recovery of temperate and Mediterranean forest (pollen zones 3b and 3c) (Fig. 3.3). In the ODP 976 pollen record, the interstadial optimum is identified in zone 3c, between 37.6 and 36.8 ka, several centuries after the Greenland GI8 optimum (Fig. 3.6). The "progressive cooling and abrupt warming" pattern for millennial oscillations usually described in the Greenland records therefore appears to be reversed at lower latitudes for the GS9 / HS4, where the cooling is abrupt and the warming progressive. Such stadial / interstadial pattern seems to be characteristic of lower latitude as previously evidenced in speleothem records (Genty et al., 2010).

For the following Stadial GS8 (not associated with a Heinrich Event), the pattern is different, with no peak abundance of *N. pachyderma* and only a small increase in *B. tepikiense* preceding the expansion of the steppe, which appears very short compared to the HS4. This shows that the water refreshing could be less intense and precedes the vegetation change, implying a different triggering mechanism for the abrupt change of ordinary stadials. This different imprint of Heinrich Events versus ordinary stadials in the Mediterranean area is less visible in the Greenland record of $\delta^{18}O$, ^{17}O-excess and methane concentration: the intensity of these indicators' shift is similar in both cold episodes, although the typical three-phase pattern of the GS9 is not identified in the GS8 in Greenland (Fig. 3.6).

3.2.6.2 The HS4 / GI8 vegetation dynamics at a regional scale

Several long palynological sequences have offered insights into the imprint of HS4 in the Iberian Peninsula region (Figs 1, 8). An extensive review of the continental palaeobotanical records in the Iberian Peninsula was recently published (Carrión et al., 2024a), although very few sites have sufficient resolution to identify the cold HS4 interval. In southern Spain, two terrestrial records, Padul peatland and Fuentillejo maar, provide low-resolution palynological data, but they both identified an expansion of the steppe and semi-desert taxa associated with the cold and arid phase of the HS4 (Camuera et al., 2019; Ortiz et al., 2013; Pons and Reille, 1988; Vegas et al., 2010, Fig. 3.8). Recently, the new continuous lacustrine record from Los Tollos in SW Spain site provided a new high-resolution palynological sequence spanning over 40 ka, and an expansion of xerophytic vegetation was identified at 38.9 ka BP compatible with GS9/HS4 timing (Carrión et al., 2024b, Fig. 3.8). Further north, the pollen sequence from El Cañizar de Villaquemado paleolake in the interior semi-arid area of NE Spain provided a discontinuous record for MIS 3 but identified a semi-desert vegetation peak around 40 ka BP, which is the most arid phase of the Last Glacial in the whole record, and is chronologically compatible with HS4 (González-Sampériz et al., 2020; Wei et al., 2021). The two long speleothem records in Ejulve cave (Spain) and Villars cave (southwestern France) were used to calibrate the timing of abrupt climate changes during the Upper Pleistocene (Genty et al., 2003, 2005, 2010; Pérez Mejías, 2019; Pérez-Mejías et al., 2019), and both identified a cold episode lasting from ~40 to 38 ka BP for Ejulve and ~ 39 to 38 ka BP for Villars (Fig. 3.8).

Deep-sea cores along the Iberian borderlands allow a high-resolution and continuous reconstruction. Although their resolution is lower than ODP 976 core, MD01-2444, MD95-2042 and MD95-2043 palynological sequences on either side of the Gibraltar Strait display a very similar 3-phased pattern during the GS9, as shown in Fig. 3.8 (Fletcher and Sánchez Goñi, 2008; Sánchez Goñi et al., 2000). Unfortunately, in Padul, the low resolution does not allow the correlation of pollen spectra to the different phases identified in deep-sea cores. At Los Tollos, the resolution is comparable to the ODP 976 record (Carrión et al., 2024), but it is hard to identify phases within GS9 probably due to the different nature of the record. Indeed, the lacustrine palynological record displays very high percentages of Amaranthaceae as a main component of the local vegetation, blurring the main imprint of HS4. However, it is to be noticed that there is a slight increase in temperate and Mediterranean vegetation after the main peak of *Artemisia*, compatible with the third GS9 phase identified in ODP 976 showing climate amelioration. In the Alboran Sea, the main phase of the GS9 evidenced by the maximum semi-desert pollen taxa corresponds to the maximum entrance of sub-polar waters through the Gibraltar Strait, as shown by the maximum occurrence of *N. pachynerma*, *B. tepikiense*, and the low SSTs in the three cores ODP 976, ODP 977, and MD95-2043, in phase with the IRD deposition on the other side of the Gibraltar strait (Fig. 3.7). During this main phase, ODP 976 and MD95-2043 pollen spectra are very similar, with the total of semi-desert taxa reaching over 60% of the total pollen sum. The same percentages are reached in the Padul and Los Tollos records, showing that the Alboran Sea deep sea records provide good insights into the expansion of semi-desert vegetation in the south of the Iberian Peninsula during HS4. Values of semi-desert taxa on the Atlantic side are lower (<50%), indicating a possible west-to-east trend of aridification in the Iberian Peninsula during GS9 / HS4. This is in agreement with previous studies showing that the impact of Heinrich stadials on the vegetation was more intense in the Mediterranean region (Roucoux et al., 2005; Sepulchre et al., 2007). In the Gulf of Lion, the core MD99-2343 shows that the semi-desert expansion is more limited, and the temperate forest appears more persistent during HS4 (Fourcade et al., 2024) (Fig. 3.8). This indicates that the vegetation response to the HS4 cold pulse was contrasted geographically with the coldest and driest conditions found in SW Mediterranean, while relatively higher precipitations persisted in the NW Mediterranean. This pattern of southern increase of aridity recalls the modern distribution of annual and seasonal precipitations in the Mediterranean region (Deitch et al., 2017; Gonzalez-Hidalgo et al., 2024).

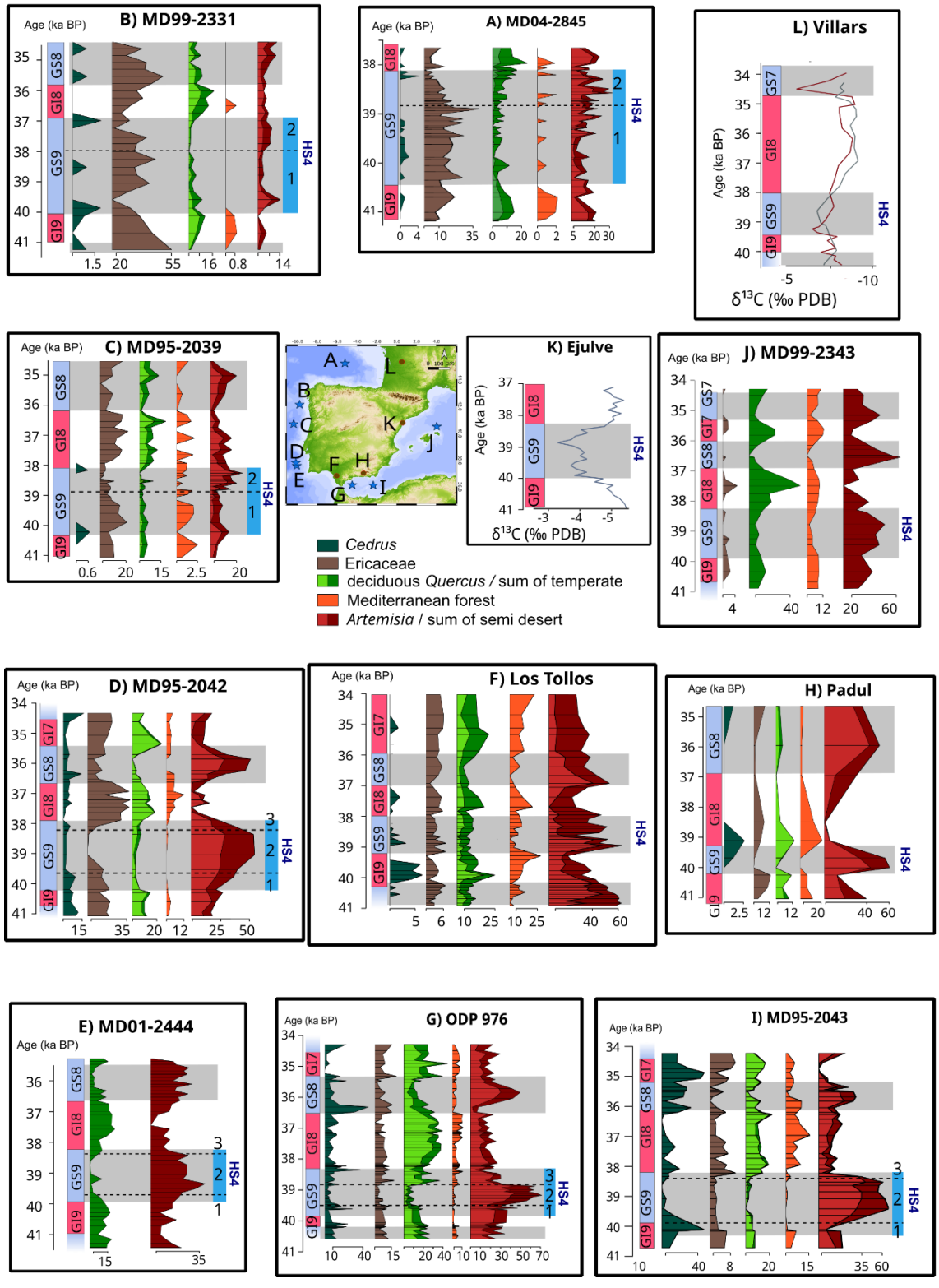


Fig. 3.8. Comparison between marine and terrestrial records around the Iberian Peninsula. Padul (Pons and Reille, 1988 ; Camuera et al., 2019), Los Tollos (Carrión et al., 2024), MD95-2043 (Fletcher and Sánchez Goñi, 2008), MD95-2042 (Sánchez Goñi et al., 2000, 2002), MD01-2444 (Margari et al., 2020), MD95-2039 (Roucoux et al., 2005), MD99-2331 (Naughton et al., 2009), MD99-2343 (Fourcade et al., 2024), MD04-2845 (Fourcade et al., 2022), and speleothem records: Ejulve cave (Pérez Mejías et al., 2019), and Villars cave (Genty et al., 2003, 2010) . The main pollen taxa and groups describing the vegetation dynamics during HS4 and GI8 are shown, together with isotope

values from speleothems records. When the resolution of the record allowed it, the phasing of GS9 was indicated by the numbers at the right of the diagram, with HS4 main fingerprint likely corresponding to phase 2 in the three-phased records.

The comparison between marine and terrestrial records around the Iberian Peninsula suggests that the internal pattern of GS9 / HS4 is different at northern latitudes on the Atlantic coast, where a two-phased pattern with wet to dry climatic trend was identified in cores MD95-2039 (Roucoux et al., 2005), MD99-2331 (Naughton et al., 2009) and MD04-2845 (Fourcade et al., 2022). The high resolution of core MD04-2845 allowed to document these two phases (Fig. 3.8). While the first phase is characterized by intense cold conditions, maximum IRD deposition and humidity as indicated by Ericaceae and specifically *Calluna vulgaris* pollen, the second phase appears drier with maximum abundance of semi-desert taxa, and still intense cold oceanic and atmospheric conditions.

How these two-phased at the north and three-phased at the south patterns for the GS9 / HS4 are related to each other remains unclear. Different scenarios were proposed to explain the different phasing during GS9 / HS4 and their geographical variability. Sánchez Goñi et al. (2000) linked the three-phased pattern observed to the provenance of IRD in the North Atlantic. While the first and third phase of the HS with a cool but still humid climate is linked to the collapse of European icebergs, the main cold and arid phase is contemporaneous with the melting of Canadian icebergs. Other models discussed the influence of the positive versus negative NAO configuration (e.g. Sánchez Goñi et al., 2002) or the shifting positions of the polar front and the Atlantic jet stream (e.g. Naughton et al., 2009). Recently, the importance of sub-regional to local processes in modulating the response to a global change was highlighted (Fourcade et al., 2024; Sánchez Goñi et al., 2021).

The transition between the HS4 and the GI8 (pollen zone 3a) in the ODP 976 record is marked by a great instability, visible in the diagram through variations of pollen abundances, particularly of steppe and semi-desert taxa, temperate and Mediterranean taxa, Ericaceae and *Cedrus*. Such an instability at the end of GS9 / HS4 is documented for the first time thanks to the ultra-high-resolution approach and recalls the pattern of the last deglaciation (~18 to 11 ka BP) described in the same core (Combourieu-Nebout et al., 2009) (Fig. 3.9). After the maximum semi-desert expansion (phase 2 of the GS9), the temperate and Mediterranean vegetation displays a first increase reminiscent of the Bölling-Alleröd forest spread following the HS1. The new smaller expansion of the semi-desert taxa could be related to an event like a very short and tiny equivalent of the “Younger Dryas” (Fig. 3.9). Then, the peak of *Cedrus* could reflect the shift towards a humidity increase followed by the development of the deciduous temperate forest at the onset of the GI8, that mimics the onset of the Holocene in the same core. Therefore, the vegetation succession during the transition HS4/GI8 is similar to a glacial/interglacial transition, although at a millennial timescale. Until now, this particular pattern has

never been recorded in other Heinrich Stadials identified in the same core (Genty et al., 2010; Combourieu-Nebout personal communication), making it the characteristic vegetation signature of the HS4/GI8 transition in the southwestern Mediterranean region, with a pattern closer to a glacial/interglacial transition than to a classic stadial/interstadial one.

The two-phased GI8 pattern characterised by the development of the temperate deciduous forest and then the expansion of Mediterranean taxa is also well-evidenced in the two cores MD95-2042 and MD95-2043. Nevertheless, the maximum expansion of deciduous temperate forest in the ODP 976 core reaches ~40%, which is comparable to those observed in core MD95-2042, while it doesn't exceed 20% in the nearby core MD95-2043. This might indicate that ODP 976 signal is more influenced by the return of Atlantic humidity and the recovery of the Atlantic Forest west of the Iberian Peninsula at the onset of GI8, as also evidenced by the high percentages of Ericaceae on the Atlantic core MD95-2042 (Fig. 3.8). Such a particular pattern in ODP 976 core record with enhanced Mediterranean aridity during HS4 and strong Atlantic humidity influence during GI8, shows that the ODP 976 core position at the gateway of Mediterranean and Atlantic climate influences trigger the enhanced expression of all climate events recorded through vegetation.

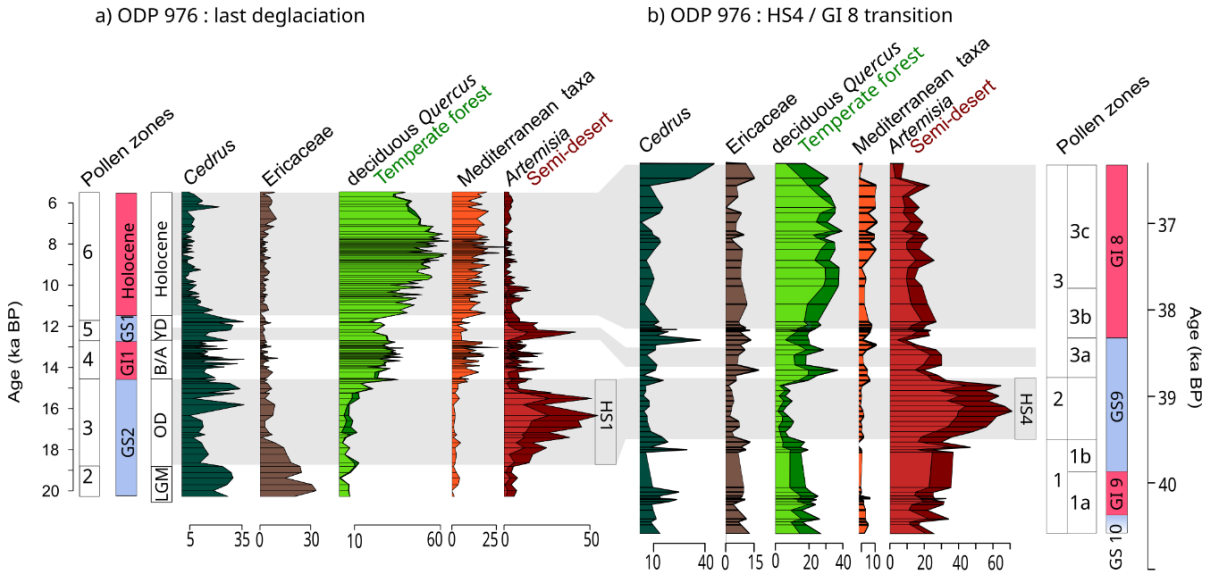


Fig. 3.9. Comparison between (a) the structure of the last deglaciation: LGM = Last Glacial Maximum; B/A = Bölling/Alleröd; YD = Younger Dryas (Combourieu-Nebout et al., 2009) and (b) the HS4 / GI8 transition (this study) in the palynological record of ODP 976. Pollen zones, Greenland events, and climatic phases are indicated on either side of the pollen diagrams.

3.2.6.3 Pollen-based climate reconstructions and climate changes at sub-millennial scale

According to the ODP 976 results, significantly dry and cold conditions are reconstructed during HS4 through all four climate reconstruction methods. The abrupt shift in annual temperatures and precipitations is mainly driven by intense cold and drought during winters and colder summers. This implies that important changes in seasonality occurred during HS4, especially in seasonal precipitations, as previously deduced by the PCA analysis (Fig. 3.4). The results indicate an abrupt perturbation of the typical Mediterranean seasonal regime, with a major hydrological stress caused by arid winters during the main GS9 phase. This supports the deterioration of the seasonal regime and the low hydrological input indicated by the contraction of the temperate and Mediterranean forest and the expansion of low water-demanding species mainly represented by *Artemisia*, Amaranthaceae and *Ephedra*.

Continental paleoclimate records for this period are rare (Liu et al., 2024). In the geochemical and palynological record of Fuentillejos maar (central Spain), the HS4 was associated with a low lake level and described as “less cold but arid” (Vegas et al., 2006), an interpretation which is supported by the ODP 976 results. The speleothem record of Ejulve cave evidenced the highest $\delta^{13}C$ values of all the sequences during HS4, indicating an extreme drop in rainfall, as also shown in the Villars cave $\delta^{13}C$ profile (Fig. 3.8) (Genty et al., 2010). In the Upper Tagus Basin, a period of intense loess deposition indicating extreme drought was identified between 43 ± 3.8 ka and 41.3 ± 4.0 ka BP, a period which could include the HS4 interval within the uncertainty of the OSL dating (Wolf et al., 2018). Temperature records from molecular biomarkers in the Eifel Volcanic Field, Germany, recently showed the importance of seasonality in the millennial-scale climate oscillations, with Heinrich Stadials affecting especially winter temperatures, while warmer seasons were less impacted (Zander et al., 2024).

Comparison with published pollen-based climate reconstructions from MD95-2042, MD95-2043, MD99-2343 and Padul records (Fig. 3.10) enables the discussion of the spatial variability of climate change in the Iberian Peninsula, although some limitations come from the low resolution, single method approach, and a limited number of reconstructed climate parameters published for these records. First, the hydroclimate reconstructions through the WA-PLS method published for Padul (Camuera et al., 2022) show a pattern very close to the ODP 976 reconstructions with the same method, with annual precipitations as low as 375 mm during the HS4 (representing a decrease of ~112 mm), winter precipitations reaching about 70 mm (representing a decrease of ~70 mm), and summer precipitations showing almost no change. This confirms that the perturbation identified through the ODP 976 reconstructions for HS4 represents well the evolution of climate seasonal conditions on the Iberian inland.

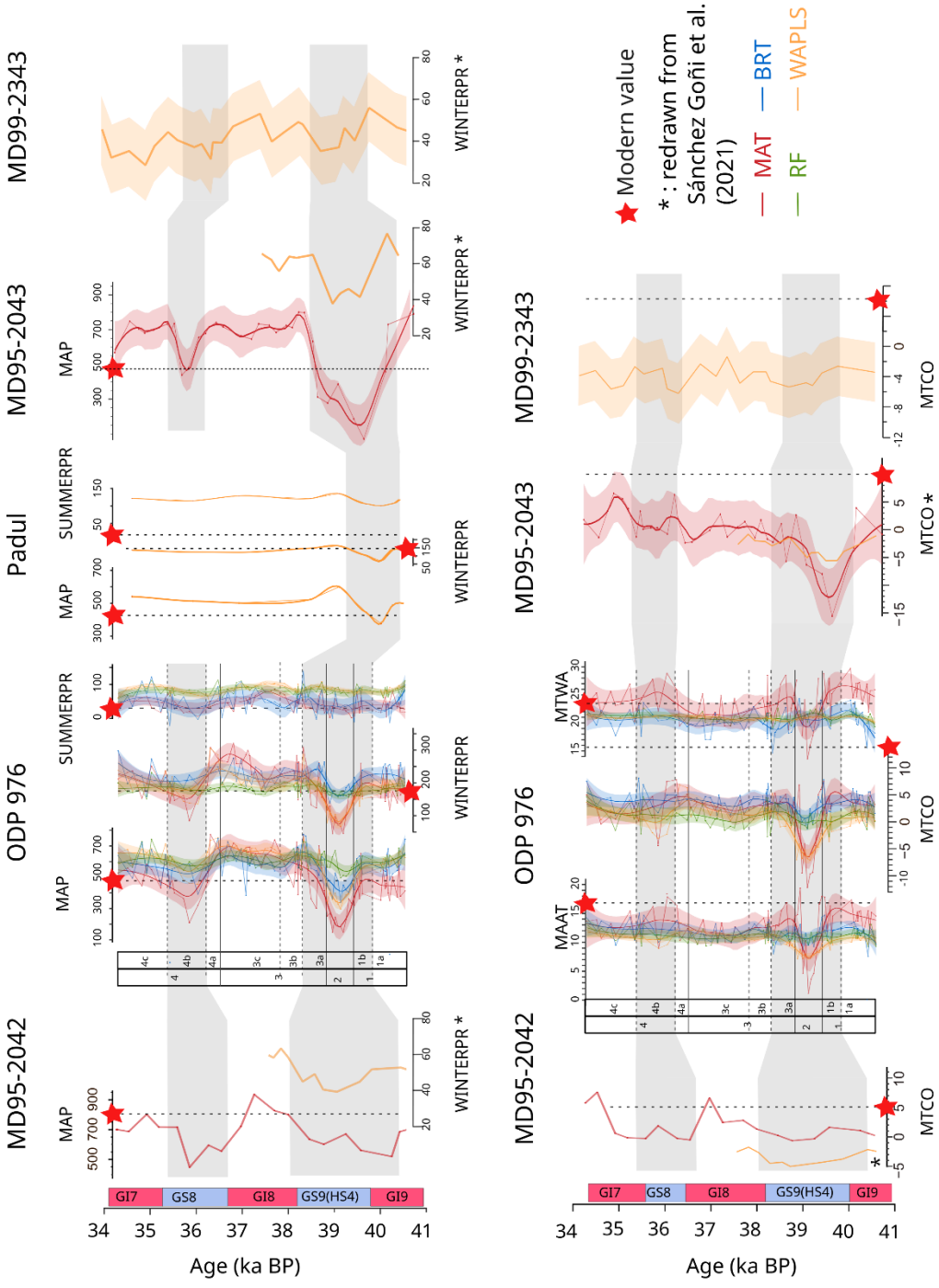


Fig 3.10. Comparison between different pollen-based climate reconstructions inferred from cores MD 95-2042 (Sánchez Goñi et al., 2002, 2021; MD95-2043, (Fletcher et al, 2010b), Padul (Camuera et al., 2019), and MD99-2343 (Sánchez Goñi et al. 2021). Different methods are used (MAT, WA-PLS) and the modern calibration dataset is different.

The very dry conditions are also identified in the MD95-2042 and MD95-2043 reconstructions (Sánchez Goñi et al., 2002), with a 200 mm shift in annual precipitations on the Atlantic side, and a 600 mm shift on the eastern Alboran seaside. The ODP 976 reconstructions, therefore, show intermediate

values and a clear pattern of aridification toward the east is identified, with increasing hydrological stress on the SW Mediterranean compared to the Atlantic side. Winter precipitations for the two cores MD95-2042 and MD95-2043 reconstructed through the WA-PLS method (Sánchez Goñi et al., 2021) show a decrease until about 40 mm, a result very close to the reconstructions of the ODP 976 core with the same method. This shows that the winter rainfall anomaly during HS4 is comparable on both sides of the Gibraltar Strait, but the consequences of such winter drought were enhanced on the Mediterranean side due to the particular seasonal regime perturbation, inducing harsher climate conditions.

For temperature reconstructions, a similar pattern of increasing cold intensity toward the east is observed, with a winter temperature anomaly of only ~2°C (from ~1.5°C to ~ -1°C) for core MD05-2042 on the Atlantic side and an extreme anomaly of around 22 °C (from 4°C to -16°C) for MD95-2043 core on the eastern Alboran Sea. Again, ODP 976 winter temperature reconstructions with the same method show intermediate values, with an anomaly of about 17°C (from 5°C to -12°C). However, the temperature anomaly here has to be interpreted with caution as it is well known that the MAT is the most sensitive method (Brewer et al., 2007; Chevalier et al., 2020) and probably not the best method for reconstructing climate from steppe pollen assemblages (Tarasov et al., 1998). The temperature decrease is less marked through the other reconstruction methods. Therefore, a multimethod approach would be necessary on the other cores to better characterize the temperature pattern and confirm or not the tendency to colder conditions on the western Mediterranean side. Winter temperatures were also recently estimated for MD95-2042, MD95-2043 and MD99-2343 cores using the WA-PLS method (Sánchez Goñi et al., 2021). Like in the ODP 976, the shift in winter temperatures from core MD95-2043 is more moderate than the one obtained through the MAT method. For core MD95-2042, however, lower winter temperatures (-5°C) are reconstructed with the WA-PLS than with the MAT method, but this is probably due to the inclusion of *Pinus* pollen in the modern and fossil samples used for the reconstructions, contrary to the ODP 976 results (see methods).

In core MD99-2343 from the Gulf of Lion, the HS4 appears much more moderate for both precipitations and temperature parameters (Sánchez Goñi et al., 2021) (Fig. 3.10), showing that the impact of HS4 on the NW Mediterranean region was less intense compared to the SW Mediterranean.

Climate model simulations of Heinrich Stadials are rare and generally focused on the ice sheet dynamics, the AMOC variations and the climate configuration at a broader geographic scale, with poor focus on the continental climate and vegetation (e.g. Alvarez-Solas et al., 2010, 2011; Kageyama et al., 2010; Menviel et al., 2014; Skinner et al., 2020). Therefore, a model-data comparison currently still represents a challenge. However, an interesting comparison can be made with the model simulations

performed with an atmospheric global circulation model at a 60 km resolution (Sepulchre et al., 2007). A west-to-east trend in aridification was evidenced, similar to the pattern described before, but with almost no change in annual temperatures in the Iberian Peninsula during the HS4. The ODP 976 climate reconstructions results do not support this pattern, with a clear temperature decrease identified with all the methods, although with different amplitudes. In addition, remarkable discrepancies between absolute values of pollen-based reconstructions and model simulations can be observed. This is probably linked to the general circulation model used and highlights the need for new paleoclimate model simulations run specifically on the Mediterranean region, which might account better for the specific features and complexities of the Mediterranean system.

3.2.6.4 Human occupations during the 42–34 ka BP climate instability

The two sets of maps (Fig. 3.11 and 3.12) inferred from our dataset enable the observation of the distribution of sites and dates within the 42–34 ca ka BP interval, with a 95% confidence range, depending on the radiometric methods and the confidence index considered. While the former map includes all the radiometric methods with confidence index 1 and 2 (see Methods section 3.5), the latter is more restrictive and includes only radiocarbon dates which were given the maximum confidence index, and tephra layers.

The maps produced show sites in which the range of dating for a given technocomplex (Middle Palaeolithic, Uluzzian, Chatelperronian, Aurignacian sensu lato) overlap with the time window considered (before, during and after GS9 / HS4). When more technocomplexes are represented on the map for a given site, it does not necessarily mean that there is an overlap between different human groups but only that the range of dating of different technocomplexes fall within their 95% confidence in the same temporal interval. For example, at Cova Eiros the two dates of Layer 3 (Middle Palaeolithic) and Layer 2 (Aurignacian SL) fall in the "after GS9 / HS4" interval within their 95% uncertainty, but they do not overlap (Lombera-Hermida et al., 2021).

The two sets of maps show a decrease in the number of sites and number of dates associated with Middle Palaeolithic, Châtelperronian and Uluzzian technocomplexes through time and an increase in sites and dates associated with Aurignacian SL technocomplexes. Selecting only the radiocarbon dates (Table 6-D and Supplementary fig. S2) significantly decreases the number of dates and sites associated with a Middle Palaeolithic technocomplex in the three intervals of time. Finally, selecting only the radiocarbon dates with index 2 and the four tephra layers reduces even more the number of sites and dates associated with a Middle Palaeolithic technocomplex (Table 6-E and Fig. 3.12). In the interval after the GS9 / HS4, the only remaining site with Middle Palaeolithic industry is Cova Eiros, with one date ranging until 37.6 ka cal BP. The authors are more prudent and claim a

Neanderthal persistence at the site until ~40 ka ca BP, waiting for more data to precisely date the timing of occupation (Lombera-Hermida et al., 2021). Therefore, based on the radiocarbon index 2 dataset, there is currently very little, if not any, evidence of Middle Palaeolithic occupation during and after the GS9 / HS4 that has not been subject to criticism. Nevertheless, with all methods and confidence index 1 and 2 considered (Table 6-C and Fig. 3.11), there are still 87 Middle Palaeolithic-associated dates from 42 different sites whose range could expand beyond the GS9 / HS4, indicating a possible persistence of Neanderthal populations beyond the arid episode, at least in the southern Mediterranean region.

These results show that a very different scenario for the MUPT can be reconstructed based on the data selected and considered valid. The growing number of dates and dating methods applied in the last years has brought new challenges to our understanding of the MUPT, reinforcing the interpretation already present more than twenty years ago of being "blind in a cloud of data" (Pettitt and Pike, 2015).

There is currently a general agreement on anatomically modern humans' presence in western Eurasia before at least 45–43 ka cal BP. In the three sets of maps, *Homo sapiens* was already well settled in western Europe prior to the GS9 / HS4, as evidenced by the presence of Aurignacian SL technocomplexes as early as ~43 ka cal BPin the Cantabrian region (Marín-Arroyo et al., 2018; Wood et al., 2014), in the Pyrenean like in Isturitz (Barshay-Szmidt et al., 2018) , in southern Spain at Bajondillo (Cortés-Sánchez et al., 2019; Zilhão but see 2021a), and around 41 ka cal BP in Portugal at Lapa do Picareiro (Haws, Benedetti, Talamo, et al., 2020). Even earlier incursions of *Homo sapiens* in western Eurasia were possibly identified at Bacho Kiro (Hublin et al., 2020) and Grotte Mandrin (Slimak et al., 2022; but see Teyssandier, 2024).

On the other hand, the chronology of the last occurrence of Neanderthals remains uncertain and strongly dependent on the data one considers valid or not. The recent effort in geochronological research has brought increasing evidence for no late survival of Neanderthal after 41–39.2 ka cal BP (Higham et al., 2014), and even earlier in specific regions like 47.9–45.1 ka cal BP in Cantabria (Marín-Arroyo et al., 2018) and 47.3–41.8 ka cal BP in the Italian peninsula (Higham et al., 2024). These estimations are based on Bayesian modelling approaches applied to robust sets of dates. However, late persistence is still claimed by a number of authors south of the Iberian Peninsula, like in Cueva Anton until ~37 ka cal BP (Zilhão et al., 2017), until at least 38.5 ka cal BP in Gruta do Caldeirão (Zilhão, et al., 2021), and ~30 ka cal BP in Carihuela (Carrión et al., 2019b). The most recent geochronological study on another Portuguese site, Foz do Enxarrique, supports the observation that the late Middle Palaeolithic is progressively more recent toward the SW Iberian Peninsula, also recognizing the validity

of the very late dates of Gorham's cave until 24 ka cal BP (Cunha et al., 2019; Finlayson et al., 2006). A similar statement is made on Salto do Boi site, where the transition is placed between 38.4 ± 1.9 ka and 34.0 ± 2.0 ka BP (Aubry et al., 2020). Indeed, as the chronology of these two sites is based on luminescence dating, they do not appear on the maps when considering only the radiocarbon dating (Fig. 3.12). Therefore, the authors of the so-called "Ebro Frontier theory" still argue that there is an apparent biogeographical frontier between late persistent Neanderthals at the south, and early *Homo sapiens* north of the Ebro valley during the 42–37 ka cal BP interval in the Iberian Peninsula (Zilhão, 2021b). This frontier is not visible in any of our maps, as recent research demonstrated that populations of *Homo sapiens* producing Aurignacian SL industries were already present in south-eastern Spain (Cortés-Sánchez et al., 2019), in Portugal (Haws, Benedetti, Talamo, et al., 2020), and even at the Abrigo de la Malia in central Spain, a region which was initially believed to be completely unpopulated as a consequence of the harsh environmental conditions (Sala et al., 2020, 2024). Therefore, if Neanderthals survived longer in the southern Iberian Peninsula as stipulated by the Ebro frontier supporters, this might indicate a long overlap of various millennia between them and early *Homo sapiens* populations. This potential long overlap is likely to be reduced as the chronology of erroneously young dated sites are being reassessed, as was the case for Gruta Oliveira, a Portuguese site which was initially key in supporting the Ebro frontier model and was then redated to MIS 5 (Zilhão et al., 2021). Furthermore, the late persistence of Middle Palaeolithic groups beyond 40 ka cal BP is also claimed in the Balkans, at Bioče and Velika Pećina (Karavanić et al., 2018, 2021; Vishnevskiy et al., 2019).

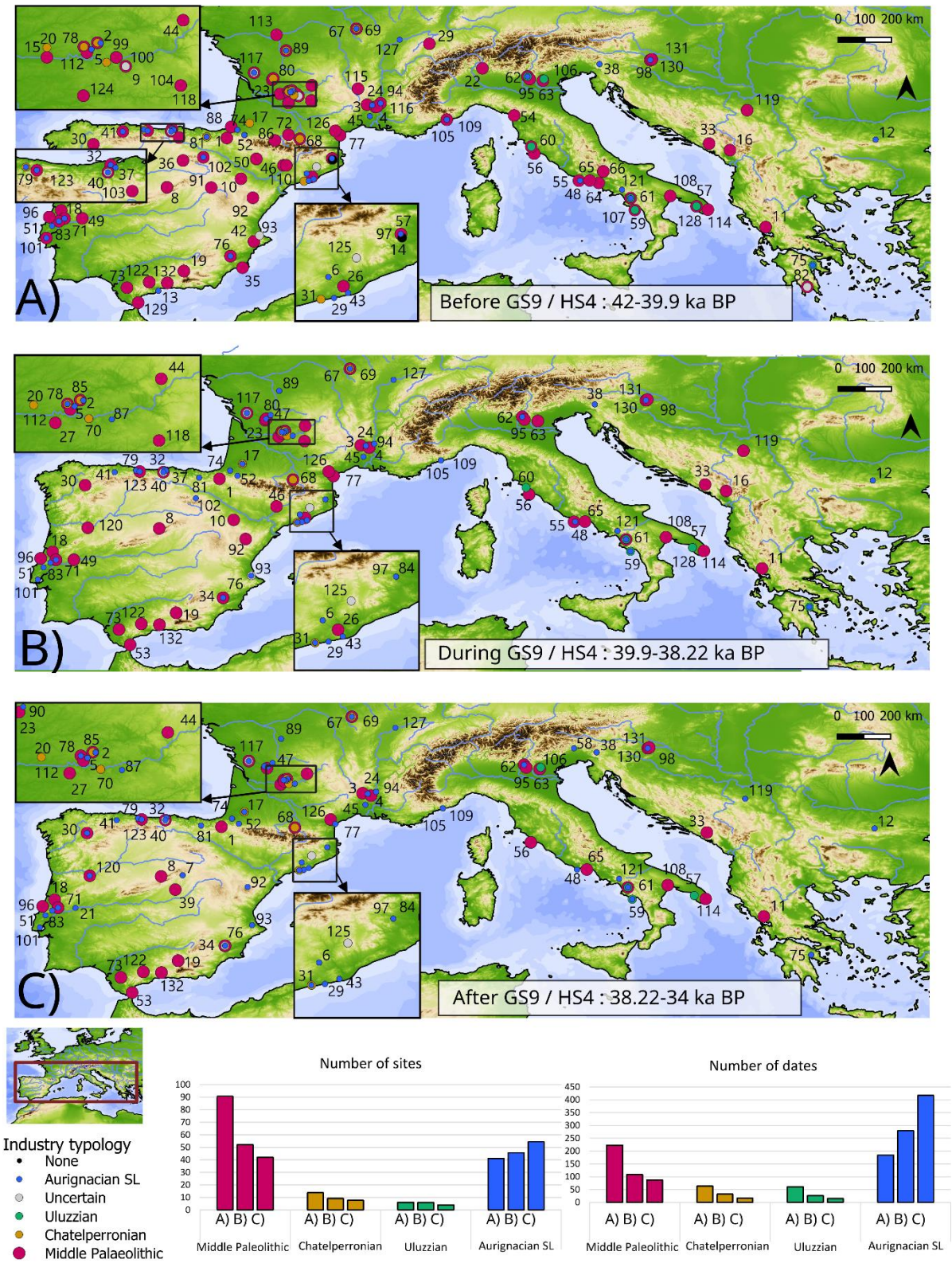


Fig. 3.11. Maps of archaeological sites and their associated technocomplexes with dates ranges falling before (A), during (B) and after (C) the GS9 / HS4. Dates from all dating methods and confidence index 1 and 2 were included (Table 6-C in results). The bar charts represent the number of sites (left) and dates (right) associated to each technocomplex for the three maps. **1**, Abauntz ; **2**, Abri Castanet ; **3**, Abri des Pêcheurs ; **4**, Abri du Maras ; **5**, Abri Pataud ; **6**, Abric Romaní ; **7**, Abrigo de la Malia ; **8**, Abrigo del molino ; **9**, Abris Peyroni ; **10**, Aguilón P7 ; **11** Asprochaliko ; **12**, Bacho

Kiro ; **13**, Bajondillo; **14**, Banyoles; **15**, Barbas III; **16**, Bioče ; **17**, Brassempouy ; **18**, Buraca Escura ; **19**, Carihuela ; **20**, Cassenade ; **21** Castelejo ; **22**, Caverna Generosa ; **23**, Chauverie ; **24**, Chauvet ; **25**, Chemin de Jupiter ; **26**, Coll Verdaguer ; **27**, Combe Capelle Bas ; **28**, Cotencher ; **29**, Cova del Gegant; **30**, Cova Eiros ; **31**, Cova Foradada ; **32**, Covalejos ; **33**, Crvena Stijena ; **34**, Cueva Antón ; **35**, Cueva de los aviones ; **36**, Cueva Millán ; **37**, Cueva Morin; **38**, Divjie Babe; **39**, El Canaveral ; **40**, El Castillo ; **41**, El Conde ; **42**, El Salt ; **43**, Els Canyars ; **44**, Espagnac ; **45**, Esquicho-Grapaou ; **46**, Estret de Tragó ; **47**, Fontechevade ; **48**, Fosselone ; **49**, Foz do Enxarrique ; **50**, Fuentes de San Cristobal ; **51**, Gato Preto ; **52**, Gatzarria ; **53**, Gorham ; **54**, Grotta all'Onda ; **55**, Grotta Breuil ; **56**, Grotta dei santi ; **57**, Grotta del Cavallo ; **58**, Grotta del Rio Secco ; **59**, Grotta della Cala ; **60**, Grotta della Fabbrica ; **61**, Grotta di Castelcività ; **62**, Grotta di Fumane ; **63**, Grotta di San Bernardino ; **64**, Grotta di San Sebastiano ; **65**, Grotta di Sant'Agostino ; **66**, Grotta Reali ; **67**, Grotte du Bison ; **68**, Grotte du Portel Ouest ; **69**, Grotte du Renne ; **70**, Grotte XVI ; **71**, Gruta do Caldeirao ; **72**, Harregi ; **73**, Higueral la Valleja ; **74**, Isturitz ; **75**, Klisoura ; **76**, La Boja ; **77**, La Crouzade ; **78**, La Ferrassie ; **79**, La Güelga ; **80**, La Quina ; **81**, Labeko Koba ; **82**, Lakonis cave I ; **83**, Lapa do Picareiro ; **84**, L'Arbreda ; **85**, Le Moustier ; **86**, Le Noisetier ; **87**, Le Piage ; **88**, Le Prissé ; **89**, Les Cottés ; **90**, Les Rois ; **91**, Los Casares ; **92**, Los Toros ; **93**, Malladetes ; **94**, Mandrin ; **95**, Mezzena ; **96**, Mira Nascente ; **97**, Mollet 1 ; **98**; Mujina Pećina ; **99**, Pech-de-l'Azé I ; **100**, Pech-de-l'Azé IV ; **101**, Pego do Diabo ; **102**, Peña Miel 1 ; **103**, Prado Vargas ; **104**, Ranc de l'Arc ; **105**, Riparo Bombrini ; **106**, Riparo del Broion ; **107**, Riparo del Poggio ; **108**, Riparo dell'Oscurusciuto ; **109**, Riparo Mochi ; **110**, Roca dels Bous ; **111**, Roc-de-Combe ; **112**, Roc-de-Marsal ; **113**, Roche cotard ; **114**, Romanelli ; **115**, Rond du Barry ; **116**, Saint-Marcel ; **117**, Saint-Césaire ; **118**, Sainte-Eulalie ; **119**, Šalitrena Pećina; **120**, Salto do Boi ; **121**, Serino ; **122**, Sima de la Palomas de Teba ; **123**, Sopeña ; **124**, Sous-les-Vignes ; **125**, Teixoneres ; **126**, Tournal ; **127**, Trou de la mère Clochette ; **128**, Uluzzo ; **129**, Vanguard ; **130**, Velika Pećina ; **131**, Vindija ; **132**, Zafarraya.

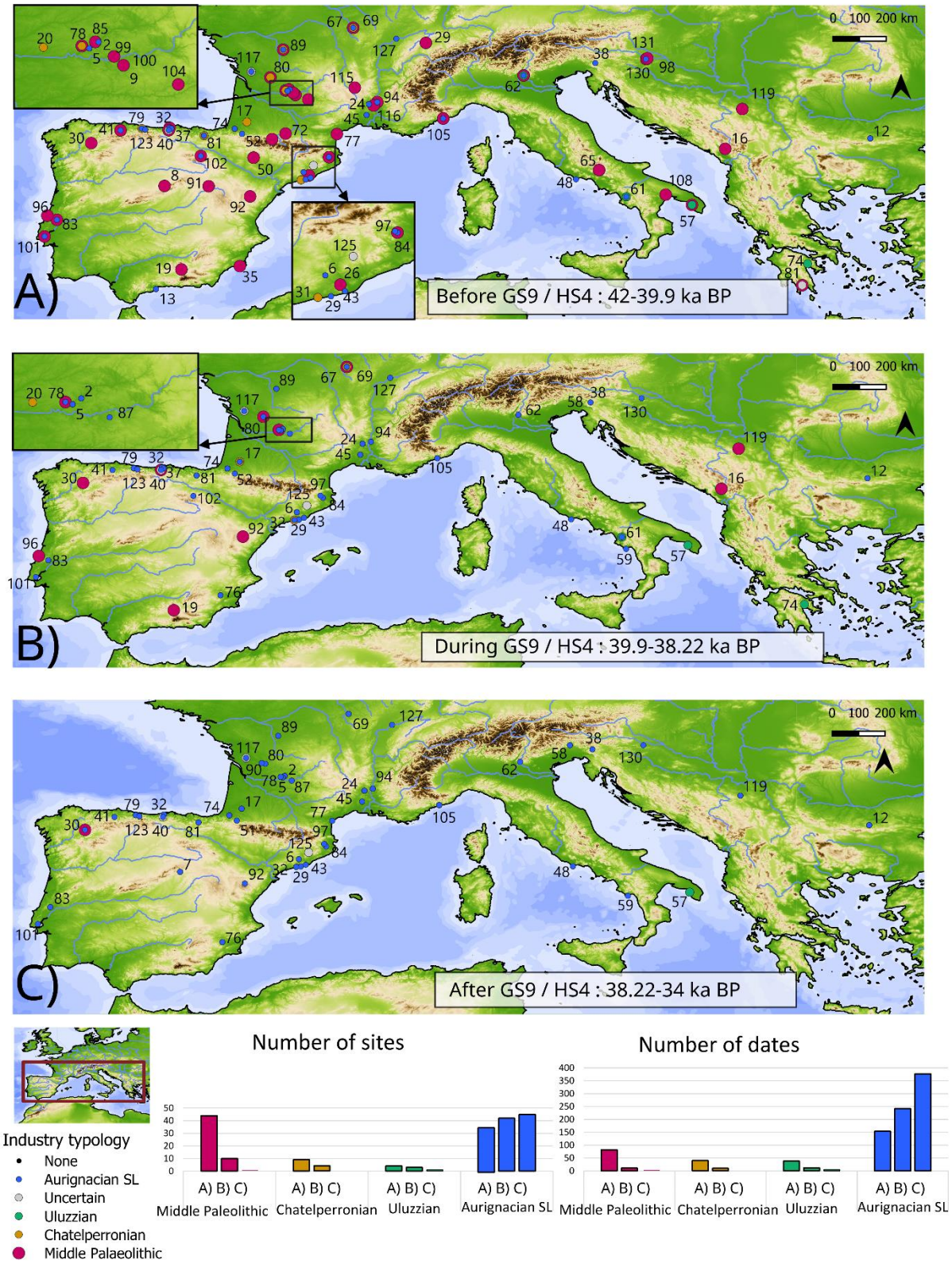


Fig. 3.12. Maps of archaeological sites and their associated technocomplexes with dates ranges at 95% falling in the interval before (A), during (B) and after (C) the GS9 / HS4. Only radiocarbon dates with confidence index 2 were included (Table 6. E in results). The bar charts represent the number

of sites (left) and dates (right) associated to each technocomplex for the three maps. For the names of the sites, refer to Fig. 3.11.

It remains very hard to place the archaeological evidence in a sub-millennial climate context and, therefore, to address with strong confidence the possible human occupation during GS9 / HS4. At some sites, the Middle Palaeolithic occupation appears to stop at the onset of GS9 / HS4, like in Coll Verdaguer (Daura et al., 2017) or possibly at los Casares (Alcaraz-Castaño et al., 2017) and Covalejos (Barquín and González, 2021). The HS5 (~48 ka BP) was identified as a possible date for Neanderthal abandonment of the site, like at El Salt (Galván et al., 2014) or Roca dels Bous (Benito-Calvo et al., 2020). At Abris du Maras, level 4 may be correlated to the HS5 or HS4 (Moncel, Chacón, et al., 2021). At other sites, the proto-Aurignacian makers enter the site during HS4, like in Les Cottés (Talamo et al., 2012), Abri Pataud (Higham et al., 2011), or Els Canyars, where a steppe environment was reconstructed thanks to the palynological analysis of coprolite remains and associated with the first *Homo sapiens* arrival at the site (Daura et al., 2013). This statement was supported by studies arguing that the *Homo sapiens* advance in Europe was favoured by the expansion of arid open landscapes like the one characteristic of HS4 (e.g. Badino et al., 2023; Banks et al., 2013; D'Errico and Sánchez Goñi, 2003; Haws et al., 2020; Sala et al., 2020). In other sites, the HS4 episode separates the Uluzzian from the Proto-Aurignacian, or the Proto from the Early Aurignacian, like in Isturitz (Barshay-Szmidt et al., 2018). In a number of Italian sites, the HS4 event / Cambrian Ignimbrite eruption layer seals the Uluzzian and sometimes Aurignacian occupation, like in Serino, Grotta di Castelcività, and Grotta del Cavallo (Falcucci et al., 2024; Higham et al., 2024; Wood et al., 2012; Zanchetta et al., 2018). Therefore, the HS4 has been discarded as a possible challenge for Italian Middle Palaeolithic groups, which would have been critically reduced, if not completely absent, before the HS4 (Falcucci et al., 2024). Furthermore, it has been shown that conditions during HS4 were more stable in Italy (Columbu et al., 2020), a statement that is supported by our regional comparison highlighting the reduced impact of HS4 on the NW Mediterranean region compared to the SW region. HS4 has rather been proposed as a trigger for an adaptative response for the first *Homo sapiens*, separating the Proto and Early Aurignacian cultures (Banks et al., 2013).

In conclusion, the potential impact of the HS4 on human populations during the MUPT in Mediterranean Europe remains poorly understood and hindered by the limitations of archaeological data available. HS4 has been used by different models in many different concurrent scenarios, depending on the timing one considers valid for the transition. If Neanderthals survived until the time of HS4 and beyond in southern Iberia, it is highly probable that they had to adapt to the harsh climate conditions that were evidenced in the ODP 976 core and many other archives. The most recent species distribution modelling studies confirmed that Neanderthal distribution was greatly influenced by

climate fluctuations during MIS4, with a habitat contraction during stadial episodes and habitat expansion during interstadials, and they also supported southwestern Europe as potential refuge areas that represented core habitat for the species during unfavourable episodes (Albouy et al., 2024; Melchionna et al., 2018). Several sites were presented as evidence of a late Neanderthal retreat in the southern Iberian Peninsula coastal refugia (Carrión et al., 2019b; Ochando et al., 2020c; Straus 2022) or in the mountain areas of the Iberian Peninsula like in Cova Eiros (Lombera-Hermida et al., 2021) or in the Balkans like in Šalitrena Pećina (Marín-Arroyo and Mihailović, 2017). According to the most reliable chronological data (Fig. 3.12), such apparent late refugia for Middle Palaeolithic populations are, for the most part, probably an artefact of unreliable chronological data, and need clarification. The most recent review of key sites for the MUPT (Zilhão et al., 2024) led to the same conclusion that, even with modelling approaches, current data is insufficient to attest the precise timing of Neanderthal replacement by *Homo sapiens*. A new paradigm for the MUPT is emerging, including complex population dynamics with regional variability especially between Eastern and Western Europe, cultural assimilation and population admixture (Zilhão et al., 2024). Thinking in term of human population, rather than Neanderthal and *Sapiens* species, now seems crucial to shedding light on the ecological implication of climate events like HS4 for the MUPT scenario in SW Europe. In the SE Iberian Peninsula, the ODP 976 record showed that the HS4 climate conditions at a regional scale were particularly extreme, and there is very few evidence of human occupation in general during and after the arid event (Fig. 3.12). Previous Heinrich Events during MIS 4 and MIS 3 were also shown to be very intense, like HS5 (Fletcher and Sánchez Goñi, 2008) which probably also weakened human populations present in SW Mediterranean Europe at that time (Galván et al., 2014). Repeated abrupt climate changes all along MIS 4-3 have likely weakened Neanderthal populations, reducing their niche repeatedly until their final extinction (Klein et al., 2023 ; Yaworsky et al., 2024). Thus, it is clear that the Neanderthal population was already declining before HS4, with increasingly isolated groups as evidenced by genetic data (Dalén et al., 2012; Slimak et al., 2023). Based on the currently available data, Neanderthal demise can, therefore, not be linked solely to an abrupt climate episode such as the HS4. However, the way they and the other human populations faced the intense and abrupt climate deterioration during GS9 / HS4 in SW Mediterranean still needs to be clarified with high-resolution, multiproxy palaeoecological studies in closer relation to the archaeological contexts.

3.2.7 Conclusion

The high-resolution palynological record of ODP 976 provided new insights into the fast dynamics of climate and vegetation changes during and after the HS4 in the southwestern Mediterranean region. A 3-phase pattern for the GS9 consistent with previous studies in Greenland and in the southern Iberian borderlands was described with a time resolution never achieved before.

The pollen assemblages in the ODP 976 core during the HS4 are dominated by steppe and semi-desert plants, representing the regional vegetation in the SE Iberian Peninsula. It was shown that a temperature decrease precedes the abrupt drop in precipitations, which is the most important signature of HS4 as the main phase of the GS9 in the SW Mediterranean, as evidenced by pollen-based climate reconstructions. Annual precipitations are the most impacted, driven by a decrease in winter precipitations, which evidences the complete disruption of the typical Mediterranean regime of precipitations during the HS4. The regional comparison shows that this extreme climate event was enhanced in SW Mediterranean compared to the Atlantic and Northern Mediterranean borderlands. In this region, the transition to the successive GI8 amelioration was characterized by great environmental instability and mimics the pattern of a deglaciation. It is still hard to evaluate the impact of such extreme and rapid climate change on Palaeolithic human groups and its role in Neanderthal demise in the region due to a complex chronological assessment of human presence in the region for this period. If Neanderthal groups were still present in the Iberian Peninsula during HS4, they were probably small groups already declining and might have been further weakened by their fast-changing environment. To clarify the pattern of the MUPT in SW Europe in the future, we need 1) technical improvement of the radiometric methods and 2) more palaeoecological data from the potential late Neanderthal and early *Homo sapiens* sites.

3.2.8 Acknowledgments

We are grateful to the two anonym reviewers for they helpful comments on this manuscript. We acknowledge the International Ocean Drilling Project and the MARUM Bremen Core Repository for making available the ODP 976 samples. The sample processing was funded by the CNRS and the MNHN. We thank Lionel Dubost for the technical assistance in the laboratory, Federica Badino for the assistance in the age model elaboration, and Nicolas Michalezyk for the extraction of climate modern values. L. Charton doctoral contract is funded by the French Ministère de l'Enseignement Supérieur et de la Recherche at the doctoral school ED 227 of the Muséum National d'Histoire Naturelle, Paris. The international cotutorship with the University of Florence is supported by the Ecole Franco-Italienne Vinci grant (project C2-166). This research was also supported by the Franco-Italian PHC Galileo project BioMed "What future for Mediterranean Biodiversity? Images from the past for a sustainable future" led by V. Lebreton and A. Bertini (project FR n°48933VE/ project IT n°2023-G23_53). This is an ISEM contribution number XXXX.

4. Rapid climatic variability and dynamics of Middle Palaeolithic human population during the last climatic cycle (MIS 5-2) in the southwestern Mediterranean

Charton Liz[1,2], Bertini Adele[2], Combourieu-Nebout Nathalie[1], Bout-Roumazeilles Viviane[3], Peyron Odile[4], Marie-Hélène Moncel[1], Lebreton Vincent[1]

**corresponding author: Liz Charton (liz.charton@mnhn.fr)*

Affiliations:

1: UMR 7194, Histoire Naturelle de l´Homme Préhistorique, CNRS-MNHN, Institut de Paléontologie Humaine, Paris, France

2: Dipartimento di Scienze della Terra, Universita di Firenze, Italy

3: UMR 8187 LOG – Laboratoire d'Océanologie et de Géosciences, CNRS, Université de Lille, Univ. Littoral Côte d'Opale, IRD, Lille, France.

4 : Institut des Sciences de l'Evolution de Montpellier, UMR CNRS 5554 ISEM, Université de Montpellier, France

4.1. Résumé en Français

Ce chapitre vise dans un premier lieu à présenter et analyser l'ensemble de l'enregistrement paléoenvironnemental d'ODP 976 sur le dernier cycle climatique (MIS 5-1, 130-11 ka BP), dont une partie des données palynologiques et minéralogiques ont déjà fait l'objet de publications scientifiques spécifiques ou de synthèses régionales (Bout-Roumazeilles et al., 2007; Charton et al., 2025; Combourieu-Nebout et al., 2002, 2009; Fletcher et al., 2010a; Masson-Delmotte et al., 2005).

Les données palynologiques complètes sont détaillées, avec des échantillons supplémentaires ajoutés par rapport à la série déjà publiée. Les reconstructions climatiques à partir du pollen à travers une approche multiméthode sont présentées pour l'intégralité du cycle, révélant l'impact des évènements abrupts et des cycles D-O sur les conditions de températures et de précipitations dans la région depuis le MIS 5. De nouvelles données minéralogiques entre 130 et 50 ka BP sont également intégrées et montrent une dynamique de circulation atmosphérique marquée par des apports éoliens africains significatifs pendant les évènements froids contemporains de l'entrée en glaciation à partir de la fin du MIS 5. Les analyses statistiques multivariées montrent que la variabilité de l'assemblage palynologique et minéralogique de la série est marquée par une nette opposition entre les marqueurs chauds et humides (forêt tempérée et méditerranéenne, plantes aquatiques, kaolinite) et les marqueurs froids (forêt d'altitude) et secs (steppe et semi-désert, palygorskite). Cette opposition permet une bonne discrimination entre les épisodes stadiaires et interstadiaires dans la séquence.

La variabilité environnementale rapide enregistrée dans la carotte ODP 976 pendant la dernière période glaciaire (MIS 4-2) puis au cours du dernier interglaciaire (MIS 5) est ensuite discutée.

Au cours des MIS 4-2, la végétation du sud-ouest méditerranéen a répondu très rapidement aux successions de stadiaires et d'interstadiaires de la dernière période glaciaire. Les principaux pics de végétation steppique et semi-désertique sont en phase avec les minimums de SSTs reconstruits en Mer d'Alboran, ainsi qu'avec les principaux dépôts d'IRDs dans l'Atlantique Nord. L'enregistrement palynologique à haute résolution de la carotte ODP 976 permet également de mettre en évidence les différents phasages et les dynamiques de végétation caractérisant les stadiaires de Heinrich 1-6. Deux stadiaires associés aux évènements de Heinrich mineurs H5a et H7 sont également enregistrés. Les interstadiaires sont marqués par un développement important de la forêt tempérée et méditerranéenne et une augmentation des températures et des précipitations, particulièrement pendant les GI17, 15, 14, 12, 8, 7, 2 et 1. Le début du MIS 3 est marqué par des conditions particulièrement humides et tempérés qui coïncident avec une longue phase de déport de niveaux riches en matière organique (ORL) en Méditerranée sud-occidentale. Les reconstructions de précipitations à partir du pollen sont en phase avec l'index d'humidité africaine, ainsi qu'avec les principales périodes humides de l'ouest méditerranéen mises en évidence dans la séquence de Padul. Une dynamique particulière des Ericaceae est mise en évidence tout au long du dernier cycle climatique, liée aux cycles d'insolation mais aussi aux évènements extrêmes de l'Atlantique Nord.

Pendant le MIS 5, l'enregistrement multi-proxies de la carotte ODP 976 enregistre à la fois la structure bien connue du dernier interglaciaire (stades et sous-stades climatiques isotopiques et palyno-stratigraphiques), et des stadiaires additionnels qui correspondent aux évènements froids de l'Atlantique Nord (C22 et évènements rapides C25-28 durant l'Eemien). Certains pics de végétation steppique et semi-désertique sont bien corrélés aux évènements de Heinrich mineurs H7a, H8, H9 et H10. L'Eemien (MIS 5e) et le St-Germain Ic (MIS 5c, corrélé au GI23 au Groënland) correspondent aux phases tempérées et humides les plus longues et intenses, au cours desquelles domine la végétation tempérée. L'entrée progressive en glaciation est marquée par une augmentation graduelle de l'abondance de pollen d'Ericaceae et de Cèdre, ainsi que par des épisodes de refroidissements plus intenses, notamment à partir du Mélisey II, corrélé au GS22 au Groënland ainsi qu'au H8 et au C21 dans l'Atlantique Nord. Les reconstructions climatiques à partir du pollen de la carotte ODP 976 montrent une bonne corrélation avec celles du lac Ohrid en Grèce, ainsi qu'avec l'index d'humidité ouest-africaine et l'enregistrement isotopique de la grotte Campanet à Majorque. Les résultats de cette étude mettent en évidence l'instabilité climatique qui a affecté le climat et la composition de la végétation du sud-ouest méditerranéen tout au long du dernier cycle climatique. Cependant, les

changements environnementaux rapides enregistrés au cours du MIS 5 sont de moindre intensité comparés à ceux des MIS 4-2.

A la lumière des changements environnementaux reconstruits, l'étude s'intéresse ensuite aux dynamiques de populations humaines du Paléolithique moyen dans la péninsule Ibérique à partir d'une synthèse de 92 sites archéologiques datés entre 130 et ~30 ka BP. Le MIS 5 apparaît comme une période particulièrement favorable aux populations néandertaliennes, avec une intensification des occupations (35 sites) et une diversification des types de sites (occupations de longue et de courte durée, en grotte ou à l'air libre, ainsi qu'en altitude). Il est encore difficile d'associer les phases d'occupation aux différents sous-stades climatiques dû aux incertitudes des datations radiométrique sur cet intervalle chronologique. Cependant, un certain nombre de sites archéologiques mettent en évidence des changements comportementaux dès la fin du MIS 5 en lien avec le refroidissement progressif qui caractérise l'entrée en glaciation. La synthèse présente un nombre similaire de sites archéologiques dont les datations couvrent au moins une partie du MIS 4 dans la péninsule Ibérique, bien que cette période soit généralement associée à une baisse de l'intensité des occupations. Plusieurs études mettent en évidence des changements importants dans la mobilité des groupes, leurs stratégies de subsistance et leurs outillages lithiques durant une phase climatique froide et sèche. La multiplication des techno-complexes lithiques dominées par le débitage Quina, particulièrement dans la région franco-cantabrique, a été interprétée comme une réponse adaptative aux conditions climatiques défavorables du MIS 4. Ainsi, l'épisode climatique froid et aride du HS6 décrit dans l'enregistrement paléoclimatique de la carotte ODP 976 pourrait représenter le principal évènement climatique défavorable ayant impacté les populations néandertaliennes au cours du MIS 4. Après 60 ka BP, une intensification des occupations néandertaliennes est visible à travers une multiplication des sites archéologiques (44 sites) qui peut être mise en lien avec les conditions particulièrement tempérées et humides enregistrée dans la carotte ODP 976 au début du MIS 3. Cette intensification des occupations coïncide avec une diversification et une régionalisation des outillages lithiques, une mobilité plus importante des groupes humains, et une spécialisation des occupations néandertaliennes. Les oscillations climatiques rapides du MIS 3 mises en évidence dans l'enregistrement de la carotte ODP 976 ont pu jouer un rôle dans ces dynamiques en favorisant des adaptations répétées et successives à un environnement instable. Un certain nombre d'études mettent en évidence la disparition de Néandertal au nord de la péninsule Ibérique successivement au HS5, tandis qu'au sud et dans certaines zones refuges une persistance plus tardive est toujours défendue par certains auteurs, au-delà du HS4 et potentiellement après 35 ka BP. Il reste difficile de replacer les chronologies des occupations humaines dans un cadre climatique millénaire dû aux incertitudes des datations radiométriques. Cependant, cette synthèse met en évidence le potentiel

impact des successions d'évènements climatiques rapides des MIS 4-3, et particulièrement des HS6-4, sur les dynamiques de peuplements néandertaliens dans la péninsule Ibérique et sur leur déclin progressif avant leur extinction.

4.2. Introduction

A growing number of studies have focused on the abrupt climate changes of the late glacial period (MIS 3-2), whereas a fewer have taken interest in the rapid events during the earlier glacial phase (MIS 4) and the last interglacial (MIS 5), which have been shown to be less intense (e.g. Sánchez Goñi, 2022a, Drysdale et al., 2007). Heinrich Stadials, the cold intervals associated to Heinrich events in the North Atlantic, are considered the most extreme cold events of the last climatic cycle (LCC) and previous glaciations in the Northern Hemisphere : HS1 to HS5 occurred during MIS 3-2, while HS6 occurred during MIS 4 (Bond et al., 1992; Broecker et al., 1992; Heinrich, 1988; Hemming, 2004). HS11, one of the longest and most intense of these events, took place during the glacial Termination II, at the transition between MIS 6 and MIS 5 (Martrat et al., 2014, see Section 5 for a focus on Termination II and HS11). Heinrich events from H10 to H7, occurring during MIS 5d to MIS 4, are usually less well identified in North-Atlantic records (Channell et al., 2012; Heinrich, 1988; Lisiecki & Stern, 2016). Their precise stratigraphical correlation with cold events recorded in Europe is still unclear, leading to their non-identification as "Heinrich Stadials" in paleoenvironmental syntheses of the last climatic cycle (e.g. Sánchez Goñi, 2022a, 2022b). Although less intense, several cold episodes have been identified during MIS 5, showing it was not as stable as previously thought for interglacial periods (Chapman & Shackleton, 1999; Oppo et al., 2001; Sassoon et al., 2025; Sinopoli et al., 2018; Tzedakis et al., 2018). Different terminologies have been used to refer to these internal climatic changes during the last interglacial and the early glacial (e.g. Sánchez Goñi, 2007, Table 4.1).

GICCO5 stratigraphy with date of start of the event (Rasmussen et al., 2014)	Global Marine Isotopic substages (MIS) based on benthic foraminifera with the date of isotopic substages peaks (Lisiecki & Raymo, 2005; Railsback et al., 2015)	North Atlantic marine isotopic cold events based on planktonic foraminifera (Chapman & Shackleton, 1999; Oppo et al., 2001, 2006; Tzedakis et al., 2018)	Heinrich Events (Lisiecki & Stern, 2016; Rasmussen et al., 2003)	Palynological stratigraphy (Sánchez Goñi, 2007; Woillard, 1978)
GI19 (72.34 b2k)	MIS 5a (82 ka)			Ognon II
GS20 (74.10 b2k)		C19		Stadial II
GI20 (76.44 b2k)				Ognon I
GS21.1 (77.76 b2k)		C20	H7a	Stadial I
GI21.2 (85.06 b2k)				St Germain II
GS22 (87.6 b2k)	MIS 5b (87 ka)	C21	H8	Mélisey II
GI22 (90.04 b2k)				St-Germain Ic
GS23.1 (90.14 b2k)	MIS 5c (96 ka)	C22		
GI23.2 (104.52 b2k)				
GS24.1 (105.44 b2k)		C23	H9	St-Germain Ib / Montaigu event
GI24.2 (108.28 b2k)		_		St-Germain Ia
GS25 (110.64 b2k)	MIS 5d (109 ka)	C24	H10	Mélisey I
GI25 (115.37 b2k)				Eemian
GS26 (119.14 b2k)		C25		
GI26	MIS 5e (123 ka)			
		C26		
		C27 a, b, c, C27’		
		C28		
	MIS 6		HS11	

Table 4.1. Tentative correlation between the terminology of climatic events identified in the different types of records from the Northern Hemisphere during MIS 5. Grey cells indicate cold events, and white cells warm events.

From a marine stratigraphy point of view, MIS 5 is composed by five isotopic substages including the three warm substages MIS 5e, 5c and 5a, and the two cold substages MIS 5b and 5d (Lisiecki & Raymo, 2005; Railsback et al., 2015). The complex succession of abrupt changes during MIS 5 was described first on palynological sequences from Western Europe, leading to the palyno-stratigraphical terms classically used to correlate changes on land and on sea. The warm intervals are referred to as the Eemian, the St-Germain Ia, St-Germain Ic, St-Germain II, Ognon I and Ognon II, while the cold episodes are referred as Melisey I, Montaigu event, Melisey II, Stadial I and Stadial II (Sánchez Goñi et al., 1999, 2005; Woillard, 1978). Furthermore, various abrupt cold events during MIS 5 identified in various marine records have been referred to as “C26” to “C19” events (Chapman & Shackleton, 1999; McManus et al., 1994; Oppo et al., 2001, 2006), before the establishment of a precise chrono-stratigraphy for stadials and interstadials in the Northern Hemisphere from the

Greenland ice core records (Rasmussen et al., 2014). Since then, it has become standard to refer to these cold episodes as Greenland Stadials (GS) based on the Greenland reference chrono-stratigraphy (e.g. Sinopoli et al., 2018). However, precise correlation between the events identified in the different records is still not completely resolved, as there is a smaller number of long multiproxy sequences covering MIS 5-4 period compared to MIS 3-2. Therefore, the correlation between North-Atlantic and European cold events and Greenland stadials is still in progress (e.g. Tzedakis et al., 2018).

From an archaeological perspective, most studies have focused on the possible impact of MIS 3 climatic variability on human population and Neanderthal replacement by *H. sapiens*, with particular attention for HS4 and to a lesser extent to HS5, a period considered as the Late Middle Palaeolithic (Albouy et al., 2024; d'Errico et al., 2006; D'Errico & Sánchez Goñi, 2003; Finlayson & Carrión, 2007; Fourcade et al., 2022; Melchionna et al., 2018; Sepulchre et al., 2007). To our knowledge, few studies have examined Neanderthal dynamics in relation to climatic instability during earlier periods (e.g. Yaworsky et al., 2024). However, this question is key to evaluate the potential role played by rapid climatic changes in Neanderthal extinction during MIS 3.

This study focuses on the time interval between 130 and 11 ka BP, corresponding to the entire LCC (MIS 5e to the beginning of MIS 1). The objectives are : i) to provide a continuous and high-resolution multiproxy (pollen, climate reconstructions, isotope and clay mineralogical composition) record for the entire climatic cycle from ODP 976, ii) to describe the various North Atlantic cold events in the Alboran Sea based on this multiproxy record, including Heinrich Stadials and Greenland Stadials, iii) to compare the structure of the most important cold events in the Alboran Sea in term of vegetation, atmospheric and water circulation changes, iv) to discuss these results in the light of the changes identified in the main paleoenvironmental sequences available in the Mediterranean region for the LCC (Fig. 4.1), and v) to provide a synthesis of the Middle Palaeolithic archaeological record in the Iberian Peninsula during the last climatic cycle allowing to discuss the potential impact of abrupt climatic changes on human population dynamics.

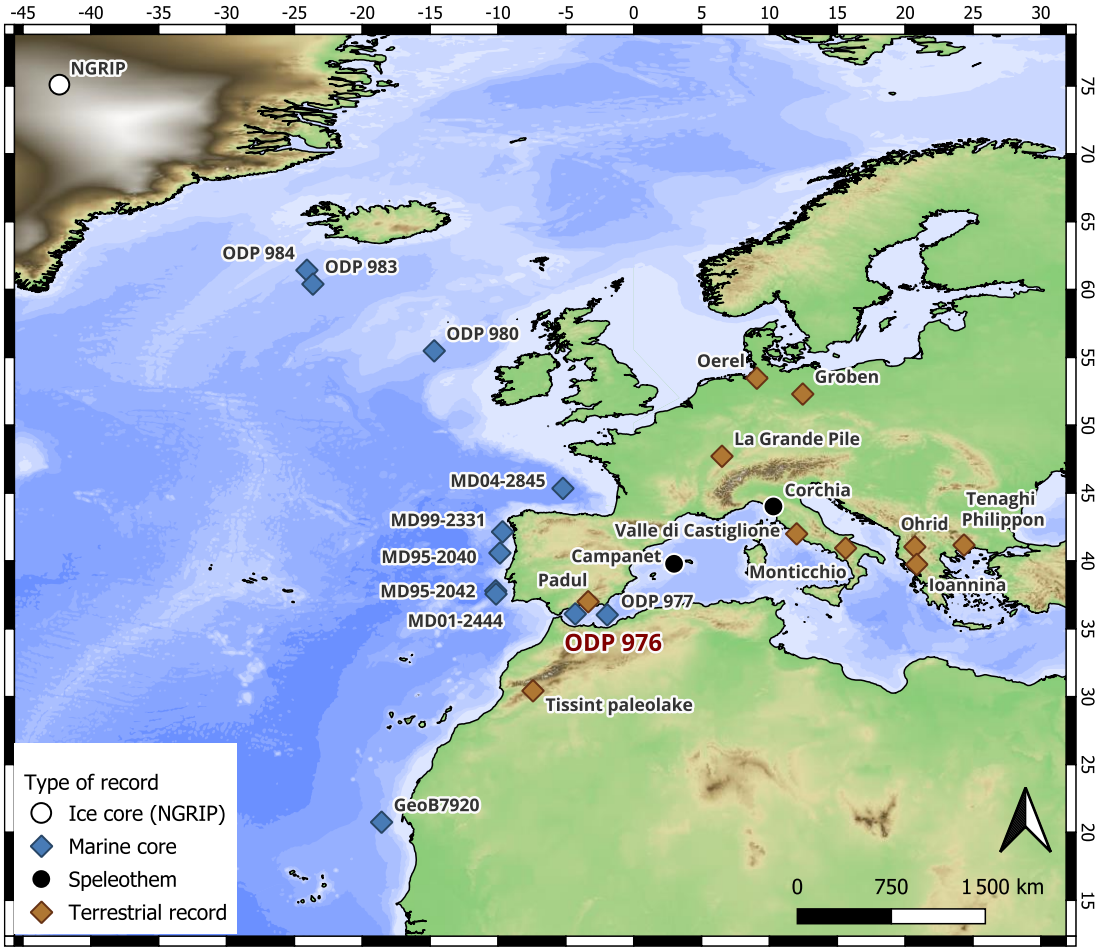


Fig. 4.1. Location of the main paleoenvironmental records mentioned in the text covering the last climatic cycle.

4.3. Age model

The age model for the ODP 976 core is based on radiocarbon dating of planktonic foraminifera for the upper 10 m (recalibrated in Charton et al. (2025), and on graphical correlation between the planktonic $\delta^{18}O$ ratio of the core and the Greenland isotopic curve on GICC05 timescale for the lower section (Table 2). The method used follows the traditional approach (Shackleton et al., 2000), taking the midpoint of the first decrease in the isotopic ratio as a control point for the start of Greenland Interstadials (Fig. 4.2).

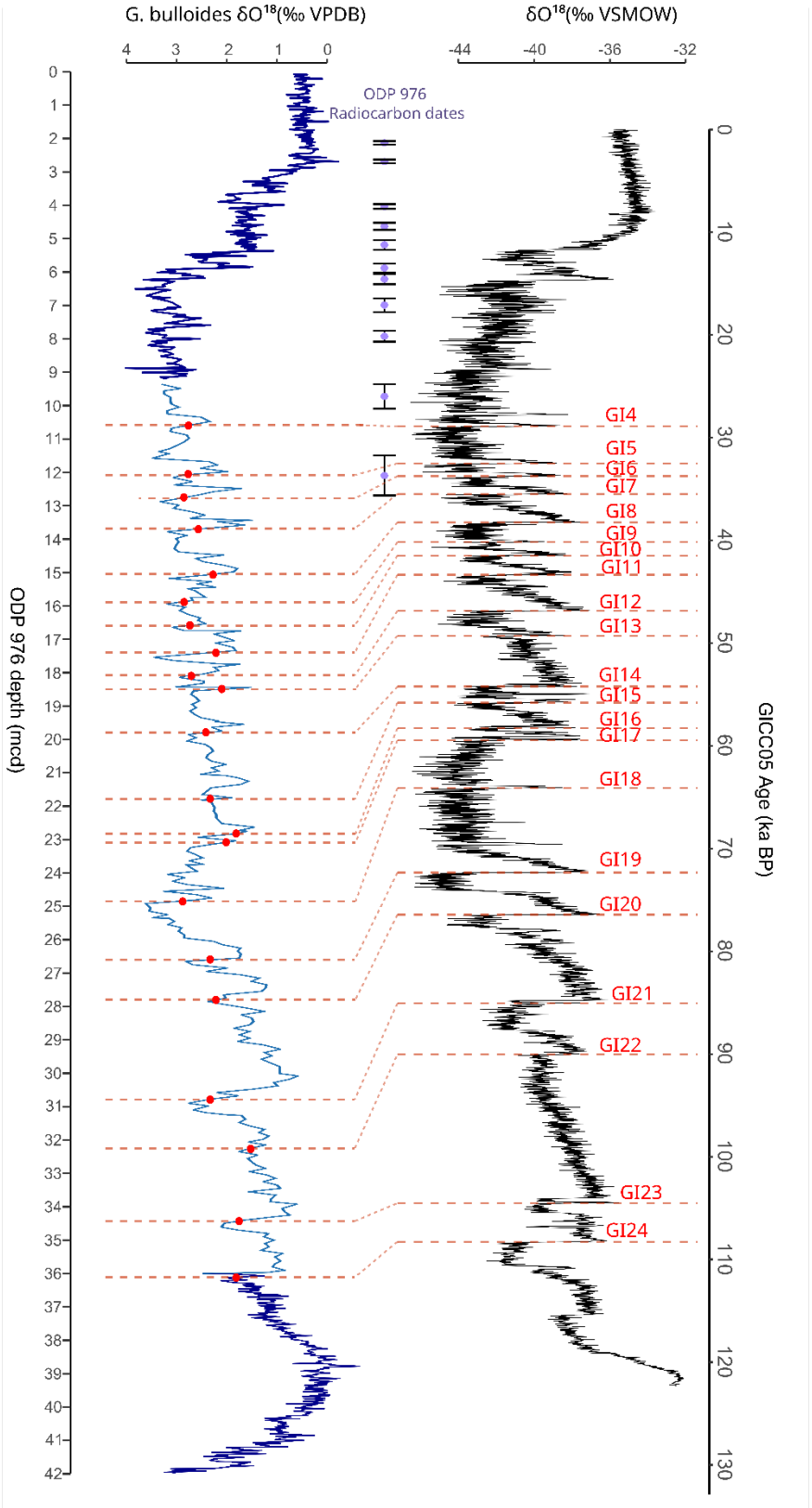


Fig. 4.2. Graphical correlation between NGRIP interstadial chronology (GICC05 and GICC05modelext ages) and ODP 976 *G. bulloides* $\delta^{18}O$: in dark blue, the data published by Jiménez-Amat & Zahn (2015), and in light blue the data partially published by Combourieu-Nebout et al. (2002 and Grafenstein et al. (1999) together with unpublished data. The eleven recalibrated radiocarbon dates retained for the age model are shown at the top (Charton et al., 2025; Combourieu-Nebout et al., 2002).

Below 36.11m (start of GI 24), we used the tie-points defined by Jiménez-Amat & Zahn (2015) and based on graphical correlation between the Mg/Ca SST curve of ODP 976 and the Dongge Cave and Corchia speleothems records of oxygen isotopic ratio (Fig. 4.3).

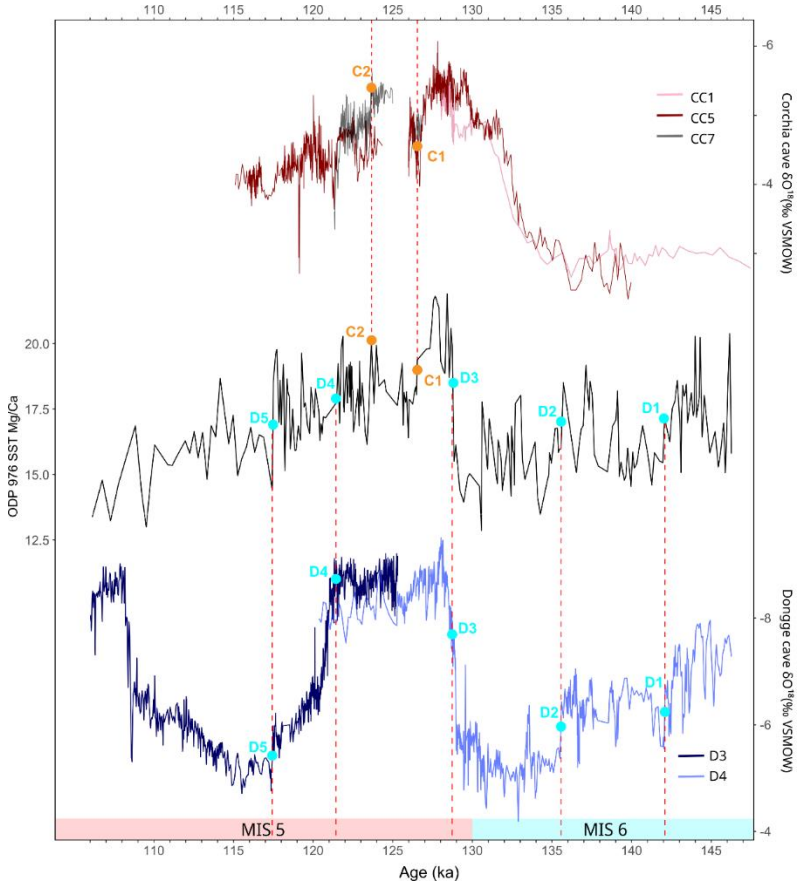


Fig. 4.3. Correlation between the ODP 976 Mg/Ca-based Sea Surface Temperatures and the Dongge Cave and Corchia Cave speleothem oxygen isotope records (adapted from Jiménez-Amat & Zahn, 2015)

The final age versus depth model spanning the last 130 ka BP is presented in Fig 4.4. Based on these 37 control points including radiocarbon ages and tie-points to Greenland and speleothem records (Table 4.2), the average sedimentation rate at the ODP 976 site over the last 130 ka BP is about 0.36 m/1000 years.

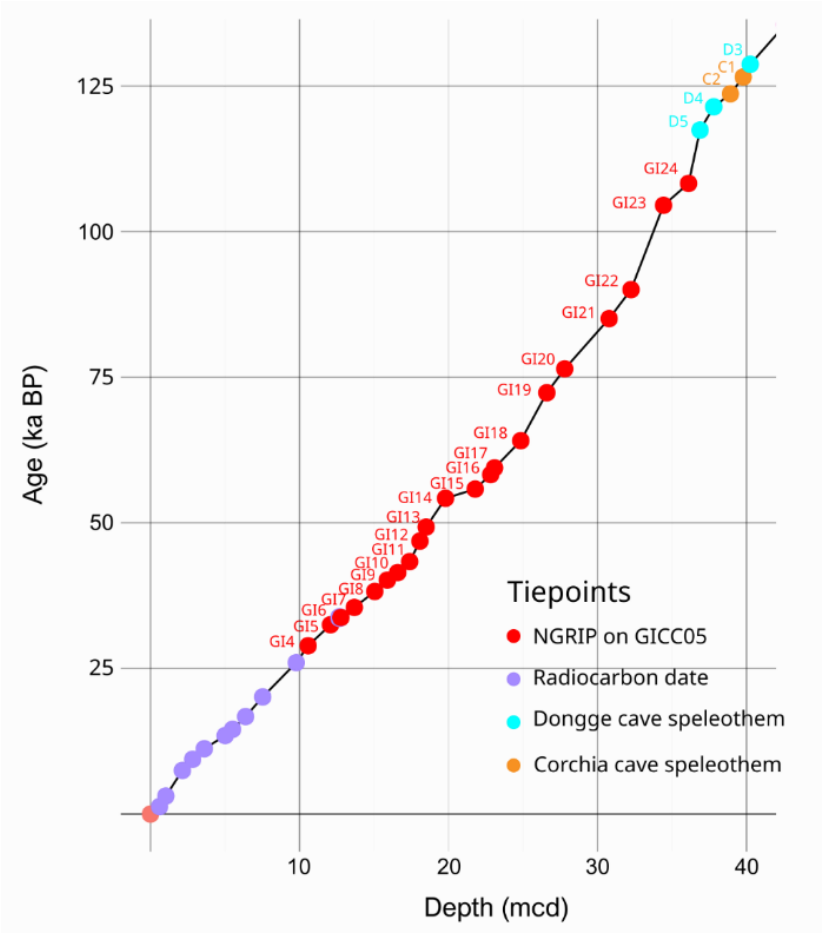


Fig. 4.4. Age versus depth model for ODP 976 from 0 to 42 m depth.

Type of point	*Depth (m)*	*Age (cal ka BP)*	*Error (ka)*	*Reference*
Radiocarbon date on sample C1H 1 60-62	0.61	1.280	-0.170 / +0.168	1
Radiocarbon date on sample C1H 1 102-104	1.03	3.100	-0.187 / + 0.203	1
Radiocarbon date on sample C1H 2 63-65	2.14	7.481	-0.166 / +0.162	1
Radiocarbon date on sample C 1H 2 132–134	2.83	9.409	-0.224 / +0.190	1
Radiocarbon date on sample C 1H 3 60–62	3.61	11.213	-0.201 / +0.251	1

Radiocarbon date on sample C 1H 4 50–52	5.01	13.466	-0.230 / +0.261	1
Radiocarbon date on sample D 2H 3 100–102	5.51	14.549	-0.391 / +0.373	1
Radiocarbon date on sample D 2H 4 37–39	6.38	16.733	-0.333 / +0.304	1
Radiocarbon date on sample D 2H 5 2–4	7.53	20.107	-0.385 / +0.372	1
Radiocarbon date on sample C 2H 3 55–57	9.78	25.986	-0.665 / +0.780	1
Start of GI4	10.58	28.9	0.898	2
Start of GI5	12.08	32.5	1.132	2
Radiocarbon date on sample C 2H 5 45–47	12.69	33.737	-1.667 / +1.482	1
Start of GI6	12.78	33.74	1.212	2
Start of GI7	13.68	34.48	1.321	2
Start of GI8	15.05	38.22	1.449	2
Start of GI9	14.89	40.16	1.58	2
Start of GI10	16.59	41.46	1.633	2
Start of GI11	17.39	43.34	1.736	2
Start of GI12	18.08	46.86	1.912	2
Start of GI13	18.5	49.28	2031	2
Start of GI14	19.8	54.22	2301	2
Start of GI15	21.79	54.8	2392	2
Start of GI16	22.83	58.28	2511	2
Start of GI17	23.09	59.44	2573	2
Start of GI18	24.85	64.1	_	2
Start of GI19	26.6	72.34	_	2
Start of GI20	27.8	76.44	_	2
Start of GI21	30.78	85.06	_	2
Start of GI22	32.25	90.04	_	2
Start of GI23	34.43	104.52	_	2
Start of GI24	36.11	108.28	_	2
Dongge Cave	36.88	117.43	_	3
Dongge Cave	37.8	121.43	_	3
Corchia Cave	38.92	123.66	_	3
Corchia Cave	39.78	126.54	_	3
Dongge Cave	40.25	128.73	_	3

Table 4.2. Control points used for the age model of ODP 976 core (130-11 ka BP). 1: Combourieu-Nebout et al., 2002 (recalibrated in Charton et al., 2025) ; 2 : Rasmussen et al., 2014 ; von Grafenstein et al., 1999 ; this study ; 3: Jiménez-Amat and Zahn, 2015 ; Kelly et al., 2006 ; Drysdale et al., 2009.

4.4. Results

4.4.1. Pollen analyses

This study focuses on 491 pollen samples from between 40.68 and 3.65 m depth, corresponding to 130 to 11 ka BP according to the age model. The mean resolution for the ODP 976 pollen record from 130 ka BP to the present is about 226 years, with a maximum resolution of 15 years during MIS 3 rapid events, and a minimum resolution of 1400 years during MIS 5 interval. The sequence was already partly published for the last 50 ka BP (Bout-Roumazeilles et al., 2007; Combourieu-Nebout et al., 1999, 2002; 2009a, 2009b), and some data for MIS 5-4 were included in regional comparison studies (Fletcher et al., 2010a; Genty et al., 2005; Masson-Delmotte et al., 2005). Here, the detailed results of palynological analyses of the LCC are presented, integrating the partially published data (Bout-Roumazeilles et al., 2007; Charton, 2025; Combourieu-Nebout et al., 1999, 2002; 2009a, 2009b; Fletcher et al., 2010a; Genty et al., 2005; Masson-Delmotte et al., 2005) as well as results from 76 new additional samples to increase the resolution of the abrupt climatic events. Pollen extraction and identification followed the traditional methods used for marine sedimentary cores (see Section 2.2 for methods details). For clarity, the complete set of results is presented in two different pollen diagrams. The first diagram presents the main pollen taxa for MIS 5-4 (~130-57 ka BP) including 215 samples (Fig. 4.5). The second diagram presents the main pollen results for samples MIS 3-2 (~ 57-11 ka BP), including 276 samples (Fig. 4.6).

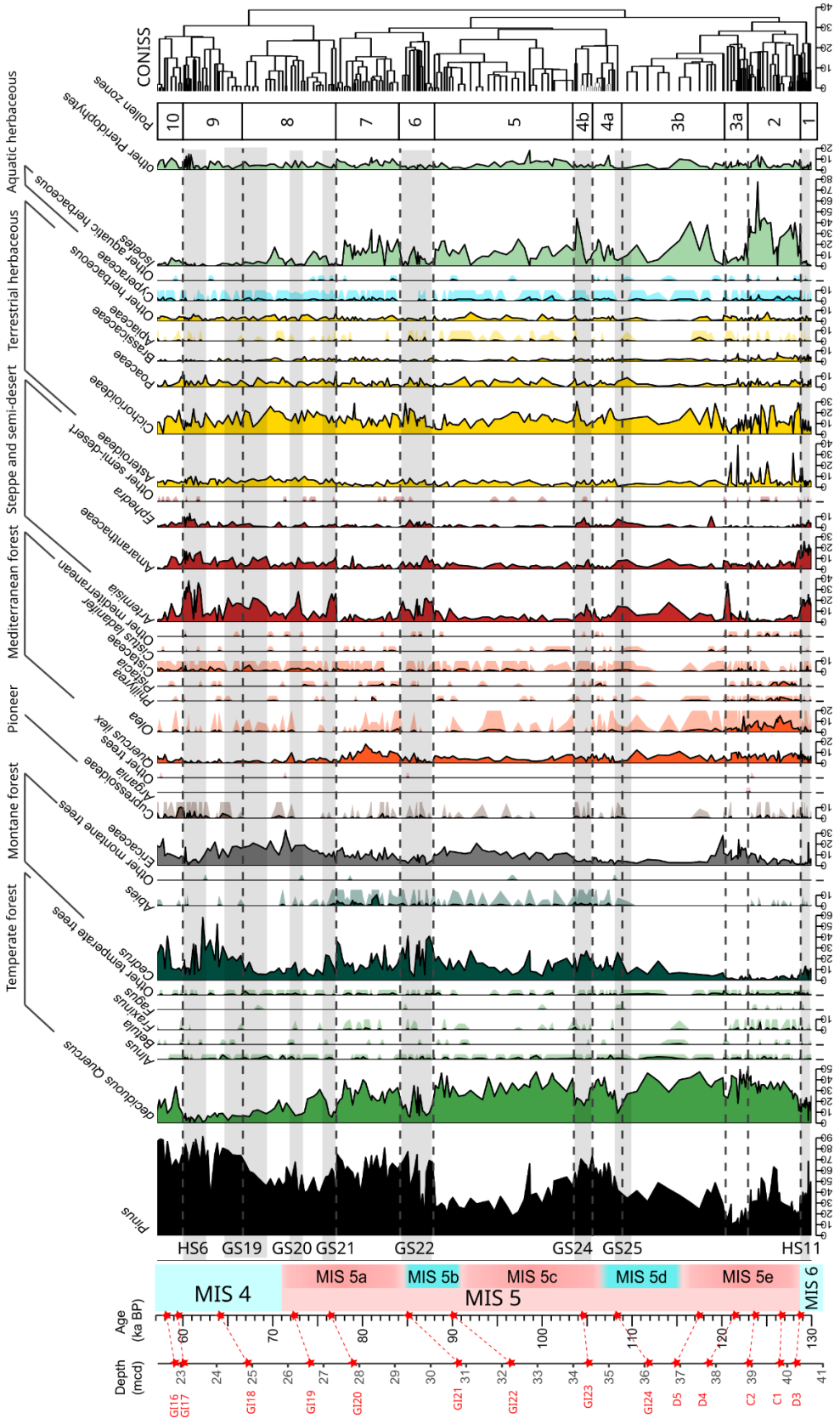


Fig. 4.5. Pollen diagram of selected taxa covering MIS 5-4 (~130-57 ka BP) plotted against age. Age-depth correspondence and tie-points to Greenland interstadials (GI) and to speleothems (D5-3 and C1-2) are shown at the left. Grey intervals show the main cooling events identified as Heinrich Stadials (HS) or Greenland Stadials (GS).

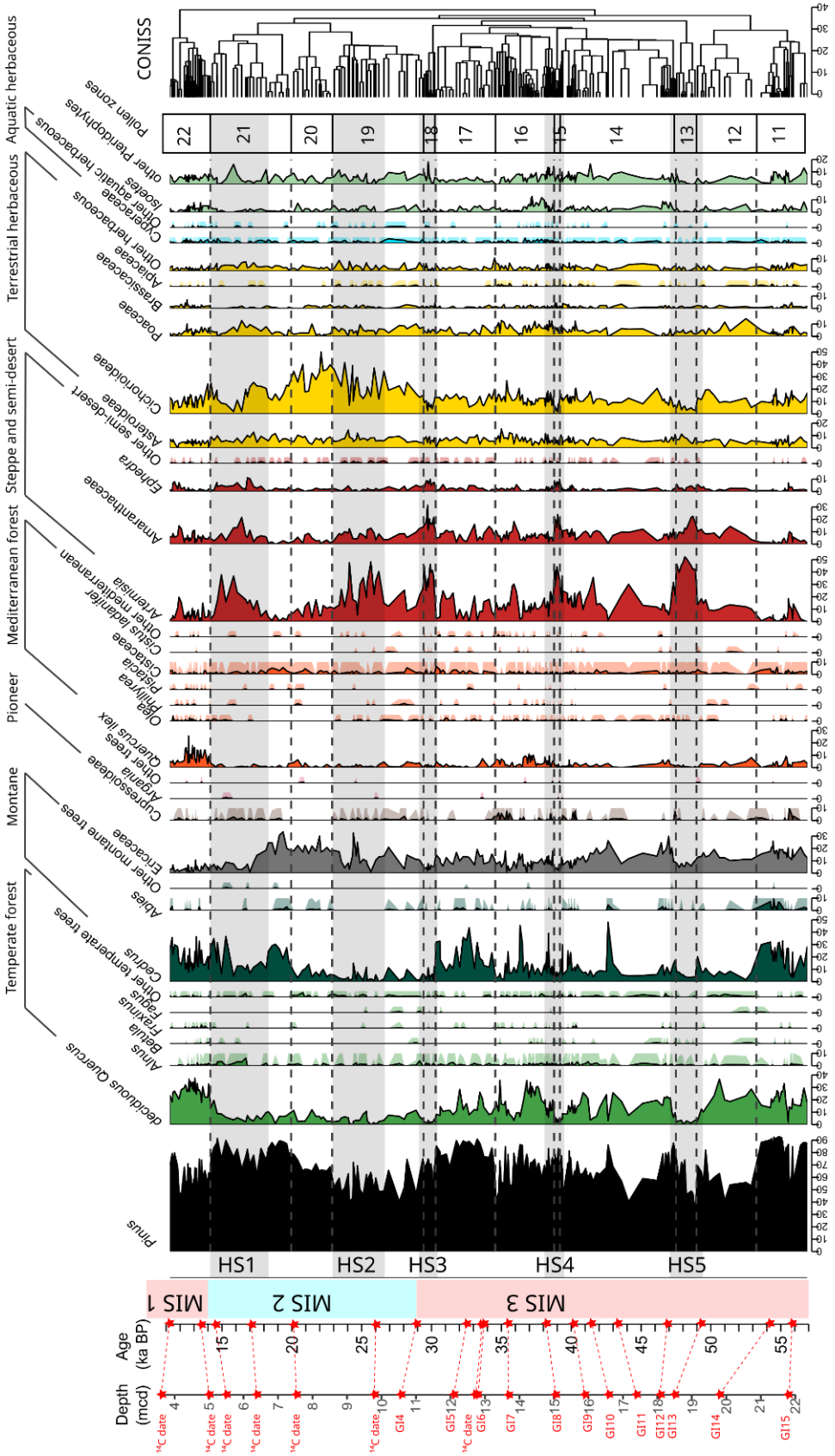


Fig. 4.6. Pollen diagram of selected taxa covering MIS 3-1 (~57-11 ka BP), plotted against age. Age-depth correspondence, radiocarbon dates and tie-points to Greenland interstadials (GI) are shown at the left. Grey intervals show the main cooling events identified as Heinrich Stadials (HS).

Table 4.3 presents the main characteristics of the pollen assemblages for each pollen zone. The base of the sequence (pollen zone 1) is characterized by high percentages of steppe and semi-desert herbaceous, corresponding to the end of the Penultimate Glacial (MIS 6). In Pollen Zone 2, temperate deciduous and Mediterranean tree pollen increase rapidly, together with aquatic herbaceous and spores of *Isoetes*, marking the onset of the MIS 5e interglacial vegetation. The temperate and Mediterranean forest taxa are dominant in the pollen assemblage through pollen zones 2 to 7, with important oscillations. Various drop in temperate tree pollen associated to peaks of *Artemisia*, Amaranthaceae and *Ephedra* pollen are recorded in Pollen Zones 3a (middle of MIS 5e), 4a and 4b (associated to MIS 5b), and 6 (associated to MIS 5d). A decreasing trend for deciduous *Quercus* can be observed from MIS 5c (Pollen Zone 5) onward, while montane vegetation (*Cedrus*) and Ericaceae increase progressively. The end of MIS 5a (Pollen Zone 8) is marked by high percentages of Ericaceae and herbaceous taxa. Pollen Zones 9 and 10 evidence high percentages of *Cedrus*, *Pinus*, semi-desert herbaceous, and low percentages of temperate trees and Mediterranean vegetation, corresponding to the MIS 4 glacial.

Pollen zones 11 to 18 are generally dominated by *Pinus*, semi-desert plants and herbaceous taxa, with important events of repeated temperate trees and Mediterranean vegetation expansion during MIS 3. Steppe and semi-desert taxa also show important variations with major events of abrupt expansion (Pollen Zones 13, 15, 18). From Pollen Zone 19 until Pollen Zone 21 (MIS 2), temperate tree and Mediterranean pollen display very low percentages, while herbaceous taxa are dominant such as *Artemisia* (Pollen Zones 19 and 21), Cichorioideae (Pollen Zones 19-20), and Ericaceae (Pollen Zones 20-21). Finally, Pollen Zone 22 is marked by the fast recolonization of temperate deciduous trees and Mediterranean vegetation during the MIS 1 interglacial.

Pollen zones	Depth and age	Pollen assemblages - main features	Climate reconstructions- main features
22	4.32-3.65 m 14.14-11.28 ka BP	deciduous *Quercus* (20-37%) and *Quercus ilex* (4-25%) are the most abundant. High percentages of *Cedrus* (7-39%), *Isoetes* (0-8%), and *Olea* (1-4%).	Warm and humid phase. MTWA close to the modern value, and precipitation above the present value.
21	7.4-4.35 m 19.77-14.20 ka BP	In the lower part, Ericaceae are abundant (up to 33%), as well as Cichorioideae (up to 25%). There are two peaks of *Cedrus* (up to 37%) at the top and at the bottom of the zone. Poaceae are abundant in the middle part (up to 13%). In the upper part, successive peaks of *Ephedra* (11%), Amaranthaceae (22%) and *Artemisia* (37%). Occurrence of *Argania* pollen at ~15 ka BP. Temperate and Mediterranean vegetation display low percentages, with a slight increase at the top.	Warm and humid conditions in the lower part of the zone. A large decrease in both temperatures and precipitation is reconstructed at the top, centred at ~16 ka BP.
20	8.54 – 7.54 m 22.74-20.14 ka BP	Ericaceae and Cichorioideae are the most abundant taxa, between 17-30 % and 18-40 % respectively. Temperate and Mediterranean vegetation display low percentages.	Relatively temperate and humid phase, with an increasing trend in

			both temperatures and precipitation.
19	10.78-8.75 m 29.38-23.03 ka BP	High percentages of Cichorioideae (up to 36%) and Ericaceae (up to 33%) all along this phase. Two major peaks of *Artemisia* (48%) and Amaranthaceae (12%) at ~24 and ~26 ka BP. Occurrence of *Argania* pollen at ~26 ka BP. Temperate and Mediterranean vegetation display low percentages.	Relatively cold and dry phase, with important variations. The lower part is warmer and wetter than the present, while the upper part displays a decrease in temperatures and precipitation, with various large oscillations below the present values.
18	11.14-10.82 m 30.24-29.48 ka BP	Peak abundance of *Artemisia* (18-46%), Amaranthaceae (13-32%) and *Ephedra* (4-10%). All tree taxa display very low percentages.	Cold and dry climate, with winter precipitation particularly low.
17	13.18-11.18 m 34.51-30.34 ka BP	*Cedrus* is the most abundant taxa (10-44%), together with deciduous *Quercus* (8-29%), Cichorioideae (5-20%) and Ericaceae (5-19%). There are various smaller peaks of *Artemisia* (up to 23%) and Amaranthaceae (up to 16%).	Generally warm and wet period, with precipitation higher than present.
16	14.28-13.23 m 38.75-34.61 ka BP	deciduous *Quercus* and *Quercus ilex* peak abundance in the lower part (up to 36% and 10% respectively). Peak of *Artemisia* (30%) and Amaranthaceae (18%) at 36 ka BP, and two peaks of *Cedrus* (~40%) at 36.3 and 38.4 ka BP.	Warm and humid conditions in the lower part, with summer temperatures higher than present. Abrupt arid and cold episode in the upper part.
15	14.46-14.3 m 39.17-38.8 ka BP	Peak abundance of *Artemisia* (28-45%), Amaranthaceae (11-24%) and *Ephedra* (3-10%). All tree taxa display very low percentages. Occurrence of *Argania* pollen.	Very abrupt cold and dry event, with winter precipitation and temperatures particularly low.
14	18.18-14.48 m 47.44-39.21	Abundant Ericaceae and deciduous *Quercus* (4-26%), although with important variations. *Artemisia* peaks (30-35%) at 41.5 and 44 ka BP, and *Cedrus* peak (48%) at 42.6 ka BP.	Rather temperate and humid climate in the lower part, with a general trend toward cold and aridity and various important oscillations.
13	18.43-18.2 48.88-47.55 ka BP	Successive peak abundance of *Ephedra* (5%), Amaranthaceae (22%) and *Artemisia* (52%). All tree taxa display very low percentages.	Very abrupt cold and dry event, with winter precipitation and temperatures particularly low.
12	19.45-18.46 m 52.89-49.05 ka BP	High percentages of deciduous *Quercus* (up to 37%), Ericaceae (up to 19%) and Cichorioideae (up to 19%).	Rather warm and humid conditions, with summer temperatures close to the present. There is a trend toward cold and aridity at the top.
11	22.25-19.64 m 56.9-53.61 ka BP	*Cedrus* is the most abundant taxa (4-33%), together with deciduous *Quercus* (2-33%) and Ericaceae (12-26%). Peak of *Artemisia* (18%), Amaranthaceae (10%) and *Ephedra* (7%) at 54.6 ka BP.	High annual and winter precipitation in the upper part. A cold and arid event is visible at the bottom ~54.6 ka BP.
10	23.24-22.35 m 59.84-57.14 ka BP	*Cedrus* (10-29%), deciduous *Quercus* (9-23%), Ericaceae (6-25%) and Cichorioideae (1-23%) are the most abundant taxa. *Quercus ilex* percentages are also significant (1-8%).	Warm and humid conditions.
9	24.35-23.35 m 66.45-60.13 ka BP	In the lower part, *Cedrus* and Ericaceae are the most abundant taxa. In the upper part, there is a peak abundance of *Artemisia*, Amaranthaceae and *Ephedra*. Low percentages of temperate and Mediterranean tree taxa.	Increasing temperatures and precipitation in the lower part, ending with an abrupt cold and arid episode in the upper part. Winter parameters are particularly low.
8	28-24.45 m 77.02-66.93 ka BP	Ericaceae (8-33%) and Cichorioideae (10-26%) are the most abundant taxa. Deciduous *Quercus* (31-6%), *Quercus ilex* (5-1%) and *Cedrus* (23-8%) decreasing trend, and three peaks	Rather warm and humid climate, with significant instability and three different episodes of abrupt

		of *Artemisia* (27%) and Amaranthaceae (8%) at 67.8, 73 and 77 ka BP.	decrease of precipitation and temperatures.
7	30.38-28.28 m 83.9-77.16 ka BP	High percentages of deciduous *Quercus* (17-40%), *Quercus ilex* (up to 18%) and *Isoetes* spores (up to 34%). *Cedrus* is also abundant (6-36%), and Ericaceae increase (6-16%). Significant presence of *Abies* (up to 5%). Very low percentages of semi-desert taxa.	Warm and humid climate, stable conditions.
6	31.58-30.58 m 87.77-84.48 ka BP	Two main peaks of *Artemisia* (19-22%), Amaranthaceae (6-12%) and *Cedrus* (41%) at 85 and 87.4 ka BP, interrupted by an abrupt increase of deciduous *Quercus* (33%) and *Isoetes* at 86 ka BP.	Moderate decrease of temperatures and precipitation.
5	34.26-31.65 m 103.4-88 ka BP	High percentages of deciduous *Quercus* (22-47%), *Quercus ilex* (2-8%), *Cedrus* (7-27%), *Isoetes* spores (up to 23%), Cichorioideae (up to 21%) and Ericaceae (up to 21%). Very low percentages of semi-desert taxa.	Warm and humid conditions, stable conditions.
4b	34.9-34.3 m 104.57-103.66 ka BP	Increase of *Artemisia* (3-16%), Amaranthaceae (9%) and *Ephedra* (9%), and slight decrease of deciduous *Quercus* (16-34%). High percentages of *Cedrus* (8-27%), Cichorioideae (8-31%) and *Isoetes* (up to 44%).	Slight decrease in temperatures and precipitations, but still warm and humid climate.
4a	36.12-35 m 108.4-104.8 ka BP	Moderate peak of *Artemisia* (14%), Amaranthaceae (8%) and *Ephedra* (8%) at the base of the zone, and successively, fast increase of deciduous *Quercus* (9-42%)	Warm and humid climate, with lower precipitation at the base.
3b	37.52-36.21 ka BP 120.21-109.47 ka BP	Peak abundance of deciduous *Quercus* (28-47%), and high percentages of *Quercus ilex* (up to 11%) and *Isoetes* (up to 41%). Moderate peak of *Artemisia* (18%), Amaranthaceae (10%) and *Ephedra* (3%) at 114 ka BP.	Warm and humid climate with peak of temperatures and precipitations at ~118 ka BP. A slight decrease in precipitation is observed at ~114 ka BP.
3a	38.5-37.62 m 122.82-120.65 ka BP	Increase of *Artemisia* (36%) and Amaranthaceae (8%), and slight decrease of deciduous *Quercus* (23%) at the top around 120 ka BP. High percentages of Ericaceae (16%) in the lower part.	Slight decrease in precipitation, still warm climate.
2	40.25-38.6 m 128.73-123.02 ka BP	Peak abundance of deciduous *Quercus* (up to 44%), *Quercus ilex* (up to 12%), *Phillyrea* (up to 4%), *Olea* (up to 14%), *Pistacia* (up to 5%) and *Isoetes* spores (up to 44%).	Peak of precipitation and temperatures at ~127 ka BP, with annual temperatures close to the present value. After the peak, decreasing trend in temperatures.
1	40.68-40.28 m 129.98-128.93 ka BP	*Artemisia* (14-25%), Amaranthaceae (11-26%) and *Ephedra* (up to 6%) are dominant, while *Cedrus* (up to 13%) and deciduous *Quercus* (11-25%) are also abundant.	Cold and arid climate, with a very fast increase in both temperatures and precipitation at the end, around 129 ka BP.

Table 4.3. Description of the pollen zones defined in Fig. 4.5 and Fig. 4.6, together with the main features of the climate reconstructions (Section 4.4.2).

4.4.2. Pollen-based climate reconstructions

Pollen-based climate reconstructions using the Modern Analogue Technique (MAT) were already run on the ODP 976 pollen record for the past 50 ka BP (Bout-Roumazeilles et al., 2007; Combourieu-Nebout, Peyron, et al., 2009). A multimethod approach was then applied to the MIS 5 pollen record of ODP 976 to investigate possible analogues for the Holocene among past interglacial

periods (Sassoon et al., 2025). Here, we run for the first time a multimethod pollen-based climate reconstructions on the complete ODP 976 pollen record for the last climatic cycle, with a focus on extreme climatic events (see Section 2 for methods details). As for pollen analyses, results of the multimethod climate reconstructions are shown in two different figures for MIS 5-4 (Fig. 4.7) and for MIS 3-1 (Fig. 4.8). Main results are given in Table 4.3. alongside the Pollen Zone.

The four methods applied here generally show consistent patterns of decreasing annual and winter temperatures and precipitations during stadial events, and the opposite pattern during interstadial events. The MAT shows the most extreme oscillations between cold and warm events, while RF appears to be the less sensitive method. Therefore, to simplify the following discussion (Section 4.4) we then chose to represent climate reconstructions as a mean value of the four methods applied in this study.

The warmest and wettest conditions are reconstructed during Pollen Zone 2 associated to MIS 5e (the Eemian) interglacial. During this phase, annual temperatures are close to the present value, while MTWA and precipitation higher than today. Following this climatic optimum, the general trend shows decreasing temperatures throughout MIS 5, with important variations of precipitation following the succession of rapid events. Throughout MIS 5, pollen-inferred temperatures and precipitation display several abrupt drops, but with reduced amplitude compared to cooling events occurring during MIS 4-2. From MIS 5a to MIS 2, higher amplitude changes are observed especially in winter and annual parameters. Summer parameters, especially precipitation, generally show very reduced variability compared to the other climatic parameters, and their pattern is less clear. During some events, like GS22 and HS1, SUMMERPR seem to increase moderately during the main cold arid phase, when MAP and WINTERP display minimum values.

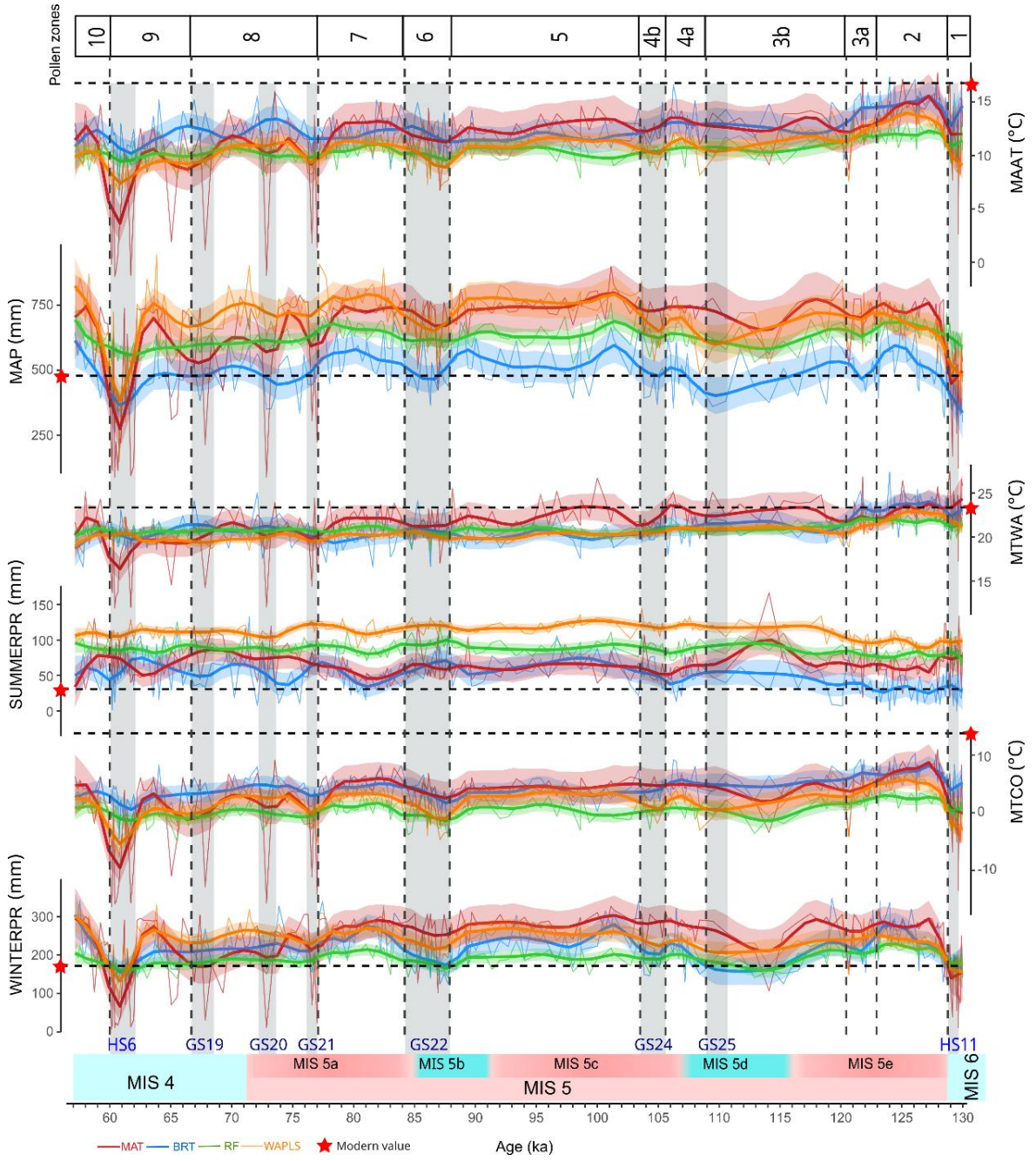


Fig. 4.7. Multimethod pollen-based climate reconstructions for MIS 5-4 interval from the ODP 976 record. MAAT (Mean Annual Temperature), MTCO (Mean Temperature of the Coldest Month), MAP (Mean Annual Precipitations), MTWA (Mean Temperature of the Warmest Month), SUMMERPR (Summer Precipitations), and WINTERPR (Winter Precipitations) for the four different methods applied: MAT (Modern Analogue Technique), WA-PLS (Weighted-Averaging Partial Least Squares), BRT (Boosted Regression Trees) and RF (Random Forest). The light-coloured interval represents the 95% confidence window, and the bold curves the loess smoothed values (alpha = 0.1). Modern values are indicated by the horizontal dashed line and the red star. Grey vertical bars indicate the main cold episodes related to the main Heinrich Stadials (HS) and Greenland Stadials (GS). The MIS boundaries follow Lisiecki & Raymo (2005).

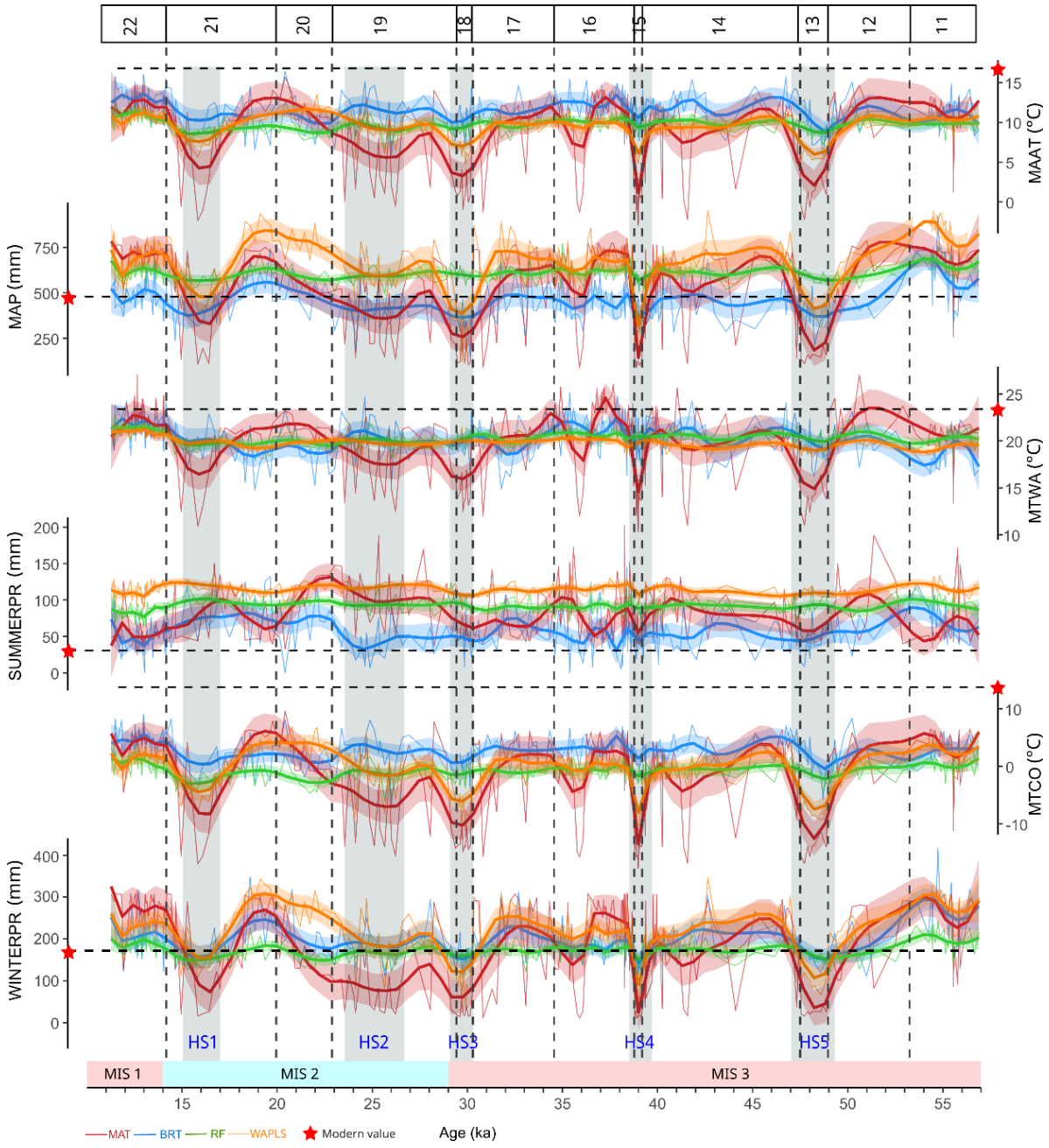


Fig. 4.8. Multimethod pollen-based climate reconstructions for MIS 3-1 interval from the ODP 976 record. MAAT (Mean Annual Temperature), MTCO (Mean Temperature of the Coldest Month), MAP (Mean Annual Precipitations), MTWA (Mean Temperature of the Warmest Month), SUMMERPR (Summer Precipitations), and WINTERPR (Winter Precipitations) for the four different methods applied: MAT (Modern Analogue Technique), WA-PLS (Weighted-Averaging Partial Least Squares), BRT (Boosted Regression Trees) and RF (Random Forest). The light-coloured interval represents the 95% confidence window, and the bold curves the loess smoothed values (alpha = 0.1). Modern values are indicated by the horizontal dashed line and the red star. Grey vertical bars indicate the main cold episodes related to the main Heinrich Stadials (HSs) The MIS boundaries follow Lisiecki & Raymo (2005).

4.4.3. Clay particles analyses

Clay mineralogical composition analyses of ODP 976 have been published for the last 50 ka BP (Bout-Roumazeilles et al., 2007; Combourieu-Nebout et al., 2009). Here, we present new data covering the last 130 ka BP, including a total of 556 samples. Results are presented in Fig. 4.9.

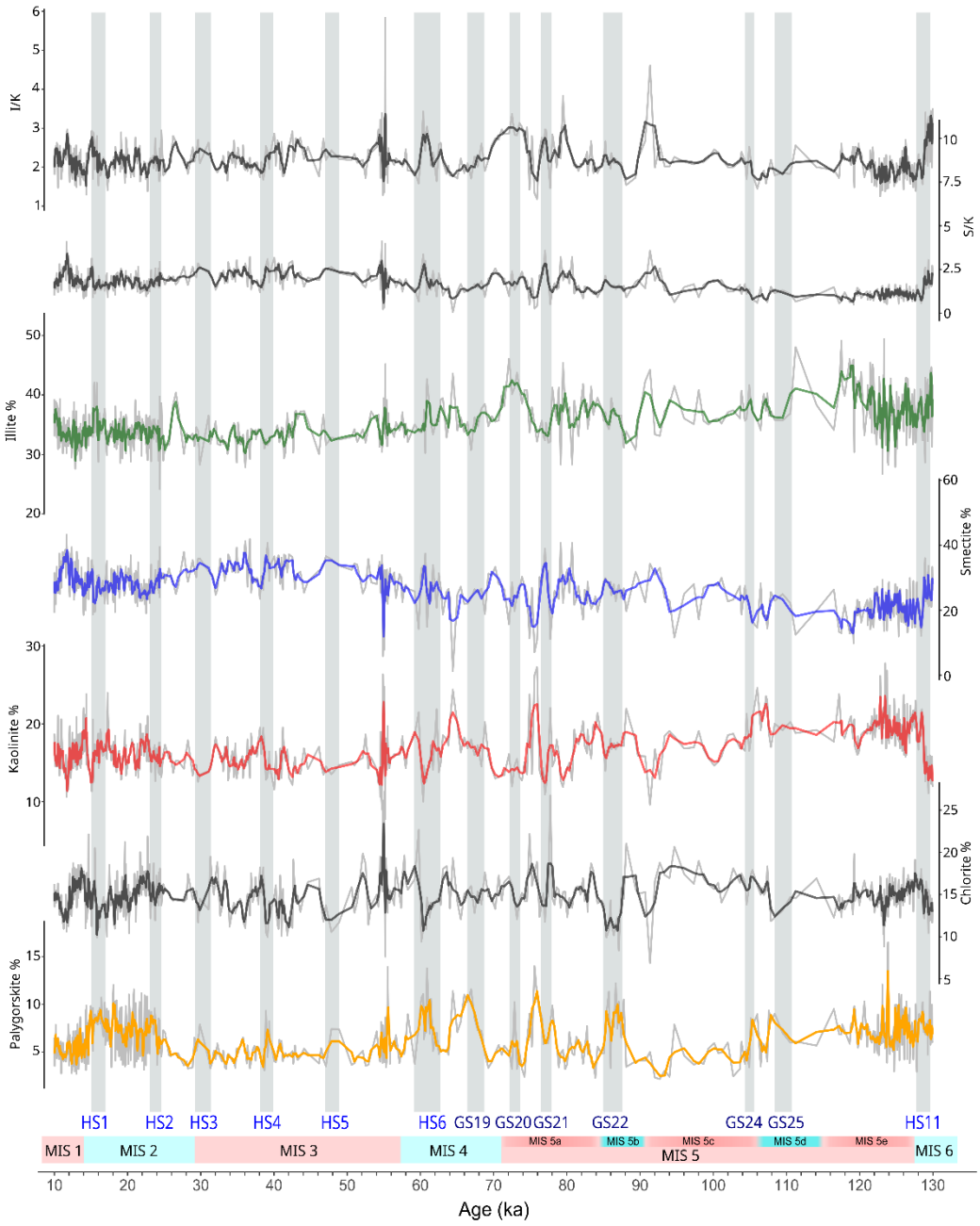


Fig. 4.9. ODP 976 clay mineralogical composition over the last climatic cycle (130-10 ka BP) (Bout-Roumazeilles et al., 2007 for the last 50 ka BP, and this study). I/K represent the illite / kaolinite ratio, and S/K the smectite / kaolinite ratio. The main cold events associated to Heinrich Stadials (HS) and Greenland Stadials (GS) are represented by the vertical grey lines.

In general, illite is the most abundant mineralogical component of ODP 976 clay sediment, followed by smectite, kaolinite, chlorite and palygorskite. Important variations in the composition can be observed, reflecting both long-term trends and rapid oscillations.

Looking at the long-term trends, kaolinite and illite are most abundant during MIS 5, and then tend to decrease while entering into the LG period (MIS 4-2). Smectite shows an opposite pattern, with increasing percentages during the LG. Chlorite and palygorskite long-term signals are more difficult to interpret. However, the palygorskite component especially is characterized by important rapid oscillations, most of them in phase with the North-Atlantic cold events (HS1-6 and GS19-26). This pattern has already been shown for the last 50 ka BP, with major palygorskite input during HS1 to HS5. Furthermore, the palygorskite percentages during previous cold events of the end of MIS 5 and MIS 4 (GS19 to GS22 and HS6) reach much higher values than during HS6-5.

4.4.4. Multivariate statistical analyses

Correlation and Principal Component Analyses were undertaken to better understand the relationship between the different paleoclimate variables and their influence on sample variability over time. The fifteen variables selected correspond to the main ecological groups of taxa and the five clay minerals: *Pinus*, Temperate Forest, Montane Forest, Ericaceae, Pioneer vegetation, semi-desert vegetation, herbaceous vegetation, Mediterranean vegetation, aquatic herbaceous, Pteridophytes (see Table 3 for the details of each group composition), and palygorskite, smectite, illite, chlorite and kaolinite. We used the *Corrplot* package for the correlation analysis (Friendly, 2002), and the *ade4* package for the PCA.

The dataset for the multivariate analysis was slightly extended at both the upper and lower limits to properly represent the Holocene and the HS11 assemblages. In addition, only samples that were analysed for both pollen and clay mineralogical composition were selected to include both pollen and clay mineralogical data in the same statistical analyses, resulting in a 406 samples dataset spanning from 7 to 133 ka BP.

The samples were grouped and coloured in the PCA according to their climatic zone, including Greenland stadials (GS), HS1-6 and HS11, the Younger-Dryas (YD), the Last Glacial Maximum (LGM) in blue, and Greenland interstadials (GI), the Holocene, the Bolling-Allerod (BA), and the Eemian in red. The distribution of samples in the distinct climatic zones was done manually, based primarily on the GI start points used for the age model, and then on the observation of the pollen assemblage changes reflecting the transition to stadial environments (Fig. 4.10).

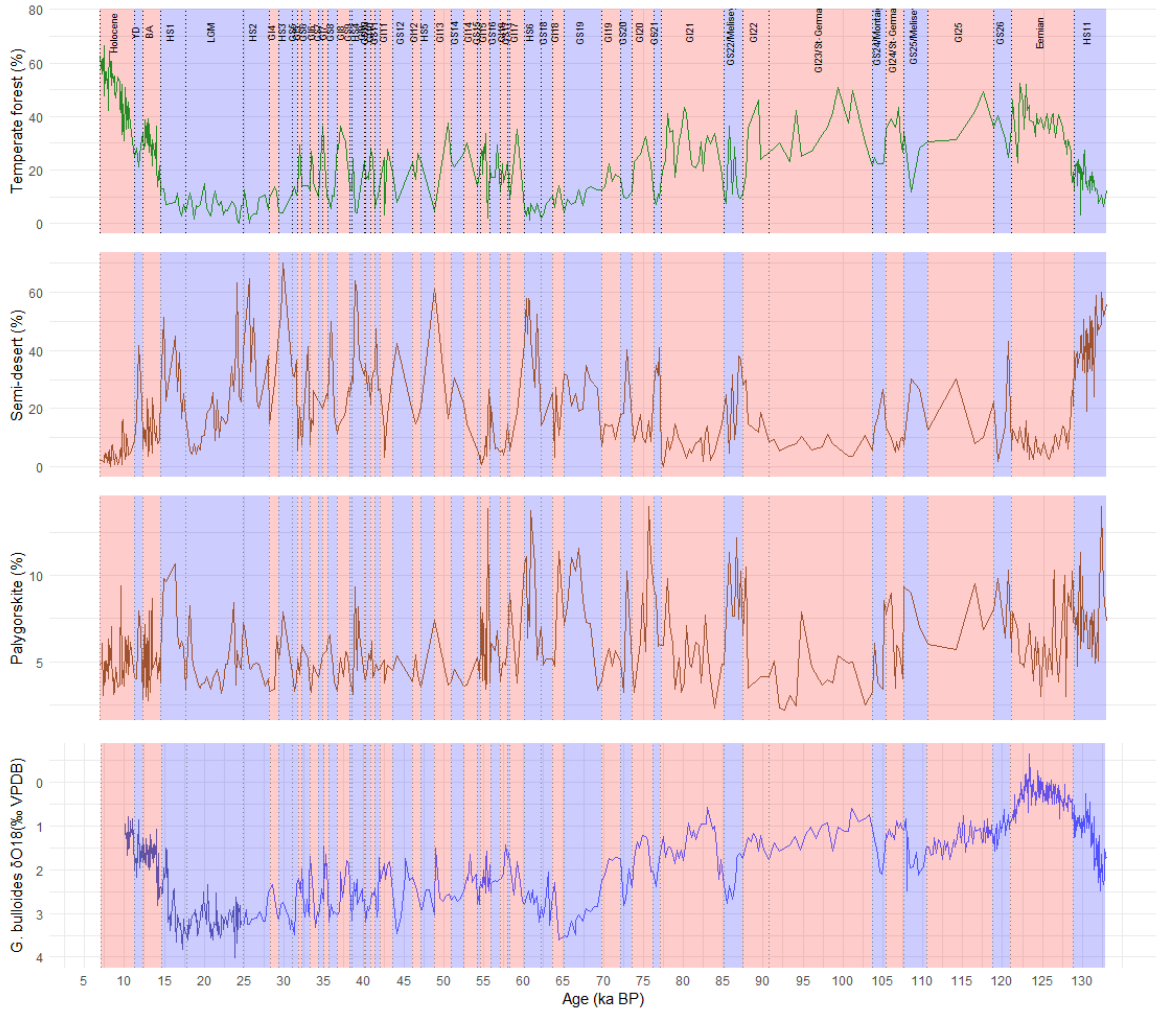


Fig. 4.10. ODP 976 multiproxy record (7-133 ka BP) used for the multivariate analyses. From top to bottom: temperate forest pollen, semi-desert pollen and Palygorskite, including a total of 406 samples common between the pollen and clay proxies. The Holocene, Younger-Dryas (YD), Bolling-Allerod (BA), Heinrich stadials (HS) 1-6, the Eemian and HS11, as well as Greenland stadials and interstadials, were placed based on the age model and the pollen assemblage, and are indicated by the blue and red vertical bars for cold and warm episodes respectively. The planktonic oxygen isotope ratio, which was used as base for the age model, is shown at the bottom for reference.

The correlation matrix shows the correlation coefficients between the fifteen variables, with positive correlation coloured in blue, and negative correlation coloured in red (Fig. 4.11). The most important positive correlations can be seen between Mediterranean and temperate forest, *Pinus* and montane forest, Pteridophytes and Mediterranean forest, and Pteridophytes and temperate forest. Other lower but still relevant positive correlations exist between *Pinus* and Ericaceae, kaolinite and chlorite, Mediterranean vegetation and aquatic herbaceous, Pteridophytes and aquatic herbaceous, kaolinite and Pteridophytes, kaolinite and Temperate Forest, kaolinite and Mediterranean vegetation, palygorskite and semi-desert vegetation, aquatic herbaceous and temperate forest. On the contrary, the most important negative correlations are observed between kaolinite and smectite, illite and smectite, semi-desert vegetation and temperate forest, smectite and chlorite. Other lower but still

relevant negative correlations exist between *Pinus* and temperate forest, semi-desert and Mediterranean vegetation, *Pinus* and Mediterranean vegetation, herbaceous vegetation and Temperate Forest.

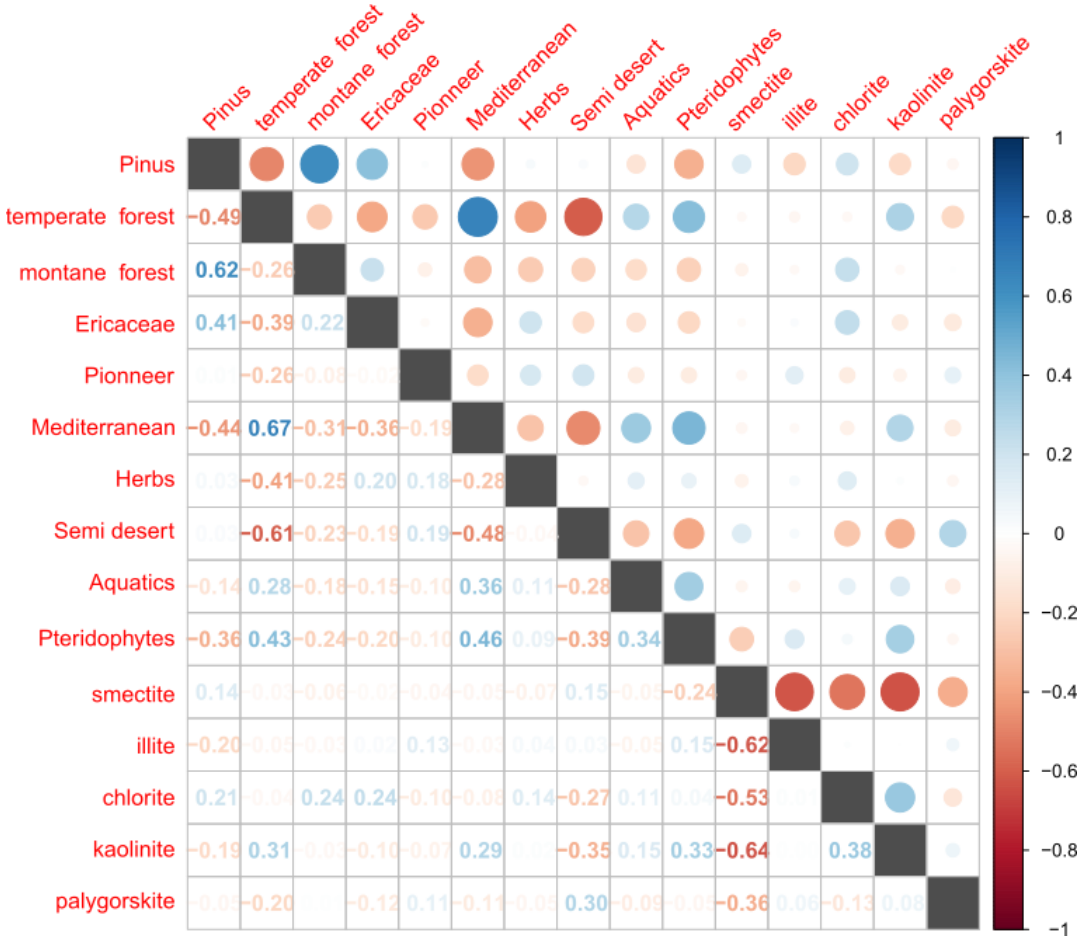


Fig. 4.11. Correlation matrix of the fifteen selected variables, including the main ecological groups of pollen taxa and the five clay minerals. The correlation coefficient is presented in the bottom part of the matrix, while the upper part shows circles coloured in blue (positive correlation) and red (negative correlation), and sized according to the coefficient's importance.

The PCA shows the ordination of the 15 variables and the 406 samples in a 2D space according to their contribution to the variance of the dataset (Fig. 4.12). The first axis represents ~25% of total variance, and mainly opposes *Pinus*, semi-desert vegetation, and Smectite in the positive values, to temperate forest, Mediterranean vegetation, Pteridophytes and Kaolinite in negative values. There is a clear opposition in the sample's ordination on axis 1, between the Eemian and the MIS 5 interstadials in negative values at the left, and the Heinrich stadials and Greenland stadials in positive values at the right. Another interesting feature is the ordination of various Greenland Interstadials (4,7,9,10,12,14, 19) in the same area than Greenland stadials at the right of the plot, indicating that their pollen assemblage and clay mineralogical composition is closer to

stadials than to the other interstadials, in particular with lower abundance of temperate taxa. On the contrary, GS25 and GS24, corresponding to the Montaigu and Melisey I events respectively in palynostratigraphy, are clearly placed at the left with the MIS 5 interstadials and the GI8, showing they were marked by a reduced importance of the cold variables (steppe and semi-desert) compared to the LG stadials.

Based on these observation, it is possible to give an interpretation of the PCA signal in term of climate conditions: axis 1 seems dominated by a temperature signal, discriminating cold variables (semi-desert, *Pinus*, montane taxa, smectite) from warm variables (Mediterranean and temperate forest, kaolinite, aquatics and Pteridophytes) and samples, while axis 2 seems more controlled by humidity, separating wet (*Pinus*, Ericaceae, montane taxa, kaolinite, chlorite, Pteridophyte) and dry (semi-desert, pioneer taxa, Mediterranean taxa) variables and samples.

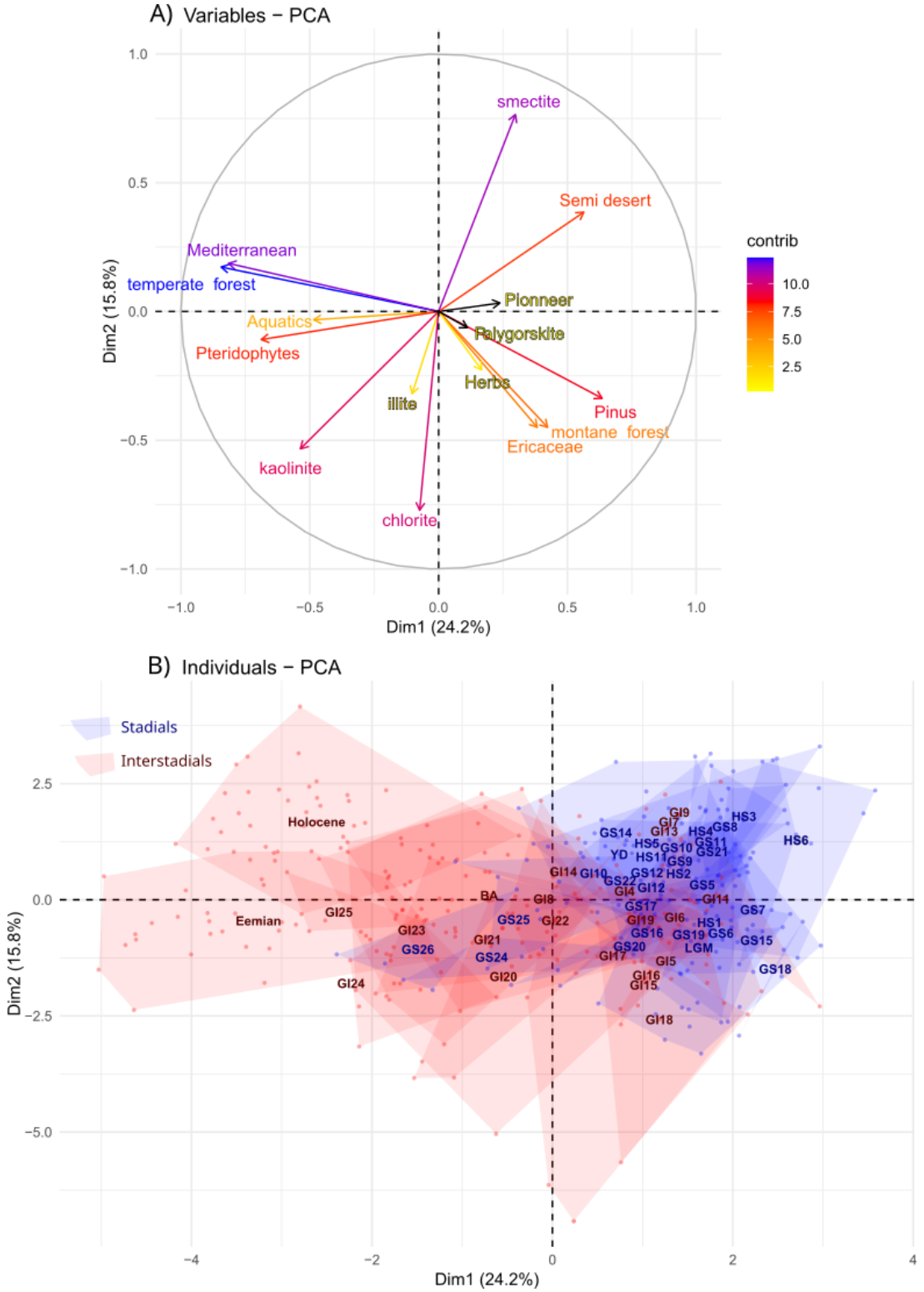


Fig. 4.12. A) PCA plot of variables, including the main ecological groups of pollen taxa and the five clay minerals coloured by their contribution to PCA axes (red: highest contribution and blue: lowest contribution), and individuals (bottom). **B)** PCA plot representing the distribution of the 406 ODP 976 samples from 7 to 133 ka BP. Samples were grouped in 55 climatic zones corresponding to stadials and interstadials, including Heinrich stadials, Greenland stadials, the Holocene, LGM, YD, BA and the Eemian (see text for details). The name of each climatic zone is placed at the epicentre of the group.

4.5. Discussion

4.5.1. The last glacial (MIS 4-2): rapid dynamics int the ODP 976 record

4.5.1.1. Overview

The last glacial (MIS 4-2) in the multiproxy record from ODP site 976 shows both long-term trends and high-amplitude sub-orbital instability well-reflected in the pollen assemblage, the clay mineralogical composition and the planktonic isotopic ratio (Fig. 4.13).

During the early MIS 4 glacial (70-65 ka BP), the pollen assemblage shows high percentages of steppe and semi-desert plants and Ericaceae. The paleo-dust record displays palygorskite percentages above 10%, among the highest values of all the last glacial record. Palygorskite mineral is produced under specific conditions of strong seasonal aridity south of the Atlas Mountains, and it therefore indicates the development of dry conditions regionally (Bout-Roumazeilles et al., 2007). Altogether, these features reflect cold and dry climatic conditions during GS19, expressed in the pollen-inferred climate reconstructions by relatively low temperature of the coldest month (Fig. 4.13). During GS19, *Cedrus* increases progressively to reach ~50% of the total pollen assemblage at the onset of GI18 (~64 ka BP), which is marked by particularly high pollen-inferred annual precipitation. Subsequently, during GS18 a major Heinrich event impacted the climate and vegetation of the southwestern Mediterranean, HS6 (62.5-60 ka BP), which is marked in the ODP 976 record by two main peaks of steppe and semi-desert vegetation percentages, of palygorskite input, and reconstructed annual precipitation below 400 mm. Following this arid event, GI17 is marked by a rapid expansion of Mediterranean and temperate deciduous vegetation. The end of MIS 4 and the beginning of MIS 3 (59.5-50 ka BP) stand out by the continuous high abundance of temperate vegetation and Mediterranean elements, but also Ericaceae and *Cedrus*, shortly interrupted by a semi-desert taxa expansion during GS16-15 (~56 ka BP), possibly linked with HS5a (Margari et al., 2020). Throughout this interval, except during GS16-15, pollen-inferred annual precipitation remains above the present value, reaching close to 800 mm /yr during GI15 (~55 ka BP). Wet conditions regionally are also supported by the presence of the thick Organic-Rich Layer (ORL) 603 (Murat, 1999) in the ODP 976 sedimentary record, starting after GI17 and ending during HS5.

After 50 ka BP, the ODP 976 multiproxy records very fast changes in the vegetation composition and climate variations following the succession of MIS 3 stadials and interstadials (Bout-Roumazeilles et al., 2007; Combourieu-Nebout et al., 2002; Masson-Delmotte et al., 2005). The succession of events is less rapid during early MIS 2, where forests are more reduced and herbaceous taxa (Ericaceae, Cichorioideae) dominate the pollen assemblage. Finally, instability returns at the end of MIS 2 during glacial termination at the transition with MIS 1, including HS1 (Oldest Dryas), GI1 (Bölling-Allerod), and

GS1 (Younger Dryas) already well-documented and studied in the region (Combourieu-Nebout et al., 2002, 2009).

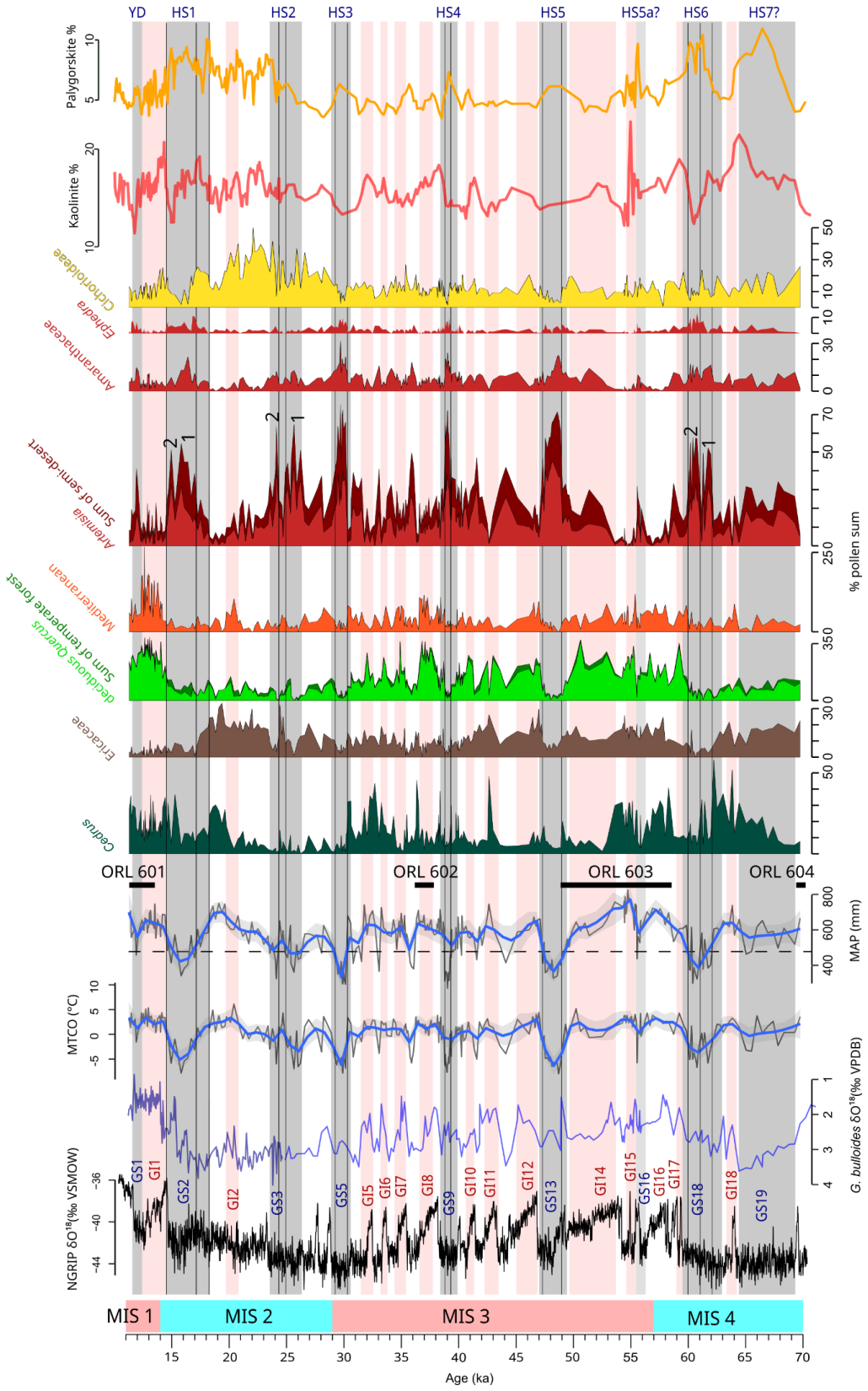


Fig. 4.13. Millennial climate oscillations during the last glacial period (MIS 4-2) recorded at ODP site 976 through multiple proxies and compared with the Greenland record on GICC05 timescale

(Rasmussen et al., 2014). From right to left: palygorskite and kaolinite percentages in the clay mineralogical composition (Bout-Roumazeilles et al., 2007; this study), main pollen taxa and ecological groups (Combourieu-Nebout et al., 2002, 2009; Genty et al., 2005, 2010; Masson-Delmotte et al., 2005; Fletcher et al., 2010a; this study); Organic-rich layers (ORLs) intervals (Murat, 1999); pollen-inferred mean annual precipitation (MAP) and temperature of the coldest month (MTCO) reconstructed through a multimethod approach; *G. bulloides* oxygen isotopic ratio (Combourieu-Nebout et al., 2002; this study). Red bars and names indicate the main Greenland Interstadials (GIs), while grey bars and blue names represent the main Greenland Stadials (GSs) associated to a Heinrich event. Numbers on the steppe and semi-desert pollen curve show the two main arid vegetation expansions during HS6, HS2 and HS1.

Greenland interstadials (GIs) are generally characterized by high percentages of temperate deciduous and Mediterranean forests, low values of steppe and semi-desert taxa, low planktonic isotopic ratio, and high input of kaolinite in the paleo-dust record. Pollen-inferred precipitations (annual and seasonal) are above the present values, and temperatures of the warmest month are close to the present value (Fig. 4.7). Annual temperature and temperature of the coldest month also increase, although the present-value remains higher (probably due to the impact of human-induced climatic warming on the extracted values from ERA 5 reanalysis between 1960 and 2022). The warmest interstadials in the ODP 976 record are represented by the GI17, GI15, GI14, GI12, GI8, GI7, GI2, and GI1, based on their high percentages of temperate deciduous and Mediterranean taxa percentages, and their higher reconstructed temperature and annual precipitation (Fig. 4.13). Despite its very long duration and important development of forest vegetation, GI14 also shows relatively high steppe and semi-desert pollen percentages in the ODP 976 record, with decreasing pollen-inferred winter temperatures and precipitation, although the lower resolution of the record during this interval may mask a more complex dynamic within GI14 (Fig. 4.13). Noteworthily, GI8 and GI1, which are among the warmest interstadials of the entire last glacial record, also concomitant with ORLs 602 and 601 deposition in the southwestern Mediterranean region, supporting enhanced rainfall during these phases (Murat, 1999).

Greenland stadials (GSs) show the opposite pattern (Fig. 4.13). They generally display a higher planktonic isotopic ratio, lower percentages of temperate deciduous and Mediterranean forest pollen, and significant palygorskite input. Pollen-inferred reconstructions support colder and drier conditions regionally during GS, with annual precipitation lower than today, and temperature of the coldest month below 0°C for some of the coldest events.

In the Greenland record, GIs are characterized by a very abrupt rise in ice temperatures, and GSs by a very abrupt decrease in ice temperature (Genty et al., 2010; Rasmussen et al., 2014). In the Alboran Sea, the opposite pattern is reflected by the pollen and isotopic records as previously evidenced by Genty et al. (2005, 2010). During GIs, warming is more gradual not only in the planktonic

isotopic ratio, but also in the pollen assemblage et pollen-inferred climate reconstructions, with some exceptions of more abrupt warming occurring during GI17, GI15, GI12 and GI10 (Fig. 4.13). During GSs, the expansion of steppe and semi-desert is generally very rapid, especially during HSs. This different timing likely reflects a longer time response of Mediterranean continental ecosystems to North Atlantic warming following the cold events of reduced AMOC.

Heinrich Stadials (HSs) represent the most extreme expression of stadial events in the ODP 976 record. The MIS 4-2 period featured six major HSs, from HS6 to HS1, which are marked in the ODP 976 by extremely high abundance of steppe and semi-desert taxa (>50%), largely dominated by *Artemisia*. Additional cooling possibly related to the less intense and less-well studied Heinrich events H7 (~66 ka BP) and H5a (~ 55 ka BP) can be recognized (Lisiecki & Stern, 2016; Rashid et al., 2003). During HSs, Mediterranean and temperate deciduous pollen taxa are very reduced, while pollen-inferred climate reconstructions show the lowest values of annual precipitation and winter temperatures recorded throughout the entire glacial (Fig. 4.13). HSs also display high percentages of palygorskite, between 5 and 10%, reflecting enhanced African input and aridity in the Alboran Sea region (Bout-Roumazeilles et al., 2007). Besides, the paleo-dust record extended beyond 50 ka BP shows a surprising new feature: the most important palygorskite input in the Alboran Sea are linked with HS1, HS6, but also HS7 and HS5a which are the less extreme events in the pollen record. In particular, HS7 features the highest percentages of palygorskite (> 10 %), while the vegetation is mostly composed by a mix of steppe taxa, Ericaceae and *Cedrus*. This pattern may reflect a non-straightforward relationship between palygorskite production and transport to the Alboran Sea, and arid conditions in the southwestern Mediterranean: during HS7, the abundance of *Cedrus* and Ericaceae pollen reflect important winter moisture availability in the region (supported by pollen-based winter precipitation higher than today).

4.5.1.2. Climatic significance of the main pollen taxa variability

The ODP 976 marine record captures a regional signal of the vegetation composition, and the limited number of long terrestrial sequences available in the Iberian Peninsula (Carrión et al., 2024) complicates the interpretation of the spatial variability and climatic significance of the different pollen taxa. However, general patterns can be described based on the knowledge of vegetation formation on the different altitudinal belts of the Alboran Sea region. In the pollen assemblage, the climatic instability of the last glacial is clearly evidenced through the opposite variations in steppe and semi-desert pollen and temperate deciduous and Mediterranean taxa, marking cold / dry and warm / humid periods respectively. The climatic significance of the three other most abundant taxa in the ODP 976 pollen record for the last glacial, *Cedrus*, Ericaceae and Cichorioideae, is more ambiguous.

Cedrus high abundance phases generally correspond to humid stadial or interstadial phases during MIS 4 and early MIS 3 (GS19, GI16, GI15, GS15) or transitional phases between interstadial and stadial periods later during MIS 3. During these phases, it is likely that montane vegetation expands in the north-African Rif, and perhaps also more moderately in the Baetic Cordillera mountains (Cheddadi et al., 2017; Jiménez-Moreno et al., 2020). *Cedrus* phases may also indicate enhanced aeolian input from North Africa (Fletcher & Sánchez Goñi, 2008), although no clear correlation is observed between *Cedrus* and dust input from Africa in the ODP 976 record (Fig. 4.11, 4.11 and 4.12).

Ericaceae generally exhibit similar dynamics to those of temperate deciduous forests, decreasing during stadials and increasing during interstadials. This pattern likely reflects the evolution of the water-demanding eurosiberian vegetation component (heathlands) on the Atlantic side of the Iberian Peninsula during periods of reduced summer dryness: previous studies correlated high percentages of Ericaceae on the Iberian margin to periods of low boreal insolation and closely linked with precession cycles (Fletcher & Sánchez Goñi, 2008; Fourcade et al., 2024; Margari et al., 2014). This pattern is also documented in the ODP 976 record (Fig. 4. 13): maximum Ericaceae abundance is observed at times of minimum insolation (~20 ka BP, ~70 ka BP, or ~95 ka BP). However, this relation is not straightforward during early interglacial periods: maximum Ericaceae are observed at two insolation maxima during MIS 5e (~125 ka BP) and during early MIS 3 (~55 ka BP). A particular dynamic is detected in the ODP 976 record, with Ericaceae progressive increase and abrupt reduction during extreme arid episodes, like HS11, C26-C25 and HS6 to HS1 (Fig. 4.13). On the other hand, Ericaceae in the ODP 976 record are also positively correlated to montane arboreal elements (*Pinus* and *Cedrus*) and herbaceous taxa, and negatively correlated to Mediterranean taxa (Fig. 4.11), indicating the development of heaths under cooler and wet conditions on the Alboran Sea borderlands. A similar interpretation can be drawn for Cichorioideae, which are the main component of the herbs group in the multivariate statistical analyses and positively correlated to Ericaceae. They display lower abundance during interstadials and seem to develop mainly during transitional phases between interstadial and stadial periods. Ericaceae and Cichorioideae also are the most abundant taxa during the last glacial maximum, between HS2 and HS1 (~23.5-18.5 ka BP), showing their high tolerance to cold conditions. Finally, it is important to considerate that Ericaceae is a large family of plants possibly including littoral heathland genus and species (*Erica arborea* and other *Erica* species), but also Mediterranean plants (*Arbutus*) or colder-adapted plants growing in altitudinal plains, which are hard to distinguish through the palynological method. Most Ericaceae identified in the ODP 976 record correspond to rather small pollen grains, which dimension falls in the rage of *Erica arborea* and *Erica vagans* types (Combourieu-Nebout, personal communication) following criteria from Oldfield, (959): these types can correspond to Atlantic and Mediterranean heath plants growing in the Iberian margins

and in the Moroccan altitudinal belt. The Atlantic heath species *Calluna vulgaris* is barely present in the ODP 976 record. Therefore, it is possible that periods of high Ericaceae percentages during interstadials, during transitional phases, and during glacial maxima may correspond to the development of different vegetation types, including Atlantic heathland, Mediterranean Ericaceae at lower altitudes, and cooler undergrowth bush Ericaceae at higher altitude.

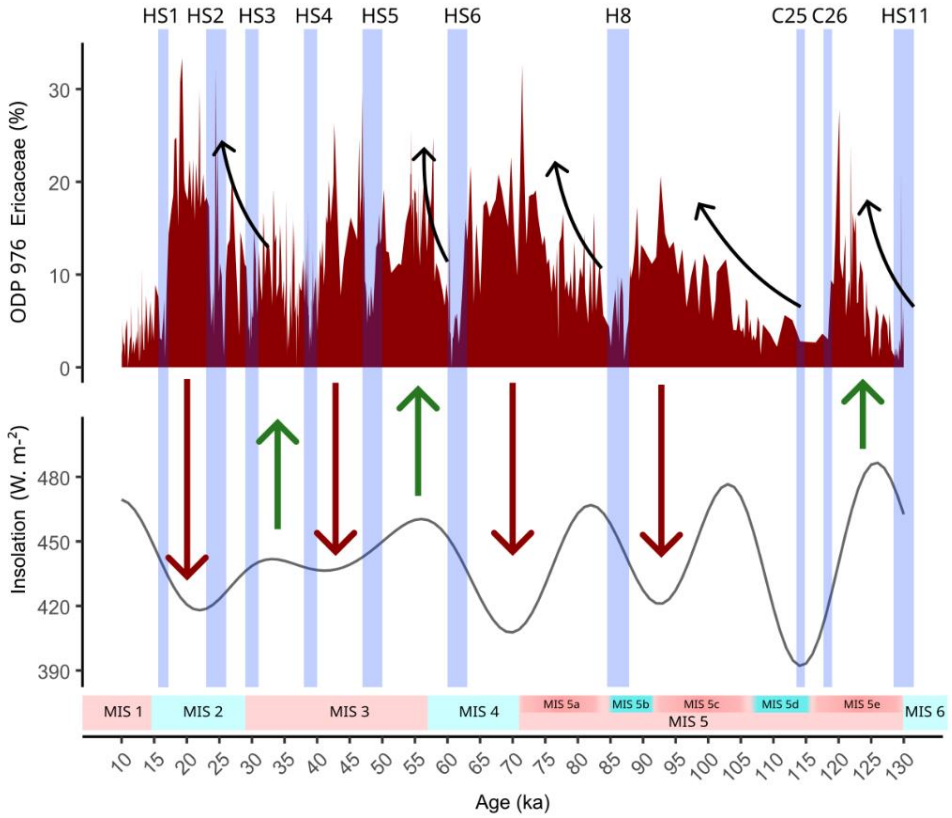


Fig. 4.14. Comparison between Ericaceae percentages in the ODP 976 pollen record and insolation at 65°N latitude (Berger & Loutre, 1991) between 130 and 10 ka BP. Black arrows show Ericaceae long-term increasing dynamics prior to abrupt extreme events. Brown arrows indicate the correspondence between maximum Ericaceae percentages and minimum insolation, while green arrows indicate Ericaceae maximum correlated to higher insolation during MIS 5e and MIS 3.

4.5.1.3. Comparison with regional and North-Atlantic records

A limited number of paleoenvironmental records allows to document continuously the complete last glacial period. Some of them have been represented in Fig. 4.15 together with the multiproxy record from ODP 976.

HS6-1 are consistent with events of intense iceberg melting in the North Atlantic evidenced from Ice-Rafted Debris (IRDs) abundance in two records from the Bay of Biscay, MD04-2845 (Sánchez Goñi et al., 2008) and the Portuguese Margin, MD95-2040 (de Abreu et al., 2003). These IRDs peaks are coeval with high percentages of the cold foraminifera *N. pachyderma* on the Portuguese margin.

Some chronological mismatches are visible in for HS5 and HS6, likely resulting from age model uncertainties. The most intense events of IRD deposition on the Portuguese margin are linked with HS2 and HS4, while HS6 features the longest duration of ice-melting. Stadial episodes evidenced in the ODP 976 pollen-inferred climate record are well-correlated to low SSTs from the nearby ODP site 977 (Martrat et al., 2007). HS4 and HS5 stand out by their particularly cold conditions, consistent in both pollen and alkenone reconstructions. However, the impact of HS3 is moderate in the SST record, while the pollen record evidence the same amplitude of freshening as HS4 and HS5. The two smaller Heinrich Stadials, HS7 and HS5a, are also characterized by IRD deposition off Portugal, but with reduced intensity and moderate cooling in the SST record of the Alboran Sea.

The sequence from Padul represents the only terrestrial record in the Iberian Peninsula continuously spanning the last climatic cycle (Camuera et al., 2019, 2022). A remarkably good correspondence is observed between the pollen-inferred reconstructions of winter precipitation in Padul (WA-PLS method) and the multimethod reconstructions from ODP 976, especially for the MIS 2-1 interval (Fig. 4.15), with some chronological misfit linked with the different age models. Based on the reconstructed past hydroclimate for the southern Iberian Peninsula, six Western Mediterranean Humid Periods (WMHP) were identified over the past 200 ka BP (Camuera et al., 2022). In the ODP 976 climate record, these WMHP are also well-identified and correspond to important winter precipitation above modern value, and high percentages of temperate forest and eurosiberian taxa (Ericaceae). Higher values of winter precipitation reconstructed during these phases in the ODP 976 record compared to Padul likely reflect the more regional image of climate of the marine sequence, capturing the conditions from the Atlantic coast of the Iberian Peninsula where the development of heaths is favoured by Atlantic moisture availability. Moreover, the humid phase during early MIS 3 (58-54 ka BP) evidenced in the ODP 976 climate reconstructions was not defined as a WMHP in Padul, although important winter precipitation also characterizes this period.

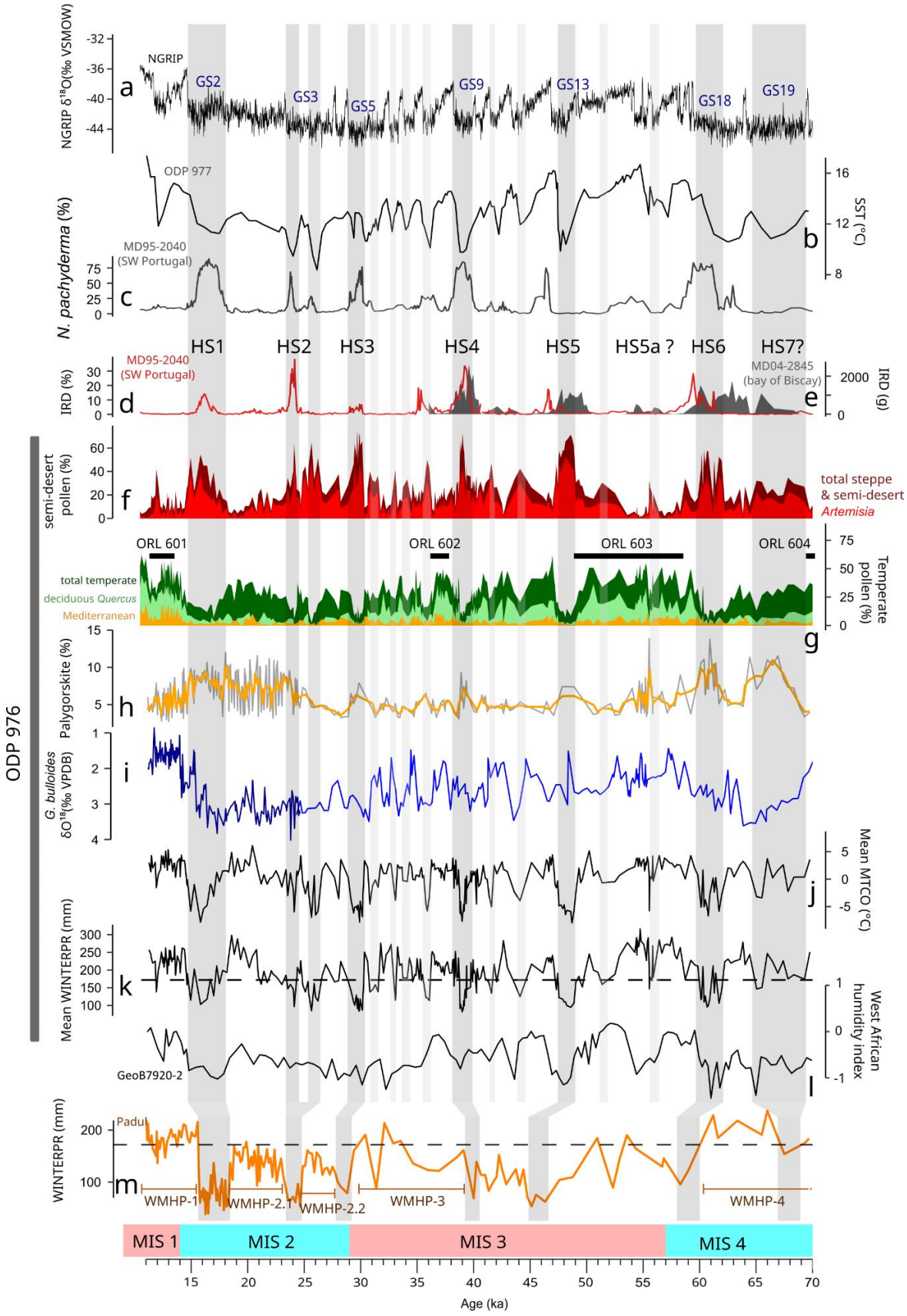


Fig. 4.15. Comparison of the ODP multiproxy record for MIS 4-1 with other records from the North Atlantic, Greenland, and the southwestern Mediterranean region. a) NGRIP ice temperature record on GICC05 timescale (Rasmussen et al., 2014 and references therein); **b)** alkenone-based sea-surface

temperatures (SSTs) from ODP 977 in the Alboran Sea (Martrat et al., 2004); **c)** *N. pachyderma* and **d)** Ice-Rafted Debris (IRD) percentages from core MD95-2040 (de Abreu et al., 2003); **e)** IRD counting from core MD04-2845 in the Bay of Biscay (Sánchez Goñi et al., 2008); the multiproxy data from ODP 976 : **f)** total semi-desert (dark red) and *Artemisia* (light red) pollen percentages, Organic-Rich Layers (ORLs) intervals (Murat, 1999), **g)** total temperate (including eurosiberian + temperate deciduous forest + Mediterranean), deciduous *Quercus*, and Mediterranean pollen percentages (Combourieu-Nebout et al., 2002, 2009; this study), **h)** palygorskite percentages (Bout-Roumazeilles et al., 2007; this study), **i)** planktonic isotopic ratio from ODP 976 (Combourieu-Nebout et al., 2002 ; Jiménez-Amat & Zahn, 2015; this study), **j)** pollen-inferred mean temperature of the coldest month (MTCO) and **k)** winter precipitation (WINTERPR) based on a mean of four methods applied in this study; **l)** West African humidity index from core GeoB7920-2 (Tjallingii et al., 2008); **m)** pollen-inferred winter precipitation from Padul record (WA-PLS method) from the Sierra Nevada (Camuera et al., 2022) with the Western Mediterranean Humid Periods (WMHP) identified. Grey bars indicate cold events in the ODP 976 record. MIS boundaries follow Lisiecki & Raymo (2005).

Interestingly, recent studies in north-western Africa showed an important African Humid Period (AHP) between 60 and 50 ka BP evidenced from paleolake Tissint reconstruction in the Anti-Atlas region (Morocco) (Nutz et al., 2024). This AHP is consistent with high winter rainfall during the same period reconstructed in the OPD 976 pollen record, showing a strong connection between African humidity and western Mediterranean climate, as already shown in Padul (Camuera et al., 2022).

4.5.1.4. Structure of the different extreme events: HS7 to HS1

Since the development of very high resolution paleoenvironmental studies from ice, speleothems and marine records, the internal structure of Heinrich Stadials have been discussed (e.g. Fletcher & Sánchez Goñi, 2008; Guillevic et al., 2014; Margari et al., 2020; Wendt et al., 2019). A 3-phases structure during the well-studied HS4 has been described in various records from the North Atlantic (Margari et al., 2020), the Mediterranean region (Charton et al., 2025; Fletcher & Sánchez Goñi, 2008), in Greenland (Guillevic et al., 2014), in Brazil (Wendt et al., 2019) and in China (Cheng et al., 2021). The ODP 976 high-resolution multiproxy record is among the few long records in the Mediterranean covering the complete last glacial period (Fletcher, Sánchez Goñi, et al., 2010) and allowing to compare the structure of the six major Heinrich events (HS6 to HS1) that impacted the regional vegetation and climate. In particular, the cluster analysis applied on the palynological record of ODP 976 allows to describe the structure of the different Heinrich Stadials in the southwestern Mediterranean (Fig 4.15)

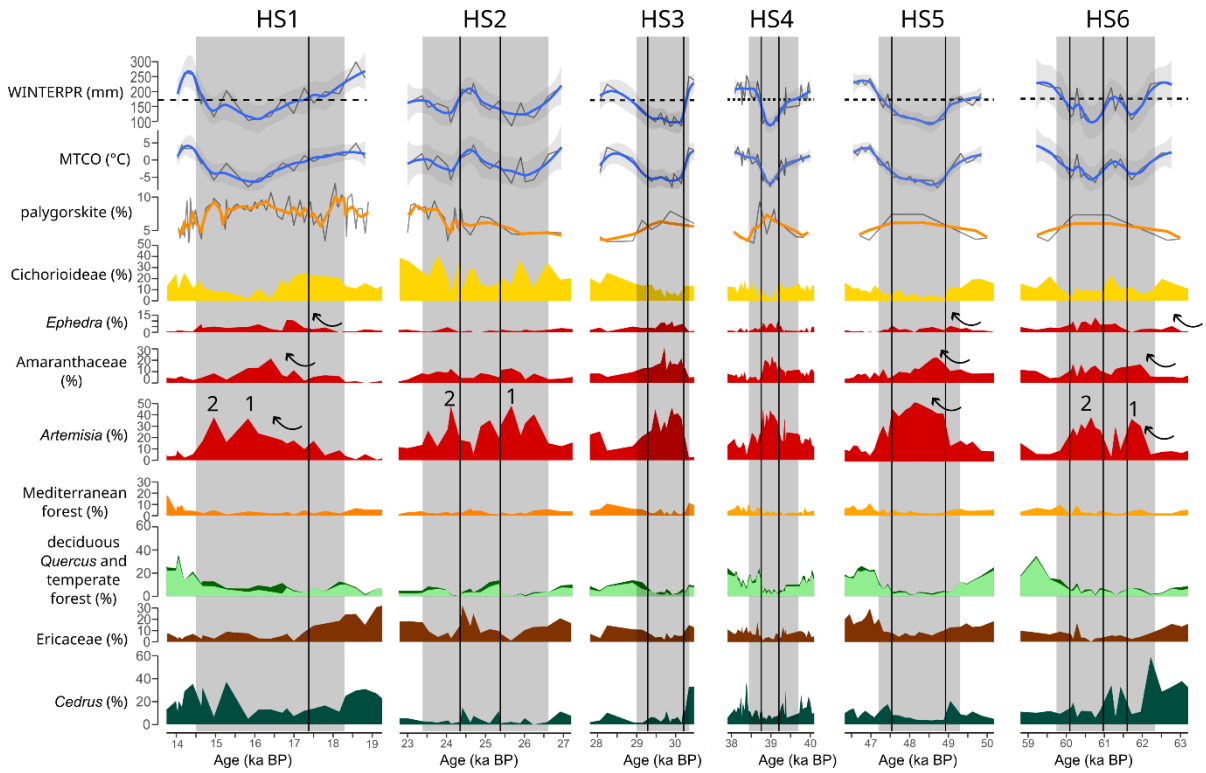


Fig. 4.16. Comparison between the structure of the HS6 to HS1 in the ODP 976 multiproxy record.

HS1 (GS2, ~18.2-14.5 ka BP) in the ODP 976 record is divided into two phases. The first is marked by a first peak in palygorskite input, and the development of herbaceous vegetation (especially Cichorioideae, and Amaranthaceae). Ericaceae and *Cedrus* are abundant, pointing toward colder but still humid conditions. Pollen-inferred reconstructions show a continuous decrease of winter temperatures and annual precipitation during this phase. The second phase displays low values of arboreal pollen, enhanced palygorskite input, and high steppe and semi-desert pollen percentages. A fast vegetation dynamic is identified, with a first *Ephedra* expansion followed Amaranthaceae and *Artemisia* increase successively, while the second phase displays two successive Artemisia peaks separated by a short *Cedrus* increase. During this second phase, climate reconstructions show very cold and dry conditions. This two-phased pattern for HS1 is compatible with other marine records from the Iberian margin, where a wet to dry climatic trend was described during HS1, HS2 and HS3 (Naughton et al., 2009), and with Indian monsoon record (Huang et al., 2019). Additionally, North Atlantic records showed that HS1 was in fact composed by two distinct layers of IRD deposition with different provenance and intensity, the second one being the most intense (Hodell et al., 2017; F. J. Sierro et al., 2020). Higher-resolution studies later evidenced a third phase of warmer conditions but still intense ice-melting in the North-Atlantic in most records from the western Mediterranean region (Naughton et al., 2016). In the Bay of Biscay record of the “Fleuve Manche” paleoriver, dinocysts data from laminated sediments revealed ultra-high resolution five phases during HS1 connected with multidecadal shifts in seasonality (Fersi et al., 2021). If higher-resolution would be necessary to assess

the consistency of the ODP 976 pollen record with these phasing, it is remarkable that the end of HS1 is marked by increased *Cedrus* and temperate pollen, and warmer and less dry conditions in the climate reconstructions, compatible with a late warming and moistening phase.

The structure of HS2 (occurring during GS3, ~26.6-23.4 ka BP) in the ODP 976 record is more complex, with two different stages of steppe and semi-desert expansion corresponding to freshening and drying events in the climate reconstructions. Between these two cool stages, the record shows a short episode of Ericaceae, *Cedrus* and temperate forest increase, and climatic warming and moistening. The second steppe and desert vegetation expansion (~24.3 ka BP) is characterized by the simultaneous increase of *Artemisia*, *Ephedra* and Amaranthaceae. While a first increase in *N. pachyderma* cold foraminifera abundance on the Portuguese margin together with a first drop in SST in the Alboran Sea are observed during the first HS2 stage (Fig. 4.14), the second stage is coincident with major IRD deposition and therefore the HE2 *sensu strico*. At the end of the event, a moderate increase of temperate deciduous and Mediterranean taxa is observed, contemporaneous to a new increase in *Artemisia* pollen. Other studies have pointed out a twofold structure during HS2 (Cui et al., 2024; F. J. Sierro et al., 2020). The ODP 976 record is compatible with such pattern through two different peaks of desert pollen, although more resolution would be needed to detail the rapid succession of changes during this shorter HS.

HS3 (GS5.1, ~30.4-29 ka BP) is divided into three different phases in the ODP 976 record. The first phase is characterized by high *Cedrus*, Ericaceae and Cichorioideae percentages, while Mediterranean taxa are also surprisingly abundant. The second phase marks the highest percentages of steppe and semi-desert taxa which increase simultaneously, together a peak in palygorskite-rich dust input. This phase coincides with the minimum reconstructed winter temperature and annual precipitation. Finally, the last phase is marked by an increase in temperate deciduous taxa, Cichorioideae, Mediterranean vegetation and Ericaceae and an increase in temperatures and precipitation. Other evidence for a three-phases pattern during HS3 come from Lake Fimone record in northern Italy (Badino et al., 2020), where the maximum arid phase is coincident with enhanced long-distance wind-transported charcoal signal, and a third intermediate phase precedes the return to full interstadial conditions.

HS4 (GS9, 39.9-38.3ka BP) displays a clear three-phases pattern in the ODP 976 multiproxy record (see Section 3 and Charton et al., 2025), compatible with Greenland (Guillevic et al., 2014) and low latitude records (Cheng et al., 2021; Wendt et al., 2019). During the main arid phase, *Artemisia*, Amaranthaceae and *Ephedra* increase together, without any delay between taxa. This main cold and

arid phase is also marked by enhanced palygorskite input in the Alboran Sea (Bout-Roumazeilles et al., 2007)

HS5 (GS13, 49.5-47 ka BP) is also characterized by three phases in the OPD 976 record which share similarities with the HS4 pattern. The first phase is marked by decreasing temperate deciduous taxa, a peak of *Cedrus*, a first increase in steppe and semi-desert taxa, and stable Ericaceae pollen percentages. The second phase is remarkably long (~1.7 ka) compared to the main HS4 phase. It displays the maximum steppe and semi-desert taxa abundance, lowest temperatures of the coldest month and winter precipitation, and palygorskite peak input. The third phase is marked by rapid vegetation succession, with a first peak of *Cedrus*, and in smaller proportion of temperate deciduous forest, followed by a new increase in *Artemisia* and Amaranthaceae, and finally an increase in Ericaceae, deciduous forest and Mediterranean taxa. Comparably to HS4, this internal three-phased structure during HS5 is consistent with data from North-Atlantic sedimentary cores (Margari et al., 2020; Sierro et al., 2020), but also with Asian Monsoon record in China where three phases connected with latitudinal movements of the ITCZ were evidenced (X. Zhang et al., 2024).

HS6 (occurring during GS18, ~62.2-59.6 ka BP) stands out in the ODP 976 record by its complex structure and long duration, close to the pattern described during HS2. After a first peak on *Cedrus* (>50% of total pollen), two main peaks of steppe and semi-desert taxa are visible. The middle phase is marked by high percentages of *Cedrus* and Cichorioideae pollen. Climate reconstructions support two minima in temperatures of the coldest month and winter precipitation associated with the two steppe and semi-desert expansions, the second of which is marked by the most extreme values. Finally, the GI17 onset at the end of HS6 is more abrupt than after other HSs, with Mediterranean and temperate deciduous forest increasing rapidly. HS6 has been less studied than other HSs, and was initially described as a very long cooling covering two North Atlantic cold events, named C17 (corresponding to GS18) and C18 (corresponding to GS19) (McManus et al., 1994; Sánchez Goñi et al., 2013). In the Bay of Biscay, intense IRD deposition is recorded continuously during GS18, preceding by several centuries the abrupt increase of steppe and semi-desert vegetation in the Alboran Sea.

In addition to these six best-studied HS, the ODP 976 pollen record shows additional cooling events compatible with two other minor IRD events named H5a and H7 events. H5a is rarely identified in paleoenvironmental records (Rashid et al., 2003). It is associated to a smaller iceberg discharge in the North Atlantic occurring during GS15 (~54.7 ka BP), and more moderate associated cooling. In the ODP 976 record, an abrupt increase in steppe and semi-desert taxa and palygorskite compatible with HS5a is detected around 55.6 ka BP, coincident with GS16. This chronological delay is likely the result of uncertain age control at times of high instability, considering the very fast succession of GS16, GI15

and GS15 and their difficult identification in the planktonic isotopic record of the Alboran Sea. During this cold episodes, two successive peaks of *Artemisia* occur, with the second one being the most intense and seeing the contemporaneous increase of Amaranthaceae and *Ephedra* together with *Artemisia*. Similarly, H7 is hardly identifiable in most paleoenvironmental records from Europe. The first description of the event came from North Atlantic sedimentary evidence from the Labrador Sea, where it was subdivided into two events (H7a and H7b), coincident with GS20 (~73 ka BP) and GS21 (~77 ka BP) (Rasmussen et al., 2003). However, in the Lisiecki & Stern LS16 regional and global stack for the last glacial cycle, H7 is placed around 67 ka BP, contemporaneous to GS19 (Lisiecki & Stern, 2016), mainly based on the IRD record from core MD03-2692 (46°N) in the Bay of Biscay (Toucanne, Zaragosi, Bourillet, Cremer, Eynaud, Van Vliet-Lanoë, Penaud, Fontanier, Turon, & Cortijo, 2009), and core GIK23415 (53°N) (Weinelt et al., 2003). However, Sánchez Goñi et al. (2013) place the cold phase during GS19 (C18 event) within the HS6 event, and not H7. In the ODP 976 record, the GS19 is characterized by one of the largest palygorskite peak of the last glacial, indicating particularly important African wind input in the Alboran Sea. The pollen assemblage is dominated by *Cedrus*, Ericaceae and steppe and semi-desert plants, although with lower percentages than classical Heinrich stadials in the core. *Artemisia* and Amaranthaceae increase synchronously, with two different peaks. Climate reconstructions show rather cool and less humid conditions, although less extreme than the other HSs. We hypothesize that this interval could correspond to H7, based on the correlation with the MD04-2845 IRD layer and LS16 IRD stack, distinct from HS6 and occurring between ~ 69.5 and ~64.7 ka BP according to our age model.

Finally, although each HS presents a different phasing, some general patterns can be identified in the ODP 976 record. First, the presence of one or two main phases of maximum steppe and semi-desert expansion and palygorskite input in the dust record, consistent with phases of minimum SST in the Alboran Sea and intense IRD deposition in the North Atlantic and on the Portuguese margin. These coldest and driest phases correspond to the maximum entrance of Atlantic freshwater through the Gibraltar Strait linked with the southernmost migration of the polar front, AMOC reduction and iceberg discharges from the Laurentide ice sheet. Secondly, transitional phases are observed before and after the main cold stage, characterized by higher percentages of montane (*Cedrus*), Ericaceae and Cichorioideae vegetation evidencing cool and relatively wet climatic conditions. Enhanced input of *Cedrus* pollen in the Alboran Sea during early phase of HSs was previously identified and linked with stronger wind-blown pollen contribution from North-Africa (Fletcher & Sánchez Goñi, 2008). This is compatible with rising palygorskite-rich dust input in general during early HS phases, although the significant presence of Ericaceae correlated with the *Cedrus* phases may also reflect relatively cold and

humid conditions regionally, favouring the development of montane vegetation in North Africa and heaths on the Alboran Sea borderlands.

Differences between HSs lies in their duration, climatic aridity intensity, in the number of cold arid phases, and the vegetation succession identified. H7 (~5 ka), HS1 ~ (4.8 ka) and HS6 (~3.4 ka) correspond the longest cold envents in the ODP 976 record, followed by HS2 (~2.8 ka), HS5 (~2.4) and HS3 (~1.7 ka). HS4 (~1.5 ka) and H5a (less than 1 ka) are the shortest events. In term of aridity intensity, maximum percentages of steppe and semi-desert taxa are recorded during HS4, HS3, HS5 (> 70 % of steppe and semi-desert taxa), while minimum annual rainfall is recorded during HS6, HS5, HS4 and HS3 (less than 350 mm/yr). Two successive peaks of steppe and semi-desert vegetation are identified during HS1, HS2, HS6, H5a and H7, while HS3, HS5 and HS4 present only one main cold and arid peak. During HS1.2, HS2.2, HS3.1, HS4 and HS6.2, the three main steppe and semi-desert taxa (*Artemisia*, *Ephedra* and Amaranthaceae) increase simultaneously. During the first stage of HS1 and HS6 and during HS5, a delay is observed between the development of *Ephedra*, Amaranthaceae, and *Artemisia* successively. This vegetation succession can indicate more progressive transition toward aridity, with increasing hydric stress favouring the expansion of halophyte vegetation formation. Therefore, based on their duration and intensity, we identify HS4 and HS3 as the most extreme events in the pollen record, characterized by very abrupt and rapid shift to arid climate conditions regionally. On the other hand, HS6 and HS5 feature a more progressive change toward dry conditions, and a longer duration.

4.5.2. The last interglacial (MIS 5)

The correspondence between Greenland cooling events, European pollens stratigraphy, and North Atlantic cooling and Heinrich events during MIS 5 has long been investigated (e.g. Sánchez Goñi, 2007; Tzedakis et al., 2018; Wohlfarth, 2013). The complete set of pollen, planktonic isotopes, clay and climate reconstructions results for MIS 5 from ODP 976 allows to assess rapid climatic variability in the Alboran Sea region during the last interglacial complex.

4.5.2.1. Overview

The internal structure of the last interglacial complex was studied in numerous continental palynological sequences in France, Germany and Italy first (Allen et al., 1999, 2000; Allen & Huntley, 2000, 2009; Behre, 1981; De Beaulieu & Reille, 2007; Reille et al., 1998; Woillard, 1978), and successively in the Eastern Mediterranean (Tzedakis, 1993, 1999, 2005; Tzedakis et al., 2003, 2006). Palyno-stratigraphical events of the last interglacial were first defined at La Grande Pile (Woillard, 1978) and recognized in other terrestrial sequences (e.g. Oerel, Gröbern, Monticchio, Tenaghi Philippon, Ioannina, see Wohlfarth (2013) for a review). Their identification in the western Iberian margin cores MD95-2042 and MD99-2331 successively helped to correlated them with north Atlantic

cooling events evidenced in marine proxies (Sánchez Goñi et al., 2005, 2007). This stratigraphy of vegetation events during MIS 5 is also well-evidenced in the ODP 976 record of the last interglacial (Fig. 4.17). Furthermore, the high-resolution ODP 976 record reveals additional events compatible with North-Atlantic cold events, especially during the Eemian (C27b-C25 events), and the GS23 / C22 event.

The MIS 6-5 transition is marked by a prominent cold event identified as HS11, and lasting until about 129 ka BP. This very cold and dry event is a particular feature of glacial Termination II and was indicated as a possible analogue for HS1 during the last deglaciation (Jiménez-Amat & Zahn, 2015; Martrat et al., 2014; see Section 5 for more information on this subject). Successively, temperate deciduous forest and Mediterranean taxa are generally the dominant taxa along the last interglacial period in the Alboran Sea, but with important oscillations. In general, *Cedrus* and Ericaceae increase progressively from MIS 5d onward, following glacial inception.

During the Eemian (MIS 5e), the Mediterranean taxa exhibit their maximum expansion between ~127.9 and ~126.2 ka BP, associated to the warmest temperatures reconstructed during the last interglacial. This implies a relatively short duration for the Eemian climatic optimum of about 1.3 ka. Successively and until 119 ka BP, Mediterranean taxa decrease progressively, and Ericaceae increase. Pollen-inferred climate reconstructions show a progressive decrease of temperatures of the coldest month starting very shortly after the Eemian optimum, after 125 ka BP. Two abrupt increases of steppe and semi-desert taxa are observed at ~121 ka BP and ~119 ka BP, associated to enhanced palygorskite input, a decrease of annual precipitation and temperatures of the coldest month, and to high planktonic isotopic values. They can be corelated to the two North-Atlantic cold events C27b and C26 respectively (Oppo et al., 2006; Tzedakis et al., 2018). A third cold event is identified in the pollen record and climate reconstruction during the Eemian at ~114.5 ka BP, compatible with C25 cold event (Oppo et al., 2006; Tzedakis et al., 2018). The end of the Eemian period is characterized by high percentages of temperate and deciduous forest and Mediterranean taxa, associated to GI26.

Successively, MIS 5d cold substage features a notable instability. The Melisey I event (~110 to 108 ka BP) in the pollen stratigraphy is marked by an increase in steppe and semi-desert taxa and a significant abrupt forest reduction, associated to GS25, to the C24 North-Atlantic cold event and to H10 (Lisiecki & Stern, 2016). A new development of temperate deciduous forest and Mediterranean taxa occurs during the St-Germain Ia event (~108 to ~105.5 ka BP), associated to GI24. The St-Germain Ib/Montaigu colt event (~105.5 to ~104 ka BP) is then well-evidenced in the pollen record as well as in the planktonic isotopic record and the climate reconstructions, correlated to GS24 in Greenland, C23 event and H9 in the North-Atlantic.

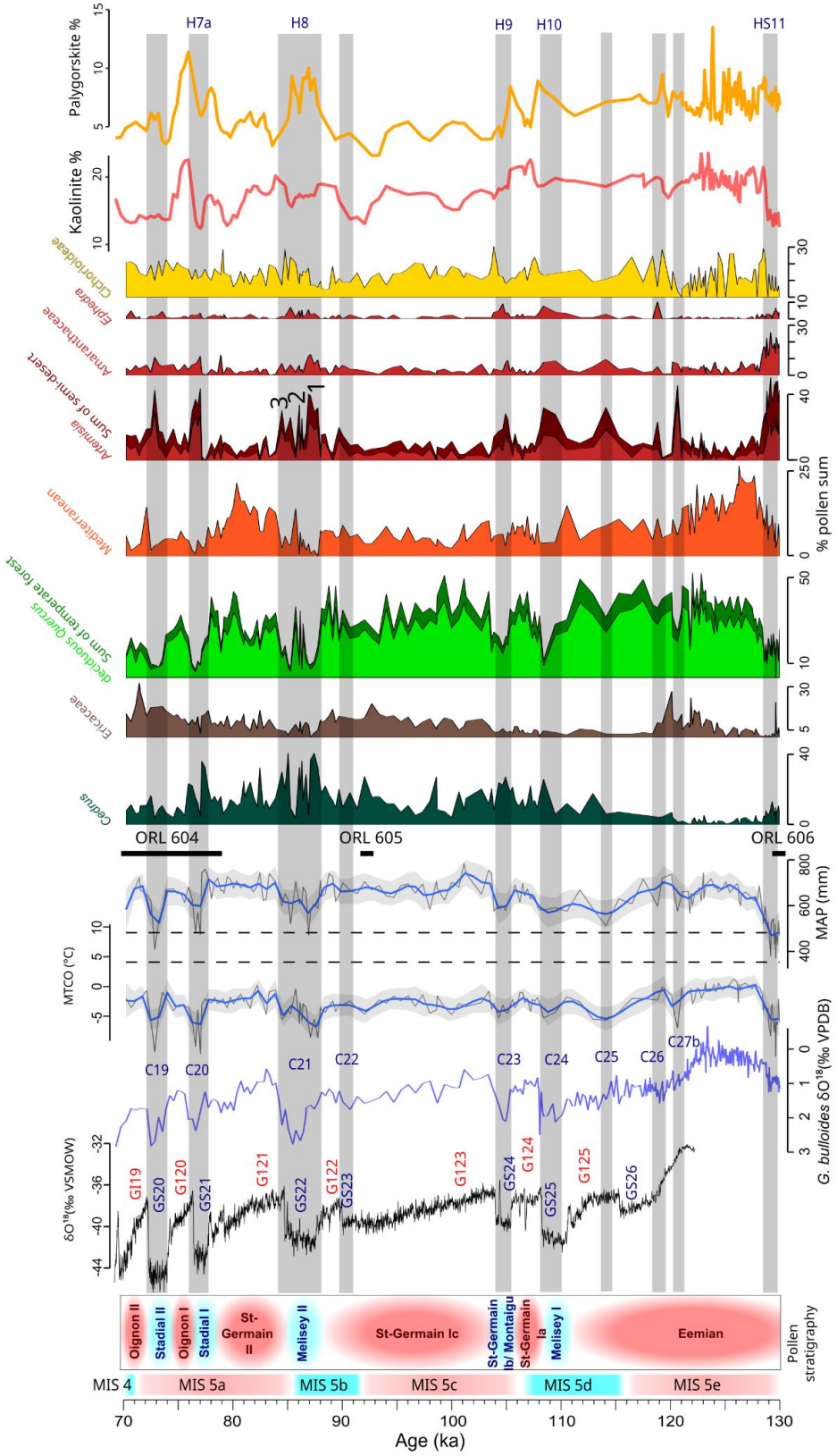


Fig. 4.17. **Millennial climate oscillations during the last interglacial (MIS 5) in the ODP 976 multiproxy record, compared with the Greenland record on GICC05modelext timescale** (Rasmussen et al., 2014). From right to left: palygorskite and kaolinite percentages in the clay mineralogical composition (this study), main pollen taxa and ecological groups (Masson-Delmotte et al., 2005; Fletcher et al., 2010a; this study); Organic-rich layers (ORLs) intervals (Murat, 1999); pollen-inferred mean annual precipitation (MAP) and temperature of the coldest month (MTCO)

reconstructed through a multimethod approach (this study); *G. bulloides* oxygen isotopic ratio (this study). Grey bars indicate the main cold events in the ODP 976 record, associated to Greenland stadials (GS) (Rasmussen et al., 2014), Heinrich Stadials (HS) (Lisiecky & Stern, 2016; Rasmussen et al., 2003), and north-Atlantic cold events (C27-C19) (Chapman & Shackleton, 1999; Oppo et al., 2001, 2006). Pollen stratigraphy follow Woillard (1978) and marine isotope stratigraphy (MIS 5e to MIS 4) follows Lisiecki & Raymo (2005) and Railsback et al. (2015).

MIS 5c stands out with a very long interstadial event between 104 and 91 ka BP identified in Greenland (GI23) and in the pollen record (St-Germain Ic). Along this interval, herbaceous taxa display generally low percentages. Temperate deciduous trees are particularly abundant at the beginning of this period, associated to higher annual rainfall than during the Eemian optimum. Successively, a progressive decrease of temperate deciduous forest, and a progressive increase in Ericaceae may indicate gradual cooling. Only one sudden cooling is recorded around 98.5 ka BP marked by a *Cedrus* increase, relatively colder temperatures, and higher planktonic isotopic ratio. A very short episode of ORL deposition (ORL 605) is also recorded at the end of this interstadial (Murat, 1999).

The beginning of MIS 5b features a moderate cold event centred around 90 ka BP correlated to GS23 and C22, followed by the GI22 interstadial. Then, the most intense and long cold event of the last interglacial is expressed in the OPD 976 multiproxy record between ~88 and ~84 ka BP, correlated to Melisey II, but also to GS22 and to C21 and H8 North-Atlantic events. This event features a very complex structure with two peaks of palygorskite percentage recorded in the clay mineralogical record, three different peaks of steppe and semi desert pollen taxa and two warm rebounds where temperate deciduous and Mediterranean pollen taxa increase very abruptly (Fig. 4.15). During this event, *Cedrus* also features three successive increases preceding the steppe and semi-desert peaks and displays the highest percentages recorded in the last interglacial, reaching nearly 40% of the total pollen sum. The first cold pulse records the lowest reconstructed precipitation and temperatures of the event, with annual rainfall falling below the modern value for the first time during the last interglacial.

MIS 5a, the final marine isotopic substage of MIS 5, starts with the long St-Germain II/GI21 interstadial, well-evidenced in the Alboran Sea pollen record between ~84 and ~78 ka BP through high percentages of temperate deciduous pollen and Mediterranean taxa, with a peak abundance at ~80.5 ka BP. Successively, important variability characterizes the end of the last interglacial. ORL 604 deposition starts at the end of the St-Germain II/Gi21 interglacial, and continuous through the fast succession of events that follows. Stadial I (~77.8 to ~76 ka BP) and Stadial II (~74 to ~72 ka BP) palyno-stratigraphical cold events correspond to GS21 and G20 respectively in the Greenland record, and to C19 and C20 in the North Atlantic records. Stadial I is also correlated to H7a (Lisiecki

& Stern, 2016). An important decrease in winter precipitation and temperatures is recorded during these two events of comparable amplitude. Oignon I (~76 to ~74 ka BP) and Oignon II (~72.2 to ~70 ka BP) interstadials are correlated to GI20 and GI19 respectively. Oignon I is expressed in the ODP 976 record by a particularly intense warm and wet rebound in the pollen-inferred climate reconstructions, but also very high input of kaolinite and palygorskite in the clay mineralogical record. This pattern may reflect enhanced African input during this phase with mixed sources from the Sahel and the northern Sahara.

To sum up, ten main cold events are recognized in the ODP 976 multiproxy record between 130 and 70 ka BP.

During the early interglacial (MIS 5e to MIS 5 c), these cold events display a moderate amplitude (with the exception of C27b event), and are coincident with still important percentages of temperate deciduous and Mediterranean taxa, contrasting with the MIS 4 to MIS 2 stadials. In particular, GS26, GS25 (H10) and GS24 (H9) in the PCA analysis clearly stand out from other Greenland stadials of the last glacial, with a variance closer to the interstadials (Fig. 4.12). The GS26 in particular is totally absent in the multiproxy record from ODP 976, implying a very limited impact of this event in the Alboran Sea.

The most intense cold episodes are represented by HS11, the C27b event, the Melisey II (C21 or H8), the Stadial I (C20 or H7a) and Stadial II (or C19) events. These five events feature steppe and semi-desert pollen percentages reaching ~40% of the total pollen sum, and pollen-inferred temperatures of the coldest month below -5°C. However, climate reconstructions show that most of these events were characterised by only moderate decrease of precipitation, with the exception of HS11, Stadial I (H8) and Stadial II events which appear drier. This pattern clearly points toward increasingly arid cold events during MIS 5 following the glacial inception.

The particular feature of H10, H9 and H8 events during MIS 5 is the abundance of *Cedrus* pollen during the main cold phase. This points toward less arid, and more humid conditions associated to Heinrich stadials during the last interglacial. Only from H7a and C19 stadial event the pattern of *Cedrus* increase during transitional phase, typical during the last glacial, begin to appear. Finally, very high palygorskite values at the end of MIS 5 during H8 and S7a also indicate enhanced African input during the glacial inception.

4.5.2.2. Regional comparison

HS11 marks the end of the penultimate glacial (MIS 6) and is well evidenced in the IRD record of the North Atlantic and Bay of Biscay (Fig. 4.18). However, the IRD record during MIS 5 is generally restricted to northernmost latitude (Fig. 4.18), like at ODP sites 980 (Oppo et al., 2006), 983 and 984 (Mokeddem et al., 2014), and south Greenland at site MD03-2664 (Irvalı et al., 2016). IRD abundance

during MIS 5 is very reduced in the Bay of Biscay as indicated by core MD95-2845 (Sánchez Goñi et al., 2013), and almost absent in the southwestern Iberian margin (de Abreu et al., 2003), indicating limited incursion of glacial water masses close to the Iberian margin during the last Interglacial. Therefore, events H7a, H8, H9 and H10 are generally more difficult to identify than the last glacial events H6-1 in most records from the North Atlantic and Europe. Nevertheless, the ODP 976 isotopic and palynological record shows that despite their reduced amplitude these events impacted the oceanographical conditions, continental climate and vegetation in the southwestern Mediterranean region. The cold events evidenced in the planktonic isotopic record from ODP 976 are consistent, within age models uncertainty, with the Alboran Sea cooling found in ODP 977 alkenone-based SSTs (Martrat et al., 2004). H8 particularly stands out for its intensity, and for its complex internal dynamics and duration (~4 ka) in the palynological record: these characteristics identify it as a precursor for the pattern observed during the following HSs occurring later in the last glacial.

Ohrid pollen-inferred climate reconstructions through WA-PLS and MAT approaches show a close dynamics to the ODP 976 multimethod reconstructions (Sassoon et al., 2025; Sinopoli et al., 2019). The Eemian climatic optimum identified at lake Ohrid between 128 and 121 ka BP is compatible with the ODP 976 climate reconstructions (Sinopoli et al., 2019). The Padul record showed that maximum moisture availability in the Southern Iberian Peninsula was reached between 124 and 115 ka BP (Camuera et al., 2022). A Western Mediterranean Humid Period is therefore defined during this phase (WMHP-5), coincident with a Green Sahara period in northern Africa (Brahim et al., 2023) and sapropel S5 deposition in the Eastern Mediterranean (Rohling et al., 2015). All these data point toward a widespread warm and humid climate in the Mediterranean region during the Eemian optimum, connected with African subtropical moisture availability. However, our comparison shows that after the rapid warming, instability started very early during MIS 5e with the abrupt C27b and C26 events well-evidenced in the ODP 976 record. Two abrupt temperature decreases are also recorded at Ohrid compatible with these events (Fig.4.17). Additional cooling events, named C28 to C27a, were identified during MIS 5e based on the correlation between the Corchia Cave isotopic stack and the multiproxy record from core MD01-2444 on the Portuguese margin (Tzedakis et al., 2018). The ODP 976 very-high resolution isotope and palynological record shows several oscillations during MIS 5e compatible with these cooling events (Fig. 4.18). Although they present a very reduced amplitude compared to the abrupt events recorded later, these episodes of abrupt North-Atlantic cooling point toward persistent instability even during the climatic optimum of the last interglacial (Tzedakis et al., 2018).

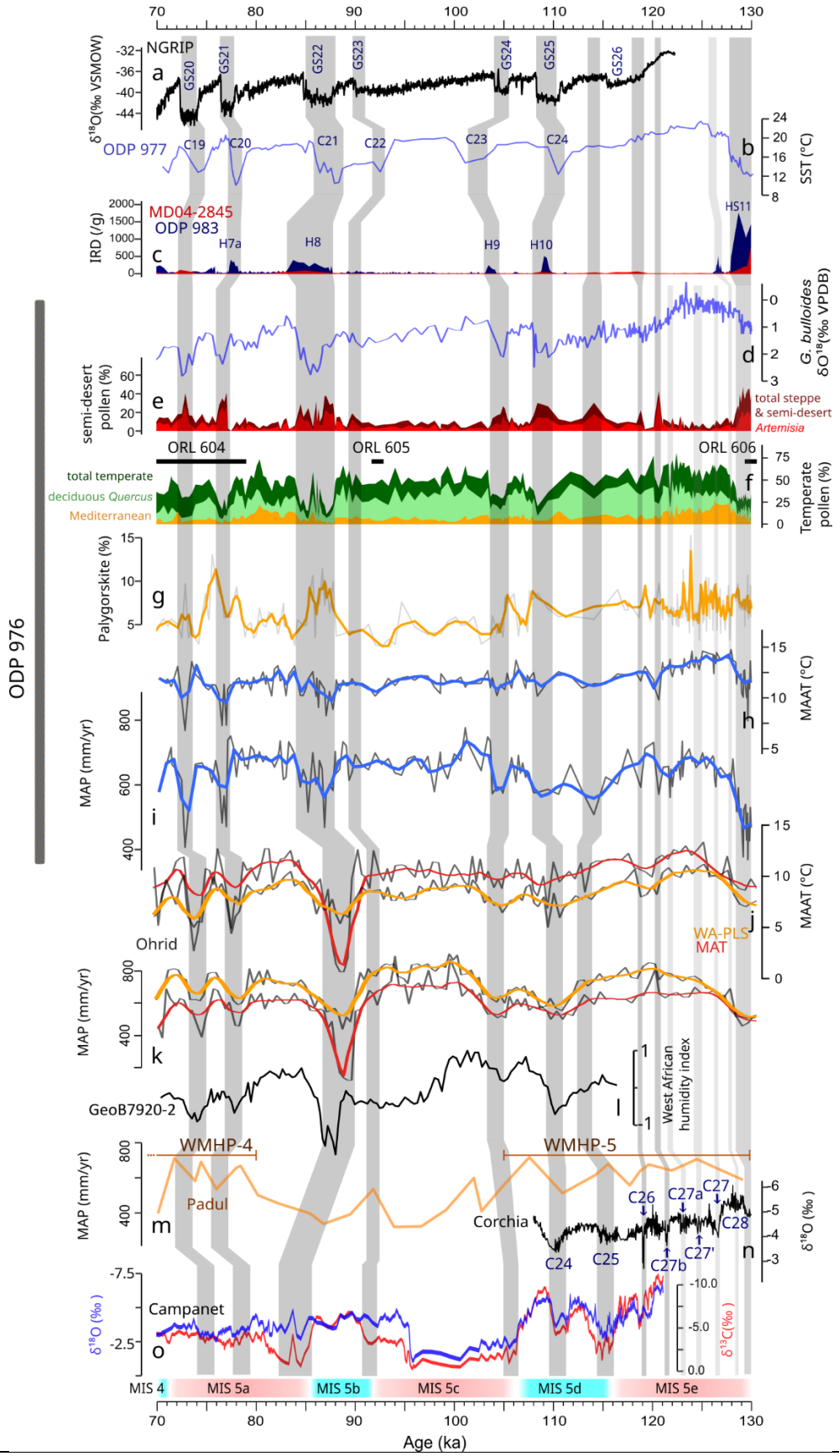


Fig. 4.18. Comparison of the ODP multiproxy record for MIS 5 with other records from the North Atlantic, Greenland, and the Mediterranean region. a) NGRIP ice temperature record on GICC05modelext timescale (Rasmussen et al., 2014 and references therein); **b)** alkenone-based sea-

surface temperatures (SSTs) from ODP 977 in the Alboran Sea (Martrat et al., 2004); **c)** Ice-Rafted Debris (IRD) counting from core MD95-2845 (red) in the Bay of Biscay (Sánchez Goñi et al., 2013) and from core ODP 983 (blue) south of Iceland (Barker et al., 2021); the multiproxy data from ODP 976 : **d)** planktonic isotopic ratio from ODP 976 (Jiménez-Amat & Zahn, 2015; this study); **e)** total semi-desert (dark red) and *Artemisia* (light red) pollen percentages, Organic-Rich Layers (ORLs) intervals (Murat, 1999), **f)** total temperate (including eurosiberian + temperate deciduous forest + Mediterranean), deciduous *Quercus*, and Mediterranean pollen percentages (Genty et al., 2005; Masson-Delmotte et al., 2005; this study), **g)** palygorskite percentages (this study), **h)** pollen-inferred mean annual temperature (MAAT) and **i)** mean annual precipitation (MAP) based on a mean of four methods applied in this study; **j)** pollen-inferred MAAT and **k)** MAP from lake Ohrid, northern Macedonia (Sinopoli et al., 2019); **l)** Western Africa humidity index from core GeoB7920-2 (Tjallingii et al., 2008); **m)** WINTERPR from Padul record (WA-PLS method) in the Sierra Nevada (Camuera et al., 2022) with the Westerm Mediterranean Humid Periods (WMHP) identified; **n)** Corchia Cave (Northern Italy) oxygen isotopic stack and the sub-millennial cold events identified based on a correlation with core MD01-2444 (Tzedakis et al., 2018); **o)** Campanet Cave (Mallorca) oxygen and carbon isotopic record (Dumitru et al., 2018). Grey bars indicate cold events recognized in the ODP 976 record, including Greenland Stadials (Rasmussen et al., 2014), C27b to C19 North-Atlantic cold events (Chapman & Shackleton, 1999; Oppo et al., 2001, 2006), and C28 to C27a event (Tzedakis et al., 2018). MIS boundaries follow Lisiecki & Raymo (2005).

Therefore, in the Alboran Sea record the first cooling event of notable intensity during MIS 5 is recorded around 120.5 ka BP and is correlated to C27b event. Successively, several cooling events are recorded from C26 to C23 pointing toward enhanced episodic cooling and drying in the Alboran Sea during the end of MIS 5e and MIS 5d. These cooling events are also well-recorded in the speleothem record from Campanet Cave from the Balearic Islands (Fig. 4.18), consistent with the rainfall decrease evidenced in the ODP 976 pollen-inferred climate reconstructions (Dumitru et al., 2018). Altogether, these data support repeated drop in precipitation and temperatures of increasing amplitude following an early glacial inception and driven by insolation decline starting as early as 125 ka BP. The pattern of mean annual precipitation in the ODP 976 record shows that wet conditions characteristic of the WMHP-5 in the Padul record were likely limited to the 129-118 ka BP interval, after which precipitations are repeatedly impacted by the cooling and drying events.

Important annual rainfall in the Alboran Sea is also evidenced at the beginning of MIS 5c between 104 and 101 ka BP coincident with GI23/ St-Germain Ic and also marked by wet conditions at lake Ohrid. However, the climate records from Padul and Campanet Cave contrast with these results, and show instead a prolonged dry episode during MIS 5c (Fig. 4.16). During this phase, steppe and semi-desert taxa are dominant in the Padul palynological record (Camuera et al., 2019, 2022), and the Balearic Islands experienced arid conditions (Dumitru et al., 2018) also supported by the deposition of aeolian dune formations on Mallorca Island at that time (Fornós et al., 2009). This divergent pattern could indicate that a strong climatic gradient existed during MIS 5c in the Iberian Peninsula, with wetter conditions under Atlantic influence in the western region and recorded in the ODP 976 regional record, while aridity characterized the south-eastern region and was recorded in Padul and the Balearic

Islands. This hypothesis is supported by important Ericaceae and temperate deciduous forest percentages in the pollen record from core MD95-2042 on the Portuguese margin during MIS 5c (Sánchez Goñi, 2005, 2007).

Interestingly, the Melisey II / C21 cooling event is also recorded in the Campanet Cave speleothem with a pattern close to the ODP 976, including a warming rebound in the middle of the event. Despite a chronological mismatch, this event is also recognized at Lake Ohrid, and represents the most extreme stadial of the record during the MIS 5 interval, with the modern analogue method showing annual temperatures below 5°C and annual precipitation below 200 mm. The last two cold events of the last interglacial complex (Stadial I / C20 and Stadial II / C19) are of similar amplitude than HS8 in the ODP 976 record, but feature more moderate cooling and drying in the Campanet Cave and Lake Ohrid records (Fig. 4.18).

4.5.3. Human occupation in the Iberian Peninsula during the last climatic cycle

4.5.3.1. Preliminary considerations

The MIS 5 interglacial is generally considered a favourable period for Neanderthals, as a higher number of sites are identified in Europe suggesting a demographic extension of Neanderthal population over Europe, with a wider latitudinal expansion compared to MIS 6, the previous very cold glacial stage (Carrión et al., 2026; Hérisson et al., 2016; Shaw et al., 2025; Weiss et al., 2022). However, contrasting views exist, related to the traditional association of Neanderthal with rather cold and open landscapes: Defleur & Desclaux (2019) presented evidence of neanderthal nutritional cannibalism from Baume Moula-Gercy site in southern France (Rhône valley) and related this behaviour with an apparent population collapse during the Eemian (MIS 5e). Their review of Middle Palaeolithic evidences in southern France and Europe presents a very limited number of sites attributed to the Eemian, which would support a drastic decline in Neandertal population as a consequence of global warming and expansion of forested landscapes. As an answer to this interpretation, Slimak & Nicholson (2020) list 75 additional Middle Palaeolithic sites in Europe, most of which have not been successfully radiometrically dated but were potentially attributed to MIS 5 based on stratigraphical interpretation. Defleur et al. (2020) strengthens their initial view by discarding many of these potential Eemian archaeological sites based on insufficient chrono-stratigraphical information. This controversy highlights two inherent problematics when trying to correlate environmental changes and human population dynamics during the last climatic cycle: i) the conflicting interpretations of Neanderthal adaptation to rather cold or rather warm environments, and ii) the difficulty to assign a robust chronology for archaeological sites beyond the radiocarbon limit, including MIS 5 to MIS 3 sites, using alternative radiometric methods like U/Th, luminescence approaches (OSL/TL/IRSL), Electron Spin

Resonnance (ESR), or amino-acid racemization (AAR), which are generally less precise than the radiocarbon method and complicates the correlation with specific climatic events. On the basis of these premises, we propose a review of the chronology of Neanderthal occupation in the Iberian Peninsula from MIS 5 to MIS 3, in light of the environmental changes evidenced in the ODP 976 sequence. In the future, this review is intended to be extended to Western Mediterranean Europe.

A total of 92 archaeological sites bearing Middle Palaeolithic industries in the Iberian Peninsula provide relatively secure absolute dating falling between MIS 5 and MIS 3 (Fig. 4.19, Fig. 4.20, Supplementary Table S5). Among them, 35 can be included into the MIS 5 period, 35 span at least a part of MIS 4, and 70 are contained into MIS 3.

4.5.3.2. MIS 5

Archaeological evidence shows that Middle Palaeolithic sites in the Iberian Peninsula during MIS 5 are mainly located in the Cantabrian region and along the western Mediterranean coast, but with some evidence also in interior Iberia like in the central Meseta (Pinilla del Valle sites), and in Portugal (Fig. 4.19). The typology of sites is very diverse, including a majority of caves but also rock shelters and open-air settlements. It was shown that during MIS 5 the intensification of settlements was related to MIS 5e climatic warming, likely favouring population growth but also technological changes linked with a better optimization of available resources (Álvarez-Alonso, 2014). From a technological point of view, MIS 5 is marked by the generalisation and standardization of Middle Palaeolithic (Mode 3 or Mousterian) lithic assemblages, dominated by the production of Levallois and Discoid-type flakes: these industries are referred to as the end of the Early Middle Palaeolithic (Álvarez-Alonso, 2014; Carmignani et al., 2017; Mathias et al., 2020; Romagnoli, Chabai, et al., 2022). However, some industries including large bifacial tools characteristic of late Lower Palaeoltihic (Mode 2 or Acheulean) persist at sites like Arlanpe layer SQ3, which is poorly dated but likely associated to the beginning of MIS 5 interglacial (Rios-Garaizar, 2017). Outside the Iberian Peninsula, late Acheulean industries are also recorded at the key site of Lazaret (southern France), possibly extended until 119.7+- 2.4 ka BP (Michel et al., 2022). This pattern of mosaic lithic assemblages presenting traditional and innovative traits is characteristic of the Lower to Middle Palaeolithic transition occurring between MIS 9 to MIS6 (Baena et al., 2017; Mathias et al., 2020), with the last industries identified as Acheulean occurring during MIS 5e (Michel et al., 2022; Panera et al., 2011; Rios-Garaizar, 2017). During the following substages of the MIS 5 interglacial, lithic assemblages evolve toward more standardization leading to the “typical Mousterian” facies (Rios-Garaizar, 2017).

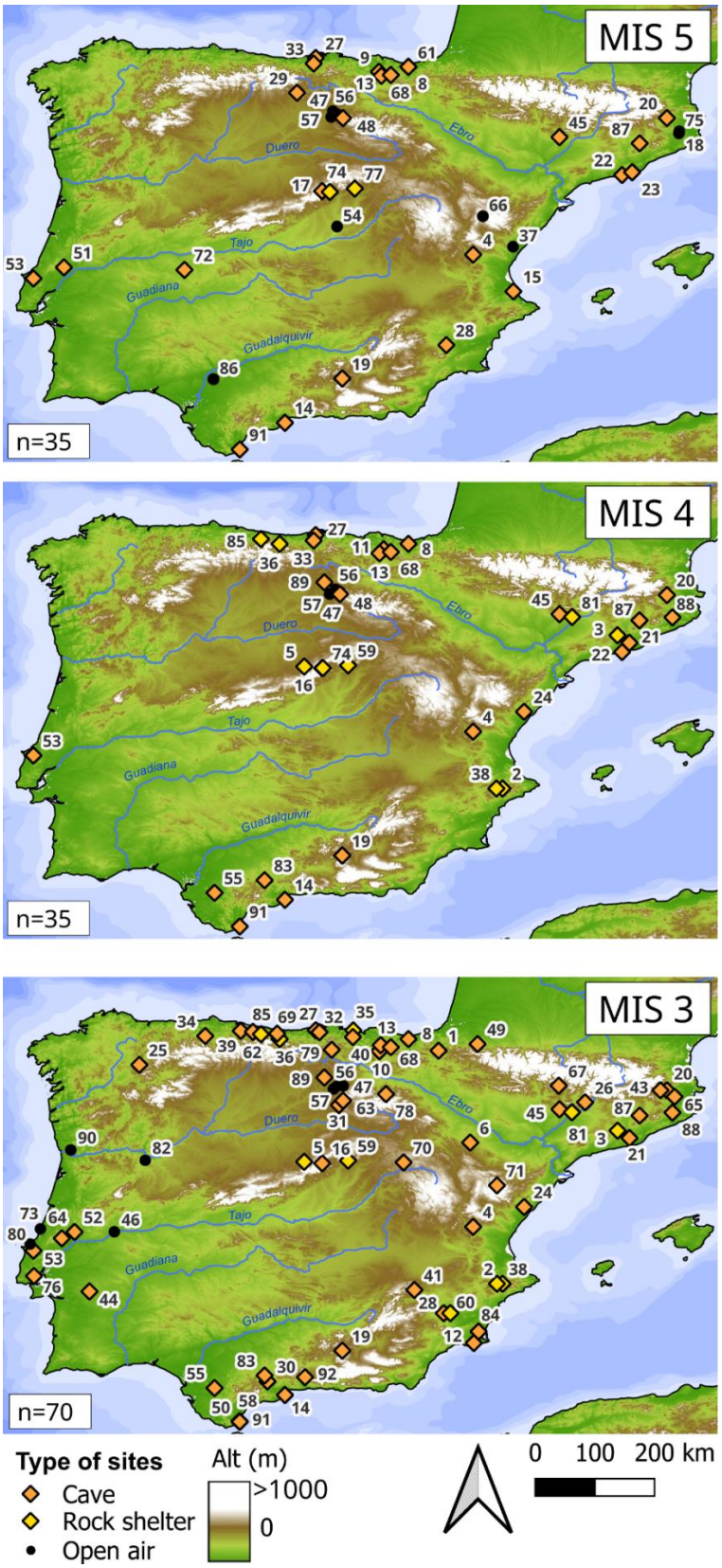


Fig. 4.19. Location of Middle Palaeolithic sites with radiometric dates falling within MIS 5, MIS 4 and MIS 3 in the Iberian Peninsula (including dating error). **1**: Abauntz; **2**: Abric del Pastor; **3**: Abric Romani; **4**: Abrigo de la Quebrada; **5**: Abrigo del Molino; **6**: Aguilon P5; **7**: Amalda I; **8**: Amalda III; **9**: Arlanpe; **10**: Arrillor; **11**: Askondo; **12**: Aviones; **13**: Axlor; **14**: Bajondillo; **15**: Bolomor; **16**: Buena Pinta Cave; **17**: Camino Cave; **18**: Can Garriga; **19**: Carihuela; **20**: Cova 120; **21**: Cova del Coll

Verdaguer; **22**: Cova del Gegant; **23**: Cova del Rinoceront; **24**: Cova del Tossal de la Font; **25**: Cova Eirós; **26:** Cova Gran; **27**: Covalejos; **28**: Cueva Anton; **29**: Cueva Corazón; **30**: Cueva de Ardales; **31**: Cueva Millan; **32:** Cueva Morin; **33**: El Castillo; **34**: El Conde; **35**: El Cuco; **36**: El Esquilleu; **37**: El Pinar; **38**: El Salt; **39**: El Sidrón; **40**: El Miron; **41**: El Niño; **42**: Els Pinyons; **43**: Ermitons; **44**: Escoural; **45**: Estret de Tragó; **46**: Foz do Enxarrique; **47**: Fuente Mudarra; **48**: Galeria de la Estatuas; **49**: Gatzarria; **50**: Gorham; **51**: Gruta da Oliveira; **52**: Gruta do Caldeirão; **53**: Gruta Nova da Columbeira; **54**: HAT; **55**: Higueral la Valleja; **56**: Hotel California; **57**: Hundidero; **58**: Ibex Cave; **59**: Jarama VI; **60**: La Boja; **61**: La Ermita; **62**: La Guelga; **63**: La Mina; **64**: Lapa do Picareiro; **65**: L'Arbreda; **66**: Las Callejuelas; **67**: Las Fuentes de San Cristobal; **68**: Lezetxiki; **69**: Llonin; **70**: Los Casares; **71**: Los Toros; **72**: Maltravieso; **73**: Mira Nascente; 74: Navalmaíllo; **75**: Pedra Dreta; **76**: Pego do Diabo; **77**: Peña Cabra; **78**: Peña Miel; **79**: Prado Vargas; **80**: Praia Rei Cortico; **81**: Roca dels Bous; **82**: Salto do Boi; **83**: Sima de las Palomas de Teba; **84**: Sima de las Palomas del cabezo gordo; **85**: Sopeña; **86**: Tarrazona; **87**: Teixoneres; **88**: Toll Cave; **89**: Valdegoba; **90**: Valongo Quarry; **91**: Vanguard Cave; **92**; Zafarraya

Very large dating range characterize the archaeological sites attributed to MIS 5, leading to a complex assignation of Neanderthal presence to a specific substage or climatic event during the long MIS 5 interglacial (Fig. 4.20).

In Central Iberia, various open-air settlements were identified in the Jarama and Manzanares valleys possibly correlated to MIS 5e and bearing Early Middle Palaeolithic assemblages, like HAT and Estragales (Moreno et al., 2019; Panera et al., 2005, 2011). Precise dating of the fluvial terraces associated to these archaeological evidences is a difficult task, and the current chronological information for these site shows large uncertainty ranges. Similar difficulties are found to precisely date the Middle Palaeolithic assemblages found in the Guadalquivir fluvial terraces like in Tarrazona locality (Caro Gómez et al., 2011).

Bolomor Cave (Valencia province) presents an outstanding record of Early Middle Palaeolithic occupations spanning MIS 8-9 to MIS 5e: the uppermost layer (IV) provided a thermoluminescence date of 121 ± 18 ka BP and evidenced warm and humid climatic conditions locally, supported by the presence of hippopotamus and an important diversity of arboreal pollen taxa identified (Ochando et al., 2019a). This layer is also associated to a more intense occupation of the cave, an increase in typical "Mousterian" lithic tools, but also a notable non-laminar microlithic component (Arsuaga, Fernández Peris, et al., 2012; Fernández-Peris et al., 2020). The presence of microlithic flakes is also evidenced in other sites attributed to MIS 5e like Las Callejuelas, el Estret de Tragó (north-eastern Spain), and southward in the Peninsula in Bajondillo Cave (layer Bj18), likely dated to MIS 5c but lacking direct chronology (López-Sáez et al., 2007; Navarro et al., 2007).

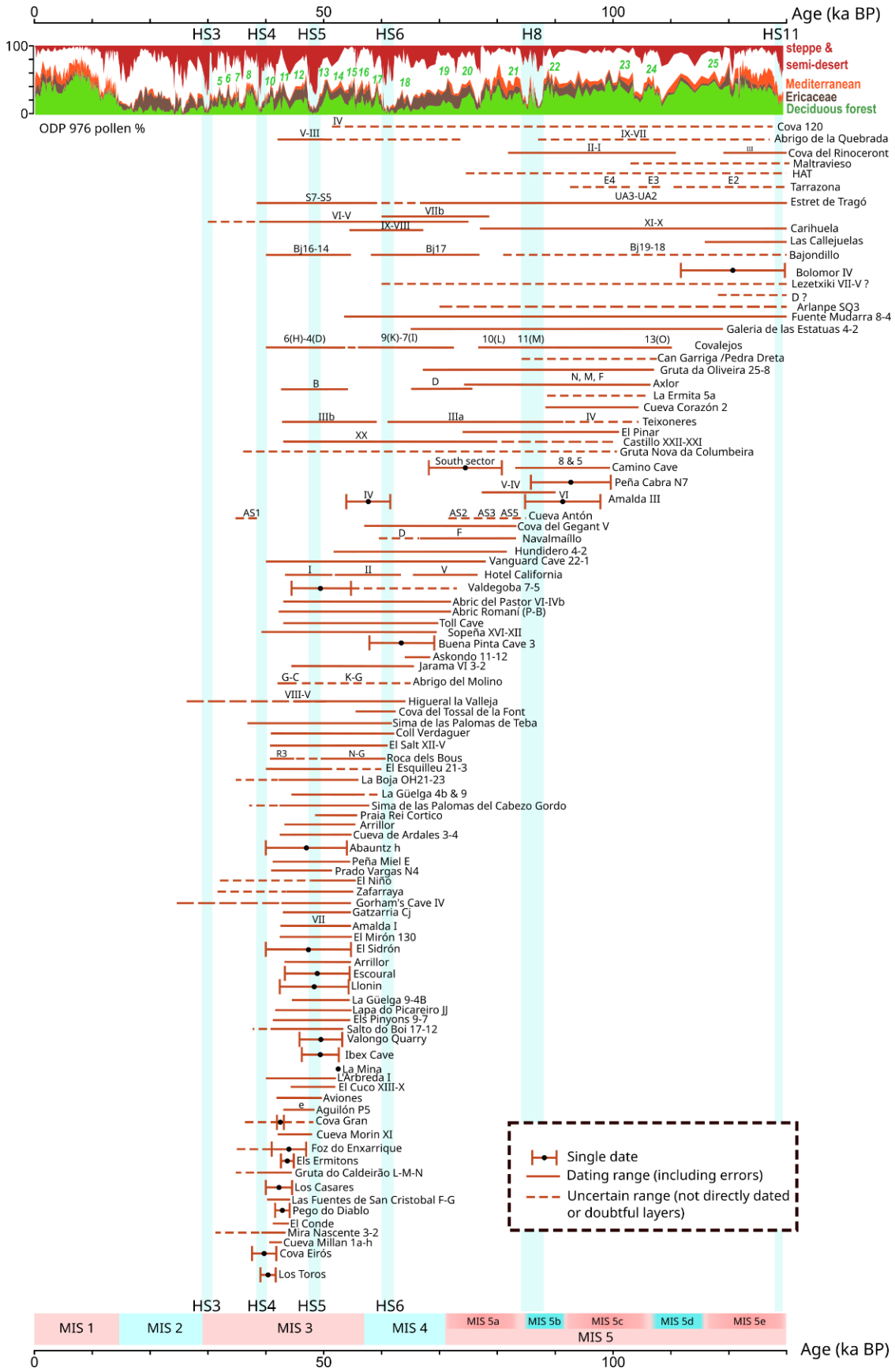


Fig. 4.20. Chronology of the main well-dated Middle Palaeolithic archaeological sites in the Iberian Peninsula during MIS 5-3 (see Supplementary Table S5). Bars represent the radiometric dating range

(including error) at each site, with multiple absolute dating methods (U/Th, OSL, TL, ESR, radiocarbon, AAR). Radiocarbon dates were recalibrated using Intcal20 curve (Charton et al., 2025). The synthetic palynological record of the Alboran Sea ODP site 976 core is placed above, with numbers Greenland Interstadials (GIs) and main Heinrich Stadials (HS) to contextualize the environment of Middle Palaeolithic populations (see text).

Carihuela Cave in southern Spain is also worth mentioning, although presenting a complex chrono-stratigraphical sequence with numerous but unprecise radiometric dates: in addition to the continuous presence of rich Mousterian lithic assemblages, the palynological study of the cave sequence evidenced important vegetation changes that were tentatively correlated to the long sequence from Padul, including several episodes of pronounced dryness at around 95, 70 and 45 ka BP (Carrión et al., 2019b).

Other sites with Middle Palaeolithic industries securely dated to MIS 5e include Cova del Rinoceront layer III in north-eastern Iberian Peninsula (Daura et al., 2015), where warm and humid similar-to-present conditions are supported by the presence of the Mediterranean tortoise, and the open-air site of Fuente Mudarra (Burgos) where archaeologists proposed the hypothesis of a continuity between the middle and upper Pleistocene human occupations in the Sierra de Atapuerca (Santamaría et al., 2021). In the nearby cave site of Galería de las Estatuas, dated by combined ESR and U-series methods to ~110-70 ka BP (Moreno et al., 2022), mitochondrial and nuclear DNA was extracted from sediments and revealed a potential population replacement in northern Spain occurring around 100-115 ka BP, maybe linked with the favourable climatic context during early MIS 5 (Vernot et al., 2021). Covalejos layer 13(O) in Cantabria provided ages compatible with a temperate phase during MIS 5e, and shows a climatic cooling toward the end (Maroto et al., 2021).

Within the MIS 5 interglacial context, multiple sites demonstrate the presence of Neanderthals at high-altitude. In central Iberia, the Navalmaíllo rock shelter (Pinilla del Valle) located at 1114 m of altitude evidence Neanderthal presence through repeated short-term hunting camp on a plateau at high altitude during MIS 5a: the local environment reconstructed through the study of pollen and herpetofauna shows the predominance of open vegetation, but temperate and humid climate around the site, supporting less arid conditions in the moutain compared to the evidences from lowland inland Iberia (Blain et al., 2022). High-altitude occupations during favourable climatic periods was also evidenced during MIS 5e in the well-dated site of Las Callejuelas, which currently represents the highest Middle Palaeolithic site of southwestern Europe at an altitude of 1400 m (Domingo et al., 2017).

Several sites provide evidence of Middle Palaeolithic short-term or longer-term occupations dated to the prolonged MIS 5c interstadial (or GI 22-23), like Camino Cave (Pinilla del Valle) (Arsuaga,

Baquedano, et al., 2012), Cueva Corazón (Diez Martín et al., 2011; Yravedra et al., 2013), Axlor Layer N-M (Demuro et al., 2023) in north-western Spain, and Cova del Rinoceront layers I-II (Daura et al., 2015) in north-eastern Spain. Although not directly dated, Castillo layers XXII and XXI (Martín-Perea et al., 2023), Teixoneres layer layer IV (Zilio et al., 2021) and Bajondillo Layers Bj19-18 (López-Sáez et al., 2007) could possibly be related to MIS 5d-c.

Finally, archaeological layers dated to late MIS 5 substages (5b-5a) at Cueva Antón (AS5) evidenced dry climatic conditions in south-eastern Iberian Peninsula, consistent with the decrease of mesothermophilous taxa in the Carihuela Cave pollen sequence through layers X-VIII (Carrión et al., 2019b). Progressive cooling following late MIS 5 glacial inception is also evidenced in layers 11(M)-10(L) of Covalejos cave in Cantabria (Montes Barquín, 2021). Other sites dated to the final MIS 5 substages include Gruta da Oliveria in Portugal (MIS 5b-5a) (Zilhão, Angelucci, Arnold, Demuro, et al., 2021), the open-air settlement of El Pinar in Valencia Province (Casabo & Gomar, 2002), and Amalda III Cave layers VI-IV which represented an occasional camp site with low concentration of lithics during periods of still humid and temperate conditions. New archaeological sequences covering late MIS 5 will be available in the future, as is the case for Abric Romani site in Catalonia, which potentially extends beyond 70 ka (the current excavated surface) until 110 ka BP (Sharp et al., 2016).

4.5.3.3. MIS 4

MIS 4 is traditionally viewed as a strongly unfavourable period for Middle Palaeolithic populations, with few sites attributed to this stage (Banks et al., 2021; Mallol et al., 2019; Terradillos-Bernal et al., 2017). In the ODP 976 record, the transition from MIS 5 to MIS 4 is not abrupt, as previously evidenced, resulting from the progressive reduction of temperate forest and various abrupt arid episodes already during MIS 5b-a. Therefore, if no clear environmental threshold seems to mark the beginning of MIS 4, a major climatic deterioration (i.e. steppe and semi-desert expansion and low reconstructed precipitation and temperatures) occurs between 62 and 60 ka BP during HS6. The intensity of cooling and drying during this stadial episode had no previous equivalence during MIS 5, and might have represented the main environmental challenge for Middle Palaeolithic population in the Iberian Peninsula. Many archaeological sites with intra-site palaeoecological information provide evidence for climatic deterioration during MIS 4, like Bajondillo cave layer Bj17 in south-eastern Spain (López-Sáez et al., 2007) or in north-western Spain Covalejos layer 9(K) (Montes Barquín, 2021).

However, a surprising aspect of the present review is that a similar number of sites spanning MIS 5 and MIS 4 (35) are identified. This contrast with the synthesis of Mallol et al. (2016), which provided important insights into Neanderthal occupation during MIS 4 from the key site of Abric del Pastor (Alicante province), and identified only 15 other sites with archaeological layers spanning MIS

4 in the Iberian Peninsula. Our updated review identifies additional sites, such as Covalejos layers 9(K) to 7(I) (Maroto et al., 2021), Amalda III (Rios-Garaizar et al., 2024), Askondo layers 11 and 12 (Garcia-Ibaibarriaga et al., 2015), Axlor layer D (Demuro et al., 2023), Cova del Gegant layer V (Daura et al., 2021), Fuente Mudarra (Santamaría et al., 2021), Galería de las Estatuas (Moreno et al., 2022), Sopeña (Pinto-Llona & Grandal-d'Anglade, 2022), Teixoneres layer III (Zilio et al., 2021). Taking into account the radiometric dating uncertainties, other sites potentially span the end of MIS 4 like El Salt layers XII-XI (Leierer et al., 2019), Abrigo del Molino (Álvarez-Alonso et al., 2018), El Esquilleu (Baena et al., 2021), Estret de Tragó (Casanova et al., 2014), Jarama VI (Navazo et al., 2020), and Cova del Coll Verdaguer (Daura et al., 2017), Higueral la Valleja layer VIII (Jennings et al., 2009), Roca dels Bous layer G (Benito-Calvo et al., 2020), Sima de las Palomas de Teba (Kehl et al., 2016). Finally, some sites provide more uncertain dating but potentially cover MIS 4 like Lezetxiki (Arriolabengoa et al., 2018), Valdegoba layer 7 (Quam et al., 2001) and Gruta nove da Columbeira (Carvalho et al., 2018), while a *terminus ante quem* indicating human potential presence during MIS 4 is identified at Cova del Tossal de la Font (Ollé et al., 2014) and Cova 120 (Agusti et al., 1991).

This apparent stability of the number of Middle Palaeolithic occurrences through MIS 5-4 could also be an artefact of the large radiometric dating uncertainties for this chronological period, or the bad preservation of the deposits. Furthermore, this review evidences very few open-air settlements during MIS 4, and an apparent emptiness of interior Iberia (Fig. 4.19). Therefore, even if a similar number of sites during MIS 4 is identified, changes in occupation patterns and spatial distribution of sites indicate some changes in Middle Palaeolithic populations dynamics. Many studies pointed toward a change in the occupation patterns during this cold stage, with important discontinuities in sites stratigraphy, and evidences of shorter-term occupations relying on local resources (Mallol et al., 2019). At Amalda III (Cantabria), the base of layer IV shows very sporadic use of the site at time of unfavourable climatic conditions during MIS 4 (Rios-Garaizar et al., 2024). Still in Cantabria, the MIS 4 layers from Covalejos also evidenced particularly cold conditions, with the presence of the steppe rhinoceros (*stephanorhinus hemitoechus*) (Maroto et al., 2021). At Axlor a turnover was identified in the sequence at the end of MIS 5 (Demuro et al., 2023). However, a recent analysis of technological variability in the MIS 4 layer from Castillo Cave and compared with the Cantabrian record showed that no drastic change could be linked with environmental constraint, and a diversity of technological behaviours allowed Neanderthals to adapt to harsh environments during MIS 4 (González Molina, 2022; González Molina et al., 2024). Strikingly, the Cantabrian region provides one of the richest archaeological records during MIS 4 in our review, supporting its potential of climatic refugia. Similarly, the Southern Iberian Peninsula was described as a region of Neanderthal persistence through glacial conditions: Vanguard Cave for example, located on the southernmost part of the Peninsula in Gibraltar,

evidenced the persistence of warm climatic conditions during MIS 4 and very fast sedimentary infill supporting its nature of climatic refugia (Carrión et al., 2018; Doerschner et al., 2019). In the same site, a specialized burning structure was identified and possibly linked with tar obtention at around 65 ka BP, revealing complex technological adaptation of these southern Iberian Neanderthals during glacial stage (Ochando et al., 2024). Looking on the southwestern area of the Peninsula, the Portuguese record of Middle Palaeolithic occupation during MIS 4 is very limited, partially due to taphonomical and dating issues: the study of coastal deposits in Portuguese Estremadura showed extensive aeolian activity and prolonged severe climate in the region during MIS 4 (Haws, Benedetti, Funk, et al., 2020). Therefore, climatic refugia during MIS 4 cold stage are mainly represented by the Cantabria region and the Mediterranean coast of the Iberian Peninsula, where possibly reduced groups of Neanderthal retreated and adapted to the harsh climatic conditions. Evidence for adaptation to unfavourable environmental conditions during MIS 4 mainly relies on the identification of a particular Middle Palaeolithic lithic techno-complex, the Quina Mousterian (Bourguignon, 1997). Quina *debitage* implies a high degree of versatility and recycling of thick flakes (including core-on-flake reductions), and was identified in a number of sites of southwestern France and the Franco-Cantabrian region mainly from the onset of MIS 4 (Castel et al., 2017; Demuro et al., 2023; Deschamps, 2019). Quina-type Mousterian assemblages were also recently identified in Northern Italy and East Asia, showing potential complex long-distances trajectories and transmission between groups for this technological adaptation, although more evidences are needed to strengthen this hypothesis (Delpiano et al., 2022; Ruan et al., 2025). An approach by eco-cultural niche modelling showed that an ecological threshold occurred for Neanderthal sometime between 80 ka BP (MIS 5a) and 60 ka BP (MIS 4), and that Quina Mousterian technologies likely spread in Western Europe, and specifically in the franco-cantabrian region, as an adaptation to unfavourable environmental conditions (Banks et al., 2021). According to the authors, “Quina system would have allowed human groups to become less tethered to specific lithic raw material sources and employ different mobility and hunting strategies paired with this novel technology.” (Banks et al., 2021). Based on the paleoenvironmental reconstructions of core ODP 976 and other North Atlantic marine sequences (e.g. Fourcade et al., 2024), this unfavourable environmental threshold triggering Middle Palaeolithic technological adaptation during MIS 4 could be represented by the HS6 arid event (~62-60 ka BP).

4.5.3.4. MIS 3 and the late Middle Palaeolithic

Nearly half (44) of the Middle Palaeolithic sites in the Iberian Peninsula identified in this review present chronologies of occupations that are apparently bracketed between ~60 to 40 ka BP, a period bounded by HS6 and HS4 (Fig. 4.20). This profusion of sites following the end of MIS 4 is likely the result of more accurate absolute dating for this time interval and better preservation of the deposits, but

might also indicate particularly favourable conditions for Neanderthals at the beginning of MIS 3, during GI 17-13 (~60-50 ka BP). During this time, the ODP 976 pollen and climate record evidence high percentages of temperate deciduous forest and Mediterranean taxa, and conditions of important annual and seasonal pollen-inferred precipitation, close to the Eemian period. Sites are mainly distributed along the Cantabrian and Western Mediterranean coasts, although several sites show evidence of Neanderthal presence in the central Meseta and in southern Portugal. A diversification of sites is observed compared to MIS 4, with more open-air settlements (Fig. 4.20). The multiplication of sites and diversification of techno-cultural behaviours in western Europe evidence complex patterns for Neanderthal occupations with no clear regional patterns, but high variability (Eixea, 2018; Eixea et al., 2020). Mobility strategies seem to have played an important role in shaping the mosaic of short-term and long-term settlements (Marín et al., 2019; Romagnoli, Chabai, et al., 2022). During the warmer early phase of MIS 3, the archaeological record of the franco-cantabrian region evidences more specialized and regional occupations with particular technological characteristics including Levallois, Quina and Discoid-type debitage associated to abundant cleavers, regrouped under the denomination of "Vasconian facies" (Deschamps, 2017, 2019; Rios-Garaizar et al., 2024). However, several studies questioned the adscription of this technological complex to a specific cultural facies, and related it to an increase in long-distance mobility and cultural exchanges between population (Herrero-Alonso et al., 2025). This higher degree of mobility in some Neanderthal groups could be related to the favourable climatic conditions at the beginning of MIS 3, similar to the pattern previously observed during MIS 5e.

In this mosaic of technological and subsistence behaviours, the intense climatic fluctuations occurring during MIS 3, including the two major cooling events during HS5 and HS4, likely affected Neanderthal territorial management strategies in the Iberian Peninsula and the general diversification of techno-cultural behaviours in western Europe. For example, the cultural succession on the Cantabrian and SW France region was described as closely related to the MIS 4-3 climatic fluctuations, including the potential intensification of Quina technology in response to HS5 (Rios-Garaizar, 2017).

Among the most important archaeological sites covering MIS 3 and the final Middle Palaeolithic, Abric Romani stands out for its long archaeological sequence which also provided a long palynological record of vegetation and climate changes following D-O cycles (Burjachs et al., 2012), and recently extended down to MIS 5d (Biltekin et al., 2019). HS5 is particularly well identified in the sequence between 47 and 49 ka BP, associated to the archaeological layer E (López-García et al., 2014). Although the radiometric dating uncertainties make it difficult to precisely place archaeological layers with respect to the extreme climatic events, other sites identified human occupation during the major environmental change associated to HS5, like Bajondillo Cave layer Bj14 (López-Sáez et al., 2007) or El

Salt layer V, where human occupation apparently stops during or slightly after the arid event (Galván et al., 2014). The same pattern of human occupation interruption during HS5 was identified at Roca dels Bous (Benito-Calvo et al., 2020).

The question of how strong environmental changes occurring during Heinrich Stadials impacted Neanderthal population remains unresolved. There is growing evidence for Neanderthal well-adaptation to forested landscapes (Carrión et al., 2026; Ochando et al., 2019; Stewart et al., 2019). A synthesis of small-vertebrate assemblages from several MIS 3 archaeological sites in north-east Iberia showed that, if Neanderthals were well-adapted to the diversity of their mosaic environments during MIS 3, the Middle Palaeolithic occupations are generally closely related to woodland formations around the site (López-García et al., 2014). The importance of forest ecosystems for Neanderthal subsistence is well-evidence in several archaeological sequences where palynological analyses were undergone, like in north-eastern sites at Teixoneres and Toll caves (Ochando, et al., 2020a, 2020b), and in several sites of the central-eastern coast, a region traditionally considered as a climatic refugia (Real et al., 2022). In the ODP 976 palynological record, forests developed rapidly during MIS 3 following D-O cycles, and especially during GI 17-13, GI 12 and GI8: during these intervals separating HS6, HS5 and HS4, the rapid expansion of deciduous forest vegetation might have favoured population development and expansion outside the refugia areas. On the contrary, it is likely that large parts of the Iberian Peninsula were highly inhospitable for humans during stadials, as also evidenced by modelling approaches through the Human Existence Potential (HEP) which showed particularly reduced HEP in most of the Peninsula during HS4 (Shao et al., 2021). The same study showcased the crucial importance of coastal areas, especially the Mediterranean and Northern Atlantic coasts, in maintaining a potentially sustainable population density. Successively, these refugia population could have been able to recolonize interior Iberia during interstadial stages. However, this potential recolonisation event didn't occur after HS4, as most evidence of Middle Palaeolithic occupation stops during or slightly after this event. Therefore, it is likely that repeated abrupt changes in the environment following MIS 3 D-O cycles and Heinrich Stadials resulted in complex spatial dynamics including abandonments of unfavourable sites (like El Salt during HS5), population contraction around refugia areas mainly represented by the Cantabrian and Mediterranean coasts, and possibly local extinctions (Wolf et al., 2018). This complex population dynamics might have triggered genetic isolation among small Neanderthal groups in refugia area as evidenced by genetic studies (Slimak et al., 2024), or even population turnovers (Dalén et al., 2012; Hajdinjak et al., 2018). These hypotheses regarding population dynamics following GI and GS during MIS 3 have already been largely tested and validated through habitat suitability and species distribution modelling approaches (Albouy et al.,

2024; Banks et al., 2008; Klein et al., 2023; Melchionna, 2018, 2018; Timmermann, 2020; Yaworsky et al., 2024).

Whether the final Middle Palaeolithic occupations are characterized by a progressive decline or an abrupt stop is still debated. Notably, considering the dating error margins, a most Middle Palaeolithic occupations in this review seems to stops before or slightly after the onset of HS4, which appears therefore as a very visual chronological boundary, with few exceptions of sites that were potentially indicated as evidences of late Neanderthal survival (Fig. 4.20). The timing and spatial character of the final Middle Palaeolithic occupations in the Iberian Peninsula is complex and needs high-resolution chronological and regional approaches (Fernández-García et al., 2023; Higham et al., 2014; Marín-Arroyo et al., 2018). An increasing number of studies supported that most occupations in the North and interior of the Iberian Peninsula seem to be very reduced and stop before 43 ka BP (Higham et al., 2014; Kehl et al., 2018; Marín-Arroyo et al., 2018; Pinto-Llona & Grandal-d'Anglade, 2022; Wood et al., 2013). Some even argue that there was a population hiatus between HS5 and HS4 (Weniger et al., 2025). In addition, several sites present a stratigraphical discontinuity correlated with HS4 and separating the last Middle Palaeolithic occupation and the first Upper Palaeolithic evidence (associated to *H. sapiens*), like in Cova Gran (Mora et al., 2018) or Covalejos (Jones et al., 2018; Maroto et al., 2021). However, a late persistence of Neanderthals is still defended in some sites of the Northern Iberian Peninsula like at El Esquilleu (Baena et al., 2017, 2021). In the southern Iberian Peninsula, a later persistence (i.e. after 39 ka BP and possibly until 32 ka BP) is also defended at key sites like Cueva Antón, Carihuela, Gorham's Cave or Gruta da Oliveira (Carrión et al., 2019b; Zilhão, 2021b). Therefore, different patterns seem to characterize the North and the South of the Iberian Peninsula during the end of Middle Palaeolithic (Weniger et al., 2025). In general, a strikingly higher number of sites are identified in northern Iberian (Fig. 4.19), probably also resulting of more intense research developed in the Cantabrian and Catalan regions, and providing more chronological studies compared to southern Iberian regions, and especially Portugal. Despite this potential bias, it could also be that reduced population density characterized the south of the Iberian Peninsula compared to the North during the last climatic cycle, with a concentration of Neanderthal presence in coastal sites in the south. One explanation for this difference could be linked with the regional environment, with the presence of wider arid areas in the south compared to the North, which shows more diverse landscapes and climates. It was shown that Heinrich Stadials could have affected differently the Northern and Southern Iberian regions, with more intense aridity in the south-eastern Iberian Peninsula compared to the north (Charton, 2025; Fourcade et al., 2024; Sepulchre et al., 2007). Therefore, these repeated abrupt extreme events during MIS 5-3, with increasing intensity from MIS 4 and during MIS 3, could

have limited population growth in the South and favoured population isolation and persistence in climatic refugia during stadials.

4.6. Conclusions

The continuous and high-resolution record of pollen, climate and clay mineralogical composition from ODP site 976 core allows a unique overview into the character of millennial-scale oscillations in the southwestern Mediterranean region during the complete last climatic cycle (MIS 5-2). The evolution of climate and vegetation in the Alboran Sea region responded to a combination of forcing, among which cold events in the North Atlantic and African subtropical humidity played a major role. During interstadials, temperate and Mediterranean vegetation increased, and pollen-inferred climatic reconstructions show a regional warming and moistening. During stadials, temperate and Mediterranean vegetation decreased significantly, and steppe and semi-desert vegetation expanded in the Iberian Peninsula and Northern Africa, while the pollen-inferred climate reconstructions show cold and dry conditions. Major inputs of African dust (palygorskite) are recorded during stadials, and especially at the end of MIS 5 and during MIS 4, showing the influence of African aridity at the onset of glaciation in the south-western Mediterranean region. Heinrich Stadials represented the most extreme expressions of these cold events, with HS11 and HS6 to HS1 being the most extreme over the last 130 ka BP. The high-resolution data from ODP 976 allowed to described internal dynamics during the different HSs, with similarities in the vegetation successions but differences in the duration, intensity and phasing of the different HSs. Additional cooling events are identified in the ODP 976 record of MIS 5 and MIS 4, linked with less-well known Heinrich events (H10-H7 and H5a), and to North Atlantic cold events C27b-C19. These results showcase the pervasive sensitivity of southwestern Mediterranean environments to millennial-scale oscillations during MIS 5 and MIS 4. However, abrupt cooling occurring during MIS 5 were generally less extreme than those recorded later during MIS 4 and MIS 3.

The review of Middle Palaeolithic occupations in the Iberian Peninsula through the last Climatic cycle supported an intensification of human presence in the Iberian Peninsula during MIS 5 interglacial, with progressive standardization of Middle Palaeolithic lithic assemblages where Levallois debitage is dominant. Population replacement during early MIS 5 and likely favoured by warm climatic conditions is suggested by genetic data from the Sierra de Atapuerca. This review evidenced the diversification and specialisation of archaeological tool kits, including both long-term and short-term occupations in caves and open-air settlements, high-altitude occupations, and micro-lithic flakes production. Although uncertainties in dating methods complicates the attribution of archaeological layers to specific climatic phase during MIS 5, some sites have been tentatively attributed to the warmest

phases during MIS 5e and MIS 5c, with episodes of cooling and reduced human presence documented at some sites. Therefore, our study supports that MIS 5 and particularly MIS 5e was a favourable period for Neanderthal populations in the Iberian Peninsula. It also shows that, although less intense and difficult to identify in the archaeological record, climatic fluctuations during MIS 5 likely influenced the pattern of occupations of Middle Palaeolithic groups.

If a similar number of sites is recorded during MIS 4 in this review, a clear change in technological and subsistence behaviours can be identified, likely following the glacial inception and particularly HS6 arid event. The expansion of Quina lithic technocomplexes in southwestern France, north-western Spain, and likely in more remote areas, might have represented a technological adaptation to the first intense cooling occurring during MIS 4, and specifically during HS6.

MIS 3 showcases the highest number of well-dated Middle Palaeolithic sites. More precise chronological information is needed to assess the precise dynamics of potential population contraction and expansion during MIS 4-3 stadials and interstadials, and more specifically during HS6 and the following HS5 and HS4. However, our review of sites supports the following observations. The Mediterranean and Cantabrian coasts provide evidence of continuous Neanderthal presence through the last climatic cycle, supporting their nature as climatic refugia. The highest concentration of sites, not only during MIS 3 but also during MIS 5 and 4, is found north of the Ebro River, in north-eastern Spain and the Cantabrian Coast, possibly indicating different population trajectories linked with different environmental variability between the North and the South of the Peninsula. Millennial-scale climatic oscillations likely shaped Neanderthal population dynamics pattern in the Iberian Peninsula since MIS 5, and particularly during MIS 4-3 when rapid D-O cycles and HS 6-4 implied fast changes in the regional landscape composition and climate. Rapid environmental dynamics is likely to have favoured the progressive diversification of Neanderthal techno-cultural behaviours during MIS 4-3, requiring versatility in resources and land management. Finally, if the spatio-temporal scenario for the final Middle Palaeolithic in the Iberian Peninsula is still very debated, HS5 and HS4 are likely to have triggered the abandonment of some sites located in unfavourable areas, but also population contraction and even local extinctions prior to the arrival of *H. sapiens* and the definitive disappearance of *H. neanderthalensis*.

5. Decoding Termination II and the onset of the last Interglacial in the Western Mediterranean

Charton Liz[1,2], Bertini Adele[2], Combourieu-Nebout Nathalie[1], Bout-Roumazeilles Viviane[3], Peyron Odile[4], Lebreton Vincent[1]

**corresponding author: Liz Charton (liz.charton@mnhn.fr)*

Affiliations:

1: UMR 7194, Histoire Naturelle de l´Homme Préhistorique, CNRS-MNHN, Institut de Paléontologie Humaine, Paris, France

2: Dipartimento di Scienze della Terra, Universita di Firenze, Italy

3: UMR 8187 LOG – Laboratoire d'Océanologie et de Géosciences, CNRS, Université de Lille, Univ. Littoral Côte d'Opale, IRD, Lille, France.

4 : Institut des Sciences de l'Evolution de Montpellier, UMR CNRS 5554 ISEM, Université de Montpellier, France

Ce chapitre correspond à un article « en préparation », et propose une focalisation sur la Terminaison II (~136-129 ka BP). Encore peu d'archives paléoclimatiques et palynologiques en Europe permettent d'évaluer la séquence d'évènements climatiques rapides au moment de l'avant-dernière déglaciation. Cette transition présente pourtant un grand intérêt stratigraphique. Un groupe de travail international de la SQS (*Subcommission on Quaternary Stratigraphy*) vient d'être mis en place dans le cadre de l'IUGS- ICS (*International Union of Geological Sciences - International Commission on Stratigraphy*) pour la définition d'un futur GSSP pour le Pléistocène supérieur (https://quaternary.stratigraphy.org/WG-Upper-Pleistocene). Dans cette optique, l'étude d'enregistrements paléoclimatiques à haute résolution et avec une chronologie robuste apparaît cruciale afin d'évaluer les successions d'évènements stratigraphiques à échelle globale.

Notre étude sur ODP 976 permet d'apporter de nouvelles données sur la végétation, le climat régional et la circulation atmosphérique en Méditerranée (à partir du pollen et des argiles) durant cette période clé, en plus des données paléo-océanographiques déjà publiées. Par ailleurs, la disponibilité de ces différents proxys continentaux et marins pour les Terminaisons I et II dans un même enregistrement permettent de tester les hypothèses sur les similarités et les différences dans les processus climatiques impliqués entre ces deux terminaisons. Les résultats préliminaires de cette étude ont été présentés au séminaire de la *Section on European Quaternary Stratigraphy* à Vienne (Autriche) en septembre 2025.

5.1. Introduction

Glacial terminations correspond to the transitional phases from a full glacial to a full interglacial state, lasting about 10 ka and during which major changes in the ice-sheet extent and global climate occur (Bajo et al., 2020; Barker & Knorr, 2021; Cheng et al., 2009). The study of past glacial terminations is of particular relevance for understanding the responses and feedbacks of the climate system to the release of large quantities of melted polar ice into the ocean, which is nowadays a result of anthropogenic climate change (Hansen et al., 2016; Li et al., 2024; Stoll et al., 2022).

Past glacial terminations were paced and shaped by cycles forced by obliquity and precession, and their timing and duration, based on marine and terrestrial records, are well constrained through the absolute dating of long speleothems (Bajo et al., 2020; Cheng et al., 2009, 2016; Kaushal et al., 2025). As periods of deep changes shaped by the interactions between the ice-cap, the atmosphere, and the ocean, terminations experienced important millennial-scale events and oscillations recorded by multiple marine and continental archives, and particularly speleothems which allow for ultra-high resolution reconstructions (e.g. Cheng et al., 2006, 2009, 2016; Drysdale et al., 2009; Moseley et al., 2015; Pawlak et al., 2021; Stoll et al., 2022; Tzedakis et al., 2018).

Termination I (T1, ~18-7 ka BP), marking the transition between the last glacial period (MIS 4-2) and the present interglacial (MIS 1), is the best-known termination and was interrupted by two millennial-scale events of intense freshwater release into the North Atlantic, AMOC shutdown and glacial conditions in Europe (Heinrich Stadial I, hereafter HS1, and the Younger Dryas) (e.g. Barker et al., 2009; Barker & Knorr, 2021; Combourieu-Nebout et al., 2002; Martrat et al., 2004). The succession of events pacing Termination II (TII, ~ 136-129 ka BP) is less well known, especially due to the absence of Greenland ice-core record spanning this interval (Chappellaz et al., 1997). High-resolution and chronologically well-resolved paleoclimatic archives for this termination are scarce (some of them are represented in Fig. 5.1 and discussed in this study). Marine sediments in the North Atlantic evidenced the presence of a major ice-rafting event, named HS11 (Heinrich, 1988; Hemming, 2004; McManus et al., 1999; Oppo et al., 2001; Rasmussen et al., 2003), whose estimated duration, between 136 and 130 ka BP, matches the timing of TII (Marino et al., 2015) and is associated to a major freshening of North Atlantic and Mediterranean sea waters, AMOC disruption, and decrease of precipitation and temperature on land (Deaney et al., 2017; Stoll et al., 2022; Tzedakis et al., 2018) . Its structure is very complex and displays a different phasing in various paleoclimatic records: it was described as a "double-u" pattern in the Alboran Sea records (Jiménez-Amat & Zahn, 2015; Martrat et al., 2014), but recent high resolution studies from the Iberian margin showed it actually corresponds to three cold

"pulses" connected with northern hemisphere icesheet releases into the North Atlantic (Tzedakis et al., 2018; Stoll et al., 2022).

The similarities and differences between Terminations I and II have been addressed by various studies, which pointed out broadly similar processes with a different pacing and timing of events (e.g. Lisiecki & Stern, 2016; Skinner & Shackleton, 2006). Moreover, major differences have been identified between both terminations with regard to the relationship between North Atlantic climate and global sea-level change, probably connected with different insolation forcing (Marino et al., 2015), and different ice-sheet configuration (Stoll et al., 2022).

From a stratigraphical point of view, the timing of Termination II corresponds to the transition from the Middle to the Upper Pleistocene, which still lacks a proper Global Boundary Stratotype Section and Point (GSSP) (Head, 2019). A main issue consists in the difficult land-sea correlation at time of deep reorganization of the climate system and enhanced millennial-scale variability, expressed by an important time lag between the onset of the interglacial in marine stratigraphy (MIS 5e), and terrestrial stratigraphy (the Eemian) (Shackleton et al., 2003; Skinner & Shackleton, 2006; Tzedakis et al., 2018).

The long paleoclimatic record of ODP 976, spanning continuously the past 200 ka BP with the study of multiple continental and marine proxies, allows to describe the sequence of events characterizing Termination II in the Western Mediterranean region, and to compare it with Termination I within the same record.

This paper aims to contribute to the study of TII in the Mediterranean by i) presenting the multiproxy record of ODP 976 for Termination II, including the already published marine proxies, and new terrestrial data (pollen and clay mineralogical composition), ii) comparing the results of pollen-inferred climate reconstructions with the various speleothem records available for TII, iii) comparing the character of the last two Terminations in the multiproxy record of ODP 976, and iv) discussing the relevance of these results for the debate on a GSSP for the Upper Pleistocene.

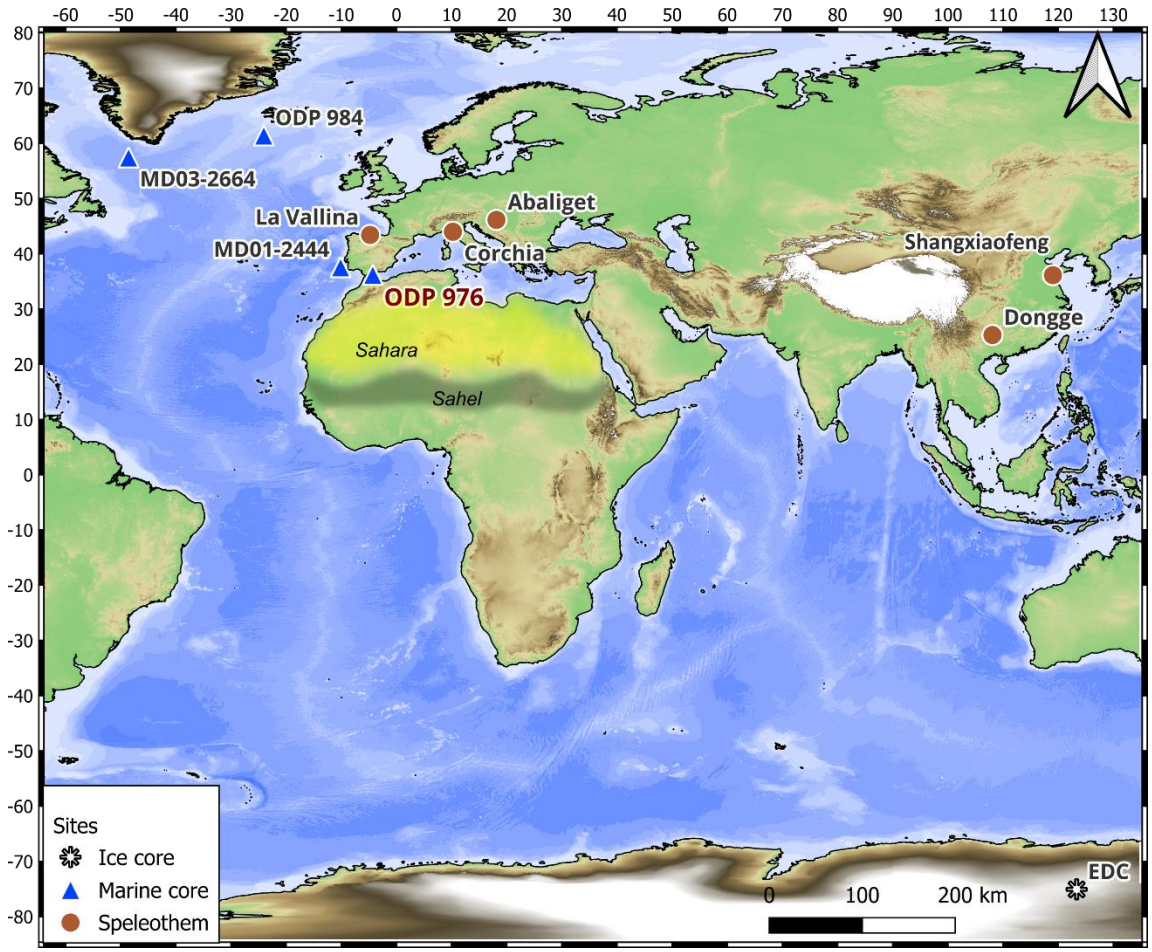


Fig. 5.1. Geographical location of ODP site 976, together with the main paleoclimatic archives covering Termination II and discussed in the text.

5.2. The multiproxy record for Termination II from ODP 976

Previously published high-resolution marine proxies from ODP 976 and covering TII included planktonic oxygen isotope, alkenone and Mg/Ca derived sea surface temperatures (SSTs) (Jiménez-Amat & Zahn, 2015; Martrat et al., 2014). These records evidenced the close response of southwestern Mediterranean surface waters to North-Atlantic freshwater pulse during HS11, with regional specifies represented by a "w shape" for the pattern of temperature decrease during this event, an Organic Rich Layer deposition (ORL606) (Murat, 1999), and an amplification of the negative temperature anomaly in the Mediterranean (Jiménez-Amat & Zahn, 2015; Martrat et al., 2014). The new terrestrial proxies from this study, including pollen counting, multimethod pollen-inferred climate reconstructions, and clay mineralogical composition, provide additional information on vegetation, climate, and atmospheric circulation changes during TII (Fig. 5.2).

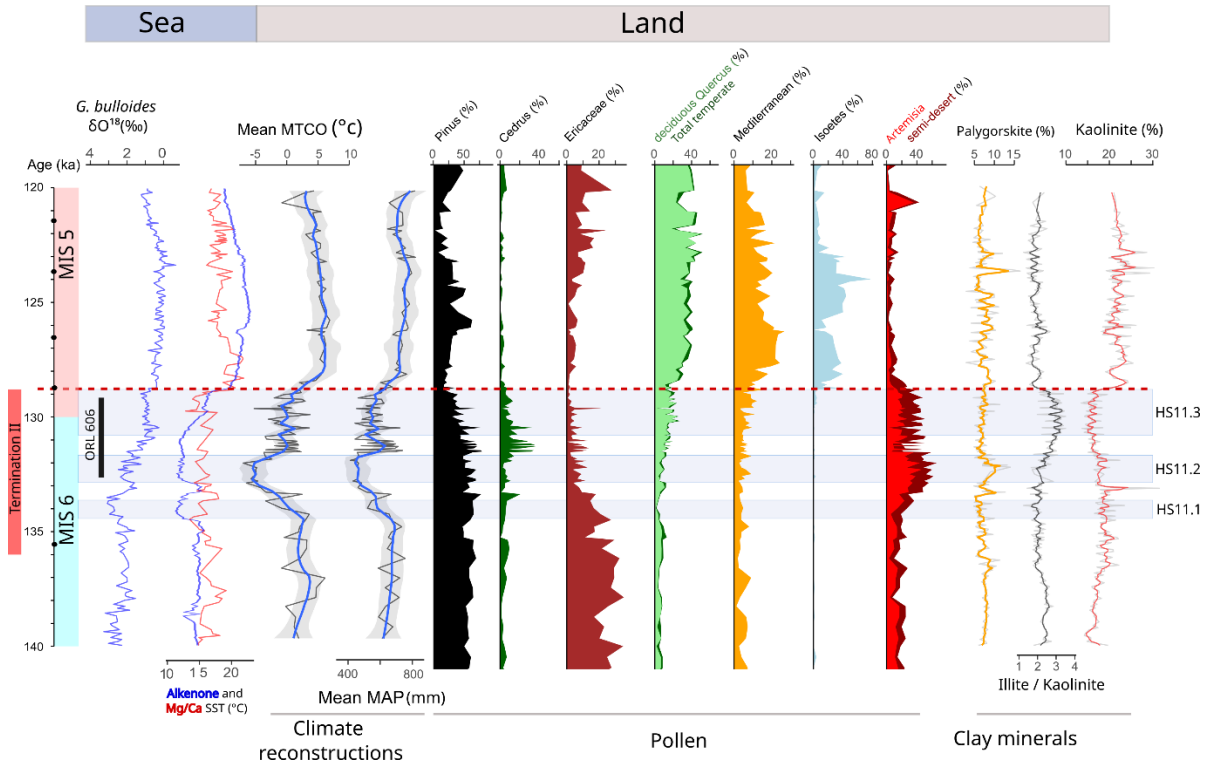


Fig. 5.2. Multiproxy record of ODP 976 between 120 and 140 ka BP. From left to right: ORL (Organic-Rich Layer) 606 interval, planktonic foraminifera isotopic ratio and Mg/Ca-based SST (Jiménez-Amat & Zahn, 2015), alkenone-based SST (Martrat et al., 2014), pollen-based reconstruction of Mean Temperature of the Coldest Month (MTCO) and Mean Annual Precipitation(MAP) based on the mean of four methods (MAT, WAPLS, BRT, RF) (this study), main pollen taxa and ecological groups percentages (this study), and main clay mineralogical percentages (this study). The timing of Termination II follow Bajo et al. (2020). The blue horizontal bars represent the three "cold" pulses of HS11 identified through the multiproxy record of ODP 976 and supported by previous studies (Stoll et al., 2022; Tzedakis et al., 2018). The red dotted line shows a major change recorded in all the different proxies from ODP 976 at the end of TII around 128.7 ka BP.

5.2.1. Pollen-inferred vegetation and climate

Pollen data and pollen-inferred climatic reconstructions depict important changes in the vegetation composition and regional climate between 140 and 120 ka BP (Fig.5.2).

The end of the penultimate glacial until ~133.5 ka BP (MIS 6) is dominated by *Pinus* and Ericaceae. Climate reconstructions indicate rather cool and humid climate, with annual precipitation above 600 mm/yr. The spread of heathland vegetation in the Iberian Peninsula during the final stages of MIS 6 probably indicates the renewed influence of Atlantic moisture through westerlies, marking the beginning of the transition toward interglacial conditions. Between ~133.5 and 128.5 ka BP, strong changes are recorded in the pollen assemblage and climate reconstructions, with a long and intense event of steppe vegetation expansion and cold-arid climate, divided in different phases. First, Ericaceae percentages decrease abruptly, while steppe and semi-desert vegetation spreads rapidly. *Artemisia*

and other steppe and semi-desert taxa remain dominant in the pollen assemblage until ~128.7 ka BP, with a mid-term phase of steppe decrease and montane elements spread, especially *Cedrus*, at 131.5-131 ka BP. Climate reconstructions show particularly cold and dry conditions during the first *Artemisia* expansion phase, between 133.5 and 131.5 ka BP. Temperatures, and especially precipitation, increase abruptly during the short event at 131.1 ka BP. In the final phase of the arid event, climate parameters depict generally cold and dry conditions, with important variations. This large multiphase event of steppe and semi-desert expansion and climatic aridity, lasting ~5 000 years, shows the impact of the North Atlantic HS11 event on southwestern Mediterranean continental environments.

The particularity of this event in the palynological and pollen-inferred climate record of ODP 976 resides in i) three phases in the pollen assemblage together with "w shape" of climate reconstructions, and ii) the continuous increase of temperate arboreal vegetation, particularly deciduous *Quercus*, together with the continuous decrease of *Pinus* during the event. The three phases include the two phases of steppe and semi-desert expansion described above, interrupted by an event of montane vegetation peak. Pollen-inferred climate parameters depict a particular "w shape" with two phases of cold and arid climate, interrupted by a short event of warming and moistening. The remarkable pattern of fast semi-desert and steppe expansion occurring in parallel with a slow but continuous increase of temperate tree taxa and decrease of *Pinus* can be interpreted as the result of superimposed global and regional climatic forcing. While the change in forest cover and composition responds to global warming and moistening during TII, steppe and semi-desert taxa respond to regional cooling linked with major freshwater release in the North Atlantic during HS11. Supporting this hypothesis, the cold-arid phases in the pollen assemblage match cold SSTs, while the continuous increase of temperate forest closely follows the trend of the oxygen isotopic ratio (Fig. 5.2).

By ~128.7 ka BP, a clear change is observed in the pollen assemblage: semi-desert and steppe vegetation collapse together with coniferous taxa (*Pinus* and *Cedrus*), while the temperate deciduous and Mediterranean forests expand very fast. Furthermore, a very fast increase of *Isoetes* spores' abundance is noticed at the same time, showing enhanced moisture availability. Pollen-inferred temperatures and precipitations also increase very fast, reaching the MIS 5e interglacial values around 128 ka. This timing for the establishment of full interglacial conditions on the continent in the Alboran Sea region exceeds by ~1 ka the end of TII, estimated at 129 ka BP based on marine and Asian monsoon records (Bajo et al., 2020). This delay likely reflects the response time of vegetation to abruptly warmer and wetter conditions, triggering the more progressive development of temperate and Mediterranean forest cover.

5.2.2. Paleo-dust record and atmospheric configuration

The evolution of clay mineralogical composition provides information on the origin of clay particles in the Alboran Sea, allowing to infer past atmospheric configuration (e.g. Bout-Roumazeilles et al., 2007; Moal-Darrigade et al., 2022). Previous clay analyses show that illite and smectite are the most abundant clay minerals in general in the ODP 976 record and are transported through a mix of water currents and aeolian input, while kaolinite and palygorskite displays generally lower abundance but are very informative to trace the origin of African winds (Bout-Roumazeilles et al., 2007). Palygorskite production originates in sub-arid environments of North Africa and requires specific conditions of seasonal aridity and strong evaporation in carbonate rocks (Elmouden et al., 2005). It is transported exclusively by wind, and has been used to trace the African origin of dust in the past, especially during North-Atlantic cold events (Bout-Roumazeilles et al., 2007). Kaolinite is typical of highly-weathered soils in equatorial regions from Africa, with a strong latitudinal (Sahara versus Sahel) and longitudinal gradient (Bout-Roumazeilles et al., 2007; Guerzoni et al., 1997). The illite/kalonite (I/K) ratio in African soils usually decreases from west to east, and from north to south (Bout-Roumazeilles et al., 2013 and references therein). Due to this spatial pattern, I/K has shown to represent a good tracer for the position of the Inter Tropical Convergence Zone (ITCZ) latitudinal following seasonal migration or large scale climatic variability (Bout-Roumazeilles et al., 2013; Skonieczny et al., 2013). When the ITCZ has a northern position, African dust rich in kaolinite is transported from the Sahel to the Alboran Sea through high-altitude winds (Saharan and North Saharan Air Layers) (Fig. 5.1), and the resulting I/K ratio in the southwestern Mediterranean is low. When the ITCZ migrates south, dust particles mainly originate from the Sahara through middle and low altitude winds, resulting in a higher I/K ratio in the southwestern Mediterranean (Bout-Roumazeilles et al., 2013; Skonieczny et al., 2013).

In the ODP 976 dust record, the end of MIS 6 is marked by an increasing trend in kaolinite input, and decreasing I/K indicating progressively enhanced dust transport from the Sahel. At 133.2 ka BP, a peak in kaolinite is synchronous with higher alkenone-SSTs and lower planktonic δ18O in the Alboran Sea, compatible with a sudden northern migration of the ITCZ. Shortly after, a peak in palygorskite mineral abundance is visible between 133 and 132 ka BP, contemporaneous with the first semi-desert expansion in the pollen assemblage and indicating arid regional climatic conditions at that time during HS11. From 132 ka BP onward, the I/K ratio increases as kaolinite input decreases. This trend of increasing I/K ratio is synchronous with the second phase of semi-desert taxa expansion visible in the pollen assemblage, and may reflect enhanced dust input from the Sahara, as the ITCZ reaches its southernmost position during the second half of HS11. Right after 129 ka BP, I/K decreases abruptly, and a large peak of kaolinite is visible in the record. This pattern expresses enhanced dust input from

the Sahel, and can indicate the northern migration of the ITCZ at the end of the arid event, and the onset of the MIS 5 interglacial. Therefore, the paleo-dust record from ODP 976 supports that internal dynamics during Heinrich Stadials are closely linked with latitudinal movements of the tropical belt, as already pointed out for other HSs (Guillevic et al., 2014; Rhodes et al., 2015; Wang et al., 2001).

5.2.3. Multiproxy land-sea correlation

Combined results from pollen, clay, isotopes and SSTs from ODP 976 provide valuable insights into the environmental response to Termination II in the sea and on the continent in the southwestern Mediterranean region (Fig. 5.2).

A climatic trend toward warmer and more humid conditions at the end of MIS 6 is evidenced by high Ericaceae pollen percentages and pollen-inferred temperatures and precipitations, a decreasing trend in planktonic isotopic ratio, an increasing trend in alkenone and Mg/Ca SSTs, and decreasing I/K (reflecting enhanced dust input from the Sahel).

A first drop in Mg/Ca SSTs at ~135 ka BP, and in Alkenone SST at 134.5 ka BP, is mirrored in the planktonic isotopic curve, and synchronous with a slight decrease in temperate deciduous forest and pollen-inferred temperature (Fig. 5.2). This first phase of freshening in the Alboran Sea and reduction of the temperate forest cover can be identified as the first phase of HS11, lasting about 1000-1500 years, until ~133.5 ka BP. However, no major expansion of steppe and semi-desert pollen is recorded, and only a moderate decrease of continental temperature and precipitation is recorded through pollen-inferred reconstruction during this HS11.1 phase. This might indicate that the first freshwater pulse during HS11 had only a limited impact on regional vegetation and climate.

The second cold-arid phase, on the contrary, is well evidenced in both marine and terrestrial proxies, starting ~132.9 and ending ~131.7 ka BP (Fig. 5.2). Minimum temperature and precipitation are reconstructed during this phase from pollen assemblages. It is also marked by the start of an "Organic-Rich Layer" (ORL 606) deposition in the Alboran Sea (Murat, 1999). ORLs in the western Mediterranean are a particular feature of deglaciations, like Sapropels, resulting from the major release of freshwater into the Mediterranean sea from multiple origins (river discharges, ice-melting, enhanced rainfall and Atlantic moisture…) and the consecutive development of deep-water anoxia (Rohling et al., 2015; Sierro et al., 2025). Therefore, the ORL start during the second cold-arid pulse of HS11 likely indicates enhanced entrance of freshwater from the North-Atlantic resulting from ice-sheet collapse and ice-rafting. Palygorskite displays higher percentages in the clay mineralogical composition of ODP 976 during this phase, supporting arid conditions regionally linked with a southern migration of the polar front and the ITCZ. The end of HS11.2 in the ODP 976 record is marked by a semi-desert vegetation retreat and a *Cedrus* increase in the pollen record, and the pollen-inferred reconstructions

indicate a relative rise in temperature and more intense increase in precipitation. *Cedrus* expansion was likely triggered by enhanced winter rainfall at that time, as supported by climate reconstructions.

A third cold pulse is recorded in the ODP 976 multiproxy record, between ~131-129 ka BP, and associated to HS11.3, with a new expansion of steppe and semi-desert pollen taxa, the decrease of precipitation and temperature reconstructed through pollen, and increasing I/K ratio pointing toward the southernmost migration of the tropical belt (Fig. 5.2).

A remarkable feature in the multiproxy record from ODP 976 is the offset of the "double-u" pattern of HS11 in the terrestrial and marine proxies (Fig. 5.2). The increase in SSTs at 133-133.5 ka BP is not clearly mirrored in the pollen-inferred climate reconstructions, and is not marked by a significant increase in tree pollen percentages. Likewise, the increase in atmospheric temperature and precipitation in the pollen-inferred reconstructions occurring at 131.5-131 ka BP finds no counterpart in the SSTs record. This pattern points toward a decoupling between SST and vegetation changes during the two climatic "warm rebounds" of HS11 in south western Mediterranean. The first warming is visible mainly in the marine SSTs record, and did not affect significantly the vegetation composition. On the contrary, the second indicates an increase in atmospheric moisture and atmospheric temperature, but was not marked by increased SSTs in the Alboran Sea. However, on the Atlantic side of the Iberian Margin, the two warm rebounds seem to be present in the marine records (Tzedakis et al., 2018) (see Fig. 5.3). One hypothesis for this pattern is that the temperature increase in the Alboran Sea during this event was limited, as supported by the regional expansion of montane elements (*Cedrus* particularly).

Another remarkable feature of the ODP 976 record is that, through all the HS11 phases, temperate deciduous and Mediterranean vegetation increase slowly but continuously, responding to progressive global warming of the deglaciation process. This pattern for HS11 contrasts with other Heinrich Stadials in Europe occurring later during MIS 4-3 (see Section 4) and evidenced through long palynological records, where the spread of steppe and semi-desert vegetation is associated with a "dip" in temperate vegetation and forest cover (Charton et al., 2025; Fletcher & Sánchez Goñi, 2008). This shows a clear difference in the pattern of HSs occurring during terminations, and HSs occurring during MIS 4-3.

At the end of HS11.3, a clear change in all the marine and terrestrial proxies indicates a deep reorganization of the ocean-atmosphere system (red dotted line in Fig. 5.2). Shortly after 129 ka, SSTs rise abruptly, while steppe and semi-desert vegetation retreat and temperate forest and Mediterranean taxa increase. Climate reconstructions show a rapid moistening and warming, with maximum temperatures and precipitation reached by 128 ka. This timing for the Eemian optimum is

fully compatible with the one from other reference and independently-dated records for TII, like Corchia speleothem and MD01-2444 marine core (Tzedakis et al., 2018).

5.3. Comparison with speleothem records and ocean-atmosphere dynamics

Speleothems are among the most valuable archives to study past glacial terminations, allowing absolute dating which can serve as reference for global calibration of marine archives (e.g. Cai et al., 2023; Cheng et al., 2006, 2009; Kaushal et al., 2024, 2025; Moseley et al., 2015; Pawlak et al., 2021; Stoll et al., 2022; Xue et al., 2019). However, although they provide ultra-high resolution proxy records, the interpretation of their climatic signal is not global and depends on regional climate influences (Kaushal et al., 2025).

ODP 976 multiproxy temperature and precipitation record was calibrated with Dongge Cave and Corchia Cave speleothem oxygen records, assuming a close connection between western Mediterranean SSTs, the intensity of rainfall in central Mediterranean, and the intensity of Asian Monsoon (Jiménez-Amat & Zahn, 2015). Based on this age model, the first warming rebound between HS11.1 and HS11.2, clearly evidenced in the SSTs record from ODP 976, is correlated to a short episode of Asian Monsoon intensification in the Dongge and Hulu Caves record (Cheng et al., 2006; Kelly et al., 2006) (Fig. 5.3). The kaolinite rise at the same time in the clay mineralogical record of ODP 976 (Fig. 5.2) supports a northern migration of the tropical belt inducing major dust transport from the African subtropical region of the Sahel to the western Mediterranean, and fully compatible with enhanced monsoonal activity in East Asia. The same process can be identified at the onset of the Eemian interglacial, characterized by abrupt increase in Asian Monsoon activity, higher precipitation and temperature in southwestern Mediterranean, and higher kaolinite-rich aeolian dust input in the Alboran Sea. Connection between North Atlantic events, southwestern Mediterranean climate, and Asian Monsoon variability, is further supported by the speleothem record from Shangxiaofeng cave (Xue et al., 2019) : the oxygen isotope record evidenced three weak monsoon events during TII coeval with the HS11 three-phases complex, with the second phase being the most intense.

North Iberian Speleothem Archive (NISA) from La Vallina Caves provides precious insight into North Atlantic freshening and warming events punctuating TII (Stoll et al., 2022). Most notably, HS11.2, the most arid and cold phase in the ODP 976 multiproxy record based on pollen and clay data, is associated with the most intense phase of freshwater release into the North Atlantic evidenced in the NISA oxygen isotope record (Fig. 5.3). The first warming event ~134 ka BP occurring between HS11.1 and HS11.2, can be linked with a reduction of freshwater, and subsequent short episode of AMOC recovery, evidenced in the NISA oxygen isotope record (Fig. 5.3). The second warming event occurring

during HS11 in the ODP 976 record around 131 ka BP is correlated to warmer conditions in the NISA carbon isotope record (Fig. 5.3), and could possibly be linked with a short reduction of freshwater input into the North Atlantic.

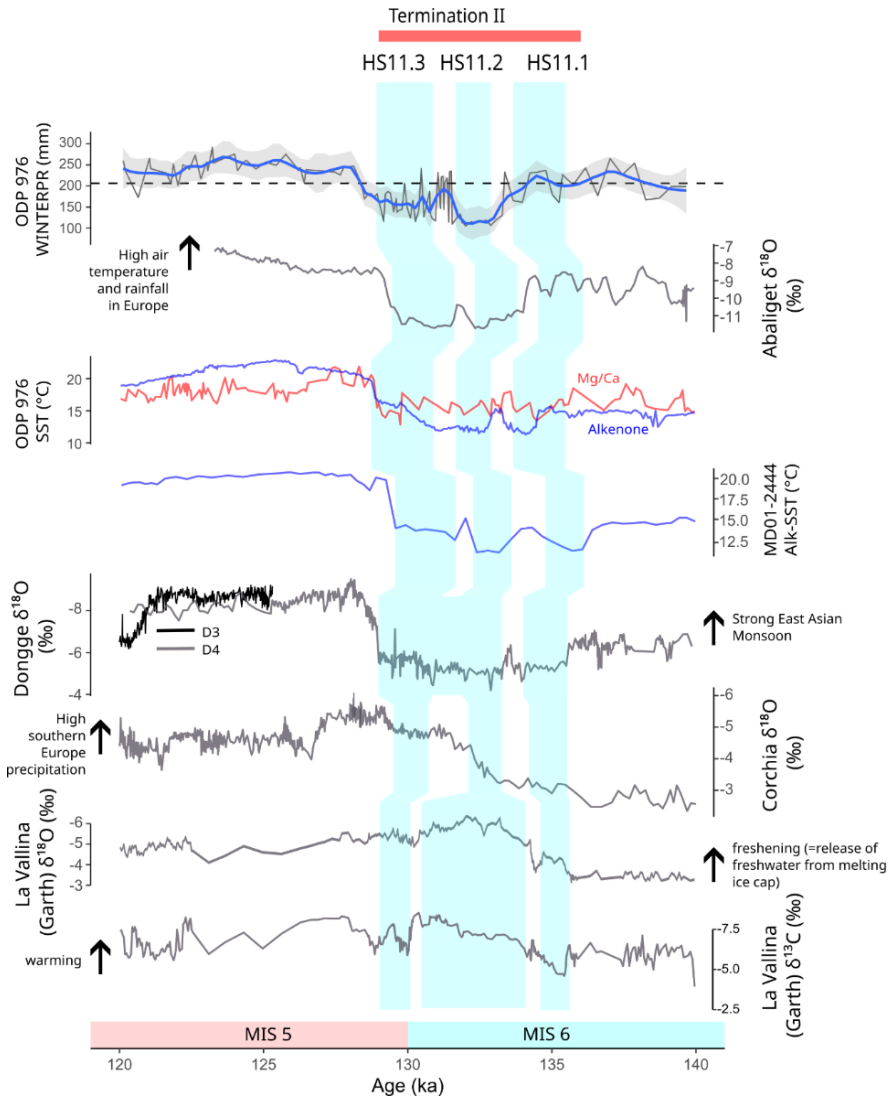


Fig. 5.3. Comparison of climate reconstructions from ODP 976 with other speleothem and marine records. From top to bottom: Abaliget cave speleothem record from southern Hungary (Koltai et al., 2017), MD01-2444 alkenone-based SSTs from the Portuguese margin (Tzedakis et al., 2018) , Dongge cave in China (Kelly et al., 2006), Corchia cave in Italy (Drysdale et al., 2009; Tzedakis et al., 2018), La Vallina complex in Northern Spain (Stoll et al., 2022). The timing for Termination II follow Bajo et al. (2020), and the interpretation of speleothem records follow the synthesis by Kaushal et al. (2025).

The southern Hungarian speleothem oxygen isotope record from Abaliget Cave is remarkably similar to the ODP 976 pollen-inferred precipitation reconstruction (Fig. 5.2). The oxygen isotope signal in the cave was interpreted as a result of air temperature changes controlling the amount of local precipitation (Koltai et al., 2017). The close match between ODP 976 and Abaliget cave paleo-precipitation records highlights the connexion between the pattern of precipitation changes in the SW

Mediterranean and in central Europe. In particular, the second warming event occurring between HS11.2 and HS11.3 in the ODP 976 pollen-inferred precipitation record is clearly correlated to higher temperatures and rainfall intensity in central Europe (Fig. 5.3). Enhanced precipitation at that time is also evidenced in the Corchia cave oxygen isotope record, and linked with the intensity of north-Atlantic moisture brought by the westerlies (Tzedakis et al., 2018).

5.4. Similarities and differences between the last and the penultimate deglaciations

Abundant Ericaceae pollen, as well as cool and humid conditions, similarly mark the end of the last glacial and penultimate glacial periods in the southwestern Mediterranean. However, steppe and semi-desert pollen was less abundant during the end of the last glacial, pointing toward less arid climatic conditions compared to the end of the penultimate glacial. Supporting this view, pollen-inferred winter precipitation is higher in the ODP 976 record at the end of MIS 2 (~16 ka) compared to the end of MIS 6 (~136 ka) (Fig. 5.4).

The last deglaciation was characterized by a well-known succession of rapid millennial-scale events pacing the transition to the present interglacial (e.g. Barker et al., 2009; Carlson & Clark, 2012; Combourieu-Nebout et al., 1998; Dormoy et al., 2009; Fletcher et al., 2010b; Martrat et al., 2014). In the ODP 976 multiproxy record, these rapid climatic events are well evidenced in the marine and terrestrial proxies (Bout-Roumazeilles et al., 2007; Combourieu-Nebout et al., 2002, 2009; Jiménez-Amat & Zahn, 2015). The HS1, associated to Greenland Stadial (GS) 2 in Greenland stratigraphy (Rasmussen et al., 2014), is marked by cold SSTs, high percentages of semi-desert pollen taxa, cold pollen-inferred mean temperature of the coldest month and low winter precipitation (Fig. 5.4). Following this cold event, a ~2 ka warming is evidenced in the SSTs, in the pollen assemblage, and the in the pollen-inferred climate reconstructions, corresponding to the Bölling-Alleröd (B-A) event, or Greenland Interstadial (GI) 1 (Rasmussen et al., 2014). Finally, the Younger Dryas (GS1) is marked by a new decrease in SSTs and pollen-inferred precipitation and temperatures, with a first *Artemisia* expansion followed by an increase in *Cedrus* pollen. The clay mineralogical record also shows important changes across Termination I, compatible with latitudinal migration of the subtropical belt: enhanced palygorskite input and increased I/K ratio during HS1 and the YD reflects enhanced dust input from North Africa and the Sahara, while higher kaolinite percentages during the B-A event likely reflects more dust input from the Sahel subtropical region.

The pattern of vegetation and climate changes in the ODP 976 record during TII and described in the previous sections is very different compared to TI. HS11 stands out for its very long duration (~6 ka, compared to less than 4 ka for HS1), and its complex structure with three cold pulses and an offset

of terrestrial and marine warm rebounds, contrasting with the B-A clear imprint in all proxies during TI. Some similarities can be recognized in the start of the first cold event (HS11 and HS1) in both glaciation: the "double-u" pattern of HS1 is comparable to HS11 in the planktonic isotope and SST record, with the warming evidenced at 15.5 ka analogous to the 133.5 ka increase. However, the following succession of events differs significantly, and the most striking difference is the absence of a prolonged B-A-type warming event during TII.

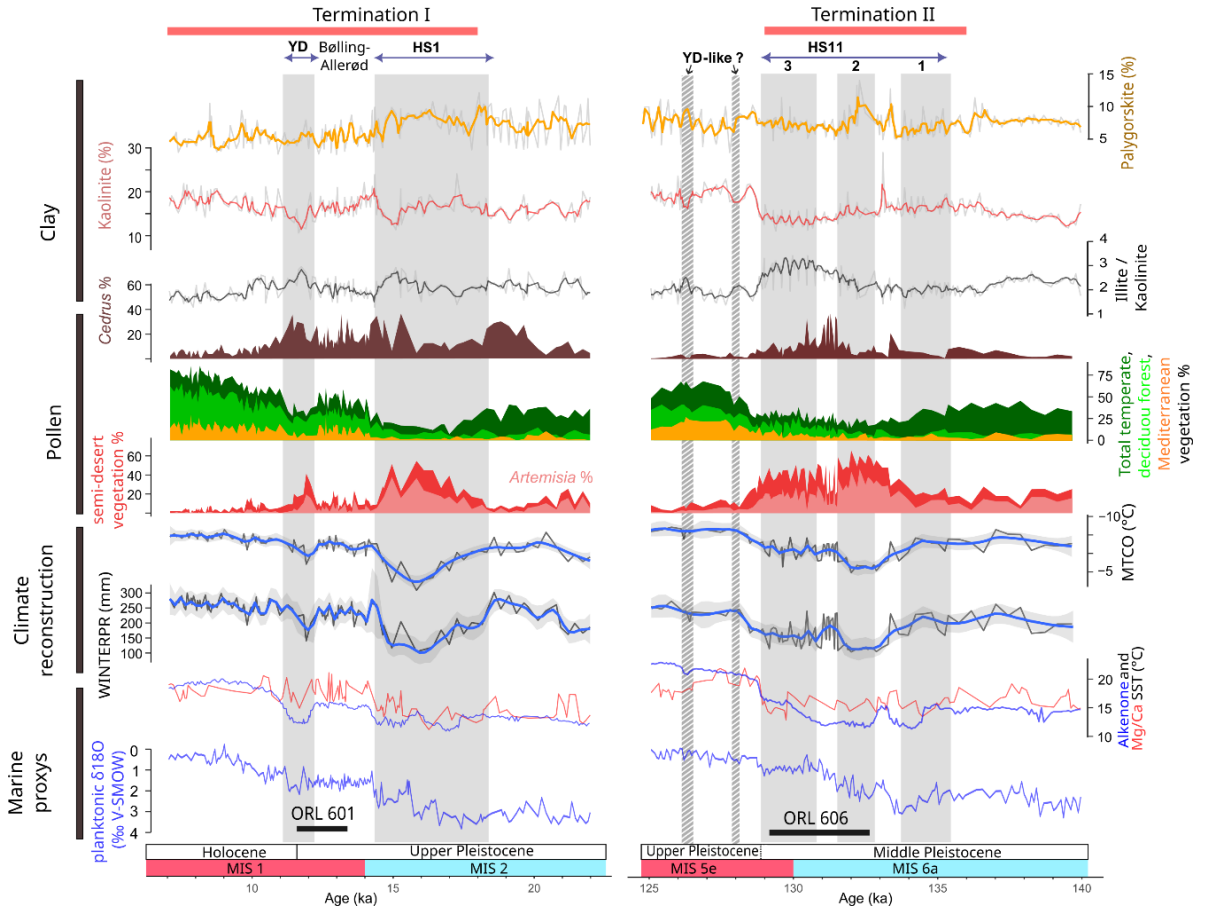


Fig. 5.4. Comparison between the two terminations in the ODP 976 multiproxy record. From bottom to top: *G. bulloides* oxygen isotope ratio and Mg/Ca Sea surface temperatures (SSTs) (Jiménez-Amat & Zahn, 2015); alkenone-based SSTs (Martrat et al., 2014); pollen-inferred climate reconstructions averaged between the four methods applied in this study: MTCO (Mean Temperature of the Coldest Month) and WINTERPR (total Winter Precipitation); main pollen group of taxa (Combourieu-Nebout et al., 2002, 2009; this study); main clay mineralogical percentages (Bout-Roumazeilles et al., 2007; this study). The timing of terminations follows Bajo et al. (2020), the MIS boundaries follow Lisiecki & Raymo (2005), and the Quaternary subdivisions follow Head (2019). Grey intervals mark the cold sub-orbital events, and the grey dashed bars the possible analogue events for the Younger Dryas during TII (see text).

The start of ORL deposition is also different in TI and TII (Fig. 5.4). During TII, ORL 606 occurs during the second HS11 cold pulse corresponding to the most intense freshwater release in the North Atlantic and the coldest temperatures reconstructed in the Alboran Sea region. During TI, the start of

ORL 601 deposition is clearly correlated to the B-A warming (Pérez-Asensio et al., 2020), a period marked by enhanced winter precipitation reconstructed through the pollen approach. The ORL 606 deposition event during TII is also longer than its counterpart during TI, probably indicating a prolongated impact of intense freshwater release in the North Atlantic during TII compared to the last deglaciation. These differences point toward a different mechanism for ORL formation in the Alboran Sea during both Terminations, and probably a different prevalent freshwater source at the origin of the deep-water anoxia events.

Previous studies already put forward major differences between TI and TII in term of duration, millennial-scale events, and deglacial processes implicated (e.g. Clark et al., 2020; Lisiecki & Stern, 2016; Martrat et al., 2014; Menviel et al., 2019). Lisiecki & Stern (2016) proposed that the shorter duration of TII compared to TI was linked with a stronger insolation forcing resulting in less millennial-scale variability and more intense ice-rafting event during TII. Supporting this view, different studies have shown that most of the sea-level rise of the penultimate deglaciation occurred during HS11, resulting from the fast North Atlantic ice-melting (e.g. Clark et al., 2020; Grant et al., 2014; Marino et al., 2015; Menviel et al., 2019). In contrast, during TI, most of the sea-level rise occurred after HS1, during the Bolling-Allerod interval and after the Younger-Dryas, resulting from enhanced Antarctic ice-melting (Carlson & Clark, 2012; Gregoire et al., 2012; Weaver et al., 2003). The longer period of AMOC weakening during HS11 compared to HS1 would therefore be linked with a faster and higher sea-level rise during Termination II compared to Termination I (Clark et al., 2020; Stoll et al., 2022). This fast deglacial process during TII was accompanied by the largest CO_2 release of the past nine deglaciations, and a continuous increase of methane concentration in Antarctic (Delmotte et al., 2004; Lourantou et al., 2010). In addition to a stronger insolation forcing rapid degassing, the greater extent of Eurasia Ice Sheet during MIS 6 compared to MIS 2 may also explain the longer and more intense release of ice-originated freshwater in the North Atlantic during the penultimate deglaciation (Colleoni et al., 2016; Rohling et al., 2017). This difference resulted in more intense and pronounced ice rafting event during TII compared to TI, and was also taken as the cause for the pervasiveness of cold sub-orbital events during MIS 5 (Tzedakis et al., 2018).

Our multiproxy land and sea record from ODP 976 fully supports a view where different forcing and ice-sheet configuration shaped distinctly the last and the penultimate deglaciations. A continuous, longer and stronger release of freshwater in the North Atlantic during TII resulted in a prolonged AMOC shutdown which apparently did not recover fully before the onset of the Eemian ~ 129 ka. The two warm rebounds that punctuated HS11 during TII did not affect equally ocean and continental environments, and lasted for shorter periods of time, preventing any analogy with the B-A/ GI1 event during TI. These short warm rebounds could correspond to internal ice-ocean-atmosphere feedbacks

usually occurring during Heinrich stadials (Alvarez-Solas et al., 2013; Marcott et al., 2011; Martrat et al., 2014), and contrasting with the full interstadial state observed during the B-A/ GI1.

While many studies have pointed out the absence of a Y-D analogue event during TII (e.g. Deaney et al., 2017; Tzedakis et al., 2018), other have proposed the occurrence of such an event, like in the Shangxiaofeng cave speleothem record where a weak monsoon interval was identified around 128.3 ka (Xue et al., 2019). The ODP 976 multiproxy record shows some features compatible with this event with lower Mg/Ca SSTs and Kaolinite input, and higher I/K ratio (Fig. 5.4) Based on the SSTs record from ODP 976, Jimenez-Amat and Zahn (2015) also suggested that the alkenone SSTs decrease observed at ~126 ka BP could represent an analogue of the Y-D. These two potential Y-D-like events are shown in Fig. 5.4. However, none of them present a significant reduction of temperate forest, expansion of steppe and semi-desert pollen, and decrease in pollen-inferred temperature and precipitation, contrasting with the clear Y-D imprint on the ODP 976 palynological record during TI. Furthermore, it is important to notice that these two events post-date the end of the termination estimated from the Asian monsoon and sea-level rise record, around 129 ka BP (Bajo et al., 2020; Clark et al., 2020). Based on our results, we therefore argue that there was no equivalent of the YD in the southwestern Mediterranean during TII. Our multiproxy record supports the idea that, if YD-like events are a pervasive feature of past deglaciations as proposed by Xue et al (2019), their expression, length and intensity can vary significantly in different regions of the globe. The emerging pattern for Termination II is therefore the absence of a clearly globally-recognized YD-like event.

5.5. Relevance for the discussion on Pleistocene Series boundaries

The last two deglaciations both cover a global stratigraphical boundary, between the Middle and the Upper Pleistocene for Termination II, and between the Upper Pleistocene to the Holocene for Termination I (Head, 2019). The Global Stratotype Section and Point (GSSP) for the Holocene Serie has been defined based on the NGRIP2 ice core in Greenland, and positioned at 11.7 ka b2k (before 2000 CE), corresponding to the climatic warming at the end of the Youger Dryas event / GS1 event (Walker et al., 2009). It was the first time a GSSP was defined based on an ice core record. To date, no official GSSP has been ratified for the Upper Pleistocene boundary. A main difficulty resided in the important leads and lags between marine and terrestrial responses to the interglacial warming, and therefore the difficult establishment of a globally recognized signal for the Upper Pleistocene onset.

Candidates to the GSSP have been proposed first in various terrestrial sections, such as Amersfoort in the Netherlands which is the type-section for the Eemian (Bosch et al., 2000; Litt & Gibbard, 2008), the Fronte section in Taranto, southern Italy (Negri et al., 2015), and Lake Monticchio in central Italy (Brauer et al., 2007). More recently, the abrupt increase in methane concentration at

128.51 ka BP recorded in EPICA Dome C core in Antarctica has been proposed as a potential GSSP (Head, 2019) (Fig. 5.5). Although not officially proposed, good candidates are also represented by speleothems, which provide absolutely calibrated high-resolution records sometimes continuously spanning long periods of time including various terminations (Kaushal et al., 2025). Among them, Corchia cave in Italy (Drysdale et al., 2009; Tzedakis et al., 2018), Dongge and Sanbao cave in China (Kelly et al., 2006; Wang et al., 2008), or La Vallina cave complex in northern Spain (Stoll et al., 2022) represent the most valuable speleothem archives for Termination II. Due to their good representativeness of global climate parameters (temperatures, precipitations, monsoon activity) and their robust calibration, many paleoclimatic records (including ODP 976) are chronologically tied to one of these reference speleothems.

Although depending on the absolute calibration of Dongge and Corchia caves, the multiproxy record from ODP 976 provides precious new data to help understanding the succession of events leading to the Eemian onset. The temperate tree pollen percentages in the Alboran Sea follow a trend of slow but continuous increase, similar to the global temperature record evidenced in the benthic $\delta^{18}O$ from the North Atlantic (Fig. 5.5 e) and in the Antarctica δDe (Fig. 5.5 b). In contrast, the steppe and semi desert pollen, together with SSTs, clay mineralogical composition, and pollen-inferred climate reconstructions, express millennial-scale changes connected with North Atlantic cold events and latitudinal migrations of the subtropical belt. Most strikingly, a good correlation is established between kaolinite input in the Alboran Sea, a northern position of the ITCZ, and strong Asian monsoonal activity. Supporting this interpretation, the evolution of methane concentration in Antarctica also seems well correlated with kaolinite concentration in the Alboran Sea (Fig. 5.5 a and j). The connection between global methane concentration and Asian monsoonal activity had already been established previously (Kelly et al., 2006; Cheng, 2016). Here, we extend this connection between methane concentration, monsoonal activity, and clay mineralogical composition in the Alboran Sea, with enhanced kaolinite input from the Sahel region at times of northern position of the ITCZ, when Asian monsoons are strong.

Following our interpretation, the peak in methane concentration observed at 128.51 in Antarctica is well-correlated (on the Asian monsoon chronology) with a peak in kaolinite concentration in the Alboran Sea clay mineralogical record at 40.2m (128.5 ka BP). This event is also marked by warm SSTs, and the end of HS11 in the palynological and paleoclimate record from ODP 976. Therefore, to our view, the future GSSP site for the Upper Pleistocene should provide a proper record of the global warming and moistening occurring at the end of the HS11 and marking the onset of the Eemian interglacial on land.

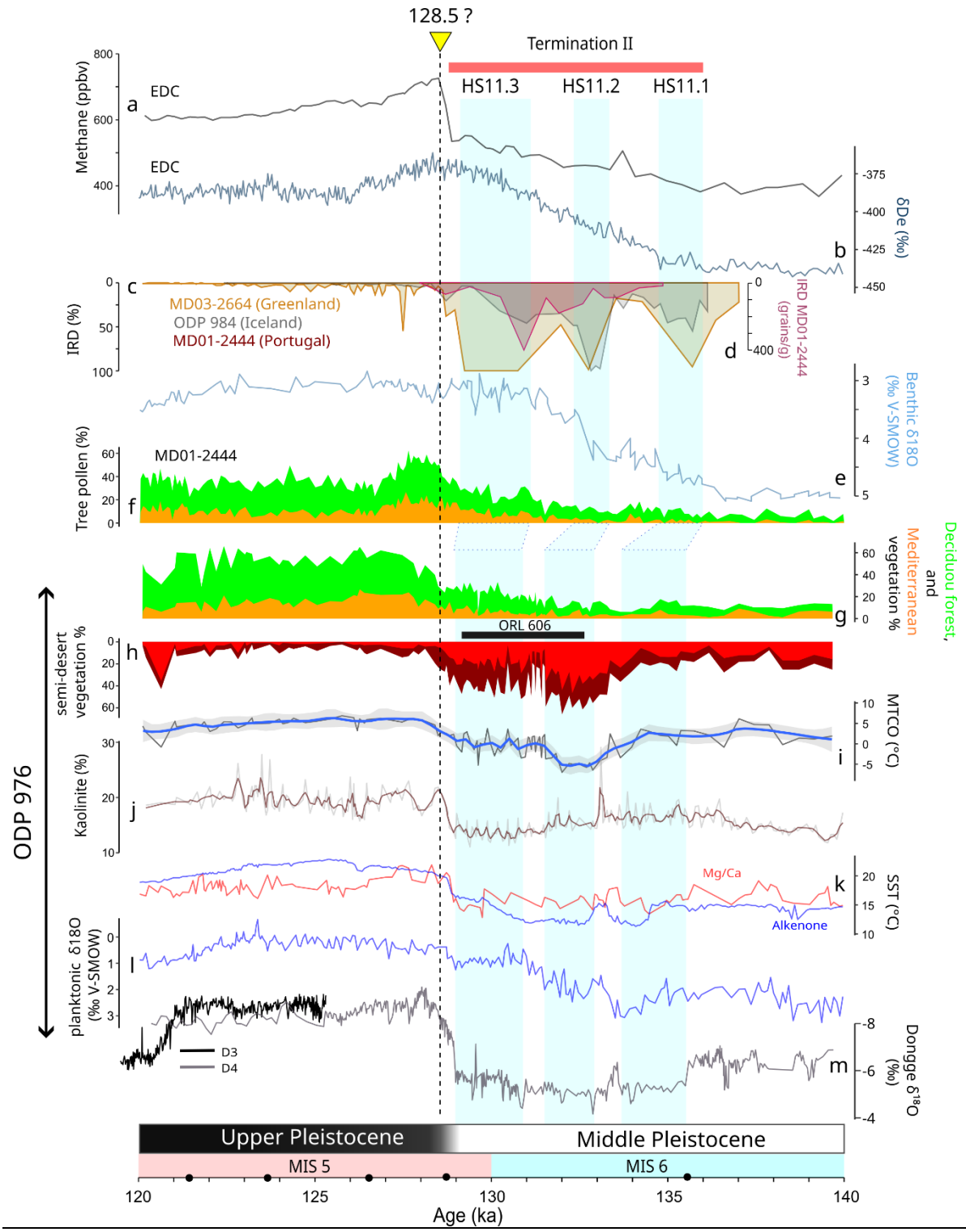


Fig. 5.5. Comparison of climate records from Antarctic, North-Atlantic, and the Alboran Sea between 140 and 120 ka BP. a) EPICA Dome C methane and **b)** deuterium records (Bazin et al., 2013; Jouzel et al., 2007); **c)** IRD percentages at sites ODP 984, southern Iceland (Mokeddem et al., 2014) and MD03-2664, southern Greenland (Irvalı et al., 2016), **d)** IRD from MD01-2444, southern Portugal (Skinner & Shackleton, 2006), **e)** benthic isotopic ratio and **f)** temperate tree pollen (temperate deciduous forest and Mediterranean taxa) from site MD01-2444 (Tzedakis et al., 2018), **g)** temperate tree pollen and **h)** semi-desert pollen from ODP 976 (this study), **i)** pollen-based reconstruction of the Mean Temperature of the Coldest Month (MTCO) based on a mean of multiple methods (MAT, WAPLS, BRT, RF) (this study), **j)** kaolinite mineral percentages in ODP 976 clay particles (this study), **k)** Mg/Ca-based SST (Jiménez-Amat & Zahn, 2015), alkenone-based SST, and **l)**

planktonic foraminifera isotopic ratio from ODP 976 (Martrat et al., 2014). Dotted line and yellow triangle show the potential GSSP proposed by Head (2019) based on the methane increase in Antarctica. Black dots show the tie-points from ODP 976 Mg/Ca SST to Dongge and Corchia Caves (Jiménez-Amat & Zahn, 2015).

5.6. Conclusions

Our study provided new terrestrial paleoclimatic data from ODP site 976, complementing the already published marine data.

This new multiproxy record from the Alboran Sea sheds light on the succession of events taking place during the penultimate deglaciation, including a major event of ice-rafting and AMOC disruption identified as HS11. This very long event evidenced in the SSTs and palynological records contains three different cold phases and two warm rebounds, the latter of which are disconnected in the marine and continental records. This land-sea offset in the warm rebounds during HS11 points toward complex feedback mechanisms resulting from the pace of deglacial freshwater release into the North Atlantic. By contrast to the steppe and semi-desert pollen which mainly reflects North-Atlantic events, the temperate deciduous pollen taxa increase continuously in the Alboran Sea record during TII, mirroring the evolution of global temperature, sea-level rise, and degassing. The paleo-dust record revealed important changes in the winds sources in the Alboran Sea during Termination II, resulting from the southward migration of the ITCZ starting from the second cold surge of HS11. Pollen-inferred climate reconstructions are consistent with different temperature and precipitation records from various speleothems worldwide, and particularly with Abaliget Cave in southern Hungary, supporting a connection between the intensity of southwestern Mediterranean precipitation and central Europe temperatures.

A comparison with Termination I from the same archive and climate proxies supports strong differences between the last two deglaciation, in the duration and pacing of events (including Organic-Rich Layer deposition). During Termination II, no clear analogues of the Bölling-Alleröd (GI1) and the Younger Dryas (GS1) are evidenced in the Alboran Sea. In contrast, during TII, HS11 stands out for its long duration (~6ka) and its complex internal structure that differentiate it from the HS1 (GS2) event occurring during TI. Our study supports a different succession of suborbital events during the last two Terminations, probably resulting from different insolation forcing and ice-sheet configuration.

The end of HS11 and the start of the Eemian interglacial in the Alboran Sea record is clearly evidenced and in all the different proxies. A Kaolinite peak in the clay mineralogical record stands out, expressing major aeolian input from the Sahel region resulting from the northern migration of the ITCZ. This kaolinite peak in ODP 976 (40.2 m depth, ~128.5 ka BP) is remarkably correlated with the abrupt

methane peak evidenced in the Antarctica record at 128.5 ka BP and proposed as a potential GSSP for the Upper Pleistocene. Our study therefore supports the global signature of the abrupt warming and northern migration of the ITCZ occurring at the end of HS11 and marking the onset of the Eemian interglacial.

Future studies should explore further the potential of speleothem records for absolute calibration of the different high-resolution marine paleoclimate archives available for Termination II. These efforts could greatly help to precise the timing of events in different regions of the world, in order to choose the most adequate GSSP of the Upper Pleistocene, reflecting global change toward interglacial conditions.

6. The Penultimate Glacial (MIS 6) in the SW Mediterranean: vegetation, climate and human dynamics.

6.1. Résumé en français

Cet article a été soumis à la revue *Climate of the Past*, et est en cours d'évaluation. L'étude se concentre sur l'avant-dernière période glaciaire (MIS 6), entre 190 et 128 ka BP environ. Considérée comme l'une des glaciations du Pléistocène les plus intenses en Europe, un petit nombre d'archives existent à ce jour pour en documenter les dynamiques ainsi que l'impact sur les environnements méditerranéens. Des séquences palynologiques longues à haute résolution sont disponibles dans la péninsule Balkanique, en Italie, et sur la côte Ibérique atlantique, tandis qu'une seule séquence à basse résolution, Padul, existe en Méditerranée sud-occidentale pour cet intervalle. Par ailleurs, si la question de l'impact des variations climatiques rapides de la dernière période glaciaire (MIS 4-2) sur Néandertal en Europe a fait l'objet de nombreuses études, très peu d'articles ont pris en considération les oscillations climatiques dans les périodes glaciaires précédente, et en particulier pendant le MIS 6. D'un point de vue archéologique, cette période couvre la fin de la transition du Paléolithique inférieur au Paléolithique moyen, qui voit la généralisation progressive des industries du Mode 3 et le début du « monde néandertalien classique » à partir du MIS 5. Cette étude explore ces thématiques à travers l'enregistrement palynologique d'ODP 976. Les résultats de deux cents échantillons palynologiques sont présentés, ainsi que des reconstructions climatiques avec une approche multiméthode. Il s'agit de la première étude proposant des reconstitutions climatiques basées sur le pollen et avec une approche multiméthode pour l'intégralité du MIS 6. Une synthèse des occupations néandertaliennes de la période est proposée pour le monde méditerranéen occidental, incluant la péninsule Ibérique, le sud de la France, et l'Italie. Les résultats principaux montrent :

(i) Une division en trois grandes phases de l'enregistrement palynologique et paléoclimatique d'ODP 976 pour le MIS 6 (Fig. 6.3 et 6.5): une première phase avec des taux importants de taxons de forêt tempérée et d'altitude marquant des conditions plus humides et tempérées, et une importante variabilité rapide ; une deuxième phase dominée par la végétation herbacée, steppique et semi-désertique, caractérisée par un climat plus froid et aride et moins d'oscillations rapides ; une troisième phase avec une présence notoire d'Ericaceae, marquant des conditions plus humides mais toujours froides à la fin du MIS 6.

(ii) La corrélation de deux niveaux de dépôts d'*Organic Rich Layers* (ORLs) identifiés dans la carotte sédimentaire (Murat, 1999) avec une phase plus chaude et humide au cours du

MIS 6e pour l'un (Fig. 6.5 et 6.8), et d'un évènement de Heinrich majeur pendant la Terminaison glaciaire pour l'autre (Fig. 6.5 et 6. 7).

(iii) L'impact majeur de l'événement de Heinrich 11 (HS11) sur la végétation régionale pendant la Terminaison glaciaire (TII), à la fin du MIS 6 (Fig. 6.3 et 6.7). Trois phases successives sont identifiées au sein de l'évènement, avec une phase intermédiaire plus humide. Les taxons de la forêt tempérée et méditerranéenne augmentent progressivement et de manière continue pendant l'évènement aride, marquant l'activation de la transition vers l'interglaciaire du MIS 5.

(iv) Une corrélation encore difficile des évènements climatiques rapides avec les séquences palynologiques longues dues aux incertitudes de modèle d'âge et aux différences de résolutions (Fig. 6.6).

(v) La réponse de la végétation aux oscillations climatiques à échelle sub-millénaires de type D-O pendant le MIS 6 en Méditerranée sud-occidentale (Fig. 6.6). La dynamique de ces oscillations partage des similitudes, mais aussi des différences majeures, avec celles du MIS 4-2 (Fig. 6.9): la fréquence et l'amplitude des oscillations de l'avant-dernier glaciaire apparaissent réduites en comparaison de la dernière période glaciaire, à l'exception du HS11 (Heinrich Stadial 11), qui est particulièrement long et intense dans l'enregistrement d'ODP 976.

(vi) La présence continue de Néandertal en Méditerranée du sud-ouest pendant le MIS 6 (Fig. 6.10), malgré les données peu abondantes, avec une mosaïque d'industries traditionnelles (Mode 2) et innovantes (Mode 3). L'Italie manque particulièrement de sites bien datés pour documenter les occupations néandertaliennes du MIS 6. Il est possible que les conditions très peu favorables pendant le HS11 aient joué un rôle dans la diminution des occupations et dans l'abandon définitif des technologies de Mode 2 à la fin du MIS 6.

6.2. Paper 2 (*Climate of the Past*): How unstable was the environment during the Penultimate Glacial in the South-Western Mediterranean? Vegetation, climate and human dynamics during MIS 6.

Charton Liz[1,2], **Combourieu-Nebout** Nathalie[1], **Bertini** Adele[2], **Peyron** Odile[3], **Robles** Mary[3], **Lebreton** Vincent[1], **Moncel**, Marie-Hélène [1].

1 : UMR 7194 HNHP- « Histoire Naturelle des Humanités Préhistorique », MNHN / CNRS / UPVD, Paris, France. liz.charton@mnhn.fr

2 : Dipartimento di Scienze della Terra, Università degli Studi di Firenze, Florence, Italy.

3: UMR 5554, ISEM-Institut des Sciences de l'Evolution de Montpellier, CNRS, Université de Montpellier, Montpellier, France.

6.2.1. Abstract

The impact of rapid climate variability on Neanderthal population in Europe during the Last Glacial (Marine Isotope Stages 4-2), including Dansgaard-Oeschger cycles and Heinrich events, has been the subject of a long-standing debate. However, few studies have focused on the nature and impact of such rapid variations on human population during earlier periods. A growing number of high-resolution paleoclimatic archives supports the persistence of rapid oscillations during the penultimate glaciation (MIS 6), and the close response of Mediterranean ecosystems to these. Still, few palynological sequences in the Mediterranean region offer sufficient resolution to document vegetation dynamics during this time. Pollen records are especially lacking in the western Mediterranean, a key region to understand the connection between North Atlantic and Mediterranean climatic influences. This region is also traditionally considered a climatic refugium for human population during unfavourable periods. We provide new palynological data covering MIS 6 from the long and continuous marine record of ODP 976 in the Alboran Sea. A total of 200 samples, spanning the interval from 196 to 127 ka Before Present (BP), reveal both long-term trends and rapid fluctuations in regional vegetation composition. A multi-method approach, including modern analogues, regression, and machine learning approaches, was applied to ODP 976 pollen assemblages to reconstruct the annual/seasonal temperatures and precipitation. Results show that three phases can be identified. The first phase (187-166 ka BP) is characterized by significant oscillations of temperate trees and rather cool and humid conditions during early MIS 6, coincident with a sapropel layer deposition in both the western and eastern Mediterranean. In the second phase (165-144 ka BP), arid herbaceous vegetation is dominant, marking the main imprint of glacial maxima conditions and reduced climate variability. The third phase (144-129 ka BP) is marked by the development of Ericaceae and increased annual precipitations. At the end of MIS 6 glaciation, a strong cooling and intense episode of steppe and semi-desert expansion is identified as Heinrich Stadial 11 (135-129 ka BP),

marking a distinct pattern for Termination II in the Western Mediterranean. Rapid oscillations appear like a pervasive feature of the Penultimate glacial in the SW Mediterranean, though they present reduced amplitude and frequency compared to the Last Glacial. A synthesis of human occupation shows that a mosaic of traditional (Mode 2) and innovative (Mode 3) technological features is observed. Although the data are scarce, Neanderthals seem to have continuously inhabited Western Mediterranean regions across the penultimate glacial. The severe climate conditions during Heinrich Stadial 11 (~133-129 ka BP) might have played a role in the apparent population contraction at the end of MIS 6, and perhaps also in the definitive abandonment of Lower Palaeolithic industries.

6.2.2. Introduction

Rapid climate oscillations occurred during the last Glacial period (MIS 4-2). Dansgaard-Oeschger (DO) cycles have been well identified in ice-core records (Bond et al., 1999; Dansgaard et al., 1993; Johnsen et al., 1992; Rasmussen et al., 2014) and recognized in Atlantic sedimentary cores (e.g. Bond et al., 1993, 1997; Roucoux et al., 2005; Sánchez Goñi et al., 2002; Shackleton et al., 2000, Zumaque et al., 2025). Short periods of intense cold named Heinrich Stadials (HS) and linked with intense iceberg discharges were also evidenced in Atlantic sediments (Bond et al., 1992; Heinrich, 1988; Hemming, 2004; Rasmussen et al., 2003; Ruddiman, 1977; Shackleton et al., 2004). Major cooling events also occurred during MIS 5 and the penultimate deglaciation (e.g. Chapman & Shackleton, 1999; Oppo et al., 2001). These high-frequency oscillations reflect major changes at global scale in the oceanic circulation and the Atlantic Meridional Overturning Circulation (AMOC), that are important features particularly during glacial terminations (Barker & Knorr, 2021). The Mediterranean region has been very sensitive to the rapid climate oscillations of MIS 5 to MIS 1, with changes recorded in both marine and continental environments (Cacho et al., 1999, 2006; Combourieu-Nebout et al., 2002, 2009; Fletcher et al., 2010a; Martrat et al., 2007; Penaud et al., 2016; Sánchez Goñi et al., 2002, 2022).

The penultimate glacial (MIS 6), took place between ~185 and 130 ka BP and presented a different ice-sheet and global climate configuration compared to the last glacial (MIS 4-2). It is considered among the coldest glacial periods of the past 800 ka BP (Masson-Delmotte et al., 2010), characterized by larger European Ice-Sheet and smaller Laurentide ice-sheet extension (Colleoni et al., 2016; Ehlers et al., 2018; Ehlers & Gibbard, 2007; Rohling et al., 2017). In Europe, it corresponds to the Riss glaciation in the Alpine area, and to the late Saalian glaciation complex in northern and central Europe, with two major ice-sheet advances identified in Germany: the Drenthe advance (~170-155 ka BP) characterized by the maximum ice extent in Europe, and the less extensive Warthe advance during the younger stage of MIS 6 (Ehlers et al., 2011). The exact chronology of the Penultimate Glacial Maximum (i.e. the maximum extension of the northern hemisphere ice-sheet) is still not well

constrained (Svendsen et al., 2004), but is usually considered around 140 ka BP (Colleoni et al., 2016). Five marine isotopic substages were identified from MIS 6e to 6a, reflecting variations of global sea temperatures : three cold substages (6e : ~180 ka BP, 6c : ~160 ka BP, 6a : ~136 ka BP) with increasing cold intensity, and two warm substages (6d : ~170 ka BP and 6b : ~149 ka BP) (Railsback et al., 2015). Different speleothem records revealed that MIS 6 glaciation in Europe, including the Mediterranean region, was characterized by wetter conditions in comparison with the last glacial (Ayalon et al., 2002; Koltai et al., 2017; Nehme et al., 2018; Regattieri et al., 2014). Furthermore, various studies highlighted the apparent higher stability of the Laurentide ice-sheets during the penultimate glacial, leading to the absence of typical "Heinrich layers" in the North Atlantic sediments, with the exception of the large event recorded at the MIS 6 to MIS 5 transition, HS11 (~135-129 ka BP) (de Abreu et al., 2003; McCarron et al., 2021; McManus et al., 1999; Obrochta et al., 2014; Ovsepyan & Murdmaa, 2017; Shackleton et al., 2003).

Human Palaeolithic groups in Europe were likely affected by rapid climate changes (Bradtmöller et al., 2012; Dennell et al., 2011; Raia et al., 2020; Willis et al., 2004). The South-Western Mediterranean probably played a major role as one of the climate refugia area around the Mediterranean Basin during the most unfavourable climatic periods, permitting the persistence of "source" population able to recolonize the northernmost areas during more favourable periods (Bailey et al., 2008; Bicho & Carvalho, 2022). Many studies focused on the potential impact of abrupt environmental changes on Neanderthal populations, especially those associated with Heinrich Stadials during MIS 3 (e.g. Charton et al., 2025; D'Errico & Sánchez Goñi, 2003; Finlayson & Carrión, 2007; Melchionna et al., 2018). During the previous climatic cycles of the Middle Pleistocene, when Early to Middle Palaeolithic cultures developed, repeated climate instability has been brought forward as an explanation for the large variability in the lithic production (Dennell et al., 2011; Foerster et al., 2022; Sánchez-Yustos & Diez-Martín, 2015), and the non-linearity of the biological processes linked with Neanderthal evolution (Bermúdez de Castro & Martinón-Torres, 2013; Hublin, 2009). Still, the short and long-term resilience of human populations in a globally unstable environment is poorly understood, and partially hindered by our limited knowledge of fast millennial-scale climate oscillations in older glaciations prior to MIS 4-2.

While the Greenland ice does not provide an adequate record for periods older than 123 ka BP (Chappellaz et al., 1997), the description of a precise stratigraphy of climate events at sub millennial scale for the previous glacial/interglacial cycles remains complex, and relies on the Antarctic isotope record (Bazin et al., 2013; Jouzel et al., 2007), the study of marine sediments (de Abreu et al., 2003; Lisiecki & Raymo, 2005; Margari et al., 2010, 2014; McManus et al., 1999; Obrochta et al., 2014) and high-resolution continental archives such as speleothems (Burns et al., 2019; Held et al., 2024; Hodge

et al., 2008; Wainer et al., 2013; Wang et al., 2018; Wang et al., 2001). Benthic and planktonic isotopic ratios together with Sea Surface Temperatures (SSTs) reconstructions in the North Atlantic and the Western Mediterranean showcased the persistence of D-O-like events and interhemispheric bipolar see-saw heat transport during MIS 6, in addition to important reorganization of the water circulation during sapropel S6 deposition ~175 ka BP (Margari et al., 2010, 2014; Martrat et al., 2004, 2007, 2014; Rousseau et al., 2020; Sierro & Andersen, 2022). Nevertheless, MIS 6 is much less well documented than the last glacial in Mediterranean Europe. Few palynological sequences are available to document the vegetation changes across this interval (Camuera et al., 2019, 2022; Follieri et al., 1988; Margari et al., 2010; Okuda et al., 2001; Roucoux et al., 2011; Sadori et al., 2016; Sinopoli et al., 2019; Tzedakis et al., 2006; Wilson et al., 2021). Among them, only one in SW Europe provides sufficient resolution to document high-frequency changes : the deep-sea core MD01-2444 (Margari et al., 2010, 2014). While D-O like events impacting the vegetation have been identified in this record especially during the lower MIS 6, the core is located out of the Mediterranean Sea along the Portuguese margin in the Atlantic Ocean. Therefore, questions remain open concerning the impact of such events on the Western Mediterranean region, considered a Pleistocene refugium for human populations.

To fill this gap, our study provides high-resolution pollen data and quantitative climate reconstructions from ODP site 976 in south-western Mediterranean focusing on MIS 6. We aim to (i) reconstruct the vegetation and climate changes in the SW Mediterranean during the penultimate glacial, (ii) identify abrupt climatic changes including potential Heinrich-like and D-O like events and connect them with other Atlantic and Mediterranean paleoenvironmental records, (iii) compare the nature of millennial-scale climate and vegetation dynamics during the last glacial period and the penultimate glacial using a single, continuous pollen record and (iv) explore the potential impact of these climatic changes for Early Middle Palaeolithic human groups, with particular attention to the presence of climate refugia during the most extreme glacial phases.

6.2.3. Study site

Ocean Drilling Program (ODP) Site 976 (36°12 N, 4°18W, 1108 m depth) core was retrieved in 1995 in the Alboran Sea (Zahn et al., 1999). The site is located about 110 km east of the Gibraltar Strait, 70 km south of the Spanish coast, and 100 km north of Morocco (Fig. 6.1).

The Alboran Sea is the westernmost extensional basin of the Mediterranean Sea, bordered to the north by the Betic Cordillera and to the south by the Moroccan Rif mountains. Oceanic currents result from the water masses exchanges between the Atlantic Ocean and the Mediterranean Sea through the Gibraltar Strait. The surface currents are governed by the inflow of low-salinity Atlantic waters (Atlantic Jet) forming two anticyclonic gyres named Western and Eastern Alboran Gyres (WAG

and EAG) (Renault et al., 2012) (Fig. 6.1). The Mediterranean high-salinity water masses flow out in the Atlantic basin through the intermediate depth currents.

The modern climate in the Alboran Sea region is typically Mediterranean, defined by long, hot, dry summers and mild and cool winters (Lionello et al., 2006; Pons and Quézel, 1998). Atlantic westerlies dominate during winter, while subtropical high pressure masses generate intense drought during summer (Sumner et al., 2001). The current vegetation distribution on the Alboran borderlands follows a strong altitudinal climatic gradient : dry steppe elements such as *Artemisia* and *Lygeum* grow in the most arid lowlands along the coast, sclerophyllous evergreen taxa, including *Quercus ilex*, *Olea* and *Pistacia* are the main representatives of the thermo-to meso-Mediterranean belts, while temperate vegetation with deciduous trees constitutes the overlying supra-Mediterranean belt (Quézel, 2000). Finally, coniferous forests of *Abies* and *Pinus* grow in the oro-Mediterranean belt (above approximately 1200 m), with the presence of *Cedrus* in altitudinal vegetation of the Moroccan Rif mountains.

The main sedimentation processes in the area originate from the strong erosion in the Betic Cordillera (Alonso et al., 1999; Liquete et al., 2005; Lobo et al., 2006) and the material transported by the surface Atlantic waters (Auffret et al., 1974), although a significant but unknown proportion of particles including pollen was transported by African winds as evidenced by the presence of Saharan clay particles and *Cedrus* pollen across the Pleistocene (Bout-Roumazeilles et al., 2007; Jiménez-Moreno et al., 2020; Magri & Parra, 2002). Therefore, the pollen assemblage is interpreted as reflecting the regional vegetation of the southern Iberian Peninsula, with smaller but variable contribution from Northern Africa. Previous studies have shown that the Alboran Sea palynological record displays close similarities with the Padul record in SE Spain (Camuera et al., 2019), indicating that ODP 976 is a valid archive to reconstruct the southern Iberian Peninsula vegetation changes (Fletcher & Sánchez Goñi, 2008; Charton et al., 2025).

Two Organic-Rich Layers (ORLs) were identified in ODP 976 core during the MIS 6 interval, bed 607 (50.43-49.93 m), and bed 606 (41.6-40.4 m) (Murat, 1999). The ages were recalculated based on the updated age model for MIS 6 presented here, giving 178.07-174.53 ka BP for bed 607, and 132.64-129.16 ka BP for bed 606. With a Total Organic Carbon (TOC) of 1.18% and 1.85% respectively, these layers have been described as “ghost sapropels”, as they present a lower organic matter content than the Eastern Mediterranean sapropels (Rogerson et al., 2008). Their relevance for hydrological and climatic inferences in the Alboran Sea will be discussed in the light of the vegetation dynamics.



Fig. 6.1. Map showing the location of ODP 976 core together with other paleoenvironmental and paleoclimate records covering part or all of MIS 6, as discussed in the text.

6.2.4. Methods

6.2.4.1. Age Model

The age model for the study interval uses three previously published tie-points between ODP 976 Mg/Ca-derived SST (Jiménez-Amat & Zahn, 2015) and the speleothem temperature records from Dongge cave in China (Kelly et al., 2006). Several other marine records covering MIS 6 in the region are chronologically tunned to speleothems (e.g. Sierro & Anderson, 2022; Tzedakis et al., 2018). For the lower interval, the low resolution of planktonic isotopic data available for ODP 976 did not allow direct orbital or temperature calibration (von Grafenstein et al., 1999). Instead, we chose to align the higher-resolution pollen record produced in this study with the one from MD01-2444 core on the Portuguese margin (Margari et al., 2010, 2014; Tzedakis et al., 2018). Previous studies highlighted the strong similarities between pollen records on the Atlantic margin and the Alboran Sea during the last glacial

period (Fletcher et al., 2010a; Fletcher & Sánchez Goñi, 2008; Sánchez Goñi et al., 2002), supporting this approach. MD01-2444 chronology is based on the alignment of benthic isotopic events with the Antarctic temperature record, on AICC2012 timescale (Jouzel et al., 2007; Margari et al., 2010; Shin et al., 2020). Five peaks of temperate forest in MD01-2444 were used as control-points for ODP 976 (Table 1).

Event type	ODP 976 Depth (mcd)	Age (ka BP)	References
Dongge cave speleothem D3	40.25	128.73	Jiménez-Amat and Zahn, 2015; Kelly et al., 2006
Dongge cave speleothem D2	42.61	135.57	Jiménez-Amat and Zahn, 2015; Kelly et al., 2006
Dongge cave speleothem D1	44.14	142.09	Jiménez-Amat and Zahn, 2015; Kelly et al., 2006
Temperate pollen peak in MD01-2444	46.4	149.43	(Margari et al., 2010; Shin et al., 2020)
Temperate pollen peak in MD01-2444	48.5	160.00	(Margari et al., 2010; Shin et al., 2020)
Temperate pollen peak in MD01-2444	49.3	170.07	(Margari et al., 2010; Shin et al., 2020)
Temperate pollen peak in MD01-2444	50.48	178.42	(Margari et al., 2010; Shin et al., 2020)
Temperate pollen peak in MD01-2444	53.2	193.758	(Margari et al., 2010; Shin et al., 2020)

Table 6.1. List of control points used to calibrate the ODP 976 record for the MIS 6 interval. The tie-points on MD01-2444 temperate pollen curve are on AICC2012 timescale.

A linear regression was applied to obtain a continuous age for the study interval, spanning from 126.4 to 196.6 ka BP, with a mean resolution of about 350 years for the record (Fig. 6.2).

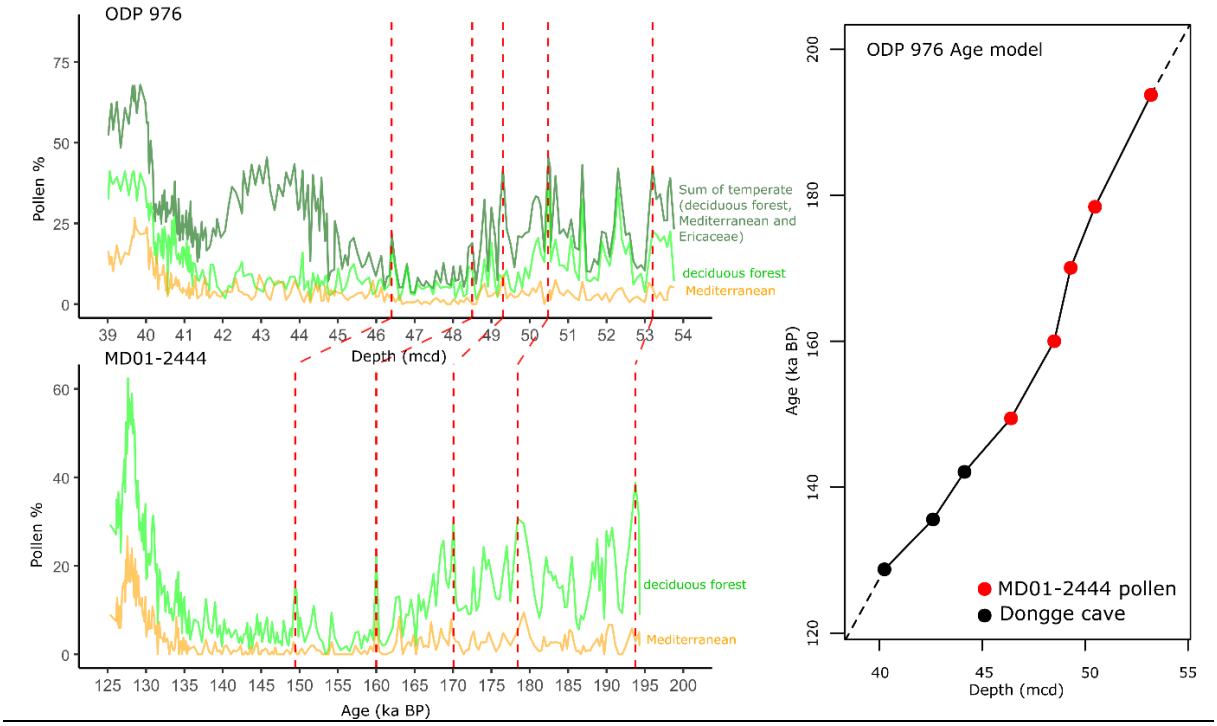


Fig. 6.2. Age versus depth model for the MIS 6 part of ODP 976 record, based on correlation between the Mg/Ca-based SST curve (Jiménez-Amat and Zahn, 2015) and the Dongge cave speleothem temperature record (Kelly et al., 2006) (black dots), and graphical correlation of the temperate pollen curve with the MD01-2444 palynological record (red dots and dotted lines) on AICC2012 timescale (Margari et al., 2010; Shin et al., 2020).

6.2.4.2. Pollen analyses

Two hundred samples have been analysed in this study, between 40 and 54 m (mcd) depth. The sample processing followed the traditional steps used for pollen extraction (Faegri & Iversen, 1964) and previously applied to the ODP 976 core (Combourieu-Nebout et al., 2002; 2009; Sassoon et al., 2023, Charton et al., 2025). It included sample weighing between 5 and 10 g of sediments, a 150 µm sieving for the retrieving of macrofossils and macroparticles, followed by 10% HCl, 40% HF, 20% HCl and a final 10 µm sieving.

A minimum of 150 pollen grains were counted for each sample, excluding *Pinus* as it is usually overrepresented in marine sequences (e.g. Combourieu-Nebout et al., 2002; Fletcher et al., 2010b; Mudie, 2011 and references therein), and represents often more than 50% of the total pollen sum in the study interval (see Fig. 6.3).

Ecological groups of pollen taxa were defined following previous studies of the ODP 976 record (Charton et al, 2025; Combourieu-Nebout et al., 2009; Sassoon et al., 2023). The percentage pollen diagram was constructed using the *rioja* R package (Juggins, 2023). Constrained Incremental Sum-of-

Squares (CONISS) cluster analysis was applied for pollen zonation, using the *vegan* package on R (Oksanen et al., 2024).

6.2.4.3. Pollen-inferred climate reconstructions: a multi-method approach

Four methods were applied to the ODP 976 record to reconstruct past climate changes during MIS 6. This is the first time this approach is used for the entire MIS 6 interval (Sinopoli et al., 2019). The multi-method approach allows for a more accurate climate reconstruction (trends and rapid events) compared to the traditional single-method approach (Chevalier et al., 2020; Peyron et al., 2011, 2013; Salonen et al., 2019; Sassoon et al., 2025). It also allows to compare the reliability and biases of the different methods, which are based on different ecological principles and mathematical algorithms. Four methods were used in this study.

The Modern Analogue Technique (MAT) is the first "assemblage" method ever developed to estimate climate parameters based on pollen assemblages, and is still the most widely used (Guiot, 1990). It is based on the calculation of a dissimilarity index between the fossil samples and samples from a modern pollen dataset. The values of the closest modern analogues selected (here, 4) are averaged to reconstruct the climate parameters for each fossil sample. Weighted Averaging Partial Least Squares (WA-PLS) (ter Braak and Juggins, 1993) is the second most widely used method, and is based on a different mathematical approach using non-linear regression. Assuming that taxa are most abundant where they find their optimum climatic conditions, WA-PLS models the plant/climate relationships from the modern calibration dataset, weighing the climatic values based on the pollen taxa percentage. These plant pollen abundance / climate transfer functions are then used to calculate the climate parameters of the fossil samples. The last two methods, Random Forest (RF) and Boosted Regression Trees (BRT), rely on a completely different approach using machine learning: they generate a large set of regression trees based on a randomised pollen dataset by bootstrapping (with pollen taxa selected randomly). Contrary to RF (Prasad et al., 2006), BRT (Salonen et al., 2012) assigns a higher probability to select samples that have not been selected before (boosting), increasing the performance of the model for elements that are less well predicted (Chevalier et al., 2020). The application of these machine learning methodologies in paleoclimatology is very promising, especially for BRT, and they have already been validated through different European and Mediterranean pollen records, for different time periods (Charton et al, 2025; D'Oliveira et al., 2023; Robles et al., 2022, 2023; Salonen et al., 2019; Sassoon et al., 2025).

The four methods were run on R using packages *Rioja* for MAT and WA-PLS (Juggins, 2024), *dismo* for BRT (Hijmans et al., 2023) and *randomForest* for RF (Liaw and Wiener, 2022).

We used the modern pollen dataset compiled by Peyron et al. (2013, 2017) and updated by Dugerdil et al. (2021a) and Robles et al. (2023). Samples belonging to non-relevant biomes for this study were excluded (Taiga, Tundra, Pioneer Forest, warm steppe and hot desert), resulting in 2373 samples for calibration dataset spanning across Eurasia and NW Africa.

Six climate variables were reconstructed: PANN (annual precipitations), MAAT (annual temperatures), SUMMERPR (summer precipitations), WINTERPR (winter precipitations), MTWA (mean temperature of the warmest month) and MTCO (mean temperature of the coldest month). SUMMERPR and MTWA values were poorly reconstructed according to the accuracy indicators (Table 2). This is in agreement with previous studies showing the poor reliability of summer parameters (e.g. Camuera et al., 2022). Therefore, we chose to represent seasonal parameters as contrast values for a better visualization: TCON (temperature contrast) = MTCO - MTWA, and PCON (precipitation contrast) = WINTERPR – SUMMERPR. The MTWA and SUMMERPR results can be found in Supplementary (Fig. S3).

For comparison with the present-day climate, and the calculation of anomalies, the modern values were extracted from ERA 5 reanalysis of the ECMWF (European Centre for Medium-Range Weather Forecasts), based on data assimilation into meteorological modelling from 1960 to 2022 (Hersbach et al., 2020). Pollen dispersal is reduced beyond a radius of 175 km (Rojo et al., 2016). However, other studies suggest that pollen can be transported up to distances of 200-300 km (Fernández-Rodríguez et al., 2014) and even over distances greater than 500 km (Bayr et al., 2023; Damialis et al., 2017). Sediments from marine cores such as ODP 976 can therefore include close and long-distance pollen. To account for these observations, an averaged value of the climate parameters on a 400 km radius around the ODP 976 site was extracted, giving MAP = 478 mm, MAAT = 16.78°C, MTCO = 13.78 ◦C, WINTERPR = 172 mm, TCON = -9.59, PCON = 141.5 mm. These values for modern climate, averaged temporally and spatially, provide a better basis for understanding the nature of the climate signal extracted from a marine palynological sequence at a regional pluri-annual scale.

The reliability of the different methods and climate parameters reconstructed is evaluated with bootstrapping cross-validation through two indicators: the correlation coefficient between the variables (R^2) and the root mean square error (RMSE).

6.2.5. Results

6.2.5.1. Pollen record

The pollen diagram shows the vegetation dynamics between 196.6 and 127.5 ka BP, spanning late MIS 7 to early MIS 5 (Fig. 6.3). Five pollen zones were separated by CONISS cluster analysis, with zone 4 being divided in three subzones (Table 2).

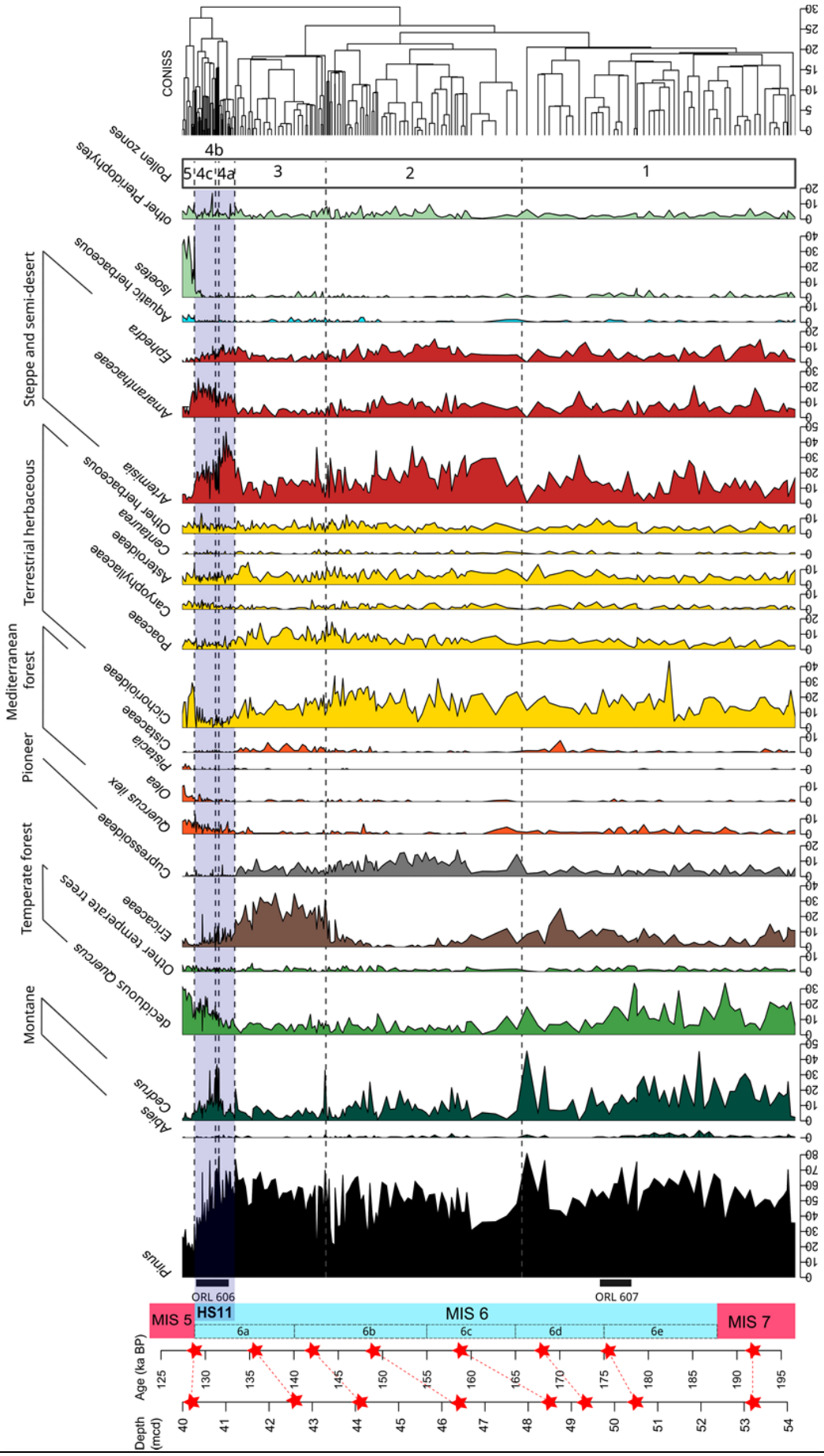

CONISS
Pollen zones
4b
5
4c
4a
3
2
1
other Pteridophytes
Steppe and semi-desert
Aquatic herbaceous
Isoetes
Ephedra
Amaranthaceae
Terrestrial herbaceous
Artemisia
Other herbaceous
Centaurea
Asteroideae
Caryophyllaceae
Poaceae
Mediterranean forest
Pioneer
Cichorioideae
Cistaceae
Pistacia
Olea
Quercus ilex
Cupressoideae
Temperate forest
Ericaceae
Other temperate trees
deciduous Quercus
Montane
Abies
Cedrus
Pinus
ORL 606
ORL 607
MIS 5
HS11
MIS 6
MIS 7
6a
6b
6c
6d
6e
Age (ka BP)
Depth (mcd)

Fig. 6.3. Pollen diagram of selected taxa for MIS 6 interval in the ODP 976 record, plotted against age. Taxa are grouped by ecological groups (see Table 2). Red stars indicate control points used for the age calibration, and their correspondence with mcd (meters composite depth) (see Table 6.1). The blue bar indicates Heinrich Stadial 11.ORL : Organic Rich Layers from ODP 976 (Murat, 1999).

Zone 1 most represented taxa are deciduous *Quercus* and *Cedrus*, with important abundance variability showing an unstable phase at the transition from MIS 7 to MIS 6e and 6d. Zone 2 displays the maximum expansion of steppe and semi-desert vegetation together with other open vegetation taxa and Cupressoideae during the MIS 6b and 6c. An additional noteworthy observation within this interval is the presence of gastropod shells identified as *Limacina retroversa* (Jeanne Rampal, personal communication, 2023), recovered during sieving of a sample at 46.4 m, corresponding to around 155.5 ka BP (Fig. 4). This species is usually most abundant in temperate to subpolar waters in the North-Atlantic (Thabet et al., 2015). Zone 3 is mainly characterized by the abundance of Ericaceae at the final stage of MIS 6 (6b and 6a). Zone 4, at the end of MIS 6a, is divided into 3 subzones which display fast vegetation changes during the transition from MIS 6 to MIS 5 (Termination II), and Heinrich Stadial 11. The fast expansion of steppe and semi-desert taxa (*Artemisia*, Amaranthaceae, *Ephedra*) occurs simultaneously with the first increase of deciduous temperate and Mediterranean forest indicative of the initialization of interglacial conditions (zone 4a). This episode of arid vegetation dominance is interrupted in zone 4b by the fast expansion of montane vegetation mainly represented by *Cedrus*. A new steppe and semi-desert vegetation increase is observed in zone 4c, while the deciduous temperate forest and the Mediterranean vegetation continue to expand. Finally, zone 5 is characterized by the maximum abundance of mesophilous and thermophilous elements, mainly represented by deciduous *Quercus* and *Quercus ilex*, typical of the MIS 5 interglacial.

Pollen zone	*Depth (mcd) and Age (ka BP)*	*Description of the pollen assemblage (Fig. 6.3)*	*Climate reconstructions (Fig. 6.5)*
5	40.25-39.98 m 128.73-127.47 ka BP	Peak abundance of deciduous *Quercus* (up to 32%), *Quercus ilex* (4-10%), *Olea* (2-11%), *Pistacia* (up to 4%), aquatic herbaceous (up to 5%) and *Isoetes* (up to 38%). High values of Cichorioideae (up to 30%). Low percentages of *Pinus* (<35%), *Artemisia* (<11%), Amaranthaceae (<18%) and *Ephedra* (<3%).	Rapid increase of temperature, precipitation and seasonal contrast close to the modern value
4c	41.08-40.28 m 131.13-128.81 ka BP	New increase of *Artemisia* (up to 29%) and Amaranthaceae (up to 26%). High values of *Cedrus* (5-28%), and increasing percentages of deciduous *Quercus* (10-23%), Cichorioideae (0-14%) and *Quercus ilex* (1-13%). Decrease of Ericaceae (13-0%). Increasing percentages of *Isoetes* (0-5%) and Pteridophytes spores (0-17%).	First decrease, and then increase in temperatures and precipitations, with low PCON.
4b	41.21-41.09 m 131.51-131.16 ka BP	Peak abundance of *Cedrus* (up to 37%). Decrease of *Artemisia* (30-7%), Amaranthaceae (6-13%) and *Ephedra* (6-4%). Notable abundance of deciduous *Quercus* (6-15%) and *Quercus ilex* (1-3%).	Abrupt rise in precipitation contrast, but still cold conditions.
4a	41.82-41.22 m 133.28-131.54 ka BP	Peak abundance of Artemisia, (24-47%), Amaranthaceae (14-6%) and *Ephedra* (5-11%). Decreasing trend of Ericaceae percentages (12-2%), and progressive increasing of deciduous *Quercus* (4-11%) and *Quercus ilex* (1-8%). Decrease of Cichorioideae (<11%) and Cupressoideae (<8%).	Rapid decrease in temperature, precipitation and seasonal contrast.
3	44.57-41.85 m 143.49-133.37 ka BP	Peak abundance of Ericaceae (12-35 %), and high values of Cichorioideae (8-22%). Notable presence of Cupressoideae (2-11%). Peak abundance of *Artemisia* (37%) at 44.28 m / 142.54 ka BP and *Cedrus* (33%) at 44.57 m/143.49 ka BP.	Increase of temperatures (but still lower than present), and important precipitations rise until values higher-than-present. Seasonal contrast close to present-day.

2	48.91-44.63 m 165.16-143.68 ka BP	High percentages of Cichorioideae (11-34 %), Poaceae (4-18%), *Artemisia* (4-37%), Amaranthaceae (3-16%) and *Ephedra* (3-12%). Cupressoideae maximum between 150-160 ka BP (up to 17%), and abundant *Cedrus* (up to 25%). Very low values of deciduous *Quercus* (<10%), Mediterranean taxa (<4%) and Ericaceae (<12%), with minimum values between 150 and 158 ka BP.	Decline of temperatures and precipitations, both lower than the modern values, reaching a minimum between ~164-155 ka BP. Afterwards, progressive rise in temperature, precipitation and seasonal contrast.
1	53.76-49 m 196.15-166.29 ka BP	High percentages of *Cedrus* (8 to 45%) and deciduous *Quercus* (4 to 34%), with important variations. Abundant Cichorioideae (up to 43%) and Ericaceae (up to 25%), with notable presence of *Abies* (up to 5%), *Quercus ilex* (up to 6%) and *Isoetes* (up to 6%). Relatively low values of semi-desert elements (*Artemisia*, Amaranthaceae, *Ephedra*) but with two increases at 49.6 m /172 ka BP and at 51.6 m / 185 ka BP.	Rather stable conditions expressed by the smoothed lines, but important and numerous rapid oscillations. In general, values of precipitation and seasonal contrast are close or higher that the modern value, while temperature is cooler than present.

Table 6.2. **Description of the pollen zones identified through CONISS cluster analysis**, including the main characteristics of their pollen assemblage and associated climate reconstructions.

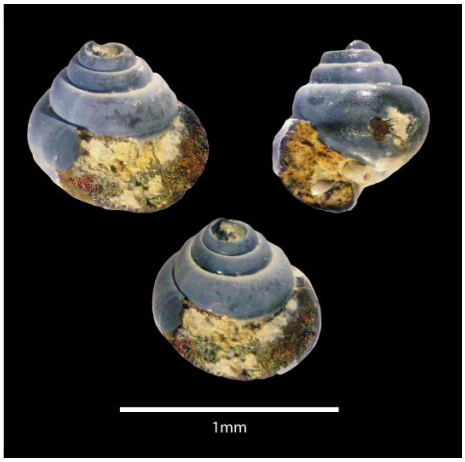


Fig. 6.4. *Limacina retroversa* specimen found in sample B6H4 130-132 (identification: Jeanne Rampal personal communication, 2023). Photo: Dael Sassoon.

6.2.5.2. Pollen-inferred climate reconstructions

Results show significant temperatures and precipitation variations in connection with the glacial / interglacial cyclicity and shorter-term variability (Fig. 6.5, Table 6.2). The most reliable methods according to the two R^2 and RMSE indicators are MAT and BRT, and the most accurately reconstructed parameters are MAAT and MTCO (Table 6.3). The four methods are in agreement for the general trends, although MAT shows the widest amplitude of variations, and RF has the smoothest curve.

Temperatures are lower than the present during the complete MIS 6 interval, except at the onset of MIS 5. A cooling trend is reconstructed during the final stage of MIS 7 (pollen zone 1, MIS 6e and 6d), while MTCO and the seasonal temperature contrast (TCON) are stable. The methods do not agree on the precipitation patterns during this phase, with MAT showing a trend toward aridity, decreasing WINTERPR and seasonal precipitation contrast (PCON), while the three other methods display a slight precipitation increase and stable PCON. From 166 ka BP onward (pollen zone 2, MIS 6c and 6b), both temperatures and precipitation decrease, and the seasonal contrast between winter and summer climate conditions reduced progressively. The MIS 6 minimum temperatures and precipitation are reconstructed in pollen zone 2 between around 150 and 160 ka BP, corresponding to the transition between MIS 6c and 6b. Subsequently, both temperatures and precipitation increase progressively in the late pollen zone 2 and early pollen zone 3 (MIS 6b to 6a). Between 140-135 ka BP (early MIS 6a), the four methods reconstruct temperatures similar to late MIS 7, a seasonal contrast close to the present, and precipitation higher than the present (except for BRT). This climate optimum is abruptly interrupted by the HS11 extreme arid event between ~134 and ~129 ka BP (pollen zone 4, late MIS 6a), during which temperatures, precipitation and seasonal contrasts are significantly reduced, reaching climate conditions similar to the MIS 6 glacial maxima ~155 ka BP. A short climate amelioration is evidenced at ~132 ka BP (pollen zone 4b), where precipitation and seasonal contrasts increase abruptly. Finally, after 130 ka BP the climate amelioration toward the MIS 5 interglacial conditions happens very fast (pollen zone 5).

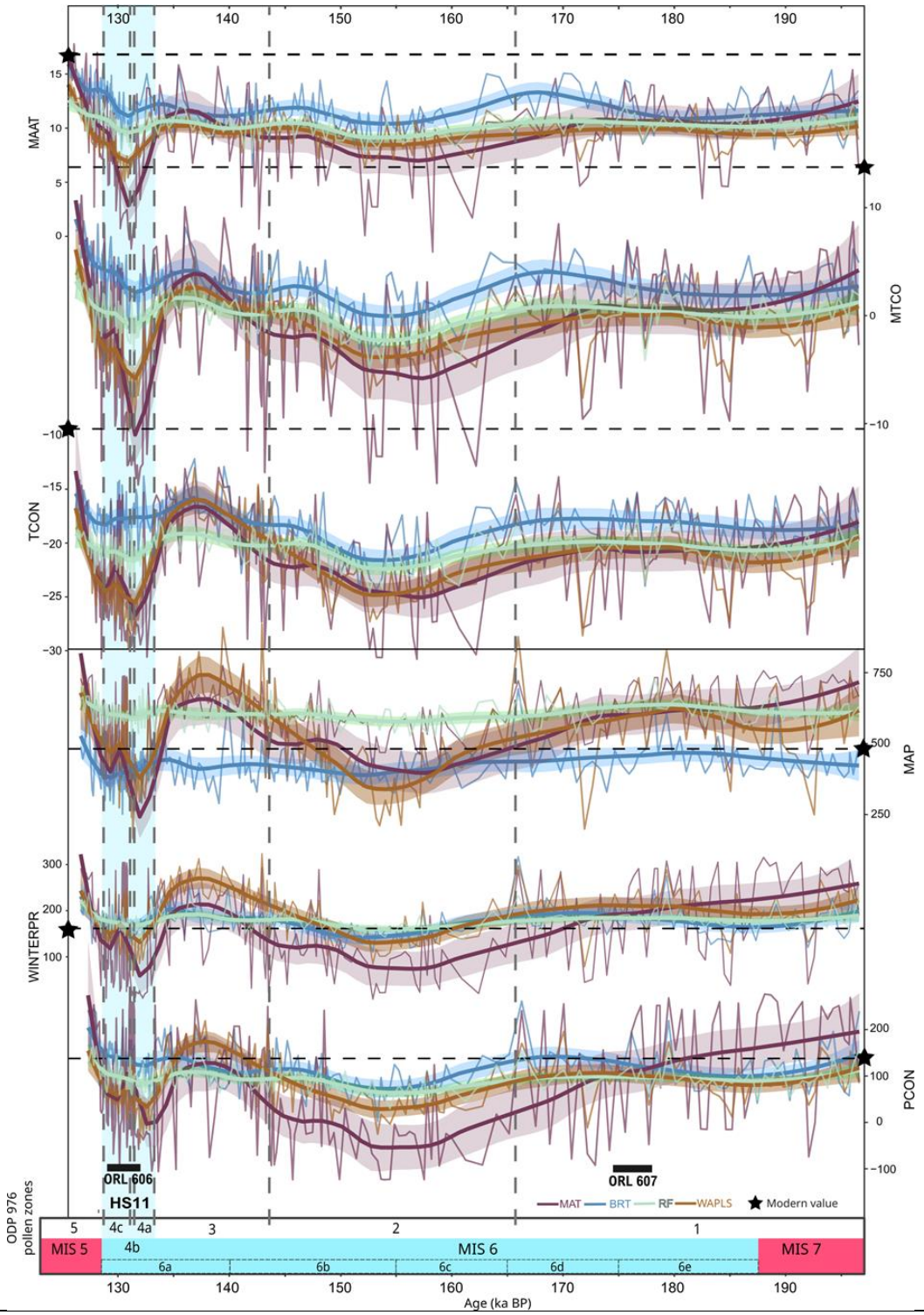


Fig. 6.5. Pollen-based climate reconstructions for MIS 6 interval from the ODP 976 record. MAAT (Mean Annual Temperature), MTCO (Mean Temperature of the Coldest Month), TCON (Temperature Contrast, see methods), MAP (Mean Annual Precipitations), WINTERPR (Winter Precipitations) and PCON (Precipitation contrast, see methods) for the four different methods applied: MAT (Modern Analogue Technique), WA-PLS (Weighted-Averaging Partial Least Square), BRT (Boosted Regression Trees) and RF (Random Forest). The light-coloured interval represents the 95% confidence window, and the bold curves the loess smoothed values (alpha = 0.25). Modern values are indicated by the horizontal dashed line and the black stars (see methods). Grey vertical dashed lines separate the pollen zones defined by CONISS cluster analysis.

	BRT		MAT		WA-PLS		RF	
	R^2	RMSE	R^2	RMSE	R^2	RMSE	R^2	RMSE
MTCO	**0.87**	2.96	**0.88**	3.19	**0.71**	4.44	**0.77**	3.88
MAAT	0.83	2.31	0.83	2.48	0.66	3.22	0.69	3.00
SUMMERPR	0.77	44.86	0.82	46.61	0.52	66.87	0.65	56.48
MAP	0.77	148.52	0.79	163.70	0.50	225.68	0.66	182.32
MTWA	0.76	**2.25**	0.79	**2.33**	0.53	**3.16**	0.61	**2.81**
WINTERPR	0.69	60.69	0.72	65.81	0.43	82.58	0.59	69.34

Table 6.3. R^2 (coefficient of determination) and RMSE (Root Mean Square Error) values for the different climate parameters reconstructed with the four methods applied. The lower the RMSE and the higher the R2 (in bold for each method), the more reliable the reconstruction.

6.2.6. Discussion

6.2.6.1. Paleoenvironment of MIS 6 and Termination II in the western Mediterranean

Important changes are recorded during MIS 6, that are consistent with orbital-scale variability during the different glacial substages.

Three phases can be discerned. The early phase (pollen zone 1) spans late MIS 7, MIS 6e and 6d (~196-166 ka) and is characterized by high percentages of deciduous *Quercus*, *Cedrus* and Cichorioideae, with marked variability and several abrupt semi-desert and steppe increases under cool and humid climate conditions, with seasonal contrast similar to present-day. The middle phase (pollen zone 2) extends from MIS 6c to late 6b (~165-143 ka), and displays the maximum expansion of steppe and semi-desert taxa together with very low temperatures and precipitation between ~160 and ~150 ka BP, a chronology compatible with the maximum Drenthe ice advance (Ehlers et al., 2011). Finally, the late phase (pollen zone 3), spanning late MIS 6b and 6a (~143-133 ka), is marked by a major expansion of Ericaceae vegetation associated with higher reconstructed precipitation and winter temperatures, as well as enhanced seasonal contrast during this phase.

Previous studies are consistent with a subdivision of MIS 6 into three phases characterized by different general trends and amplitude of millennial-scale oscillations (Margari et al., 2014; Nehme et al., 2020). Margari et al. (2014) described an early phase between 185 and 160 ka BP, with warmer and wetter conditions and important rapid climate variability, a middle transitional phase between 160 and 150 ka BP, and a late phase with stable glacial conditions between 150 and 135 ka BP. This three-phasing for MIS 6 glaciation matches our interpretation of ODP 976 pollen zones 1, 2 and 3.

The final phase of MIS 6 is characterized by important changes in vegetation and climate, indicating a rapid modification of vegetation communities and atmospheric configuration at the transition between MIS 6 and MIS 5. Termination II (TII), defined as the period of fast reorganization of the climate system from full glacial (MIS 6) to full interglacial (MIS 5) conditions, is indeed characterized by extreme and fast internal dynamics including a major Heinrich Stadial, HS11 (Broecker & Henderson, 1998; Gouzy et al., 2004; Martrat et al., 2014; Moseley et al., 2015; Ovsepyan & Murdmaa, 2017). The Timing for TII has been estimated based on the initialisation and termination of Weak Asian Monsoon evidenced in the Dongge cave speleothems, lasting from ~136 to 129 ka BP (Bajo et al., 2020; Kelly et al., 2006; Menviel et al., 2019). These boundaries for TII give a total duration of about 7 ka. The timing of TII in the ODP 976 marine record is directly dependent on Dongge Cave chronology (see methods, section 6.2.4.1). Approximately the same duration is observed in the Alboran Sea vegetation response to TII, but with ~1 ka delay. The imprint of HS11 on the vegetation in the Western Mediterranean region is recorded here between 133.3 – 128.8 ka BP (pollen zone 4). This delay in marine and terrestrial proxies may reflect the vegetation response to the first cold pulse of HS11. ODP 976 provides for the first time a very detailed record of vegetation successions during this arid event (pollen zones 4a, 4b and 4c), in agreement with other SSTs and speleothem records that depict a three-phases or "W" pattern for the event (see section 6.2.6.4). After the first rapid increase of steppe and semi-desert taxa (pollen zone 4a), the middle phase shows an abrupt decrease of steppe and semi-desert vegetation, and a fast increase of montane trees (mainly *Cedrus*) percentages (pollen zone 4b). Climate reconstructions reflect this event through a fast increase of both precipitation and temperatures. This pattern is fully compatible with the ODP 976 SSTs trend (Jiménez-Amat & Zahn, 2015; Martrat et al., 2014), although a delay of about 1 kyr is observed between the abrupt drop in alkenone-based SST and the expansion of steppe and semi-desert vegetation. The same way, the abrupt sea surface warming in the middle of HS11 (~133 ka BP) is shifted in the pollen record, to around 131.5 ka BP (pollen zone 4b).

6.2.6.2. Hydroclimate connection with ORLs deposition during MIS 6

Pollen analyses help us to characterize the processes behind Organic Rich Layers (ORLs) deposition in this western Mediterranean region. Like sapropels, ORLs reveal important changes in the water stratification and circulation, with reduced bottom water ventilation and enhanced organic productivity in straight connection with (i) increase in the freshwaters Atlantic inflow at times of deglaciation and (ii) enhanced rivers runoff regionally linked with increased precipitation (Murat, 1999; Pérez-Asensio et al., 2020; Rogerson et al., 2008). Although they are often considered as "ghost sapropels", their timing and the mechanism behind them may differ from those of Eastern Mediterranean sapropels (Rogerson et al., 2008).

ORL bed 607 coincides with a period of enhanced precipitation around 176 ka reconstructed through our pollen-based approach (Fig. 6.7). Its basis appears almost synchronous with the onset of Sapropel S6 layer deposition in the Eastern Mediterranean (Emeis et al., 2003; Rohling et al., 2015; Savannah et al., 2024). Its duration also appears shorter than Sapropel S6, possibly indicating an interruption of favourable climate conditions in the Western Mediterranean region by a stadial event occurring around 172 ka BP and marked by an abrupt decrease in precipitation (Fig. 6.7).

ORL bed 606 was deposited during the second half of Termination II, at a time of deglaciation and directly following the first aridity pulse of HS11. Pollen-based reconstructions show enhanced precipitation and seasonal contrast during this time, suggesting intense precipitation together with deglacial freshwater input as combined causes for ORL deposition in the Western Mediterranean, which finds no counterpart in the Eastern Mediterranean. The implications of such organic layer deposition occurring at times of enhanced precipitations or deglaciation will be furtherly discussed in section 6.2.6.4.

6.2.6.3. Mediterranean vegetation changes during the penultimate glaciation: a synthesis

The ODP 976 pollen record documents MIS 6 vegetation changes in the Western Mediterranean with a temporal resolution comparable to the most detailed terrestrial palynological sequences from the Eastern Mediterranean (Tenaghi Philippon and Ioannina). A W-E transect of Mediterranean palynological records offers valuable insights on the spatial pattern of vegetation changes during the penultimate glaciation (Fig. 6.6).

At the MIS 7-6 transition, no abrupt decline of temperate forest is recorded in the ODP 976 and Padul records, in contrast with central and Eastern pollen records such as Tenaghi Philippon, Ioannina, Ohrid and Castiglione where the transition is very abrupt (Follieri et al., 1988; Koutsodendris et al., 2023; Roucoux et al., 2011; Sadori et al., 2016). At these sites, a higher contrast has been described between interglacial periods with very high percentages of temperate deciduous forest taxa and glacial periods with very reduced tree cover (P. C. Tzedakis, 1993; P. C. Tzedakis et al., 2006). The western Mediterranean region, at the contrary, was generally characterized by a high proportion of herbaceous taxa, even during interglacial periods, attenuating the vegetation contrasts during transitions to glacial periods.

The first half of MIS 6 (~185-165 ka BP) is marked by relatively high percentages of arboreal pollen across all records, especially deciduous forest (Roucoux et al., 2011; Margari et al., 2010, 2014). The abundance of montane taxa (mainly *Cedrus*) is characteristic of ODP 976 record, and reflects the development of altitudinal trees on the Moroccan mountains. Montane elements also increase during

early MIS 6 at Valle di Castiglione, mainly represented by *Fagus* and *Abies* (Follieri et al., 1988), and at Ioannina, mainly represented by *Pinus* (Roucoux et al., 2011). No equivalent pattern is recorded in Padul where herbaceous vegetation is largely dominant. The scarcity of palynological data from the western Mediterranean, especially from North Africa, limits our understanding of the spatio-temporal significance of *Cedrus* expansions during MIS 6, and past glaciations in general.

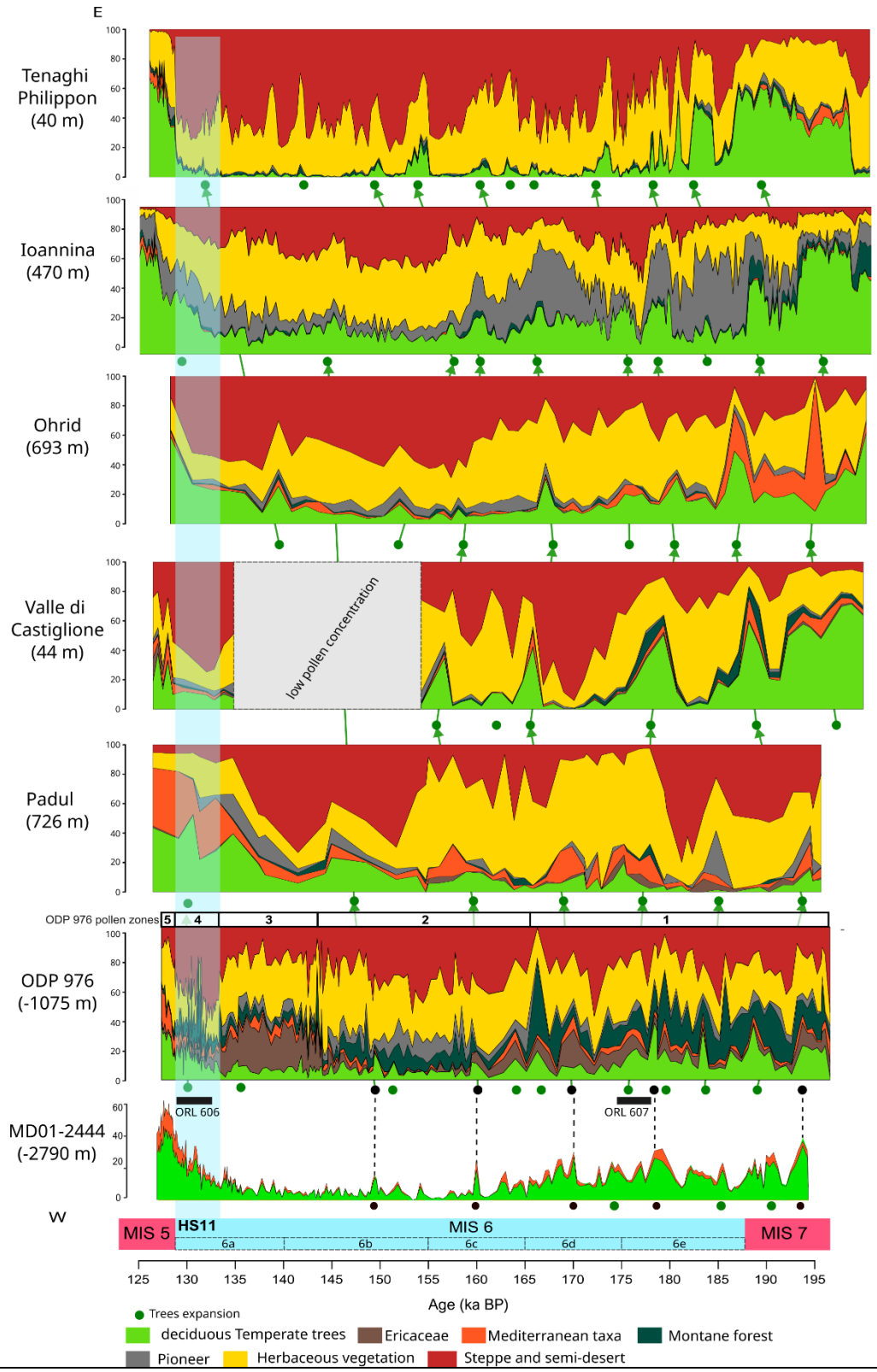


Fig. 6.6. Synthesis of vegetation changes in the Mediterranean during MIS 6 based on available palynological sequences, from west (bottom) to east (top): MD01-2444 (Margari et al., 2010; Tzedakis et al., 2018), ODP 976 (this study), Padul (Camuera et al., 2019), Valle di Castiglione (Follieri et al., 1988), Ohrid (Sadori et al., 2016), Ioannina (Roucoux et al., 2011), Tenaghi Philippon (Koutsodendris et al., 2023). Each synthetic pollen diagram is plotted according to its own age model. ODP 976 and Ioannina's chronologies are based on alignment with MD01-2444 temperate pollen curve on AICC2012 timescale. The ecological groups are the same as for ODP 976, except

Pinus was included in pioneer vegetation at Ioannina, as it is the only record where *Pinus* is not over-represented. Green dots indicate temperate vegetation increases, with tentative correlations between records. The two Organic Rich Layers (ORLs) identified in the ODP 976 core (Murat, 1999), were placed at the bottom.

The main phase of steppe and semi-arid vegetation is recorded between ~165-145 ka BP in the Alboran Sea record, consistent with Ohrid and Ioannina pollen sequences (Fig. 6.6). In Padul, however, the maximum expansion of steppe and semi-desert taxa occurs later, between ~155 and ~137 ka BP. This time window corresponds to the glacial maximum recorded at Azzano X (northern Italy) between 148 and 135 ka BP (Pini et al., 2009), and to a period of low pollen concentration at Valle di Castiglione, likely reflecting full glacial conditions. The ~10 ka lag in the vegetation glacial maxima between ODP 976 and Padul is probably the result of the low temporal resolution of the latter, in addition to differences in the age models used. However, the presence of pioneer vegetation and to a lesser extent of montane elements in Padul during the maximum glacial phase matches the ODP 976 pattern in pollen zone 2, where Cupressoideae and *Cedrus* display high abundance.

A distinctive feature of the Western Mediterranean vegetation recorded during the final stage of MIS 6 (pollen zone 3) is the marked increase in Ericaceae observed in ODP 976 record, and almost absent in the rest of the Mediterranean region. A similar expansion is observed in the Atlantic margin, where core MD01-2444 recorded patterns of Ericaceae expansion matching the three insolation minima during MIS 6 (Margari et al., 2014). Ericaceae development during minimal summer insolation is particularly favoured by reduced summer evaporation at times of low seasonal contrast in precipitation, as already noted in the Alboran Sea during the last glacial (Fletcher & Sánchez Goñi, 2008b) . Following the same interpretation, the expansion of heathland vegetation in the Iberian Peninsula as recorded in ODP 976 during the final stage of MIS 6 may therefore mark the renewed influence of westerlies and Atlantic moisture preceding the onset of the transition to MIS 5 interglacial (Margari et al., 2014). Supporting this state, an increase in temperate deciduous forest at the end of MIS 6 is also seen in Padul, Ohrid and Ioannina records before the transition to MIS 5.

Despite some discrepancies due to the differences in age models and temporal resolutions, all records display comparable variations in temperate pollen percentages during the penultimate glacial. These variations support the persistent sensitivity of Mediterranean plant ecosystems to global-scale millennial climate variability during the penultimate glaciation, with modulation of the vegetation response depending on the local geography. Strong similarities can be observed between ODP 976 and Padul, despite the lower temporal resolution of Padul record. In both sequences, temperate pollen percentages reached ~30 % of total pollen as a maximum during the rapid forest expansions events in the first half of MIS 6. This similarity supports the validity of the ODP 976 marine record to reconstruct

the SW Iberian Peninsula temperate forest history. However, ODP 976 sequence provides a more regional image of the vegetation, including higher percentages of Ericaceae pollen coming from the Atlantic coast, and *Cedrus* pollen from the Moroccan mountains (Jiménez-Moreno et al., 2020), compared to Padul where percentages of Mediterranean taxa and hygrophyte herbaceous are higher due to the local nature of the signal (Camuera et al., 2019). Looking further east, Valle di Castiglione recorded various temperate trees expansions and contractions during the lower MIS 6, before the full glacial conditions. In the Italian Peninsula, various interstadials have also been identified further north at Azzano X (Pini et al., 2009). This pattern was already described during the last climatic cycle and reflects the exacerbated vegetation dynamics locally, with episodes of rapid and enhanced colonization by tree vegetation (Koutsodendris et al., 2023; P. C. Tzedakis, 2005; P. C. Tzedakis et al., 2004). This has been mainly explained by the location of the site in a low altitudinal plain characterized by a more continental climate with lower winter precipitation: tree population at lower altitudinal location are closer to their ecological threshold in term of precipitations, and are likely to be very affected even by minimal changes in the amount of rainfall. On the contrary, the Ioannina record shows the highest deciduous forest percentages of all the records presented here, supporting its character as a local trees refugium (Roucoux et al., 2011).

Termination II displays a particular pattern in vegetation records from the Mediterranean region: while the expansion of trees and temperate vegetation is fast and continuous, HS11 represents at the same time a remarkable episode of abrupt steppe and semi-desert expansion. Although this event is visible in almost all the records, it is particularly prominent in ODP 976 record (pollen zone 4), and appears less pronounced in the eastern Mediterranean sequences. In Padul, no major expansion of xerophyte vegetation is detected, but a small decrease of temperate deciduous taxa was interpreted as the HS11 imprint (Camuera et al., 2019), and the signal might be hindered by the low resolution of the record. A pattern of fast arid vegetation increase contemporaneous to the temperate forest expansion is also found in central Italy at Lago Grande di Monticchio, which was not presented in Fig. 6.6 as its record does not extend beyond 132 ka BP (Allen & Huntley, 2009; Brauer et al., 2007).

Finally, all palynological sequences reveal high-frequency oscillations of temperate and semi-desert pollen, compatible at first look with DO-like variability based on their duration and intensity. They represent a particularly distinctive feature of the lower part of MIS 6.

6.2.6.4. Rapid climate variability during MIS 6: a regional multiproxy comparison

In order to investigate the character of rapid climate variability during MIS 6, a comparison with regional and global climatic archives is essential. The events of arboreal pollen increase observed in the ODP 976 record show percentages and timing comparable to those from the Portuguese margin

core MD01-2444 (Margari et al., 2010, 2014; Tzedakis et al., 2018) (Fig. 7, m). However, the ODP 976 record generally presents lower values of temperate deciduous pollen percentages compared to the Atlantic record, due to its more semiarid Mediterranean influence as previously evidenced for the last glacial period (Charton et al., 2025; Fletcher et al., 2010b). To better capture temperate vegetation dynamics, we added Ericaceae, a clear marker of Atlantic influence in the ODP 976 record, to the deciduous temperate forest, to obtain a "total temperate pollen sum" which enhances the main warming peaks and strengthens the correlation between the two marine cores on both sides of Gibraltar Strait (Fig. 6.7, m and l). The ODP 976 pollen-inferred climate reconstructions show generally consistent patterns with the SSTs trends based on alkenones (Martrat et al., 2004, 2007), and the southern Iberian humidity recorded in the speleothem from Cueva Gitana (Hodge et al., 2008) (Fig. 7, e and g). The ODP 976 pollen record therefore appears to reflect well regional variations in both temperature and humidity across MIS 6.

Warm events in the northern hemisphere are generally well-correlated to peaks in the ODP 976 temperate pollen curve (Fig. 7, c and l). An active bipolar seesaw dynamics was described during the penultimate glacial Davtian & Bard, 2023; EPICA Community Members, 2006; Stocker, 1998), and the Antarctic record was used to elaborate the Greenland GL_T-syn (Greenland temperature synthetic) curve showing predicted $\delta^{18}O$ millennial-scale events for the past glacial eight climatic cycles, which are not directly recorded in Greenland ice (Barker et al., 2011; Bazin et al., 2013; Jouzel et al., 2007). Six Antarctic Isotopic maxima (AIM) events were recognized on the Deuterium curve during MIS 6 (6i to 6vi), correlated with increases in CO2 concentrations and benthic isotope minima in the North Atlantic (Barker et al., 2011; Hodell et al., 2023; Margari et al., 2010, 2014; Shin et al., 2020) (Fig. 6.7, a-c). These AIM and benthic minima in the Atlantic are not easily correlated with steppe expansions in the ODP 976 record, indicating a limited response of vegetation in the Western Mediterranean to the Antarctic warm events.

Barker et al. (2011) predicted the occurrence of eleven millennial-scale warming events during MIS 6 (Fig. 6.7, c), while nine interstadials were recognized in the Alboran Sea from the alkenone record (Fig. 6.7, e), (Martrat et al., 2004, 2007). In the loess record of Harletz in central Europe, ten interstadials were described (Rousseau et al., 2020), strongly matching the Chinese speleothems records of stadial and interstadial events related to the Asian Monsoon dynamics (Cheng et al., 2006; Li et al., 2014; Wang et al., 2018; Wang et al., 2001; Xue et al., 2019). The global nature of fast climate oscillations in the northern hemisphere thus appears controlled by the coupled influence of Atlantic cold events, and tropical monsoon variations as evidenced by the eastern Mediterranean speleothems records from Sofular, Soreq and Kanaan caves (Ayalon et al., 2002; Held et al., 2024; Matthews et al., 2021; Nehme et al., 2018).

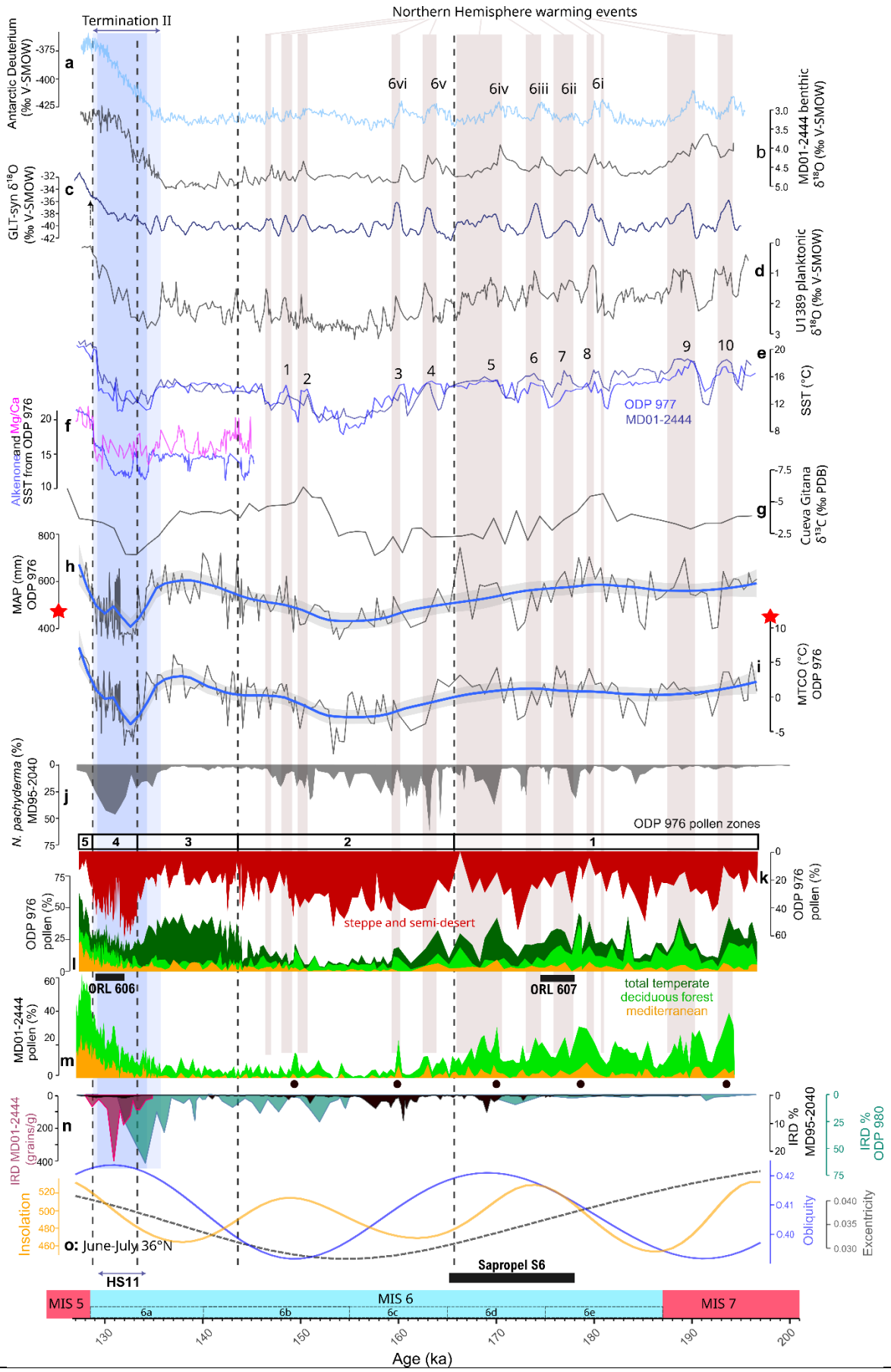


Fig. 6.7. Millennial climate changes during MIS 6. **a)** Antarctic Dome C δD (Bazin et al., 2013; Jouzel et al., 2007); **b)** Benthic $\delta^{18}O$ from MD01-2444 (Margari et al., 2010); **c)** Greenland synthetic $\delta^{18}O$

(Barker et al., 2011); **d)** Planktonic $\delta^{18}O$ from U1389 (Sierro & Andersen, 2022); **e)** alkenone-based SST from ODP 977 (darker blue) and MD01-2444 (lighter blue) (Martrat et al., 2004, 2007)**; f)** Alkenone-based SST (Martrat et al., 2014) and Mg/Ca-based SST (Jiménez-Amat & Zahn, 2015) from ODP 976; **g)** $\delta^{18}C$ from Cueva Gitana (Hodge et al., 2008); **h)** Mean Annual Precipitation (MAP) reconstructed from ODP 976 pollen assemblage, mean of the four methods used in this study (MAT, WA-PLS, RF, BRT), with the red star showing the modern value ; **i)** Mean Temperature of the Coldest Month (MTCO) reconstructed from ODP 976 pollen assemblage, mean of the four methods used in this study (MAT, WA-PLS, RF, BRT)), with the red star showing the modern value; **j)** *N. pachyderma* percentages from MD95-2040 (de Abreu et al., 2003; Voelker & de Abreu, 2011); **k)** ODP 976 pollen percentages of semi-desert and steppe taxa, with ODP 976 pollen zones (this study); **l)** ODP 976 pollen percentages of total temperate taxa including temperate deciduous forest + Ericaceae + Mediterranean (dark green), deciduous forest (light green), Mediterranean (orange) (this study); **m)** MD01-2444 pollen percentages of temperate tree (light green) and Mediterranean (orange) taxa (Margari et al., 2010; Tzedakis et al., 2018); **n)** Ice-Rafted Debris (IRD) percentages from MD01-2444, 37° N (pink) (Skinner & Shackleton, 2006) redrawn from Tzedakis et al. (2018), MD95-2040 (black), 40°N (de Abreu et al., 2003) and ODP 980 (blue), 55°N (McManus et al., 1999; Oppo et al., 2001, 2006); **o)** orbital parameters (Laskar et al., 2004) calculated for June-July at 36°N: Eccentricity (black), Obliquity (blue) and Insolation (yellow). The black rectangle indicates the interval of deposition of Sapropel layer S6 in the eastern Mediterranean (Ziegler et al., 2010). The marine substages MIS 6a-e follow (Railsback et al., 2015). All data are plotted on AICC2012 chronology (Bazin et al., 2013) following Sierro et al. (2020, 2022), except for the IRD records and Gitana Cave which is plotted on its own age model based on U-series absolute dating. The vertical grey bars indicate the Northern Atlantic interstadial events based on the planktonic isotope record and the predicted D-O events from Greenland synthetic record, with the numbers of the Alboran interstadials (AI-1 to AI-10) from Martrat et al. (2004, 2007). Numbers 6i-6vi correspond to the Antarctic Isotope Maxima (AIM) from Margari et al. (2010). The vertical blue bar represents Heinrich Stadial 11 (HS11). Black dots and dotted lines show the five temperate pollen peaks in MD01-2444 used as control points for ODP 976 chronology.

The three phases identified during MIS 6 based on the ODP 976 vegetation and climate record can be compared with regional and global records to be interpreted in a broader context, based on general climatic trends and the expression of climatic instability:

Early MIS 6 (187-166 ka BP): warm/wet conditions and instability. The first phase encompasses the two substages MIS 6e and 6d, and is characterized by humid and rather warm climate conditions in the Mediterranean at the transition from MIS 7 to MIS 6. This phase aligns well with the deposition of ORL bed 607 in the Alboran Sea, and the sapropel layer S6 in the Eastern Mediterranean, associated with the maximum summer insolation and increased intensification of the summer monsoonal system in the eastern Mediterranean between 178.5 to 165.5 ka (Emeis et al., 2003; Rohling et al., 2015; Ziegler et al., 2010). At the same time of S6 deposition, Cheddadi and Rossignol-Strick (1995) described an increase in temperate pollen in the Nile region, and Soreq cave speleothem records climatic conditions typical of an interglacial (Ayalon et al., 2002). Sapropel depositions usually occur during interglacial periods as MIS 1 (Holocene), which makes sapropel S6 an exceptional feature of early MIS 6. It reflects particularly warm and humid conditions, and intense freshwater input in the

Mediterranean which can result from various sources, including increased rainfall and monsoon activity, Atlantic freshwater entrance, and enhanced river discharges (Sierro & Andersen, 2022). The long speleothem records in China report a period of northern shift of the Intertropical Convergence Zone associated with enhanced Asian Monsoon activity during this phase (Wang et al., 2018). Higher pluviometry is also supported by foraminifera isotopic and SSTs signal throughout the Mediterranean Sea, which were used to reconstruct past salinity and freshwater budget regionally (Kallel et al., 2000). Enhanced rainfall in the Balkans is evidenced by the Ioannina lake deepening (Wilson et al., 2021), and a more humid period is documented in speleothem records from Argentarola cave in Italy (Bard et al., 2002) and Gitana cave in southern Spain (Hodge et al., 2008) (Fig. 6.7, g). Therefore, humid conditions during this phase were not restricted to the eastern Mediterranean where the sapropel deposition occurred. ODP 976 organic layer 607 together with the pollen-based climate reconstructions support this view, with enhanced seasonal precipitation contrast during this interval driven by enhanced winter precipitations (Fig. 6.5). Comparison with Padul pollen-based hydroclimate reconstructions (Camuera et al., 2022) further strengthens this scenario: despite the chronological delay between the two sequences, this early MIS 6 humid phase and ORL deposition likely matches the Western Mediterranean Humid Period (WMHP 6) dated between 180-155 ka BP (Fig. 6.8). The same study made the case for a co-occurrence of humid periods in the Western Mediterranean and in West Africa (African Humid Periods) during periods of high precipitations seasonality and enhanced West African Monsoon. Pollen-inferred climate reconstructions from lake Ohrid have also shown the phase relationship between African Monsoons and periods of high winter precipitations in the Mediterranean region (Wagner et al., 2019; Sinopoli et al., 2019).

Another characteristic of this early MIS 6 phase is the strong variations in pollen and isotopic curves in the Atlantic and Western Mediterranean (Fig. 6.7, a-d and l-m). Variations in temperate deciduous and Ericaceae percentages are observed in the ODP 976 record, in close correspondence with the Atlantic record from MD01-2444. The largest interstadial peak in ODP 976 around 179 ka BP is also identified in all the different records and marked by warmer conditions in the sea, and more effective precipitations in SE Iberia (Hodge et al., 2008). It is well correlated with the stadial following Antarctic event 6i (Margari et al., 2010), the associated predicted millennial-scale warming event in Greenland synthetic curve, and the Alboran Sea SST interstadial event 8 (Martrat et al., 2004). In Padul record, the temperate deciduous, Mediterranean and *Abies* percentages increase correlates well with this event (Camuera et al., 2019). It could also match the WMHP 6.1 interstadial (Camuera et al., 2022) (Fig. 6.8). This large interstadial was suggested to be at the origin of the initialisation of the sapropel S6 deposition (Sierro & Andersen, 2022), and could also have participated in the initialization of ORL 607 deposition in the Alboran Sea (Murat, 1999). On the other hand, the most important tree

population decline and semi-desert expansion in ODP 976 is recorded at ~172 ka BP, which could match Antarctic event 6iv, and is associated to a moderate increase of IRD deposition at the latitude of ODP 980 (Fig. 6.7, n). A similar stadial can be observed in the Ioannina and Tenaghi Philippon records with a close chronology (Roucoux et al., 2011) (Fig. 6.6). Dry conditions at this time are also recorded in the eastern Mediterranean as shown in the Pentadactylos and Soreq speleothems (Ayalon et al., 2002; Nehme et al., 2018).

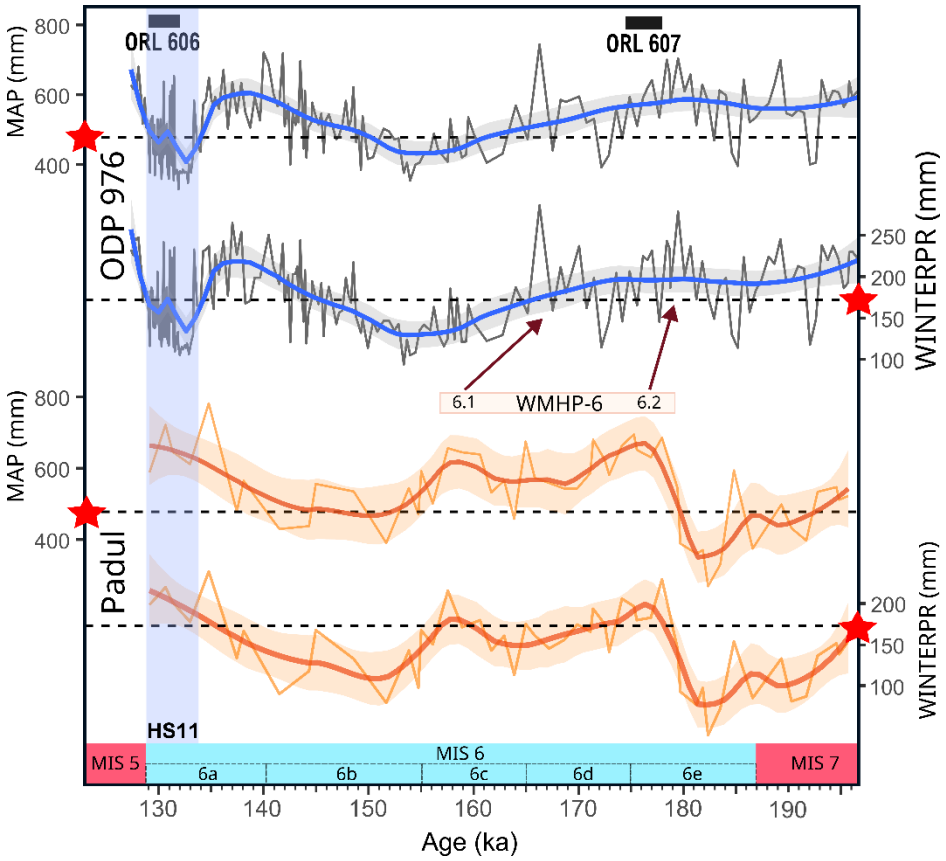


Fig. 6.8. Comparison between the precipitation pattern reconstructed from ODP 976 with our multi-method approach (mean) (this study) and from Padul with only the WA-PLS method (Camuera et al., 2022). Mean Annual Precipitation (MAP) and Winter Precipitation (WINTERPR) are represented, together with the two Organic Rich Layers (ORLs) identified in ODP 976 (Murat, 1999) and the Western Mediterranean Humid Period (WMHP) 6 defined by Camuera et al. (2022). Red arrows indicate tentative correlation between the two phases of WMHP 6, and the precipitation reconstructions from ODP 976. Red stars and dashed lines indicate the modern climate value (see methods).

Middle MIS 6 (165-144 ka BP): maximum glacial conditions and stability. This phase is marked by the maximum expansion of semi-desert vegetation and the almost complete collapse of forest vegetation between ~163 and 150 ka BP, according to the ODP 976 pollen and MD01-2444 records, synchronous with the minimum in orbital eccentricity. This is in agreement with the lowest SSTs values reconstructed in the Alboran Sea from the alkenone record occurring around 155 ka BP, and low SSTs in the Gulf of Lions too (Cortina et al., 2015). At the same time, high percentages of the cold species *N.*

pachyderma, together with important ice-detritus pulses, are recorded on the Portuguese margin (de Abreu et al., 2003), (Fig. 6.7, j and n). The occurrence of the cold Atlantic species *Limacina retroversa* shells in the ODP 976 sediments at ~155 ka BP is consistent with the enhanced entrance of cold subpolar water masses in the Alboran sea at the time of full glacial conditions. In parallel, there is an intensification of "Fleuve Manche" paleo river discharges evidenced in various sedimentary cores from the Bay of Biscay (Boswell et al., 2019; Eynaud et al., 2007; Penaud et al., 2009, 2016; Toucanne, Zaragosi, Bourillet, Cremer, Eynaud, Van Vliet-Lanoë, Penaud, Fontanier, Turon, Cortijo, et al., 2009), and a fluvial aggradation linked with reduced vegetation cover in Spanish river basins (Macklin et al., 2002). A long-term aridification is recorded in SE Spain in Gitana cave close to the ODP 976 location (Hodge et al., 2008). The glacial maximum in Soreq cave speleothem is also recorded around 154 ka BP (Bard et al., 2002), and might be responsible for the hiatus in the Pentadactylos speleothem in Cyprus (Nehme et al., 2020). In Italy, the Tana che Urla cave also recorded cooling and aridification between 159-132 ka BP, indicated by both the carbon and oxygen isotopic ratio (Regattieri et al., 2014). The coolest phase in Abaliget Cave speleothem in central Europe is also recorded at that time (Koltai et al., 2017). Climate conditions reconstructed at ODP 976 site during this phase show the maximum aridity and cold temperatures, which are consistent and fall within the range of reconstructed temperatures and precipitations at the same time at Ohrid (Sinopoli et al., 2019). This main phase of glaciation in Europe took place after 163 ka BP, corresponding to the Drenthe glacial advance (Ehlers et al., 2018; Margari et al., 2014). The maximum ice expansion probably led to the almost complete collapse of temperate vegetation across the Mediterranean region, except in specific climate refugia's like Ioannina or Padul (Fig. 6.6). The Mediterranean vegetation taxa were particularly affected and almost disappeared at this time in the ODP 976 record.

Few interstadial events are observed during this cold and dry phase, probably due to the extended ice volume reaching a critical threshold (McManus et al., 1999) and leading to higher climate stability at time of glacial maximum expansion (F. J. Sierro & Andersen, 2022). One moderate interstadial event around 150 ka BP is expressed in the ODP 976 and MD01-2444 records through an increase in temperate deciduous tree taxa (Fig. 6.7, l and m). It may correspond to the interstadial recognized in Gitana Cave speleothem approximately at the same time, and is compatible with the Alboran Interstadial events 1 or 2 (Martrat et al., 2004), while a larger trees increase in Padul record is also observed (Camuera et al., 2019) (Fig. 6.6). It is also compatible with interstadials recognized in other speleothem records in eastern and central Mediterranean (Ayalon et al., 2002; Bard et al., 2002; Regattieri et al., 2014). Sierro et al. (2022) described a major event of low Mediterranean overturning and high freshwater entrance through the Gibraltar Strait at that time and contemporaneous to the insolation maximum (Fig. 6.7, o). This configuration was similar to the one contemporaneous to

sapropel S6 and ORL 607 deposition during early MIS 6, but did not lead to any new sapropel deposition at 150 ka BP, probably because the climate conditions were more favourable but not enough for a sapropel deposition.

Late MIS 6 (144-129 ka BP): increased precipitation during the last glacial, and arid conditions during HS11. Between 150 and 140 ka BP, warmer and wetter conditions are indicated by ODP 976 pollen percentages of Ericaceae (pollen zone 3). Ericaceae expansions in the Iberian margin sediments were found to be associated to insolation minima in core MD01-2444 (Margari et al., 2014). This pattern is consistent with the ODP 976 Ericaceae curve (Fig. 6.7, l). The climate reconstructions evidenced high precipitations and especially high WINTERPR values. These higher humidity and temperature values are supported by the carbon isotope record from Gitana Cave (Hodge et al., 2008) and the Alboran Sea SSTs (Martrat et al., 2007). In central Europe, Abaliget Cave speleothem also show more favourable climate conditions during this phase (Koltai et al., 2017). Climatic oscillations appear subdued in the Western Mediterranean pollen records during this last phase. The high resolution ODP 976 record shows some SST variations (Jiménez-Amat & Zahn, 2015; Martrat et al., 2014) : Ericaceae pollen contractions and semi-desert elements expansions could be correlated to three abrupt drops in alkenone-based SSTs at 144, 142, and 139 ka BP (Fig. 6.7, f, k and l). Fifteen Chinese Interstadials (CIS) were identified at Hulu Cave during late MIS 6, linked with Asian Monsoon dynamics (Wang et al., 2018), and the ultra-high-resolution record of planktonic isotope ratio at U1389 by Sierro and Andersen (2022) also expresses some variability. However, the vegetation response in the SW Mediterranean was apparently limited.

Following the Ericaceae expansion, the most prominent feature of the late MIS 6 phase is the large and fast expansion of steppe and semi-desert vegetation during HS11, between 133 and 129 ka BP (pollen zone 4). It is characterized by a first large IRD peak at high latitude (ODP 980) around 134 ka BP, and later at the MD01-2444 latitude, around 131 ka BP (Skinner & Shackleton, 2006; Tzedakis et al., 2018). This event also corresponds to an increase in the oxygen isotopic ratio at the Portuguese margin (especially planktonic, starting around 136 ka BP), also broadly synchronous to an important decrease in SSTs of the Atlantic and the Mediterranean Sea (Jiménez-Amat & Zahn, 2015; Martrat et al., 2004, 2007, 2014). A pronounced increase in *N. pachyderma* (sinistral) abundance is also recorded on the Portuguese margin (Voelker & de Abreu, 2011). Climate reconstructions show particularly harsh conditions in the Western Mediterranean region during this event, compatible with the reconstructions from Lake Ohrid (Sinopoli et al., 2019) and from three French sites (Les Echets, la Grande Pile and Le Bouchet) for the latest phase of MIS 6 (Guiot et al., 1989, 1993). An arid phase is also evidenced at Gitana Cave (Hodge et al., 2008), which closely matches the trend of the ODP 976 precipitation curve (Fig. 6.8). Aridity is evidenced in other speleothem records in Europe like Villars

(Wainer et al., 2011), Sieben in the Alps (Moseley et al., 2015), and Abaliget cave in central Europe (Koltai et al., 2017). Dryness over western Europe is also supported by an episode of intense loess deposition in Rodderberg crater in northern Germany between 136-129 ka BP (J. Zhang et al., 2024). If HS11 is also recorded in China speleothems (Wang et al., 2018), it appears subdued in the eastern palynological Mediterranean records (Fig. 6.6), indicating that the Western Mediterranean region was more severely impacted by the dry and cold pulse of HS11. The "double u" shape of HS11 described in section 5.1 for the ODP 976 record matches well the Hulu cave record, where the particular event in the middle of HS11 was linked with a strong Asian Monsoon episode that could represent an analogue to the Bølling-Allerød during Termination I (Wang et al., 2018). The fast and multiphase vegetation and climate dynamics evidenced in the ODP 976 record is in agreement with the description of a "HS11 complex" with multiple phases (Tzedakis et al., 2018), and will require more focused attention in the future.

HS11 has been described as a "pause" in the glacial termination II (Gouzy et al., 2004; Hodge et al., 2008). However, in the ODP 976 and MD01-2444 records, temperate vegetation keeps increasing all along the event, despite the supposed cessation of the warming and moistening trend for almost 2000 years. Therefore, the trend toward increased temperate vegetation during Termination II did not seem to be strongly affected by the abrupt arid event, following the continuous climate amelioration described in various speleothem records from Italy covering Termination II, at Corchia cave, Tana che Urla and Argentarola (Bard et al., 2002; Drysdale et al., 2005; Regattieri et al., 2014). On the contrary, the Gitana Cave speleothem records a strong moisture deficit (Fig. 6.7, g), supporting a stronger impact of HS11 in the SW Mediterranean compared to the Italian Peninsula.

Finally, it is to be pointed out that HS12, occurring around 140 ka BP (Lisiecki & Stern, 2016), apparently did not have any imprint on the vegetation record of ODP 976, implying a subdued impact of this event on Mediterranean vegetation compared to HS11.

6.2.6.5. Comparison of MIS 6 with the last glacial period (MIS 4-2)

Various studies have pointed out strong similarities between the millennial-scale oscillations of the last glacial period and the penultimate glacial period, with the division between MIS 3 and MIS 2 being analogous to the early and mid-late phase of MIS 6 respectively (Held et al., 2024; Margari et al., 2010, 2014; Roucoux et al., 2011; Rousseau et al., 2020; Shin et al., 2020; Sierro et al., 2020). The same studies argued in favour of pervasive impact of stadial events on the continental climate and vegetation in the Mediterranean region, even in absence of typical Heinrich layers (Roucoux et al., 2011). The ODP 976 record shows a cooling and aridification trend during the first half of MIS 6 (Fig.

6.9), with decreasing intensity of interstadials events, that recalls the pattern of MIS 3 D-O cycles (Bond et al., 1993).

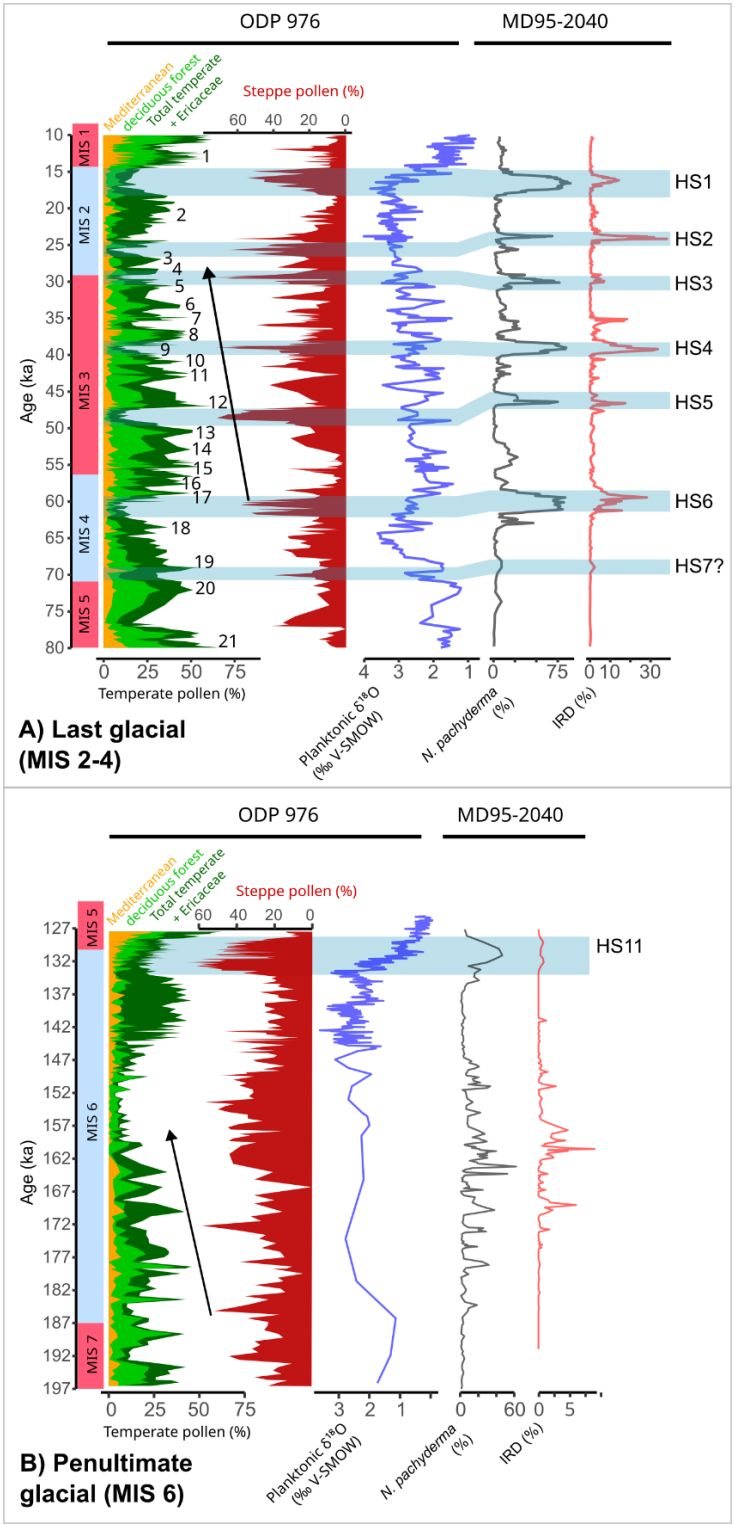


Fig. 6.9. Comparison of millennial changes during A) the last glacial (MIS 2-4) and B) the penultimate glacial (MIS 6), including the main pollen data from ODP 976 (Charton et al., 2025; Combourieu-Nebout et al., 2002, 2009, and unpublished data for the last climatic cycle, and this

study for MIS 6), the ODP 976 planktonic isotopic ratio from *G. bulloides* (Combourieu-Nebout et al., 2002; Jiménez-Amat & Zahn, 2015; von Grafenstein et al., 1999, and unpublished data), and the *N. pachyderma* and IRD record from core MD95-2040 (de Abreu et al., 2003; Voelker & de Abreu, 2011). Marine Isotope Stages follow the boundaries from Lisiecki & Raymo (2005). Numbers on the Last Glacial correspond to the Greenland D-O events chronology (Fletcher et al., 2010a; Rasmussen et al., 2014). Black arrows mark the aridification trend and decreasing interstadials intensity during MIS 3 and early MIS 6.

However, the absence of clear successions of stadial events and especially Heinrich stadials, together with the more subdued expression of interstadials in the vegetation record, limits the resemblance between the two glacial periods. The pacing of interstadial peaks also seems to be reduced compared to the last glacial period high-frequency oscillations, as previously highlighted from the high-resolution speleothem record from Sofular cave in Turkey (Held et al., 2024).

A comparison of millennial-scale changes during the past two glacial periods based on the ODP 976 and MD95-2040 records, on either side of the Gibraltar Strait, support our view (Fig. 6.9). The last glacial period (encompassing MIS 4 to MIS 2) was characterized in the Alboran Sea by high-intensity oscillations in both temperate and semi-desert vegetation correlated with D-O cycles and intense ice-rafting events HE1 to HE7 in MD95-2040. During interstadial events, temperate and Mediterranean vegetation (deciduous forest + Mediterranean + Ericaceae) could reach values above 60 % of total pollen; during stadial events, the semi-desert pollen values reached values as high as 70% of total pollen (during HS3, HS4 and HS5). In comparison, the penultimate glacial (MIS 6) displays much lower intensity events, with interstadials characterized by 45% as a maximum value for temperate vegetation, and stadials with 65% for the steppe and semi-desert vegetation (during HS11). High-intensity cold episodes during MIS 6 are limited to the HS11, and the ~172 ka BP event. This is consistent with the multiproxy record of core MD95-2040 on the Portuguese margin, which evidenced reduced variability in the *N. pachyderma* abundance and IRD deposition during the penultimate glacial compared to the last glacial (de Abreu et al., 2003). The ice rafting episodes appear to be of different nature during MIS 6 (Hodell et al., 2008; Liu et al., 2018; McCarron et al., 2021), with the main iceberg discharges originating from the European ice sheet, contrary to the typical Hudson Strait origin of the last glacial Heinrich events. SST reconstructions in the western Mediterranean also show less intense cooling during MIS 6 than during MIS 3 (Martrat et al., 2004, 2007), supporting limited incursions of polar waters in the Mediterranean during MIS 6 compared to MIS 3 coldest stadials, and especially Heinrich stadials (Cacho et al., 1999).

Like ODP 976, Ioannina records lower intensity arboreal pollen oscillations during early MIS 6 compared to the last glacial (Roucoux et al., 2011). In comparison, the Atlantic pollen record from MD01-2444 core displays similar amplitude of tree percentages during the last and the penultimate

glacial (Margari et al., 2010). This difference can be explained by the different climate conditions, and the higher sensitivity to cold and aridity of sclerophyllous and deciduous forest vegetation on the Mediterranean side, as recorded in the ODP 976 and Ioannina palynological sequence. It appears that temperate vegetation in SW Mediterranean responded to millennial climate oscillations with higher intensity during the last glacial compared to the penultimate, probably because the climate in Europe was colder during MIS 6 compared to MIS 2. This is supported by larger European ice-sheet extension during the penultimate glacial (Ehlers et al., 2011; Ehlers & Gibbard, 2007; Shackleton, 1987), favouring the long-term establishment of open landscapes mainly composed by steppe and semi-desert plants. The differences in humidity might not be as easily interpretable, with an early MIS 6 more humid, and a MIS 6 glacial maximum more arid, compared to MIS 3 and MIS 2 as also suggested by the Ioannina record (Roucoux et al., 2011). Future climate reconstructions applied to the complete last glacial cycle in ODP 976 and other Mediterranean long pollen sequences will help understanding the different climate configurations between the last two glacial periods.

6.2.6.6. Human occupation during MIS 6 in SW Europe

Only a limited number of sites in South-Western Europe has yielded archaeological layers attributed to MIS 6, and even fewer of them have been radiometrically dated allowing for a robust comparison with the environmental changes during MIS 6 (Fig. 6.10, Supplements table S5). The environmental proxies available in the archaeological layers (pollen, charcoal, macro and microfauna) can help the chronological attribution, but are often insufficient to establish a precise correlation with the high-resolution chrono-environmental framework of marine and glacial archives. Even when absolute dates are available, their large uncertainty range and the poor resolution of the archaeological record represent a major limitation and make it difficult to correlate the human occupation phases with a specific substage of MIS 6.

It is generally accepted that the northern part of Europe was almost completely depopulated during MIS 6, with very few sites identified compared to the southern European fringes, indicating discontinuous occupation during more favourable climatic episodes (Hérisson et al., 2016) or total abandonment like in the British lands (Scott, 2011; Shaw et al., 2016; White & Pettitt, 2011). Southern France, Italy and the Iberian Peninsula could have represented climate refugia during the most extreme ice-cap advances (Bicho & Carvalho, 2022). Notably, Italy is particularly deprived of sites well-dated to MIS 6 including the isolated Neanderthal of Altamura, the short episode of elephant scavenging at Poggetti Vecchi, and the long sequence of San Bernardino cave which chronological range extends up to ~154 ka BP, a period marked by the most extensive glacial conditions of MIS 6. Some other few archaeological layers have been attributed to MIS 6, but they lack a robust chronological attribution

(Aureli & Ronchitelli, 2018; Fontana et al., 2010, Fig. 6.10). One can hypothesise that regional climate conditions in the peninsula were particularly harsh after 150 ka, and that potential refugia sites remain to be identified in Italy. Palaeoecological reconstructions at the Poggetti Vecchi site indicated cold and dry open environment (Aranguren et al., 2019; Benvenuti et al., 2017). Interestingly, the chronological range for the site could coincide with a major stadial event at 171 ka BP identified in the ODP 976 core, and particularly well expressed in the Valle di Castiglione record (Fig. 6.6).

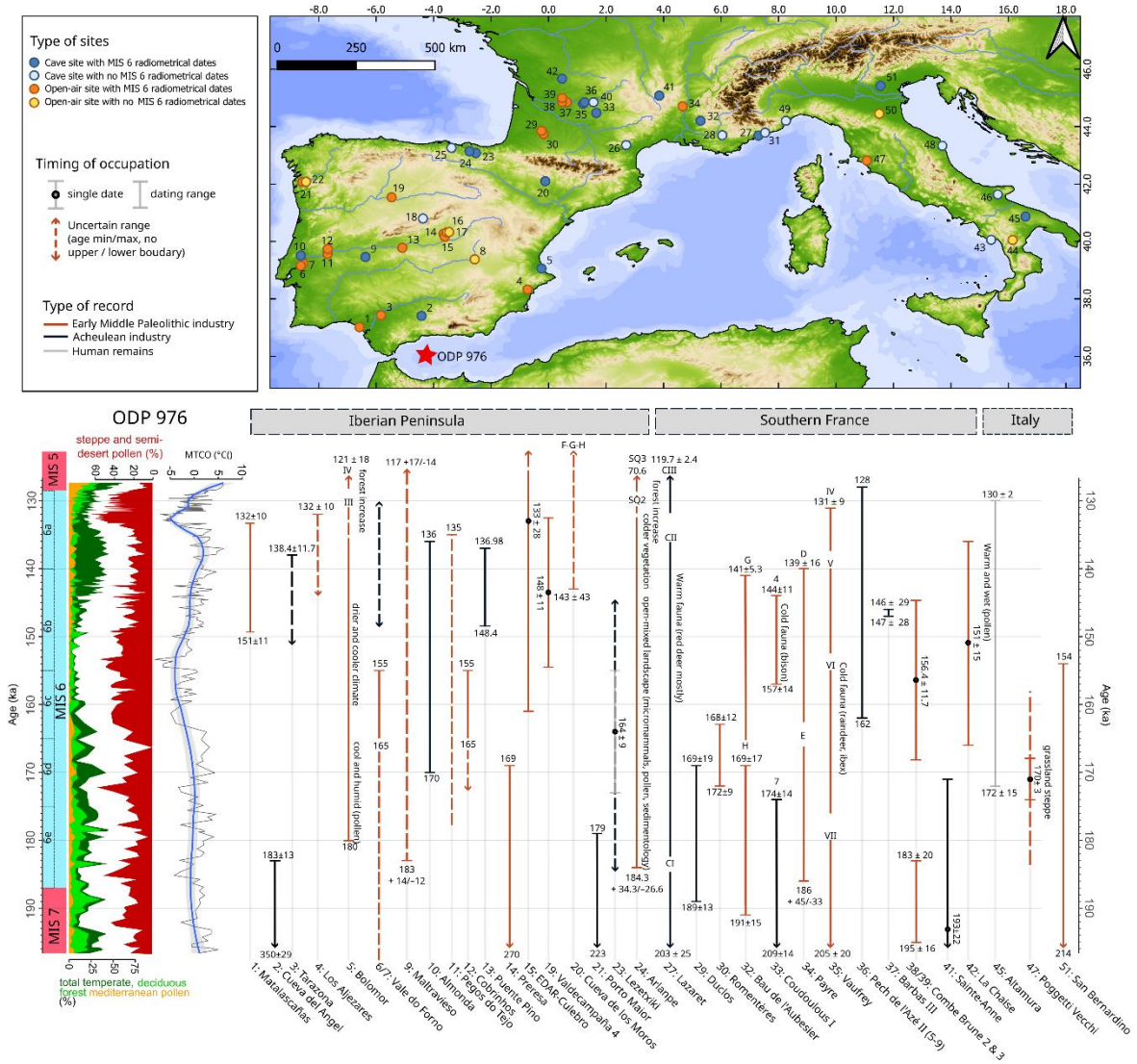


Fig. 6.10. Distribution of archaeological sites and radiometrically dated human occupation in western Mediterranean attributed to MIS 6, with some relevant palaeoecological information when available. The dates used and references can be found in Supplementary table S3. Sites on the map are numbered from south to north in each country: **1**: Matalascañas ; **2**: Cueva del Angel ; **3**: Tarazona ; **4**: Los Aljezares ; **5**: Cueva del Bolomor ; **6**: Vale do Forno ; **7**: VF3 (Milharos) ; 8: El Provencio ; **9**: Cueva de Maltravieso ; **10**: Almonda ; **11**: Pegos do Tejo ; **12**: Cobrinhos ; **13**: Puente Pino ; **14**: Preresa ; **15**: EDAR-Culebro 2 ; **16**: Arriaga II/III ; **17**: Arganda II (Valdocarros) ; **18**: Villacastin ; **19**: Valdecampana ; **20**: Cueva de los Moros de Gabasa; **21**: Porto Maior; **22** : Arbo; **23**: Lezetxiki ; **24** : Arlanpe ; **25**: Ventalaperra ; **26**: Aldènes ; **27** : Grotte du Lazaret ; **28** : Baume Bonne ; **29** : Duclos ; **30**: Romenteres ; **31**: Grotte du Prince ; **32**: Bau de l'Aubesier; **33**: Coudoulous I ; **34**: Payre ; **35**:

Grotte Vaufrey ; **36** : Pech de l'Aze II ; **37**: Barbas III ; **38**: Combe Brune 3 ; **39**: Combe Brune 2 ; **40**: Grotte Sirogne; **41**: Sainte -Anne ; **42**: La Chaise ; **43**: Riparo del Poggio; **44**: Rosaneto; **45**: Altamura; **46**: Riparo Paglicci; **47**: Poggetti Vecchi ; **48**: Monte Conero; **49**: Grotta del Colombo; **50**: Due Pozzi/Scornetta; **51**: Grotta di San Bernardino.

In Southern France and the Iberian Peninsula, according to available radiometric dates, human occupation appears to have been continuous across MIS 6, even during the glacial maximum, with both cave and open-air sites. France provides a comparable number of cave and open-air sites mainly concentrated in the southwestern region. The Portuguese record is mainly constituted by open-air sites in fluvial terrace systems of the lower Tagus, offering important insights into short-term occupations during the full-glacial stage, but with complex chronological attribution (Cunha et al., 2012, 2017; Pereira et al., 2019). The Spanish record includes various open-air settlements in the upper Tagus valley (Panera et al., 2011, 2014; Yravedra et al., 2019), as well as the Duero (Diez-Martín, 2010) and the Guadalquivir (Caro Gómez et al., 2011) valleys. Cave sites are fewer and are mainly located closer to the coast (Cueva del Bolomor, Cueva del Angel, Lezetxiki, Arlanpe, Ventalaperra), with the two exceptions of Cueva de Maltravieso and Villacastín. Key sites like Lazaret Cave (Late Acheulean, France) and Cueva del Bolomor (Middle Palaeolithic, Spain) evidence the persistence of human groups in possible climate refugia (Ochando et al., 2019a; Valensi et al., 2005).

MIS 6 in Europe saw the final stage of the cultural transition from the Lower to the Middle Palaeolithic industries (MIS 8-5), mainly characterized by the emergence of more complex core technologies such as Levallois debitage and changes in subsistence strategies. No rupture is observed between the technocomplexes, as cultural diversity and the permanence of Acheulean bifacial tools associated to technological innovation mark these Early Middle Palaeolithic industries in Southern Europe (Santonja et al., 2016; Terradillos-Bernal et al., 2023). The distribution of archaeological sites and timing of human occupation in South-Western Mediterranean at that time reflect this pattern. A mosaic of traditional and innovative behavioural traits can be observed, with late Acheulean and Early Middle Palaeolithic coexisting continuously (Cueto et al., 2016; de Lumley, 2018; Mathias et al., 2020; Moncel et al., 2025; Santonja et al., 2022; Torres et al., 2024; Valensi et al., 2013). Acheulean technocomplexes are progressively abandoned during MIS 6 in Europe (Álvarez-Alonso, 2014; Key et al., 2021), with the latest chronologies found possibly in the Manzanares basin in central Iberia at Arriaga sites (Panera et al., 2014; Rubio-Jara et al., 2016; Rubio-Jara & Panera, 2019; Silva et al., 2013), or at Lazaret cave (Michel et al., 2022), and dated to the beginning of MIS 5. No clear explanation is accepted for the emergence and generalization of the Levallois debitage, and while cognition might not be the only factor, some authors suggested that MIS 6 glaciation could have played a role in the final abandonment of Acheulean industries (Moncel et al., 2020; Valensi et al., 2005). It is hard to claim that specific environmental pressures favoured Levallois technology over bifacial production, as these

lithic technologies seem to have co-existed in Western Europe since MIS 12-11 over several glacial/interglacial cycles (Baena et al., 2017; Moncel et al., 2020), including extremely cold stages (like MIS 12 and 10). This "mosaic" pattern for the lower to middle palaeolithic transition, although at least partly imputable to the large dating uncertainties, points toward more complex processes leading to the generalization of Middle Palaeolithic industries from MIS 5. Interestingly, the end of the Lower to Middle Palaeolithic transition is also associated with a shift in the morphology of human remains, from "Early Neanderthals" (MIS 7-5) to "Classical Neanderthals" (MIS 5-3) (Di Vincenzo & Manzi, 2023). Sites like La Chaise (Abri Suard), Lazaret and Altamura provide fossil evidence for these "Early Neanderthals" which share characteristics with earlier Middle Pleistocene populations, and with later Neanderthals (Buzi et al., 2025; Couture-Veschambre et al., 2021; de Lumley, 2018). Genetic data also support an important population shift in western Europe sometimes around the transition from MIS 6 to MIS 5 (Peyrégne et al., 2019). Therefore, an important population reorganization seems to have occurred at the time of the final Acheulean industries, leading to the onset of the so-called "Classical neanderthal world" in western Eurasia, with generalized Middle Palaeolithic industries and established Neanderthal morphological features. The role of environmental changes occurring during MIS 6 in this population reorganization remains poorly understood.

Changes in land use and mobility pattern have been evidenced in north-central Iberia, and can be viewed as adaptations to the severe climatic conditions of MIS 6 evidenced in the ODP 976 sequence during pollen zone/phase 2: increasing mobility, more short-term occupations and reliance on more local resources for subsistence strategies (Diez-Martín, 2010; Diez-Martín et al., 2008; Rios-Garaizar, 2016; Sánchez-Yustos, 2009). However, identifying cultural phases in the archaeological sequences linked with specific climatic episodes is generally hindered by the poor resolution of the archaeological record and chronological data. Among the sites identified in this synthesis, Lazaret and Bolomor caves probably present the most informative and well-dated sequences with several archaeological layers dated to MIS 6.

Cueva del Bolomor stands out in the Iberian Peninsula record as it provided an exceptionally long and continuous record of human presence, and the oldest evidence of fire use in Spain during the Middle Palaeolithic (Vidal-Matutano et al., 2019). Climate changes during MIS 6 documented in Bolomor's sediments through multiple proxies are consistent with the different phases identified in the ODP 976 record, with a more humid and cool phase at the beginning of MIS 6, and the most arid phase taking place at the middle of Phase III (layers X-VIII) (Arsuaga, Fernández Peris, et al., 2012; Fernández Peris et al., 2008). The site is described as a climatic refugium where Mediterranean vegetation persisted during the colder phase of MIS 6 thanks to the coastal reservoir character of the site (Ochando et al., 2019). No clear change in lithic production has been identified in the MIS 6 layers

of Bolomor: according to Fernández Peris (2008), archaeological layers XII to VII (Phase III, MIS 6) are all dominated by limestone flakes with few retouches, few recycling, and the presence non-Acheulean macro-lithic elements. These layers are characterized by expeditive flaking (including Levallois *débitage*) relying on local raw-material, pointing toward a high degree of mobility and search for immediate effectiveness. It is thus hard to distinguish different techno-cultural tendencies during this phase. The most visible change in the archaeological sequence occurs in layer VI (MIS 5) which shows an intensification of lithic production dominated by flint, the production of more specialized tools including microlithic elements and associated to more intense and stable occupation in the cave (Fernández Peris et al., 2008). Therefore, a clear behavioural change in the technological and economical exploitation of raw materials is identified at the beginning of MIS 5. Faunal remains show a large and constant diversity, including abundant micro supporting both short-term and long-term not-specialized occupation, with no clear change in the site's function across the sequence (Blasco et al., 2013).

Lazaret Cave, in south-eastern France, shows a very distinct scheme: the lower to middle Palaeolithic transition is well documented in the archaeological sequence (Unit CII and CIII), with the progressive replacement of large bifacial tools production by more standardized and smaller flakes (Cauche, 2012). Levallois *débitage* is already present and well-mastered in the lower MIS 6 levels, although rare, and becomes dominant in the upper levels (early MIS 5). Therefore, a subdivision of unit CII can be made with a lower interval rich in handaxes, and an upper layer characterized as "final Acheulean" with rare handaxes and more abundant flakes. Faunal assemblages are very constant throughout MIS 6, with the large dominance of red deers and rare presence of cold species (*Rangifer tarandus*, *Coelodonta antiquitatis*). Thus, the climatic oscillations of MIS 6 do not seem to have influenced different hunting strategies or prey selection by human populations at Lazaret Cave, as large game hunting of red deer prevailed (Valensi et al., 2013).

Therefore, Lazaret and Bolomor caves are examples of different strategies of site exploitation and technological evolution during MIS 6: Lazaret Cave represents a specialized red-deer hunting camp evidencing a progressive change from Lower to Middle Palaeolithic tools, while Cueva del Bolomor can be characterized as a short-term camp with more generalized hunting and stable expeditive Middle Palaeolithic industry. Despite these differences both sites provide evidence for a change in lithic assemblages occurring at the end of MIS 6/ beginning of MIS 5: the disappearance of handaxes and generalization of Levallois flakes in Lazaret, and the intensification and standardization of flint flaxes in Bolomor.

The fast climate dynamics during Termination II as evidenced in the ODP 976 paleoenvironmental record could have represented a critical period for human population. At the end of MIS 6, more sites have been identified in the Iberian Peninsula than Southern France, showing the latter could have represented a climate refugium at the time of maximum glacial expansion, with more intense human occupation regionally. Many of these late MIS 6 sites present a chronological boundary at the top of the sequence compatible with the onset of Termination II around 136 ka BP, and with HS11, within the dating uncertainty: Matalascañas, Tarrazona, Los Aljezares, Bolomor Unit III, Almonda, Pegos do Tejo, Puente Pino, Arlanpe Unit SQ2, Lazaret Unit CII, Payre layer D, Vauffrey unit IV, and Pech de l'Azé II layer 5. The extreme character of this event in the South-Western Mediterranean as expressed in the ODP 976 sequence could have put further environmental pressure on hominin groups already diminished. A niche modelling approach based on 41 sites of Western Eurasia since 145 ka BP has shown that the projected potential niche space for Neanderthals at the end of MIS 6 (~145ka BP) was very reduced and concentrated in Western Europe (Yaworsky et al., 2024). This coincides with the end of pollen zone/phase 2 in the ODP 976 record, the most cold and arid phase of the penultimate Glacial before HS11. Then, the authors reconstruct a progressive expansion of Neanderthal potential niche space between 145 and 130 ka, compatible with the climatic warming and moistening during pollen zone/phase 3 in the ODP 976 record (Yaworsky et al., 2024). The temporal resolution of the model (1000 years) does not allow to detect the impact of HS11 on the niche projection, and only a small slowdown and decline of the projected niche is visible at ~130 ka BP, before the MIS 5e optimum (Yaworsky et al., 2024, Fig. 5). A regional study focused on North-Western Spain argued in favour of a demographic vacuum at the end of MIS 6, compatible with HS11 and leading to a population reorganization implying contraction or micro-extinction, before the generalization of Middle Palaeolithic industries during MIS 5 (Sánchez-Yustos & Diez-Martín, 2015). According to the same authors, following this crisis, Neanderthal population entered a "reorganisation phase" leading to demographical stability and more technological standardization, visible in the explosion of the number of sites in Europe in general, especially after the MIS 5e climatic optimum (Bringmans, 2007; Lewis et al., 2011; Wenzel, 2007). This statement is supported by niche modelling which shows a peak in projected potential niche space of Neanderthal during MIS 5e (Yaworsky et al., 2024), and by recent genetic data which provided evidence for at least two radiation events linked with the environmental conditions of the last interglacial (Vernot, Zavala, Gómez-Olivencia, Jacobs, Slon, Mafessoni, Romagné, Pearson, Petr, Sala, Pablos, Aranburu, Bermúdez de Castro, et al., 2021), and Neanderthal population continuity since ~120 ka BP (Peyrégne et al., 2019). Thus, HS11 did not lead to complete extinction of hominin groups but might have induced deep demographical and technological reorganization, representing the first and one of the most intense abrupt changes that Neanderthal population had to face in South-Western Europe before the Last Glacial largest oscillations (HS6-4). According to this

view, the emergence of the “classical Neanderthal” world in Europe after the MIS 6/5 transition corresponds to the initialization of dynamics of repeated population contraction and expansion in response to the Upper Pleistocene instability, especially during MIS 4-2 (Sánchez-Yustos, 2009). In that sense, the subdued environmental instability during MIS 6 evidenced in the OD P976 record compared to the last glacial period (Section 6.2.6.5 and Fig. 6.9) could also have implications for human populations, with less fragmented (although harsh) habitats and more stable (although reduced) population during MIS 6. This hypothesis remains however hard to test based on the very different nature and quality of preservation of the archaeological record during MIS 6 compared to MIS 4-2 (e.g. Charton et al., 2025).

6.2.7. Conclusion

The ODP 976 record shed light on the environmental and climate changes during MIS 6 in the SW Mediterranean. The sequence is characterized by the high representation of *Cedrus* and Ericaceae pollen, resulting from the combined influence of African and Atlantic input respectively. ODP 976 position, at the confluence of Mediterranean versus Atlantic, and Eurasian versus African climatic areas, is ideal to decipher the processes behind orbital and sub-orbital climate dynamics during past glaciations. Three main phases have been distinguished during MIS 6 with different trends in vegetation and climate changes. Millennial-scale oscillations are recorded especially during the early part of MIS 6 (~187-166 ka BP) through the rapid increases of temperate and Mediterranean pollen, some of which are similar to millennial-scale warming events identified in the ice-core and marine temperature records, as well as other palynological sequences in the Mediterranean region. This Early MIS 6 phase is characterized by overall warmer and wetter climate conditions, in agreement with other paleoclimate archives in the Mediterranean showing enhanced moisture availability at the beginning of MIS 6. This phase of enhanced moisture availability was likely connected with enhanced Asian and African monsoon activity and was probably at the origin of the deposition of the Organic Rich Layer 607 in the Alboran Sea and sapropel S6 in the eastern Mediterranean. The second phase (165-144 ka BP) shows the establishment of full glacial conditions in the Mediterranean, with the maximum spread of steppe and semi-desert vegetation associated to cold and arid climate conditions and limited rapid oscillations. Finally, the final stages of MIS 6 are marked by increased humidity and the development of Ericaceae, with moderate millennial-scale oscillations seen in the vegetation record. Termination II is very particular in the ODP 976 record, with the continuous increase of temperate and Mediterranean vegetation being contemporaneous to a major episode of steppe expansion and aridity increase identified as HS11. This event shows a particular three phases or “W” shape, in agreement with other records, and probably had a major impact on the SW Mediterranean environments. A comparison with the changes occurring during the last glacial period (MIS 4-2) inferred from the same core highlighted

the limited duration, frequency and intensity of MIS 6 millennial climate events compared the last Glacial D-O cycles and Heinrich Events (MIS 4-2). These results support a subdued impact of the millennial-scale climate oscillations on the continental vegetation in the Mediterranean region during the Penultimate glaciation compared to the Last Glacial. The only exception is HS11, which stands out by its notable intensity and duration and is of particular interest to understand the mechanisms behind Termination II.

Human populations continuously inhabited the SW Mediterranean territory during MIS 6. While few sites are available and robustly dated to MIS 6 in Italy, Southern France and the Iberian Peninsula appear to have been intensely populated, supporting their nature of Pleistocene Climate refugia. More ecological data from well-dated archaeological sites during MIS 6 would be needed to increase the quality of human-environmental dynamics comparison. However, the synthesis drawn in the present study highlights the extreme nature of events characterizing Termination II, and particularly HS11, which could have represented an important environmental crisis for human population at that time, catalysing the end of the Lower to Middle Palaeolithic Transition and the onset of the “classical” Neanderthal world through a drastic population bottleneck.

6.2.8. Acknowledgments

We want to thank the three anonymous reviewers for their very helpful comments on this manuscript. We acknowledge the International Ocean Drilling Project and the MARUM Bremen Core Repository for making available the ODP 976 samples. The sample processing was funded by the CNRS and the MNHN. We thank the European Research Council (ERC) under the European Union’s HORIZON1.1 research program (LATEUROPE project, grant agreement ID 101052653) for funding. L. Charton doctoral contract is funded by the French Ministère de l’Enseignement Supérieur et de la Recherche at the doctoral school ED 227 of the Muséum National d’Histoire Naturelle, Paris. The international cotutorship with the University of Florence is supported by the Ecole Franco-Italienne Vinci grant (project C2-166). We thank Lionel Dubost for assistance in laboratory treatment of samples to HF. We are grateful to Francisco Sierro for sharing the isotopic data on AICC2012 timescale, to Jon Camuera for the pollen data from Padul and to Katherine Roucoux for the pollen data from Ioannina. This is an ISEM contribution.

7. Discussion générale

7.1. Cadre interprétatif et limites méthodologiques

Cette étude interdisciplinaire a permis d'intégrer des données palynologiques sur la végétation en Méditerranée sud-occidentale avec des données climatiques régionales et globales, et des données archéologiques. Cette approche croisée a mis en lien les changements environnementaux et climatiques avec les dynamiques de population au cours des derniers 200 000 ans. Comme toute étude paléoenvironnementale fondée sur des archives marines, celle-ci s'appuie sur un ensemble de contraintes inhérentes à la nature même de l'enregistrements et des méthodes. Ces contraintes définissent le cadre interprétatif dans lequel les résultats doivent être compris et permettent d'identifier les pistes les plus prometteuses pour de futures recherches. Nous présentons ici les principales contraintes de l'approche, ainsi que leur portée pour l'interprétation des dynamiques environnementales et humaines

Enjeu 1 : Définir la zone source du pollen dans un contexte marin intercontinental. La méthode palynologique appliquée en contexte marin tient compte d'une représentation très large de la végétation à échelle régionale voir sub-régionale, liée aux modalités de transport et de déport du pollen sur de longues distances (e.g. Heusser & Balsam, 1977; Prentice, 1985; Stanley, 1966). La comparaison des assemblages palynologiques actuels d'échantillons marins de surface sur le littoral ouest-Ibérique avec ceux d'échantillons terrestres, et notamment des principaux estuaires, a montré une bonne correspondance entre l'image de la végétation régionale dans les archives marines et dans les échantillons terrestres (Naughton et al., 2007). Selon cette même étude, les carottages marins de la marge ouest-ibérique permettent une bonne différenciation des grands domaines de végétation (eurosibérien / méditerranéens) entre le nord et le sud de la péninsule. Ce contrôle actuel de la zone source du pollen n'existe pas pour la Mer d'Alboran. Ainsi, si les études palynologiques en Mer d'Alboran reposent sur l'hypothèse qu'une majorité des grains de pollen provient du sud de la péninsule Ibérique (de l'est mais aussi de l'ouest comme le montre l'abondance du pollen d'Ericaceae), une quantité inconnue et potentiellement variable de matériel provient également du Nord de l'Afrique, comme indiqué par la présence de taxons endémiques (*Argania*, *Cedrus* dont l'abondance peut parfois atteindre 60% de l'assemblage pollinique). Cette composante africaine de l'assemblage pollinique d'ODP 976 semble majoritairement liée au transport éolien, au vu de l'activité très limitée du système hydrographique marocain sur la côte méditerranéenne. Le transport éolien de particules depuis l'Afrique vers la Méditerranée augmente pendant les épisodes de sécheresse, comme indiqué dans de nombreuses études (dont celle-ci) à travers l'analyse des poussières et minéraux argileux (e.g. Bout-Roumazeilles et al., 2007; Guerzoni et al., 1997). Il est ainsi probable qu'une quantité plus

importante de grains de pollen africains soient présents dans l'assemblage pollinique d'ODP 976 pendant les épisodes stadiaires (GS et HS), bien qu'il soit actuellement impossible d'estimer précisément cette composante. Cette limitation avait constitué l'un des arguments centraux de la critique de Carrión (2004) face à l'étude de d'Errico et Sánchez Goñi (2003) sur le lien entre l'extinction de Néandertal et les oscillations rapides du MIS 3 mises en évidence dans les carottes marines au large de la péninsule Ibérique (carottes atlantiques et méditerranéennes). Les changements dans la composition du spectre pollinique en Mer d'Alboran représenteraient une alternance d'apports préférentiels terrestres (pendant les interstadiaires) et éoliens (pendant les stadiaires) plutôt que des changements de végétation régionale. Si l'étude consécutive de Naughton et al. (2007) a permis de renforcer l'interprétation des spectres polliniques sur le côté atlantique, la question reste encore ouverte pour la Mer d'Alboran. Cependant, comme souligné à plusieurs reprises dans cette étude et celles qui l'ont précédé, la forte ressemblance des changements des spectres polliniques observés dans la carotte ODP 976 avec ceux de séquences terrestres dans la péninsule Ibérique (Padul, Villarquemado, Carihuela, Abric Romani) soutient l'interprétation de nos résultats comme reflétant majoritairement les changements de végétation dans la péninsule Ibérique. Le manque d'archives palynologiques dans le Nord de l'Afrique sur le Pléistocène récent (au-delà de l'Holocène) empêche en revanche d'évaluer la proportion de la composante africaine dans l'assemblage pollinique d'ODP 976 pendant le dernier glaciaire et les périodes antérieures.

Enjeu 2 : Spatialisation et hétérogénéité des environnements. L'approche régionale de la palynologie en contexte marin produit une synthèse de la végétation sur une aire géographique difficile à estimer, qui s'étend potentiellement sur des centaines de kilomètres, et qui peine à rendre compte de l'hétérogénéité spatiale des environnements. La comparaison avec d'autres enregistrements (marins et continentaux) permet de mieux comprendre les différences spatiales de la végétation, comme dans la Section 3.2.6.2, où la signature différentielle du HS4 en Méditerranée sud-occidentale par rapport à l'Atlantique a été mis en évidence par les comparaisons régionales. Ces comparaisons régionales sont plus limitées pour les périodes antérieures, pour lesquelles un plus petit nombre de séquences paléoenvironnementales est disponible. De manière générale, très peu d'enregistrements terrestres continus et bien datés sont disponibles pour la péninsule Ibérique. Cette limitation de la spatialisation des reconstructions est importante pour la problématique concernant les dynamiques de populations humaines, et l'existence de refuges climatiques. Si l'enregistrement palynologique de la carotte ODP 976 montre une prédominance de la végétation steppique et semi-désertique pendant les stadiaires (et particulièrement les HS) au niveau régional, ceci n'entre pas en contradiction avec l'existence de refuges tempérés et de spots de biodiversité le long du littoral

(Carrión et al., 2008, 2018; Real et al., 2022; Straus, 2022), comme indiqué par la présence continue de taxons polliniques d'affinité méditerranéenne pendant les HS (Fig. 4.16).

Enjeu 3 : Reconstruction climatique et bases de données de référence. Les reconstructions climatiques à partir du pollen présentées dans cette étude possèdent également plusieurs limitations. La première tient à la difficile reconstruction des paramètres climatiques d'été mise en évidence notamment pour le MIS 6 (voir section 6.2.5.2). La seconde tient à la composition de la base de données de référence servant aux reconstructions: l'ajout d'un plus grand nombre d'échantillons couvrant les biomes nord-africains, mais également de steppes européennes, et d'environnements eurosibériens dans la péninsule Ibérique (voir Fig. 2.11) permettrait de mieux reconstituer les paramètres climatiques associés aux assemblages dominés respectivement par le Cèdre (*Cedrus atlantica*, qui n'est pas différencié de *Cedrus libani* par la palynologie et peut induire une confusion entre les bases de données actuelle et fossile), par les formations à *Artemisia*, Amaranthaceae et *Ephedra*, et par les Ericaceae. Ces assemblages polliniques sont en effet fréquents au cours du Pléistocène en Méditerranée sud-occidentale, et impliquent une recherche d'analogues parfois lointains pour les reconstructions climatiques (Turquie pour les assemblages à Cèdre, Tibet pour les assemblages de steppe froide).

Enjeu 4 : Contraintes chronologiques et corrélations inter-régionales. La difficile construction d'un modèle chronologique robuste pour les carottes marines représente un des enjeux principaux. L'attribution d'âges relatifs au-delà de 40 000 ans par corrélation avec d'autres enregistrements de référence parfois lointains (Chine, Antarctique…), comme cela est le cas pour la carotte ODP 976 (voir section 2.3), limite grandement notre compréhension des relations entre évènements climatiques dans différentes régions, en créant une logique circulaire qu'il faut prendre en compte avec prudence. L'indisponibilité d'un enregistrement isotopique à haute résolution couvrant les 200 000 ans pour ODP 976 et permettant une meilleure calibration chronologique relative constitue l'une des principales limitations de cette étude. Ainsi, les corrélations avec la chronologie des évènements isotopiques du Groënland pourraient être améliorées, tout comme les points de contrôle du MIS 6, par l'augmentation de la résolution de la série. La potentielle élaboration d'un modèle d'âge plus robuste pour la séquence pourrait également prendre en compte les enregistrements directement datés disponibles dans la région, comme les spéléothèmes (e.g. Held et al., 2024; Kaushal et al., 2025; Tzedakis et al., 2018).

Enjeu 5 : Articuler chronologies environnementales et occupations humaines. Enfin, l'étude des relations Homme / environnement est aussi grandement limitée par les différences d'approches chronologiques entre les enregistrements paléoenvironnement aux dépourvus de datations absolues (comme ODP 976) et les sites archéologiques, témoins des occupations humaines dans le passé et dont

la chronologie est aussi, souvent, incertaine. Ces difficiles corrélations entre changements environnementaux et bio-culturels sont connus de longues dates (e.g. D'Errico & Sánchez Goñi, 2003; Fourcade, 2022; Fourcade et al., 2022; Tzedakis et al., 2007). Or, l'aspect chronologique est fondamental afin d'éviter les fausses interprétations sur les liens entre changements environnementaux et dynamiques de populations humaines au Paléolithique (Van Andel & Tzedakis, 1996). Il convient donc de rester prudent dans les conclusions, et d'éviter toute vision déterministe qui poserait le contexte environnemental et climatique uniquement comme une contrainte pour les populations humaines paléolithiques. Par ailleurs, de récents efforts dans la compilation de bases de données uniformisées de sites archéologiques paléolithiques datés (Kandel et al., 2023), avec des indices de confiance clairement explicités et reproductibles (Albouy et al., 2023, 2024) pourrait améliorer l'interprétation des interactions Homme / environnement dans de futures études.

Malgré ces contraintes, les convergences observées entre la carotte ODP 976 et plusieurs séquences, ainsi que l'intégration d'approches palynologiques, climatiques et archéologiques, permettent d'obtenir une image cohérente de l'histoire environnementale en Méditerranée sud-occidentale au cours des derniers 200 000 ans. Les limitations, clairement identifiées, constituent autant de pistes pour affiner les modèles chronologiques, améliorer les bases de données polliniques et renforcer les futurs travaux sur les interactions Homme–environnement.

7.2. Dynamiques de la végétation et du climat en Méditerranée depuis 200 000 ans : une synthèse de l'enregistrement d'ODP 976

Cette thèse a permis de compléter et d'étendre l'enregistrement multi-proxy de la carotte ODP 976 sur 200 000 ans, qui comporte maintenant des données isotopiques (bien qu'à faible résolution sur le MIS 6), des données palynologiques à haute résolution, des quantifications climatiques multiméthode à partir du pollen, et des données minéralogiques à haute résolution (Fig. 7.1). La représentation de l'ensemble de ces données sur toute la période d'étude mises en parallèle de la courbe de référence du Groenland met bien en évidence les liens entre les dynamiques paléo-océanographiques (isotopes), paléo-atmosphériques (minéraux argileux) ainsi que de végétation et de climat (pollen et reconstructions climatiques) sur le long terme et à échelle sub-millénaire.

Pendant le dernier cycle climatique, la courbe des isotopes planctoniques d'ODP 976 suit étroitement les variations isotopiques observées dans l'enregistrement polaire, montrant une bonne corrélation entre l'évolution globale des températures et les températures des eaux profondes en Méditerranée sud-occidentale enregistrées par les foraminifères. La composition de la végétation régionale en Méditerranée sud-occidentale représentée par les assemblages polliniques de la carotte ODP 976 a subi d'importants changements au cours des derniers 200 000 ans, répondant à la fois aux

grandes cyclicités orbitales glaciaire/interglaciaire et aux dynamiques climatiques à échelle sub-millénaire. Les reconstructions des paramètres climatiques à partir du pollen montrent une très grande sensibilité du climat régional aux oscillations climatiques rapides de type D-O ainsi qu'aux évènements de Heinrich. Des conditions de froid et d'aridité extrêmes sont reconstituées pendant les HS majeurs, représentés par le HS11 et les HS6-1, où les taxons caractéristiques d'une végétation steppique et semi-désertique dominent les assemblages polliniques.

Les reconstructions climatiques à partir du pollen ont montré que la saisonnalité est un facteur particulièrement important pendant les évènements sub-millénaires du dernier cycle climatique. Lors des stadiaires, et particulièrement des HS, les paramètres climatiques d'hiver subissent les chutes les plus prononcées impliquant une perturbation du régime saisonnier typique des précipitations et des températures en région méditerranéenne. Les paramètres d'été montrent généralement des tendances plus ambiguës. Les précipitations d'été, déjà très peu abondantes dans la région, sont plus modérément affectées par les évènements extrêmes dans le passé. Les températures d'été montrent également des variations réduites pendant certains HS. Ceci peut-être une conséquence directe des méthodes de reconstruction basées sur le pollen : *Artemisia*, l'un des taxons le plus déterminants pour la reconstruction pendant les HS, est compatible avec des environnements plus chauds, notamment pendant l'été (Subally & Quézel, 2002; Toucanne et al., 2022).

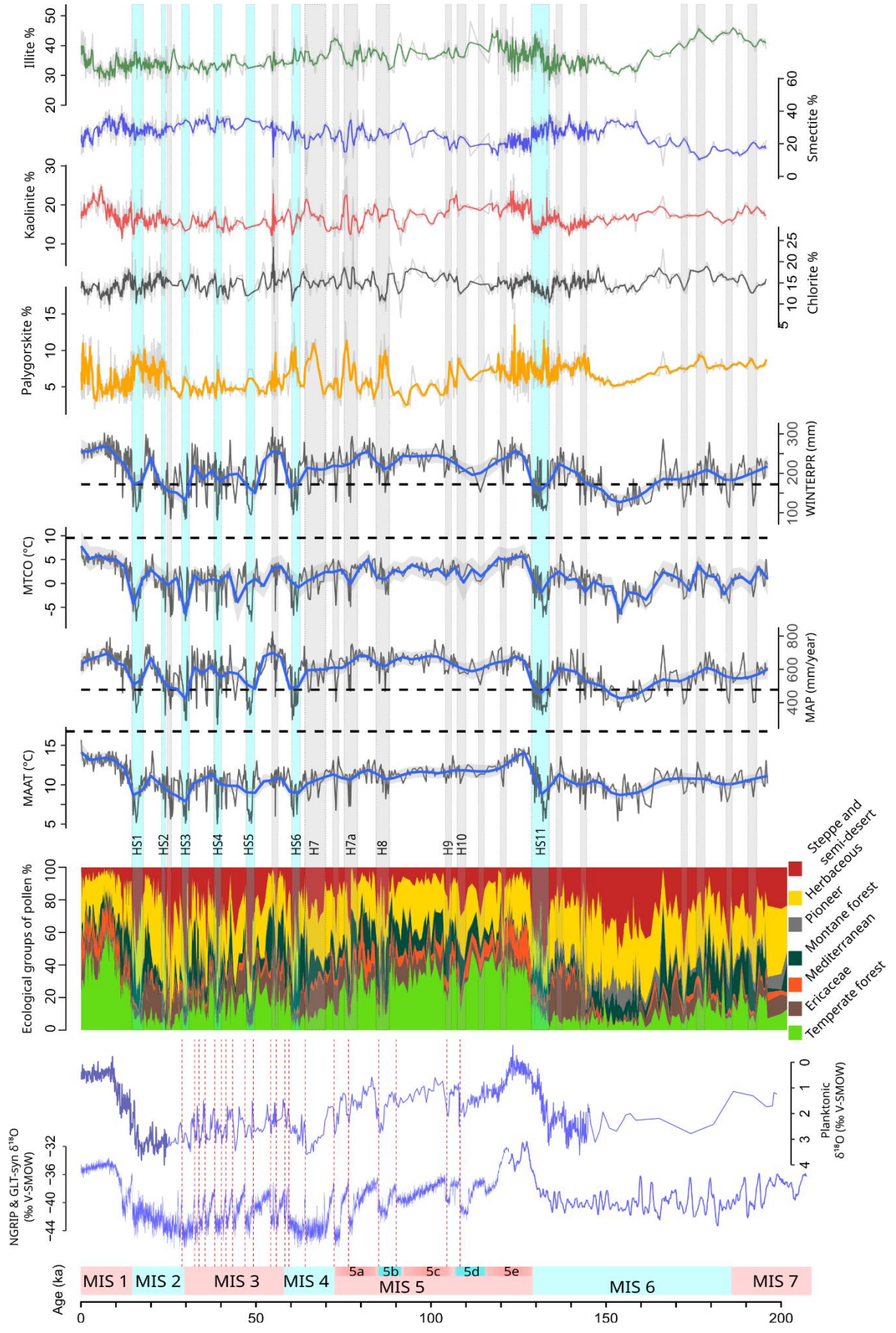


Fig. 7.1. Synthèse des données disponibles pour la carotte ODP 976 sur 200 000 ans présentées dans cette thèse et mises en parallèle de la courbe isotopique du Groënland entre 0 et 123 ka BP

(Rasmussen et al., 2014; Seierstad et al., 2014) et la courbe synthétique pour la période antérieure (Barker et al., 2011). De bas en haut: rapport des isotopes planctoniques (*G. bulloides*) (Combourieu-Nebout et al., 2002; Grafenstein et al., 1999; Jiménez-Amat & Zahn, 2015, et données inédites de R. Zahn présentées dans la section 4), pourcentages polliniques des principaux groupes écologiques (Combourieu-Nebout et al., 1999, 2002; Combourieu-Nebout et al., 2009, et cette thèse), moyenne des reconstructions climatiques multiméthode à partir des assemblages polliniques (MAAT: température moyenne annuelle, MAP: précipitations annuelles, MTCO: température moyenne du mois le plus froid, WINTERPR: précipitations d'hiver), composition minéralogique des argiles (Bout-Roumazeilles et al., 2007 et données inédites de V. Bout-Roumazeilles présentées en partie dans la section 4). Les lignes rouges en pointillé indiquent les points de calage entre les évènements isotopiques au Groënland (Rasmussen et al., 2014) et la courbe isotopique d'ODP 976 utilisés dans le modèle d'âge.

L'interprétation de la composition minéralogique des argiles sur toute la série devra être développée plus en détail dans de futures recherches. Cependant, les interprétations préliminaires présentées dans les sections 4 et 5 montrent l'importance de la palygorskite et de la kaolinite comme indicateurs de sources éoliennes du nord de l'Afrique et du Sahel respectivement. Ces minéraux argileux représentent un proxy intéressant dans les archives sédimentaires de la marge ibérique pour retracer les mouvements de la zone de convergence intertropicale dans le passé, en lien avec les périodes plus sèches ou humides africaines, les cyclicités glaciaires / interglaciaires et les cyclicités D-O. Les données de compositions d'argiles concernant le MIS 6 n'avaient pas été intégrées à la section 6 car elles semblaient peu informatives, et méritent d'être brièvement commentées ici. Il apparait en effet que les dynamiques rapides observées en particulier pour la palygorskite et la kaolinite au cours des MIS 5-1 sont très réduites, voire absente pendant l'avant-dernier glaciaire. Les pourcentages de minéraux argileux en général montrent une faible variabilité sub-millénaire, mais expriment tout de même des tendances plurimillénaires. En particulier, la courbe d'abondance de la palygorskite montre un « plateau » à la base du MIS 6, puis une tendance claire à la diminution entre 170 et 150 ka BP qui semble suivre l'évolution vers le maximum glaciaire du MIS 6. Cette évolution indique donc des apports éoliens du nord de l'Afrique relativement important au début du MIS 6, qui deviennent très réduits pendant l'avant-dernier maximum glaciaire, puis augmentent à nouveau à la fin du glaciaire. Il semble ainsi que la palygorskite pendant l'avant-dernière période glaciaire montre une corrélation positive avec les précipitations et les températures reconstruites à partir du pollen, dynamique qui contraste avec l'anti-corrélation observée au cours des MIS 5-1 (Fig. 7.1). Ces résultats tendent vers des apports éoliens en Mer d'Alboran potentiellement réduits pendant l'avant-dernier glaciaire. La smectite montre en revanche une signature « glaciaire » très marquée, avec des pourcentages particulièrement élevés entre l'avant-dernier maximum glaciaire et la fin du MIS 6. La smectite est un marqueur d'origine fluvial, dont la source principale en Méditerranée est représentée par le Nil, mais aussi par les autres fleuves majeurs comme le Rhône, le Pô ou le Guadalquivir (Bout-Roumazeilles et al., 2007, 2013; Moal-Darrigade et al., 2022). Ainsi, la prédominance de la smectite pendant le maximum

glaciaire du MIS 6 peut indiquer un phénomène d'aggradation fluviale en Méditerranée favorisé par les conditions particulièrement froides et sèches.

L'analyse en composante principale (ACP) appliquée à l'ensemble de la série sur 200 000 ans permet une visualisation claire des relations entre variables incluses dans cette étude (groupes écologiques polliniques, paramètres climatiques et minéraux argileux) et échantillons sédimentaires d'ODP 976 (Fig. 7.2). L'axe 1 porte 29.4 % de variance et montre une opposition très nette entre taxons steppiques et semi-désertique associés à la smectite et à la palygorskite dans les valeurs positives, et les taxons de forêt tempérée et méditerranéens associés aux paramètres climatiques (précipitations annuelles, températures et précipitations d'hiver) ainsi qu'à la kaolinite dans les valeurs négatives. L'axe 2 porte 15.1 % de variance et montre surtout une opposition entre la smectite et le rapport S/K en haut, et les autres minéraux argileux en bas (surtout la kaolinite). Ce deuxième axe peut indiquer l'opposition entre la prédominance d'apports fluviatiles (en haut) et d'apports éoliens (en bas) dans les échantillons sédimentaires d'ODP 976. Sur le graphique montrant la variance des échantillons (Fig. 7.2, B), une opposition très nette apparaît suivant l'axe 1 entre les échantillons correspondant aux évènements interglaciaires/interstadiaires et ceux des évènements glaciaires / stadiaires. Ainsi, il apparaît que l'ensemble des indicateurs pollen / minéraux argileux / reconstructions climatiques permettent une très bonne différenciation des évènements sub-millénaires froids et chauds. Les évènements froids les plus extrêmes (dans les valeurs positives de l'axe 1, à droite) sont représentés par les HS11, HS6, HS4 et les HS3-1, ainsi que la phase 6.2 du MIS 6 (correspondant à l'avant-dernier maximum glaciaire), et les GS12, 8, 21, 5, 9. La position intermédiaire du HS5 dans la PCA est liée à la faible résolution pour cet évènement après rééchantillonnage des échantillons communs entre le pollen et les minéraux argileux (voir section 4.4.4, Fig. 4.10).

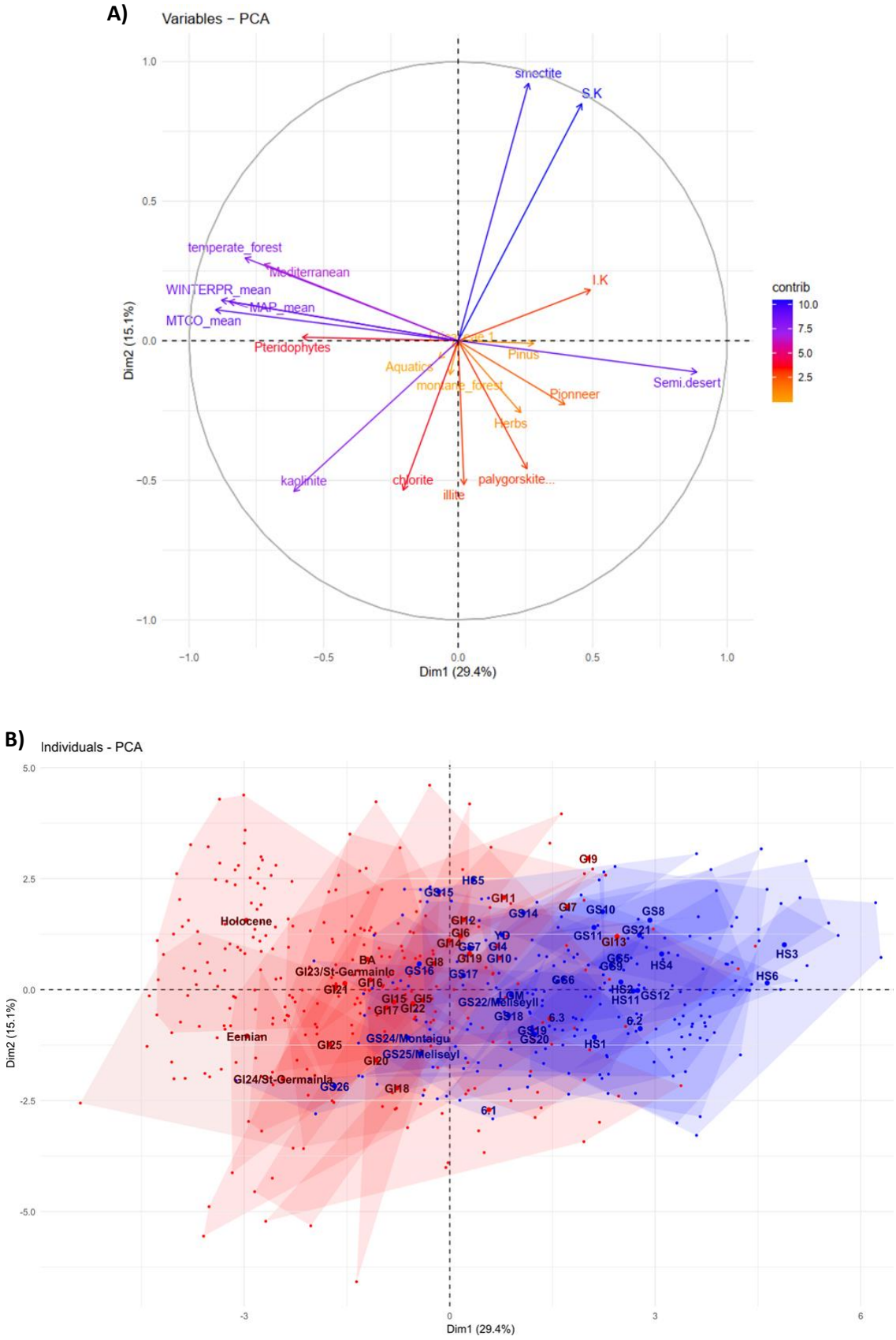


Fig. 7.2 Analyse en Composantes Principales (PCA) appliquée à l'enregistrement ODP 976 sur 200 000 ans (incluant 498 échantillons communs entre les analyses palynologiques et de composition d'argiles). A) Contributions des variables (principaux groupes écologiques et taxons polliniques ainsi

que les minéraux argileux). **B)** Contributions des individus (échantillons d'ODP 976). Les échantillons ont été groupés en fonction de leur appartenance à une phase interglaciaire / interstadiaire en rouge, ou à une phase glaciaire/stadiaire en bleu. Ces groupes incluent: les stadiaires de Heinrich (HS11 et HS6-1), les stadiaires du Groënland (GS), les interstadiaries du Groënland (GI), l'Holocene, le dernier maximum glaciaire (LGM), le Dryas récent (YD), le Bölling-Alleröd (BA), l'Eemien, ainsi que les trois grandes phases du MIS 6 (correspondant aux zones polliniques 6.1, 6.2 et 6.3 dans la section 6). Voir la section 4.4.4. pour les détails sur la méthode.

7.3. Différences, similarités et modulation orbitale des oscillations sub-millénaires au cours des derniers 200 000 ans

L'une des problématiques centrales de cette thèse était d'explorer les similarités et les différences entre les oscillations climatiques à échelle sub-millénaire pendant le dernier cycle climatique et l'avant-dernière période glaciaire. La période d'étude peut ainsi être divisée en trois fenêtres chronologiques d'une durée d'environ 60 000 ans chacune (Fig. 7.3): entre 190 et 130 ka BP (correspondant au MIS 6, l'avant-dernière période glaciaire), entre 130 et 70 ka BP (correspondant au MIS 5, le dernier interglaciaire), et entre 70 et 10 ka BP (correspondant au MIS 4-1, la dernière période glaciaire et le début de l'Holocène).

La partie inférieure du MIS 6 (~190-165 ka BP) est caractérisée par des variations importantes dans la composition de la végétation dans l'assemblage palynologique de la carotte ODP 976, ainsi que des oscillations rapides et significatives des paramètres climatiques. Ces oscillations sub-millénaires partagent des similarités avec celles des cycles D-O de la dernière période glaciaire, avec une alternance de phases de réchauffement et d'expansion de la forêt tempérée, et des phases plus froides et sèches où la végétation steppique et semi-désertique domine l'assemblage. Les évènements arides les plus notoires sont situés à ~185 et ~172 ka BP (Fig. 7.3). Cependant, dans la limite de la résolution de l'enregistrement palynologique obtenue sur cet intervalle, ces oscillations rapides semblent se distinguer de celles du MIS 3 par leur fréquence réduite et leur intensité moindre. A partir de 165 ka BP, le couvert forestier est drastiquement réduit dans l'enregistrement palynologique et montre ainsi l'absence d'évènements interstadiaires type D-O marqués. La période entre 165 et 150 ka BP est particulièrement froide et aride, marquée par des conditions glaciaires similaires à celles des stadiaires de Heinrich du MIS 3, sur une période de temps prolongée qui coïncide avec le minimum d'excentricité de l'orbite terrestre (Fig. 7.3). Enfin, le réchauffement graduel qui marque la fin du MIS 6 à partir de ~150 ka BP est également caractérisé par une variabilité environnementale et climatique réduite, l'absence d'évènements stadiaires et interstadiaires d'intensité marquée.

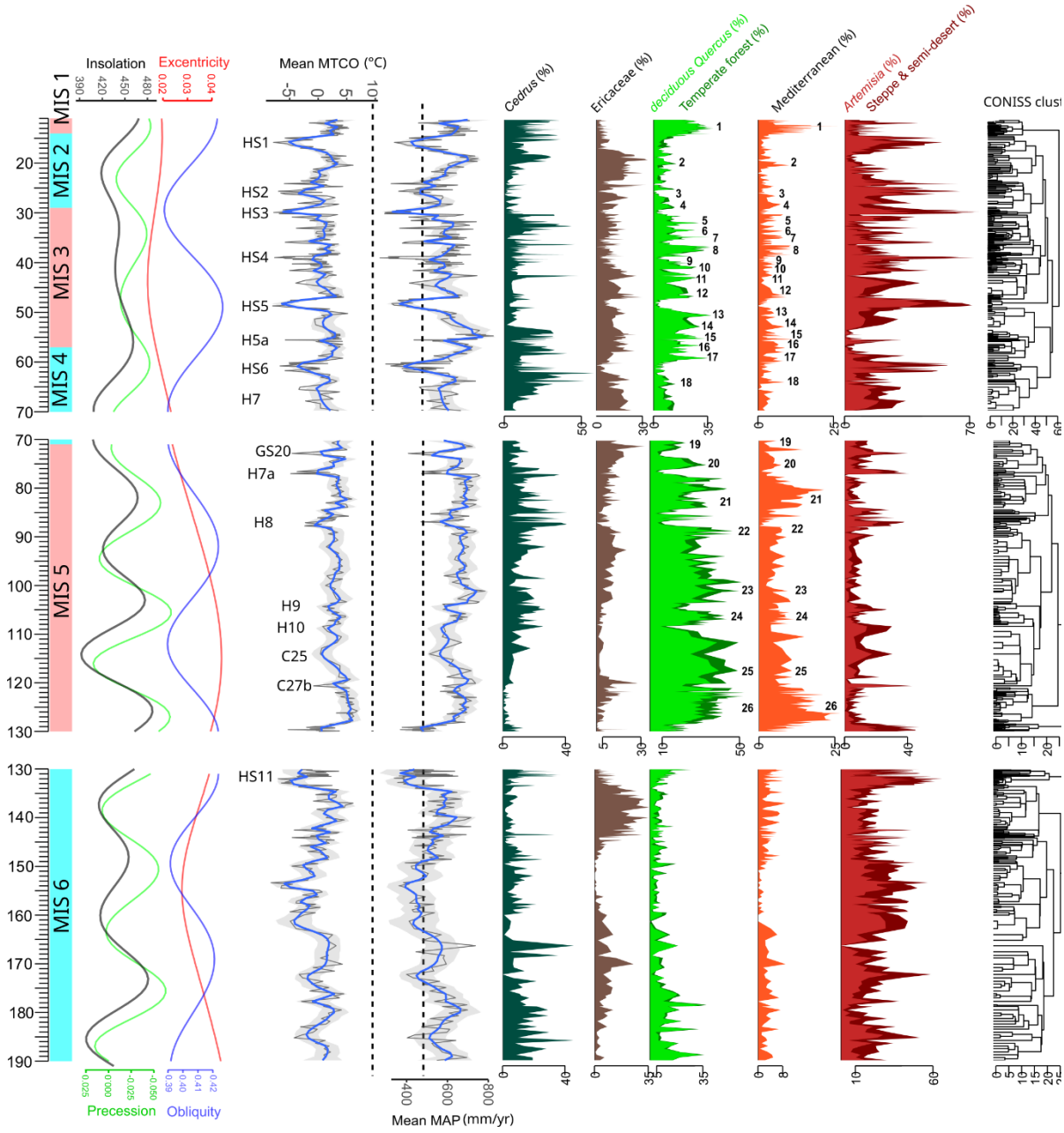


Fig. 7.3. Comparaison des changements rapides de végétation et de climat dans l'enregistrement d'ODP 976 pendant la dernière période glaciaire (MIS 4-2), le dernier interglaciaire (MIS 5), et l'avant-dernier glaciaire (MIS 6). L'évolution des paramètres orbitaux est montrée à gauche (Berger & Loutre (1991) pour l'insolation à 65°N; Laskar et al. (2004) pour les autres paramètres), suivi des températures du mois la plus froid (MTCO, moyenne des quatre méthodes de reconstructions climatiques à partir du pollen appliquées dans cette étude), des précipitations annuelles (MAP, idem), et des cinq taxons polliniques et groupes écologiques les plus importants dans l'enregistrement d'ODP 976.

Ainsi, cette étude soutient une nature différente des oscillations suborbitales pendant le MIS 6 en Méditerranée sud-occidentale par rapport au dernier glaciaire, avec des évènements climatiques moins intenses et moins fréquents, concentrés dans la partie inférieure du MIS 6.

La deuxième fenêtre chronologique, représentée par le MIS 5, apparaît comme la phase la plus « stable » de la période d'étude par rapport aux deux périodes glaciaires qui l'encadrent. Les oscillations visibles dans l'assemblage palynologique et les reconstructions climatiques y sont moins intenses ; le couvert forestier reste toujours très important et la végétation steppique et semi-désertique ne dépasse pas 40% dans l'assemblage palynologique de la carotte ODP 976. Une succession de 8 cycles D-O est mise en évidence avec des interstadiaires particulièrement longs et des stadiaires peu marqués.

Enfin, à partir de la fin du MIS 4 et jusqu'à la fin de la dernière période glaciaire, l'enregistrement palynologique de la carotte ODP 976 montre une instabilité extrême et à très haute fréquence. La succession de dix-huit cycles D-O ponctués par six HS majeurs (HS6-1) et deux autres mineurs (H7 et H5a) dans l'enregistrement palynologique de la carotte ODP 976 montre la rapidité et l'intensité de la réponse de la végétation du sud-ouest méditerranéen aux variations climatiques sub-millénaires du dernier glaciaire.

Ainsi, les résultats principaux de cette étude soulignent le caractère sans précédent des oscillations sub-millénaires du MIS 4-2 au cours des derniers 200 000 ans dans la Méditerranée sud-occidentale. Si les périodes précédentes (MIS 6 et MIS 5) ont également été marquées par une instabilité environnementale et climatique à échelle sub-millénaire, l'amplitude et la fréquence des variations observées restent relativement faibles comparées à la dernière période glaciaire (MIS 4-2). Les raisons et les mécanismes responsables de ces différences devront être explorées plus en détail dans de futures recherches. Une hypothèse relative aux différences de configuration orbitales pourrait être proposée, bien que les mécanismes concrets à travers lesquels les variations des paramètres orbitaux ont impacté le climat global et la végétation en Europe restent encore mal compris (Paillard, 2010). L'influence de l'excentricité est généralement liée à l'étendue des calottes polaires et au contrôle des cyclicités glaciaires/interglaciaires globales. De cette façon, la réduction de la calotte arctique pendant le MIS 5 liée au maximum d'excentricité peut expliquer en partie la moindre intensité des évènements stadiaires enregistrés en Méditerranée pendant cette période. Des débâcles d'icebergs moins importantes pendant les évènements de type Heinrich au cours du MIS 5 auraient limité la pénétration des eaux subpolaires aux hautes latitudes de l'Atlantique Nord. Cette hypothèse serait cohérente avec la mise en évidence d'évènements stadiaires de moindre intensité au début du MIS 6, lorsque l'excentricité est encore élevée et la calotte polaire encore relativement peu étendue. (Fig. 7.3) L'intensité croissante des événements froids entre la fin du MIS 5 et le MIS 3 coïncide également avec une diminution progressive de l'excentricité et le développement de la calotte polaire arctique. Ces observations soutiennent un contrôle des épisodes stadiaires en Méditerranée occidentale principalement lié aux mécanismes de hautes latitudes impliquant la couverture glaciaire.

Par ailleurs, différentes études ont montré que l'expression régionale des oscillations climatiques sub-millénaires a pu être modulée par la précession et l'obliquité, avec des mécanismes impliquant l'insolation, la variabilité saisonnière et les cycles de moussons asiatiques et africaines (Cheng et al., 2016; Drysdale et al., 2009; Fletcher & Sánchez Goñi, 2008; Magri & Tzedakis, 2000; Sánchez Goñi et al., 2008; Ziegler et al., 2010). Ainsi, les cycles de précession et d'obliquité ont été présenté comme les « *pacemakers* » des oscillations climatiques suborbitales (Cheng et al., 2016), particulièrement pendant les terminaisons glaciaires, à travers leur influence sur l'insolation dans l'hémisphère Nord et les liens avec les phénomènes hydro-climatiques aux basses latitudes. Magri et Tzedakis (2000) ont mis en évidence pour la première fois la réponse de la végétation méditerranéenne aux cycles de précession, notamment à travers la longue série italienne de Valle di Castiglione (Follieri et al., 1988): les périodes de passage du périhélie en hiver (associés à une insolation réduite) sont toujours associés à une contraction de la végétation tempérée, tandis que certains pics de végétation méditerranéenne sont associés aux périodes de passage du périhélie en été (forte insolation boréale). L'étude de la carotte MD95-2043 (en mer d'Alboran orientale) a corroboré cette interprétation en montrant l'influence de la précession sur les dynamiques de végétation du sud-ouest Méditerranéen pendant le MIS 3, à travers une expansion marquée de la forêt tempérée et méditerranéenne durant les GI 8-5 coïncidant avec le minimum de précession / le maximum d'insolation boréale (Fletcher & Sánchez Goñi, 2008). La séquence ODP 976 couvrant de multiples cycles de précession permet de confirmer ces interprétations : des phases d'expansion de la végétation tempérée coïncidant avec les minimums de précession et maximum d'insolation sont identifiés au début du MIS 3 pendant les GI 17-13 (~60-50 ka BP), mais aussi au cours du MIS 5 pendant le GI 21 (~85-80 ka BP), le GIS 24 (~108-105 ka BP) et l'Eemien (« GI 26 », ~128-120 ka BP). Ces liens entre précession, insolation et végétation tempérée et méditerranéenne sont en revanche moins évidents pendant le MIS 6: le maximum d'insolation / minimum de précession centré autours 173 ka BP coïncide avec une phase de développement de la steppe et du semi-désert (Fig. 7.3).

Finalement, l'influence de l'obliquité sur les dynamiques climatiques et de végétation en Méditerranée au cours du Pléistocène récent a été relativement peu exploré, et centré sur son rôle dans les terminaisons glaciaires (Bajo et al., 2020; Tzedakis, 2005). Les variations de l'obliquité de l'axe de rotation de la Terre ont un impact sur la saisonnalité, principalement aux hautes latitudes, avec des saisons plus marquées lorsque l'obliquité est importante (Berger & Loutre, 2004). De manière frappante, la première moitié du MIS 3 coïncide avec une période de faible excentricité, faible insolation boréale et haute obliquité, une configuration unique au cours des derniers 200 000 ans qui pourrait expliquer le caractère sans précédent de la variabilité climatique durant cette période. Cette thèse montre, à travers les reconstructions climatiques basées sur le pollen, que les changements de

saisonnalité ont joué un rôle clé dans les dynamiques de végétation en Méditerranée et les phases d'expansion et de contraction de la végétation tempérée et Méditerranéenne. Par conséquent, il apparaît crucial d'explorer contrôle du régime saisonnier Méditerranéen par les paramètres orbitaux impliquant à la fois des mécanismes de hautes latitudes (obliquité, excentricité) et de basses latitudes (précession) pour comprendre la variabilité des oscillations climatiques sub-millénaires au cours des différents cycles climatiques passés.

7.4. Mise en perspective de l'enregistrement palynologique d'ODP 976 à échelle globale ainsi qu'avec les principales longues séquences méditerranéennes

L'enregistrement paléoclimatique à haute résolution d'ODP 976 sur 200 000 ans permet de comprendre l'impact de la variabilité climatique à haute fréquence en Méditerranée sud-occidentale par comparaison avec les courbes climatiques globales de référence (Fig. 7.4).

Des corrélations claires apparaissent entre les dynamiques de végétation mises en évidence dans l'enregistrement palynologique de la carotte ODP 976, et les changements climatiques à échelle globale représentés principalement par les courbes isotopiques en Arctique et en Atlantique Nord (Fig. 7.4. d-f). Ainsi, les changements du couvert forestier en Méditerranée sud-occidental sur le long-terme ont principalement répondu aux grandes variations de températures globales et aux dynamiques des calottes polaires. Une bonne correspondance entre les principaux pics de forêt tempérée en Méditerranée sud-occidentale et la concentration atmosphérique de méthane dans l'enregistrement d'EPICA Dome C (Jouzel et al., 2007) (Fig. 7.4. c & k) montre également un lien entre le développement des forêts en Méditerranée et l'activité des zones humides émettrices de méthane à échelle globale (Rhodes et al., 2017). Les changements de la végétation steppique et semi-désertique ont également suivi les grandes tendances climatiques globales, avec une prédominance pendant les glaciaires (MIS 6 et MIS 4-2). Dans la limite des modèles d'âges employés pour chaque enregistrement, cette comparaison montre également la composante suborbitale de la dynamique environnementale à travers des changement rapides (millénaires et submillénaires) qui semblent bien corrélés entre les courbes de la végétation steppique et semi-désertique et des reconstructions climatiques de la carotte OPD 976 (Fig. 7.4. a, i & j), et l'enregistrement des IRD et des isotopes planctoniques dans l'Atlantique nord (Fig. 7.4. b & f), ainsi que des températures de surfaces en Mer d'Alboran (Fig. 7.4. g) et de l'humidité ouest-africaine (Fig. 7.4. h).

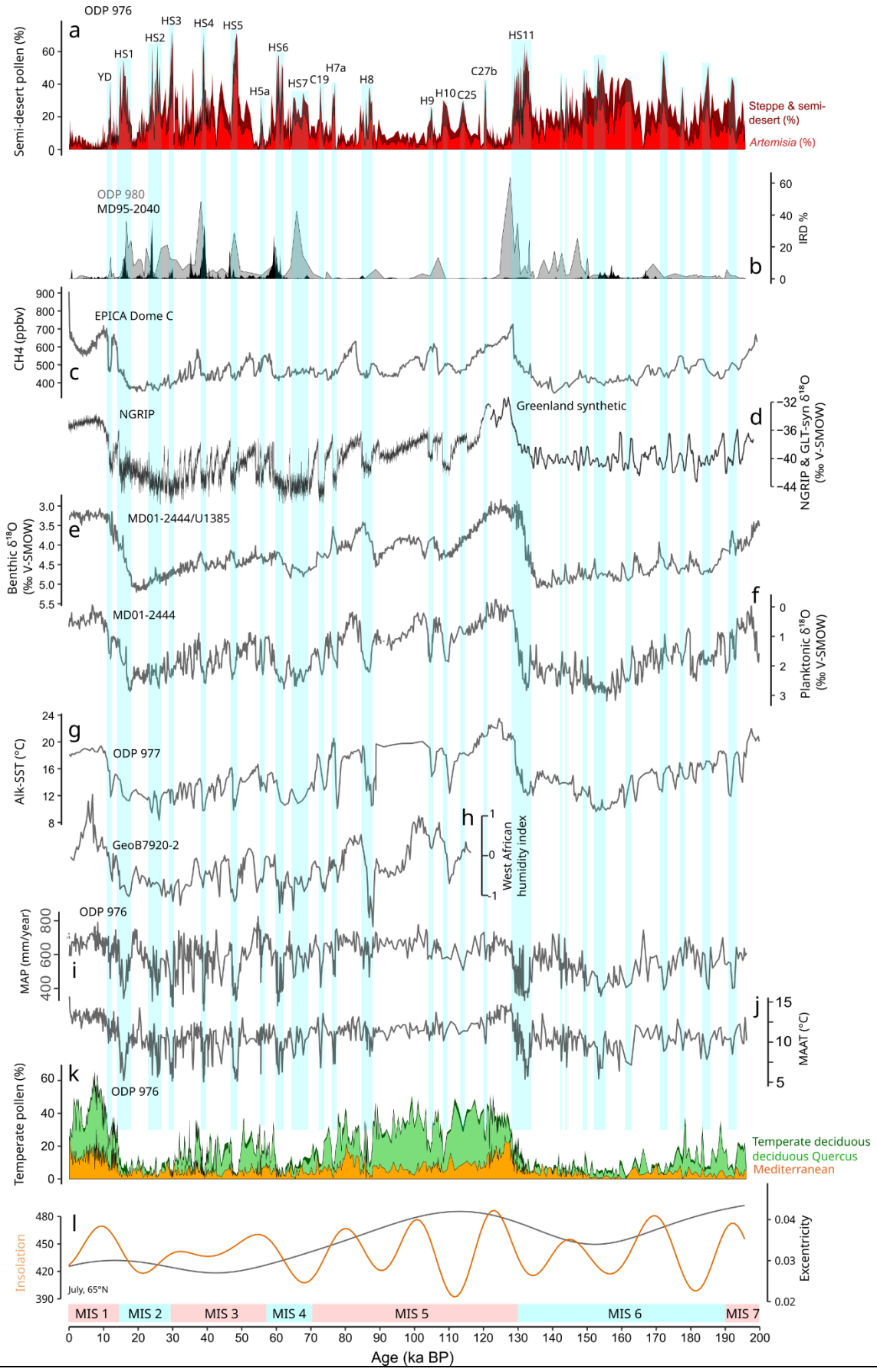


Fig. 7.4. Comparaison des changements climatiques et de végétation en Méditerranée sud-occidentale depuis 200 000 ans avec les principales courbes paléoclimatiques de référence

globale. a: pourcentages polliniques de la végétation steppique et semi-désertique de la carotte ODP 976 (Charton et al., 2025; Combourieu-Nebout et al., 1999, 2002; Combourieu-Nebout et al., 2009, et cette thèse) ; **b**: pourcentages d'Ice-Rafted Debris (IRD) des carottes ODP 980 (Nord-Est Atlantique, McManus et al., 1999) et MD95-2040 (marge ouest-ibérique, de Abreu et al., 2003) ; **c** : concentration en méthane du carottage Antarctique EPICA Dome C (chronologie AICC2012, Jouzel et al., 2007) ; **d**: rapport isotopique de l'oxygène du carottage arctique NGRIP (chronologie GICC05, Rasmussen et al., 2014) et courbe synthétique du Groënland entre 125 et 200 ka BP (Barker et al., 2011) ; **e**: rapport isotopique de l'oxygène benthique des carottes compilées MD01-2444 et U1385 au sud-ouest de la péninsule Ibérique (Hodell et al., 2023) ; **f**: rapport isotopique de l'oxygène planktonique de la carotte MD01-2444 (Sierro et al., 2020) ; **g**: températures de surface (SST) reconstruites à partir des alkénones de la carotte ODP 977 en Mer d'Alboran (Martrat et al., 2004) ; **h** : index d'humidité continentale ouest-africaine de la carotte GeoB7920-2 sur la côte mauritanienne (Tjallingii et al., 2008) ; **i** : températures moyennes du mois le plus froid reconstituées à partir des assemblages polliniques de al carotte ODP 976 avec une approche multi-méthodes (cette étude) ; **j**: excentricité de l'orbite terrestre (Laskar et al., 2004) et insolation à 65° N (Berger & Loutre, 1991). Les stades isotopiques marins (MIS) suivent Lisiecki et Raymo (2005). Les barres verticales bleues indiquent les principaux évènements froids mis en évidence dans la carotte ODP 976.

Les reconstructions des SSTs à partir des alkénones de la carotte ODP 977 (Martrat et al., 2004) sont cohérentes avec les reconstructions des températures à partir du pollen dans la carotte ODP 976, notamment à travers les évènements abrupts froids depuis 200 000 ans (dans la limite de la résolution temporelle et du modèle d'âge d'ODP 977). La corrélation précise entre les pics de végétation steppique et semi-désertique dans l'enregistrement d'ODP 976 et les pics d'IRD dans l'Atlantique Nord est rendue difficile par l'absence d'enregistrement d'IRD à haute résolution continu sur 200 000 ans avec une calibration chronologique robuste. Si les pics enregistrés dans les deux carottes ODP 980 et MD95-2040 (de Abreu et al., 2003 ; McManus et al., 1990) semblent montrer globalement une bonne correspondance avec les refroidissements abrupts mis en évidence dans la carotte ODP 976, des décalages temporels sont visibles, artefacts des différences de modèle d'âge. La mise au point d'une courbe de référence d'IRD à haute résolution dans l'Atlantique Nord sur plusieurs cycles climatiques aiderait à préciser ces corrélations, particulièrement pour les évènements de Heinrich moins connus (H5a, H7-10), avec une différenciation latitudinale pour comprendre l'intensité des évènements de débâcles d'icebergs et leur impact sur les environnements méditerranéens. Enfin, une correspondance notoire est observée entre les diminutions abruptes de précipitations reconstruites à partir du pollen dans la carotte ODP 976, et les épisodes de sécheresse africaine visibles dans la courbe de l'index d'humidité ouest-africaine et construite à partir de données sédimentaires au large de la Mauritanie (bien que disponible pour les derniers 115 ka BP seulement). Cette correspondance souligne un lien étroit entre les périodes humides et sèches africaines et le climat méditerranéen (Blanchet et al., 2021; Tjallingii et al., 2008). Les périodes répétées de sécheresse et de faible activité des systèmes hydriques en Afrique du Nord ont pu participer à accentuer les épisodes d'aridité en Méditerranée, particulièrement durant la transition MIS 5-MIS 4 et la progression de la glaciation.

Ainsi, cette comparaison globale montre que les oscillations climatiques millénaires sont une caractéristique pérenne du système climatique dans l'hémisphère nord et particulièrement des environnements méditerranéens au cours des derniers 200 000 ans, bien que leur amplitude soit limitée pendant le MIS 6 dû à l'intensité de la glaciation à ce moment, ainsi que durant l'interglaciaire du MIS 5 pendant lequel des conditions relativement humides et tempérées se sont maintenues (Hodell et al., 2023 ; Margari et al., 2010 ; ce travail sections 4.5.2 et 6). Les évènements climatiques abrupts enregistrés dans la séquence palynologique et paléoclimatique de la carotte ODP 976 sont mis en lien avec des processus globaux impliquant à la fois les hautes latitudes (liés aux paramètres d'excentricité et d'obliquité, à l'extension des calottes polaires, aux températures polaires et aux débâcles d'icebergs) et les basses latitudes (à travers les cycles de précession, les moussons et les périodes humides et sèches africaines).

La carotte ODP 976 peut désormais être intégrée parmi les principales longues séquences méditerranéennes ayant enregistré les changements environnementaux et climatiques sur 200 000 ans. Sur la figure 7.5, seules les principales longues séquences et dont les données sont disponibles ont été représentées, tandis que d'autres séquences couvrant le dernier cycle climatique existent mais ne sont pas ou seulement partiellement disponibles, comme la carotte MD04-2845 (Sánchez Goñi, 2021, 2022), les enregistrements continentaux des séries du Bouchet (Reille et al., 1998), des Echets (de Beaulieu & Reille, 2008), de Lagaccione (Magri, 1999), de Fimone (Pini et al., 2010), d'Azzano Decimo (Pini et al., 2009), ou encore du lac Van (Litt et al., 2014). L'étude de la carotte marine ODP 976 permet donc de combler une lacune géographique et temporelle en présentant une séquence palynologique continue et à haute résolution pour la Méditerranée occidentale, complémentaire de la séquence continentale de Padul (Camuera et al., 2019). Un tel enregistrement continu sur 200 000 ans à haute résolution manque encore en Méditerranée centrale, mais devrait être bientôt représenté par la séquence de Fucino (Giaccio et al., 2024), ainsi que sur la côte ouest-ibérique où des études sont encore en cours (Donders et al., 2024). Finalement, la contribution de cette thèse permet d'enrichir notre connaissance des changements de végétation et de climat au cours des deux derniers cycles climatiques à l'échelle de tout le bassin méditerranéen, panorama qui devrait être complété par les études à venir prochainement en Italie et sur la côte atlantique. Cette première comparaison à l'échelle de la Méditerranée sur un transect ouest-est permet déjà de mettre en évidence la variabilité spatiale de la réponse de la végétation méditerranéenne en réponse aux cyclicités orbitales et millénaires.

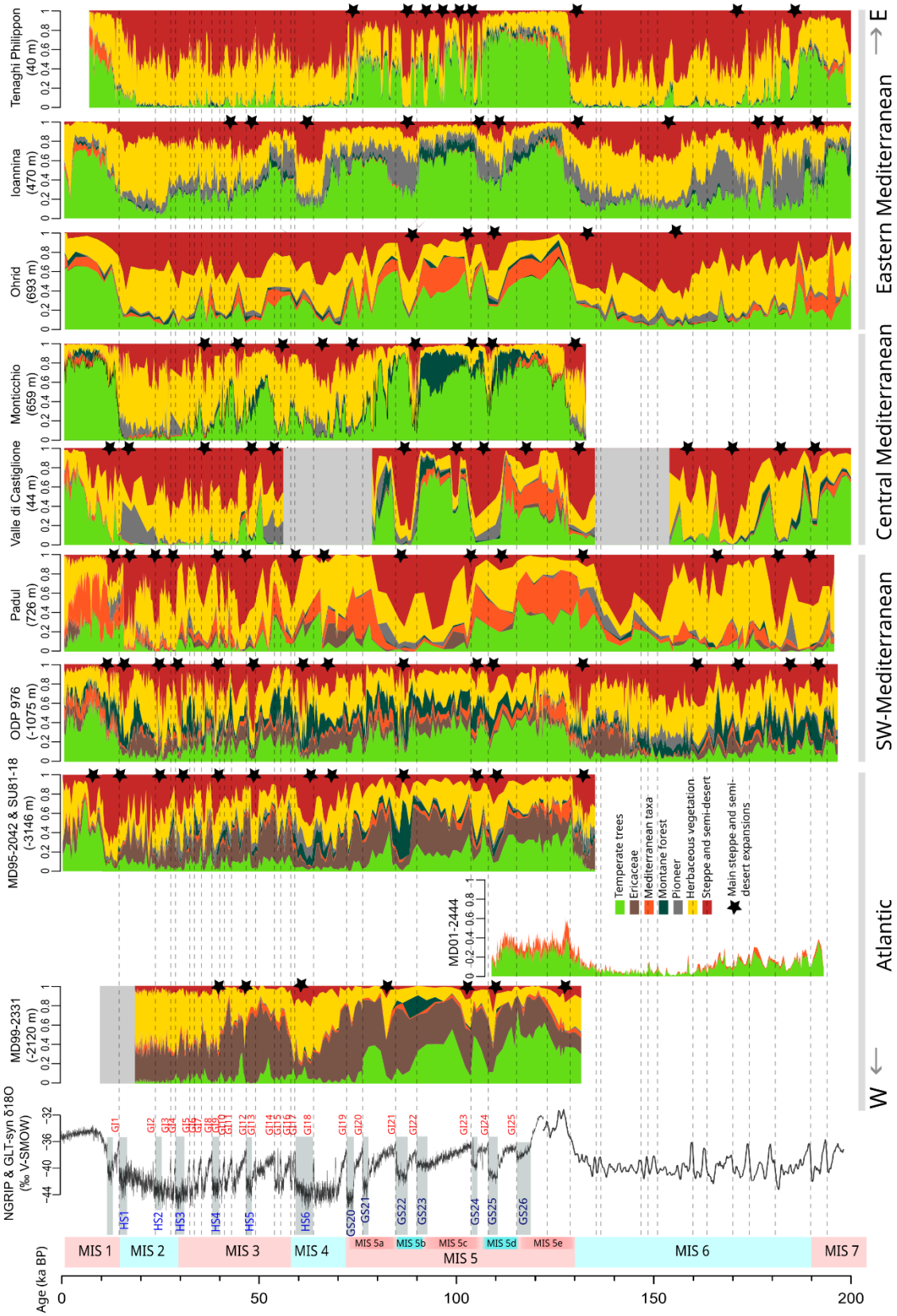


Fig. 7.5. Dynamique de la végétation Méditerranéenne depuis 200 000 ans : comparaison entre l'enregistrement palynologique synthétique d'ODP 976 et les principales autres longues séquences palynologiques couvrant les derniers 200 000 ans et disponibles en région méditerranéenne et en marge de la péninsule Ibérique, sur un transect ouest-est : MD99-2331 2331 (Naughton et al., 2007, 2009; Sánchez Goñi et al., 2005, 2008, 2017), MD01-2444 (Margari et al., 2010, 2014; Tzedakis et

al., 2018), MD95-2042 & SU81-18 (Sánchez Goñi et al., 1999, 2000, 2009, 2017), ODP 976 (This study, Charton, 2025; Combourieu-Nebout et al., 1999, 2002, 2009a, 2009b), Padul (Camuera et al., 2019), Valle di Castiglione (Follieri et al., 1988), Monticchio (Allen et al., 2000; Allen & Huntley, 2009; Brauer et al., 2007), Ohrid (Sadori et al., 2016; Sinopoli et al., 2018), Ioannina (Roucoux et al., 2011; Tzedakis et al., 2002, 2003, 2004 et données inédites communiquées personnellement par Katherine Roucoux en 2025), Tenaghi Philippon (Koutsodendris et al., 2023; Milner et al., 2012, 2013, 2016; Tzedakis et al., 2006). Les groupes écologiques suivent ceux établis pour ODP 976, et *Pinus* a été exclu des assemblages pour une meilleure comparaison, sauf pour Ioannina où il a été inclus dans le groupe des taxons pionniers suivant Roucoux et al., (2011). La courbe isotopique du Groënland est donnée pour référence des oscillations rapides incluant les interstadiaires (GI, en rouge) et les stadiaires (GS et HS, en bleu) (Rasmussen et al., 2014).

A échelle orbitale, toutes les séquences montrent un développement rapide et important de la forêt tempérée pendant le MIS 5, avec une composante d'arbres décidus largement plus importante dans les séquences de Monticchio, Ioannina et Tenaghi Philippon, et une composante méditerranéenne majoritaire à Padul, Valle di Castiglione et Ohrid. Les transitions glaciaire / interglaciaire (MIS 6 / MIS 5) puis l'entrée en glaciation (MIS 5/ MIS 4) apparaissent beaucoup plus abruptes dans les séquences de la Méditerranée orientale et centrale, tandis que des transitions plus progressives sont mises en évidence dans les séquences de la Méditerranée occidentale et de l'Atlantique. Les phases glaciaires (MIS 6 et MIS 4-2) sont particulièrement marquées à Tenaghi Philippon, où la végétation arborée est très réduite, voire absente pendant les évènements stadiaires (Tzedakis, 2005). Toujours à Tenaghi Philippon, un nombre plus important de changements abrupts et extrêmes pendant le MIS 5 a été identifié (Milner et al., 2013), clairement visibles dans notre comparaison. Ces particularités à Tenaghi Philippon indiquent des conditions spécifiques au site liées à la topographie (basse plaine éloignée des montagnes) impliquant un seuil de réponse rapide aux changements de température et d'humidité dans la région. Au contraire, à Ioannina la forêt tempérée s'est maintenue dans des proportions relativement importantes tout au long des derniers 200 000 ans, soulignant sa position de refuge climatique plus en altitude (Roucoux et al., 2011). Une observation similaire peut être faite à Ohrid, où la forêt mésophile est maintenue même pendant les stadiaires, et malgré leur intensité et leur caractère très abrupt (Sadori et al., 2016; Sinopoli et al., 2018, 2019). A Valle di Castiglione, malgré une résolution plus faible de l'enregistrement, les dynamiques de végétation semblent très similaires à celles de Tenaghi Philippon avec des glaciaires très prononcés où la végétation arborée est drastiquement réduite, des transitions glaciaire/interglaciaire abruptes, et des épisodes d'expansion de steppe très rapides pendant le MIS 5. Ces similarités peuvent être expliquées par la faible altitude de ces deux sites induisant des seuils de tolérance proches aux changements des conditions climatiques.

De manière frappante, il est moins facile d'identifier les changements de végétation abrupts liés aux cycles D-O pendant les glaciaires en Méditerranée orientale par rapport à la Méditerranée

occidentale. En effet, les phases d'expansion de la forêt tempérée pendant les GIs sont plus prononcées en Méditerranée occidentale par rapport à la Méditerranée orientale. De même, les stadiaires et particulièrement les HS sont beaucoup plus marqués dans les séquences occidentales. Ces deux observations combinées mettent en évidence un contraste plus important entre évènements stadiaires et interstadiaires dans les séquences de la Méditerranée occidentale par rapport à la Méditerranée orientale pendant les glaciaires. Pendant l'interglaciaire du MIS 5, ce schéma semble s'inverser, avec un contraste entre stadiaires et interstadiaires plus important dans les séquences orientales de Tenaghi Philippon, Ohrid, ainsi que celles de la Méditerranée centrale par rapport aux séquences occidentales.

Ce patron différentiel entre Méditerranée occidentale et orientale pendant les glaciaires avait déjà été mis en évidence par des comparaison régionales (Tzedakis, 2005), qui avaient également souligné l'absence de discrimination entre stadiaires « modérés » (type GS) et stadiaires plus « extrêmes » (type HS) dans les séquences orientales et dans les séquences de l'Atlantique Nord (MD99-2331 dans notre comparaison, mais aussi carotte MD04-2845 (Fourcade et al., 2022; Sánchez Goñi, 2022b), contrairement aux séquences de la Méditerranée occidentale et centrale. L'impact comparable des GS et des HS en Méditerranée orientale (à Tenaghi Philippon) et dans les séquences de l'Atlantique Nord a été expliqué par la présence déjà très limitée de la forêt tempérée tout au long du glaciaire dans ces régions, et donc un seuil de tolérance plus bas aux conditions de froid et d'aridité pendant le stadiaires. Cependant, la particularité des séquences atlantiques réside dans l'importance de la végétation eurosibérienne et en particulier des Ericaceae, qui se développent pendant les interstadiaires suite à l'augmentation des précipitations d'hiver. Par comparaison, les interstadiaires dans les séquences de la Méditerranée occidentale (ODP 976 et Padul) sont marqués par une expansion plus importante de la forêt tempérée et méditerranéenne.

Les deux enregistrements palynologiques de la carotte marine ODP 976 et de la séquence continentale de Padul offrent une vision complémentaire des changements de végétation du sud-ouest Méditerranéen sur 200 000 ans. Malgré la plus faible résolution de la série de Padul, une bonne correspondance est observée de manière générale entre les deux enregistrements, particulièrement dans la réponse de la végétation aux cycles D-O du dernier glaciaire. Plusieurs différences notoires sont cependant observables entre les deux séquences, notamment dans la représentation des principaux taxa polliniques : la carotte ODP 976 présente une proportion plus importante de pollen d'Ericaceae et de *Cedrus*, conséquence de l'aire de captation plus importante de la séquence qui enregistre une synthèse des environnements du sud-ibérique et du nord de l'Afrique. L'expansion du domaine eurosibérien dans la péninsule Ibérique pendant les phases interstadiaires est ainsi certainement à l'origine de l'apport majeur de pollen d'Ericaceae dans la carotte ODP 976. Le caractère plus « local »

de l'enregistrement de Padul est indiqué par la représentation plus importante des taxons méditerranéens, mais aussi des plantes hygrophiles non représentées dans notre comparaison (Camuera et al., 2019). Les différences dans les dynamiques de végétation enregistrées dans les deux enregistrements peuvent donc indiquer une divergence entre les tendances régionales (représentées par la carotte ODP 976) et locales (représentées par la série de Padul). Ainsi, au cours du dernier interglaciaire Padul montre une tendance à l'aridité très précoce au cours du MIS 5c (dès ~100 ka BP), avec l'expansion rapide de la végétation herbacée et steppique, tandis qu'au même moment ODP 976 montre une prédominance de la forêt tempérée et des conditions interstadiaires prolongées (Fig. 7.4). La sécheresse mise en évidence à Padul peut être reliée à l'index d'humidité africaine (Fig. 7.3., Tjallingii et al., 2008) qui montre une baisse abrupte de l'activité des systèmes hydriques ouest-africains dès 100 ka BP, et qui a pu avoir un impact sur les environnements continentaux du sud-est ibérique. L'enregistrement de la carotte ODP 976 durant cette période apparaît en revanche majoritairement lié à l'influence atlantique, vu les conditions tempérées très similaires visibles dans la carotte MD95-2042 au large de la péninsule Ibérique (Fig. 7.4). La Méditerranée sud-occidentale, représentée par les séquences du site ODP 976 et de Padul, apparaît donc comme une région intermédiaire, qui partage des similarités avec les séquences atlantiques (domaine eurosibérien et influence des évènements froids de l'Atlantique Nord) et les séquences du reste de la Méditerranée (importance de la forêt tempérée et méditerranéenne pendant l'interglaciaire et les interstadaires). Si la végétation tempérée et méditerranéenne dans ces deux séquences semble plus stable pendant le MIS 5 et s'est maintenue pendant le dernier glaciaire avec des phases d'expansion majeures pendant les GI, elle s'est aussi montrée plus sensible aux évènements arides et particulièrement aux HS par rapport aux autres séquences méditerranéennes et atlantiques.

Cette comparaison soutient ainsi les conclusions de Tzedakis et al. (2004, 2005) qui ont souligné à la fois des réponses aux variations climatiques abruptes globalement différentes en Méditerranée orientale, centrale et occidentale aux variations climatiques abruptes, mais aussi l'importance des caractéristiques géographiques et climatiques locales qui modulent la réponse de la végétation à ces variations. L'enregistrement palynologique du site ODP 976 se situe dans une zone de transition entre le domaine ibéro-atlantique (représenté par les Ericaceae, l'influence des vents d'ouest, et l'importance des stadiaires nord-atlantiques), le domaine méditerranéen (représenté par la végétation méditerranéenne et tempérée résiliente tout au long du dernier cycle climatique) et le domaine nord-africain (à travers les formations à *Cedrus* en altitude et l'influence de l'aridité africaine). Les fluctuations climatiques mises en évidences dans l'enregistrement palynologique et paléoclimatique de la carotte ODP 976 montrent une prédominance de l'influence nord-atlantique pendant les interstadiaires, et une prédominance de l'influence méditerranéenne et nord-africaine

pendant les stadiaires. Cette position au carrefour de trois domaines bioclimatiques explique la sensibilité extrême de la région aux variations abruptes des températures pendant les glaciaires, avec un contraste très important entre GS / HS froids et arides, et GI tempérés et humides.

7.5. Néandertal dans son environnement instable depuis 200 000 ans en Méditerranée occidentale

Ce travail de synthèse a montré la présence continue de Néandertal en Méditerranée occidentale entre 200 000 et environ 35 000 ans BP, à travers des environnements changeants.

Au cours de l'avant-dernière période glaciaire (MIS 6), un nombre très limité de sites archéologiques bien datés sont disponibles, témoignant à la fois d'un potentiel biais taphonomique et de lacunes dans la recherche, mais également d'une population néandertalienne possiblement réduite pendant cette période. Un environnement froid et aride où domine la steppe a été reconstitué à partir de l'enregistrement de la carotte ODP 976 dans le sud-ouest méditerranéen pendant l'avant-dernier maximum glaciaire entre ~165 et ~150 ka BP. La coexistence d'industries lithiques traditionnelles (Mode 2 – Paléolithique inférieur ou Acheuléen tardif) et d'industries innovantes (Mode 3 – Paléolithique moyen ancien aussi appelé « Moustérien ») témoigne de la fin d'une longue période de transition où semblent avoir cohabité sur le territoire différentes populations humaines. A la fin du MIS 6, différentes études mettent en évidence une contraction des populations (Sánchez-Yustos & Diez-Martín, 2015; Yaworsky et al., 2024) qui précède l'abandon définitif des dernières industries lithiques acheuléennes au tout début de l'interglaciaire du MIS 5. Cette étude propose pour la première fois de mettre en relation cette contraction apparente des populations à la fin du MIS 6 et l'épisode de refroidissement et de sécheresse intense enregistré au cours du HS11 (~134-129 ka BP).

Un nombre plus important de sites archéologiques datant du MIS 5 est connu, indiquant potentiellement une période d'expansion démographique liée à un environnement favorable. Ces sites sont associés en grande majorité à des assemblages lithiques typiquement « moustériens » où domine le débitage Levallois. Les études génétiques montrent l'arrivée de nouvelles populations dans la péninsule Ibérique pendant cette phase (Vernot et al., 2021).

Par la suite, une diversification progressive des assemblages lithiques est observée à partir de la fin du MIS 5 et au cours des MIS 4-3, semblant accompagner le refroidissement progressif qui caractérise l'entrée en glaciaire. L'apparition d'industries nouvelles et « régionales » telles que les faciès Quina et Vasconien dans la région franco-cantabrique a été présentée comme témoignant de changements dans les comportements de subsistance des groupes néandertaliens, qui ont pu représenter des réponses adaptatives à un environnement de plus en plus instable (e.g. Banks et al., 2021; Rios-Garaizar, 2017).

Ainsi, s'il est encore très difficile d'établir des synchronies précises entre changements environnementaux enregistrés dans les archives paléoclimatiques marines et occupations humaines, l'intensité des occupations indiquée par le nombre de sites datés connus au cours du temps montre de potentielles phases d'expansion (MIS 5 et début du MIS 3) et de contraction (MIS 6, MIS 4, fin du MIS 3, ainsi que le HS11 et les HS6-4) des populations néandertaliennes (Fig. 7.6).

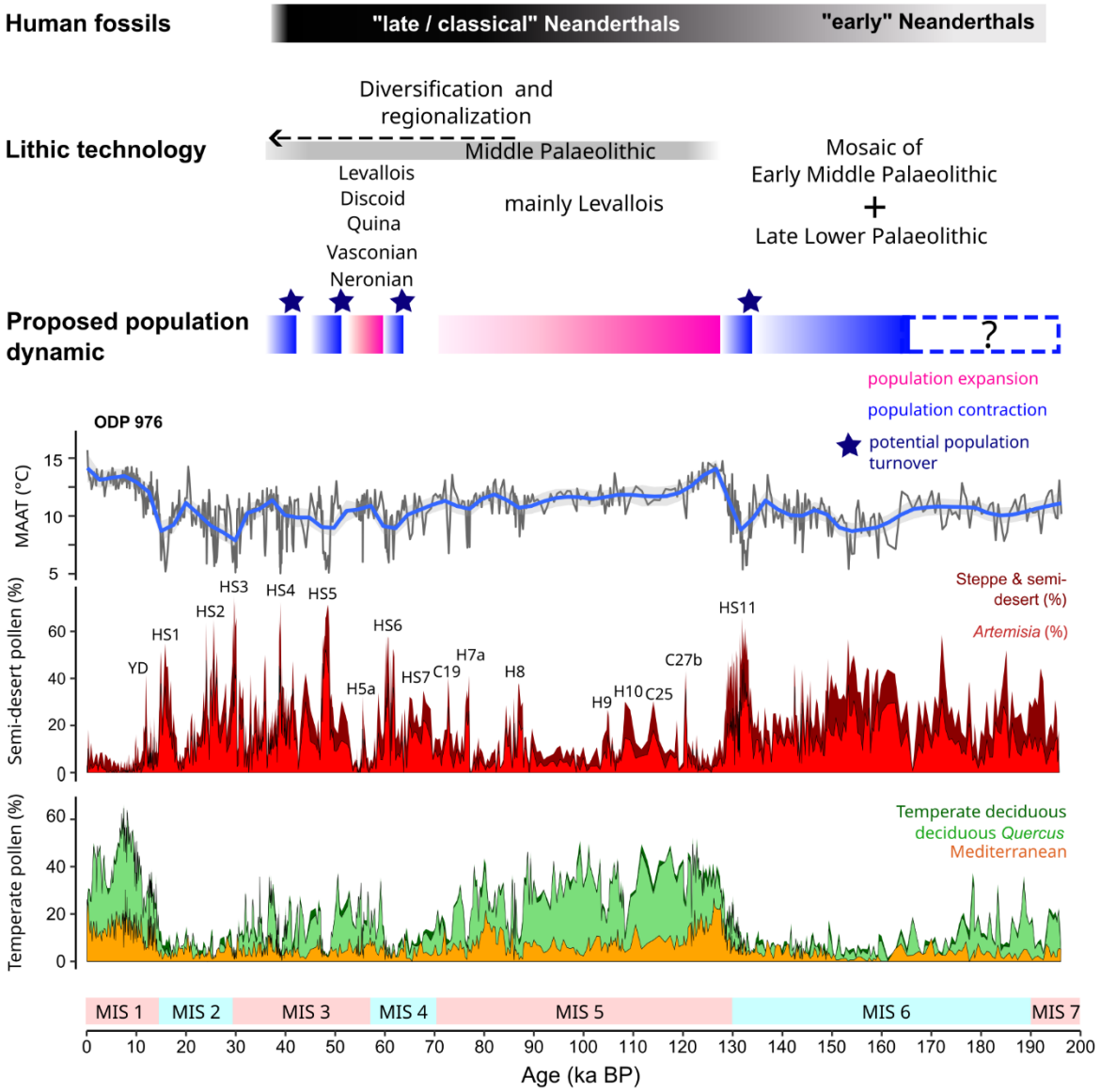


Fig. 7.6. Schéma synthétique des dynamiques de population en Méditerranée occidentale depuis 200 000 ans mises en perspective de l'enregistrement paléoclimatique de la carotte ODP 976 (pollen et températures moyennes annuelles – MAAT). Les principales phases d'accroissement et de replis démographique proposées à partir de cette synthèse sont présentées, ainsi que les potentiels évènements de crise majeure ayant pu mener à une modification de la population.

Cette figure propose une représentation schématique et hypothétique des dynamiques de population humaine au cours des derniers 200 000 ans, basée sur les interprétations qui ont émergé de la synthèse archéologique présentée dans les différentes parties de cette thèse. L'émergence du

« monde néandertalien classique », caractérisé par les industries du Paléolithique moyen et des fossiles néandertaliens dits « classiques », apparait postérieur à la transition MIS 6/MIS 5 et semble correspondre à l'établissement d'un climat régional tempéré et humide relativement stable, où les forêts tempérées et méditerranéennes occupent une proportion importante du territoire de la péninsule. Cette thèse montre que les principaux évènements froids et secs les plus intenses ayant pu avoir un impact sur les peuplements néandertaliens au niveau régional correspondent aux stadiaires de Heinrich le plus extrêmes, les HS11 et les HS6-4. L'hypothèse de contractions répétées de populations pendant ces évènements reste encore difficile à tester à partir des données archéologiques. L'incertitude des datations des sites archéologiques rend difficile l'estimation des potentielles phases de contraction et d'expansion à échelle millénaire en lien avec les alternances de stadiaires et interstadiaires au cours des MIS 5-3. La multiplication récente des études chronologiques sur sites archéologiques prenant pour référence les courbes de température du Groënland et la chronologie des évènements GI et GS (e.g. Demuro et al., 2023; Rios-Garaizar et al., 2024) permet de mieux replacer les évidences archéologiques dans un contexte climatique global de référence, et ainsi d'améliorer les corrélations Homme/environnement. La poursuite de ces efforts dans les futures études contribuera grandement à améliorer la corrélation entre les occupations humaines et le contexte environnemental et climatique : une perspective est donc de généraliser cette approche en créant une base de données de niveaux archéologiques qui peuvent être attribués de manière fiable à un épisode stadiaire ou interstadiaire, avec une attention particulière pour les HS (Albouy et al., 2023).

Ainsi, il est probable que la variabilité plus importante du climat au cours des MIS 4-3 ait eu un impact sur les dynamiques de peuplement néandertaliennes. Nous avons montré que cette variabilité était inédite dans la région au cours des derniers 200 000 ans. Les périodes précédentes ont été marquées par une moindre amplitude et une moindre fréquence des variations de températures et de précipitations au cours de l'avant-dernier glaciaire (MIS 6) et du dernier interglaciaire (MIS 5). Si cette hypothèse de l'impact de la variabilité climatique sur Néandertal reste difficile à tester, plusieurs mécanismes peuvent être envisagés, à travers lesquels elle a pu influencer les dynamiques de populations :

Mécanisme 1 : fragmentation des habitats. La variabilité climatique rapide a pu favoriser un contraste marqué pendant les stadiaires entre zones de steppe et semi-désert, et zones refuges où persistait la végétation tempérée et méditerranéenne. Cette fragmentation des environnements a pu pousser les populations à déserter certains territoires inhospitaliers et se replier dans des régions plus favorables, restreintes spatialement. Récemment, de nombreuses études ont modélisé la niche écologique de Néandertal en Europe occidentale (e.g. Albouy et al., 2024; Banks et al., 2008, 2021; Melchionna et al., 2018). Celle-ci correspond à l'espace géographique où les conditions

environnementales et climatiques permettent la survie et la reproduction de l'espèce. La plupart de ces études ont montré une préférence de Néandertal pour les environnements chauds et humides, où la végétation arborée est abondante (Benito et al., 2017; Yaworsky et al., 2024), et présentent au contraire les environnements froids et secs comme plus défavorables (Banks et al., 2021 ; Melchionna et al., 2018). Selon Albouy et al. (2024), la stabilité de l'environnement est un facteur plus important que les conditions de températures et de précipitations : les régions moins sensibles aux changements abrupts du MIS 3 et représentant des refuges glaciaires seraient préférées par Néandertal. Ainsi, l'intensité et la fréquence croissante des variations climatiques rapides à partir de la fin du MIS 5 a pu provoquer une diminution de la niche écologique de Néandertal en favorisant une instabilité croissante des environnements et la diminution des zones refuges. Yaworsky et al. (2024) ont reconstruit l'évolution de la niche fondamentale de Néandertal en Europe depuis 145 000 ans, et ont montré une réduction progressive de celle-ci au fur et à mesure de la progression du dernier glaciaire, et particulièrement après 65 ka BP. Ce timing est compatible avec la contraction des occupations observées pendant le MIS 4 (Banks et al., 2021), et avec le HS6, l'un des évènements froids et arides les plus intenses identifiés dans l'enregistrement de la carotte ODP 976.

Mécanisme 2 : réduction des ressources disponibles pendant les stadiaires. La modification de l'environnement a affecté la composition de la faune et de la flore en réduisant potentiellement les ressources disponibles pour l'alimentation des groupes néandertaliens. La disponibilité des ressources peut être estimée par le calcul de la productivité primaire nette (NPP, qui correspond à la biomasse végétale et animale), un indicateur qui semble déterminant pour la densité de population des groupes de chasseurs-cueilleurs (Zhu et al., 2021). Vidal-Cordasco et al. (2022) ont modélisé les changements de NPP dans la péninsule Ibérique pour la période comprise entre 50 et 30 ka BP. Cette étude a montré l'impact différentiel des oscillations climatiques rapides du MIS 3 sur la disponibilité des ressources dans la péninsule Ibérique en fonction des grandes zones bioclimatiques (eurosibérienne, supra-méditerranéenne, méso-méditerranéenne, thermo-méditerranéenne). Dans la zone eurosibérienne, ces variations auraient été beaucoup plus prononcées, et l'extinction de Néandertal aurait été corrélée à une diminution de la NPP durant le GS12, au cours d'une période située entre le HS5 et le HS4. Au contraire, la zone thermo-méditerranéenne au sud de la péninsule Ibérique aurait été marquée par une plus grande stabilité de la disponibilité en ressources et moins affectée par la variabilité climatique rapide. Ces conditions auraient permis la survie plus tardive de Néandertal dans la région.

Mécanisme 3 : contractions démographiques répétées. Il est encore très difficile d'estimer l'évolution démographique des populations néandertaliennes en Europe. Les études génétiques ont fourni des informations clé sur l'histoire démographique de Néandertal. La plupart estiment une petite taille de métapopulation néandertalienne, ainsi qu'une structure de population très nette avec une

division géographique en petits groupes de néandertaliens (Mafessoni et al., 2020; Mafessoni & Prüfer, 2017; Rogers, 2024; Rogers et al., 2017). Par ailleurs, la taille de la métapopulation semble avoir varié au cours du temps, avec des épisodes de contractions et de substitution (« *population turnovers* ») (Dalén et al., 2012; Fabre et al., 2009; Vernot et al., 2021). La petite taille des groupes géographiquement séparés semble aussi avoir favorisé une faible diversité génétique, estimée à travers l'hétérozygotie au sein d'une population (Castellano et al., 2014; Rogers, 2024). Ces caractéristiques peuvent amener à penser que la réduction répétée des habitats des groupes néandertaliens au cours des fluctuations climatiques a pu fragiliser la démographie des groupes en favorisant leur isolement, leur réduction, voire des extinctions localisées. Les approches par modélisation multi-agents ont également montré que des caractéristiques inhérentes aux groupes néandertaliens tels que le taux de mortalité, le taux de reproduction et la mobilité ont pu participer au déclin puis à l'extinction des populations néandertaliennes dans la péninsule Ibérique (Cucart-Mora et al., 2018).

Ces trois mécanismes sont fortement interconnectés : dans le cadre d'un environnement hautement instable, la fragmentation géographique des habitats et la diminution des ressources disponibles ont pu fragiliser des populations déjà peu nombreuses et fortement subdivisées. Ces mécanismes doivent être compris à échelle pluri-générationnelle, de l'ordre de quelques centaines d'années, temps qui correspond à la réponse observée de la végétation entre les périodes stadiaires et interstadiaires dans l'enregistrement de la carotte ODP 976. Finalement, il apparaît crucial d'étudier l'impact spatial de la variabilité climatique à haute fréquence, notamment sur l'aire de répartition des biomes, et donc des habitats de Néandertal. La notion de refuge climatique apparaît également centrale : en accord avec les résultats des modélisations de niches, cette étude montre l'existence de potentielle zones refuge dans des régions comme la Cantabrie, le littoral du sud-est ibérique, ou le littoral du sud-est de la France. Cependant, cette vision des zones refuges est potentiellement biaisée par l'important effort de recherche déployé dans certaines régions comme la Cantabrie, et doit être mieux comprise et étayée par de nouvelles données archéologiques et paléoécologiques pour en préciser la définition (Jones, 2022).

8. Conclusions et perspectives

Dans la lignée de précédentes études, cette thèse a montré le potentiel et les limitations des corrélations entre dynamiques humaines et environnementales au Paléolithique à partir des enregistrements paléoclimatiques marins. La séquence paléoclimatique à haute résolution du site ODP 976 permet de reconstruire pour la première fois les environnements de Néandertal et des premiers *Homo sapiens* en Méditerranée sud-occidentale depuis 200 000 ans. Elle montre des dynamiques de végétation et de climat à plusieurs échelles de temps au cours de l'avant-dernière période glaciaire (MIS 6) et du dernier cycle climatique (MIS 5-2). Une forte instabilité climatique, inédite depuis 200 ka BP, a caractérisé les MIS 4-3, période au cours de laquelle il est proposé que les populations néandertaliennes ont décliné progressivement avant leur extinction. Ce travail souligne l'importance du sud-ouest Méditerranéen pour mieux comprendre (i) l'impact de la variabilité climatique rapide sur les environnements terrestres méditerranéens et (ii) les dynamiques des peuplements paléolithiques au cours du Pléistocène dans le cadre de ces variations. La région se situe en effet au carrefour de l'océan Atlantique, de la mer Méditerranée, de l'Afrique et de la péninsule Ibérique, une position qui permet d'évaluer les interactions entre plusieurs influences climatiques au cours des variations abruptes du climat. Il a ainsi été montré que les environnements du sud-ouest méditerranéens se sont montrés très sensibles aux refroidissements abrupts de l'Atlantique Nord ainsi qu'aux épisodes de sécheresse africaine, tandis que la végétation tempérée et méditerranéenne s'est maintenue dans les zones refuges de la péninsule Ibérique y compris pendant les évènements froids et arides les plus extrêmes. La région a pu aussi représenter un refuge pour les populations humaines paléolithiques, et notamment pour Néandertal lors des périodes glaciaires et des épisodes stadiaires les plus intenses. Une survie plus tardive des néandertaliens au sud de la péninsule Ibérique après le HS4 est toujours soutenue par plusieurs études, bien que cette hypothèse doive encore être renforcée par de nouvelles datations. Les évènements climatiques les plus extrêmes identifiés dans l'enregistrement de la carotte ODP 976 et qui ont pu affecter les populations néandertaliennes sont représentés par le stadiaire de Heinrich (HS) 11, ainsi que les HS6-1. Bien qu'il soit encore difficile de corréler précisément l'enregistrement marin du site ODP 976 avec les chronologies des sites archéologiques, cette synthèse soutient une contraction des populations humaines néandertaliennes pendant ces évènements, et particulièrement pendant les HS6-4 qui ont précédé l'extinction de Néandertal.

Ces hypothèses pourront être testées dans de futures études à travers des synthèses plus exhaustives des chronologies d'occupations néandertaliennes mises en lien avec les changements environnementaux mis en évidence dans la carotte ODP 976. Des corrélations plus précises entre changements environnementaux et dynamiques de peuplement humain pourraient être établies à travers une approche par modélisation bayésienne qui permettrait de mettre au point une synthèse

chronologique robuste des occupations néandertaliennes à échelles régionales ainsi qu'à échelle de la péninsule Ibérique. Cette synthèse chronologique poussée existe à l'échelle de l'Europe occidentale (Higham et al., 2014) et pour la péninsule italienne (Higham et al., 2024), mais doit encore être complétée pour l'ensemble de la péninsule Ibérique (Marín-Arroyo et al., 2018; Vidal-Cordasco et al., 2022), région clé pour comprendre le scénario de l'extinction de Neandertal.

Des approches statistiques et géostatistiques plus poussées pourraient également être envisagées afin d'estimer quantitativement les changements démographiques des populations néandertaliennes (Schmidt et al., 2021 et références citées). Cette évolution démographique reconstituée pourrait être mise en parallèle des courbes environnementales et climatiques de référence (comme celle de la carotte ODP 976) afin de tester l'hypothèse de contractions démographiques durant les périodes froides et sèches et d'expansions démographiques durant les périodes plus tempérées et humides.

Des approches de modélisations appliquées à la végétation pourraient aussi être développées afin de mieux comprendre les dynamiques spatiales des changements environnementaux dans la péninsule Ibérique en réponse aux changements climatiques rapides, et de les comparer avec les enregistrements fossiles. La réponse des populations humaines aux changements climatiques rapides pourrait également être explorée à travers des approches de modélisation (modèles de prédiction de répartition, modèles multi-agents prenant en compte l'environnement…), avec une attention renforcée pour la composante spatiale dans la péninsule Ibérique. L'identification des potentiels refuges climatiques comme la Cantabrie, la Catalogne ou le sud-est de la péninsule Ibérique, pourrait ainsi être testée à travers ces approches.

L'hétérogénéité spatiale des environnements au cours du temps pourra être explorée à travers des synthèses paléoenvironnementales plus exhaustives, prenant mieux en compte les archives paléobotaniques terrestres dans la péninsule Ibérique. Même si celles-ci sont généralement discontinues et difficilement datées, il serait très intéressant d'approfondir leur lien avec la nouvelle longue série palynologique de la carotte ODP 976, afin d'enrichir notre vision des changements de végétation dans la péninsule Ibérique (Carrión et al., 2024; Ochando et al., 2020, 2022). Par ailleurs, il apparaît prometteur de mettre en perspective cette nouvelle longue série palynologique avec d'autres longues séquences palynologiques du pourtour méditerranéen qui seront bientôt disponibles, comme celle de la carotte MD01-2444 (Margari et al., 2010, 2014 ; Tzedakis et al., 2018). La comparaison des changements de végétation enregistrés de part et d'autre du détroit de Gibraltar sur 200 000 ans permettra de mieux comprendre les variations d'influences atlantiques et méditerranéennes sur les environnements sud-ibériques à long terme et au cours des variations rapides. Cette synthèse des

archives palynologiques marines et continentales permettrait d'obtenir une image intégrée des changements de végétation dans la péninsule Ibérique sur le temps longs et en prenant mieux en compte la composante spatiale.

Parmi les perspectives de cette étude se trouve aussi l'exploration plus poussée des relations entre dynamiques des environnements du sud-ouest méditerranéens et influences africaines. De nouvelles archives paléoenvironnementales au Maroc et en Algérie permettraient d'évaluer la composante africaine dans l'enregistrement de la carotte ODP 976, et de mieux comprendre les liens entre les dynamiques environnementales sur les deux versants de la Méditerranée au cours du Pléistocène.

Au terme de ce travail, l'étude palynologique de la séquence ODP 976 présente un enregistrement paléoenvironnemental et paléoclimatique continu sur 200 000 ans qui pourra servir de référence afin de contextualiser les occupations néandertaliennes dans la région clé du sud-ouest Méditerranéen. Cette thèse s'inscrit également dans le projet d'étude palynologique sur 1.2 million d'années de la carotte ODP 976, qui fournira ainsi l'un des enregistrements les plus longs et complets en Méditerranée sur le Pléistocène.

9. Liste des figures

Fig. 1.1. Carte représentant la répartition des aires d'étagement de végétation méditerranéenne, ainsi que la zone d'étude (mer d'Alboran) et le lieu de forage de la carotte ODP 976……p.7

Fig. 1.2. Carte de la région de la Mer d'Alboran représentant les principales caractéristiques géographiques et physiques, ainsi que les principaux courants marins……..p.10

Fig. 1.3. Comparaison des deux configurations de l'Oscillation Nord Atlantique (NAO) et impact sur les anomalies de précipitations en Europe occidentale……..p.12

Fig. 1.3. Coupe verticale du bassin Méditerranéen occidental montrant le gradient de salinité et la stratification des masses d'eau……p.13

Fig. 1.4. Structure climato-stratigraphique globale et évolution des paramètres orbitaux au cours des derniers 200 000 ans……..p.17

Fig. 1.5. Structure théorique des cycles D-O et d'un cycle de Bond……p.20

Fig. 1.6. Courbes de références pour les changements suborbitaux au cours du dernier cycle climatique……..p.22

Fig. 1.7. Principales séquences palynologiques longues et continues disponibles pour les derniers 200 000 ans en Méditerranée et sur la côte Atlantique……..p.24

Fig. 1.8. Cartes des principaux sites ayant livré des restes humains attribués à Néandertal en Eurasie occidentale……p.27

Fig. 1.9. Synthèse des principales trajectoires climatiques, humaines et culturelles en Europe occidentale au cours des derniers 200 000 ans……p.29

Fig. 1.10. Aire de répartition d'*Homo neanderthalensis* avec les voies principales de migration ayant amené à la colonisation de l'Eurasie par *Homo sapiens*……p.33

Fig. 1.11. Principaux sites du MIS 3 présentant des restes humains attribués à *H. sapiens*, datés d'avant 30 ka BP, avec les aires de répartition des principales cultures dites « de transition »……..p.35

Fig. 2.1. Mission d'échantillonnage à Brême (Avril 2022)……..p.45

Fig. 2.2. Trois spécimens de *Limacina retroversa* identifiés dans le refus de tamis de l'échantillon B6H4 130-132 (profondeur : 47.40 m), correspondant au MIS 6 ……..p.47

Fig. 2.3. Comparaison du facies de deux échantillons proches traités à l'HF 40% et à l'HF 70%.....p.48

Fig. 2.4. Comparaison du facies d'un même échantillon traité durant la thèse à l'HF 40% (à gauche) et à 70% (à droite)……..p.48

Fig. 2.5. Exemples de palynomorphes pyritisés……p. 49

Fig. 2.6. Concentration pollinique calculée pour les 120 échantillons traités et analysés au cours de la thèse……p.50

Fig. 2.7. Comparaison entre les deux modèles d'âge basés sur les datations au radiocarbone uniquement et sur les points de calage avec la stratigraphie des interstadiaires du Groënland…….p.55

Fig. 2.8. Modèle d'Age pour ODP 976 construit dans cette étude couvrant les derniers 200 000 ans……p.59

Fig. 2.9. Schéma du principe sur lequel reposent les méthodes de reconstructions climatiques à partir du pollen……p.62

Fig. 2.10. Cartes des valeurs modernes des six paramètres climatiques en Méditerranée occidentale à partir du modèle ERA 5 1960-2022 du ECMRWF……p.65

Fig. 2.11. Distribution des échantillons actuels constituant la base de données eurasiatique de référence……p.66

Fig. 2.12. Spectres de tolérance des principaux taxons identifiés dans la carotte ODP 976 aux six paramètres climatiques reconstruits à partir de la base de données eurasiatique de référence……p.68

Fig. 3.1: Vegetation distribution and position of the marine and terrestrial sites discussed in the text……p.79

Fig. 3.2. Age model for ODP 976 based on radiocarbon dates (upper 10 m) and correlation with Greenland interstadials chronology……p.82

Fig. 3.3. Synthetic pollen diagram representing the main pollen taxa identified in the sequence across the time……p.88

Fig. 3.4: PCA biplot of variables (ecological groups of taxa) and samples.p……p.91

Fig. 3.5. Pollen-based climate reconstructions……p.93

Fig. 3.6. Correlation of the Greenland NEEM record with the main proxy available for ODP 976 core……p.96

Fig. 3.7. Correlation between Greenland NEEM record, IRD deposition (brown curve for the Atlantic records) and the main marine proxies available for the six marine cores……p.98

Fig. 3.8. Comparison between marine and terrestrial records around the Iberian Peninsula……p.102

Fig. 3.9. Comparison between (a) the structure of the last deglaciation and (b) the HS4 / GI8 transition (this study) in the palynological record of ODP 976……p.104

Fig 3.10. Comparison between different pollen-based climate reconstructions ……p.106

Fig. 3.11. Maps of archaeological sites and their associated technocomplexes with dates ranges falling before (A), during (B) and after (C) the GS9 / HS4. Dates from all dating methods and confidence index 1 and 2 were included……p.111

Fig. 3.12. Maps of archaeological sites and their associated technocomplexes with dates ranges at 95% falling in the interval before (A), during (B) and after (C) the GS9 / HS4. Only radiocarbon dates with confidence index 2 were included……p.113

Fig. 4.1. Location of the main paleoenvironmental records mentioned in the text covering the last climatic cycle……p.123

Fig. 4.2. Graphical correlation between NGRIP interstadial chronology (GICC05 and GICC05modelext ages) and ODP 976 *G. bulloides* $\delta^{18}O$……p.124

Fig. 4.3. Correlation between the ODP 976 Mg/Ca-based Sea Surface Temperatures and the Dongge Cave and Corchia Cave speleothem oxygen isotope records……p.125

Fig. 4.4. Age versus depth model for ODP 976 from 0 to 42 m depth……p.126

Fig. 4.5. Pollen diagram of selected taxa covering MIS 5-4 (~130-57 ka BP) plotted against age……..p.129

Fig. 4.6. Pollen diagram of selected taxa covering MIS 3-1 (~57-11 ka BP), plotted against age……p.130

Fig. 4.7. Multimethod pollen-based climate reconstructions for MIS 5-4 interval from the ODP 976 record……..p.135

Fig. 4.8. Multimethod pollen-based climate reconstructions for MIS 3-1 interval from the ODP 976 record……p.136

Fig. 4.9. ODP 976 clay mineralogical composition over the last climatic cycle (130-10 ka BP)……p.137

Fig. 4.10. ODP 976 multiproxy record (7-133 ka BP) used for the multivariate analyses……p.139

Fig. 4.11. Correlation matrix of the fifteen selected variables, including the main ecological groups of pollen taxa and the five clay minerals……p.140

Fig. 4.12. PCA plot of variables, including the main ecological groups of pollen taxa and the five clay minerals……p.142

Fig. 4.13. Millennial climate oscillations during the last glacial period (MIS 4-2) recorded at ODP site 976 through multiple proxies and compared with the Greenland record on GICC05 timescale……..p.144

Fig. 4.14. Comparison between Ericaceae percentages in the ODP 976 pollen record and insolation at 65°N latitude……p.148

Fig. 4.15. Comparison of the ODP multiproxy record for MIS 4-1 with other records from the North Atlantic, Greenland, and the southwestern Mediterranean region……p.150

Fig. 4.16. Comparison between the structure of the HS6 to HS1 in the ODP 976 multiproxy record……p.152

Fig. 4.17. Millennial climate oscillations during the last interglacial (MIS 5) in the ODP 976 multiproxy record, compared with the Greenland record on GICC05modelext timescale……p.158

Fig. 4.18. Comparison of the ODP multiproxy record for MIS 5 with other records from the North Atlantic, Greenland, and the Mediterranean region……p.162

Fig. 4.19. Location of Middle Palaeolithic sites with radiometric dates falling within MIS 5, MIS 4 and MIS 3 in the Iberian Peninsula……p.166

Fig. 4.20. Chronology of the main well-dated Middle Palaeolithic archaeological sites in the Iberian Peninsula during MIS 5-3……p.168

Fig. 5.1. Geographical location of ODP site 976, together with the main paleoclimatic archives covering Termination II and discussed in the text……p.182

Fig. 5.2. Multiproxy record of ODP 976 between 120 and 140 ka BP……p.183

Fig. 5.3. Comparison of climate reconstructions from ODP 976 with other speleothem and marine records……p.189

Fig. 5.4. Comparison between the two terminations in the ODP 976 multiproxy record……..p.192

Fig. 5.5. Comparison of climate records from Antarctic, North-Atlantic, and the Alboran Sea between 140 and 120 ka BP……..p.195

Fig. 6.1. Map showing the location of ODP 976 core together with other paleoenvironmental and paleoclimate records covering part or all of MIS 6……..p.206

Fig. 6.2. Age versus depth model for the MIS 6 part of ODP 976 record……..p.207

Fig. 6.3. Pollen diagram of selected taxa for MIS 6 interval in the ODP 976 record, plotted against age……...p.211

Fig. 6.4. *Limacina retroversa* specimen found in sample B6H4 130-132……p.214

Fig. 6.5. Pollen-based climate reconstructions for MIS 6 interval from the ODP 976 record……..p.216

Fig. 6.6. Synthesis of vegetation changes in the Mediterranean during MIS 6 based on available palynological sequences……...p.221

Fig. 6.7. Millennial climate changes during MIS 6……p.225

Fig. 6.8. Comparison between the precipitation pattern reconstructed from ODP 976 with our multi-method approach (mean) (this study) and from Padul……p.228

Fig. 6.9. Comparison of millennial changes during the last glacial (MIS 2-4) and the penultimate glacial (MIS 6)……p.232

Fig. 6.10. Distribution of archaeological sites and radiometrically dated human occupation in western Mediterranean attributed to MIS 6……p.235

Fig. 7.1. Synthèse des données disponibles pour la carotte ODP 976 sur 200 000 ans présentées dans cette thèse et mises en parallèle de la courbe isotopique du Groënland……p.248

Fig. 7.2 Analyse en Composantes Principales (PCA) appliquée à l'enregistrement ODP 976 sur 200 000 ans (incluant 498 échantillons communs entre les analyses palynologiques et de composition d'argiles)……p.251

Fig. 7.3. Comparaison des changements rapides de végétation et de climat dans l'enregistrement d'ODP 976 pendant la dernière période glaciaire (MIS 4-2), le dernier interglaciaire (MIS 5), et l'avant-dernier glaciaire (MIS 6)……p.253

Fig. 7.4. Comparaison des changements climatiques et de végétation en Méditerranée sud-occidentale depuis 200 000 ans avec les principales courbes paléoclimatiques de référence globale……p.257

Fig. 7.5. Dynamique de la végétation Méditerranéenne depuis 200 000 ans……..p.260

Fig. 7.6. Schéma synthétique des dynamiques de population en Méditerranée occidentale depuis 200 000 ans mises en perspective de l'enregistrement paléoclimatique de la carotte ODP 976……p.265

10. Liste des tableaux

Tableau 2.1. Principaux groupes écologiques et groupes de taxons végétaux utilisés pour l'interprétation des données palynologiques d'OPD 976……..p.52

Tableau 2.2. Liste des datations et points de contrôle utilisés pour construire le modèle d'âge d'ODP 976 sur 200 000 ans……p.58

Table 3.1. Recalibrated 14C dates for ODP 976 (OxCal 3.4), using the marine20 calibration curve and ΔR = -175 ± 35 correction for the Alboran Sea reservoir……p.81

Table 3.2. Tie points of ODP 976 core temperate pollen curve to Greenland GICC05 stratigraphy (Rasmussen et al., 2014) used to build the age model for the core……..p.82

Table 3.3. List of taxa identified in the ODP 976 record and their ecological group attribution……p.87

Table 3.4. Description of the main pollen zone with the main characteristics of the pollen assemblage, the vegetation and climate interpretation, and the associated Greenland Chronology……p.90

Table 3.5. R2 (Pearson correlation coefficient) and RMSE (Root Mean Square Error) values for the climate parameters reconstructed and the four methods……..p.94

Table 3.6. Synthesis of the dataset with a number of dates and sites included for each time range and confidence index……p.95

Table 4.1. Tentative correlation between the terminology of climatic events identified in the different types of records from the Northern Hemisphere during MIS 5……..p.121

Table 4.2. Control points used for the age model of ODP 976 core (130-11 ka BP)……..p.127

Table 4.3. Description of the pollen zones defined in Fig. 4.5 and Fig. 4.6, together with the main features of the climate reconstructions……p.133

Table 6.1. List of control points used to calibrate the ODP 976 record for the MIS 6 interval……..p.207

Table 6.2. Description of the pollen zones identified through CONISS cluster analysis……..p.213

Table 6.3. R^2 (coefficient of determination) and RMSE (Root Mean Square Error) values for the different climate parameters reconstructed with the four methods applied……..p.217

11. Déclaration sur l'utilisation de l'IA générative

L'Intelligence Artificielle (IA) générative a été utilisée ponctuellement au cours de ce travail pour deux fonctions spécifiques :

i) L'amélioration et le débogage des scripts R ayant servi aux plots, aux analyses statistiques, à la chronologie, et aux reconstructions climatiques.
ii) L'amélioration de la qualité d'expression en Anglais, à travers la recherche de synonymes et d'expressions alternatives dans des cas de phrases spécifiques.

Aucun texte, aucune analyse ni interprétation de données dans ce travail n'ont été générés par IA. Je reconnais l'impact social et environnemental ainsi que les dangers de l'utilisation de l'IA générative, et en prône un usage très modéré, limité à des tâches « mécaniques » qui représentent un réel gain de temps dans le cadre d'une thèse en trois ans.

12. Références bibliographiques

Adler, D. S., Wilkinson, K. N., Blockley, S., Mark, D. F., Pinhasi, R., Schmidt-Magee, B. A., Nahapetyan, S., Mallol, C., Berna, F., Glauberman, P. J., Raczynski-Henk, Y., Wales, N., Frahm, E., Jöris, O., MacLeod, A., Smith, V. C., Cullen, V. L., & Gasparian, B. (2014). Early Levallois technology and the Lower to Middle Paleolithic transition in the Southern Caucasus. Science, 345(6204), 1609–1613. https://doi.org/10.1126/science.1256484

Agusti, B., Alcalde, G., Güell, A., Juan-Muns, N., Rueda, J. M., & Terradas, X. (1991). La cova 120, parada de caçadors—Recollectors del paleolític mitjà. Cypsela: Revista de Prehistòria i Protohistòria; Núm.: 9, 9.

Agustí, J., & Rubio-Campillo, X. (2017). Were Neanderthals responsible for their own extinction? Quaternary International, 431, 232–237. https://doi.org/10.1016/j.quaint.2016.02.017

Albouy, B., Paquin, S., Hinz, M., Wren, C. D., & Burke, A. (2023). The Last of Them: Investigating the Palaeogeography of the Last Neanderthals in Europe (Marine Isotopic Stage 3). In S. Seuru & B. Albouy (Eds.), Modelling Human-Environment Interactions in and beyond Prehistoric Europe (pp. 27–45). Springer International Publishing. https://doi.org/10.1007/978-3-031-34336-0_2

Albouy, B., Paquin, S., Riel-Salvatore, J., Kageyama, M., Vrac, M., & Burke, A. (2024). Evaluating the impact of climate change and millennial variability on the last Neanderthal populations in Europe (Marine Isotope Stage 3). Quaternary Science Reviews, 338, 108812. https://doi.org/10.1016/j.quascirev.2024.108812

Alcaraz-Castaño, M., Alcolea-González, J., Kehl, M., Albert, R.-M., Baena-Preysler, J., Balbín-Behrmann, R. de, Cuartero, F., Cuenca-Bescós, G., Jiménez-Barredo, F., López-Sáez, J.-A., Piqué, R., Rodríguez-Antón, D., Yravedra, J., & Weniger, G.-C. (2017). A context for the last Neandertals of interior Iberia: Los Casares cave revisited. PLOS ONE, 12(7), e0180823. https://doi.org/10.1371/journal.pone.0180823

Allen, J. R. M., Brandt, U., Brauer, A., Hubberten, H.-W., Huntley, B., Keller, J., Kraml, M., Mackensen, A., Mingram, J., Negendank, J. F. W., Nowaczyk, N. R., Oberhänsli, H., Watts, W. A., Wulf, S., & Zolitschka, B. (1999). Rapid environmental changes in southern Europe during the last glacial period. Nature, 400(6746), Article 6746. https://doi.org/10.1038/23432

Allen, J. R. M., & Huntley, B. (2000). Weichselian palynological records from southern Europe: Correlation and chronology. Quaternary International, 73–74, 111–125. https://doi.org/10.1016/S1040-6182(00)00068-9

Allen, J. R. M., & Huntley, B. (2009). Last Interglacial palaeovegetation, palaeoenvironments and chronology: A new record from Lago Grande di Monticchio, southern Italy. Quaternary Science Reviews, 28(15), 1521–1538. https://doi.org/10.1016/j.quascirev.2009.02.013

Allen, J. R. M., Watts, W. A., & Huntley, B. (2000). Weichselian palynostratigraphy, palaeovegetation and palaeoenvironment; the record from Lago Grande di Monticchio, southern Italy. Quaternary International, 73–74, 91–110. https://doi.org/10.1016/S1040-6182(00)00067-7

Alley, R. B. (1998). Icing the North Atlantic. Nature, 392(6674), 335–337. https://doi.org/10.1038/32781

Alonso, B., Ercilla, G., Martinez-Ruiz, F., Baraza, J., & Galimont, A. (1999). Pliocene-Pleistocene sedimentary facies at Site 976: Depositional history in the northwestern Alboran Sea. Proceedings of the Ocean Drilling Program: Scientific Results, 161. https://doi.org/10.2973/odp.proc.sr.161.206.1999

Álvarez-Alonso, D. (2014). First Neanderthal settlements in northern Iberia: The Acheulean and the emergence of Mousterian technology in the Cantabrian region. Quaternary International, 326–327, 288–306. https://doi.org/10.1016/j.quaint.2012.12.023

Álvarez-Alonso, D., de Andrés-Herrero, M., Díez-Herrero, A., Medialdea, A., & Rojo-Hernández, J. (2018). Neanderthal settlement in central Iberia: Geo-archaeological research in the Abrigo del Molino site, MIS 3 (Segovia, Iberian Peninsula). Quaternary International, 474, 85–97. https://doi.org/10.1016/j.quaint.2016.05.027

Alvarez-Solas, J., Charbit, S., Ritz, C., Paillard, D., Ramstein, G., & Dumas, C. (2010). Links between ocean temperature and iceberg discharge during Heinrich events. Nature Geoscience, 3(2), 122–126. https://doi.org/10.1038/ngeo752

Alvarez-Solas, J., & Ramstein, G. (2011). On the triggering mechanism of Heinrich events. Proceedings of the National Academy of Sciences, 108(50), E1359–E1360. https://doi.org/10.1073/pnas.1116575108

Alvarez-Solas, J., Robinson, A., Montoya, M., & Ritz, C. (2013). Iceberg discharges of the last glacial period driven by oceanic circulation changes. Proceedings of the National Academy of Sciences, 110(41), 16350–16354. https://doi.org/10.1073/pnas.1306622110

Amorós, G., & Carrión, J. S. (2026). The Mismeasure of Neanderthals. Earth History and Biodiversity, 7, 100036. https://doi.org/10.1016/j.hisbio.2025.100036

Andersen, K., Azuma, N., Barnola, J. M., Bigler, M., Biscaye, P., Caillon, N., Chappellaz, J., Clausen, H., Dahl-Jensen, D., Fischer, H., Flückiger, J., Fritzsche, D., Fujii, Y., Goto-Azuma, K., Grønvold, K., Gundestrup, N., Hansson, M., Huber, C., Hvidberg, C., & White, J. (2004). High-resolution record of Northern Hemisphere climate extending into the last interglacial period. Nature, 431, 147–151. https://doi.org/10.1038/nature02805

Andersen, K. K., Svensson, A., Johnsen, S. J., Rasmussen, S. O., Bigler, M., Röthlisberger, R., Ruth, U., Siggaard-Andersen, M.-L., Peder Steffensen, J., Dahl-Jensen, D., Vinther, B. M., & Clausen, H. B. (2006). The Greenland Ice Core Chronology 2005, 15–42ka. Part 1: Constructing the time scale. Quaternary Science Reviews, 25(23), 3246–3257. https://doi.org/10.1016/j.quascirev.2006.08.002

Anderson, L., Reynolds, N., & Teyssandier, N. (2019). No reliable evidence for a very early Aurignacian in Southern Iberia. Nature Ecology & Evolution, 3(5), Article 5. https://doi.org/10.1038/s41559-019-0885-3

Aranguren, B., Grimaldi, S., Benvenuti, M., Capalbo, C., Cavanna, F., Cavulli, F., Ciani, F., Comencini, G., Giuliani, C., Grandinetti, G., Mariotti Lippi, M., Masini, F., Mazza, P. P. A., Pallecchi, P., Santaniello, F., Savorelli, A., & Revedin, A. (2019). Poggetti Vecchi (Tuscany, Italy): A late Middle Pleistocene case of human–elephant interaction. Journal of Human Evolution, 133, 32–60. https://doi.org/10.1016/j.jhevol.2019.05.013

Arriolabengoa, M., Iriarte, E., Aranburu, A., Yusta, I., Arnold, L. J., Demuro, M., & Arrizabalaga, A. (2018). Reconstructing the sedimentary history of Lezetxiki II cave (Basque Country, northern

Iberian Peninsula) using micromorphological analysis. Sedimentary Geology, 372, 96–111. https://doi.org/10.1016/j.sedgeo.2018.05.006

Arsuaga, J. L., Baquedano, E., Pérez-González, A., Sala, N., Quam, R. M., Rodríguez, L., García, R., García, N., Álvarez-Lao, D. J., Laplana, C., Huguet, R., Sevilla, P., Maldonado, E., Blain, H.-A., Ruiz-Zapata, M. B., Sala, P., Gil-García, M. J., Uzquiano, P., Pantoja, A., & Márquez, B. (2012). Understanding the ancient habitats of the last-interglacial (late MIS 5) Neanderthals of central Iberia: Paleoenvironmental and taphonomic evidence from the Cueva del Camino (Spain) site. Quaternary International, 275, 55–75. https://doi.org/10.1016/j.quaint.2012.04.019

Arsuaga, J. L., Fernández Peris, J., Gracia-Téllez, A., Quam, R., Carretero, J. M., Barciela González, V., Blasco, R., Cuartero, F., & Sañudo, P. (2012). Fossil human remains from Bolomor Cave (Valencia, Spain). Journal of Human Evolution, 62(5), 629–639. https://doi.org/10.1016/j.jhevol.2012.02.002

Ashton, N., & Scott, B. (2016). The British Middle Palaeolithic. Quaternary International, 411, 62–76. https://doi.org/10.1016/j.quaint.2015.06.011

Aubry, T., Dimuccio, L., Barbosa, A., Luis, L., Santos, A., Silvestre, M., Thomsen, K., Rades, E. F., Autzen, M., & Murray, A. (2020). Timing of the Middle-to-Upper Palaeolithic transition in the Iberian inland (Cardina-Salto do Boi, Côa Valley, Portugal). Quaternary Research, 1–21. https://doi.org/10.1017/qua.2020.43

Auffret, G.-A., Pastouret, L., Chamley, H., & Lanoix, F. (1974). Influence of the prevailing current regime on sedimentation in the Alboran Sea. Deep Sea Research and Oceanographic Abstracts, 21(10), 839–849. https://doi.org/10.1016/0011-7471(74)90003-5

Aureli, D., & Ronchitelli, A. (2018). The Lower Tyrrhenian Versant: Was it a techno-cultural area during the Middle Palaeolithic? Evolution of the lithic industries of the Riparo del Molare sequence in the frame of Neanderthal peopling dynamics in Italy. in: Borgia, V. and E. Cristiani (eds.) Palaeolithic Italy. Advanced studies on early human adaptations in the Apennine peninsula, Sidestone Press Academics (Leiden), pp. 59-94.

Ayalon, A., Bar-Matthews, M., & Kaufman, A. (2002). Climatic conditions during marine oxygen isotope stage 6 in the eastern Mediterranean region from the isotopic composition of speleothems of Soreq Cave, Israel. Geology, 30(4), 303. https://doi.org/10.1130/0091-7613(2002)030<0303:CCDMOI>2.0.CO;2

Badino, F., Pini, R., Ravazzi, C., Margaritora, D., Arrighi, S., Bortolini, E., Figus, C., Giaccio, B., Lugli, F., Marciani, G., Monegato, G., Moroni, A., Negrino, F., Oxilia, G., Peresani, M., Romandini, M., Ronchitelli, A., Spinapolice, E. E., Zerboni, A., & Benazzi, S. (2020). An overview of Alpine and Mediterranean palaeogeography, terrestrial ecosystems and climate history during MIS 3 with focus on the Middle to Upper Palaeolithic transition. Quaternary International, 551, 7–28. https://doi.org/10.1016/j.quaint.2019.09.024

Baena, J., Moncel, M.-H., Cuartero, F., Chacón Navarro, M. G., & Rubio, D. (2017). Late Middle Pleistocene genesis of Neanderthal technology in Western Europe: The case of Payre site (south-east France). Quaternary International, 436, 212–238. https://doi.org/10.1016/j.quaint.2014.08.031

Baena, J., Pardo, J. F. J., Santafe, E. C., Navas, C. T., Gonzalez, P. C., & Terreros, J. Y. S. D. L. (2021). A road to nowhere? The non-transitional sequence at El Esquilleu (Cantabria, Spain). Comptes Rendus Palevol, 16. https://doi.org/10.5852/cr-palevol2021v20a16

Bailey, G., Carrión, J., Fa, D., Finlayson, C., Finlayson, G., & Vidal, J. (2008). The coastal shelf of the Mediterranean and beyond: Corridor and refugium for human populations in the Pleistocene Introduction. Quaternary Science Reviews, 27, 2095–2099. https://doi.org/10.1016/j.quascirev.2008.08.005

Bajo, P., Drysdale, R. N., Woodhead, J. D., Hellstrom, J. C., Hodell, D., Ferretti, P., Voelker, A. H. L., Zanchetta, G., Rodrigues, T., Wolff, E., Tyler, J., Frisia, S., Spötl, C., & Fallick, A. E. (2020). Persistent influence of obliquity on ice age terminations since the Middle Pleistocene transition. Science, 367(6483), 1235–1239. https://doi.org/10.1126/science.aaw1114

Balzeau, A., Turq, A., Talamo, S., Daujeard, C., Guérin, G., Welker, F., Crevecoeur, I., Fewlass, H., Hublin, J.-J., Lahaye, C., Maureille, B., Meyer, M., Schwab, C., & Gómez-Olivencia, A. (2020). Pluridisciplinary evidence for burial for the La Ferrassie 8 Neandertal child. Scientific Reports, 10(1), 21230. https://doi.org/10.1038/s41598-020-77611-z

Bandarupalli, D., Jones, E. B. G., Ghate, S. D., & Sarma, V. V. (2021). Biodiversity of marine fungi in mangroves with reference to Muthupet mangroves, Tamil Nadu, east coast of India. Marine Biodiversity, 51(6), 88. https://doi.org/10.1007/s12526-021-01214-8

Banks, W. E., d'Errico, F., Peterson, A. T., Kageyama, M., Sima, A., & Sánchez-Goñi, M.-F. (2008). Neanderthal Extinction by Competitive Exclusion. PLOS ONE, 3(12), e3972. https://doi.org/10.1371/journal.pone.0003972

Banks, W. E., d'Errico, F., & Zilhão, J. (2013). Human–climate interaction during the Early Upper Paleolithic: Testing the hypothesis of an adaptive shift between the Proto-Aurignacian and the Early Aurignacian. Journal of Human Evolution, 64(1), 39–55. https://doi.org/10.1016/j.jhevol.2012.10.001

Banks, W. E., Moncel, M.-H., Raynal, J.-P., Cobos, M. E., Romero-Alvarez, D., Woillez, M.-N., Faivre, J.-P., Gravina, B., d'Errico, F., Locht, J.-L., & Santos, F. (2021). An ecological niche shift for Neanderthal populations in Western Europe 70,000 years ago. Scientific Reports, 11(1), 5346. https://doi.org/10.1038/s41598-021-84805-6

Barbante, C., Barnola, J.-M., Becagli, S., Beer, J., Bigler, M., Boutron, C., Blunier, T., Castellano, E., Cattani, O., Chappellaz, J., Dahl-Jensen, D., Debret, M., Delmonte, B., Dick, D., Falourd, S., Faria, S., Federer, U., Fischer, H., Freitag, J., … EPICA Community Members. (2006). One-to-one coupling of glacial climate variability in Greenland and Antarctica. Nature, 444(7116), 195–198. https://doi.org/10.1038/nature05301

Bard, E., Antonioli, F., & Silenzi, S. (2002). Sea-level during the penultimate interglacial period based on a submerged stalagmite from Argentarola Cave (Italy). Earth and Planetary Science Letters, 196(3), 135–146. https://doi.org/10.1016/S0012-821X(01)00600-8

Bard, E., Delaygue, G., Rostek, F., Antonioli, F., Silenzi, S., & Schrag, D. P. (2002). Hydrological conditions over the western Mediterranean basin during the deposition of the cold Sapropel 6 (ca. 175 kyr BP). Earth and Planetary Science Letters, 202(2), 481–494. https://doi.org/10.1016/S0012-821X(02)00788-4

Barker, S., Chen, J., Gong, X., Jonkers, L., Knorr, G., & Thornalley, D. (2015). Icebergs not the trigger for North Atlantic cold events. Nature, 520(7547), Article 7547. https://doi.org/10.1038/nature14330

Barker, S., Diz, P., Vautravers, M. J., Pike, J., Knorr, G., Hall, I. R., & Broecker, W. S. (2009). Interhemispheric Atlantic seesaw response during the last deglaciation. Nature, 457(7233), 1097–1102. https://doi.org/10.1038/nature07770

Barker, S., & Knorr, G. (2021). Millennial scale feedbacks determine the shape and rapidity of glacial termination. Nature Communications, 12(1), Article 1. https://doi.org/10.1038/s41467-021-22388-6

Barker, S., Knorr, G., Edwards, R. L., Parrenin, F., Putnam, A. E., Skinner, L. C., Wolff, E., & Ziegler, M. (2011a). 800,000 Years of Abrupt Climate Variability. Science, 334(6054), 347–351. https://doi.org/10.1126/science.1203580

Barker, S., Knorr, G., Edwards, R. L., Parrenin, F., Putnam, A. E., Skinner, L. C., Wolff, E., & Ziegler, M. (2011b). 800,000 Years of Abrupt Climate Variability. Science, 334(6054), 347–351. https://doi.org/10.1126/science.1203580

Barker, S., Zhang, X., Jonkers, L., Lordsmith, S., Conn, S., & Knorr, G. (2021). Strengthening Atlantic Inflow Across the Mid-Pleistocene Transition. Paleoceanography and Paleoclimatology, 36(4), e2020PA004200. https://doi.org/10.1029/2020PA004200

Barquín, R. M., & González, J. S. (2021). La cueva de Covalejos (Velo de Piélagos, Cantabria): Ocupaciones neandertales y sapiens en la cueva baja del río Pas. Actuaciones arqueológicas, 1997-1999 y 2002. Museo de Prehistoria y Arqueología de Cantabria. https://dialnet.unirioja.es/servlet/libro?codigo=857858

Barshay-Szmidt, C., Normand, C., Flas, D., & Soulier, M.-C. (2018). Radiocarbon dating the Aurignacian sequence at Isturitz (France): Implications for the timing and development of the Protoaurignacian and Early Aurignacian in western Europe. Journal of Archaeological Science: Reports, 17, 809–838. https://doi.org/10.1016/j.jasrep.2017.09.003

Bazin, L., Landais, A., Lemieux-Dudon, B., Toyé Mahamadou Kele, H., Veres, D., Parrenin, F., Martinerie, P., Ritz, C., Capron, E., Lipenkov, V., Loutre, M.-F., Raynaud, D., Vinther, B., Svensson, A., Rasmussen, S. O., Severi, M., Blunier, T., Leuenberger, M., Fischer, H., … Wolff, E. (2013). An optimized multi-proxy, multi-site Antarctic ice and gas orbital chronology (AICC2012): 120–800 ka. Climate of the Past, 9(4), 1715–1731. https://doi.org/10.5194/cp-9-1715-2013

Been, E., & Barzilai, O. (2024). Neandertal burial practices in Western Asia: How different are they from those of the early Homo sapiens? L'Anthropologie, 128(3), 103281. https://doi.org/10.1016/j.anthro.2024.103281

Behre, K.-E. (1981). The interpretation of anthropogenic indicators in pollen diagrams. January 1981. https://www.researchgate.net/publication/233772643

Benabid, A. (1982). Bref aperçu sur la zonation altitudinale de la végétation climacique du Maroc. Ecologia Mediterranea, 8(1), 301–315. https://doi.org/10.3406/ecmed.1982.1956

Benazzi, S., Douka, K., Fornai, C., Bauer, C. C., Kullmer, O., Svoboda, J., Pap, I., Mallegni, F., Bayle, P., Coquerelle, M., Condemi, S., Ronchitelli, A., Harvati, K., & Weber, G. W. (2011). Early dispersal

of modern humans in Europe and implications for Neanderthal behaviour. Nature, 479(7374), Article 7374. https://doi.org/10.1038/nature10617

Benazzi, S., Slon, V., Talamo, S., Negrino, F., Peresani, M., Bailey, S. E., Sawyer, S., Panetta, D., Vicino, G., Starnini, E., Mannino, M. A., Salvadori, P. A., Meyer, M., Pääbo, S., & Hublin, J.-J. (2015). The makers of the Protoaurignacian and implications for Neandertal extinction. Science, 348(6236), 793–796. https://doi.org/10.1126/science.aaa2773

Benito, B. M., Svenning, J.-C., Kellberg-Nielsen, T., Riede, F., Gil-Romera, G., Mailund, T., Kjaergaard, P. C., & Sandel, B. S. (2017). The ecological niche and distribution of Neanderthals during the Last Interglacial. Journal of Biogeography, 44(1), 51–61. https://doi.org/10.1111/jbi.12845

Benito-Calvo, A., Arnold, L. J., Mora, R., Martínez-Moreno, J., & Demuro, M. (2020). Reconstructing Mousterian landscapes in the southeastern Pyrenees (Roca dels Bous site, Pre-Pyrenees ranges, Spain). Quaternary Research, 97, 167–186. https://doi.org/10.1017/qua.2020.29

Bennett, K. D. (1996). Determination of the number of zones in a biostratigraphical sequence. New Phytologist, 132(1), 155–170. https://doi.org/10.1111/j.1469-8137.1996.tb04521.x

Bennett, K. D., Tzedakis, P. C., & Willis, K. J. (1991). Quaternary Refugia of North European Trees. Journal of Biogeography, 18(1), 103–115. https://doi.org/10.2307/2845248

Benvenuti, M., Bahain, J.-J., Capalbo, C., Capretti, C., Ciani, F., D'Amico, C., Esu, D., Giachi, Gi., Giuliani, C., Gliozzi, E., Lazzeri, S., Macchioni, N., Lippi, M. M., Masini, F., Mazza, P. P. A., Pallecchi, P., Revedin, A., Savorelli, A., Spadi, M., … Aranguren, B. (2017). Paleoenvironmental context of the early Neanderthals of Poggetti Vecchi for the late middle Pleistocene of Central Italy. Quaternary Research, 88(2), 327–344. https://doi.org/10.1017/qua.2017.51

Berger, A. (1980). The Milankovitch astronomical theory of paleoclimates: A modern review. Vistas in Astronomy, 24, 103–122. https://doi.org/10.1016/0083-6656(80)90026-4

Berger, A., & Loutre, M. F. (1991). Insolation values for the climate of the last 10 million years. Quaternary Science Reviews, 10(4), 297–317. https://doi.org/10.1016/0277-3791(91)90033-Q

Berger, A., & Loutre, M. F. (2004). Théorie astronomique des paléoclimats. Comptes Rendus. Géoscience, 336(7–8), 701–709. https://doi.org/10.1016/j.crte.2004.02.006

Bermúdez de Castro, J. M., & Martinón-Torres, M. (2013). A new model for the evolution of the human Pleistocene populations of Europe. Quaternary International, 295, 102–112. https://doi.org/10.1016/j.quaint.2012.02.036

Beug, H. J. Leitfaden der Pollenbestimmung für Mitteleuropa und angrenzende Gebiete. Pfeil, F, München, 2004. 542 p.

Bicho, N., & Carvalho, M. (2022). Peninsular southern Europe refugia during the Middle Palaeolithic: An introduction. Journal of Quaternary Science, 37(2), 133–135. https://doi.org/10.1002/jqs.3410

Biltekin, D., Burjachs, F., Vallverdú, J., Sharp, W. D., Mertz-Kraus, R., Chacón, M. G., Saladié, P., Bischoff, J. L., & Carbonell, E. (2019). Vegetation and climate record from Abric Romaní (Capellades, northeast Iberia) during the Upper Pleistocene (MIS 5d−3). Quaternary Science Reviews, 220, 154–164. https://doi.org/10.1016/j.quascirev.2019.07.035

Bird, M. I., Ayliffe, L. K., Fifield, L. K., Turney, C. S. M., Cresswell, R. G., Barrows, T. T., & David, B. (1999). Radiocarbon Dating of "Old" Charcoal Using a Wet Oxidation, Stepped-Combustion Procedure. Radiocarbon, 41(2), 127–140. https://doi.org/10.1017/S0033822200019482

Bisschop, K., Mortier, F., Etienne, R. S., & Bonte, D. (2019). Transient local adaptation and source–sink dynamics in experimental populations experiencing spatially heterogeneous environments. Proceedings of the Royal Society B: Biological Sciences, 286(1905), 20190738. https://doi.org/10.1098/rspb.2019.0738

Blain, H.-A., Laplana, C., Sánchez-Bandera, C., Fagoaga, A., Blanco Lapaz, Á., Martínez-Monzón, A., Bisbal-Chinesta, J. F., Moclán, A., Martín-Perea, D. M., Domínguez-García, Á. C., Álvarez-Vena, A., Sevilla, P., Ruiz Zapata, M. B., Gil García, M. J., Márquez, B., Huguet, R., Pérez-González, A., Arsuaga, J. L., & Baquedano, E. (2022). A warm and humid paleoecological context for the Neanderthal mountain settlement at the Navalmaíllo rockshelter (Iberian Central System, Madrid). Quaternary Science Reviews, 293, 107727. https://doi.org/10.1016/j.quascirev.2022.107727

Blanchet, C. L., Osborne, A. H., Tjallingii, R., Ehrmann, W., Friedrich, T., Timmermann, A., Brückmann, W., & Frank, M. (2021). Drivers of river reactivation in North Africa during the last glacial cycle. Nature Geoscience, 14(2), 97–103. https://doi.org/10.1038/s41561-020-00671-3

Blockley, S. P. E., Lane, C. S., Hardiman, M., Rasmussen, S. O., Seierstad, I. K., Steffensen, J. P., Svensson, A., Lotter, A. F., Turney, C. S. M., & Ramsey, C. B. (2012). Synchronisation of palaeoenvironmental records over the last 60,000 years, and an extended INTIMATE 1 event stratigraphy to 48,000 b2k. Quaternary Science Reviews, 36, 2–10. https://doi.org/10.1016/j.quascirev.2011.09.017

Bocquet-Appel, J.-P., & Degioanni, A. (2013). Neanderthal Demographic Estimates. Current Anthropology, 54(S8), S202–S213. https://doi.org/10.1086/673725

Bohn, U., Zazanashvili, N., & Nakhutsrishvili, G. (2007). The Map of the Natural Vegetation of Europe and its application in the Caucasus Ecoregion. Bulletin of the Georgia Academy of Science, 175.

Bolar, K. (2019). STAT: Interactive Document for Working with Basic Statistical Analysis (Version 0.1.0) [Computer software]. https://cran.r-project.org/web/packages/STAT/index.html

Bon, F. (2002). A brief overview of Aurignacian cultures in the context of the industries of the transition from the Middle to the Upper Paleolithic. Trabalhos de Arqueologia, 133–144.

Bond, G., Broecker, W., Johnsen, S., McManus, J., Labeyrie, L., Jouzel, J., & Bonani, G. (1993). Correlations between climate records from North Atlantic sediments and Greenland ice. Nature, 365(6442), Article 6442. https://doi.org/10.1038/365143a0

Bond, G. C., Showers, W., Elliot, M., Evans, M., Lotti, R., Hajdas, I., Bonani, G., & Johnson, S. (1999). The North Atlantic's 1-2 kyr climate rhythm: Relation to Heinrich events, Dansgaard/Oeschger cycles and the Little Ice Age. Washington DC American Geophysical Union Geophysical Monograph Series, 112, 35–58. https://doi.org/10.1029/GM112p0035

Bond, G., Heinrich, H., Broecker, W., Labeyrie, L., McManus, J., Andrews, J., Huon, S., Jantschik, R., Clasen, S., Simet, C., Tedesco, K., Klas, M., Bonani, G., & Ivy, S. (1992). Evidence for massive discharges of icebergs into the North Atlantic Ocean during the last glacial period. Nature, 360(6401), Article 6401. https://doi.org/10.1038/360245a0

Bond, G., Showers, W., Cheseby, M., Lotti, R., Almasi, P., Demenocal, P., Priore, P., Cullen, H., Hajdas, I., & Bonani, G. (1997). A pervasive millennial-scale cycle in the North Atlantic Holocene and glacial climates. Science, 278, 1257. https://doi.org/10.1126/science.278.5341.1257

Bordes, Brun-Ricalens, F., Castel, J.-C., Ducasse, S., Faivre, J.-P., Feruglio, V., Henry-Gambier, Lacrampe-Cuyaubere, Laroulandie, V., Arnaud, L., Martin, Maureille, Morala, Morin, E., Renard, Rendu, W., Solange, R., Rougier, Szmidt, & Teyssandier, N. (2009). Les débuts du Paléolithique supérieur dans le Sud-Ouest de la France: Nouvelles fouilles au Piage (2004-2006). Problématique et premiers résultats. In «Les sociétés Paléolithiques d'un grand Sud-Ouest : nouveaux gisements, nouvelles méthodes, nouveaux résultats». Mémoire XLVII de la Société préhistorique française. Bordeaux, France. pp.261-288.

Bordes, J.-G. (2006). News from the West: A reevaluation of the classical Aurignacian sequence of the Périgord. Towards a Definition of the Aurignacian. In Bar Yosef O. and Zilhao J. (Eds.). Towards a definition of the Aurignacian., Instituto Portuges de Arqueologia, Trabalhos de Arqueologia 45. pp.147-71.

Bosch, J. H. A., Cleveringa, P., & Meijer, T. (2000). The Eemian stage in the Netherlands: History, character and new research. Geologie en Mijnbouw / Netherlands Journal of Geosciences, 79 (2/3): 135-145.

Boswell, S. M., Toucanne, S., Pitel-Roudaut, M., Creyts, T. T., Eynaud, F., & Bayon, G. (2019). Enhanced surface melting of the Fennoscandian Ice Sheet during periods of North Atlantic cooling. Geology, 47(7), 664–668. https://doi.org/10.1130/G46370.1

Bouchet, M., Landais, A., Grisart, A., Parrenin, F., Prié, F., Jacob, R., Fourré, E., Capron, E., Raynaud, D., Lipenkov, V. Y., Loutre, M.-F., Extier, T., Svensson, A., Legrain, E., Martinerie, P., Leuenberger, M., Jiang, W., Ritterbusch, F., Lu, Z.-T., & Yang, G.-M. (2023). The Antarctic Ice Core Chronology 2023 (AICC2023) chronological framework and associated timescale for the European Project for Ice Coring in Antarctica (EPICA) Dome C ice core. Climate of the Past, 19(11), 2257–2286. https://doi.org/10.5194/cp-19-2257-2023

Bourguignon, L. (1997). Le Moustérien de type Quina: Nouvelles définitions d'une entité technique. Thèse de doctorat, Paris 10. https://theses.fr/1997PA100064

Bout-Roumazeilles, V., Combourieu Nebout, N., Peyron, O., Cortijo, E., Landais, A., & Masson-Delmotte, V. (2007). Connection between South Mediterranean climate and North African atmospheric circulation during the last 50,000yrBP North Atlantic cold events. Quaternary Science Reviews, 26(25–28), 3197–3215. https://doi.org/10.1016/j.quascirev.2007.07.015

Bout-Roumazeilles, V., Combourieu-Nebout, N., Desprat, S., Siani, G., Turon, J.-L., & Essallami, L. (2013). Tracking atmospheric and riverine terrigenous supplies variability during the last glacial and the Holocene in central Mediterranean. Climate of the Past, 9(3), 1065–1087. https://doi.org/10.5194/cp-9-1065-2013

Bradtmöller, M., Pastoors, A., Weninger, B., & Weniger, G.-C. (2012). The repeated replacement model – Rapid climate change and population dynamics in Late Pleistocene Europe. Quaternary International, 247, 38–49. https://doi.org/10.1016/j.quaint.2010.10.015

Brahim, Y. A., Sha, L., Wassenburg, J. A., Azennoud, K., Cheng, H., Cruz, F. W., & Bouchaou, L. (2023). The spatiotemporal extent of the Green Sahara during the last glacial period. Science, 26(7). https://doi.org/10.1016/j.isci.2023.107018

Brauer, A., Allen, J. R. M., Mingram, J., Dulski, P., Wulf, S., & Huntley, B. (2007). Evidence for last interglacial chronology and environmental change from Southern Europe. Proceedings of the National Academy of Sciences, 104(2), 450–455. https://doi.org/10.1073/pnas.0603321104

Breiman, L., Cutler, A., Liaw, A., & Wiener, M. (2024). randomForest: Breiman and Cutlers Random Forests for Classification and Regression (Version 4.7-1.2) [Computer software]. https://cran.r-project.org/web/packages/randomForest/index.html

Brewer, S., Guiot, J., & Barboni, D. (2007). Use of Pollen as Climate Proxies. In Encyclopedia of Quaternary Science (pp. 2497–2508). Elsevier. https://doi.org/10.1016/B0-444-52747-8/00177-0

Brewer, S., Guiot, J., Sánchez-Goñi, M. F., & Klotz, S. (2008). The climate in Europe during the Eemian: A multi-method approach using pollen data. Quaternary Science Reviews, 27(25), 2303–2315. https://doi.org/10.1016/j.quascirev.2008.08.029

Bringmans, P. (2007). First Evidence of Neanderthal Presence in Northwest Europe during the Late Saalian 'Zeifen Interstadial' (MIS 6.01) found at the VLL and VLB Sites at Veldwezelt-Hezerwater, Belgium. Journal of Archaeology of Northwest Europe, 1.

Broecker, W., Bond, G., Klas, M., Clark, E., & McManus, J. (1992). Origin of the northern Atlantic's Heinrich events. Climate Dynamics, 6, 265–273. https://doi.org/10.1007/BF00193540

Broecker, W. S., & Henderson, G. M. (1998). The sequence of events surrounding Termination II and their implications for the cause of glacial-interglacial CO2 changes. Paleoceanography, 13(4), 352–364.

Brown, K. S., Marean, C. W., Jacobs, Z., Schoville, B. J., Oestmo, S., Fisher, E. C., Bernatchez, J., Karkanas, P., & Matthews, T. (2012). An early and enduring advanced technology originating 71,000 years ago in South Africa. Nature, 491(7425), 590–593. https://doi.org/10.1038/nature11660

Burjachs, F., & Julià, R. (1994). Abrupt climatic changes during the last glaciation based on pollen analysis of the abric romani, catalonia, spain. Quaternary Research, 42(3), 308–315. https://doi.org/10.1006/qres.1994.1081

Burjachs, F., López-García, J. M., Allué, E., Blain, H. A., Rivals, F., Bennàsar, M., & Expósito, I. (2012). Palaeoecology of Neanderthals during Dansgaard-Oeschger cycles in northeastern Iberia (Abric Romaní): From regional to global scale. Quaternary International, 247(1), 26–37. https://doi.org/10.1016/j.quaint.2011.01.035

Burns, S. J., Welsh, L. K., Scroxton, N., Cheng, H., & Edwards, R. L. (2019). Millennial and orbital scale variability of the South American Monsoon during the penultimate glacial period. Scientific Reports, 9(1), 1234. https://doi.org/10.1038/s41598-018-37854-3

Cacho, I., Grimalt, J. O., Pelejero, C., Canals, M., Sierro, F. J., Flores, J. A., & Shackleton, N. (1999). Dansgaard-Oeschger and Heinrich event imprints in Alboran Sea paleotemperatures. Paleoceanography, 14(6), 698–705. https://doi.org/10.1029/1999PA900044

Cacho, I., Grimalt, J. O., Sierro, F. J., Shackleton, N., & Canals, M. (2000). Evidence for enhanced Mediterranean thermohaline circulation during rapid climatic coolings. Earth and Planetary Science Letters, 183(3), 417–429. https://doi.org/10.1016/S0012-821X(00)00296-X

Cacho, I., Shackleton, N., Elderfield, H., Sierro, F. J., & Grimalt, J. O. (2006). Glacial rapid variability in deep-water temperature and δ18O from the Western Mediterranean Sea. Quaternary Science Reviews, 25(23), 3294–3311. https://doi.org/10.1016/j.quascirev.2006.10.004

Cai, Y., Cheng, H., Cheng, X., Shi, Z., Lu, Y., Ma, L., Pérez-Mejías, C., Zhang, H., Wei, Y., Xue, G., Li, H., He, M., Wang, T., Edwards, R. L., & An, Z. (2023). Orbital- to millennial-scale variation of the speleothem δ18O record during Marine Isotope Stages 5 to 3 on the southeast Chinese Loess Plateau and its climatic and environmental implications. Journal of Quaternary Science, 38(3), 295–307. https://doi.org/10.1002/jqs.3489

Camiz, S. (2005). The Guttman effect: Its interpretation and a new redressing method. Data Analysis Bulletin, 5, 7–35.

Camuera, J., Jiménez-Moreno, G., Ramos-Román, M. J., García-Alix, A., Toney, J. L., Anderson, R. S., Jiménez-Espejo, F., Bright, J., Webster, C., Yanes, Y., & Carrión, J. S. (2019). Vegetation and climate changes during the last two glacial-interglacial cycles in the western Mediterranean: A new long pollen record from Padul (southern Iberian Peninsula). Quaternary Science Reviews, 205, 86–105. https://doi.org/10.1016/j.quascirev.2018.12.013

Camuera, J., Jiménez-Moreno, G., Ramos-Román, M. J., García-Alix, A., Toney, J. L., Anderson, R. S., Jiménez-Espejo, F., Kaufman, D., Bright, J., Webster, C., Yanes, Y., Carrión, J. S., Ohkouchi, N., Suga, H., Yamame, M., Yokoyama, Y., & Martínez-Ruiz, F. (2018). Orbital-scale environmental and climatic changes recorded in a new ~200,000-year-long multiproxy sedimentary record from Padul, southern Iberian Peninsula. Quaternary Science Reviews, 198, 91–114. https://doi.org/10.1016/j.quascirev.2018.08.014

Camuera, J., Ramos-Román, M. J., Jiménez-Moreno, G., García-Alix, A., Ilvonen, L., Ruha, L., Gil-Romera, G., González-Sampériz, P., & Seppä, H. (2022). Past 200 kyr hydroclimate variability in the western Mediterranean and its connection to the African Humid Periods. Scientific Reports, 12(1), 9050. https://doi.org/10.1038/s41598-022-12047-1

Carlson, A. E., & Clark, P. U. (2012). Ice sheet sources of sea level rise and freshwater discharge during the last deglaciation. Reviews of Geophysics, 50, RG4007. https://doi.org/10.1029/2011RG000371

Carmignani, L., Moncel, M.-H., Fernandes, P., & Wilson, L. (2017). Technological variability during the Early Middle Palaeolithic in Western Europe. Reduction systems and predetermined products at the Bau de l'Aubesier and Payre (South-East France). PLOS ONE, 12(6), e0178550. https://doi.org/10.1371/journal.pone.0178550

Caro Gómez, J. A., Díaz Del Olmo, F., Artigas, R. C., Recio Espejo, J. M., & Barrera, C. B. (2011). Geoarchaeological alluvial terrace system in Tarazona: Chronostratigraphical transition of Mode 2 to Mode 3 during the middle-upper pleistocene in the Guadalquivir River valley (Seville, Spain). Quaternary International, 243(1), 143–160. https://doi.org/10.1016/j.quaint.2011.04.022

Carrión, J. et al., coords. (2024). Iberian paleoflora and paleovegetation. Vol. II: Pleistocene. Cartagena: Universidad Politécnica, 626 p. https://doi.org/10.31428/10317/16814

Carrión, J., Amorós, G., Amorós, A., & Marín-Arroyo, A. B. (2026). Beyond the cold steppes: Neanderthal landscapes and the neglect of flora. Quaternary Science Reviews, 371, 109673. https://doi.org/10.1016/j.quascirev.2025.109673

Carrión, J. S. (2004). The use of two pollen records from deep sea cores to frame adaptive evolutionary change for humans: A comment on “Neanderthal extinction and the millennial scale climate variability of OIS 3” by F. d’Errico and M.F. Sánchez Goñi. Quaternary Science Reviews, 23(9–10), 1217–1219. https://doi.org/10.1016/j.quascirev.2004.01.003

Carrión, J. S., Dupré, M., Fumanal, M. P., & Montes, R. (1995). A Palaeoenvironmental Study in Semi-arid Southeastern Spain: The Palynological and Sedimentological Sequence at Perneras Cave (Lorca, Murcia). Journal of Archaeological Science, 22(3), 355–367. https://doi.org/10.1006/jasc.1995.0037

Carrión, J. S., Lalueza-Fox, C., & Stewart, J. (2019a). Neanderthals: Ecology and evolution. Quaternary Science Reviews, 217, 1–6. https://doi.org/10.1016/j.quascirev.2019.05.008

Carrión, J. S., Fernández, S., Jiménez-Arenas, J. M., Munuera, M., Ochando, J., Amorós, G., Ponce de León, M., Zollikofer, C., Martín-Lerma, I., Toro-Moyano, I., Hajdas, I., & Walker, M. J. (2019b). The sequence at Carihuela Cave and its potential for research into Neanderthal ecology and the Mousterian in southern Spain. Quaternary Science Reviews, 217, 194–216. https://doi.org/10.1016/j.quascirev.2019.04.012

Carrión, J. S., & Leroy, S. A. G. (2010). Iberian floras through time: Land of diversity and survival. Review of Palaeobotany and Palynology, 162(3), 227–230. https://doi.org/10.1016/j.revpalbo.2010.07.002

Carrión, J. S., Munuera, M., Navarro, C., Burjachs, F., Dupré, M., & Walker, M. J. (1999). The palaeoecoloical potential of pollen records in caves: The case of Mediterranean Spain. Quaternary Science Reviews, 18(8), 1061–1073. https://doi.org/10.1016/S0277-3791(98)00002-X

Carrión, J. S., Ochando, J., Fernández, S., Blasco, R., Rosell, J., Munuera, M., Amorós, G., Martín-Lerma, I., Finlayson, S., Giles, F., Jennings, R., Finlayson, G., Giles-Pacheco, F., Rodríguez-Vidal, J., & Finlayson, C. (2018). Last Neanderthals in the warmest refugium of Europe: Palynological data from Vanguard Cave. Review of Palaeobotany and Palynology, 259, 63–80. https://doi.org/10.1016/j.revpalbo.2018.09.007

Carrión, J. S., Ochando, J., Michelangeli, F., Jiménez-Espejo, F., Ojeda, F., Amorós, G., Munuera, M., Marín-Arroyo, A. B., González-Sampériz, P., Rodríguez-Vidal, J., Di Rita, F., & Magri, D. (2024). Tracing 40,000 years of vegetation change in the Baetic-Rifan biodiversity hotspot. Review of Palaeobotany and Palynology, 105202. https://doi.org/10.1016/j.revpalbo.2024.105202

Carrión, J. S., & Walker, M. J. (2019). Background to Neanderthal presence in Western Mediterranean Europe. Quaternary Science Reviews, 217, 7–44. https://doi.org/10.1016/j.quascirev.2018.10.011

Carrión, J. S., Yll, E. I., Walker, M. J., Legaz, A. J., Chaín, C., & López, A. (2003). Glacial refugia of temperate, Mediterranean and Ibero-North African flora in south-eastern Spain: New evidence from cave pollen at two Neanderthal man sites. Global Ecology and Biogeography, 12(2), 119–129. https://doi.org/10.1046/j.1466-822X.2003.00013.x

Carrión, J., Scott, L., Arribas, A., Fuentes, N., Gil-Romera, G., & Montoya, E. (2007). Pleistocene landscapes in Central Iberia inferred from pollen analysis of hyena coprolites. Journal of Quaternary Science, 22, 191–202. https://doi.org/10.1002/jqs.1024

Cartapanis, O., Bard, E., Leroy, S. A.G. Chevalier, M., Flas, D., Devièse, T. (2025). Regional climatic dynamics and cultural divergence in glacial western Europe. Quaternary Science Reviews. https://doi.org/10.1016/j.quascirev.2025.109429

Carvalho, M., & Bicho, N. (2022). Complexity in the Middle to Upper Paleolithic Transition in Peninsular Southern Europe and application of refugium concepts. Journal of Quaternary Science, 37(2), 380–393. https://doi.org/10.1002/jqs.3350

Carvalho, M., Pereira, T., & Manso, C. (2018). Rabbit exploitation in the Middle Paleolithic at Gruta Nova da Columbeira, Portugal. Journal of Archaeological Science: Reports, 21, 821–832. https://doi.org/10.1016/j.jasrep.2018.09.003

Casabo, J., & Gomar, M. (2002). El Paleolítico Medio en el Valle del río Palancia. Saguntum: Papeles del Laboratorio de Arqueología de Valencia, ISSN-e 2174-517X, ISSN 0210-3729, Nº 34, pp. 9-28.

Casanova, J., Roda Gilabert, X., Martínez-Moreno, J., & Torcal, R. (2014). Débitage, Façonnage et Diversité des Systèmes Techniques du Moustérien à Tragó (Prepyrénées de Lleida, Catalogne). Transitions, Ruptures et Continuité En Préhistoire. XXVIIe Congrès Préhistorique de France – Bordeaux-Les Eyzies, 139–154.

Castel, J.-C., Discamps, E., Soulier, M.-C., Sandgathe, D., Dibble, H. L., McPherron, S. J. P., Goldberg, P., & Turq, A. (2017). Neandertal subsistence strategies during the Quina Mousterian at Roc de Marsal (France). Quaternary International, 433, 140–156. https://doi.org/10.1016/j.quaint.2015.12.033

Castellano, S., Parra, G., Sánchez-Quinto, F. A., Racimo, F., Kuhlwilm, M., Kircher, M., Sawyer, S., Fu, Q., Heinze, A., Nickel, B., Dabney, J., Siebauer, M., White, L., Burbano, H. A., Renaud, G., Stenzel, U., Lalueza-Fox, C., de la Rasilla, M., Rosas, A., … Pääbo, S. (2014). Patterns of coding variation in the complete exomes of three Neandertals. Proceedings of the National Academy of Sciences, 111(18), 6666–6671. https://doi.org/10.1073/pnas.1405138111

Catrain, M., Combourieu-Nebout, N., Lebreton, V., Fauquette, S., Joannin, S., & Moncel, M.-H. (2025). Vegetation and climate dynamics in the south-western mediterranean during MIS 37–31 (∼1.25 - ∼1. 06 Ma): Insights from the marine core ODP site 976. Quaternary Science Reviews, 369. https://doi.org/10.1016/j.quascirev.2025.109635

Channell, J. E. T., Hodell, D. A., Romero, O., Hillaire-Marcel, C., de Vernal, A., Stoner, J. S., Mazaud, A., & Röhl, U. (2012). A 750-kyr detrital-layer stratigraphy for the North Atlantic (IODP Sites U1302–U1303, Orphan Knoll, Labrador Sea). Earth and Planetary Science Letters, 317–318, 218–230. https://doi.org/10.1016/j.epsl.2011.11.029

Chapman, M. R., & Shackleton, N. J. (1999). Global ice-volume fluctuations, North Atlantic ice-rafting events, and deep-ocean circulation changes between 130 and 70 ka. Geology, 27, 795. https://doi.org/10.1130/0091-7613(1999)027<0795:GIVFNA>2.3.CO;2

Chappellaz, J., Brook, E., Blunier, T., & Malaizé, B. (1997). CH4 and δ18 O of O2 records from Antarctic and Greenland ice: A clue for stratigraphic disturbance in the bottom part of the Greenland Ice Core Project and the Greenland Ice Sheet Project 2 ice cores. Journal of Geophysical Research: Oceans, 102(C12), 26547–26557. https://doi.org/10.1029/97JC00164

Chappellaz, J., Stowasser, C., Blunier, T., Baslev-Clausen, D., Brook, E., Dallmayr, R., Faïn, X., Lee, J., Mitchell, L., Pascual, O., Romanini, D., Rosen, J., & Schüpbach, S. (2013). High-resolution glacial and deglacial record of atmospheric methane by continuous-flow and laser spectrometer

analysis along the NEEM ice core. Climate of the Past, 9, 2579–2593. https://doi.org/10.5194/cp-9-2579-2013

Charton, L., Combourieu-Nebout, N., Bertini, A., Lebreton, V., Peyron, O., Robles, M., Sassoon, D., & Moncel, M.-H. (2025). Vegetation and climate changes during the Middle to Upper Palaeolithic transition in the southwestern Mediterranean: What happened to the last Neanderthals during Heinrich stadial 4? Quaternary Science Reviews, 359, 109345. https://doi.org/10.1016/j.quascirev.2025.109345

Cheddadi, R., Henrot, A.-J., François, L., Boyer, F., Bush, M., Carré, M., Coissac, E., De Oliveira, P. E., Ficetola, F., Hambuckers, A., Huang, K., Lézine, A.-M., Nourelbait, M., Rhoujjati, A., Taberlet, P., Sarmiento, F., Abel-Schaad, D., Alba-Sánchez, F., & Zheng, Z. (2017). Microrefugia, Climate Change, and Conservation of Cedrus atlantica in the Rif Mountains, Morocco. Frontiers in Ecology and Evolution, 5. https://doi.org/10.3389/fevo.2017.00114

Cheddadi, R., Lamb, H., Joel, G., & van der Kaars, S. (1998). Holocene climatic change in Morocco: A quantitative reconstruction from pollen data. Climate Dynamics, 14, 883–890. https://doi.org/10.1007/s003820050262

Cheddadi, R., & Rossignol-Strick, M. (1995). Eastern Mediterranean Quaternary paleoclimates from pollen and isotope records of marine cores in the Nile Cone Area. Paleoceanography, 10(2), 291–300. https://doi.org/10.1029/94PA02672

Cheng, H., Edwards, R. L., Broecker, W. S., Denton, G. H., Kong, X., Wang, Y., Zhang, R., & Wang, X. (2009). Ice Age Terminations. Science, 326(5950), 248–252. https://doi.org/10.1126/science.1177840

Cheng, H., Edwards, R. L., Sinha, A., Spötl, C., Yi, L., Chen, S., Kelly, M., Kathayat, G., Wang, X., Li, X., Kong, X., Wang, Y., Ning, Y., & Zhang, H. (2016). The Asian monsoon over the past 640,000 years and ice age terminations. Nature, 534(7609), 640–646. https://doi.org/10.1038/nature18591

Cheng, H., Edwards, R. L., Wang, Y., Kong, X., Ming, Y., Kelly, M. J., Wang, X., Gallup, C. D., & Liu, W. (2006). A penultimate glacial monsoon record from Hulu Cave and two-phase glacial terminations. Geology, 34(3), 217–220. https://doi.org/10.1130/G22289.1

Cheng, H., Xu, Y., Dong, X., Zhao, J., Li, H., Baker, J., Sinha, A., Spötl, C., Zhang, H., Du, W., Zong, B., Jia, X., Kathayat, G., Liu, D., Cai, Y., Wang, X., Strikis, N. M., Cruz, F. W., Auler, A. S., … Edwards, R. L. (2021). Onset and termination of Heinrich Stadial 4 and the underlying climate dynamics. Communications Earth & Environment, 2(1), 1–11. https://doi.org/10.1038/s43247-021-00304-6

Chevalier, M., Davis, B. A. S., Heiri, O., Seppä, H., Chase, B. M., Gajewski, K., Lacourse, T., Telford, R. J., Finsinger, W., Guiot, J., Kühl, N., Maezumi, S. Y., Tipton, J. R., Carter, V. A., Brussel, T., Phelps, L. N., Dawson, A., Zanon, M., Vallé, F., … Kupriyanov, D. (2020). Pollen-based climate reconstruction techniques for late Quaternary studies. Earth-Science Reviews, 210. https://doi.org/10.1016/j.earscirev.2020.103384

Chmura, G. L., Smirnov, A., & Campbell, I. D. (1999). Pollen transport through distributaries and depositional patterns in coastal waters. Palaeogeography, Palaeoclimatology, Palaeoecology, 149(1), 257–270. https://doi.org/10.1016/S0031-0182(98)00205-3

Churchill, S. E. (2006). Bioenergetic perspectives on Neanderthal thermoregulatory and activity budgets. In J.-J. Hublin, K. Harvati, & T. Harrison (Eds.), Neanderthals Revisited: New Approaches and Perspectives (pp. 113–133). Springer Netherlands. https://doi.org/10.1007/978-1-4020-5121-0_7

Clark, P. U., He, F., Golledge, N. R., Mitrovica, J. X., Dutton, A., Hoffman, J. S., & Dendy, S. (2020). Oceanic forcing of penultimate deglacial and last interglacial sea-level rise. Nature, 577(7792), 660–664. https://doi.org/10.1038/s41586-020-1931-7

Colleoni, F., Wekerle, C., Näslund, J.-O., Brandefelt, J., & Masina, S. (2016). Constraint on the penultimate glacial maximum Northern Hemisphere ice topography (≈140 kyrs BP). Quaternary Science Reviews, 137, 97–112. https://doi.org/10.1016/j.quascirev.2016.01.024

Columbu, A., Chiarini, V., Spötl, C., Benazzi, S., Hellstrom, J., Cheng, H., & De Waele, J. (2020). Speleothem record attests to stable environmental conditions during Neanderthal–modern human turnover in southern Italy. Nature Ecology & Evolution, 4(9), Article 9. https://doi.org/10.1038/s41559-020-1243-1

Comas, M. C., Zahn, R., & Klaus, A. (1996). Proceedings of the Ocean Drilling Program, Initial Reports (Vol. 161).

Combourieu-Nebout, N., Bout-Roumazeilles, V., Dormoy, I., & Peyron, O. (2009). Sécheresses récurrentes en Méditerranée au cours des derniers 50000 ans. Sécheresse, 20(2), 210–216. https://doi.org/10.1684/sec.2009.0181

Combourieu-Nebout, N., Londeix, L., Baudin, F., Jean Louis, T., R., V., & R., Z. (1999). Quaternary marine and continental paleoenvironments in the western Mediterranean (Site 976, Alboran Sea): Palynological evidence. In Proceedings of the Ocean Drilling Program, Scientific Results. (Zahn, R., Comas, M.C., and Klaus, A., Vol. 161, pp. 457–468). https://doi.org/10.2973/odp.proc.sr.161.238.1999

Combourieu-Nebout, N., Paterne, M., Turon, J.-L., & Siani, G. (1998). A high-resolution record of the last deglaciation in the central Mediterranean sea: Palaeovegetation and palaeohydrological evolution. Quaternary Science Reviews, 17(4–5), 303. https://doi.org/10.1016/S0277-3791(97)00039-5

Combourieu-Nebout, N., Peyron, O., Dormoy, I., Desprat, S., Célia, B., Kotthoff, U., & Marret, F. (2009). Rapid climatic variability in the west Mediterranean during the last 25 000 years from high resolution pollen data. Climate of the Past, 5, 503–521. https://doi.org/10.5194/cpd-5-671-2009

Combourieu-Nebout, N., Turon, J. L., Zahn, R., Capotondi, L., Londeix, L., & Pahnke, K. (2002). Enhanced aridity and atmospheric high-pressure stability over the western Mediterranean during the North Atlantic cold events of the past 50 k.y. Geology, 30(10), 863. https://doi.org/10.1130/0091-7613(2002)030<0863:EAAAHP>2.0.CO;2

Cooper, A., Turney, C. S. M., Palmer, J., Hogg, A., McGlone, M., Wilmshurst, J., Lorrey, A. M., Heaton, T. J., Russell, J. M., McCracken, K., Anet, J. G., Rozanov, E., Friedel, M., Suter, I., Peter, T., Muscheler, R., Adolphi, F., Dosseto, A., Faith, J. T., … Zech, R. (2021a). A global environmental crisis 42,000 years ago. Science, 371(6531), 811–818. https://doi.org/10.1126/science.abb8677

Cooper, A., Turney, C. S. M., Palmer, J., Hogg, A., McGlone, M., Wilmshurst, J., Lorrey, A. M., Heaton, T. J., Russell, J. M., McCracken, K., Anet, J. G., Rozanov, E., Friedel, M., Suter, I., Peter, T., Muscheler, R., Adolphi, F., Dosseto, A., Faith, J. T., … Zech, R. (2021b). Response to Comment on "A global environmental crisis 42,000 years ago". Science, 374(6570), eabi9756. https://doi.org/10.1126/science.abi9756

Corrick, E. C., Drysdale, R. N., Hellstrom, J. C., Capron, E., Rasmussen, S. O., Zhang, X., Fleitmann, D., Couchoud, I., & Wolff, E. (2020). Synchronous timing of abrupt climate changes during the last glacial period. Science (New York, N.Y.), 369(6506), 963–969. https://doi.org/10.1126/science.aay5538

Cortés-Sánchez, M., Jiménez-Espejo, F. J., Simón-Vallejo, M. D., Stringer, C., Lozano Francisco, M. C., García-Alix, A., Vera Peláez, J. L., Odriozola, C. P., Riquelme-Cantal, J. A., Parrilla Giráldez, R., Maestro González, A., Ohkouchi, N., & Morales-Muñiz, A. (2019). An early Aurignacian arrival in southwestern Europe. Nature Ecology & Evolution, 3(2), Article 2. https://doi.org/10.1038/s41559-018-0753-6

Cortijo, E., Labeyrie, L., Vidal, L., Vautravers, M., Chapman, M., Duplessy, J.-C., Elliot, M., Arnold, M., Turon, J.-L., & Auffret, G. (1997). Changes in sea surface hydrology associated with Heinrich event 4 in the North Atlantic Ocean between 40° and 60°N. Earth and Planetary Science Letters, 146(1), 29–45. https://doi.org/10.1016/S0012-821X(96)00217-8

Cortina, A., Sierro, F. J., Flores, J. A., Martrat, B., & Grimalt, J. O. (2015). The response of SST to insolation and ice sheet variability from MIS 3 to MIS 11 in the northwestern Mediterranean Sea (Gulf of Lions). Geophysical Research Letters, 42(23), 10,366-10,374. https://doi.org/10.1002/2015GL065539

Coussin, V. (2021). Gradients climatiques continentaux et hydrologiques au cours de l'Holocène dans la marge Algérienne au Golfe du Lion: Approche multi-proxies : palynologie, sédimentologie, biomarqueurs moléculaires et reconstructions climatiques. Thèse de Université de Bretagne occidentale, Brest, 368 p. https://theses.hal.science/tel-03783723

Cucart-Mora, C., Lozano, S., & Fernández-López De Pablo, J. (2018). Bio-cultural interactions and demography during the Middle to Upper Palaeolithic transition in Iberia: An agent-based modelling approach. Journal of Archaeological Science, 89, 14–24. https://doi.org/10.1016/j.jas.2017.11.001

Cueto, S., Preysler, J., Pérez-González, A., Torres, C., Pérez, I., & Miguel, J. (2016). Acheulian flint quarries in the Madrid Tertiary basin, central Iberian Peninsula: First data obtained from geoarchaeological studies. Quaternary International, 411. https://doi.org/10.1016/j.quaint.2016.01.041

Cugny, C., Mazier, F., & Galop, D. (2010). Modern and fossil non-pollen palynomorphs from the Basque mountains (western Pyrenees, France): The use of coprophilous fungi to reconstruct pastoral activity. Vegetation History and Archaeobotany, 19(5), 391–408. https://doi.org/10.1007/s00334-010-0242-6

Cui, Y., Xu, H., Liang, Y., Zhao, K., Chen, J., Wang, Y., Cong, J., Cheng, H., & Tan, L. (2024). Chronological features of Heinrich Stadial 2 based on a high-resolution analysis of δ18O stalagmite records from China, and possible links to changes in Atlantic Meridional Overturning Circulation. Palaeogeography, Palaeoclimatology, Palaeoecology, 633, 111875. https://doi.org/10.1016/j.palaeo.2023.111875

Cunha, P. P., Almeida, N. A. C., Aubry, T., Martins, A. A., Murray, A. S., Buylaert, J.-P., Sohbati, R., Raposo, L., & Rocha, L. (2012). Records of human occupation from Pleistocene river terrace and aeolian sediments in the Arneiro depression (Lower Tejo River, central eastern Portugal). Geomorphology, 165–166, 78–90. https://doi.org/10.1016/j.geomorph.2012.02.017

Cunha, P. P., Martins, A. A., Buylaert, J.-P., Murray, A. S., Gouveia, M. P., Font, E., Pereira, T., Figueiredo, S., Ferreira, C., Bridgland, D. R., Yang, P., Stevaux, J. C., & Mota, R. (2019). The Lowermost Tejo River Terrace at Foz do Enxarrique, Portugal: A Palaeoenvironmental Archive from c. 60–35 ka and Its Implications for the Last Neanderthals in Westernmost Iberia. Quaternary, 2(1), Article 1. https://doi.org/10.3390/quat2010003

Cunha, P. P., Martins, A. A., Buylaert, J.-P., Murray, A. S., Raposo, L., Mozzi, P., & Stokes, M. (2017). New data on the chronology of the Vale do Forno sedimentary sequence (Lower Tejo River terrace staircase) and its relevance as a fluvial archive of the Middle Pleistocene in western Iberia. Quaternary Science Reviews, 166, 204–226. https://doi.org/10.1016/j.quascirev.2016.11.001

d'Errico, F., & Sánchez Goñi, M. F. (2003). Neandertal extinction and the millennial scale climatic variability of OIS 3. Quaternary Science Reviews, 22(8–9), 769–788. https://doi.org/10.1016/S0277-3791(03)00009-X

d'Errico, F., & Sánchez Goñi, M. F. (2004). "A Garden of Eden for the Gibraltar Neandertals? A reply to Finlayson et al." Quaternary Science Reviews, 23(9–10), 1210–1216. https://doi.org/10.1016/j.quascirev.2003.12.016

d'Errico, F., Sanchez Goñi, M., & Vanharen, M. (2006). L'impact de la variabilité climatique rapide des OIS3-2 sur le peuplement de l'Europe. In Bard, E. (Eds), L'Homme face au climat, Travaux du Collège de France, Odile Jacob. pp. 265-282.

Dahl-Jensen, D., Albert, M. R., Aldahan, A., Azuma, N., Balslev-Clausen, D., Baumgartner, M., Berggren, A.-M., Bigler, M., Binder, T., Blunier, T., Bourgeois, J. C., Brook, E. J., Buchardt, S. L., Buizert, C., Capron, E., Chappellaz, J., Chung, J., Clausen, H. B., Cvijanovic, I., … NEEM community members. (2013). Eemian interglacial reconstructed from a Greenland folded ice core. Nature, 493(7433), Article 7433. https://doi.org/10.1038/nature11789

Dalén, L., Orlando, L., Shapiro, B., Brandström-Durling, M., Quam, R., Gilbert, M. T. P., Díez Fernández-Lomana, J. C., Willerslev, E., Arsuaga, J. L., & Götherström, A. (2012). Partial Genetic Turnover in Neandertals: Continuity in the East and Population Replacement in the West. Molecular Biology and Evolution, 29(8), 1893–1897. https://doi.org/10.1093/molbev/mss074

Dansgaard, W., Johnsen, S. J., Clausen, H. B., Dahl-Jensen, D., Gundestrup, N. S., Hammer, C. U., Hvidberg, C. S., Steffensen, J. P., Sveinbjörnsdottir, A. E., & Jouzel, J. (1993). Evidence for general instability of past climate from a 250-kyr ice-core record. Nature, 364, 218–220.

Daura, J., Sanz, M., Allué, E., Vaquero, M., López-García, J. M., Sánchez-Marco, A., Domènech, R., Martinell, J., Carrión, J. S., Ortiz, J. E., Torres, T., Arnold, L. J., Benson, A., Hoffmann, D. L., Skinner, A. R., & Julià, R. (2017). Palaeoenvironments of the last Neanderthals in SW Europe (MIS 3): Cova del Coll Verdaguer (Barcelona, NE of Iberian Peninsula). Quaternary Science Reviews, 177, 34–56. https://doi.org/10.1016/j.quascirev.2017.10.005

Daura, J., Sanz, M., Demuro, M., Arnold, L. J., Costa, A. M., Moreno, J., da Conceição Freitas, M., Lopes, V., Égüez, N., Hoffmann, D. L., Benson, A., Cabanes, D., García-Targa, J., & Fullola, J. M. (2021).

A new chronological framework and site formation history for Cova del Gegant (Barcelona): Implications for Neanderthal and Anatomically Modern Human occupation of NE Iberian Peninsula. Quaternary Science Reviews, 270, 107141. https://doi.org/10.1016/j.quascirev.2021.107141

Daura, J., Sanz, M., García, N., Allué, E., Vaquero, M., Fierro, E., Carrión, J. S., López-García, J. M., Blain, H. A., Sánchez-Marco, A., Valls, C., Albert, R. M., Fornós, J. J., Julià, R., Fullola, J. M., & Zilhão, J. (2013). Terrasses de la Riera dels Canyars (Gavà, Barcelona): The landscape of Heinrich Stadial 4 north of the "Ebro frontier" and implications for modern human dispersal into Iberia. Quaternary Science Reviews, 60, 26–48. https://doi.org/10.1016/j.quascirev.2012.10.042

Daura, J., Sanz, M., Julià, R., García-Fernández, D., Fornós, J. J., Vaquero, M., Allué, E., López-García, J. M., Blain, H. A., Ortiz, J. E., Torres, T., Albert, R. M., Rodríguez-Cintas, À., Sánchez-Marco, A., Cerdeño, E., Skinner, A. R., Asmeron, Y., Polyak, V. J., Garcés, M., … Zilhão, J. (2015). Cova del Rinoceront (Castelldefels, Barcelona): A terrestrial record for the Last Interglacial period (MIS 5) in the Mediterranean coast of the Iberian Peninsula. Quaternary Science Reviews, 114, 203–227. https://doi.org/10.1016/j.quascirev.2015.02.014

Davis, B. A. S., Brewer, S., Stevenson, A. C., & Guiot, J. (2003). The temperature of Europe during the Holocene reconstructed from pollen data. Quaternary Science Reviews, 22(15), 1701–1716. https://doi.org/10.1016/S0277-3791(03)00173-2

Davis, B. A. S., Fasel, M., Kaplan, J. O., Russo, E., & Burke, A. (2022). The climate and vegetation of Europe, North Africa and the Middle East during the Last Glacial Maximum (21,000 years BP) based on pollen data. Climate of the Past Discussions. https://doi.org/10.5194/cp-2022-59

Davtian, N., & Bard, E. (2023). A new view on abrupt climate changes and the bipolar seesaw based on paleotemperatures from Iberian Margin sediments. Proceedings of the National Academy of Sciences, 120(12), e2209558120. https://doi.org/10.1073/pnas.2209558120

de Abreu, L., Shackleton, N. J., Schönfeld, J., Hall, M., & Chapman, M. (2003). Millennial-scale oceanic climate variability off the Western Iberian margin during the last two glacial periods. Marine Geology, 196(1), 1–20. https://doi.org/10.1016/S0025-3227(03)00046-X

de Beaulieu, J.-L., & Reille, M. (2008). A long Upper Pleistocene pollen record from Les Echets, near Lyon, France. Boreas, 13, 111–132. https://doi.org/10.1111/j.1502-3885.1984.tb00066.x

de Beaulieu, J.-L., & Reille, M. (1992). The last climatic cycle at La Grande Pile (Vosges, France) a new pollen profile. Quaternary Science Reviews, 11(4), 431–438. https://doi.org/10.1016/0277-3791(92)90025-4

De Beaulieu, J.-L., & Reille, M. (2007). The Pollen Sequence of Les Échets (France): A New Element for the Chronology of the Upper Pleistocene. Géographie physique et Quaternaire, 38(1), 3–9. https://doi.org/10.7202/032531ar

De Kaenel, E., Siesser, W., & Murat, A. (1999). Pleistocene calcareous nannofossil biostratigraphy and the Western Mediterranean sapropels, Sites 974 to 977 and 979. Proceedings of the Ocean Drilling Program: Scientific Results, 161. https://doi.org/10.2973/odp.proc.sr.161.250.1999

de la Torre, I., Martínez-Moreno, J., & Mora, R. (2013). Change and Stasis in the Iberian Middle Paleolithic: Considerations on the Significance of Mousterian Technological Variability. Current Anthropology, 54(S8), S320–S336. https://doi.org/10.1086/673861

de Lombera-Hermida, A., Rodríguez-Álvarez, X. P., Mosquera, M., Ollé, A., García-Medrano, P., Pedergnana, A., Terradillos-Bernal, M., López-Ortega, E., Bargalló, A., Rodríguez-Hidalgo, A., Saladié, P., Bermúdez de Castro, J. M., & Carbonell, E. (2020). The dawn of the Middle Paleolithic in Atapuerca: The lithic assemblage of TD10.1 from Gran Dolina. Journal of Human Evolution, 145, 102812. https://doi.org/10.1016/j.jhevol.2020.102812

de Lumley, M. A. (2018). Les restes humains fossiles de la grotte du Lazaret. Généralités, approche démographique. In Les restes humains fossiles de la grotte du Lazaret, Nice, Alpes-Maritimes. Des Homo erectus européens évolués en voie de néandertalisation (pp. 217–220). CNRS Editions. https://hal.science/hal-02265863

Deaney, E. L., Barker, S., & van de Flierdt, T. (2017). Timing and nature of AMOC recovery across Termination 2 and magnitude of deglacial CO2 change. Nature Communications, 8(1), Article 1. https://doi.org/10.1038/ncomms14595

Defleur, A. R., & Desclaux, E. (2019). Impact of the last interglacial climate change on ecosystems and Neanderthals behavior at Baume Moula-Guercy, Ardèche, France. Journal of Archaeological Science, 104, 114–124. https://doi.org/10.1016/j.jas.2019.01.002

Defleur, A. R., Desclaux, E., Jabbour, R. S., & Richards, G. D. (2020). The Eemian: Global warming, ecosystem upheaval, demographic collapse and cannibalism at Moula-Guercy. A reply to Slimak and Nicholson (2020). Journal of Archaeological Science, 117, 105113. https://doi.org/10.1016/j.jas.2020.105113

Degioanni, A., Bonenfant, C., Cabut, S., & Condemi, S. (2019). Living on the edge: Was demographic weakness the cause of Neanderthal demise? PLOS ONE, 14(5), e0216742. https://doi.org/10.1371/journal.pone.0216742

Degioanni, A., Cabut, S., Condemi, S., & Smith, R. S. (2025). Climate change in Europe between 90 and 50 kyr BP and Neanderthal territorial habitability. PLOS ONE, 20(2), e0308690. https://doi.org/10.1371/journal.pone.0308690

Deitch, M., Sapundjieff, M., & Feirer, S. (2017). Characterizing Precipitation Variability and Trends in the World's Mediterranean-Climate Areas. Water, 9(4), 259. https://doi.org/10.3390/w9040259

Delagnes, A., & Meignen, L. (2007). Diversity of Lithic Production Systems During the Middle Paleolithic in France. In Transitions before the Transition: Evolution and Stability in the Middle Paleolithic and Middle Stone Age (pp. 85–107). https://doi.org/10.1007/0-387-24661-4_5

Delagnes, A., & Rendu, W. (2011). Shifts in Neandertal mobility, technology and subsistence strategies in western France. Journal of Archaeological Science, 38(8), 1771–1783. https://doi.org/10.1016/j.jas.2011.04.007

Delmotte, M., Chappellaz, J., Brook, E., Yiou, P., Barnola, J. M., Goujon, C., Raynaud, D., & Lipenkov, V. I. (2004). Atmospheric methane during the last four glacial-interglacial cycles: Rapid changes and their link with Antarctic temperature. Journal of Geophysical Research: Atmospheres, 109(D12). https://doi.org/10.1029/2003JD004417

Delpiano, D., Zupancich, A., Bertola, S., Martellotta, E. F., Livraghi, A., Cristiani, E., & Peresani, M. (2022). Flexibility within Quina lithic production systems and tool-use in Northern Italy: Implications on Neanderthal behavior and ecology during early MIS 4. Archaeological and Anthropological Sciences, 14(12), 219. https://doi.org/10.1007/s12520-022-01684-2

Demuro, M., Arnold, L., Gonzalez-Urquijo, J., Lazuen, T., & Frochoso, M. (2023). Chronological constraint of Neanderthal cultural and environmental changes in southwestern Europe: MIS 5–MIS 3 dating of the Axlor site (Biscay, Spain). Journal of Quaternary Science, 38. https://doi.org/10.1002/jqs.3527

Dennell, R. W., Martinón-Torres, M., & Bermúdez de Castro, J. M. (2011). Hominin variability, climatic instability and population demography in Middle Pleistocene Europe. Quaternary Science Reviews, 30(11–12), 1511–1524. https://doi.org/10.1016/j.quascirev.2009.11.027

Depaepe, P. (2022). Sociétés humaines et changements climatiques: Une longue histoire. L'homme de Neandertal pendant les stades isotopiques 11 à 4. In Les sociétés humaines face aux changements climatiques (Archaeopress, Vol. 1).

Deschamps, M. (2017). Late Middle Palaeolithic assemblages with flake cleavers in the western Pyrenees: The Vasconian reconsidered. Quaternary International, 433, 33–49. https://doi.org/10.1016/j.quaint.2016.01.043

Deschamps, M. (2019). Identification of Quina and Vasconian technocomplexes in Gatzarria Cave (north-western Pyrenees), based on the stratigraphic, taphonomic and technological revision of the Georges Laplace collections. Comptes Rendus Palevol, 18(5), 569–586. https://doi.org/10.1016/j.crpv.2019.04.001

Di Vincenzo, F., & Manzi, G. (2023). Homo heidelbergensis as the Middle Pleistocene common ancestor of Denisovans, Neanderthals and modern humans. Journal of Mediterranean Earth Sciences, Vol. 15 (2023): In progress. https://doi.org/10.13133/2280-6148/18074

Diez Martín, F., Sánchez Yustos, P., Gómez González, J. A., Gómez De La Rúa, D., Yravedra Sáinz De Los Terreros, J., & Díaz Muñoz, I. (2011). La ocupación neandertal en el Cañón de La Horadada (Mave, Palencia, España): Nuevas perspectivas arqueológicas en Cueva Corazón. MUNIBE (Antropologia-Arkeologia), 62, 65–85.

Diez-Martín, F. (2010). Evaluating the effect of plowing on the archaeological record: The early middle palaeolithic in the river Duero basin plateaus (north-central Spain). Quaternary International, 214(1), 30–43. https://doi.org/10.1016/j.quaint.2009.10.024

Diez-Martín, F., Sánchez-Yustos, P., Gómez-González, J. Á., & Gómez De La Rúa, D. (2008). Earlier Palaeolithic Settlement Patterns: Landscape Archaeology on the River Duero Basin Plateaus (Castilla y León, Spain). Journal of World Prehistory, 21(2), 103–137. https://doi.org/10.1007/s10963-008-9012-0

Diodato, N., Bellocchi, G., Romano, N., & Chirico, G. B. (2011). How the aggressiveness of rainfalls in the Mediterranean lands is enhanced by climate change. Climatic Change, 108(3), 591–599. https://doi.org/10.1007/s10584-011-0216-4

Doerschner, N., Fitzsimmons, K. E., Blasco, R., Finlayson, G., Rodríguez-Vidal, J., Rosell, J., Hublin, J.-J., & Finlayson, C. (2019). Chronology of the Late Pleistocene archaeological sequence at Vanguard Cave, Gibraltar: Insights from quartz single and multiple grain luminescence dating. Quaternary International, 501, 289–302. https://doi.org/10.1016/j.quaint.2018.02.020

D'Oliveira, L., Dugerdil, L., Ménot, G., Evin, A., Muller, S., Ansanay-Alex, S., Azuara, J., Bonnet, C., Bremond, L., Shah, M., & Peyron, O. (2023). Reconstructing 15 000 years of southern France temperatures from coupled pollen and molecular (branched glycerol dialkyl glycerol

tetraether) markers (Canroute, Massif Central). Climate of the Past, 19, 2127–2156. https://doi.org/10.5194/cp-19-2127-2023

Domingo, R., Peña-Monné, J. L., de Torres, T., Ortiz, J. E., & Utrilla, P. (2017). Neanderthal highlanders: Las Callejuelas (Monteagudo del Castillo, Teruel, Spain), a high-altitude site occupied during MIS 5. Quaternary International, 435, 129–143. https://doi.org/10.1016/j.quaint.2015.09.088

Donders, T. H., Oliveira, D., Goñi, M. F. S., & Sadori, L. (2024). A 1.1-million-year vegetation history of the Mediterranean region: Scientific drilling reveals sensitivities of forest ecosystems. PAGES Magazine, 32(2).

Donders, T., Panagiotopoulos, K., Koutsodendris, A., Bertini, A., Mercuri, A. M., Masi, A., Combourieu-Nebout, N., Joannin, S., Kouli, K., Kousis, I., Peyron, O., Torri, P., Florenzano, A., Francke, A., Wagner, B., & Sadori, L. (2021). 1.36 million years of Mediterranean forest refugium dynamics in response to glacial–interglacial cycle strength. Proceedings of the National Academy of Sciences, 118(34), e2026111118. https://doi.org/10.1073/pnas.2026111118

Dormoy, I., Peyron, O., Combourieu-Nebout, N., Goring, S., Kotthoff, U., Magny, M., & J, P. (2009). Terrestrial climate variability and seasonality changes in the Mediterranean region between 15000 and 4000 years BP deduced from marine pollen records. Climate of the Past Discussions, 5. https://doi.org/10.5194/cpd-5-735-2009

Douka, K., & Higham, T. (2017). The Chronological Factor in Understanding the Middle and Upper Paleolithic of Eurasia. Current Anthropology, 58(S17), S480–S490. https://doi.org/10.1086/694173

Douka, K., Higham, T. F. G., Wood, R., Boscato, P., Gambassini, P., Karkanas, P., Peresani, M., & Ronchitelli, A. M. (2014). On the chronology of the Uluzzian. Journal of Human Evolution, 68, 1–13. https://doi.org/10.1016/j.jhevol.2013.12.007

Dray, S., Dufour, A.-B., Thioulouse, J., Chessel, D., Jombart, T., Pavoine, S., Lobry, J. R., Ollier, S., Borcard, D., Legendre, P., Bougeard, S., & Siberchicot, A. (2025). ade4: Analysis of Ecological Data: Exploratory and Euclidean Methods in Environmental Sciences (Version 1.7-23) [Computer software]. https://cran.r-project.org/web/packages/ade4/index.html

Drysdale, R. N., Hellstrom, J. C., Zanchetta, G., Fallick, A. E., Sánchez Goñi, M. F., Couchoud, I., McDonald, J., Maas, R., Lohmann, G., & Isola, I. (2009). Evidence for obliquity forcing of glacial Termination II. Science (New York, N.Y.), 325(5947), 1527–1531. https://doi.org/10.1126/science.1170371

Drysdale, R. N., Zanchetta, G., Hellstrom, J. C., Fallick, A. E., & Zhao, J. (2005). Stalagmite evidence for the onset of the Last Interglacial in southern Europe at 129 ± 1 ka. Geophysical Research Letters, 32(24). https://doi.org/10.1029/2005GL024658

Drysdale, R., Zanchetta, G., Hellstrom, J., Fallick, A. E., McDonald, J., & Cartwright, I. (2007). Stalagmite evidence for the precise timing of North Atlantic cold events during the last glacial. Geology, 35. https://doi.org/10.1130/G23161A.1

Dugerdil, L., Joannin, S., Peyron, O., Jouffroy-Bapicot, I., Vannière, B., Boldgiv, B., Unkelbach, J., Behling, H., & Ménot, G. (2021). Climate reconstructions based on GDGT and pollen surface datasets from Mongolia and Baikal area: Calibrations and applicability to extremely cold–dry environments over the Late Holocene. Climate of the Past, 17(3), 1199–1226. https://doi.org/10.5194/cp-17-1199-2021

Dumitru, O. A., Onac, B. P., Polyak, V. J., Wynn, J. G., Asmerom, Y., & Fornós, J. J. (2018). Climate variability in the western Mediterranean between 121 and 67 ka derived from a Mallorcan speleothem record. Palaeogeography, Palaeoclimatology, Palaeoecology, 506, 128–138. https://doi.org/10.1016/j.palaeo.2018.06.028

Duprat-Oualid, F. (2019). 50 000 ans d'histoire de la végétation et du climat en Europe occidentale: Étude pollinique et approche multi-proxy sur la séquence sédimentaire du Bergsee (Forêt Noire, Allemagne). Thèse de l'Université de Bourgogne Franche-Compté. 272 p.

Ehlers, J., & Gibbard, P. L. (2007). The extent and chronology of Cenozoic Global Glaciation. Quaternary International, 164–165, 6–20. https://doi.org/10.1016/j.quaint.2006.10.008

Ehlers, J., Gibbard, P. L., & Hughes, P. D. (2018). Chapter 4—Quaternary Glaciations and Chronology. In J. Menzies & J. J. M. van der Meer (Eds.), Past Glacial Environments (Second Edition) (pp. 77–101). Elsevier. https://doi.org/10.1016/B978-0-08-100524-8.00003-8

Ehlers, J., Grube, A., Stephan, H.-J., & Wansa, S. (2011). Pleistocene Glaciations of North Germany—New Results. In Developments in Quaternary Sciences (Vol. 15, pp. 149–162). Elsevier. https://doi.org/10.1016/B978-0-444-53447-7.00013-1

Eixea, A. (2018). Middle palaeolithic lithic assemblages in western Mediterranean Europe from MIS 5 to 3. Journal of Archaeological Science: Reports, 21, 643–666. https://doi.org/10.1016/j.jasrep.2018.08.039*

Eixea, A., Chacón, M. G., Bargalló, A., Sanchis, A., Romagnoli, F., Vaquero, M., & Villaverde, V. (2020). Neanderthal Spatial Patterns and Occupation Dynamics: A Focus on the Central Region in Mediterranean Iberia. Journal of World Prehistory, 33(3), 267–324. https://doi.org/10.1007/s10963-020-09143-3

Ejarque, A., Julià, R., Castanyer, P., Orengo, H. A., Palet, J. M., & Riera, S. (2022). Landscape footprints of peopling and colonisation from the Late Bronze Age to Antiquity in the coastal hinterland of Emporion-Emporiae, NE Iberia. The Holocene, 32(4), 280–296. https://doi.org/10.1177/09596836211066597

Elith, J., Leathwick, J. R., & Hastie, T. (2008). A working guide to boosted regression trees. Journal of Animal Ecology, 77(4), 802–813. https://doi.org/10.1111/j.1365-2656.2008.01390.x

Elmouden, A., Bouchaou, L., & Snoussi, M. (2005). Constraints on alluvial clay mineral assemblages in semiarid regions. The Souss Wadi Basin (Morocco, Northwestern Africa). Geologica Acta: An International Earth Science Journal, ISSN 1695-6133, Vol. 3, No. 1, 2005, Pags. 3-14, 3. https://doi.org/10.1344/105.000001410

Emeis, K., Schulz, H., Struck, U., Rossignol-Strick, M., Erlenkeuser, H., Howell, M., Kroon, D., Mackensen, A., Ishizuka, S., Oba, T., Sakamoto, T., & Koizumi, I. (2003). Eastern Mediterranean surface water temperatures and δ18O composition during deposition of sapropels in the late Quaternary. Paleoceanography, 18, 1005. https://doi.org/10.1029/2000PA000617

Emiliani, C. (1955). Pleistocene Temperatures. The Journal of Geology, 63(6), 538–578. https://doi.org/10.1086/626295

Eynaud, F., Zaragosi, S., Scourse, J. D., Mojtahid, M., Bourillet, J. F., Hall, I. R., Penaud, A., Locascio, M., & Reijonen, A. (2007). Deglacial laminated facies on the NW European continental margin: The hydrographic significance of British-Irish Ice Sheet deglaciation and Fleuve Manche paleoriver

discharges. Geochemistry, Geophysics, Geosystems, 8(6). https://doi.org/10.1029/2006GC001496

Fa, J. E., Stewart, J. R., Lloveras, L., & Vargas, J. M. (2013). Rabbits and hominin survival in Iberia. Journal of Human Evolution, 64(4), 233–241. https://doi.org/10.1016/j.jhevol.2013.01.002

Fabre, V., Condemi, S., & Degioanni, A. (2009). Genetic Evidence of Geographical Groups among Neanderthals. PLOS ONE, 4(4), e5151. https://doi.org/10.1371/journal.pone.0005151

Fabres, J., Calafat, A., Sanchez-Vidal, A., Canals, M., & Heussner, S. (2002). Composition and spatio-temporal variability of particle fluxes in the Western Alboran Gyre, Mediterranean Sea. Journal of Marine Systems, 33–34, 431–456. https://doi.org/10.1016/S0924-7963(02)00070-2

Faegri, K., & Iversen, J. (1964). Textbook of Pollen Analysis (4th Edition). John Wiley and Sons. https://www.abebooks.com/9780471921783/Textbook-Pollen-Analysis-Faegri-Iversen-0471921785/plp

Falcucci, A., Arrighi, S., Spagnolo, V., Rossini, M., Higgins, O. A., Muttillo, B., Martini, I., Crezzini, J., Boschin, F., Ronchitelli, A., & Moroni, A. (2024). A pre-Campanian Ignimbrite techno-cultural shift in the Aurignacian sequence of Grotta di Castelcivita, southern Italy. Scientific Reports, 14(1), 12783. https://doi.org/10.1038/s41598-024-59896-6

Fernández Peris, J., Barciela, V., Blasco, R., Cuartero, F., & Sañudo, P. (2008). El Paleolítico Medio en el territorio valenciano y la variabilidad tecno-económica de la Cova del Bolomor. Treballs d'Arqueologia, 14, 141–169.

Fernández-García, M., Vidal-Cordasco, M., Jones, J. R., & Marín-Arroyo, A. B. (2023). Reassessing palaeoenvironmental conditions during the Middle to Upper Palaeolithic transition in the Cantabrian region (Southwestern Europe). Quaternary Science Reviews, 301, 107928. https://doi.org/10.1016/j.quascirev.2022.107928

Fernández-Peris, J., Cuartero, F., Barciela, V., Blasco, R., & Sañudo, P. (2020). The flake microlithism in the European Pleistocene: The case of Bolomor Cave (MIS 9-5, Valencia, Spain). Journal of Archaeological Science: Reports, 31, 102305. https://doi.org/10.1016/j.jasrep.2020.102305

Fersi, W., Penaud, A., Wary, M., Toucanne, S., Waelbroeck, C., Rossignol, L., & Eynaud, F. (2021). Imprint of seasonality changes on fluvio-glacial dynamics across Heinrich Stadial 1 (NE Atlantic Ocean). Global and Planetary Change, 204, 103552. https://doi.org/10.1016/j.gloplacha.2021.103552

Finlayson, C. (2008). On the importance of coastal areas in the survival of Neanderthal populations during the Late Pleistocene. Quaternary Science Reviews, 27(23), 2246–2252. https://doi.org/10.1016/j.quascirev.2008.08.033

Finlayson, C., & Carrión, J. S. (2007). Rapid ecological turnover and its impact on Neanderthal and other human populations. Trends in Ecology & Evolution, 22(4), 213–222. https://doi.org/10.1016/j.tree.2007.02.001

Finlayson, C., Fa, D. A., Finlayson, G., Pacheco, F. G., & Vidal, J. R. (2004). Did the moderns kill off the Neanderthals? A reply to F. d'Errico and Sánchez Goñi. Quaternary Science Reviews, 23(9–10), 1205–1209. https://doi.org/10.1016/j.quascirev.2003.12.017

Finlayson, C., Fa, D. A., Jiménez Espejo, F., Carrión, J. S., Finlayson, G., Giles Pacheco, F., Rodríguez Vidal, J., Stringer, C., & Martínez Ruiz, F. (2008). Gorham's Cave, Gibraltar—The persistence of

a Neanderthal population. Quaternary International, 181(1), 64–71. https://doi.org/10.1016/j.quaint.2007.11.016

Finlayson, C., Giles Pacheco, F., Rodríguez-Vidal, J., Fa, D. A., María Gutierrez López, J., Santiago Pérez, A., Finlayson, G., Allue, E., Baena Preysler, J., Cáceres, I., Carrión, J. S., Fernández Jalvo, Y., Gleed-Owen, C. P., Jimenez Espejo, F. J., López, P., Antonio López Sáez, J., Antonio Riquelme Cantal, J., Sánchez Marco, A., Giles Guzman, F., … Sakamoto, T. (2006a). Late survival of Neanderthals at the southernmost extreme of Europe. Nature, 443(7113), 850–853. https://doi.org/10.1038/nature05195

Fitzsimmons, K. E., Hambach, U., Veres, D., & Iovita, R. (2013). The Campanian Ignimbrite Eruption: New Data on Volcanic Ash Dispersal and Its Potential Impact on Human Evolution. PLOS ONE, 8(6), e65839. https://doi.org/10.1371/journal.pone.0065839

Fletcher, W. J., Müller, U. C., Koutsodendris, A., Christanis, K., & Pross, J. (2013). A centennial-scale record of vegetation and climate variability from 312 to 240 ka (Marine Isotope Stages 9c–a, 8 and 7e) from Tenaghi Philippon, NE Greece. Quaternary Science Reviews, 78, 108–125. https://doi.org/10.1016/j.quascirev.2013.08.005

Fletcher, W. J., & Sánchez Goñi, M. F. (2008). Orbital- and sub-orbital-scale climate impacts on vegetation of the western Mediterranean basin over the last 48,000 yr. Quaternary Research, 70(3), 451–464. https://doi.org/10.1016/j.yqres.2008.07.002

Fletcher, W. J., Sánchez Goñi, M. F., Allen, J. R. M., Cheddadi, R., Combourieu-Nebout, N., Huntley, B., Lawson, I., Londeix, L., Magri, D., Margari, V., Müller, U. C., Naughton, F., Novenko, E., Roucoux, K., & Tzedakis, P. C. (2010a). Millennial-scale variability during the last glacial in vegetation records from Europe. Quaternary Science Reviews, 29(21), 2839–2864. https://doi.org/10.1016/j.quascirev.2009.11.015

Fletcher, W. J., Sanchez Goñi, M. F., Peyron, O., & Dormoy, I. (2010b). Abrupt climate changes of the last deglaciation detected in a Western Mediterranean forest record. Climate of the Past, 6(2), 245–264. https://doi.org/10.5194/cp-6-245-2010

Foerster, V., Asrat, A., Bronk Ramsey, C., Brown, E. T., Chapot, M. S., Deino, A., Duesing, W., Grove, M., Hahn, A., Junginger, A., Kaboth-Bahr, S., Lane, C. S., Opitz, S., Noren, A., Roberts, H. M., Stockhecke, M., Tiedemann, R., Vidal, C. M., Vogelsang, R., … Trauth, M. H. (2022). Pleistocene climate variability in eastern Africa influenced hominin evolution. Nature Geoscience, 15(10), 805–811. https://doi.org/10.1038/s41561-022-01032-y

Follieri, M., Magri, D., & Sadori, L. (1988). A 250 000-years pollen record from Valle di Castiglione (Roma). Pollen et Spores, 30, 329–356.

Follieri, M., Magri, D., & Sadori, L. (1989). Pollen stratigraphical synthesis from Valle di Castiglione (Roma). Quaternary International, 3–4, 81–84. https://doi.org/10.1016/1040-6182(89)90076-1

Fontana, F., Nenzioni, G., & Peretto, C. (2010). The southern Po plain area (Italy) in the mid-late Pleistocene: Human occupation and technical behaviours. Quaternary International, 223, 465–471. https://doi.org/10.1016/j.quaint.2010.02.013

Fornós, J. J., Clemmensen, L. B., Gómez-Pujol, L., & Murray, A. S. (2009). Late Pleistocene carbonate aeolianites on Mallorca, Western Mediterranean: A luminescence chronology. Quaternary Science Reviews, 28(25), 2697–2709. https://doi.org/10.1016/j.quascirev.2009.06.008

Fourcade, T. (2022). Changements culturels et adaptations aux changements climatiques et environnementaux des derniers Néandertaliens dans le sud de la France. Thèse de l'Université Bordeaux Montaigne. 411 p.

Fourcade, T., Sánchez Goñi, M. F., Lahaye, C., Rossignol, L., & Philippe, A. (2022). Environmental changes in SW France during the Middle to Upper Paleolithic transition from the pollen analysis of an eastern North Atlantic deep-sea core. Quaternary Research, 1–18. https://doi.org/10.1017/qua.2022.21

Fourcade, T., Sánchez Goñi, M. F., Lesven, J., Lahaye, C., & Philippe, A. (2024). Vegetation response in NW Mediterranean borderlands to the millennial-scale climate variability of the last glacial period. Quaternary Science Reviews, 334, 108722. https://doi.org/10.1016/j.quascirev.2024.108722

Fu, Q., Hajdinjak, M., Moldovan, O. T., Constantin, S., Mallick, S., Skoglund, P., Patterson, N., Rohland, N., Lazaridis, I., Nickel, B., Viola, B., Prüfer, K., Meyer, M., Kelso, J., Reich, D., & Pääbo, S. (2015). An early modern human from Romania with a recent Neanderthal ancestor. Nature, 524(7564), 216–219. https://doi.org/10.1038/nature14558

Fu, Q., Posth, C., Hajdinjak, M., Petr, M., Mallick, S., Fernandes, D., Furtwängler, A., Haak, W., Meyer, M., Mittnik, A., Nickel, B., Peltzer, A., Rohland, N., Slon, V., Talamo, S., Lazaridis, I., Lipson, M., Mathieson, I., Schiffels, S., … Reich, D. (2016). The genetic history of Ice Age Europe. Nature, 534(7606), 200–205. https://doi.org/10.1038/nature17993

Galván, B., Hernández, C. M., Mallol, C., Mercier, N., Sistiaga, A., & Soler, V. (2014). New evidence of early Neanderthal disappearance in the Iberian Peninsula. Journal of Human Evolution, 75, 16–27. https://doi.org/10.1016/j.jhevol.2014.06.002

Gamble, C. (1999). The Palaeolithic societies of Europe (Transferred to digital print). Cambridge Univ. Press.

García, M., López-García, J., Royer, A., Lécuyer, C., Rivals, F., Rufà, A., Blasco, R., & Rosell Ardèvol, J. (2022). New insights in Neanderthal palaeoecology using stable oxygen isotopes preserved in small mammals as palaeoclimatic tracers in Teixoneres Cave (Moià, northeastern Iberia). Archaeological and Anthropological Sciences, 14, 106. https://doi.org/10.1007/s12520-022-01564-9

García-Diez, M., & Ochoa, B. (2013). Neanderthal Graphic Behavior: The Pecked Pebble from Axlor Rockshelter. Journal of Anthropological Research, 69, 397. https://doi.org/10.3998/jar.0521004.0069.307

Garcia-Ibaibarriaga, N., Rofes, J., Bailon, S., Garate, D., Rios-Garaizar, J., Martínez-García, B., & Murelaga, X. (2015). A palaeoenvironmental estimate in Askondo (Bizkaia, Spain) using small vertebrates. Quaternary International, 364, 244–254. https://doi.org/10.1016/j.quaint.2014.09.069

Garcia-Ibaibarriaga, N., Suárez Bilbao, A., Bailon, S., Arrizabalaga, A., Iriarte-Chiapusso, M.-J., Arnold, L., Demuro, M., & Murelaga, X. (2018). Paleoenvironmental and paleoclimatic interpretation of the stratigraphic sequence of Lezetxiki II Cave (Basque Country, Iberian Peninsula) inferred from small vertebrate assemblages. Quaternary Research, 90, 1–16. https://doi.org/10.1017/qua.2018.17

Gelorini, V., Verschuren, D., & Verbeken, A. (2011). Diversity and palaeoecological significance of non-pollen palynomorph assemblages in East African lake sediments. Afrika Focus, 24(2), 19–20. https://doi.org/10.21825/af.v24i2.18046

Genty, D., Blamart, D., Ouahdi, R., Gilmour, M., Baker, A., Jouzel, J., & Van-Exter, S. (2003). Precise dating of Dansgaard–Oeschger climate oscillations in western Europe from stalagmite data. Nature, 421(6925), 833–837. https://doi.org/10.1038/nature01391

Genty, D., Combourieu Nebout, N., Hatté, C., Blamart, D., Ghaleb, B., & Isabello, L. (2005). Rapid climatic changes of the last 90 kyr recorded on the European continent. Comptes Rendus Geoscience, 337(10), 970–982. https://doi.org/10.1016/j.crte.2005.04.010

Genty, D., Combourieu-Nebout, N., Peyron, O., Blamart, D., Wainer, K., Mansuri, F., Ghaleb, B., Isabello, L., Dormoy, I., von Grafenstein, U., Bonelli, S., Landais, A., & Brauer, A. (2010). Isotopic characterization of rapid climatic events during OIS3 and OIS4 in Villars Cave stalagmites (SW-France) and correlation with Atlantic and Mediterranean pollen records. Quaternary Science Reviews, 29(19), 2799–2820. https://doi.org/10.1016/j.quascirev.2010.06.035

Giaccio, B., Hajdas, I., Isaia, R., Deino, A., & Nomade, S. (2017). High-precision 14C and 40Ar/39Ar dating of the Campanian Ignimbrite (Y-5) reconciles the time-scales of climatic-cultural processes at 40 ka. Scientific Reports, 7(1), Article 1. https://doi.org/10.1038/srep45940

Giaccio, B., Wagner, B., Zanchetta, G., Bertini, A., Cavinato, G. P., De Franco, R., Florindo, F., Hodell, D., Neubauer, T., Pereira, A., Sadori, L., Satolli, S., Tzedakis, C., Albert, P., Boncio, P., Jonge, C., Francke, A., Heim, C., & Paine, A. (2024). International Continental Scientific Drilling Program (ICDP) workshop on the Fucino paleolake project: The longest continuous terrestrial archive in the MEditerranean recording the last 5 Million years of Earth system history (MEME). Scientific Drilling, 33, 249–266. https://doi.org/10.5194/sd-33-249-2024

Gicqueau, A., Schuh, A., Henrion, J., Viola, B., Partiot, C., Guillon, M., Golovanova, L., Doronichev, V., Gunz, P., Hublin, J.-J., & Maureille, B. (2023). Anatomically modern human in the Châtelperronian hominin collection from the Grotte du Renne (Arcy-sur-Cure, Northeast France). Scientific Reports, 13(1), 12682. https://doi.org/10.1038/s41598-023-39767-2

Gilpin, W., Feldman, M. W., & Aoki, K. (2016). An ecocultural model predicts Neanderthal extinction through competition with modern humans. Proceedings of the National Academy of Sciences of the United States of America, 113(8), 2134–2139. https://doi.org/10.1073/pnas.1524861113

Giorgi, F., & Lionello, P. (2008). Climate change projections for the Mediterranean region. Global and Planetary Change, 63(2), 90–104. https://doi.org/10.1016/j.gloplacha.2007.09.005

Gkinis, V., Vinther, B. M., Popp, T. J., Quistgaard, T., Faber, A.-K., Holme, C. T., Jensen, C.-M., Lanzky, M., Lütt, A.-M., Mandrakis, V., Ørum, N.-O., Pedersen, A.-S., Vaxevani, N., Weng, Y., Capron, E., Dahl-Jensen, D., Hörhold, M., Jones, T. R., Jouzel, J., … White, J. W. C. (2021). A 120,000-year long climate record from a NW-Greenland deep ice core at ultra-high resolution. Scientific Data, 8(1), Article 1. https://doi.org/10.1038/s41597-021-00916-9

Golovanova, L. V., Doronichev, V. B., Cleghorn, N. E., Koulkova, M. A., Sapelko, T. V., & Shackley, M. S. (2010). Significance of Ecological Factors in the Middle to Upper Paleolithic Transition. Current Anthropology, 51(5), 655–691. https://doi.org/10.1086/656185

González Molina, I. (2022). Ocupaciones neandertales en el MIS 4: Análisis tecnológico de la industria lítica de la Unidad XXf de la Cueva de El Castillo (Cantabria, España). Mémoire de master de l'Universitat Rovira i Virgili. 130p.

González Molina, I., Maillo-Fernández, J., Vaquero, M., Neira, A., Quirós, F., & Marín, J. (2024). Technological variability in El Castillo cave during MIS 4. Archaeological and Anthropological Sciences, 16. https://doi.org/10.1007/s12520-024-02041-1

Gonzalez-Hidalgo, J. C., Trullenque-Blanco, V., Beguería, S., & Peña-Angulo, D. (2024). Seasonal precipitation changes in the western Mediterranean Basin: The case of the Spanish mainland, 1916–2015. International Journal of Climatology, 44(5), 1800–1815. https://doi.org/10.1002/joc.8412

González-Sampériz, P., Leroy, S. A. G., Carrión, J. S., Fernández, S., García-Antón, M., Gil-García, M. J., Uzquiano, P., Valero-Garcés, B., & Figueiral, I. (2010). Steppes, savannahs, forests and phytodiversity reservoirs during the Pleistocene in the Iberian Peninsula. Review of Palaeobotany and Palynology, 162(3), 427–457. https://doi.org/10.1016/j.revpalbo.2010.03.009

Gouveia, C., Trigo, R. M., DaCamara, C. C., Libonati, R., & Pereira, J. M. C. (2008). The North Atlantic Oscillation and European vegetation dynamics. International Journal of Climatology, 28(14), 1835–1847. https://doi.org/10.1002/joc.1682

Gouzy, A., Malaizé, B., Pujol, C., & Charlier, K. (2004). Climatic "pause" during Termination II identified in shallow and intermediate waters off the Iberian margin. Quaternary Science Reviews, 23(14), 1523–1528. https://doi.org/10.1016/j.quascirev.2004.03.002

Granata, F., Zhu, S., & Di Nunno, F. (2025). Hydrological extremes in the Mediterranean basin: Interactions, impacts, and adaptation in the face of climate change. Regional Environmental Change, 25(3), 100. https://doi.org/10.1007/s10113-025-02432-7

Grant, K. M., Rohling, E. J., Ramsey, C. B., Cheng, H., Edwards, R. L., Florindo, F., Heslop, D., Marra, F., Roberts, A. P., Tamisiea, M. E., & Williams, F. (2014). Sea-level variability over five glacial cycles. Nature Communications, 5(1), 5076. https://doi.org/10.1038/ncomms6076

Gravina, B., Bachellerie, F., Caux, S., Discamps, E., Faivre, J.-P., Galland, A., Michel, A., Teyssandier, N., & Bordes, J.-G. (2018). No Reliable Evidence for a Neanderthal-Châtelperronian Association at La Roche-à-Pierrot, Saint-Césaire. Scientific Reports, 8(1), 15134. https://doi.org/10.1038/s41598-018-33084-9

Greenbaum, G., Getz, W. M., Rosenberg, N. A., Feldman, M. W., Hovers, E., & Kolodny, O. (2019). Disease transmission and introgression can explain the long-lasting contact zone of modern humans and Neanderthals. Nature Communications, 10(1), 5003. https://doi.org/10.1038/s41467-019-12862-7

Gregoire, L., Payne, A., & Valdes, P. (2012). Deglacial rapid sea level rises caused by ice-sheet saddle collapses. Nature, 487, 219–222. https://doi.org/10.1038/nature11257

Grimm, E. (1987). CONISS: A FORTRAN 77 program for stratigraphically constrained cluster analysis by the method of incremental sum of squares. Computers & Geosciences, 13, 13–35. https://doi.org/10.1016/0098-3004(87)90022-7

Grootes, P. M., Stuiver, M., White, J. W. C., Johnsen, S., & Jouzel, J. (1993). Comparison of oxygen isotope records from the GISP2 and GRIP Greenland ice cores. Nature, 366, 552–554. https://doi.org/10.1038/366552a0

Groucutt, H. S., Petraglia, M. D., Bailey, G., Scerri, E. M. L., Parton, A., Clark-Balzan, L., Jennings, R. P., Lewis, L., Blinkhorn, J., Drake, N. A., Breeze, P. S., Inglis, R. H., Devès, M. H., Meredith-Williams, M., Boivin, N., Thomas, M. G., & Scally, A. (2015). Rethinking the dispersal of Homo sapiens out of Africa. Evolutionary Anthropology: Issues, News, and Reviews, 24(4), 149–164. https://doi.org/10.1002/evan.21455

Guerzoni, S., Molinaroli, E., & Chester, R. (1997). Saharan dust inputs to the western Mediterranean Sea: Depositional patterns, geochemistry and sedimentological implications. Deep Sea Research Part II: Topical Studies in Oceanography, 44(3), 631–654. https://doi.org/10.1016/S0967-0645(96)00096-3

Guibert, P., Bechtel, F., Bourguignon, L., Brenet, M., Couchoud, I., Delagnes, A., Delpech, F., Detrain, L., Duttine, M., Folgado, M., Jaubert, J., Lahaye, C., Lenoir, M., Maureille, B., Texier, J.-P., Turq, A., Vieillevigne, E., & Villeneuve, G. (2008). Une base de données pour la chronologie du Paléolithique moyen dans le Sud-Ouest de la France. Bulletin de La Société Préhistorique Française, 47, 19–40.

Guillevic, M., Bazin, L., Landais, A., Stowasser, C., Masson-Delmotte, V., Blunier, T., Eynaud, F., Falourd, S., Michel, E., Minster, B., Popp, T., Prié, F., & Vinther, B. (2014). Evidence for a three-phase sequence during Heinrich Stadial 4 using a multiproxy approach based on Greenland ice core records. Climate of the Past, 10, 2115–2133. https://doi.org/10.5194/cp-10-2115-2014

Guion, A., Turquety, S., Polcher, J., Pennel, R., Bastin, S., & Arsouze, T. (2022). Droughts and heatwaves in the Western Mediterranean: Impact on vegetation and wildfires using the coupled WRF-ORCHIDEE regional model (RegIPSL). Climate Dynamics, 58(9), 2881–2903. https://doi.org/10.1007/s00382-021-05938-y

Guiot, J. (1987). Late Quaternary Climatic Change in France Estimated from Multivariate Pollen Time Series. Quaternary Research, 28(1), 100–118. https://doi.org/10.1016/0033-5894(87)90036-6

Guiot, J. (1990). Methodology of the last climatic cycle reconstruction in France from pollen data. Palaeogeography, Palaeoclimatology, Palaeoecology, 80(1), 49–69. https://doi.org/10.1016/0031-0182(90)90033-4

Guiot, J., De Beaulieu, J. L., Cheddadi, R., David, F., Ponel, P., & Reille, M. (1993). The climate in Western Europe during the last Glacial/Interglacial cycle derived from pollen and insect remains. Palaeogeography, Palaeoclimatology, Palaeoecology, 103(1–2), 73–93. https://doi.org/10.1016/0031-0182(93)90053-L

Guiot, J., Pons, A., De Beaulieu, J. L., & Reille, M. (1989). A 140,000-year continental climate reconstruction from two European pollen records. Nature, 338(6213), 309–313. https://doi.org/10.1038/338309a0

Hajdinjak, M., Fu, Q., Hübner, A., Petr, M., Mafessoni, F., Grote, S., Skoglund, P., Narasimham, V., Rougier, H., Crevecoeur, I., Semal, P., Soressi, M., Talamo, S., Hublin, J.-J., Gušić, I., Kućan, Ž., Rudan, P., Golovanova, L. V., Doronichev, V. B., … Kelso, J. (2018). Reconstructing the genetic history of late Neanderthals. Nature, 555(7698), 652–656. https://doi.org/10.1038/nature26151

Hajdinjak, M., Mafessoni, F., Skov, L., Vernot, B., Hübner, A., Fu, Q., Essel, E., Nagel, S., Nickel, B., Richter, J., Moldovan, O. T., Constantin, S., Endarova, E., Zahariev, N., Spasov, R., Welker, F., Smith, G. M., Sinet-Mathiot, V., Paskulin, L., … Pääbo, S. (2021). Initial Upper Palaeolithic humans in Europe had recent Neanderthal ancestry. Nature, 592(7853), Article 7853. https://doi.org/10.1038/s41586-021-03335-3

Hansen, J., Sato, M., Hearty, P., Ruedy, R., Kelley, M., Masson-Delmotte, V., Russell, G., Tselioudis, G., Cao, J., Rignot, E., Velicogna, I., Tormey, B., Donovan, B., Kandiano, E., von Schuckmann, K., Kharecha, P., Legrande, A. N., Bauer, M., & Lo, K.-W. (2016). Ice melt, sea level rise and superstorms: Evidence from paleoclimate data, climate modeling, and modern observations that 2 °C global warming could be dangerous. Atmospheric Chemistry and Physics, 16(6), 3761–3812. https://doi.org/10.5194/acp-16-3761-2016

Hardy, K. (2022). Chapter 9—The use of plants by Neanderthals as food, medicine, and raw materials. In F. Romagnoli, F. Rivals, & S. Benazzi (Eds.), Updating Neanderthals (pp. 145–161). Academic Press. https://doi.org/10.1016/B978-0-12-821428-2.00004-4

Harvati, K., Röding, C., Bosman, A. M., Karakostis, F. A., Grün, R., Stringer, C., Karkanas, P., Thompson, N. C., Koutoulidis, V., Moulopoulos, L. A., Gorgoulis, V. G., & Kouloukoussa, M. (2019). Apidima Cave fossils provide earliest evidence of Homo sapiens in Eurasia. Nature, 571(7766), 500–504. https://doi.org/10.1038/s41586-019-1376-z

Harvati, K., & Roksandic, M. (2016). The Human Fossil Record from Romania: Early Upper Paleolithic European Mandibles and Neanderthal Admixture. In K. Harvati & M. Roksandic (Eds.), Paleoanthropology of the Balkans and Anatolia: Human Evolution and its Context (pp. 51–68). Springer Netherlands. https://doi.org/10.1007/978-94-024-0874-4_4

Hautavoine, H., Arnaud, J., Balzeau, A., & Mounier, A. (2024). Quantifying hominin morphological diversity at the end of the middle Pleistocene: Implications for the origin of Homo sapiens. American Journal of Biological Anthropology, 184(2), e24915. https://doi.org/10.1002/ajpa.24915

Hawks, J. (2021). Comment on “A global environmental crisis 42,000 years ago”. Science, 374(6570), eabh1878. https://doi.org/10.1126/science.abh1878

Haws, J. A., Benedetti, M. M., Bicho, N. F., Cascalheira, J., Ellis, M. G., Carvalho, M. M., Friedl, L., Pereira, T., & Talamo, S. (2021). The early Aurignacian at Lapa do Picareiro really is that old: A comment on ‘The late persistence of the Middle Palaeolithic and Neandertals in Iberia: A review of the evidence for and against the “Ebro Frontier” model’. Quaternary Science Reviews, 274, 107261. https://doi.org/10.1016/j.quascirev.2021.107261

Haws, J. A., Benedetti, M. M., Funk, C. L., Bicho, N. F., Pereira, T., Marreiros, J., Daniels, J. M., Forman, S. L., Minckley, T. A., & Denniston, R. F. (2020). Late Pleistocene Landscape and Settlement Dynamics of Portuguese Estremadura. Journal of Field Archaeology, 45(4), 222–248. https://doi.org/10.1080/00934690.2020.1733780

Haws, J. A., Benedetti, M. M., Talamo, S., Bicho, N., Cascalheira, J., Ellis, M. G., Carvalho, M. M., Friedl, L., Pereira, T., & Zinsious, B. K. (2020). The early Aurignacian dispersal of modern humans into westernmost Eurasia. Proceedings of the National Academy of Sciences, 117(41), 25414–25422. https://doi.org/10.1073/pnas.2016062117

Head, M. J. (2019). Formal subdivision of the Quaternary System/Period: Present status and future directions. Quaternary International, 500, 32–51. https://doi.org/10.1016/j.quaint.2019.05.018

Head, M. J. (2023). Quaternary. In N. Wallenhorst & C. Wulf (Eds.), Handbook of the Anthropocene: Humans between Heritage and Future (pp. 373–378). Springer International Publishing. https://doi.org/10.1007/978-3-031-25910-4_57

Heaton, T. J., Köhler, P., Butzin, M., Bard, E., Reimer, R. W., Austin, W. E. N., Ramsey, C. B., Grootes, P. M., Hughen, K. A., Kromer, B., Reimer, P. J., Adkins, J., Burke, A., Cook, M. S., Olsen, J., & Skinner, L. C. (2020). Marine20—The Marine Radiocarbon Age Calibration Curve (0–55,000 cal BP). Radiocarbon, 62(4), 779–820. https://doi.org/10.1017/RDC.2020.68

Heinrich, H. (1988). Origin and Consequences of Cyclic Ice Rafting in the Northeast Atlantic Ocean During the Past 130,000 Years. Quaternary Research, 29, 142–152. https://doi.org/10.1016/0033-5894(88)90057-9

Held, F., Cheng, H., Edwards, R. L., Tüysüz, O., Koç, K., & Fleitmann, D. (2024). Dansgaard-Oeschger cycles of the penultimate and last glacial period recorded in stalagmites from Türkiye. Nature Communications, 15(1), 1183. https://doi.org/10.1038/s41467-024-45507-5

Hemming, S. R. (2004). Heinrich events: Massive late Pleistocene detritus layers of the North Atlantic and their global climate imprint. Reviews of Geophysics, 42(1). https://doi.org/10.1029/2003RG000128

Henrion, J., Hublin, J.-J., & Maureille, B. (2023). New Neanderthal remains from the Châtelperronian-attributed layer X of the Grotte du Renne (Arcy-sur-Cure, France). Journal of Human Evolution, 181, 103402. https://doi.org/10.1016/j.jhevol.2023.103402

Henry, L. G., McManus, J. F., Curry, W. B., Roberts, N. L., Piotrowski, A. M., & Keigwin, L. D. (2016). North Atlantic ocean circulation and abrupt climate change during the last glaciation. Science, 353(6298), 470–474. https://doi.org/10.1126/science.aaf5529

Hérisson, D., Brenet, M., Cliquet, D., Moncel, M.-H., Richter, J., Scott, B., Van Baelen, A., Di Modica, K., Loecker, D., Ashton, N., Bourguignon, L., Delagnes, A., Faivre, J.-P., Folgado-Lopez, M., Locht, J.-L., Pope, M., Raynal, J.-P., Roebroeks, W., Santagata, C., & Peer, P. (2016). The emergence of the Middle Palaeolithic in north-western Europe and its southern fringes. Quaternary International, 411. https://doi.org/10.1016/j.quaint.2016.02.049

Herrero-Alonso, D., Maíllo-Fernández, J.-M., Abellán-Beltrán, N., Moral, M., González-Molina, I., Solano-Megías, I., Luzón-Ruiz, S., Marín, J., Álvarez-Vena, A., Martín-Perea, D., Neira, A., Bernaldo de Quirós, F., & Tarriño, A. (2025). Neanderthal mobility over very long distances: The case of El Castillo cave (northern Spain) and the 'Vasconian' Mousterian. Journal of Human Evolution, 205, 103715. https://doi.org/10.1016/j.jhevol.2025.103715

Hersbach, H., Bell, B., Berrisford, P., Hirahara, S., Horányi, A., Muñoz-Sabater, J., Nicolas, J., Peubey, C., Radu, R., Schepers, D., Simmons, A., Soci, C., Abdalla, S., Abellan, X., Balsamo, G., Bechtold, P., Biavati, G., Bidlot, J., Bonavita, M., … Thépaut, J.-N. (2020). The ERA5 global reanalysis. Quarterly Journal of the Royal Meteorological Society, 146(730), 1999–2049. https://doi.org/10.1002/qj.3803

Hershkovitz, I., Weber, G. W., Quam, R., Duval, M., Grün, R., Kinsley, L., Ayalon, A., Bar-Matthews, M., Valladas, H., Mercier, N., Arsuaga, J. L., Martinón-Torres, M., Bermúdez de Castro, J. M., Fornai,

C., Martín-Francés, L., Sarig, R., May, H., Krenn, V. A., Slon, V., … Weinstein-Evron, M. (2018). The earliest modern humans outside Africa. Science, 359(6374), 456–459. https://doi.org/10.1126/science.aap8369

Herzschuh, U., Böhmer, T., Chevalier, M., Hébert, R., Dallmeyer, A., Li, C., Cao, X., Peyron, O., Nazarova, L., Novenko, E. Y., Park, J., Rudaya, N. A., Schlütz, F., Shumilovskikh, L. S., Tarasov, P. E., Wang, Y., Wen, R., Xu, Q., & Zheng, Z. (2023). Regional pollen-based Holocene temperature and precipitation patterns depart from the Northern Hemisphere mean trends. Climate of the Past, 19(7), 1481–1506. https://doi.org/10.5194/cp-19-1481-2023

Heusser, L., & Balsam, W. L. (1977). Pollen Distribution in the Northeast Pacific Ocean. Quaternary Research, 7(1), 45–62. https://doi.org/10.1016/0033-5894(77)90013-8

Hidalgo-Triana, N., Solakis, A., Casimiro-Soriguer, F., Choe, H., Navarro, T., Pérez-Latorre, A. V., & Thorne, J. H. (2023). The high climate vulnerability of western Mediterranean forests. Science of The Total Environment, 895, 164983. https://doi.org/10.1016/j.scitotenv.2023.164983

Higham, T., Brock, F., Peresani, M., Broglio, A., Wood, R., & Douka, K. (2009). Problems with radiocarbon dating the Middle to Upper Palaeolithic transition in Italy. Quaternary Science Reviews, 28(13–14), 1257–1267. https://doi.org/10.1016/j.quascirev.2008.12.018

Higham, T., Douka, K., Wood, R., Ramsey, C., Brock, F., Basell, L., Camps, M., Arrizabalaga, A., Preysler, J., Barroso, C., Bergman, C., Boitard, C., Boscato, P., Caparrós, M., Conard, N., Draily, C., Froment, A., Galvan, B., Gambassini, P., & Jacobi, R. (2014). The timing and spatiotemporal patterning of Neanderthal disappearance. Nature, 512. https://doi.org/10.1038/nature13621

Higham, T. F. G., Jacobi, R. M., & Ramsey, C. B. (2006). AMS Radiocarbon Dating of Ancient Bone Using Ultrafiltration. Radiocarbon, 48(2), 179–195. https://doi.org/10.1017/S0033822200066388

Higham, T., Frouin, M., Douka, K., Ronchitelli, A., Boscato, P., Benazzi, S., Crezzini, J., Spagnolo, V., McCarty, M., Marciani, G., Falcucci, A., Rossini, M., Arrighi, S., Dominici, C., Devièse, T., Schwenninger, J.-L., Martini, I., Moroni, A., & Boschin, F. (2024). Chronometric data and stratigraphic evidence support discontinuity between Neanderthals and early Homo sapiens in the Italian Peninsula. Nature Communications, 15(1), Article 1. https://doi.org/10.1038/s41467-024-51546-9

Higham, T., Jacobi, R., Basell, L., Ramsey, C. B., Chiotti, L., & Nespoulet, R. (2011). Precision dating of the Palaeolithic: A new radiocarbon chronology for the Abri Pataud (France), a key Aurignacian sequence. Journal of Human Evolution, 61(5), 549–563. https://doi.org/10.1016/j.jhevol.2011.06.005

Hijmans, R. J., Phillips, S., Leathwick, J., & Elith, J. (2024). dismo: Species Distribution Modeling (Version 1.3-16) [Computer software]. https://cran.r-project.org/web/packages/dismo/index.html

Hockett, B., & Haws, J. A. (2005). Nutritional ecology and the human demography of Neandertal extinction. Quaternary International, 137(1), 21–34. https://doi.org/10.1016/j.quaint.2004.11.017

Hodell, D. A., Channell, J. E. T., Curtis, J. H., Romero, O. E., & Röhl, U. (2008). Onset of "Hudson Strait" Heinrich events in the eastern North Atlantic at the end of the middle Pleistocene transition (~640 ka)? Paleoceanography, 23(4), 2008PA001591. https://doi.org/10.1029/2008PA001591

Hodell, D. A., Crowhurst, S. J., Lourens, L., Margari, V., Nicolson, J., Rolfe, J. E., Skinner, L. C., Thomas, N. C., Tzedakis, P. C., Mleneck-Vautravers, M. J., & Wolff, E. W. (2023). A 1.5-million-year record of orbital and millennial climate variability in the North Atlantic. Climate of the Past, 19(3), 607–636. https://doi.org/10.5194/cp-19-607-2023

Hodell, D. A., Nicholl, J. A., Bontognali, T. R. R., Danino, S., Dorador, J., Dowdeswell, J. A., Einsle, J., Kuhlmann, H., Martrat, B., Mleneck-Vautravers, M. J., Rodríguez-Tovar, F. J., & Röhl, U. (2017). Anatomy of Heinrich Layer 1 and its role in the last deglaciation. Paleoceanography, 32(3), 284–303. https://doi.org/10.1002/2016PA003028

Hodge, E., Richards, D., Smart, P., Andreo, B., Hoffmann, D., Mattey, D., & González-Ramón, A. (2008). Effective precipitation in southern Spain (~ 266 to 46 ka) based on a speleothem stable carbon isotope record. Quaternary Research, 69, 447–457. https://doi.org/10.1016/j.yqres.2008.02.013

Hoffecker, J. F. (2009). The spread of modern humans in Europe. Proceedings of the National Academy of Sciences, 106(38), 16040–16045. https://doi.org/10.1073/pnas.0903446106

Hoffmann, D. L., Angelucci, D. E., Villaverde, V., Zapata, J., & Zilhão, J. (2018). Symbolic use of marine shells and mineral pigments by Iberian Neandertals 115,000 years ago. Science Advances, 4(2), eaar5255. https://doi.org/10.1126/sciadv.aar5255

Holliday, T. W. (1997). Postcranial evidence of cold adaptation in European Neandertals. American Journal of Physical Anthropology, 104(2), 245–258. https://doi.org/10.1002/(SICI)1096-8644(199710)104:2<245::AID-AJPA10>3.0.CO;2-#

Horan, R. D., Bulte, E., & Shogren, J. F. (2005). How trade saved humanity from biological exclusion: An economic theory of Neanderthal extinction. Journal of Economic Behavior & Organization, 58(1), 1–29. https://doi.org/10.1016/j.jebo.2004.03.009

Hortolà, P., & Martínez-Navarro, B. (2013). The Quaternary megafaunal extinction and the fate of Neanderthals: An integrative working hypothesis. Quaternary International, 295, 69–72. https://doi.org/10.1016/j.quaint.2012.02.037

Houldcroft, C. J., & Underdown, S. J. (2016). Neanderthal genomics suggests a pleistocene time frame for the first epidemiologic transition. American Journal of Physical Anthropology, 160(3), 379–388. https://doi.org/10.1002/ajpa.22985

Huang, J., Wan, S., Li, A., & Li, T. (2019). Two-phase structure of tropical hydroclimate during Heinrich Stadial 1 and its global implications. Quaternary Science Reviews, 222, 105900. https://doi.org/10.1016/j.quascirev.2019.105900

Hublin, J. J. (2009). The origin of Neandertals. Proceedings of the National Academy of Sciences, 106(38), 16022–16027. https://doi.org/10.1073/pnas.0904119106

Hublin, J.-J. (2002). Climatic Changes, Paleogeography, and the Evolution of the Neandertals. In T. Akazawa, K. Aoki, & O. Bar-Yosef (Eds.), Neandertals and Modern Humans in Western Asia (pp. 295–310). Kluwer Academic Publishers. https://doi.org/10.1007/0-306-47153-1_18

Hublin, J.-J. (2015). The modern human colonization of western Eurasia: When and where? Quaternary Science Reviews, 118, 194–210. https://doi.org/10.1016/j.quascirev.2014.08.011

Hublin, J.-J., & Roebroeks, W. (2009). Ebb and flow or regional extinctions? On the character of Neandertal occupation of northern environments. Comptes Rendus Palevol, 8(5), 503–509. https://doi.org/10.1016/j.crpv.2009.04.001

Hublin, J.-J., Sirakov, N., Aldeias, V., Bailey, S., Bard, E., Delvigne, V., Endarova, E., Fagault, Y., Fewlass, H., Hajdinjak, M., Kromer, B., Krumov, I., Marreiros, J., Martisius, N. L., Paskulin, L., Sinet-Mathiot, V., Meyer, M., Pääbo, S., Popov, V., … Tsanova, T. (2020). Initial Upper Palaeolithic Homo sapiens from Bacho Kiro Cave, Bulgaria. Nature, 581(7808), 299–302. https://doi.org/10.1038/s41586-020-2259-z

Hublin, J.-J., Talamo, S., Julien, M., David, F., Bodu, P., Vandermeersch, B., & Richards, M. (2012). Radiocarbon dates from the Grotte du Renne and Saint-Cesaire support a Neandertal origin for the Chatelperronian. Proceedings of the National Academy of Sciences of the United States of America, 109. https://doi.org/10.1073/pnas.1212924109

Huguet, R., Rodríguez-Álvarez, X. P., Martinón-Torres, M., Vallverdú, J., López-García, J. M., Lozano, M., Terradillos-Bernal, M., Expósito, I., Ollé, A., Santos, E., Saladié, P., de Lombera-Hermida, A., Moreno-Ribas, E., Martín-Francés, L., Allué, E., Núñez-Lahuerta, C., van der Made, J., Galán, J., Blain, H.-A., … Bermúdez de Castro, J. M. (2025). The earliest human face of Western Europe. Nature, 640(8059), 707–713. https://doi.org/10.1038/s41586-025-08681-0

Hurrell, J. W. (1995). Decadal Trends in the North Atlantic Oscillation: Regional Temperatures and Precipitation. Science, 269(5224), 676–679. https://doi.org/10.1126/science.269.5224.676

Iasi, L. N. M., Chintalapati, M., Skov, L., Mesa, A. B., Hajdinjak, M., Peter, B. M., & Moorjani, P. (2024). Neanderthal ancestry through time: Insights from genomes of ancient and present-day humans. Science, 386(6727), eadq3010. https://doi.org/10.1126/science.adq3010

Irvalı, N., Ninnemann, U., Kleiven, K. H., Galaasen, E., Morley, A., & Rosenthal, Y. (2016). Evidence for regional cooling, frontal advances, and East Greenland Ice Sheet changes during the demise of the last interglacial. Quaternary Science Reviews, 150. https://doi.org/10.1016/j.quascirev.2016.08.029

Israelevich, P., Ganor, E., Alpert, P., Kishcha, P., & Stupp, A. (2012). Predominant transport paths of Saharan dust over the Mediterranean Sea to Europe. Journal of Geophysical Research: Atmospheres, 117(D2). https://doi.org/10.1029/2011JD016482

Jaubert, J., Maureille, B., & Peresani, M. (2022). Spiritual and symbolic activities of Neanderthals. In Updating Neanderthals: Understanding Behavioural Complexity in the Late Middle Palaeolithic (pp. 261–274). https://doi.org/10.1016/B978-0-12-821428-2.00005-6

Jaubert, J., Verheyden, S., Genty, D., Soulier, M., Cheng, H., Blamart, D., Burlet, C., Camus, H., Delaby, S., Deldicque, D., Edwards, R. L., Ferrier, C., Lacrampe-Cuyaubère, F., Lévêque, F., Maksud, F., Mora, P., Muth, X., Régnier, É., Rouzaud, J.-N., & Santos, F. (2016). Early Neanderthal constructions deep in Bruniquel Cave in southwestern France. Nature, 534(7605), 111–114. https://doi.org/10.1038/nature18291

Jennings, R. P., Giles Pacheco, F., Barton, R. N. E., Collcutt, S. N., Gale, R., Gleed-Owen, C. P., Gutiérrez López, J. M., Higham, T. F. G., Parker, A., & Price, C. (2009). New dates and palaeoenvironmental evidence for the Middle to Upper Palaeolithic occupation of Higueral de Valleja Cave, southern Spain. Quaternary Science Reviews, 28(9–10), 830–839. https://doi.org/10.1016/j.quascirev.2008.11.014

Jiménez-Amat, P., & Zahn, R. (2015). Offset timing of climate oscillations during the last two glacial-interglacial transitions connected with large-scale freshwater perturbation. Paleoceanography, 30(6), 768–788. https://doi.org/10.1002/2014PA002710

Jiménez-Espejo, F. J., Martínez-Ruiz, F., Finlayson, C., Paytan, A., Sakamoto, T., Ortega-Huertas, M., Finlayson, G., Iijima, K., Gallego-Torres, D., & Fa, D. (2007). Climate forcing and Neanderthal extinction in Southern Iberia: Insights from a multiproxy marine record. Quaternary Science Reviews, 26, 836–852. https://doi.org/10.1016/j.quascirev.2006.12.013

Jiménez-Moreno, G., Anderson, R. S., Ramos-Román, M. J., Camuera, J., Mesa-Fernández, J. M., García-Alix, A., Jiménez-Espejo, F. J., Carrión, J. S., & López-Avilés, A. (2020). The Holocene Cedrus pollen record from Sierra Nevada (S Spain), a proxy for climate change in N Africa. Quaternary Science Reviews, 242, 106468. https://doi.org/10.1016/j.quascirev.2020.106468

Joannin, S., Bassinot, F., Nebout, N. C., Peyron, O., & Beaudouin, C. (2011). Vegetation response to obliquity and precession forcing during the Mid-Pleistocene Transition in Western Mediterranean region (ODP site 976). Quaternary Science Reviews, 30(3–4), 280–297. https://doi.org/10.1016/j.quascirev.2010.11.009

Joannin, S., Brugiapaglia, E., de Beaulieu, J.-L., Bernardo, L., Magny, M., Peyron, O., Goring, S., & Vannière, B. (2012). Pollen-based reconstruction of Holocene vegetation and climate in southern Italy: The case of Lago Trifoglietti. Climate of the Past, 8(6), 1973–1996. https://doi.org/10.5194/cp-8-1973-2012

Johnsen, S. J., Clausen, H. B., Dansgaard, W., Fuhrer, K., Gundestrup, N., Hammer, C. U., Iversen, P., Jouzel, J., Stauffer, B., & Steffensen, J. P. (1992). Irregular glacial interstadials recorded in a new Greenland record. Nature, 359, 311–313.

Jones, E. L. (2022). What is a refugium? Questions for the Middle–Upper Palaeolithic transition in peninsular southern Europe. Journal of Quaternary Science, 37(2), 136–141. https://doi.org/10.1002/jqs.3274

Jones, E., Pang, K.-L., Abdel-Wahab, M., Scholz, B., Hyde, K., Boekhout, T., Rateb, M., Henderson, L., Sakayaroj, J., Suetrong, S., Dayarathne, M., Kumar, V., Raghukumar, S., Sridhar, K., Bahkali, A., Gleason, F., & Norphanphoun, C. (2019). An online resource for marine fungi. Fungal Diversity, 96, 347–433. https://doi.org/10.1007/s13225-019-00426-5

Jones, J. R., Richards, M. P., Straus, L. G., Reade, H., Altuna, J., Mariezkurrena, K., & Marín-Arroyo, A. B. (2018). Changing environments during the Middle-Upper Palaeolithic transition in the eastern Cantabrian Region (Spain): Direct evidence from stable isotope studies on ungulate bones. Scientific Reports, 8(1), 14842. https://doi.org/10.1038/s41598-018-32493-0

Jouzel, J., Masson-Delmotte, V., Cattani, O., Dreyfus, G., Falourd, S., Hoffmann, G., Minster, B., Nouet, J., Barnola, J. M., Chappellaz, J., Fischer, H., Gallet, J. C., Johnsen, S., Leuenberger, M., Loulergue, L., Luethi, D., Oerter, H., Parrenin, F., Raisbeck, G., … Wolff, E. W. (2007). Orbital and millennial Antarctic climate variability over the past 800,000 years. Science (New York, N.Y.), 317(5839), 793–796. https://doi.org/10.1126/science.1141038

Juggins, S. (2024). rioja: Analysis of Quaternary Science Data (Version 1.0-7) [Computer software]. https://cran.r-project.org/web/packages/rioja/index.html

Kageyama, M., Nebout, N. C., Sepulchre, P., Peyron, O., Krinner, G., Ramstein, G., & Cazet, J.-P. (2005). The Last Glacial Maximum and Heinrich Event 1 in terms of climate and vegetation around the

Alboran Sea: A preliminary model-data comparison. Comptes Rendus Geoscience, 337(10), 983–992. https://doi.org/10.1016/j.crte.2005.04.012

Kageyama, M., Roche, D. M., & Combourieu-Nebout, N. (2013). Variabilité climatique rapide: Description et mécanismes. In Paléoclimatologie—Enquête sur les climats anciens—Tome II (pp. 293–323). EDP Sciences. https://hal.science/hal-02897860

Kallel, N., Duplessy, J.-C., Labeyrie, L., Fontugne, M., Paterne, M., & Montacer, M. (2000). Mediterranean pluvial periods and sapropel formation over the last 200 000 years. Palaeogeography, Palaeoclimatology, Palaeoecology, 157(1), 45–58. https://doi.org/10.1016/S0031-0182(99)00149-2

Kandel, A. W., Sommer, C., Kanaeva, Z., Bolus, M., Bruch, A. A., Groth, C., Haidle, M. N., Hertler, C., Heß, J., Malina, M., Märker, M., Hochschild, V., Mosbrugger, V., Schrenk, F., & Conard, N. J. (2023). The ROCEEH Out of Africa Database (ROAD): A large-scale research database serves as an indispensable tool for human evolutionary studies. PLOS ONE, 18(8), e0289513. https://doi.org/10.1371/journal.pone.0289513

Karavanić, I., Hellstrom, J., Rabeder, G., Vukosavljević, N., Banda, M., & Smith, F. (2021). New U-Th dates from Vindija, Velika pećina (Kličevica) and Mujina pećina and their implications for chronology of the Middle Paleolithic in Croatia. Collegium Antropologicum, 45, 1–10. https://doi.org/10.5671/ca.45.1.1

Karavanić, I., Vukosavljević, N., Janković, I., Ahern, J. C. M., & Smith, F. H. (2018). Paleolithic hominins and settlement in Croatia from MIS 6 to MIS 3: Research history and current interpretations. Quaternary International, 494, 152–166. https://doi.org/10.1016/j.quaint.2017.09.034

Kassambara, A., & Mundt, F. (2020). factoextra: Extract and Visualize the Results of Multivariate Data Analyses (Version 1.0.7) [Computer software]. https://cran.r-project.org/web/packages/factoextra/index.html

Kaushal, N., Lechleitner, F. A., Wilhelm, M., Azennoud, K., Bühler, J. C., Braun, K., Ait Brahim, Y., Baker, A., Burstyn, Y., Comas-Bru, L., Fohlmeister, J., Goldsmith, Y., Harrison, S. P., Hatvani, I. G., Rehfeld, K., Ritzau, M., Skiba, V., Stoll, H. M., Szűcs, J. G., … SISAL Working Group members. (2024). SISALv3: A global speleothem stable isotope and trace element database. Earth System Science Data, 16(4), 1933–1963. https://doi.org/10.5194/essd-16-1933-2024

Kaushal, N., Pérez-Mejías, C., & Heather, S. (2025). Perspective on ice age terminations from absolute chronologies provided by global speleothem records. Climate of the Past, 21, 1633–1660. https://doi.org/10.5194/cp-21-1633-2025

Kehl, M., Álvarez-Alonso, D., Andrés-Herrero, M. de, Díez-Herrero, A., Klasen, N., Rethemeyer, J., & Weniger, G.-C. (2018). The rock shelter Abrigo del Molino (Segovia, Spain) and the timing of the late Middle Paleolithic in Central Iberia. Quaternary Research, 90(1), 180–200. https://doi.org/10.1017/qua.2018.13

Kehl, M., Burow, C., Cantalejo, P., Domínguez-Bella, S., Durán, J. J., Henselowsky, F., Klasen, N., Linstädter, J., Medianero, J., Pastoors, A., Ramos, J., Reicherter, K., Schmidt, C., & Weniger, G.-C. (2016). Site formation and chronology of the new Paleolithic site Sima de Las Palomas de Teba, southern Spain. Quaternary Research, 85(2), 313–331. https://doi.org/10.1016/j.yqres.2016.01.007

Kelly, M., Edwards, R., Cheng, H., Yuan, D., Cai, Y., Zhang, M., Lin, Y., & An, Z. (2006). High resolution characterization of the Asian Monsoon between 146,000 and 99,000 years B.P. from Dongge Cave, China and global correlation of events surrounding Termination II. Palaeogeography, Palaeoclimatology, Palaeoecology, 236, 20–38. https://doi.org/10.1016/j.palaeo.2005.11.042

Key, A. J. M., Jarić, I., & Roberts, D. L. (2021). Modelling the end of the Acheulean at global and continental levels suggests widespread persistence into the Middle Palaeolithic. Humanities and Social Sciences Communications, 8(1), 55. https://doi.org/10.1057/s41599-021-00735-8

King, W. (1864). The reputed fossil man of the Neanderthal. The Quarterly Journal of Science, 1, 88--97.

Klein, K., Weniger, G.-C., Ludwig, P., Stepanek, C., Zhang, X., Wegener, C., & Shao, Y. (2023). Assessing climatic impact on transition from Neanderthal to anatomically modern human population on Iberian Peninsula: A macroscopic perspective. Science Bulletin, 68(11), 1176–1186. https://doi.org/10.1016/j.scib.2023.04.025

Koltai, G., Spötl, C., Shen, C.-C., Wu, C.-C., Rao, Z., Palcsu, L., Kele, S., Surányi, G., & Bárány-Kevei, I. (2017). A penultimate glacial climate record from southern Hungary. Journal of Quaternary Science, 32(7), 946–956. https://doi.org/10.1002/jqs.2968

Koumouzelis, M., Ginter, B., Kozlowski, J. K., Pawlikowski, M., Bar-Yosef, O., Albert, R. M., Litynska-Zajac, M., Stworzewicz, E., Wojtal, P., Lipecki, G., Tomek, T., Bochenski, Z. M., & Pazdur, A. (2001). The Early Upper Palaeolithic in Greece: The Excavations in Klisoura Cave. Journal of Archaeological Science, 28(5), 515–539. https://doi.org/10.1006/jasc.2000.0599

Koutsodendris, A., Dakos, V., Fletcher, W. J., Knipping, M., Kotthoff, U., Milner, A. M., Müller, U. C., Kaboth-Bahr, S., Kern, O. A., Kolb, L., Vakhrameeva, P., Wulf, S., Christanis, K., Schmiedl, G., & Pross, J. (2023). Atmospheric CO2 forcing on Mediterranean biomes during the past 500 kyrs. Nature Communications, 14(1), 1664. https://doi.org/10.1038/s41467-023-37388-x

Kuhn, S., & Stiner, M. (2006). What's a Mother To Do? The Division of Labor among Neandertals and Modern Humans in Eurasia. Current Anthropology - CURR ANTHROPOL, 47, 953–981. https://doi.org/10.1086/507197

Lari, M., Di Vincenzo, F., Borsato, A., Ghirotto, S., Micheli, M., Balsamo, C., Collina, C., De Bellis, G., Frisia, S., Giacobini, G., Gigli, E., Hellstrom, J. C., Lannino, A., Modi, A., Pietrelli, A., Pilli, E., Profico, A., Ramirez, O., Rizzi, E., … Manzi, G. (2015). The Neanderthal in the karst: First dating, morphometric, and paleogenetic data on the fossil skeleton from Altamura (Italy). Journal of Human Evolution, 82, 88–94. https://doi.org/10.1016/j.jhevol.2015.02.007

Laskar, J., Robutel, P., Joutel, F., Gastineau, M., Correia, A. C. M., & Levrard, B. (2004). A long-term numerical solution for the insolation quantities of the Earth. Astronomy & Astrophysics, 428(1), Article 1. https://doi.org/10.1051/0004-6361:20041335

Lebreton, V., Messager, E., Marquer, L., & Renault-Miskovsky, J. (2010). A neotaphonomic experiment in pollen oxidation and its implications for archaeopalynology. Review of Palaeobotany and Palynology, 162(1), 29–38. https://doi.org/10.1016/j.revpalbo.2010.05.002

Leierer, L., Jambrina-Enríquez, M., Herrera-Herrera, A. V., Connolly, R., Hernández, C. M., Galván, B., & Mallol, C. (2019). Insights into the timing, intensity and natural setting of Neanderthal occupation from the geoarchaeological study of combustion structures: A micromorphological

and biomarker investigation of El Salt, unit Xb, Alcoy, Spain. PLOS ONE, 14(4), e0214955. https://doi.org/10.1371/journal.pone.0214955

Lewis, S., Ashton, N., & Jacobi, R. (2011). 9 - Testing Human Presence During the Last Interglacial (MIS 5e): A Review of the British Evidence. In N. Ashton, S. G. Lewis, & C. Stringer (Eds.), Developments in Quaternary Sciences (Vol. 14, pp. 125–164). Elsevier. https://doi.org/10.1016/B978-0-444-53597-9.00009-1

Li, D., DeConto, R. M., Pollard, D., & Hu, Y. (2024). Competing climate feedbacks of ice sheet freshwater discharge in a warming world. Nature Communications, 15(1), 5178. https://doi.org/10.1038/s41467-024-49604-3

Li, T.-Y., Shen, C.-C., Huang, L.-J., Jiang, X.-Y., Yang, X.-L., Mii, H.-S., Lee, S.-Y., & Lo, L. (2014). Stalagmite-inferred variability of the Asian summer monsoon during the penultimate glacial–interglacial period. Climate of the Past, 10(3), 1211–1219. https://doi.org/10.5194/cp-10-1211-2014

Liang, Y.-J., Chen, S.-T., Wang, Y.-J., Zhao, K., Yang, S.-H., Wang, Z.-J., Huang, Y.-Z., Cheng, H., & Edwards, R. L. (2022). Asian monsoon intensity coupled to Antarctic climate during Dansgaard–Oeschger 8 and Heinrich 4 glacial intervals. Communications Earth & Environment, 3(1), 1–9. https://doi.org/10.1038/s43247-022-00633-0

Lionello, P., Malanotte-Rizzoli, P., Boscolo, R., Alpert, P., Artale, V., Li, L., Luterbacher, J., May, W., Trigo, R., Tsimplis, M., Ulbrich, U., & Xoplaki, E. (2006). The Mediterranean climate: An overview of the main characteristics and issues. In P. Lionello, P. Malanotte-Rizzoli, & R. Boscolo (Eds.), Developments in Earth and Environmental Sciences (Vol. 4, pp. 1–26). Elsevier. https://doi.org/10.1016/S1571-9197(06)80003-0

Lionello, P., & Scarascia, L. (2018). The relation between climate change in the Mediterranean region and global warming. Regional Environmental Change, 18(5), 1481–1493. https://doi.org/10.1007/s10113-018-1290-1

Liquete, C., Arnau, P., Canals, M., & Colas, S. (2005). Mediterranean river systems of Andalusia, southern Spain, and associated deltas: A source to sink approach. Marine Geology, 222–223, 471–495. https://doi.org/10.1016/j.margeo.2005.06.033

Lisiecki, L. E., Jones, A. M., Rand, D., Lee, T., & Lawrence, C. E. (2022). Comparing age model techniques for the last glacial cycle: A case study of ten Iberian Margin sediment cores. Quaternary Science Reviews, 287, 107559. https://doi.org/10.1016/j.quascirev.2022.107559

Lisiecki, L. E., & Stern, J. V. (2016). Regional and global benthic δ18O stacks for the last glacial cycle. Paleoceanography, 31(10), 1368–1394. https://doi.org/10.1002/2016PA003002

Lisiecki, L., & Raymo, M. (2005). Pliocene-Pleistocene stack of 57 globally distributed benthic 18O records. Paleoceanography, 20. https://doi.org/10.1029/2004PA001071

Litt, T., & Gibbard, P. (2008). Definition of a Global Stratotype Section and Point (GSSP) for the base of the Upper (Late) Pleistocene Subseries (Quaternary System/Period). Episodes Journal of International Geoscience, 31(2), 260–263. https://doi.org/10.18814/epiiugs/2008/v31i2/015

Litt, T., Pickarski, N., Heumann, G., Stockhecke, M., & Tzedakis, C. (2014). A 600,000 year long continental pollen record from Lake Van, eastern Anatolia (Turkey). Quaternary Science Reviews, 104. https://doi.org/10.1016/j.quascirev.2014.03.017

Liu, J., Fang, N., Wang, F., Yang, F., & Ding, X. (2018). Features of ice-rafted debris (IRD) at IODP site U1312 and their palaeoenvironmental implications during the last 2.6 Myr. Palaeogeography, Palaeoclimatology, Palaeoecology, 511, 364–378. https://doi.org/10.1016/j.palaeo.2018.09.002

Liu, M., Prentice, I. C., & Harrison, S. P. (2024). A global analysis of reconstructed land climate changes during Dansgaard-Oeschger events. Climate of the Past Discussions, 1–26. https://doi.org/10.5194/cp-2024-12

Lombera-Hermida, A. de, Rodríguez-Álvarez, X.-P., Iglesias, A. A., Rodríguez, M. D., Iván REY-RODRÍGUEZ, undefined, Tejedor, I. V., Pérez-Alberti, A., Cunha, P. P., García, H. B., Moreira, X. A., Salgueiro, C. L., Castro, T. M., & Valcarce, R. F. (2021). Between two worlds: Cova Eirós and the Middle-Upper Palaeolithic transition in NW Iberia. Comptes Rendus Palevol, 42. https://doi.org/10.5852/cr-palevol2021v20a42

López-García, J. M., Blain, H.-A., Bennàsar, M., & Fernández-García, M. (2014). Environmental and climatic context of Neanderthal occupation in southwestern Europe during MIS3 inferred from the small-vertebrate assemblages. Quaternary International, 326–327, 319–328. https://doi.org/10.1016/j.quaint.2013.09.010

López-González, N., Alonso, B., Juan, C., Ercilla, G., Bozzano, G., Cacho, I., Casas, D., Palomino, D., Vázquez, J.-T., Estrada, F., Bárcenas, P., d'Acremont, E., Gorini, C., & Moumni, B. E. (2019). 133,000 Years of Sedimentary Record in a Contourite Drift in the Western Alboran Sea: Sediment Sources and Paleocurrent Reconstruction. Geosciences, 9(8), 345. https://doi.org/10.3390/geosciences9080345

López-Sáez, J. A., Lopez, P., & Sánchez, M. (2007). Paleovegetación del Cuaternario reciente: Estudio arqueopalinológico. Cueva Bajondillo (Torremolinos). Secuencia Cronocultural y Paleoambiental Del Cuaternario Reciente En La Bahía de Málaga, 139–156.

Lourantou, A., Chappellaz, J., Barnola, J.-M., Masson-Delmotte, V., & Raynaud, D. (2010). Changes in atmospheric CO2 and its carbon isotopic ratio during the penultimate deglaciation. Quaternary Science Reviews, 29(17), 1983–1992. https://doi.org/10.1016/j.quascirev.2010.05.002

Luterbacher, J., García-Herrera, R., Akcer-On, S., Allan, R., & Alvarez-Castro, M.-C. (2012). A Review of 2000 Years of Paleoclimatic Evidence in the Mediterranean. In G. Benito, J. Booth, U. Büntgen, N. Cagatay, D. Colombaroli, B. Davis, J. Esper, T. Felis, D. Fleitmann, D. Frank, D. Gallego, E. Garcia-Bustamante, R. Glaser, F. J. Gonzalez-Rouco, H. Goosse, T. Kiefer, M. G. Macklin, S. W. Manning, P. Montagna, … E. Zorita, The Climate of the Mediterranean Region (pp. 87–185). Elsevier. https://doi.org/10.1016/b978-0-12-416042-2.00002-1

MacDonald, K., Martinón-Torres, M., Dennell, R. W., & Bermúdez de Castro, J. M. (2012). Discontinuity in the record for hominin occupation in south-western Europe: Implications for occupation of the middle latitudes of Europe. Quaternary International, 271, 84–97. https://doi.org/10.1016/j.quaint.2011.10.009

Macklin, M. G., Fuller, I. C., Lewin, J., Maas, G. S., Passmore, D. G., Rose, J., Woodward, J. C., Black, S., Hamlin, R. H. B., & Rowan, J. S. (2002). Correlation of fluvial sequences in the Mediterranean basin over the last 200 ka and their relationship to climate change. Quaternary Science Reviews, 21(14), 1633–1641. https://doi.org/10.1016/S0277-3791(01)00147-0

Mafessoni, F., Grote, S., de Filippo, C., Slon, V., Kolobova, K. A., Viola, B., Markin, S. V., Chintalapati, M., Peyrégne, S., Skov, L., Skoglund, P., Krivoshapkin, A. I., Derevianko, A. P., Meyer, M., Kelso, J., Peter, B., Prüfer, K., & Pääbo, S. (2020). A high-coverage Neandertal genome from Chagyrskaya Cave. Proceedings of the National Academy of Sciences, 117(26), 15132–15136. https://doi.org/10.1073/pnas.2004944117

Mafessoni, F., & Prüfer, K. (2017). Better support for a small effective population size of Neandertals and a long shared history of Neandertals and Denisovans. Proceedings of the National Academy of Sciences of the United States of America, 114(48), E10256–E10257. https://doi.org/10.1073/pnas.1716918114

Magri, D. (1999). Late Quaternary vegetation history at Lagaccione near Lago di Bolsena (central Italy). Review of Palaeobotany and Palynology, 106(3), 171–208. https://doi.org/10.1016/S0034-6667(99)00006-8

Magri, D., Di Rita, F., Aranbarri, J., Fletcher, W., & González-Sampériz, P. (2017). Quaternary disappearance of tree taxa from Southern Europe: Timing and trends. Quaternary Science Reviews, 163, 23–55. https://doi.org/10.1016/j.quascirev.2017.02.014

Magri, D., & Parra, I. (2002). Late Quaternary western Mediterranean pollen records and African winds. Earth and Planetary Science Letters, 200(3–4), 401–408. https://doi.org/10.1016/S0012-821X(02)00619-2

Magri, D., & Tzedakis, P. C. (2000). Orbital signatures and long-term vegetation patterns in the Mediterranean. Quaternary International, 73–74, 69–78. https://doi.org/10.1016/S1040-6182(00)00065-3

Malinsky-Buller, A. (2016). Lost and found: Technological trajectories within Lower/Middle Paleolithic transition in Western Europe, North of the Pyrenees. Quaternary International, 409, 104–148. https://doi.org/10.1016/j.quaint.2015.09.079

Mallol, C., Hernández, C., Mercier, N., Falguères, C., Carrancho, Á., Cabanes, D., Vidal-Matutano, P., Connolly, R., Pérez, L., Mayor, A., Ben Arous, E., & Galván, B. (2019). Fire and brief human occupations in Iberia during MIS 4: Evidence from Abric del Pastor (Alcoy, Spain). Scientific Reports, 9(1), 18281. https://doi.org/10.1038/s41598-019-54305-9

Manzano, S., Carrión, J. S., López-Merino, L., González-Sampériz, P., Munuera, M., Fernández, S., Martín-Lerma, I., & Gómez Ferreras, M. del C. (2017). Mountain strongholds for woody angiosperms during the Late Pleistocene in SE Iberia. CATENA, 149, 701–712. https://doi.org/10.1016/j.catena.2016.03.008

Marcott, S. A., Clark, P. U., Padman, L., Klinkhammer, G. P., Springer, S. R., Liu, Z., Otto-Bliesner, B. L., Carlson, A. E., Ungerer, A., Padman, J., He, F., Cheng, J., & Schmittner, A. (2011). Ice-shelf collapse from subsurface warming as a trigger for Heinrich events. Proceedings of the National Academy of Sciences, 108(33), 13415–13419. https://doi.org/10.1073/pnas.1104772108

Marean, C. W. (2005). From the tropics to the colder climates: Contrasting faunal exploitation adaptations of modern humans and Neanderthals. In F. d'Errico & L. Backwell (Eds.), From Tools to Symbols: From Early Hominids to Modern Humans (pp. 333–371). Wits University Press. https://www.cambridge.org/core/books/from-tools-to-symbols/from-the-tropics-to-the-colder-climates-contrasting-faunal-exploitation-adaptations-of-modern-humans-and-neanderthals/3486247DB127C77F8D51BC995F30AC31

Margari, V., Skinner, L. C., Menviel, L., Capron, E., Rhodes, R. H., Mleneck-Vautravers, M. J., Ezat, M. M., Martrat, B., Grimalt, J. O., Hodell, D. A., & Tzedakis, P. C. (2020). Fast and slow components of interstadial warming in the North Atlantic during the last glacial. Communications Earth & Environment, 1(1), 1–9. https://doi.org/10.1038/s43247-020-0006-x

Margari, V., Skinner, L. C., Tzedakis, P. C., Ganopolski, A., Vautravers, M., & Shackleton, N. J. (2010). The nature of millennial-scale climate variability during the past two glacial periods. Nature Geoscience, 3(2), Article 2. https://doi.org/10.1038/ngeo740

Margari, V., Skinner, L., Hodell, D., Martrat, B., Toucanne, S., Gibbard, P., Lunkka, J., & Tzedakis, C. (2014). Land-ocean changes on orbital and millennial time scales and the penultimate glaciation. Geology. https://doi.org/10.1130/G35070.1

Marín, J., Rodríguez-Hidalgo, A., Vallverdú, J., Gómez De Soler, B., Rivals, F., Rabuñal, J. R., Pineda, A., Chacón, M. G., Carbonell, E., & Saladié, P. (2019). Neanderthal logistic mobility during MIS3: Zooarchaeological perspective of Abric Romaní level P (Spain). Quaternary Science Reviews, 225, 106033. https://doi.org/10.1016/j.quascirev.2019.106033

Marín-Arroyo, A. B., Rios-Garaizar, J., Straus, L. G., Jones, J. R., Rasilla, M. de la, Morales, M. R. G., Richards, M., Altuna, J., Mariezkurrena, K., & Ocio, D. (2018). Chronological reassessment of the Middle to Upper Paleolithic transition and Early Upper Paleolithic cultures in Cantabrian Spain. PLOS ONE, 13(4), e0194708. https://doi.org/10.1371/journal.pone.0194708

Marín-Arroyo, A. B., Terlato, G., Vidal-Cordasco, M., & Peresani, M. (2023). Subsistence of early anatomically modern humans in Europe as evidenced in the Protoaurignacian occupations of Fumane Cave, Italy. Scientific Reports, 13(1), 3788. https://doi.org/10.1038/s41598-023-30059-3

Marín-Arroyo, A., & Mihailović, B. (2017). The Chronometric Dating and Subsistence of Late Neanderthals and Early Anatomically Modern Humans in the Central Balkans: Insights from Šalitrena Pećina (Mionica, Serbia). Journal of Anthropological Research, 73, 000–000. https://doi.org/10.1086/693054

Marino, G., Rohling, E. J., Rodríguez-Sanz, L., Grant, K. M., Heslop, D., Roberts, A. P., Stanford, J. D., & Yu, J. (2015). Bipolar seesaw control on last interglacial sea level. Nature, 522(7555), Article 7555. https://doi.org/10.1038/nature14499

Maroto, J., Montes, R., & Rasines, P. (2021). Dataciones numéricas del yacimiento, resultados y contextualización. In La Cueva de Covalejos (Velo de Piélagps, Cantabria). Ocupaciones neandertales y sapiens en la cuenca baja del río Pas. Actuaciones arqueológicas 1997–1999 y 2002 (Montes Barquín R, Sanguino González J (Eds.), Vol. 2, pp. 382–401). Museo de Prehistoria y Arqueología de Cantabria.

Marquet, J.-C., Lorblanchet, M., Egels, Y., Esquerre-Pourtère, J., & Hesse, M.-S. (2014). Symbolic character productions in the mousterian site of La Roche-Cotard in Langeais (Indre-et-Loire, France) and their geological context. Paléo, 25, 169–194. https://doi.org/10.4000/paleo.3013

Marsaglia, K. M., Latter, K. K., & Cline, V. (1999). Sand provenance in the Alboran and Tyrrhenian Basins. In Proceedings of the Ocean Drilling Program. Ocean Drilling Program. https://doi.org/10.2973/odp.proc.sr.161.205.1999

Martínez Navarro, B., Turq, A., Ballester, J. A., & Oms, O. (1997). Fuente Nueva-3 (Orce, Granada, Spain) and the first human occupation of Europe. Journal of Human Evolution, 33(5), 611–620. https://doi.org/10.1006/jhev.1997.0158

Martínez-Navarro, B. (2020). El sapiens asesino y el ocaso de los neandertales. Almuzara. 240 p.

Martín-Perea, D. M., Maíllo-Fernández, J.-M., Marín, J., Arroyo, X., & Asiaín, R. (2023). A step back to move forward: A geological re-evaluation of the El Castillo Cave Middle Palaeolithic lithostratigraphic units (Cantabria, northern Iberia). Journal of Quaternary Science, 38(2), 221–234. https://doi.org/10.1002/jqs.3473

Martín-Puertas, C., Brauer, A., Wulf, S., Ott, F., Lauterbach, S., & Dulski, P. (2014). Chronology and annual proxy data of Lago Grande di Monticchio sediments [Dataset publication series]. Supplement to: Martín-Puertas, C et al. (2014): Annual Proxy Data from Lago Grande Di Monticchio (Southern Italy) between 76 and 112 Ka: New Chronological Constraints and Insights on Abrupt Climatic Oscillations. Climate of the Past, 10(6), 2099-2114, Https://Doi.Org/10.5194/Cp-10-2099-2014; https://doi.org/10.1594/PANGAEA.837248

Martrat, B., Grimalt, J. O., Lopez-Martinez, C., Cacho, I., Sierro, F. J., Flores, J. A., Zahn, R., Canals, M., Curtis, J. H., & Hodell, D. A. (2004). Abrupt Temperature Changes in the Western Mediterranean over the Past 250,000 Years. Science, 306(5702), 1762–1765. https://doi.org/10.1126/science.1101706

Martrat, B., Grimalt, J. O., Shackleton, N. J., de Abreu, L., Hutterli, M. A., & Stocker, T. F. (2007). Four Climate Cycles of Recurring Deep and Surface Water Destabilizations on the Iberian Margin. Science, 317(5837), 502–507. https://doi.org/10.1126/science.1139994

Martrat, B., Jimenez-Amat, P., Zahn, R., & Grimalt, J. O. (2014). Similarities and dissimilarities between the last two deglaciations and interglaciations in the North Atlantic region. Quaternary Science Reviews, 99, 122–134. https://doi.org/10.1016/j.quascirev.2014.06.016

Maslin, M. A., & Brierley, C. M. (2015). The role of orbital forcing in the Early Middle Pleistocene Transition. Quaternary International, 389, 47–55. https://doi.org/10.1016/j.quaint.2015.01.047

Masson-Delmotte, V., Landais, A., Combourieu-Nebout, N., von Grafenstein, U., Jouzel, J., Caillon, N., Chappellaz, J., Dahl-Jensen, D., Johnsen, S. J., & Stenni, B. (2005). Rapid climate variability during warm and cold periods in polar regions and Europe. Comptes Rendus Geoscience, 337(10), 935–946. https://doi.org/10.1016/j.crte.2005.04.001

Masson-Delmotte, V., Stenni, B., Pol, K., Braconnot, P., Cattani, O., Falourd, S., Kageyama, M., Jouzel, J., Landais, A., Minster, B., Barnola, J. M., Chappellaz, J., Krinner, G., Johnsen, S., Röthlisberger, R., Hansen, J., Mikolajewicz, U., & Otto-Bliesner, B. (2010). EPICA Dome C record of glacial and interglacial intensities. Quaternary Science Reviews, 29(1), 113–128. https://doi.org/10.1016/j.quascirev.2009.09.030

Mathias, C., Bourguignon, L., Brenet, M., Grégoire, S., & Moncel, M.-H. (2020). Between new and inherited technical behaviours: A case study from the Early Middle Palaeolithic of Southern France. Archaeological and Anthropological Sciences, 12(7), 146. https://doi.org/10.1007/s12520-020-01114-1

Mathias, C., & Moncel, M. (2020). Transition et temporalité. La transition entre Paléolithique inférieur et moyen à l'épreuve du temps. Les Nouvelles de l'archéologie, 161, 19–26. https://doi.org/10.4000/nda.10366

Matthews, A., Affek, H. P., Ayalon, A., Vonhof, H. B., & Bar-Matthews, M. (2021). Eastern Mediterranean climate change deduced from the Soreq Cave fluid inclusion stable isotopes and carbonate clumped isotopes record of the last 160 ka. Quaternary Science Reviews, 272, 107223. https://doi.org/10.1016/j.quascirev.2021.107223

Mauri, A., Davis, B. A. S., Collins, P. M., & Kaplan, J. O. (2015). The climate of Europe during the Holocene: A gridded pollen-based reconstruction and its multi-proxy evaluation. Quaternary Science Reviews, 112, 109–127. https://doi.org/10.1016/j.quascirev.2015.01.013

McCarron, A. P., Bigg, G. R., Brooks, H., Leng, M. J., Marshall, J. D., Ponomareva, V., Portnyagin, M., Reimer, P. J., & Rogerson, M. (2021). Northwest Pacific ice-rafted debris at 38°N reveals episodic ice-sheet change in late Quaternary Northeast Siberia. Earth and Planetary Science Letters, 553, 116650. https://doi.org/10.1016/j.epsl.2020.116650

McManus, J. F., Bond, G. C., Broecker, W. S., Johnsen, S., Labeyrie, L., & Higgins, S. (1994). High-resolution climate records from the North Atlantic during the last interglacial. Nature, 371(6495), Article 6495. https://doi.org/10.1038/371326a0

McManus, J. F., Oppo, D. W., & Cullen, J. L. (1999). A 0.5-Million-Year Record of Millennial-Scale Climate Variability in the North Atlantic. Science, 283(5404), 971–975. https://doi.org/10.1126/science.283.5404.971

Médail, F. (2017). The specific vulnerability of plant biodiversity and vegetation on Mediterranean islands in the face of global change. Regional Environmental Change, 17(6), 1775–1790. https://doi.org/10.1007/s10113-017-1123-7

Médail, F., Baumel, A., Diadema, K., & Migliore, J. (2012). La biodiversité végétale méditerranéenne, organisation et évolution [Société Française d'Ecologie]. Regards et débats sur la biodiversité (38). https://sfecologie.org/regard/r38-frederic-medail-et-al/

Médail, F., & Diadema, K. (2009). Glacial refugia influence plant diversity patterns in the Mediterranean Basin. Journal of Biogeography, 36(7), 1333–1345. https://doi.org/10.1111/j.1365-2699.2008.02051.x

Médail, F., & Quézel, P. (2003). Conséquences écologiques possibles des changements c1imatiques sur la flore et la végétation du bassin méditerranéen. Bocconea, 16(1), 397–422.

MedECC. (2020). Climate and Environmental Change in the Mediterranean Basin – Current Situation and Risks for the Future. First Mediterranean Assessment Report (Version 1). MedECC Reports. MedECC Secretariat, Marseille, France. https://doi.org/10.5281/ZENODO.7224821

Melchionna, M. (2018). Small and isolated: Ecology and fragmentation of Neanderthals. In S. Bartolini Lucenti, Fossilia—Reports in Palaeontology (pp. 53–56). Saverio Bartolini Lucenti. https://doi.org/10.32774/FosRepPal.20.1810.075356

Melchionna, M., Di Febbraro, M., Carotenuto, F., Rook, L., Mondanaro, A., Castiglione, S., Serio, C., Vero, V. A., Tesone, G., Piccolo, M., Diniz-Filho, J. A. F., & Raia, P. (2018). Fragmentation of Neanderthals' pre-extinction distribution by climate change. Palaeogeography,

Palaeoclimatology, Palaeoecology, 496, 146–154. https://doi.org/10.1016/j.palaeo.2018.01.031

Mellars, P. (2004). Neanderthals and the modern human colonization of Europe. Nature, 432(7016), Article 7016. https://doi.org/10.1038/nature03103

Mellars, P. (2005). The impossible coincidence. A single-species model for the origins of modern human behavior in Europe. Evolutionary Anthropology: Issues, News, and Reviews, 14(1), 12–27. https://doi.org/10.1002/evan.20037

Mellars, P. (2006). Archeology and the dispersal of modern humans in Europe: Deconstructing the "Aurignacian". Evolutionary Anthropology: Issues, News, and Reviews, 15(5), 167–182. https://doi.org/10.1002/evan.20103

Mellars, P., & French, J. C. (2011). Tenfold population increase in Western Europe at the Neandertal-to-modern human transition. Science (New York, N.Y.), 333(6042), 623–627. https://doi.org/10.1126/science.1206930

Menviel, L., Capron, E., Govin, A., Dutton, A., Tarasov, L., Abe-Ouchi, A., Drysdale, R. N., Gibbard, P. L., Gregoire, L., He, F., Ivanovic, R. F., Kageyama, M., Kawamura, K., Landais, A., Otto-Bliesner, B. L., Oyabu, I., Tzedakis, P. C., Wolff, E., & Zhang, X. (2019). The penultimate deglaciation: Protocol for Paleoclimate Modelling Intercomparison Project (PMIP) phase 4 transient numerical simulations between 140 and 127 ka, version 1.0. Geoscientific Model Development, 12(8), 3649–3685. https://doi.org/10.5194/gmd-12-3649-2019

Menviel, L., Skinner, L., Tarasov, L., & Tzedakis, C. (2020). An ice-climate oscillatory framework for Dansgaard-Oeschger cycles. Nature Reviews Earth & Environment, 1. https://doi.org/10.1038/s43017-020-00106-y

Meyer, M., Arsuaga, J.-L., De Filippo, C., Nagel, S., Aximu-Petri, A., Nickel, B., Martínez, I., Gracia, A., De Castro, J. M. B., Carbonell, E., Viola, B., Kelso, J., Prüfer, K., & Pääbo, S. (2016). Nuclear DNA sequences from the Middle Pleistocene Sima de los Huesos hominins. Nature, 531(7595), 504–507. https://doi.org/10.1038/nature17405

Michel, V., Delanghe-Sabatier, D., Bard, E., & Barroso Ruiz, C. (2013). U-series, ESR and 14C studies of the fossil remains from the Mousterian levels of Zafarraya Cave (Spain): A revised chronology of Neandertal presence. Quaternary Geochronology, 15, 20–33. https://doi.org/10.1016/j.quageo.2012.12.008

Michel, V., Shen, G., Shen, C.-C., Duval, M., Woodhead, J., Chou, Y.-M., Hu, H.-M., Wu, C.-C., Kan, Y.-C., Yang, H., Yu, T.-L., Gallet, S., & Valensi, P. (2022). Datations radioisotopiques (U-Th, U-Pb) et paléodosimétriques (ESR) des plus anciens sites préhistoriques des Alpes-Maritimes: La grotte du Vallonnet, le site de plein air de Terra Amata et la grotte du Lazaret. In Bulletin du Musée d'Anthropologie préhistorique de Monaco (Vol. 61, pp. 65–80).

Milanković, M. (1941). Canon of insolation and the ice-age problem (Kanon der Erdbestrahlung und seine Anwendung auf das Eiszeitenproblem), Belgrade, 1941.

Milner, A., Collier, R., Roucoux, K., Müller, U., Pross, J., Kalaitzidis, S., Christanis, K., & Tzedakis, C. (2012). Enhanced seasonality of precipitation in the Mediterranean during the early part of the Last Interglacial. Geology, 40, 919–922. https://doi.org/10.1130/G33204.1

Milner, A., Müller, U., Roucoux, K., Collier, R., Pross, J., Kalaitzidis, S., Christanis, K., & Tzedakis, C. (2013). Environmental variability during the Last Interglacial: A new high-resolution pollen record from Tenaghi Philippon, Greece. Journal of Quaternary Science, 28, 113–117. https://doi.org/10.1002/jqs.2617

Milner, A., Roucoux, K. H., Collier, R. E. L., Müller, U. C., Pross, J., & Tzedakis, P. C. (2016). Vegetation responses to abrupt climatic changes during the Last Interglacial Complex (Marine Isotope Stage 5) at Tenaghi Philippon, NE Greece. Quaternary Science Reviews, 154, 169–181. https://doi.org/10.1016/j.quascirev.2016.10.016

Miras, Y. (2021). Tracking plant, fungal and algal diversity through a data mining approach: Towards an improved analysis of holocene lake Aydat (Puy- de-Dôme, France) dynamics and ecological legacies. 85.

Miras, Y., Ejarque, A., Orengo, H., Riera, S., Martínez, J. M., & Alexandre, P. (2010). Prehistoric impact on landscape and vegetation at high altitudes: An integrated palaeoecological and archaeological approach in the eastern Pyrenees (Perafita valley, Andorra). Plant Biosystems, 144. https://doi.org/10.1080/11263504.2010.491980

Miras, Y., Mariani, M., Couderc, F., Lavrieux, M., & Ledger, P. M. (2023). Addressing the Complexity of the Paleoenvironmental Impact of Prehistoric Settlement and Protohistoric Urbanism in the Auvergne Mountains (Massif Central, France).

Moal-Darrigade, P., Ducassou, E., Bout-Roumazeilles, V., Hanquiez, V., Perello, M.-C., Mulder, T., & Giraudeau, J. (2022). Source-to-sink pathways of clay minerals in the cadiz contourite system over the last 25 kyrs: The segregational role of mediterranean outflow water. Marine Geology, 443, 106697. https://doi.org/10.1016/j.margeo.2021.106697

Mokeddem, Z., McManus, J. F., & Oppo, D. W. (2014). Oceanographic dynamics and the end of the last interglacial in the subpolar North Atlantic. Proceedings of the National Academy of Sciences, 111(31), 11263–11268. https://doi.org/10.1073/pnas.1322103111

Moncel, M. hélène, & Schreve, D. (2016). The Acheulean in Europe: Origins, evolution and dispersal. Quaternary International, 411, 1–8. https://doi.org/10.1016/j.quaint.2016.08.039

Moncel, M., Vaissié, E., Marin, J., Fernandes, P., Abrunhosa, A., Hardy, B., Richard, M., Torres, C., & Baena, J. (2025). Early Middle Palaeolithic Occupations Dated to MIS 7 at the Abri du Maras (Ardèche, Southeast France). Journal of Paleolithic Archaeology.

Moncel, M.-H., Ashton, N., Arzarello, M., Fontana, F., Lamotte, A., Scott, B., Muttillo, B., Berruti, G., Nenzioni, G., Tuffreau, A., & Peretto, C. (2020). Early Levallois core technology between Marine Isotope Stage 12 and 9 in Western Europe. Journal of Human Evolution, 139, 102735. https://doi.org/10.1016/j.jhevol.2019.102735

Moncel, M.-H., Chacón, M. G., Vettese, D., Courty, M.-A., Daujeard, C., Eixea, A., Fernandes, P., Allué, E., Hardy, B., Rivals, F., Béarez, P., Gallotti, R., & Puaud, S. (2021). Late Neanderthal short-term and specialized occupations at the Abri du Maras (South-East France, level 4.1, MIS 3). Archaeological and Anthropological Sciences, 13(3), 45. https://doi.org/10.1007/s12520-021-01285-5

Moncel, M.-H., García-Medrano, P., Despriée, J., Arnaud, J., Voinchet, P., & Bahain, J.-J. (2021). Tracking behavioral persistence and innovations during the Middle Pleistocene in Western Europe. Shift

in occupations between 700 and 450 ka at la Noira site (Centre, France). Journal of Human Evolution, 156, 103009. https://doi.org/10.1016/j.jhevol.2021.103009

Moncel, M.-H., Moigne, A.-M., & Combier, J. (2012). Towards the Middle Palaeolithic in Western Europe: The case of Orgnac 3 (southeastern France). Journal of Human Evolution, 63(5), 653–666. https://doi.org/10.1016/j.jhevol.2012.08.001

Moncel, M.-H., & Voisin, J.-L. (2006). Les « industries de transition » et le mode de spéciation des groupes néandertaliens en Europe entre 40 et 30 ka. Comptes Rendus Palevol, 5(1), 183–192. https://doi.org/10.1016/j.crpv.2005.09.010

Montes Barquín, J. (2021). 21. Interpretación paleoambiental y crono-cultural del registro estratigrafico. In La Cueva de Covalejos (Velo de Piélagps, Cantabria). Ocupaciones neandertales y sapiens en la cuenca baja del río Pas. Actuaciones arqueológicas 1997–1999 y 2002 (Montes Barquín R, Sanguino González J (Eds.), Vol. 2, pp. 417–443). Museo de Prehistoria y Arqueología de Cantabria.

Mora, C. C. (2022). Aplicación de métodos computacionales al estudio de las dinámicas demográficas del Pleistoceno superior y las redes sociales del Holoceno inicial de la Península Ibérica. Thèse de l'Universidad de Alicante, 319 p.

Mora, R., Martínez-Moreno, J., Roy Sunyer, M., Benito Calvo, A., Polo-Díaz, A., & Samper Carro, S. (2018). Contextual, technological and chronometric data from Cova Gran: Their contribution to discussion of the Middle-to-Upper Paleolithic transition in northeastern Iberia. Quaternary International, 474, 30–43. https://doi.org/10.1016/j.quaint.2016.05.017

Morales, J. I., Cebrià, A., Burguet-Coca, A., Fernández-Marchena, J. L., García-Argudo, G., Rodríguez-Hidalgo, A., Soto, M., Talamo, S., Tejero, J.-M., Vallverdú, J., & Fullola, J. M. (2019). The Middle-to-Upper Paleolithic transition occupations from Cova Foradada (Calafell, NE Iberia). PLOS ONE, 14(5), e0215832. https://doi.org/10.1371/journal.pone.0215832

Moreno, A., Cacho, I., Canals, M., Prins, M. A., Sánchez-Goñi, M.-F., Grimalt, J. O., & Weltje, G. J. (2002). Saharan Dust Transport and High-Latitude Glacial Climatic Variability: The Alboran Sea Record. Quaternary Research, 58(3), 318–328. https://doi.org/10.1006/qres.2002.2383

Moreno, D., Duval, M., Rubio-Jara, S., Panera, J., Bahain, J.-J., Shao, Q., Pérez-González, A., & Falguères, C. (2019). ESR dating of Middle Pleistocene archaeo-paleontological sites from the Manzanares and Jarama river valleys (Madrid basin, Spain). Quaternary International, 520, 23–38. https://doi.org/10.1016/j.quaint.2017.09.003

Moreno, D., Ortega, A. I., Falguères, C., Shao, Q., Tombret, O., Gómez-Olivencia, A., Aranburu, A., Trompier, F., Bermúdez de Castro, J. M., Carbonell, E., & Arsuaga, J. L. (2022). ESR/U-series chronology of the Neanderthal occupation layers at Galería de las Estatuas (Sierra de Atapuerca, Spain). Quaternary Geochronology, 72, 101342. https://doi.org/10.1016/j.quageo.2022.101342

Moseley, G. E., Spötl, C., Cheng, H., Boch, R., Min, A., & Edwards, R. L. (2015). Termination-II interstadial/stadial climate change recorded in two stalagmites from the north European Alps. Quaternary Science Reviews, 127, 229–239. https://doi.org/10.1016/j.quascirev.2015.07.012

Moulin, C., Lambert, C. E., Dulac, F., & Dayan, U. (1997). Control of atmospheric export of dust from North Africa by the North Atlantic Oscillation. Nature, 387(6634), 691–694. https://doi.org/10.1038/42679

Mudie, P. (2011). Pollen distribution in recent marine sediments, eastern Canada. Canadian Journal of Earth Sciences, 19, 729–747. https://doi.org/10.1139/e82-062

Müller, U. C., Pross, J., Tzedakis, P. C., Gamble, C., Kotthoff, U., Schmiedl, G., Wulf, S., & Christanis, K. (2011). The role of climate in the spread of modern humans into Europe. Quaternary Science Reviews, 30(3), 273–279. https://doi.org/10.1016/j.quascirev.2010.11.016

Murat, A. (Ed.). (1999). Chapitre 41: Pliocene–pleistocene occurrence of sapropels in the western mediterranean sea and their relation to eastern mediterranean sapropels. In Proceedings of the Ocean Drilling Program, 161 Scientific Results (Vol. 161). Ocean Drilling Program. https://doi.org/10.2973/odp.proc.sr.161.1999

Nabais, M., Dupont, C., & Zilhão, J. (2023). The exploitation of crabs by Last Interglacial Iberian Neanderthals: The evidence from Gruta da Figueira Brava (Portugal). Frontiers in Environmental Archaeology, 2, 1097815. https://doi.org/10.3389/fearc.2023.1097815

Naughton, F., Sanchez Goñi, M. F., Desprat, S., Turon, J.-L., Duprat, J., Malaizé, B., Joli, C., Cortijo, E., Drago, T., & Freitas, M. C. (2007). Present-day and past (last 25000 years) marine pollen signal off western Iberia. Marine Micropaleontology, 62(2), 91–114. https://doi.org/10.1016/j.marmicro.2006.07.006

Naughton, F., Sánchez Goñi, M. F., Kageyama, M., Bard, E., Duprat, J., Cortijo, E., Desprat, S., Malaizé, B., Joly, C., Rostek, F., & Turon, J.-L. (2009). Wet to dry climatic trend in north-western Iberia within Heinrich events. Earth and Planetary Science Letters, 284(3), 329–342. https://doi.org/10.1016/j.epsl.2009.05.001

Naughton, F., Sanchez Goñi, M. F., Rodrigues, T., Salgueiro, E., Costas, S., Desprat, S., Duprat, J., Michel, E., Rossignol, L., Zaragosi, S., Voelker, A. H. L., & Abrantes, F. (2016). Climate variability across the last deglaciation in NW Iberia and its margin. Quaternary International, 414, 9–22. https://doi.org/10.1016/j.quaint.2015.08.073

Navarro, A., Palma, J., Merelo, I., Simón-Vallejo, M., Albert, R., Bergadà, M., Bao, J., López-Sáez, J. A., Lopez, P., de la Rubia de Gracia, J., Rodríguez, I., Abad, M., Navarro, B., Cáceres Puro, L., Cantos, F., Valcero, J., Montero, M., Rodríguez, V., Moreno, P., & Vera Peláez, J. L. (2007). Cueva Bajondillo (Torremolinos). Secuencia cronocultural y paleoambiental del Cuaternario reciente de la Bahía de Málaga.

Navazo, M., Jordá Pardo, J., Burow, C., Kehl, M., Pastoors, A., Weniger, G.-C., & Wood, R. (2020). Last Neanderthal occupations at Central Iberia: The lithic industry of Jarama VI rock shelter (Valdesotos, Guadalajara, Spain). Archaeological and Anthropological Sciences, 12. https://doi.org/10.1007/s12520-019-00974-6

Negri, A., Amorosi, A., Antonioli, F., Bertini, A., Florindo, F., Lurcock, P. C., Marabini, S., Mastronuzzi, G., Regattieri, E., Rossi, V., Scarponi, D., Taviani, M., Zanchetta, G., & Vai, G. B. (2015). A potential global boundary stratotype section and point (GSSP) for the Tarentian Stage, Upper Pleistocene, from the Taranto area (Italy): Results and future perspectives. Quaternary International, 383, 145–157. https://doi.org/10.1016/j.quaint.2014.08.057

Nehme, C., Kluge, T., Verheyden, S., Nader, F., Charalambidou, I., Weissbach, T., Gucel, S., Cheng, H., Edwards, R. L., Satterfield, L., Eiche, E., & Claeys, P. (2020). Speleothem record from Pentadactylos cave (Cyprus): New insights into climatic variations during MIS 6 and MIS 5 in

the Eastern Mediterranean. Quaternary Science Reviews, 250, 106663. https://doi.org/10.1016/j.quascirev.2020.106663

Nehme, C., Verheyden, S., Breitenbach, S. F. M., Gillikin, D. P., Verheyden, A., Cheng, H., Edwards, R. L., Hellstrom, J., Noble, S. R., Farrant, A. R., Sahy, D., Goovaerts, T., Salem, G., & Claeys, P. (2018). Climate dynamics during the penultimate glacial period recorded in a speleothem from Kanaan Cave, Lebanon (central Levant). Quaternary Research, 90(1), 10–25. https://doi.org/10.1017/qua.2018.18

Ntinou, M. (2021). Vegetation change in southeastern Greece during the Late Pleistocene. The wood charcoal record from Klissoura Cave 1 (Peloponnese, Greece). Quaternary International, 593–594, 104–117. https://doi.org/10.1016/j.quaint.2020.11.002

Nutz, A., Kwiecien, O., Buylaert, J. P., Guihou, A., Khabouchi, I., Deschamps, P., Breitenbach, S. F. M., Poirier, P., Dietrich, P., Kabiri, L., Essafraoui, B., & Bodin, S. (2024). A 60–50 ka African Humid Period modulated by stadial Heinrich events HE6 and HE5a in northwestern Africa. Palaeogeography, Palaeoclimatology, Palaeoecology, 635, 111952. https://doi.org/10.1016/j.palaeo.2023.111952

Obrochta, S. P., Crowley, T. J., Channell, J. E. T., Hodell, D. A., Baker, P. A., Seki, A., & Yokoyama, Y. (2014). Climate variability and ice-sheet dynamics during the last three glaciations. Earth and Planetary Science Letters, 406, 198–212. https://doi.org/10.1016/j.epsl.2014.09.004

Ochando, J., Amorós, G., Carrión, J. S., Fernández, S., Munuera, M., Camuera, J., Jiménez-Moreno, G., González-Sampériz, P., Burjachs, F., Marín-Arroyo, A. B., Roksandic, M., & Finlayson, C. (2022). Iberian Neanderthals in forests and savannahs. Journal of Quaternary Science, 37(2), 335–362. https://doi.org/10.1002/jqs.3339

Ochando, J., Carrión, J. S., Blasco, R., Fernández, S., Amorós, G., Munuera, M., Sañudo, P., & Fernández Peris, J. (2019). Silvicolous Neanderthals in the far West: The mid-Pleistocene palaeoecological sequence of Bolomor Cave (Valencia, Spain). Quaternary Science Reviews, 217, 247–267. https://doi.org/10.1016/j.quascirev.2019.03.015

Ochando, J., Carrión, J. S., Blasco, R., Rivals, F., Rufà, A., Amorós, G., Munuera, M., Fernández, S., & Rosell, J. (2020a). The Late Quaternary pollen sequence of Toll Cave, a palaeontological site with evidence of human activities in northeastern Spain. Quaternary International, 554, 1–14. https://doi.org/10.1016/j.quaint.2020.06.048

Ochando, J., Carrión, J. S., Blasco, R., Rivals, F., Rufà, A., Demuro, M., Arnold, L. J., Amorós, G., Munuera, M., Fernández, S., & Rosell, J. (2020b). Neanderthals in a highly diverse, mediterranean-Eurosiberian forest ecotone: The pleistocene pollen record of Teixoneres Cave, northeastern Spain. Quaternary Science Reviews, 241, 106429. https://doi.org/10.1016/j.quascirev.2020.106429

Ochando, J., Jiménez-Espejo, F. J., Giles-Guzmán, F., Neto de Carvalho, C., Carrión, J. S., Muñiz, F., Rubiales, J. M., Cura, P., Belo, J., Finlayson, S., Martrat, B., van Drooge, B. L., Jiménez-Moreno, G., García-Alix, A., Lozano Rodríguez, J. A., Albert, R. M., Ohkouchi, N., Ogawa, N., Suga, H., … Finlayson, C. (2024). A Neanderthal's specialised burning structure compatible with tar obtention. Quaternary Science Reviews, 346, 109025. https://doi.org/10.1016/j.quascirev.2024.109025

Ochando, J., López-Sáez, J. A., Pérez-Díaz, S., Ramos-Fernández, J., Munuera, M., Fernández, S., Galacho-Jiménez, F. B., Luelmo-Lautenschlaeger, R., & Carrión, J. S. (2020c). A new pollen sequence from southern Iberia suggesting coastal Pleistocene phytodiversity hotspot. Review of Palaeobotany and Palynology, 281, 104281. https://doi.org/10.1016/j.revpalbo.2020.104281

Ocobock, C., Lacy, S., & Niclou, A. (2021). Between a rock and a cold place: Neanderthal biocultural cold adaptations. Evolutionary Anthropology, 30(4), 262–279. https://doi.org/10.1002/evan.21894

Okuda, M., Yasuda, Y., & Setoguchi, T. (2001). Middle to Late Pleistocene vegetation history and climatic changes at Lake Kopais, Southeast Greece. Boreas, 30(1), 73–82. https://doi.org/10.1111/j.1502-3885.2001.tb00990.x

Oldfield, F. (1959). The pollen morphology of some of the West European Ericales-Preliminary descriptions and a tentative key to their identification. Pollen et Spores, 1, 19–48.

Ollé, A., Saladié, P., Vallverdu, J., Cáceres, I., van der Made, J., Expósito Barea, I., Casas, F., López-Polín, L., Lorenzo, C., Bennàsar, M., Salazar-García, D., & Olària, C. (2014). La Cova de Dalt del Tossal de la Font (pp. 413–417).

Oppo, D. W., Keigwin, L. D., McManus, J. F., & Cullen, J. L. (2001). Persistent suborbital climate variability in marine isotope stage 5 and termination II. Paleoceanography, 16(3), 280–292. https://doi.org/10.1029/2000PA000527

Oppo, D. W., McManus, J. F., & Cullen, J. L. (2006). Evolution and demise of the Last Interglacial warmth in the subpolar North Atlantic. Quaternary Science Reviews, 25(23), 3268–3277. https://doi.org/10.1016/j.quascirev.2006.07.006

Ortiz, J. E., Moreno, L., Torres, T., Vegas, J., Ruiz-Zapata, B., García-Cortés, Á., Galán, L., & Pérez-González, A. (2013). A 220 ka palaeoenvironmental reconstruction of the Fuentillejo maar lake record (Central Spain) using biomarker analysis. Organic Geochemistry, 55, 85–97. https://doi.org/10.1016/j.orggeochem.2012.11.012

Ovsepyan, E. A., & Murdmaa, I. O. (2017). Response of the bering sea to Heinrich Event 11. Lithology and Mineral Resources, 52(6), 442–446. https://doi.org/10.1134/S0024490217060062

Oxilia, G., Bortolini, E., Marciani, G., Menghi Sartorio, J. C., Vazzana, A., Bettuzzi, M., Panetta, D., Arrighi, S., Badino, F., Figus, C., Lugli, F., Romandini, M., Silvestrini, S., Sorrentino, R., Moroni, A., Donadio, C., Morigi, M. P., Slon, V., Piperno, M., … Benazzi, S. (2022). Direct evidence that late Neanderthal occupation precedes a technological shift in southwestern Italy. American Journal of Biological Anthropology, 179(1), 18–30. https://doi.org/10.1002/ajpa.24593

Pagano, A. S., Márquez, S., & Laitman, J. T. (2019). Reconstructing the Neanderthal Eustachian Tube: New Insights on Disease Susceptibility, Fitness Cost, and Extinction. The Anatomical Record, 302(12), 2109–2125. https://doi.org/10.1002/ar.24248

Paillard, D. (2010). Climate and the orbital parameters of the Earth. Comptes Rendus Geoscience, 342(4), 273–285. https://doi.org/10.1016/j.crte.2009.12.006

Panera, J., Pérez-González, A., Rubio-Jara, S., & Sesé, C. (2005). El yacimiento paleolítico de HAT en el Valle del Jarama: Una aportación del Cuaternario de la cuenca de Madrid al debate sobre el

inicio del Paleolítico Medio. In Geoarqueología y Patrimonio en la Península Ibérica y El Entorno Mediterráneo (pp. 251–260).

Panera, J., Rubio-Jara, S., Yravedra, J., Blain, H.-A., Sesé, C., & Pérez-González, A. (2014). Manzanares Valley (Madrid, Spain): A good country for Proboscideans and Neanderthals. Quaternary International, 326–327, 329–343. https://doi.org/10.1016/j.quaint.2013.09.009

Panera, J., Torres, T., Pérez-González, A., Ortiz, J. E., Rubio-Jara, S., & Val, D. U. del. (2011). Geocronología de la Terraza Compleja de Arganda en el valle del río Jarama (Madrid, España). Estudios Geológicos, 67(2), Article 2. https://doi.org/10.3989/egeol.40550.204

Paquin, S., Albouy, B., Kageyama, M., Vrac, M., & Burke, A. (2024). Anatomically modern human dispersals into Europe during MIS 3: Climate stability, paleogeography and habitat suitability. Quaternary Science Reviews, 330, 108596. https://doi.org/10.1016/j.quascirev.2024.108596

Park, C.-E., Jeong, S.-J., Joshi, M., Osborn, T. J., Ho, C.-H., Piao, S., Chen, D., Liu, J., Yang, H., Park, H., Kim, B.-M., & Feng, S. (2018). Keeping global warming within 1.5 °C constrains emergence of aridification. Nature Climate Change, 8(1), 70–74. https://doi.org/10.1038/s41558-017-0034-4

Pastor, F., Paredes-Fortuny, L., & Khodayar, S. (2024). Mediterranean marine heatwaves intensify in the presence of concurrent atmospheric heatwaves. Communications Earth & Environment, 5(1), 797. https://doi.org/10.1038/s43247-024-01982-8

Pawlak, J., Błaszczyk, M., Hercman, H., & Matoušková, Š. (2021). Palaeoenvironmental conditions during MIS 6/MIS 5 transition recorded in speleothems from the Tatra Mountains. Boreas, 50(1), 224–241. https://doi.org/10.1111/bor.12472

Pearce, E., Stringer, C., & Dunbar, R. (2013). New insights into differences in brain organization between Neanderthals and anatomically modern humans. Proceedings. Biological Sciences / The Royal Society, 280, 20130168. https://doi.org/10.1098/rspb.2013.0168

Pederzani, S., Britton, K., Aldeias, V., Bourgon, N., Fewlass, H., Lauer, T., McPherron, S. P., Rezek, Z., Sirakov, N., Smith, G. M., Spasov, R., Tran, N.-H., Tsanova, T., & Hublin, J.-J. (2021). Subarctic climate for the earliest Homo sapiens in Europe. Science Advances, 7(39), eabi4642. https://doi.org/10.1126/sciadv.abi4642

Penaud, A., Eynaud, F., Sánchez-Goñi, M., Malaizé, B., Turon, J. L., & Rossignol, L. (2011). Contrasting sea-surface responses between the western Mediterranean Sea and eastern subtropical latitudes of the North Atlantic during abrupt climatic events of MIS 3. Marine Micropaleontology, 80(1), 1–17. https://doi.org/10.1016/j.marmicro.2011.03.002

Penaud, A., Eynaud, F., Turon, J. L., Zaragosi, S., Malaizé, B., Toucanne, S., & Bourillet, J. F. (2009). What forced the collapse of European ice sheets during the last two glacial periods (150 ka B.P. and 18 ka cal B.P.)? Palynological evidence. Palaeogeography, Palaeoclimatology, Palaeoecology, 281(1), 66–78. https://doi.org/10.1016/j.palaeo.2009.07.012

Penaud, A., Eynaud, F., Voelker, A. H. L., & Turon, J.-L. (2016). Palaeohydrological changes over the last 50 ky in the central Gulf of Cadiz: Complex forcing mechanisms mixing multi-scale processes. Biogeosciences, 13(18), 5357–5377. https://doi.org/10.5194/bg-13-5357-2016

Pereira, T., Cunha, P. P., Martins, A. A., Nora, D., Paixão, E., Figueiredo, O., Raposo, L., Henriques, F., Caninas, J., Moura, D., & Bridgland, D. R. (2019). Geoarchaeology of the Cobrinhos site (Vila

Velha de Ródão, Portugal)—A record of the earliest Mousterian in western Iberia. Journal of Archaeological Science: Reports, 24, 640–654. https://doi.org/10.1016/j.jasrep.2018.11.026

Peresani, M. (2022). Inspecting human evolution from a cave. Late Neanderthals and early sapiens at Grotta di Fumane: Present state and outlook. Journal of Anthropological Sciences, 100, 71–107. https://doi.org/doi. 10.4436/jass10016

Peresani, M., Bertola, S., Delpiano, D., Benazzi, S., & Romandini, M. (2019). The Uluzzian in the north of Italy: Insights around the new evidence at Riparo Broion. Archaeological and Anthropological Sciences, 11. https://doi.org/10.1007/s12520-018-0770-z

Peresani, M., Fiore, I., Gala, M., Romandini, M., & Tagliacozzo, A. (2011). Late Neandertals and the intentional removal of feathers as evidenced from bird bone taphonomy at Fumane Cave 44 ky B.P., Italy. Proceedings of the National Academy of Sciences of the United States of America, 108(10), 3888–3893. https://doi.org/10.1073/pnas.1016212108

Pérez Mejías, C. (2019). The Ejulve cave speleothemic record:from monitoring control to abrupt climate changes during the Pleistocene in the Eastern Iberian Range (Teruel). Zaragoza.

Pérez-Asensio, J. N., Frigola, J., Pena, L. D., Sierro, F. J., Reguera, M. I., Rodríguez-Tovar, F. J., Dorador, J., Asioli, A., Kuhlmann, J., Huhn, K., & Cacho, I. (2020). Changes in western Mediterranean thermohaline circulation in association with a deglacial Organic Rich Layer formation in the Alboran Sea. Quaternary Science Reviews, 228, 106075. https://doi.org/10.1016/j.quascirev.2019.106075

Pérez-Mejías, C., Moreno, A., Sancho, C., Martín-García, R., Spötl, C., Cacho, I., Cheng, H., & Edwards, R. L. (2019). Orbital-to-millennial scale climate variability during Marine Isotope Stages 5 to 3 in northeast Iberia. Quaternary Science Reviews, 224, 105946. https://doi.org/10.1016/j.quascirev.2019.105946

Petr, M., Hajdinjak, M., Fu, Q., Essel, E., Rougier, H., Crevecoeur, I., Semal, P., Golovanova, L. V., Doronichev, V. B., Lalueza-Fox, C., de la Rasilla, M., Rosas, A., Shunkov, M. V., Kozlikin, M. B., Derevianko, A. P., Vernot, B., Meyer, M., & Kelso, J. (2020). The evolutionary history of Neanderthal and Denisovan Y chromosomes. Science (New York, N.Y.), 369(6511), 1653–1656. https://doi.org/10.1126/science.abb6460

Pettitt, P., & Pike, A. W. G. (2015). Blind in a cloud of data: Problems with the chronology of Neanderthal extinction and anatomically modern human expansion. Antiquity, 75. https://doi.org/10.1017/S0003598X0006107X

Peyrégne, S., Slon, V., Mafessoni, F., de Filippo, C., Hajdinjak, M., Nagel, S., Nickel, B., Essel, E., Le Cabec, A., Wehrberger, K., Conard, N. J., Kind, C. J., Posth, C., Krause, J., Abrams, G., Bonjean, D., Di Modica, K., Toussaint, M., Kelso, J., … Prüfer, K. (2019). Nuclear DNA from two early Neandertals reveals 80,000 years of genetic continuity in Europe. Science Advances, 5(6), eaaw5873. https://doi.org/10.1126/sciadv.aaw5873

Peyron, O., Combourieu-Nebout, N., Brayshaw, D., Goring, S., Andrieu-Ponel, V., Desprat, S., Fletcher, W., Gambin, B., Ioakim, C., Joannin, S., Kotthoff, U., Kouli, K., Montade, V., Pross, J., Sadori, L., & Magny, M. (2017). Precipitation changes in the Mediterranean basin during the Holocene from terrestrial and marine pollen records: A model–data comparison. Climate of the Past, 13(3), 249–265. https://doi.org/10.5194/cp-13-249-2017

Peyron, O., Goring, S., Dormoy, I., Kotthoff, U., Pross, J., de Beaulieu, J.-L., Drescher-Schneider, R., Vannière, B., & Magny, M. (2011). Holocene seasonality changes in the central Mediterranean region reconstructed from the pollen sequences of Lake Accesa (Italy) and Tenaghi Philippon (Greece). The Holocene, 21(1), 131–146. https://doi.org/10.1177/0959683610384162

Peyron, O., Guiot, J., Cheddadi, R., Tarasov, P., Reille, M., de Beaulieu, J.-L., Bottema, S., & Andrieu, V. (1998). Climatic Reconstruction in Europe for 18,000 YR B.P. from Pollen Data. Quaternary Research, 49(2), 183–196. https://doi.org/10.1006/qres.1997.1961

Peyron, O., Magny, M., Goring, S., Joannin, S., de Beaulieu, J.-L., Brugiapaglia, E., Sadori, L., Garfi, G., Kouli, K., Ioakim, C., & Combourieu-Nebout, N. (2013). Contrasting patterns of climatic changes during the Holocene across the Italian Peninsula reconstructed from pollen data. Climate of the Past, 9(3), 1233–1252. https://doi.org/10.5194/cp-9-1233-2013

Picin, A., Moroni, A., & Benazzi, S. (2022). The arrival of Homo sapiens in the Near East and Europe. In F. Romagnoli, F. Rivals, & S. Benazzi (Eds.), Updating Neanderthals (pp. 321–347). Academic Press. https://doi.org/10.1016/B978-0-12-821428-2.00021-4

Pigott, E. M., Cheshmedzhieva, K., Zeller, E., van der Sluis, L. G., Pal Chowdhury, M., Gianni, M., Végh, E., Uthmeier, T., Chabai, V., Patou-Mathis, M., Šimková, P. G., Voglmayr, J. N., Weber, G. W., Pinhasi, R., Timmermann, A., Kuhlwilm, M., Douka, K., & Higham, T. (2025). A new late Neanderthal from Crimea reveals long-distance connections across Eurasia. Proceedings of the National Academy of Sciences, 122(45), e2518974122. https://doi.org/10.1073/pnas.2518974122

Pini, R., Ravazzi, C., & Donegana, M. (2009). Pollen stratigraphy, vegetation and climate history of the last 215 ka in the Azzano Decimo core (plain of Friuli, north-eastern Italy). Quaternary Science Reviews, 28(13), 1268–1290. https://doi.org/10.1016/j.quascirev.2008.12.017

Pini, R., Ravazzi, C., & Reimer, P. J. (2010). The vegetation and climate history of the last glacial cycle in a new pollen record from Lake Fimon (southern Alpine foreland, N-Italy). Quaternary Science Reviews, 29(23), 3115–3137. https://doi.org/10.1016/j.quascirev.2010.06.040

Pinto-Llona, A. C., & Grandal-d'Anglade, A. (2022). Sorting the riddle of the Neanderthal to anatomically modern human boundary in Sopeña (Asturias, Spain): New dates and a preliminar Bayesian analysis. Journal of Archaeological Science: Reports, 45, 103607. https://doi.org/10.1016/j.jasrep.2022.103607

Pitarch Martí, A., Zilhão, J., d'Errico, F., Cantalejo-Duarte, P., Domínguez-Bella, S., Fullola, J. M., Weniger, G. C., & Ramos-Muñoz, J. (2021). The symbolic role of the underground world among Middle Paleolithic Neanderthals. Proceedings of the National Academy of Sciences, 118(33), e2021495118. https://doi.org/10.1073/pnas.2021495118

Pons, A., & Quézel, P. (1998). A propos de la mise en place du climat méditerranéen. Compte-Rendus de l'Académie Des Sciences de Paris, Sciences de La Terre et Des Planètes, 327, 755–760.

Pons, A., & Reille, M. (1988). The holocene- and upper pleistocene pollen record from Padul (Granada, Spain): A new study. Palaeogeography, Palaeoclimatology, Palaeoecology, 66(3), 243–263. https://doi.org/10.1016/0031-0182(88)90202-7

Posth, C., Wißing, C., Kitagawa, K., Pagani, L., van Holstein, L., Racimo, F., Wehrberger, K., Conard, N. J., Kind, C. J., Bocherens, H., & Krause, J. (2017). Deeply divergent archaic mitochondrial

genome provides lower time boundary for African gene flow into Neanderthals. Nature Communications, 8(1), 16046. https://doi.org/10.1038/ncomms16046

Prasad, A. M., Iverson, L. R., & Liaw, A. (2006). Newer Classification and Regression Tree Techniques: Bagging and Random Forests for Ecological Prediction. Ecosystems, 9(2), 181–199. https://doi.org/10.1007/s10021-005-0054-1

Prentice, C., Guiot, J., Huntley, B., Jolly, D., & Cheddadi, R. (1996). Reconstructing biomes from palaeoecological data: A general method and its application to European pollen data at 0 and 6 ka. Climate Dynamics, 12(3), 185–194. https://doi.org/10.1007/BF00211617

Prentice, I. C. (1985). Pollen representation, source area, and basin size: Toward a unified theory of pollen analysis. Quaternary Research, 23(1), 76–86. https://doi.org/10.1016/0033-5894(85)90073-0

Prentice, I. C., Cramer, W., Harrison, S. P., Leemans, R., Monserud, R. A., & Solomon, A. M. (1992). Special Paper: A Global Biome Model Based on Plant Physiology and Dominance, Soil Properties and Climate. Journal of Biogeography, 19(2), 117–134. https://doi.org/10.2307/2845499

Price, M. H., Capriles, J. M., Hoggarth, J. A., Bocinsky, R. K., Ebert, C. E., & Jones, J. H. (2021). End-to-end Bayesian analysis for summarizing sets of radiocarbon dates. Journal of Archaeological Science, 135(105473). https://doi.org/10.1016/j.jas.2021.105473

Prüfer, K., Racimo, F., Patterson, N., Jay, F., Sankararaman, S., Sawyer, S., Heinze, A., Renaud, G., Sudmant, P. H., de Filippo, C., Li, H., Mallick, S., Dannemann, M., Fu, Q., Kircher, M., Kuhlwilm, M., Lachmann, M., Meyer, M., Ongyerth, M., … Pääbo, S. (2014). The complete genome sequence of a Neanderthal from the Altai Mountains. *Nature*, *505*(7481), 43–49. https://doi.org/10.1038/nature12886

Prüfer, K., Posth, C., Yu, H., Stoessel, A., Spyrou, M. A., Deviese, T., Mattonai, M., Ribechini, E., Higham, T., Velemínský, P., Brůžek, J., & Krause, J. (2021). A genome sequence from a modern human skull over 45,000 years old from Zlatý kůň in Czechia. Nature Ecology & Evolution, 5(6), 820–825. https://doi.org/10.1038/s41559-021-01443-x

Quam, R. M., Arsuaga, J.-L., Bermúdez de Castro, J.-M., Díez, C. J., Lorenzo, C., Carretero, M., García, N., & Ortega, A. I. (2001). Human remains from Valdegoba Cave (Huérmeces, Burgos, Spain). Journal of Human Evolution, 41(5), 385–435. https://doi.org/10.1006/jhev.2001.0486

Quézel, P. (1995). La flore du bassin méditerranéen: Origine, mise en place, endémisme. Ecologia mediterranea, 21(1), 19–39. https://doi.org/10.3406/ecmed.1995.1752

Quézel, P. (2000). Réflexions sur l'évolution de la flore et de la végétation au Maghreb Méditerranéen (Ibis Press).

Rae, T. C., Koppe, T., & Stringer, C. B. (2011a). Hyperpneumatized Neanderthals? Reply to Holton et al. (2011). Journal of Human Evolution, 61(5), 628–629. https://doi.org/10.1016/j.jhevol.2011.08.002

Rae, T. C., Koppe, T., & Stringer, C. B. (2011b). The Neanderthal face is not cold adapted. Journal of Human Evolution, 60(2), 234–239. https://doi.org/10.1016/j.jhevol.2010.10.003

Raia, P., Mondanaro, A., Melchionna, M., Di Febbraro, M., Diniz-Filho, J. A., Rangel, T., Holden, P., Carotenuto, F., Edwards, N., Lima-Ribeiro, M., Profico, A., Maiorano, L., Castiglione, S., Serio,

C., & Rook, L. (2020). Past Extinctions of Homo Species Coincided with Increased Vulnerability to Climatic Change. One Earth, 3, 480–490. https://doi.org/10.1016/j.oneear.2020.09.007

Railsback, L. B., Gibbard, P. L., Head, M. J., Voarintsoa, N. R. G., & Toucanne, S. (2015). An optimized scheme of lettered marine isotope substages for the last 1.0 million years, and the climatostratigraphic nature of isotope stages and substages. Quaternary Science Reviews, 111, 94–106. https://doi.org/10.1016/j.quascirev.2015.01.012

Ramsey, C. (1995). Radiocarbon Calibration and Analysis of Stratigraphy: The OxCal Program. Radiocarbon, 37(2), 425–430.

Rashid, H., Hesse, R., & Piper, D. J. W. (2003). Evidence for an additional Heinrich event between H5 and H6 in the Labrador Sea. Paleoceanography, 18(4), 2003PA000913. https://doi.org/10.1029/2003PA000913

Rasmussen, S., Andersen, K., Svensson, A., Steffensen, J., Vinther, B., Clausen, H. B., Siggaard-Andersen, M.-L., Johnsen, S. J., Larsen, L. B., Dahl-Jensen, D., Bigler, M., & Röthlisberger, R. (2006). A new Greenland ice core chronology for the Last Glacial termination. Journal of Geophysical Research, 111. https://doi.org/10.1029/2005JD006079

Rasmussen, S. O., Bigler, M., Blockley, S. P., Blunier, T., Buchardt, S. L., Clausen, H. B., Cvijanovic, I., Dahl-Jensen, D., Johnsen, S. J., Fischer, H., Gkinis, V., Guillevic, M., Hoek, W. Z., Lowe, J. J., Pedro, J. B., Popp, T., Seierstad, I. K., Steffensen, J. P., Svensson, A. M., … Winstrup, M. (2014). A stratigraphic framework for abrupt climatic changes during the Last Glacial period based on three synchronized Greenland ice-core records: Refining and extending the INTIMATE event stratigraphy. Quaternary Science Reviews, 106, 14–28. https://doi.org/10.1016/j.quascirev.2014.09.007

Rasmussen, T. L., Oppo, D. W., Thomsen, E., & Lehman, S. J. (2003). Deep sea records from the southeast Labrador Sea: Ocean circulation changes and ice-rafting events during the last 160,000 years. Paleoceanography, 18(1). https://doi.org/10.1029/2001PA000736

Real, C., Martínez-varea, C. M., Carrión, Y., Badal, E., Sanchis, A., Guillem, P., Martínez-valle, R., & Villaverde, V. (2022). Could the central-eastern Iberian Mediterranean region be defined as a refugium? Fauna and flora in MIS 5–3 and their implications for Palaeolithic human behaviour. Journal of Quaternary Science, 37(2), 363–379. https://doi.org/10.1002/jqs.3285

Reddad, H., El Talibi, H., Perri, F., El Moussaoui, S., Zerdeb, M. A., Zaghloul, M. N., & Critelli, S. (2016). Textural and compositional controls on modern fluvial and beach sands of Mediterranean coastal Rif belt (Northern Rif, Morocco). Italian Journal of Geosciences, 135(2), 336–349. https://doi.org/10.3301/ijg.2015.33

Regattieri, E., Zanchetta, G., Drysdale, R. N., Isola, I., Hellstrom, J. C., & Roncioni, A. (2014). A continuous stable isotope record from the penultimate glacial maximum to the Last Interglacial (159–121 ka) from Tana Che Urla Cave (Apuan Alps, central Italy). Quaternary Research, 82(2), 450.

Reille, M. (1990). Leçons de palynologie et d'analyse pollinique / Maurice Reille. Centre national de la recherche scientifique. Paris. https://bm-grenoble.fr/Default/doc/SYRACUSE/804989/lecons-de-palynologie-et-d-analyse-pollinique-maurice-reille

Reille, M. (1992). Pollen et spores d'Europe et d'Afrique du Nord. Laboratoire de Botanique Historique et Palynologie. 582p.

Reille, M., Andrieu, V., De beaulieu, J.-L., Guenet, P., & Goeury, C. (1998). A long pollen record from Lac du Bouchet, Massic Central, France for the period ca. 325 to 100 ka BP (OIS 9c to OIS 5e). Quaternary Science Reviews, 17(12), 1107–1123. https://doi.org/10.1016/S0277-3791(97)00093-0

Reille, M., Joel, G., & de Beaulieu, jacques-L. (1992). The Montaigu Event: An Abrupt Climatic Change During the Early Wurm in Europe (pp. 85–95). https://doi.org/10.1007/978-3-642-76954-2_7

Reimer, P. J. (2020). Composition and consequences of the IntCal20 radiocarbon calibration curve. Quaternary Research, 96, 22–27. https://doi.org/10.1017/qua.2020.42

Reimer, P. J., & Reimer, R. W. (2001). A Marine Reservoir Correction Database and On-Line Interface. Radiocarbon, 43(2A), 461–463. https://doi.org/10.1017/S0033822200038339

Renault, L., Oguz, T., Pascual, A., Vizoso, G., & Tintore, J. (2012). Surface circulation in the Alborán Sea (western Mediterranean) inferred from remotely sensed data. Journal of Geophysical Research: Oceans, 117(C8), 2011JC007659. https://doi.org/10.1029/2011JC007659

Rendu, W., Beauval, C., Crevecoeur, I., Bayle, P., Balzeau, A., Bismuth, T., Bourguignon, L., Delfour, G., Faivre, J.-P., Lacrampe-Cuyaubère, F., Muth, X., Pasty, S., Semal, P., Tavormina, C., Todisco, D., Turq, A., & Maureille, B. (2016). Let the dead speak…comments on Dibble et al.'s reply to "Evidence supporting an intentional burial at La Chapelle-aux-Saints". Journal of Archaeological Science, 69, 12–20. https://doi.org/10.1016/j.jas.2016.02.006

Revelles, J. (2017). Archaeoecology of Neolithisation. Human-environment interactions in the NE Iberian Peninsula during the Early Neolithic. Journal of Archaeological Science: Reports, 15, 437–445. https://doi.org/10.1016/j.jasrep.2016.02.004

Revelles, J. (2019). The role of non-pollen palynomorphs analysis in archaeopalynology. Taphonomic evaluation of emerged and waterlogged sectors at the Neolithic site of LaDraga (Banyoles, NE Iberia) (pp. 0–40). Institut Català de Paleoecologia Humana i Evolució Social (IPHES).

Revelles, J., Burjachs, F., Morera, N., Barceló, J. A., Berrocal, A., López-Bultó, O., Maicher, C., Le Bailly, M., Piqué, R., Palomo, A., & Terradas, X. (2017). Use of space and site formation processes in a Neolithic lakeside settlement. Pollen and non-pollen palynomorphs spatial analysis in La Draga (Banyoles, NE Iberia). Journal of Archaeological Science, 81, 101–115. https://doi.org/10.1016/j.jas.2017.04.001

Rhodes, R. H., Brook, E. J., Chiang, J. C. H., Blunier, T., Maselli, O. J., McConnell, J. R., Romanini, D., & Severinghaus, J. P. (2015). Paleoclimate. Enhanced tropical methane production in response to iceberg discharge in the North Atlantic. Science (New York, N.Y.), 348(6238), 1016–1019. https://doi.org/10.1126/science.1262005

Rhodes, R. H., Brook, E. J., McConnell, J. R., Blunier, T., Sime, L. C., Faïn, X., & Mulvaney, R. (2017). Atmospheric methane variability: Centennial-scale signals in the Last Glacial Period. Global Biogeochemical Cycles, 31(3), 575–590. https://doi.org/10.1002/2016GB005570

Richard, M., Falguères, C., Pons-Branchu, E., Bahain, J.-J., Voinchet, P., Lebon, M., Valladas, H., Dolo, J.-M., Puaud, S., Rué, M., Daujeard, C., Moncel, M.-H., & Raynal, J.-P. (2015). Contribution of ESR/U-series dating to the chronology of late Middle Palaeolithic sites in the middle Rhône valley, southeastern France. Quaternary Geochronology, 30, 529–534. https://doi.org/10.1016/j.quageo.2015.06.002

Richard, M., Pons-Branchu, E., Genuite, K., Jaillet, S., Joannes-Boyau, R., Wang, N., Genty, D., Cheng, H., Price, G. J., Pierre, M., Dapoigny, A., Falguères, C., Tombret, O., Voinchet, P., Bahain, J.-J., & Moncel, M.-H. (2021). Timing of Neanderthal occupations in the southeastern margins of the Massif Central (France): A multi-method approach. Quaternary Science Reviews, 273, 107241. https://doi.org/10.1016/j.quascirev.2021.107241

Richter, J. (2016). Leave at the height of the party: A critical review of the Middle Paleolithic in Western Central Europe from its beginnings to its rapid decline. Quaternary International, 411, 107–128. https://doi.org/10.1016/j.quaint.2016.01.018

Riding, J. B. (2021). A guide to preparation protocols in palynology. Palynology, 45(S1), 1–110. https://doi.org/10.1080/01916122.2021.1878305

Ríos, L., Kivell, T. L., Lalueza-Fox, C., Estalrrich, A., García-Tabernero, A., Huguet, R., Quintino, Y., de la Rasilla, M., & Rosas, A. (2019). Skeletal Anomalies in The Neandertal Family of El Sidrón (Spain) Support A Role of Inbreeding in Neandertal Extinction. Scientific Reports, 9(1), 1697. https://doi.org/10.1038/s41598-019-38571-1

Rios-Garaizar, J. (2016). Early Middle Palaeolithic occupations at Ventalaperra cave (Cantabrian Region, Northern Iberian Peninsula). Journal of Lithic Studies, 3. https://doi.org/10.2218/jls.v3i1.1287

Rios-Garaizar, J. (2017). A new chronological and technological synthesis for Late Middle Paleolithic of the Eastern Cantabrian Region. Quaternary International, 433, 50–63. https://doi.org/10.1016/j.quaint.2016.02.020

Rios-Garaizar, J., Garate, D., Gómez-Olivencia, A., Iriarte, E., Aranburu, A., Arceredillo, D., García, A., Ortiz, J., Torres, T., San Pedro Calleja, Z., & Zapata-Peña, L. (2011). The Lower to Middle Palaeolithic transition in northern Iberia: New data from Arlanpe Cave. Antiquity, 85.

Rios-Garaizar, J., Sánchez-Romero, L., Arriolabengoa, M., Benito-Calvo, A., Expósito, I., Del Val, M., Karambaglidis, T., Marín-Arroyo, A. B., Pérez-Garrido, C., Arenas-Sorriqueta, E., Eixea, A., Gómez-Olivencia, A., Agudo-Pérez, L., San Emeterio, A., & Antxieta Arkeologi Taldea. (2024). MIS5-MIS3 Neanderthal occupations at Amalda III cave (Northern Iberian Peninsula). Quaternary Science Reviews, 333, 108666. https://doi.org/10.1016/j.quascirev.2024.108666

Robles, M. (2022). Végétation, climat et sociétés humaines du bassin méditerranéen du Tardiglaciaire à l'Holocène: Approche multi-proxy (pollen, NPP, brGDGT, XRF) de l'Italie (lac Matese) à l'Arménie (lac Sévan) Thèse de l'Université de Montpellier et de l'Università degli studi del Molise, 283 p.

Robles, M., Andrieu, V., Rochette, P., Fauquette, S., Peyron, O., Demory, F., Parlak, O., Charrat, E., Gambin, B., & Alçiçek, M. C. (2025). Vegetation and climate changes at the Early-Late Pliocene Transition around the Mediterranean basin: A case from the Burdur Basin in Southwestern Anatolia. EGUsphere, 1–33. https://doi.org/10.5194/egusphere-2025-174

Robles, M., Peyron, O., Ménot, G., Brugiapaglia, E., Wulf, S., Appelt, O., Blache, M., Vannière, B., Dugerdil, L., Paura, B., Ansanay-Alex, S., Cromartie, A., Charlet, L., Guédron, S., De Beaulieu, J.-L., & Joannin, S. (2022). Climate changes during the Lateglacial in South Europe: New insights based on pollen and brGDGTs of Lake Matese in Italy. https://doi.org/10.5194/cp-2022-54

Robles, M., Peyron, O., Ménot, G., Brugiapaglia, E., Wulf, S., Appelt, O., Blache, M., Vannière, B., Dugerdil, L., Paura, B., Ansanay-Alex, S., Cromartie, A., Charlet, L., Guédron, S., de Beaulieu, J.-L., & Joannin, S. (2023). Climate changes during the Late Glacial in southern Europe: New

insights based on pollen and brGDGTs of Lake Matese in Italy. Clim. Past, 19(2), 493–515. https://doi.org/10.5194/cp-19-493-2023

Rodríguez-Hidalgo, A., Morales, J. I., Cebrià, A., Courtenay, L. A., Fernández-Marchena, J. L., García-Argudo, G., Marín, J., Saladié, P., Soto, M., Tejero, J.-M., & Fullola, J.-M. (2019). The Châtelperronian Neanderthals of Cova Foradada (Calafell, Spain) used imperial eagle phalanges for symbolic purposes. Science Advances, 5(11), eaax1984. https://doi.org/10.1126/sciadv.aax1984

Rogers, A. R. (2024). Genetic Evidence for Geographic Structure within the Neanderthal Population. Peer Community Journal, 4. https://doi.org/10.24072/pcjournal.448

Rogers, A. R., Bohlender, R. J., & Huff, C. D. (2017). Early history of Neanderthals and Denisovans. Proceedings of the National Academy of Sciences of the United States of America, 114(37), 9859–9863. https://doi.org/10.1073/pnas.1706426114

Rogerson, M., Cacho, I., Jimenez-Espejo, F., Reguera, M. I., Sierro, F. J., Martinez-Ruiz, F., Frigola, J., & Canals, M. (2008). A dynamic explanation for the origin of the western Mediterranean organic-rich layers. Geochemistry, Geophysics, Geosystems, 9(7). https://doi.org/10.1029/2007GC001936

Rohling, E. J., Hibbert, F. D., Williams, F. H., Grant, K. M., Marino, G., Foster, G. L., Hennekam, R., de Lange, G. J., Roberts, A. P., Yu, J., Webster, J. M., & Yokoyama, Y. (2017). Differences between the last two glacial maxima and implications for ice-sheet, δ18O, and sea-level reconstructions. Quaternary Science Reviews, 176, 1–28. https://doi.org/10.1016/j.quascirev.2017.09.009

Rohling, E. J., Marino, G., & Grant, K. M. (2015). Mediterranean climate and oceanography, and the periodic development of anoxic events (sapropels). Earth-Science Reviews, 143, 62–97. https://doi.org/10.1016/j.earscirev.2015.01.008

Romagnoli, F., Chabai, V., Gravina, B., Hérisson, D., Hovers, E., Moncel, M.-H., Peresani, M., Uthmeier, T., Bourguignon, L., Chacón, M. G., Modica, K. D., Faivre, J.-P., Kolobova, K., Malinsky-Buller, A., Neruda, P., Garaizar, J. R., Weiss, M., Wiśniewski, A., & Sykes, R. W. (2022). Chapter 10 - Neanderthal technological variability: A wide-ranging geographical perspective on the final Middle Palaeolithic. In F. Romagnoli, F. Rivals, & S. Benazzi (Eds.), Updating Neanderthals (pp. 163–205). Academic Press. https://doi.org/10.1016/B978-0-12-821428-2.00012-3

Romagnoli, F., Rivals, F., & Benazzi, S. (2022). Updating Neanderthals: Taking stock of more than 160 years of studies. In F. Romagnoli, F. Rivals, & S. Benazzi (Eds.), Updating Neanderthals (pp. 1–15). Academic Press. https://doi.org/10.1016/B978-0-12-821428-2.00020-2

Rosas, A., Bastir, M., & García-Tabernero, A. (2022). Chapter 5 - Neanderthals: Anatomy, genes, and evolution. In F. Romagnoli, F. Rivals, & S. Benazzi (Eds.), Updating Neanderthals (pp. 71–87). Academic Press. https://doi.org/10.1016/B978-0-12-821428-2.00007-X

Rosas, A., Bastir, M., García-Tabernero, A., Alarcón Pérez, J. A., Rosas, A., Bastir, M., García-Tabernero, A., & Alarcón Pérez, J. A. (2025). Mosaic evolution. An example in the origin of Neandertals. Spanish Journal of Palaeontology, 40(1), 97–114. https://doi.org/10.7203/SJP.30506

Roucoux, K. H., de Abreu, L., Shackleton, N. J., & Tzedakis, P. C. (2005). The response of NW Iberian vegetation to North Atlantic climate oscillations during the last 65kyr. Quaternary Science Reviews, 24(14–15), 1637–1653. https://doi.org/10.1016/j.quascirev.2004.08.022

Roucoux, K. H., Tzedakis, P. C., de Abreu, L., & Shackleton, N. J. (2006). Climate and vegetation changes 180,000 to 345,000 years ago recorded in a deep-sea core off Portugal. Earth and Planetary Science Letters, 249(3), 307–325. https://doi.org/10.1016/j.epsl.2006.07.005

Roucoux, K. H., Tzedakis, P. C., Lawson, I. T., & Margari, V. (2011). Vegetation history of the penultimate glacial period (Marine isotope stage 6) at Ioannina, north-west Greece. Journal of Quaternary Science, 26(6), 616–626. https://doi.org/10.1002/jqs.1483

Rousseau, D.-D., Antoine, P., Boers, N., Lagroix, F., Ghil, M., Lomax, J., Fuchs, M., Debret, M., Christine, H., Moine, O., Gauthier, C., Jordanova, D., & Jordanova, N. (2020). Dansgaard-Oeschger-like events of the penultimate climate cycle: The loess point of view. Climate of the Past, 16, 713–727. https://doi.org/10.5194/cp-16-713-2020

Roussel, M., Soressi, M., & Hublin, J.-J. (2016). The Châtelperronian conundrum: Blade and bladelet lithic technologies from Quinçay, France. Journal of Human Evolution, 95, 13–32. https://doi.org/10.1016/j.jhevol.2016.02.003

Ruan, Q.-J., Li, H., Xiao, P.-Y., Li, B., Monod, H., Sumner, A., Zhao, K.-L., Liu, J.-H., Jia, Z.-X., Wang, C.-X., Fan, A.-C., Moncel, M.-H., Marwick, B., Peresani, M., Wang, Y.-P., Chen, F.-H., & Delpiano, D. (2025). Quina lithic technology indicates diverse Late Pleistocene human dynamics in East Asia. Proceedings of the National Academy of Sciences, 122(14), e2418029122. https://doi.org/10.1073/pnas.2418029122

Rubio-Jara, S., & Panera, J. (2019). Unravelling an essential archive for the European Pleistocene. The human occupation in the Manzanares valley (Madrid, Spain) throughout nearly 800,000 years. Quaternary International, 520, 5–22. https://doi.org/10.1016/j.quaint.2018.08.007

Rubio-Jara, S., Panera, J., Rodríguez-de-Tembleque, J., Santonja, M., & Pérez-González, A. (2016). Large flake Acheulean in the middle of Tagus basin (Spain): Middle stretch of the river Tagus valley and lower stretches of the rivers Jarama and Manzanares valleys. Quaternary International, 411, 349–366. https://doi.org/10.1016/j.quaint.2015.12.023

Ruddiman, W. F. (1977). Late Quaternary deposition of ice-rafted sand in the subpolar North Atlantic (lat 40° to 65°N). Geological Society of America Bulletin, 88(12), 1813. https://doi.org/10.1130/0016-7606(1977)88<1813:LQDOIS>2.0.CO;2

Ruddiman, W. F. (2008). Earth's Climate, Past and Future. Clancy Marshall. 445 p.

Ruddiman, W. F., Raymo, M., & McIntyre, A. (1986). Matuyama 41,000-year cycles: North Atlantic Ocean and northern hemisphere ice sheets. Earth and Planetary Science Letters, 80(1–2), 117–129. https://doi.org/10.1016/0012-821X(86)90024-5

Sadori, L., Koutsodendris, A., Panagiotopoulos, K., Masi, A., Bertini, A., Combourieu-Nebout, N., Francke, A., Kouli, K., Joannin, S., Mercuri, A. M., Peyron, O., Torri, P., Wagner, B., Zanchetta, G., Sinopoli, G., & Donders, T. H. (2016). Pollen-based paleoenvironmental and paleoclimatic change at Lake Ohrid (south-eastern Europe) during the past 500 ka. Biogeosciences, 13(5), 1423–1437. https://doi.org/10.5194/bg-13-1423-2016

Sala, N., Alcaraz-Castaño, M., Arriolabengoa, M., Martínez-Pillado, V., Pantoja-Pérez, A., Rodríguez-Hidalgo, A., Téllez, E., Cubas, M., Castillo, S., Arnold, L. J., Demuro, M., Duval, M., Arteaga-Brieba, A., Llamazares, J., Ochando, J., Cuenca-Bescós, G., Marín-Arroyo, A. B., Seijo, M. M.,

Luque, L., … Pablos, A. (2024). Nobody's land? The oldest evidence of early Upper Paleolithic settlements in inland Iberia. Science Advances, 10(26), eado3807. https://doi.org/10.1126/sciadv.ado3807

Sala, N., Pablos, A., Gómez-Olivencia, A., Sanz, A., Villalba, M., Pantoja-Pérez, A., Laplana, C., Arsuaga, J. L., & Algaba, M. (2020). Central Iberia in the middle MIS 3. Paleoecological inferences during the period 34–40 cal kyr BP. Quaternary Science Reviews, 228, 106027. https://doi.org/10.1016/j.quascirev.2019.106027

Sala, N., Téllez, E., Arteaga-Brieba, A., Rodríguez-Iglesias, D., Rodríguez-Almagro, M., Pantoja-Pérez, A., Grabbe, J., & Pablos, A. (2025). Iberian Neandertal fossils: Exploring funerary practices in a paleoclimatic context. Journal of Archaeological Science: Reports, 66, 105316. https://doi.org/10.1016/j.jasrep.2025.105316

Salonen, J. S., Korpela, M., Williams, J. W., & Luoto, M. (2019). Machine-learning based reconstructions of primary and secondary climate variables from North American and European fossil pollen data. Scientific Reports, 9(1), 15805. https://doi.org/10.1038/s41598-019-52293-4

Salonen, J. S., Luoto, M., Alenius, T., Heikkilä, M., Seppä, H., Telford, R. J., & Birks, H. J. B. (2014). Reconstructing palaeoclimatic variables from fossil pollen using boosted regression trees: Comparison and synthesis with other quantitative reconstruction methods. Quaternary Science Reviews, 88, 69.

Salonen, J. S., Seppä, H., Luoto, M., Bjune, A. E., & Birks, H. J. B. (2012). A North European pollen–climate calibration set: Analysing the climatic responses of a biological proxy using novel regression tree methods. Quaternary Science Reviews, 45, 95–110. https://doi.org/10.1016/j.quascirev.2012.05.003

Sánchez Goñi, M. (1993). The identification of European Upper Palaeolithic interstadials from cave sequences. Aspects of Archaeological Palynology: Methodology and Applications, 29, 161–182.

Sánchez Goñi, M. (1996). Les changements climatiques du Paléolithique Supérieur. Enquête sur le rapport entre Paléoclimatologie et Préhistoire. Zephyrus: Revista de Prehistoria y Arqueología, ISSN 0514-7336, No 49, 1996, Pags. 3-36, 49.

Sánchez Goñi, M. (2020). Regional impacts of climate change and its relevance to human evolution. Evolutionary Human Sciences, 2, 1–27. https://doi.org/10.1017/ehs.2020.56

Sánchez Goñi, M. (2022a). An overview of the Last Glacial Cycle. In An overview of the Last Glacial Cycle. (Palacios, D., Hugues, P.D., Garcia-Ruiz, J.M., and Andrés, N., pp. 165–169). Chennai: Elsevier. https://doi.org/10.1016/B978-0-12-823498-3.00012-1

Sánchez Goñi, M. (2022b). The climatic and environmental context of the Late Pleistocene. In Updating Neanderthals. Understanding Behavioural Complexity in the Late Middle Palaeolithic. (Romagnoli, Rivals and Benazzi, pp. 165–169). Elsevier/Academic Press. https://doi.org/10.1016/B978-0-12-823498-3.00012-1

Sanchez Goñi, M., Bakker, P., Desprat, S., Carlson, A., Van Meerbeeck, C., Peyron, O., Naughton, F., Fletcher, W., Eynaud, F., Rossignol, L., & Renssen, H. (2012). European climate optimum and enhanced Greenland melt during the Last Interglacial. Geology, 40, 627–630. https://doi.org/10.1130/G32908.1

Sánchez Goñi, M., Bard, E., Landais, A., Rossignol, L., & d'Errico, F. (2013). Air-sea temperature decoupling in western Europe during the last interglacial-glacial transition. Nature Geoscience, 6, 837–841. https://doi.org/10.1038/ngeo1924

Sánchez Goñi, M., Cacho, I., Jean Louis, T., Joel, G., Sierro, F., Peypouquet, J., Grimalt, J., & Shackleton, N. (2002). Synchroneity between marine and terrestrial responses to millennial scale climatic variability during the last glacial period in the Mediterranean region. Climate Dynamics, 19, 95–105. https://doi.org/10.1007/s00382-001-0212-x

Sánchez Goñi, M., & d'Errico, F. (2005). La historia de la vegetación y el clima del último ciclo climático (OIS5-OIS1, 140.000-10.000 años BP) en la Península Ibérica y su posible impacto sobre los grupos paleolíticos. Monografías, 20, 115–129.

Sánchez Goñi, M. F. (2007). Introduction to Climate and Vegetation in Europe During MIS5. Developments in Quaternary Science, 7, 197–205.

Sánchez Goñi, M. F. (2010). Millennial-scale variability during the last glacial in vegetation records from Europe. Quaternary Science Reviews. https://www.academia.edu/4858846/Millennial_scale_variability_during_the_last_glacial_in_vegetation_records_from_Europe

Sánchez Goñi, M. F., Desprat, S., Daniau, A.-L., Bassinot, F. C., Polanco-Martínez, J. M., Harrison, S. P., Allen, J. R. M., Anderson, R. S., Behling, H., Bonnefille, R., Burjachs, F., Carrión, J. S., Cheddadi, R., Clark, J. S., Combourieu-Nebout, N., Mustaphi, C. J. C., Debusk, G. H., Dupont, L. M., Finch, J. M., … Yamamoto, M. (2017). The ACER pollen and charcoal database: A global resource to document vegetation and fire response to abrupt climate changes during the last glacial period. Earth System Science Data, 9(2), 679–695. https://doi.org/10.5194/essd-9-679-2017

Sánchez Goñi, M. F., Desprat, S., Fletcher, W. J., Morales-Molino, C., Naughton, F., Oliveira, D., Urrego, D. H., & Zorzi, C. (2018). Pollen from the Deep-Sea: A Breakthrough in the Mystery of the Ice Ages. Frontiers in Plant Science, 9. https://doi.org/10.3389/fpls.2018.00038

Sánchez Goñi, M. F., Eynaud, F., Turon, J.-L., & Shackleton, N. J. (1999). High resolution palynological record off the Iberian margin: Direct land-sea correlation for the Last Interglacial complex. Earth and Planetary Science Letters, 171, 123–137.

Sánchez Goñi, M. F., Fourcade, T., Salonen, S., Lesven, J., Frigola, J., Swingedouw, D., & Sierro, F. J. (2021). Muted cooling and drying of NW Mediterranean in response to the strongest last glacial North American ice surges. GSA Bulletin, 133(3–4), 451–460. https://doi.org/10.1130/B35736.1

Sánchez Goñi, M. F., Landais, A., Cacho, I., Duprat, J., & Rossignol, L. (2009). Contrasting intrainterstadial climatic evolution between high and middle North Atlantic latitudes: A close-up of Greenland Interstadials 8 and 12. Geochemistry, Geophysics, Geosystems, 10(4). https://doi.org/10.1029/2008GC002369

Sánchez Goñi, M. F., Landais, A., Fletcher, W. J., Naughton, F., Desprat, S., & Duprat, J. (2008). Contrasting impacts of Dansgaard–Oeschger events over a western European latitudinal transect modulated by orbital parameters. Quaternary Science Reviews, 27(11–12), 1136–1151. https://doi.org/10.1016/j.quascirev.2008.03.003

Sánchez Goñi, M. F., Loutre, M. F., Crucifix, M., Peyron, O., Santos, L., Duprat, J., Malaizé, B., Turon, J.-L., & Peypouquet, J.-P. (2005). Increasing vegetation and climate gradient in Western Europe

over the Last Glacial Inception (122–110 ka): Data-model comparison. Earth and Planetary Science Letters, 231(1–2), 111–130. https://doi.org/10.1016/j.epsl.2004.12.010

Sánchez Goñi, M. F., Turon, J.-L., Eynaud, F., & Gendreau, S. (2000). European Climatic Response to Millennial-Scale Changes in the Atmosphere–Ocean System during the Last Glacial Period. Quaternary Research, 54(3), 394–403. https://doi.org/10.1006/qres.2000.2176

Sánchez Goñi, M., & Harrison, S. (2010). Millennial-scale climate variability and vegetation changes during the Last Glacial: Concepts and terminology. Quaternary Science Reviews, 29, 2823–2827. https://doi.org/10.1016/j.quascirev.2009.11.014

Sánchez Goñi, M., Cacho, I., Jean Louis, T., Joel, G., Sierro, F., Peypouquet, J., Grimalt, J., Shackleton, N. (2002). Synchroneity between marine and terrestrial responses to millennial scale climatic variability during the last glacial period in the Mediterranean region. Climate Dynamics, 19(1), 95–105. https://doi.org/10.1007/s00382-001-0212-x

Sánchez-Laulhé, J. M., Jansa, A., & Jiménez, C. (2021). Alboran Sea Area Climate and Weather. In J. C. Báez, J.-T. Vázquez, J. A. Camiñas, & M. Malouli Idrissi (Eds.), Alboran Sea—Ecosystems and Marine Resources (pp. 31–83). Springer International Publishing. https://doi.org/10.1007/978-3-030-65516-7_3

Sánchez-Yustos, P. (2009). El paleolítico antiguo en la cuenca del Duero. Instrumentos teóricos para la construcción de un modelo interpretativo de arqueología económica.

Sánchez-Yustos, P., & Diez-Martín, F. (2015). Dancing to the rhythms of the Pleistocene? Early Middle Paleolithic population dynamics in NW Iberia (Duero Basin and Cantabrian Region). Quaternary Science Reviews, 121. https://doi.org/10.1016/j.quascirev.2015.05.005

Santamaría, M., Navazo, M., Benito-Calvo, A., Alonso, R., López, G. I., & Carbonell, E. (2021). Atapuerca Neanderthal landscape at Fuente Mudarra site in Burgos, Spain, during Marine Isotope Stages 5–3. Quaternary Research, 99, 248–269. https://doi.org/10.1017/qua.2020.65

Santonja, M., Pérez-González, A., Baena, J., Panera, J., Méndez-Quintas, E., Uribelarrea, D., Demuro, M., Arnold, L., Abrunhosa, A., & Rubio-Jara, S. (2022). The Acheulean of the Upper Guadiana River Basin (Central Spain). Morphostratigraphic Context and Chronology. Frontiers in Earth Science, 10. https://doi.org/10.3389/feart.2022.912007

Santonja, M., Pérez-González, A., Panera, J., Rubio-Jara, S., & Méndez-Quintas, E. (2016). The coexistence of Acheulean and Ancient Middle Palaeolithic techno-complexes in the Middle Pleistocene of the Iberian Peninsula. Quaternary International, 411, 367–377. https://doi.org/10.1016/j.quaint.2015.04.056

Santonja, M., Rubio-Jara, S., Panera, J., Sánchez-Romero, L., Tarriño, A., & Pérez-González, A. (2018). Ambrona revisited: The Acheulean lithic industry in the Lower Stratigraphic Complex. Quaternary International, 480, 95–117. https://doi.org/10.1016/j.quaint.2017.01.021

Sassoon, D., Combourieu-Nebout, N., Peyron, O., Bertini, A., Toti, F., Lebreton, V., & Moncel, M.-H. (2025). Pollen-based climatic reconstructions for the interglacial analogues of MIS 1 (MIS 19, 11, and 5) in the southwestern Mediterranean: Insights from ODP Site 976. Climate of the Past, 21(2), 489–515. https://doi.org/10.5194/cp-21-489-2025

Sassoon, D., Lebreton, V., Combourieu-Nebout, N., Peyron, O., & Moncel, M.-H. (2023). Palaeoenvironmental changes in the southwestern Mediterranean (ODP site 976, Alboran sea)

during the MIS 12/11 transition and the MIS 11 interglacial and implications for hominin populations. Quaternary Science Reviews, 304, 108010. https://doi.org/10.1016/j.quascirev.2023.108010

Savannah, M., Eelco, R., Timme, D., Katharine, G., Jörg, K., Gianluca, M., Francesca, S., Francesca, C., Caterina, M., Anna, S., & Alessandra, N. (2024). The "glacial" sapropel S6 (172 ka; MIS 6): A multiproxy approach to solve a Mediterranean "cold case". Palaeogeography, Palaeoclimatology, Palaeoecology, 650, 112384. https://doi.org/10.1016/j.palaeo.2024.112384

Schmidt, I., Hilpert, J., Kretschmer, I., Peters, R., Broich, M., Schiesberg, S., Vogels, O., Wendt, K. P., Zimmermann, A., & Maier, A. (2021). Approaching prehistoric demography: Proxies, scales and scope of the Cologne Protocol in European contexts. Philosophical Transactions of the Royal Society B: Biological Sciences, 376(1816), 20190714. https://doi.org/10.1098/rstb.2019.0714

Scott, B. (2011). Becoming Neanderthals: The earlier British middle palaeolithic. Oxbow books.

Seierstad, I. K., Abbott, P. M., Bigler, M., Blunier, T., Bourne, A. J., Brook, E., Buchardt, S. L., Buizert, C., Clausen, H. B., Cook, E., Dahl-Jensen, D., Davies, S. M., Guillevic, M., Johnsen, S. J., Pedersen, D. S., Popp, T. J., Rasmussen, S. O., Severinghaus, J. P., Svensson, A., & Vinther, B. M. (2014). Consistently dated records from the Greenland GRIP, GISP2 and NGRIP ice cores for the past 104 ka reveal regional millennial-scale δ18O gradients with possible Heinrich event imprint. Quaternary Science Reviews, 106, 29–46. https://doi.org/10.1016/j.quascirev.2014.10.032

Sepulchre, P., Ramstein, G., Kageyama, M., Vanhaeren, M., Krinner, G., Sánchez-Goñi, M.-F., & d'Errico, F. (2007). H4 abrupt event and late Neanderthal presence in Iberia. Earth and Planetary Science Letters, 283–292.

Shackleton, N. J. (1987). Oxygen isotopes, ice volume and sea level. Quaternary Science Reviews, 6(3), 183–190. https://doi.org/10.1016/0277-3791(87)90003-5

Shackleton, N. J., Fairbanks, R. G., Chiu, T., & Parrenin, F. (2004). Absolute calibration of the Greenland time scale: Implications for Antarctic time scales and for Δ14C. Quaternary Science Reviews, 23(14), 1513–1522. https://doi.org/10.1016/j.quascirev.2004.03.006

Shackleton, N. J., Hall, M. A., & Vincent, E. (2000). Phase relationships between millennial-scale events 64,000–24,000 years ago. Paleoceanography, 15(6), 565–569. https://doi.org/10.1029/2000PA000513

Shackleton, N. J., Sánchez-Goñi, M. F., Pailler, D., & Lancelot, Y. (2003). Marine Isotope Substage 5e and the Eemian Interglacial. Global and Planetary Change, 36(3), 151–155. https://doi.org/10.1016/S0921-8181(02)00181-9

Shao, Y., Klein, K., Ludwig, P., Maier, A., Richter, J., Schmidt, I., & Weniger, G.-C. (2021). 6. Modelling Human Mobility in Space and Time (pp. 269–307).

Sharp, W. D., Mertz-Kraus, R., Vallverdu, J., Vaquero, M., Burjachs, F., Carbonell, E., & Bischoff, J. L. (2016). Archeological deposits at Abric Romaní extend to 110 ka: U-series dating of a newly cored, 30 meter-thick section. Journal of Archaeological Science: Reports, 5, 400–406. https://doi.org/10.1016/j.jasrep.2015.12.015

Shaw, A., Bates, M., Conneller, C., Gamble, C., Julien, M.-A., McNabb, J., Pope, M., & Scott, B. (2016). The archaeology of persistent places: The Palaeolithic case of La Cotte de St Brelade, Jersey. Antiquity, 90(354), 1437–1453. https://doi.org/10.15184/aqy.2016.212

Shaw, A., Dobbie, J., Toms, P., & Wood, J. (2025). A long chronology for the British Late Middle Palaeolithic: MIS 5–MIS 3 occupation at Great Pan Farm (Isle of Wight, England). Quaternary International, 736–737, 109846. https://doi.org/10.1016/j.quaint.2025.109846

Shea, J., & Sisk, M. (2010). Complex projectile technology and Homo sapiens dispersal into Western Eurasia. PaleoAnthropology, 2010, 100–122.

Shin, J., Nehrbass-Ahles, C., Grilli, R., Chowdhry Beeman, J., Parrenin, F., Teste, G., Landais, A., Schmidely, L., Silva, L., Schmitt, J., Bereiter, B., Stocker, T. F., Fischer, H., & Chappellaz, J. (2020). Millennial-scale atmospheric CO2 variations during the Marine Isotope Stage 6 period (190–135 ka). Climate of the Past, 16(6), 2203–2219. https://doi.org/10.5194/cp-16-2203-2020

Shumilovskikh, L. S., Schlütz, F., Achterberg, I., Bauerochse, A., & Leuschner, H. H. (2015). Non-pollen palynomorphs from mid-holocene peat of the raised bog borsteler moor (Lower saxony, Germany). Studia Quaternaria, 32(1), 5–18. https://doi.org/10.1515/squa-2015-0001

Shumilovskikh, L., van Geel, B., & Gafarov, A. (2016). Non-Pollen Palynomorph Image Database. http://non-pollen-palynomorphs.uni-goettingen.de/index.html

Siani, G., Paterne, M., Arnold, M., Bard, E., Métivier, B., Tisnerat, N., & Bassinot, F. (2000). Radiocarbon Reservoir Ages in the Mediterranean Sea and Black Sea. Radiocarbon, 42(2), 271–280. https://doi.org/10.1017/S0033822200059075

Sierro, F. J., & Andersen, N. (2022). An exceptional record of millennial-scale climate variability in the southern Iberian Margin during MIS 6: Impact on the formation of sapropel S6. Quaternary Science Reviews, 286, 107527. https://doi.org/10.1016/j.quascirev.2022.107527

Sierro, F. J., Hodell, D. A., Andersen, N., Azibeiro, L. A., Jimenez-Espejo, F. J., Bahr, A., Flores, J. A., Ausin, B., Rogerson, M., Lozano-Luz, R., Lebreiro, S. M., & Hernandez-Molina, F. J. (2020). Mediterranean Overflow Over the Last 250 kyr: Freshwater Forcing From the Tropics to the Ice Sheets. Paleoceanography and Paleoclimatology, 35(9), e2020PA003931. https://doi.org/10.1029/2020PA003931

Sierro, F. J., Tarruella, J., Jiménez-Espejo, F., & Hodell, D. (2025). Atlantic atmospheric rivers and the pulse of deep Mediterranean respiration. https://doi.org/10.21203/rs.3.rs-5678981/v1

Silva, P. G., López-Recio, M., Tapias, F., Roquero, E., Morín, J., Rus, I., Carrasco-García, P., Giner-Robles, J. L., Rodríguez-Pascua, M. A., & Pérez-López, R. (2013). Stratigraphy of the Arriaga Palaeolithic sites. Implications for the geomorphological evolution recorded by thickened fluvial sequences within the Manzanares River valley (Madrid Neogene Basin, Central Spain). Geomorphology, 196, 138–161. https://doi.org/10.1016/j.geomorph.2012.10.019

Silvestrini, S., Romandini, M., Marciani, G., Arrighi, S., Carrera, L., Fiorini, A., López-García, J. M., Lugli, F., Ranaldo, F., Slon, V., Tassoni, L., Higgins, O. A., Bortolini, E., Curci, A., Meyer, M., Meyer, M. C., Oxilia, G., Zerboni, A., Benazzi, S., & Spinapolice, E. E. (2022). Integrated multidisciplinary ecological analysis from the Uluzzian settlement at the Uluzzo C Rock Shelter, south-eastern Italy. Journal of Quaternary Science, 37(2), 235–256. https://doi.org/10.1002/jqs.3341

Sinopoli, G., Masi, A., Regattieri, E., Wagner, B., Francke, A., Peyron, O., & Sadori, L. (2018). Palynology of the Last Interglacial Complex at Lake Ohrid: Palaeoenvironmental and palaeoclimatic inferences. Quaternary Science Reviews, 180, 177–192. https://doi.org/10.1016/j.quascirev.2017.11.013

Sinopoli, G., Peyron, O., Masi, A., Holtvoeth, J., Francke, A., Wagner, B., & Sadori, L. (2019). Pollen-based temperature and precipitation changes in the Ohrid Basin (western Balkans) between 160 and 70 ka. Climate of the Past, 15(1), 53–71. https://doi.org/10.5194/cp-15-53-2019

Skilbeck, C. G., & Tribble, J. S. (1999). Description, classification, and origin of upper Pliocene–Holocene marine sediments in the Alboran Basin. In Proceedings of the Ocean Drilling Program, Scientific Results (Comas, M.C., Zahn, R., and Klaus, A., et al., Vol. 161). Ocean Drilling Program. https://doi.org/10.2973/odp.proc.sr.161.1999

Skinner, L. C., & Shackleton, N. J. (2006). Deconstructing Terminations I and II: Revisiting the glacioeustatic paradigm based on deep-water temperature estimates. Quaternary Science Reviews, 25(23–24), 3312–3321. https://doi.org/10.1016/j.quascirev.2006.07.005

Skonieczny, C., Bory, A., Bout-Roumazeilles, V., Abouchami, W., Galer, S. J. G., Crosta, X., Diallo, A., & Ndiaye, T. (2013). A three-year time series of mineral dust deposits on the West African margin: Sedimentological and geochemical signatures and implications for interpretation of marine paleo-dust records. Earth and Planetary Science Letters, 364, 145–156. https://doi.org/10.1016/j.epsl.2012.12.039

Skov, L., Peyrégne, S., Popli, D., Iasi, L. N. M., Devièse, T., Slon, V., Zavala, E. I., Hajdinjak, M., Sümer, A. P., Grote, S., Bossoms Mesa, A., López Herráez, D., Nickel, B., Nagel, S., Richter, J., Essel, E., Gansauge, M., Schmidt, A., Korlević, P., … Peter, B. M. (2022). Genetic insights into the social organization of Neanderthals. Nature, 610(7932), 519–525. https://doi.org/10.1038/s41586-022-05283-y

Slimak, L. (2008). The Neronian and the historical structure of cultural shifts from Middle to Upper Palaeolithic in Mediterranean France. Journal of Archaeological Science, 35(8), 2204–2214. https://doi.org/10.1016/j.jas.2008.02.005

Slimak, L. (2019). For a cultural anthropology of the last Neanderthals. Quaternary Science Reviews, 217, 330–339. https://doi.org/10.1016/j.quascirev.2018.12.019

Slimak, L., & Nicholson, C. (2020). Cannibals in the forest: A comment on Defleur and Desclaux (2019). Journal of Archaeological Science, 117, 105034. https://doi.org/10.1016/j.jas.2019.105034

Slimak, L., Zanolli, C., Higham, T., Frouin, M., Schwenninger, J.-L., Arnold, L. J., Demuro, M., Douka, K., Mercier, N., Guérin, G., Valladas, H., Yvorra, P., Giraud, Y., Seguin-Orlando, A., Orlando, L., Lewis, J. E., Muth, X., Camus, H., Vandevelde, S., … Metz, L. (2022). Modern human incursion into Neanderthal territories 54,000 years ago at Mandrin, France. Science Advances, 8(6), eabj9496. https://doi.org/10.1126/sciadv.abj9496

Slimak, L., Vimala, T., Seguin-Orlando, A., Metz, L., Zanolli, C., Joannes-Boyau, R., Frouin, M., Arnold, L. J., Demuro, M., Devièse, T., Comeskey, D., Buckley, M., Camus, H., Muth, X., Lewis, J. E., Bocherens, H., Yvorra, P., Tenailleau, C., Duployer, B., … Sikora, M. (2023). A late Neanderthal reveals genetic isolation in their populations before extinction (p. 2023.04.10.536015). bioRxiv. https://doi.org/10.1101/2023.04.10.536015

Slimak, L., Vimala, T., Seguin-Orlando, A., Metz, L., Zanolli, C., Joannes-Boyau, R., Frouin, M., Arnold, L. J., Demuro, M., Devièse, T., Comeskey, D., Buckley, M., Camus, H., Muth, X., Lewis, J. E., Bocherens, H., Yvorra, P., Tenailleau, C., Duployer, B., … Sikora, M. (2024). Long genetic and social isolation in Neanderthals before their extinction. Cell Genomics, 4(9). https://doi.org/10.1016/j.xgen.2024.100593

Smith, F. H., Ahern, J. C. M., Janković, I., & Karavanić, I. (2017). The Assimilation Model of modern human origins in light of current genetic and genomic knowledge. Quaternary International, 450, 126–136. https://doi.org/10.1016/j.quaint.2016.06.008

Smith, F., Janković, I., & Karavanić, I. (2005). The Assimilation Model, Modern Human Origins in Europe, and the Extinction of Neandertals. Quaternary International, 137, 7–19. https://doi.org/10.1016/j.quaint.2004.11.016

Sørensen, B. (2011). Demography and the extinction of European Neanderthals. Journal of Anthropological Archaeology, 30(1), 17–29. https://doi.org/10.1016/j.jaa.2010.12.003

Spikins, P., Needham, A., Wright, B., Dytham, C., Gatta, M., & Hitchens, G. (2019). Living to fight another day: The ecological and evolutionary significance of Neanderthal healthcare. Quaternary Science Reviews, 217, 98–118. https://doi.org/10.1016/j.quascirev.2018.08.011

Spinapolice, E. E., Zerboni, A., Meyer, M. C., Talamo, S., Mariani, G. S., Gliganic, L. A., Buti, L., Fusco, M., Maiorano, M. P., Silvestrini, S., Sorrentino, R., Vazzana, A., Romandini, M., Fiorini, A., Curci, A., & Benazzi, S. (2022). Back to Uluzzo – archaeological, palaeoenvironmental and chronological context of the Mid–Upper Palaeolithic sequence at Uluzzo C Rock Shelter (Apulia, southern Italy). Journal of Quaternary Science, 37(2), 217–234. https://doi.org/10.1002/jqs.3349

Stanley, E. A. (1966). The application of palynology to oceanology with reference to the northwestern Atlantic. Deep Sea Research and Oceanographic Abstracts, 13(5), 921–939. https://doi.org/10.1016/0011-7471(76)90911-6

Staubwasser, M., Drăguşin, V., Onac, B., Assonov, S., Ersek, V., Hoffmann, D., & Veres, D. (2018). Impact of climate change on the transition of Neanderthals to modern humans in Europe. Proceedings of the National Academy of Sciences, 115, 201808647. https://doi.org/10.1073/pnas.1808647115

Steegmann, A., Cerny, F., & Holliday, T. (2002). Neandertal cold adaptation: Physiological and energetic factors. American Journal of Human Biology : The Official Journal of the Human Biology Council, 14, 566–583. https://doi.org/10.1002/ajhb.10070

Stewart, J. R. (2004). Neanderthal–modern human competition? A comparison between the mammals associated with Middle and Upper Palaeolithic industries in Europe during OIS 3. International Journal of Osteoarchaeology, 14(34), 178–189. https://doi.org/10.1002/oa.754

Stewart, J. R. (2005). The ecology and adaptation of Neanderthals during the non-analogue environment of Oxygen Isotope Stage 3. Quaternary International, 137(1), 35–46. https://doi.org/10.1016/j.quaint.2004.11.018

Stewart, J. R., García-Rodríguez, O., Knul, M. V., Sewell, L., Montgomery, H., Thomas, M. G., & Diekmann, Y. (2019). Palaeoecological and genetic evidence for Neanderthal power locomotion as an adaptation to a woodland environment. Quaternary Science Reviews, 217, 310–315. https://doi.org/10.1016/j.quascirev.2018.12.023

Stocker, T. F. (1998). The Seesaw Effect. Science, 282(5386), 61–62. https://doi.org/10.1126/science.282.5386.61

Stoll, H. M., Cacho, I., Gasson, E., Sliwinski, J., Kost, O., Moreno, A., Iglesias, M., Torner, J., Perez-Mejias, C., Haghipour, N., Cheng, H., & Edwards, R. L. (2022). Rapid northern hemisphere ice sheet melting during the penultimate deglaciation. Nature Communications, 13(1), 3819. https://doi.org/10.1038/s41467-022-31619-3

Straus, L. G. (2022). Neanderthal last stand? Thoughts on Iberian refugia in late MIS 3. Journal of Quaternary Science, 37(2), 283–290. https://doi.org/10.1002/jqs.3252

Stringer, C. B., Finlayson, J. C., Barton, R. N. E., Fernández-Jalvo, Y., Cáceres, I., Sabin, R. C., Rhodes, E. J., Currant, A. P., Rodríguez-Vidal, J., Giles-Pacheco, F., & Riquelme-Cantal, J. A. (2008). Neanderthal exploitation of marine mammals in Gibraltar. Proceedings of the National Academy of Sciences, 105(38), 14319–14324. https://doi.org/10.1073/pnas.0805474105

Stringer, C., & Crété, L. (2022). Mapping Interactions of H. neanderthalensis and Homo sapiens from the Fossil and Genetic Records. PaleoAnthropology, 2022(2). https://doi.org/10.48738/2022.iss2.130

Stringer, C., Palike, H., Van Andel, T., Huntley, B., Valdes, P., & Allen, J. (2004). Climatic Stress and the Extinction of the Neanderthals. In T. Van Andel & W. Davies (Eds.), Neanderthals and Modern Humans in the European Landscape During the Last Glaciation: Archaeological Results of the Stage 3 Project (pp. 233–240). McDonald Institute for Archaeological Research, University of Cambridge.

Subally, D., & Quézel, P. (2002). Glacial or interglacial: Artemisia, a plant indicator with dual responses. Review of Palaeobotany and Palynology, 120(1), 123–130. https://doi.org/10.1016/S0034-6667(01)00143-9

Sümer, A. P., Rougier, H., Villalba-Mouco, V., Huang, Y., Iasi, L. N. M., Essel, E., Bossoms Mesa, A., Furtwaengler, A., Peyrégne, S., de Filippo, C., Rohrlach, A. B., Pierini, F., Mafessoni, F., Fewlass, H., Zavala, E. I., Mylopotamitaki, D., Bianco, R. A., Schmidt, A., Zorn, J., … Krause, J. (2025). Earliest modern human genomes constrain timing of Neanderthal admixture. Nature, 638(8051), 711–717. https://doi.org/10.1038/s41586-024-08420-x

Sumner, G., Homar, V., & Ramis, C. (2001). Precipitation seasonality in eastern and southern coastal Spain. International Journal of Climatology, 21(2), 219–247. https://doi.org/10.1002/joc.600

Svendsen, J. I., Alexanderson, H., Astakhov, V. I., Demidov, I., Dowdeswell, J. A., Funder, S., Gataullin, V., Henriksen, M., Hjort, C., Houmark-Nielsen, M., Hubberten, H. W., Ingólfsson, Ó., Jakobsson, M., Kjær, K. H., Larsen, E., Lokrantz, H., Lunkka, J. P., Lysså, A., Mangerud, J., … Stein, R. (2004). Late Quaternary ice sheet history of northern Eurasia. Quaternary Science Reviews, 23(11), 1229–1271. https://doi.org/10.1016/j.quascirev.2003.12.008

Svensson, A., Andersen, K. K., Bigler, M., Clausen, H. B., Dahl-Jensen, D., Davies, S. M., Johnsen, S. J., Muscheler, R., Parrenin, F., Rasmussen, S. O., Röthlisberger, R., Seierstad, I., Steffensen, J. P., & Vinther, B. M. (2008). A 60 000 year Greenland stratigraphic ice core chronology. Climate of the Past, 4(1), 47–57. https://doi.org/10.5194/cp-4-47-2008

Talamo, S., Aldeias, V., Goldberg, P., Chiotti, L., Dibble, H. L., Guérin, G., Hublin, J.-J., Madelaine, S., Maria, R., Sandgathe, D., Steele, T. E., Turq, A., & Mcpherron, S. J. P. (2020). The new 14C chronology for the Palaeolithic site of La Ferrassie, France: The disappearance of Neanderthals

and the arrival of Homo sapiens in France. Journal of Quaternary Science, 35(7), 961–973. https://doi.org/10.1002/jqs.3236

Talamo, S., Soressi, M., Roussel, M., Richards, M., & Hublin, J.-J. (2012). A radiocarbon chronology for the complete Middle to Upper Palaeolithic transitional sequence of Les Cottés (France). Journal of Archaeological Science, 39(1), 175–183. https://doi.org/10.1016/j.jas.2011.09.019

Tarasov, P., Cheddadi, R., Joel, G., Bottema, S., Peyron, O., Belmonte, J., Ruiz-Sanchez, V., Saadi, F., & Brewer, S. (1998). A method to determine warm and cool steppe biomes from pollen data; application to the Mediterranean and Kazakhstan Regions. Journal of Quaternary Science, 13, 335. https://doi.org/10.1002/(SICI)1099-1417(199807/08)13:43.3.CO;2-1

ter Braak, C., & Juggins, S. (1993). Weighted Averaging Partial Least Squares Regression (WA-PLS): An Improved Method for Reconstructing Environmental Variables from Species Assemblages. Hydrobiologia, 269–270, 485–502. https://doi.org/10.1007/BF00028046

Terradillos-Bernal, M., Demuro, M., Arnold, L. J., Jordá-Pardo, J. F., Clemente-Conte, I., Benito-Calvo, A., & Díez Fernández-Lomana, J. C. (2023). San Quirce (Palencia, Spain): New chronologies for the Lower to Middle Palaeolithic transition of south-west Europe. Journal of Quaternary Science, 38(1), 21–37. https://doi.org/10.1002/jqs.3460

Terradillos-Bernal, M., Díez Fernández-Lomana, J. C., Jordá Pardo, J.-F., Benito-Calvo, A., Clemente, I., & Marcos-Sáiz, F. J. (2017). San Quirce (Palencia, Spain). A Neanderthal open air campsite with short term-occupation patterns. Quaternary International, 435, 115–128. https://doi.org/10.1016/j.quaint.2015.09.082

Teyssandier, N. (2024). Us and Them: How to Reconcile Archaeological and Biological Data at the Middle-to-Upper Palaeolithic Transition in Europe? Journal of Paleolithic Archaeology, 7(1), 1. https://doi.org/10.1007/s41982-023-00166-8

Thabet, A. A., Maas, A. E., Lawson, G. L., & Tarrant, A. M. (2015). Life cycle and early development of the thecosomatous pteropod Limacina retroversa in the Gulf of Maine, including the effect of elevated CO2 levels. Marine Biology, 162(11), 2235–2249. https://doi.org/10.1007/s00227-015-2754-1

Till, C., & Guiot, J. (1990). Reconstruction of precipitation in Morocco since 1100 A.D. Based on Cedrus atlantica tree-ring widths. Quaternary Research, 33(3), 337–351. https://doi.org/10.1016/0033-5894(90)90060-X

Timmermann, A. (2020). Quantifying the potential causes of Neanderthal extinction: Abrupt climate change versus competition and interbreeding. Quaternary Science Reviews, 238, 1–14.

Tjallingii, R., Claussen, M., Stuut, J.-B. W., Fohlmeister, J., Jahn, A., Bickert, T., Lamy, F., & Röhl, U. (2008). Coherent high- and low-latitude control of the northwest African hydrological balance. Nature Geoscience, 1(10), 670–675. https://doi.org/10.1038/ngeo289

Torres, C., Tapias, F., Demuro, M., Arnold, L., Arriolabengoa, M., Pérez, S., & Preysler, J. (2024). The Acheulian site of Cantera Vieja (Madrid, Spain) and the Lower to Middle Palaeolithic transition in central Spain. https://doi.org/10.21203/rs.3.rs-4195503/v1

Toti, F., Bertini, A., Girone, A., Marino, M., Maiorano, P., Bassinot, F., Combourieu-Nebout, N., Nomade, S., & Buccianti, A. (2020). Marine and terrestrial climate variability in the western

Mediterranean Sea during marine isotope stages 20 and 19. Quaternary Science Reviews, 243, 106486. https://doi.org/10.1016/j.quascirev.2020.106486

Toucanne, S., Naughton, F., Rodrigues, T., Vázquez-Riveiros, N., & Sánchez Goñi, M. F. (2022). Abrupt (or millennial or suborbital) climatic variability: Heinrich events/stadials. In European Glacial Landscapes (pp. 181–187). Elsevier. https://doi.org/10.1016/B978-0-12-823498-3.00062-5

Toucanne, S., Zaragosi, S., Bourillet, J. F., Cremer, M., Eynaud, F., Van Vliet-Lanoë, B., Penaud, A., Fontanier, C., Turon, J. L., & Cortijo, E. (2009). Timing of massive 'Fleuve Manche' discharges over the last 350kyr: Insights into the European ice-sheet oscillations and the European drainage network from MIS 10 to 2. Quaternary Science Reviews, 28(13–14), 1238–1256. https://doi.org/10.1016/j.quascirev.2009.01.006

Trájer, A. J. (2023). Ecological evaluation of the development of Neanderthal niche exploitation. Quaternary Science Reviews, 310, 108127. https://doi.org/10.1016/j.quascirev.2023.108127

Trigo, R. M., Barriopedro, D., Garrido-Perez, J. M., Simon, A., Plecha, S. M., Teles-Machado, A., Russo, A., & Garcia-Herrera, R. (2025). The outstanding European and Mediterranean heatwave activity during summer 2022. Atmospheric Research, 323, 108195. https://doi.org/10.1016/j.atmosres.2025.108195

Trigo, R. M., Osborn, T. J., & Corte-Real, J. M. (2002). The North Atlantic Oscillation influence on Europe: Climate impacts and associated physical mechanisms. Climate Research, 20, 9–17. https://doi.org/10.3354/cr020009

Trigo, R. M., Pozo-Vázquez, D., Osborn, T. J., Castro-Díez, Y., Gámiz-Fortis, S., & Esteban-Parra, M. J. (2004). North Atlantic oscillation influence on precipitation, river flow and water resources in the Iberian Peninsula. International Journal of Climatology, 24(8), 925–944. https://doi.org/10.1002/joc.1048

Tzedakis, C. (2005). Towards an understanding of the response of southern European vegetation to orbital and suborbital climate variability. Quaternary Science Reviews, 24, 1585–1599. https://doi.org/10.1016/j.quascirev.2004.11.012

Tzedakis, P. C. (1993). Long-term tree populations in northwest Greece through multiple Quaternary climatic cycles. Nature, 364(6436), 437–440. https://doi.org/10.1038/364437a0

Tzedakis, P. C. (1999). The last climatic cycle at Kopais, central Greece. Journal of the Geological Society, 156(2), 425–434. https://doi.org/10.1144/gsjgs.156.2.0425

Tzedakis, P. C., Drysdale, R. N., Margari, V., Skinner, L. C., Menviel, L., Rhodes, R. H., Taschetto, A. S., Hodell, D. A., Crowhurst, S. J., Hellstrom, J. C., Fallick, A. E., Grimalt, J. O., McManus, J. F., Martrat, B., Mokeddem, Z., Parrenin, F., Regattieri, E., Roe, K., & Zanchetta, G. (2018). Enhanced climate instability in the North Atlantic and southern Europe during the Last Interglacial. Nature Communications, 9(1), Article 1. https://doi.org/10.1038/s41467-018-06683-3

Tzedakis, P. C., Frogley, M. R., & Heaton, T. H. E. (2003). Last Interglacial conditions in southern Europe: Evidence from Ioannina, northwest Greece. Global and Planetary Change, 36(3), 157–170. https://doi.org/10.1016/S0921-8181(02)00182-0

Tzedakis, P. C., Frogley, M. R., Lawson, I. T., Preece, R. C., Cacho, I., & de Abreu, L. (2004). Ecological thresholds and patterns of millennial-scale climate variability: The response of vegetation in Greece during the last glacial period. Geology, 32, 109. https://doi.org/10.1130/G20118.1

Tzedakis, P. C., Hooghiemstra, H., & Pälike, H. (2006). The last 1.35 million years at Tenaghi Philippon: Revised chronostratigraphy and long-term vegetation trends. Quaternary Science Reviews, 25(23), 3416–3430. https://doi.org/10.1016/j.quascirev.2006.09.002

Tzedakis, P. C., Hughen, K. A., Cacho, I., & Harvati, K. (2007). Placing late Neanderthals in a climatic context. Nature, 449(7159), 206–208. https://doi.org/10.1038/nature06117

Tzedakis, P. C., Lawson, I. T., Frogley, M. R., Hewitt, G. M., & Preece, R. C. (2002). Buffered Tree Population Changes in a Quaternary Refugium: Evolutionary Implications. Science, 297(5589), 2044–2047. https://doi.org/10.1126/science.1073083

Vaesen, K., Dusseldorp, G. L., & Brandt, M. J. (2021). An emerging consensus in palaeoanthropology: Demography was the main factor responsible for the disappearance of Neanderthals. Scientific Reports, 11(1), 4925. https://doi.org/10.1038/s41598-021-84410-7

Valensi, P., Aouraghe, H., Bailon, S., Cauche, D., Combier, J., Desclaux, E., Gagnepain, J., Gaillard, C., Khatib, S., Lumley, H., Moigne, A.-M., Moncel, M.-H., & Notter, O. (2005). Les peuplements préhistoriques dans le sud-est de la France à la fin du Pléistocène moyen: 400 - 120 000 ans. Terra Amata, Orgnac 3, Baume Bonne, Lazaret. Cadre géochronologique et biostratigraphique, paléoenvironnements et évolution culturelle des derniers anténéandertaliens. (Vol. 1352).

Valensi, P., Michel, V., El Guennouni, K., & Liouville, M. (2013). New data on human behavior from a 160,000 year old Acheulean occupation level at Lazaret cave, south-east France: An archaeozoological approach. Quaternary International, 316. https://doi.org/10.1016/j.quaint.2013.10.034

Valet, J.-P., & Valladas, H. (2010). The Laschamp-Mono lake geomagnetic events and the extinction of Neanderthal: A causal link or a coincidence? Quaternary Science Reviews, 29(27), 3887–3893. https://doi.org/10.1016/j.quascirev.2010.09.010

Vallini, L., Marciani, G., Aneli, S., Bortolini, E., Benazzi, S., Pievani, T., & Pagani, L. (2022). Genetics and Material Culture Support Repeated Expansions into Paleolithic Eurasia from a Population Hub Out of Africa. Genome Biology and Evolution, 14(4), evac045. https://doi.org/10.1093/gbe/evac045

Vallini, L., Zampieri, C., Shoaee, M. J., Bortolini, E., Marciani, G., Aneli, S., Pievani, T., Benazzi, S., Barausse, A., Mezzavilla, M., Petraglia, M. D., & Pagani, L. (2024). The Persian plateau served as hub for Homo sapiens after the main out of Africa dispersal. Nature Communications, 15(1), 1882. https://doi.org/10.1038/s41467-024-46161-7

van Geel, B. (1998). A study of non-pollen objects in pollen slides. Npp Key.

Van Geel, B. (2001). Non-Pollen Palynomorphs. In J. P. Smol, H. J. B. Birks, & W. M. Last (Eds.), Tracking Environmental Change Using LakeSediments.: Vol. Volume 3 (pp. 0–18). Kluwer Academic Publishers. https://doi.org/10.1007/0-306-47668-1

Vanhaeren, M., & d'Errico, F. (2006). Aurignacian ethno-linguistic geography of Europe revealed by personal ornaments. Journal of Archaeological Science, 33(8), 1105–1128. https://doi.org/10.1016/j.jas.2005.11.017

Vaquero, M. (2006). El tránsito Paleolítico Medio/Superior en la Península Ibérica y la Frontera del Ebro. Comentario a Zilhao (2006). Pyrenae, 37.

Vaquero, M., Maroto, J., Arrizabalaga, A., Preysler, J., Baquedano, E., Carrión, E., Jordá Pardo, J., Martinón, M., Menendez, M., Montes-Barquín, R., & Rosell Ardèvol, J. (2006). The neanderthal-modern human meeting in Iberia: A critical view of the cultural, geographical and chronological data. https://doi.org/10.13140/2.1.1697.1049

Vargas-Yáñez, M., Plaza, F., García-Lafuente, J., Sarhan, T., Vargas, J. M., & Vélez-Belchi, P. (2002). About the seasonal variability of the Alboran Sea circulation. Journal of Marine Systems, 35(3), 229–248. https://doi.org/10.1016/S0924-7963(02)00128-8

Vautard, R., Yiou, P., D'Andrea, F., de NOBLET, N., Viovy, N., Cassou, C., Polcher, J., Ciais, P., Kageyama, M., & Fan, Y. (2007). Summertime European heat and drought waves induced by wintertime Mediterranean rainfall deficit. Geophysical Research Letters, 34. https://doi.org/10.1029/2006gl028001

Vegas, J., García-Cortés, Á., Galán, L., Pérez-González, A., & Martín-Serrano, A. (2006). The lacustrine sedimentary record of the Fuentillejo Maar (Ciudad Real, Spain). Boletin Geologico y Minero, 117, 339–349.

Vegas, J., Ruiz-Zapata, B., Ortiz, J. E., Galán, L., Torres, T., García-Cortés, Á., Gil-García, M. J., Pérez-González, A., & Gallardo-Millán, J. L. (2010). Identification of arid phases during the last 50 cal. Ka BP from the Fuentillejo maar-lacustrine record (Campo de Calatrava Volcanic Field, Spain). Journal of Quaternary Science, 25(7), 1051–1062. https://doi.org/10.1002/jqs.1262

Verlaque, R., Médail, F., Quézel, P., & Babinot, J.-F. (1997). Endémisme végétal et paléogéographie dans le Bassin Méditerranéen. Geobios, 30, 159–166. https://doi.org/10.1016/S0016-6995(97)80083-6

Vernot, B., Zavala, E. I., Gómez-Olivencia, A., Jacobs, Z., Slon, V., Mafessoni, F., Romagné, F., Pearson, A., Petr, M., Sala, N., Pablos, A., Aranburu, A., de Castro, J. M. B., Carbonell, E., Li, B., Krajcarz, M. T., Krivoshapkin, A. I., Kolobova, K. A., Kozlikin, M. B., … Meyer, M. (2021). Unearthing Neanderthal population history using nuclear and mitochondrial DNA from cave sediments. Science (New York, N.Y.), 372(6542), eabf1667. https://doi.org/10.1126/science.abf1667

Vidal-Cordasco, M., Ocio, D., Hickler, T., & Marín-Arroyo, A. B. (2022). Ecosystem productivity affected the spatiotemporal disappearance of Neanderthals in Iberia. Nature Ecology & Evolution, 6(11), Article 11. https://doi.org/10.1038/s41559-022-01861-5

Vidal-Cordasco, M., & Marín-Arroyo, A. B. (2025). Novel dynamics of human-carnivore interactions linked to the arrival of *H. sapiens* in Europe. *Science Bulletin*. https://doi.org/10.1016/j.scib.2025.11.055

Vidal-Matutano, P., Blasco, R., Sañudo, P., & Fernández Peris, J. (2019). The Anthropogenic Use of Firewood During the European Middle Pleistocene: Charcoal Evidence from Levels XIII and XI of Bolomor Cave, Eastern Iberia (230–160 ka). Environmental Archaeology, 24(3), 269–284. https://doi.org/10.1080/14614103.2017.1406026

Villa, P. (2009). Discussion 3: The Lower to Middle Paleolithic transition. In Sourcebook of Paleolithic Transitions (pp. 265–270). https://doi.org/10.1007/978-0-387-76487-0_17

Villa, P., & Roebroeks, W. (2014). Neandertal Demise: An Archaeological Analysis of the Modern Human Superiority Complex. PLOS ONE, 9(4), e96424. https://doi.org/10.1371/journal.pone.0096424

Villa, P., Soriano, S., Pollarolo, L., Smriglio, C., Gaeta, M., D'Orazio, M., Conforti, J., & Tozzi, C. (2020). Neandertals on the beach: Use of marine resources at Grotta dei Moscerini (Latium, Italy). PLOS ONE, 15(1), e0226690. https://doi.org/10.1371/journal.pone.0226690

Villaverde, V., Real, C., Roman, D., Albert, R., Badal, E., Bel, M. Á., Bergadà, M., Oliveira, P., Eixea, A., Esteban, I., Martínez-Alfaro, Á., Martínez Varea, C., & PérEZ-riPoll, M. (2017). The Early Upper Palaeolithic of Cova de les Cendres. Quaternary International, 515. https://doi.org/10.1016/j.quaint.2017.11.051

Villaverde, V., Sanchis, A., Badal, E., Bel, M. Á., Bergadà, M. M., Eixea, A., Guillem, P. M., Martínez-Alfaro, Á., Martínez-Valle, R., Martínez-Varea, C. M., Real, C., Steier, P., & Wild, E. M. (2021). Cova de les Malladetes (Valencia, Spain): New Insights About the Early Upper Palaeolithic in the Mediterranean Basin of the Iberian Peninsula. Journal of Paleolithic Archaeology, 4(1), 5. https://doi.org/10.1007/s41982-021-00081-w

Vishnevskiy, A. V., Pavlenok, K. K., Kozlikin, M. B., Ulyanov, V. A., Derevianko, A. P., & Shunkov, M. V. (2019). A Neanderthal Refugium in the Eastern Adriatic. Archaeology, Ethnology & Anthropology of Eurasia, 47(4), Article 4. https://doi.org/10.17746/1563-0110.2019.47.4.003-015

Voelker, Antje H. L., and Lucia de Abreu. (2011). 'A Review of Abrupt Climate Change Events in the Northeastern Atlantic Ocean (Iberian Margin): Latitudinal, Longitudinal, and Vertical Gradients'. In *Abrupt Climate Change: Mechanisms, Patterns, and Impacts*, American Geophysical Union (AGU), 15–37. https://doi:10.1029/2010GM001021

von Grafenstein, R., Zahn, R., & Tiedemann, R. (1999). Planktonic d18O records at Sites 976 and 977, Alboran Sea: Stratigraphy, forcing, and paleoceanographic implications. In Curry, W.B., Shackleton, N.J., and Richter, C. Proceedings Ocean Drilling Program Scientific Results, 154, 299–318.

Wagner, B., Vogel, H., Francke, A., Friedrich, T., Donders, T., Lacey, J. H., Leng, M. J., Regattieri, E., Sadori, L., Wilke, T., Zanchetta, G., Albrecht, C., Bertini, A., Combourieu-Nebout, N., Cvetkoska, A., Giaccio, B., Grazhdani, A., Hauffe, T., Holtvoeth, J., … Zhang, X. (2019). Mediterranean winter rainfall in phase with African monsoons during the past 1.36 million years. Nature, 573(7773), 256–260. https://doi.org/10.1038/s41586-019-1529-0

Wainer, K., Genty, D., Blamart, D., Bar-Matthews, M., Quinif, Y., & Plagnes, V. (2013). Millennial climatic instability during penultimate glacial period recorded in a south-western France speleothem. Palaeogeography, Palaeoclimatology, Palaeoecology, 376, 122–131. https://doi.org/10.1016/j.palaeo.2013.02.026

Wainer, K., Genty, D., Blamart, D., Daëron, M., Bar-Matthews, M., Vonhof, H., Dublyansky, Y., Pons-Branchu, E., Thomas, L., Calsteren, P., Quinif, Y., & Caillon, N. (2011). Speleothem record of the last 180 ka in Villars cave (SW France): Investigation of a large δ 18O shift between MIS6 and MIS5. Quaternary Science Reviews - QUATERNARY SCI REV, 30, 130–146. https://doi.org/10.1016/j.quascirev.2010.07.004

Walker, M., Johnsen, S., Rasmussen, S. O., Popp, T., Steffensen, J.-P., Gibbard, P., Hoek, W., Lowe, J., Andrews, J., Björck, S., Cwynar, L. C., Hughen, K., Kershaw, P., Kromer, B., Litt, T., Lowe, D. J., Nakagawa, T., Newnham, R., & Schwander, J. (2009). Formal definition and dating of the GSSP (Global Stratotype Section and Point) for the base of the Holocene using the Greenland NGRIP ice core, and selected auxiliary records. Journal of Quaternary Science, 24(1), 3–17. https://doi.org/10.1002/jqs.1227

Wang, Q., Wang, Y., Shao, Q., Liang, Y., Zhang, Z., & Kong, X. (2018). Millennial-scale Asian monsoon variability during the late Marine Isotope Stage 6 from Hulu Cave, China. Quaternary Research, 90(2), 394–405. https://doi.org/10.1017/qua.2018.75

Wang, Y., Cheng, H., Edwards, R. L., Kong, X., Shao, X., Chen, S., Wu, J., Jiang, X., Wang, X., & An, Z. (2008). Millennial- and orbital-scale changes in the East Asian monsoon over the past 224,000 years. Nature, 451(7182), 1090–1093. https://doi.org/10.1038/nature06692

Wang, Y. J., Cheng, H., Edwards, R. L., An, Z. S., Wu, J. Y., Shen, C. C., & Dorale, J. A. (2001). A high-resolution absolute-dated late Pleistocene Monsoon record from Hulu Cave, China. Science (New York, N.Y.), 294(5550), 2345–2348. https://doi.org/10.1126/science.1064618

Wary, M., Eynaud, F., Kissel, C., Londeix, L., Rossignol, L., Lapuyade, J., Castéra, M.-H., & Billy, I. (2018). Spatio-temporal dynamics of hydrographic reorganizations and iceberg discharges at the junction between the Northeast Atlantic and Norwegian Sea basins surrounding Heinrich event 4. Earth and Planetary Science Letters, 481, 236–245. https://doi.org/10.1016/j.epsl.2017.10.042

Watts, W. (1996). Vegetation history and palaeoclimate of the last glacial period of Lago Grande di Monticchio, southern Italy. Quaternary Science Reviews, 15(2–3), 133.

Weaver, A. J., Saenko, O. A., Clark, P. U., & Mitrovica, J. X. (2003). Meltwater Pulse 1A from Antarctica as a Trigger of the Bølling-Allerød Warm Interval. Science, 299(5613), 1709–1713. https://doi.org/10.1126/science.1081002

Wei, T., Simko, V., Levy, M., Xie, Y., Jin, Y., Zemla, J., Freidank, M., Cai, J., & Protivinsky, T. (2024). corrplot: Visualization of a Correlation Matrix (Version 0.95) [Computer software]. https://cran.r-project.org/web/packages/corrplot/index.html

Weinelt, M., Rosell-Melé, A., Pflaumann, U., Sarnthein, M., & Kiefer, T. (2003). The role of productivity in the Northeast Atlantic on abrupt climate change over the last 80,000 years. Zeitschrift Der Deutschen Geologischen Gesellschaft, 154, 47–66. https://doi.org/10.1127/zdgg/154/2003/47

Weiss, M., Hein, M., Urban, B., Stahlschmidt, M., Heinrich, S., Hilbert, Y., Power, R., Suchodoletz, H., Terberger, T., Böhner, U., Klimscha, F., Veil, S., Breest, K., Schmidt, J., Colarossi, D., Tucci, M., Frechen, M., Tanner, D., & Lauer, T. (2022). Neanderthals in changing environments from MIS 5 to early MIS 4 in northern Central Europe – Integrating archaeological, (chrono)stratigraphic and paleoenvironmental evidence at the site of Lichtenberg. Quaternary Science Reviews, 284. https://doi.org/10.1016/j.quascirev.2022.107519

Wendt, K. A., Häuselmann, A. D., Fleitmann, D., Berry, A. E., Wang, X., Auler, A. S., Cheng, H., & Edwards, R. L. (2019). Three-phased Heinrich Stadial 4 recorded in NE Brazil stalagmites. Earth and Planetary Science Letters, 510, 94–102. https://doi.org/10.1016/j.epsl.2018.12.025

Weniger, G.-C., Kranz Bartz, M., Blumenröther, J., Bolin, V., Brückner, H., De Andrés-Herrero, M., Kehl, M., Klein, K., Linstädter, J., Otto, T., Potì, A.-S., Rotgänger, M., Val-Peón, C., Tafelmaier, Y., & Reicherter, K. (2025). 5 The Westernmost Mediterranean (pp. 205–268).

Wenzel, S. (2007). Neanderthal presence and behaviour in central and Northwestern Europe during MIS 5e. In Developments in Quaternary Sciences (pp. 173–193). https://doi.org/10.13140/2.1.2747.7442

White, M. J., & Pettitt, P. B. (2011). The British Late Middle Palaeolithic: An Interpretative Synthesis of Neanderthal Occupation at the Northwestern Edge of the Pleistocene World. Journal of World Prehistory, 24(1). https://doi.org/10.1007/s10963-011-9043-9

Wiel, K., Bloomfield, H., Lee, R., Stoop, L., Blackport, R., Screen, J., & Selten, F. (2019). The influence of weather regimes on European renewable energy production and demand. Environmental Research Letters. https://doi.org/10.1088/1748-9326/ab38d3

Willis, K. J., Bennett, K. D., Walker, D., Gamble, C., Davies, W., Pettitt, P., & Richards, M. (2004). Climate change and evolving human diversity in Europe during the last glacial. Philosophical Transactions of the Royal Society of London. Series B: Biological Sciences, 359(1442), 243–254. https://doi.org/10.1098/rstb.2003.1396

Wilson, G. P., Frogley, M. R., Hughes, P. D., Roucoux, K. H., Margari, V., Jones, T. D., Leng, M. J., & Tzedakis, P. C. (2021). Persistent millennial-scale climate variability in Southern Europe during Marine Isotope Stage 6. Quaternary Science Advances, 3, 100016. https://doi.org/10.1016/j.qsa.2020.100016

Wohlfarth, B. (2013). A review of Early Weichselian climate (MIS 5d-a) in Europe.

Woillard, G. M. (1978). Grande Pile peat bog: A continuous pollen record for the last 140,000 years. Quaternary Research, 9(1), 1–21. https://doi.org/10.1016/0033-5894(78)90079-0

Wolf, D., Kolb, T., Alcaraz-Castaño, M., Heinrich, S., Baumgart, P., Calvo, R., Sánchez, J., Ryborz, K., Schäfer, I., Bliedtner, M., Zech, R., Zöller, L., & Faust, D. (2018). Climate deteriorations and Neanderthal demise in interior Iberia. Scientific Reports, 8(1), 7048. https://doi.org/10.1038/s41598-018-25343-6

Wood, R. E., Arrizabalaga, A., Camps, M., Fallon, S., Iriarte-Chiapusso, M.-J., Jones, R., Maroto, J., de la Rasilla, M., Santamaría, D., Soler, J., Soler, N., Villaluenga, A., & Higham, T. F. G. (2014). The chronology of the earliest Upper Palaeolithic in northern Iberia: New insights from L'Arbreda, Labeko Koba and La Viña. Journal of Human Evolution, 69, 91–109. https://doi.org/10.1016/j.jhevol.2013.12.017

Wood, R. E., Barroso-Ruíz, C., Caparrós, M., Jordá Pardo, J. F., Galván Santos, B., & Higham, T. F. G. (2013). Radiocarbon dating casts doubt on the late chronology of the Middle to Upper Palaeolithic transition in southern Iberia. Proceedings of the National Academy of Sciences, 110(8), 2781–2786. https://doi.org/10.1073/pnas.1207656110

Wood, R. E., Douka, K., Boscato, P., Haesaerts, P., Sinitsyn, A., & Higham, T. F. G. (2012). Testing the ABOx-SC method: Dating known-age charcoals associated with the Campanian Ignimbrite. Quaternary Geochronology, 9, 16–26. https://doi.org/10.1016/j.quageo.2012.02.003

Wroe, S., Parr, W. C. H., Ledogar, J. A., Bourke, J., Evans, S. P., Fiorenza, L., Benazzi, S., Hublin, J.-J., Stringer, C., Kullmer, O., Curry, M., Rae, T. C., & Yokley, T. R. (2018). Computer simulations

show that Neanderthal facial morphology represents adaptation to cold and high energy demands, but not heavy biting. Proceedings of the Royal Society B: Biological Sciences, 285(1876), 20180085. https://doi.org/10.1098/rspb.2018.0085

Wynn, T. (2009). Hafted spears and the archaeology of mind. Proceedings of the National Academy of Sciences, 106(24), 9544–9545. https://doi.org/10.1073/pnas.0904369106

Xiao, S., Li, S., Wang, X., Chen, L., & Su, T. (2022). Cedrus distribution change: Past, present, and future. Ecological Indicators, 142, 109159. https://doi.org/10.1016/j.ecolind.2022.109159

Xue, G., Cai, Y., Ma, L., Cheng, X., Cheng, H., Edwards, R. L., Li, D., & Tan, L. (2019). A new speleothem record of the penultimate deglacial: Insights into spatial variability and centennial-scale instabilities of East Asian monsoon. Quaternary Science Reviews, 210, 113–124. https://doi.org/10.1016/j.quascirev.2019.02.023

Yaworsky, P. M., Nielsen, E. S., & Nielsen, T. K. (2024). The Neanderthal niche space of Western Eurasia 145 ka to 30 ka ago. Scientific Reports, 14(1), 7788. https://doi.org/10.1038/s41598-024-57490-4

Yravedra, J., Diez-Martín, F., Sánchez-Yustos, P., Gómez, D., Díaz, I. M., & Gómez, J. A. (2013). Estrategias de subsistencia durante Paleolítico medio en la submeseta norte. La Cueva Corazón Mave, Palencia. Zephyrus, 71, 45–60.

Yravedra, J., Rubio-Jara, S., Panera, J., Made, J. van der, & Pérez-González, A. (2019). Neanderthal diet in fluvial environments at the end of the Middle Pleistocene/early Late Pleistocene of PRERESA site in the Manzanares Valley (Madrid, Spain). Quaternary International, 520, 72–83. https://doi.org/10.1016/j.quaint.2018.01.030

Zaghloul, M. N., Reddad, H., & Critelli, S. (2009). Source-area controls on the composition of beach and fluvial sands on the southern side of the Gibraltar Strait and Western Alboran Sea (Flysch Basin, Internal and External, Domains, Northern Rif Chain). Journal of African Earth Sciences, 55(1), 36–46. https://doi.org/10.1016/j.jafrearsci.2008.11.001

Zahn, R., Comas, M. C., & Klaus, A. (Eds.). (1999). Proceedings of the Ocean Drilling Program, 161 Scientific Results (Vol. 161). Ocean Drilling Program. https://doi.org/10.2973/odp.proc.sr.161.1999

Zaitchik, B. F., Rodell, M., Biasutti, M., & Seneviratne, S. I. (2023). Wetting and drying trends under climate change. Nature Water, 1(6), 502–513. https://doi.org/10.1038/s44221-023-00073-w

Zampieri, M., D'Andrea, F., Vautard, R., Ciais, P., de NOBLET, N., & Yiou, P. (2009). Hot European Summers and the Role of Soil Moisture in the Propagation of Mediterranean Drought. Journal of Climate, 22, 4747–4758. https://doi.org/10.1175/2009jcli2568.1

Zanchetta, G., Giaccio, B., Bini, M., & Sarti, L. (2018). Tephrostratigraphy of Grotta del Cavallo, Southern Italy: Insights on the chronology of Middle to Upper Palaeolithic transition in the Mediterranean. Quaternary Science Reviews, 182, 65–77. https://doi.org/10.1016/j.quascirev.2017.12.014

Zander, P. D., Böhl, D., Sirocko, F., Auderset, A., Haug, G. H., & Martínez-García, A. (2024). Reconstruction of warm-season temperatures in central Europe during the past 60 000 years from lacustrine branched glycerol dialkyl glycerol tetraethers (brGDGTs). Climate of the Past, 20(4), 841–864. https://doi.org/10.5194/cp-20-841-2024

Zhang, J., Zolitschka, B., Hogrefe, I., Tsukamoto, S., Binot, F., & Frechen, M. (2024). High-resolution luminescence-dated sediment record for the last two glacial-interglacial cycles from Rodderberg, Germany. Quaternary Geochronology, 82, 101535. https://doi.org/10.1016/j.quageo.2024.101535

Zhang, X., Qiu, W., Jiang, X., Cai, B., & Shen, C.-C. (2024). East Asian summer monsoon evolution during Heinrich Stadial 5. Palaeogeography, Palaeoclimatology, Palaeoecology, 654, 112467. https://doi.org/10.1016/j.palaeo.2024.112467

Zhu, D., Galbraith, E. D., Reyes-García, V., & Ciais, P. (2021). Global hunter-gatherer population densities constrained by influence of seasonality on diet composition. Nature Ecology & Evolution, 5(11), 1536–1545. https://doi.org/10.1038/s41559-021-01548-3

Ziegler, M., Tuenter, E., & Lourens, L. (2010). The precession phase of the boreal summer monsoon as viewed from the eastern Mediterranean (ODP Site 968). Quaternary Science Reviews, 29. https://doi.org/10.1016/j.quascirev.2010.03.011

Zilhão, J. (2000). The Ebro frontier: A model for the late extinction of Iberian Neanderthals. In Neanderthals on the Edge (pp. 111–121).

Zilhão, J. (2006). Chronostratigraphy of the Middle-to- Upper Paleolithic Transition in the Iberian Peninsula. Pyrenae.

Zilhão, J. (2012). Chapter 4—Personal Ornaments and Symbolism Among the Neanderthals. In S. Elias (Ed.), Developments in Quaternary Sciences (Vol. 16, pp. 35–49). Elsevier. https://doi.org/10.1016/B978-0-444-53821-5.00004-X

Zilhão, J. (2021a). The earliest Upper Paleolithic of Southern and Western Iberia is an Evolved, not an Early Aurignacian (pp. 52–71).

Zilhão, J. (2021b). The late persistence of the Middle Palaeolithic and Neandertals in Iberia: A review of the evidence for and against the “Ebro Frontier” model. Quaternary Science Reviews, 270, 107098. https://doi.org/10.1016/j.quascirev.2021.107098

Zilhão, J. (2022). Everything you always wanted to ask about the Lapa do Picareiro Aurignacian and should not be afraid to know: A reply to ‘The early Aurignacian at Lapa do Picareiro really is that old’. Quaternary Science Reviews, 277, 107296. https://doi.org/10.1016/j.quascirev.2021.107296

Zilhão, J., Anesin, D., Aubry, T., Badal, E., Cabanes, D., Kehl, M., Klasen, N., Lucena, A., Martín-Lerma, I., Martínez, S., Matias, H., Susini, D., Steier, P., Wild, E. M., Angelucci, D. E., Villaverde, V., & Zapata, J. (2017). Precise dating of the Middle-to-Upper Paleolithic transition in Murcia (Spain) supports late Neandertal persistence in Iberia. Heliyon, 3(11), e00435. https://doi.org/10.1016/j.heliyon.2017.e00435

Zilhão, J., Angelucci, D. E., Arnold, L. J., d’Errico, F., Dayet, L., Demuro, M., Deschamps, M., Fewlass, H., Gomes, L., Linscott, B., Matias, H., Pike, A. W. G., Steier, P., Talamo, S., & Wild, E. M. (2021). Revisiting the Middle and Upper Palaeolithic archaeology of Gruta do Caldeirão (Tomar, Portugal). PLOS ONE, 16(10), e0259089. https://doi.org/10.1371/journal.pone.0259089

Zilhão, J., Angelucci, D. E., Arnold, L. J., Demuro, M., Hoffmann, D. L., & Pike, A. W. G. (2021). A revised, Last Interglacial chronology for the Middle Palaeolithic sequence of Gruta da Oliveira (Almonda

karst system, Torres Novas, Portugal). Quaternary Science Reviews, 258, 106885. https://doi.org/10.1016/j.quascirev.2021.106885

Zilhão, J., Banks, W. E., d'Errico, F., & Gioia, P. (2015). Analysis of Site Formation and Assemblage Integrity Does Not Support Attribution of the Uluzzian to Modern Humans at Grotta del Cavallo. PLOS ONE, 10(7), e0131181. https://doi.org/10.1371/journal.pone.0131181

Zilhão, J., d'Errico, F., Banks, W. E., & Teyssandier, N. (2024). A Data-Driven Paradigm Shift for the Middle-to-Upper Palaeolithic Transition and the Neandertal Debate. Quaternary Environments and Humans, 100037. https://doi.org/10.1016/j.qeh.2024.100037

Zilio, L., Hammond, H., Karampaglidis, T., Sánchez-Romero, L., Blasco, R., Rivals, F., Rufà, A., Picin, A., Chacón, M. G., Demuro, M., Arnold, L. J., & Rosell, J. (2021). Examining Neanderthal and carnivore occupations of Teixoneres Cave (Moià, Barcelona, Spain) using archaeostratigraphic and intra-site spatial analysis. Scientific Reports, 11(1), 4339. https://doi.org/10.1038/s41598-021-83741-9

13. Suppléments

Tableau S1. Sites en Eurasie occidentale ayant livré des restes fossiles néandertaliens……..p.354

Tableau S2. Sites en Eurasie occidentale ayant livré des restes fossiles *Sapiens* plus vieux que 30 ka BP……..p.359

Tableau S3. Echantillons d'ODP 976 traités au laboratoire de palynologie de l'UMR 7194 au cours de cette thèse……..p.360

Tableau S4: Liste des datations de sites archéologiques du Paléolithique moyen et supérieur initial entre 50 et 30 ka BP……p.363

Fig. S1: Map of archaeological sites used in the dataset……..p.392

Fig. S2. Maps of archaeological sites and their associated technocomplexes with dates ranges falling before (A), during (B) and after (C) the HS4. Only radiocarbon dates with confidence index 1 and 2 were included……..p.393

Tableau S5. Sites archéologiques datés du Paléolithique moyen pendant le dernier cycle climatique dans la péninsule Ibérique……p.394

Fig. S3. Reconstructions climatiques à partir du pollen des paramètres d'été pour le MIS 6……p.406

Tableau S6. Sites archéologiques attribués au MIS 6 en Méditerranée occidentale……..p.407

Planches 1 à 11. Photographies microscopiques des principaux types (pollen et spores de ptéridophytes) identifiés au cours de l'étude de la carotte ODP 976……..p.411

Planches 12 à 17. Photographies microscopiques des principaux types de spores de champignons, d'algues, restes de foraminifères et autres palynomorphes non-identifiés……..p.422

Tableau S1: sites en Eurasie occidentale ayant livré des restes fossiles néandertaliens

N°	Site	Country	Lat.	Long.	MIS 6	MIS 5	MIS 4	MIS 3	Ref
1	Gibraltar (Devil's Tower)		36.12	-5.34				■	Bokelmann et al., 2019
2	Gibraltar (Forbes' Quarry)	Spain	36.12	-5.34		■	■		Bokelmann et al., 2019
3	Apidima	Greece	36.66	22.36	■				de Lumley et al., 2020
4	Kalamakia	Greece	36.68	22.36				■	Harvati et al., 2013
5	Lakonis cave	Greece	36.76	22.56				■	Starkovich et al., 2020
6	Zafarraya	Spain	36.95	-4.13				■	Michel et al, 2013
7	Cueva del Ángel	Spain	37.41	-4.42		■			Bermúdez et al., 2023
8	Carihuela	Spain	37.44	-3.43		■	■	■	Carrión et al., 2019b
9	Sima de las Palomas	Spain	37.80	-0.90				■	Walker et al., 2012, 2014
10	Archi	Italy	38.14	15.66		■			Rolfo et al., 2023
11	Figueira Brava	Portugal	38.47	-8.99		■			Telles Antunes and Santinho Cunha, 1992; Zilhão et al., 2020
12	El Salt	Spain	38.69	-0.51				■	Dolores Garralda et al., 2014
13	Bolomor	Spain	39.06	-0.25	■	■			Ochando et al., 2019
14	Gruta Nova da Columbeira	Portugal	39.30	-9.20				■	Carvalho et al., 2018
15	Gruta da Oliveira	Portugal	39.51	-8.61			■		Zilhão et al., 2021
16	Taddeo	Italy	40.00	15.37		■			Benazzi et al., 2011
17	Riparo del Molare	Italy	40.05	15.49		■			Ronchitelli, 2005; Spagnolo et al., 2020
18	Tossal de la Font	Spain	40.11	-0.05				■	Ollé et al., 2014
19	Grotta del Cavallo	Italy	40.16	17.96				■	Zanchetta et al., 2018; Fabbri et al., 2016
20	Altamura	Spain	40.87	16.59	■				Lari et al., 2015
21	Pinilla del Valle (Camino)	Spain	40.93	-3.82		■			Arsuaga et al., 2012
22	Pinilla del Valle (Des-cubierta)	Spain	40.93	-3.82				■	Martín-Perea et al., 2025
23	Pinilla del Valle (Buena Pinta)	Spain	40.93	-3.82				■	Blain et al., 2025
24	Los Casares	Spain	40.94	-2.29				■	Alcaraz-Castaño et al, 2017
25	Los Casares	Spain	40.94	-2.29				■	Alcaraz-Castaño et al., 2017
26	Jarama VI	Spain	40.97	-3.33				■	Navazo et al., 2020
27	Roccia San Sebastiano	Italy	41.14	13.88				■	Oxilia et al., 2022

28	Bisceglie (Grotta Santa Croce)	Italy	41.18	16.47			■	■	Rolfo et al., 2023
29	Cueva Foradada	Spain	41.20	1.58		■	■		Aparicio Pérez et al., 2014
30	Cova del Gegant	Spain	41.22	1.77			■	■	Daura et al., 2021
31	Grotta del Fossellone	Italy	41.23	13.10				■	Vitagliano and Bruno, 2012
32	Grotta Breuil	Italy	41.23	13.05				■	Tafuri et al., 2015
33	Grota Guattari	Italy	41.24	13.10			■		Rolfo et al., 2023
34	Abric Romani	Spain	41.53	1.69			■		Sharp et al., 2016
35	Cova Simanya	Spain	41.67	2.01				■	Morales et al., 2023
36	Teixoneres	Spain	41.81	2.10				■	Talamo et al., 2016
37	Cueva de los Moros de Gabasa	Spain	42.07	-0.14		■			Jaouen et al., 2022
38	Banyoles	Spain	42.11	2.77				■	Keeling et al., 2023
39	Atapuerca (Galeria de las Estatuas)	Spain	42.35	-3.52		■			Vernot et al., 2021
40	Grottoni di Calascio	Italy	42.47	14.41		■	■		Rolfo et al., 2023
41	Valdegoba	Spain	42.51	-3.76			■	■	Rodríguez-Gómez et al., 2022
42	Crvena Stijena	Montenegro	42.78	18.48			■	■	Morley et al., 2009
43	Le Noisetier	France	42.92	0.37				■	Minet et al. 2021
44	Bacho Kiro	Bulgaria	42.95	25.43			■		
45	Grotte du Portel-Ouest	France	42.98	1.40				■	Becam and Chevalier, 2019
46	Ramandils	France	43.00	3.03		■			Rusch et al, 2019
47	Arrillor	Spain	43.01	-2.74				■	Romero et al., 2022
48	Soulabe-las-Maretas	France	43.02	1.33		■			Maureille et al., 1999
49	Malarnaud	France	43.02	1.34		■			Mann and Vandermeersch, 1998
50	Prado Vargas	Spain	43.03	-3.63				■	Ruiz et al, 2021
51	Lezetxiki	Spain	43.08	-2.53	■			■	de la Rua et al., 2016; López-Onaindia et al., 2023
52	La Crouzade	France	43.13	3.08				■	Saos et al., 2020
53	Axlor	Spain	43.14	-2.75		■	■	■	Demuro et al., 2023
54	Pešturina	Serbia	43.17	21.90		■			Blackwell et al., 2014
55	Grotte du Coupe-Gorge	France	43.23	0.63	■				Thiam, 2021
56	El Castillo	Spain	43.29	-3.97			■	■	Garralda et al., 2023
57	El Sidron	Spain	43.38	-5.32				■	Wood et al., 2013
58	Covalejos	Spain	43.39	-3.93				■	Montes Barquín and Sanguino González, 2021
59	Kozarnika	Bulgaria	43.65	22.70	■				Tillier et al., 2017
60	Grotte du Lazaret	France	43.69	7.30	■				de Lumley et al., 2018
61	Grotte de l'Hortus	France	43.80	3.85				■	Williams et al., 2018

62	Baume des Peyrards	France	43.82	5.31		■	■		Crégut-Bonnoure et al., 2011
63	Madonna dell'Arma	Italy	43.83	7.83		■			Giacobini et al., 2022
64	Buca del Tasso	Italy	43.95	10.33				■	Gennai, 2024
65	Bau de l'Aubesier	France	44.14	5.34		■			Carmignani and Soressi, 2023
66	Caverna delle Fate	Italy	44.20	8.37		■	■		de Lumley and Giacobini, 2013
67	Arma delle Manie	Italy	44.20	8.38			■	■	Cauche, 2007
68	Rescoundudou	France	44.41	2.58		■			Jaubert and Maureille, 2008
69	Abri des Pêcheurs	France	44.41	4.21			■	■	Richard et al., 2021
70	Grotte Mandrin	France	44.47	4.77				■	Slimak et al. 2024
71	Sous-les Vignes	France	44.48	0.93				■	Valladas et al., 1999
72	Las Pélénos	France	44.50	0.93			■	■	Scolan et al., 2012
73	Payre	France	44.71	4.66	■				Valladas et al., 2008
74	Grotte Sirogne	France	44.80	1.65	■	■			Bayle et al., 2017
75	Grotte Vaufrey	France	44.80	1.20			■		Hernandez et al., 2014
76	Pech de l'Aze I	France	44.86	1.25				■	Soressi et al, 2007
77	Combe-Grenal	France	44.87	1.23			■		Garralda et al., 2022
78	Baume Néron	France	44.89	4.85				■	Defleur et al, 1992, 1994
79	Roc-de-Marsal	France	44.91	0.97			■	■	Wroth et al., 2019
80	Baume Moula-Guerçy	France	44.93	4.87		■			Richards et al., 2025
81	La Ferrassie	France	44.96	0.94				■	Balzeau et al., 2020
82	Chapelle-aux-Saints	France	45.00	1.73				■	Grün & Stringer, 1991
83	Le Moustier	France	45.00	1.07				■	Higham et al., 2014
84	Kiik-Koba	Ukraine	45.05	34.30		■	■		Trinkaus et al., 2008
85	Regourdou	France	45.06	1.18		■			Dodat et al., 2021
86	Jaurens	France	45.07	1.53		■			Bouvier, 1983
87	Grotta di San Bernardino	Italy	45.42	11.55				■	Vacca and Alciati, 2000
88	Grotta de Nadale	Italy	45.43	11.50			■		Nava et al., 2020
89	Jonzac (Chez Pinaud)	France	45.44	-0.42				■	Richards et al., 2008
90	Ca' Verde	Italy	45.46	10.75		■	■		Rolfo et al., 2023
91	Mezzena	Italy	45.48	10.99				■	Talamo et al., 2016
92	Riparo Broion	Italy	45.49	11.59				■	Romagnoli et al., 2022
93	La Quina	France	45.51	0.30			■	■	Verna et al., 2010
94	Riparo Tagliente	Italy	45.54	11.01			■	■	Arnaud et al., 2016
95	Contrada Ianni	Italy	45.57	7.99		■			Rolfo et al., 2023
96	Grotte Castaigne	France	45.59	0.20				■	Maureille et al., 2022
97	Grotta di Fumane	Italy	45.59	10.91				■	Benazzi et al., 2011
98	Petit-Puymoyen	France	45.61	0.18			■	■	Ready and Morin, 2019
99	Fontechevade	France	45.67	0.48				■	Chase et al., 2007
100	Abri Suard Bourgeois-Delaunay	France	45.67	0.47	■	■			Couture-Veschambre et al., 2021
101	Grotte de la Tour	France	45.67	0.46				■	Puymerail et al., 2012

102	Ciota Ciara	Italy	45.71	8.31		■			Buccheri et al., 2016
103	Les Pradelles	France	45.74	0.43			■	■	Frouin et al., 2017
104	Saint-Césaire	France	45.75	-0.51				■	Valladas et al, 1999
105	Artenac	France	45.83	0.33		■			Mann et al., 2007
106	Rochelot	France	45.85	0.28		■			Tournepiche, 1994
107	Partizanska Jama	Slovenia	46.14	14.64				■	Jamnik et al., 2015
108	Krapina	Bulgaria	46.17	15.86	■				Rink et al., 1995
109	Vindija	Croatia	46.31	16.09				■	Karavanić et al, 2021
110	Vergisson	France	46.31	4.72			■	■	Condemi & Giuliani, 2022
111	Les Rochers-de-Villeneuve	France	46.42	0.74				■	Beauval et al., 2006
112	Les Cottés	France	46.67	0.83				■	Hajdinjak et al., 2018
113	Cotencher	Switzerland	46.96	6.81				■	Deák et al, 2019
114	Genay	France	47.53	4.30		■			Dolores Garralda et al., 2008
115	Grotte du Bison	France	47.59	3.77				■	Rocca et al., 2017
116	Grotte du Renne	France	47.59	3.76				■	Banks & D'Errico, 2019
117	Subalyuk cave	Hungary	48.07	21.22				■	Mester et al., 2024
118	Šaľa	Slovakia	48.15	17.87		■			Sefcakova et al., 2005
119	Hohlenstein-Stadel	Germany	48.55	10.17		■			Peyrégne et al., 2019
120	Sesselfelsgrotte	Germany	48.94	11.80		■		■	Agam et al., 2023
121	Gánovce-Hrádo	Slovakia	49.03	20.33		■			Sabol et al., 2017
122	La Cotte de St Brélade	Jersey, Channel Islands	49.18	-2.19				■	Compton et al., 2021
123	Tourville-la-rivière	France	49.33	1.11	■				Faivre et al., 2014
124	Hunas cave	Germany	49.50	11.55			■		Alt et al., 2006
125	Šipka cave	Czech Republic	49.59	18.12				■	Minugh-Purvis et al., 2000
126	Kůlna	Poland	49.67	17.22				■	Neijman et al., 2011
127	Trou de l'Abîme	Belgium	50.05	4.50				■	Toussaint et al., 2010
128	Trou Magrite	Belgium	50.23	4.91				■	Guy Straus et al., 2023
129	Ochtendung	Germany	50.38	7.42	■				Richter et al., 2017
130	Goyet	Belgium	50.45	5.01				■	Hajdinjak et al., 2018
131	Scladina	Belgium	50.48	5.03		■			Bocherens et al., 1999
132	Spy	Belgium	50.49	4.66				■	Van Peer, 2021
133	Bay Bonnet (Fonds-de-Forêt)	Belgium	50.59	5.69				■	Abrams et al., 2024
134	Walou Cave	Belgium	50.59	6.69				■	Toussaint et al., 2017
135	Engis (Schmerling cave)	Belgium	50.59	5.41				■	Devièse et al., 2021
136	Stajnia cave	Poland	50.62	19.48				■	Dąbrowski et al., 2013
137	Stajnia	Poland	50.62	19.48		■			Picin et al., 2020
138	Feldhofer cave	Germany	51.23	6.95				■	Schmitz et al., 2002
139	Zeeland Ridges	Netherlands	51.75	3.32				■	Hublin et al., 2009

140	Warendorf	Germany	51.96	7.95			[redacted]	Scholz et al., 2000
141	Salzgitter-Lebenstedt	Germany	52.17	10.33			[redacted]	Ruebens et al., 2023

Tableau S2: Sites en Eurasie occidentale ayant livré des restes fossiles *Sapiens* plus vieux que 30 ka BP

N°	SITE	COUNTRY	LATITUDE	LONGITUDE	REFERENCE
1	Ilsenhöhle	Germany	50.66	11.57	Mylopotamitaki et al., 2024
2	Kent's Cavern	UK	50.47	-3.50	Higham et al., 2011
3	Goyet	Belgium	50.45	5.01	Fu et al., 2016
4	Zlatý kůň	Czechia	49.92	14.07	Prüfer et al., 2021
5	Grotte du Renne	France	47.59	3.76	Banks & D'Errico, 2019
6	Fontechevade	France	45.67	0.48	Chase et al., 2007
7	Grotta di Fumane	Italy	45.59	10.91	Higham et al., 2009
8	Les Rois	France	45.54	0.14	Rozzi et al., 2009
9	La Quina	France	45.51	0.30	Verna et al., 2012
10	Oase	Romania	45.03	21.83	Fu et al., 2015
11	Abri Castanet	France	45.00	1.10	White et al., 2012
12	Le Piage	France	44.80	1.40	Bordes, 2009
13	Grotte Mandrin	France	44.47	4.77	Slimak et al. 2024
14	Riparo Bombrini	Italy	43.78	7.54	Benazzi et al., 2015
15	Brassempouy	France	43.64	-0.69	Henry-Gambier et al., 2004
16	Covalejos	Spain	43.39	-3.93	Montes Barquín and Sanguino González, 2021
17	La Crouzade	France	43.13	3.08	Saos et al., 2020
18	Bacho Kiro	Bulgaria	42.95	25.43	Hublin et al., 2020
19	Fossellone	Italy	41.23	13.10	Degano et al, 2019
20	Roccia di San Sebastiano	Italy	41.14	13.88	Oxilia et al., 2022
21	Grotta del Cavallo	Italy	40.16	17.96	Marciani et al., 2018
22	Carihuela	Spain	37.44	-3.43	Carrión et al., 2019b

Tableau S3: échantillons d'ODP 976 traités au laboratoire de palynologie de l'UMR 7194 au cours de cette thèse

Section de l'échantillon	Int. sup (cm)	Int. inf (cm)	Pronfondeur (m)	N° série	Poids	Volume traité	Pastilles de Lycopodes	Concentration Lycopodes	Lycopodes	Somme polliniq ue totale	Concentration pollinique(grains/g)
C-2H-5W	90	91	13.13	9	4.5	3.7	2	13761		NA	NA
C-2H-5W	100	101	13.23	9	7.4	4.7	2	13761	184	316	6387.3
C-2H-5W	110	111	13.33	9	5.6	3.4	2	13761	227	351	7599.3
C-2H-5W	120	121	13.43	9	6.4	3.9	2	13761	204	379	7989.3
C-2H-5W	130	131	13.53	9	6.6	4	2	13761	238	367.5	6439.0
C-2H-5W	140	141	13.63	9	6.5	3.2	2	13761	228	361	6704.1
C-2H-6W	0	1	13.73	9	5.1	3	2	13761	244	349.5	7729.8
C-2H-6W	10	11	13.83	9	5.1	3.2	2	13761	357	373.5	5645.9
C-2H-6W	30	32	14.03	3	5.6	4.1	2	13761	NA	NA	NA
C-2H-6W	40	42	14.13	4	5.4	3.3	2	13761	NA	NA	NA
C-2H-6W	87	89	14.60	4	5.3	3.7	2	13761	NA	NA	NA
C-2H-6W	97	99	14.70	3	4.9	3.2	2	13761	NA	NA	NA
C-2H-6W	103	105	14.76	4	inconnu	inconnu	2	13761	NA	NA	NA
D-3H-3W	137	138	15.56	9	5	3.5	2	13761	681	364.5	2946.2
D-3H-4W	51	53	16.20	12	5.5	3.2	2	13761	NA	NA	NA
D-3H-5W	0	1	17.19	13	5.5	3.2	2	13761	NA	NA	NA
C-3H-3W	125	127	19.75	14	5.5	3.3	2	13761	NA	NA	NA
C-3H-5W	5	7	21.55	12	5.5	2.8	2	13761	314.0	464.5	7402.4
C-3H-5W	27	29	21.77	13	5.5	3.1	2	13761	319	445	6980.5
C-3H-5W	33	34	21.83	14	5.6	3.3	2	13761	440	456.5	5098.9
C-3H-5W	121	122	22.71	16	5.5	3	2	13761	368	446.5	6071.4
C-3H-6W	14	16	23.14	16	3.3	2.3	2	13761	708	457.5	5389.2
C-3H-6W	49	50	23.49	11	5.6	3.3	2	13761	576	702	5989.7
C-3H-6W	58.5	59.5	23.59	16	5.7	3.7	2	13761	578	543.5	4540.2
C-3H-6W	78	79	23.78	16	5.6	3.6	2	13761	1282	428.5	1642.7
D-4H-6W	0	1	28.00	16	5.5	3.6	2	13761	472	299.5	3175.2
B-4H-5W	130.5	131.5	29.99	16	5.6	3.6	2	13761	476	324	inconnu
B-4H-6W	65.5	66.5	30.84	15	5.6	3.4	2	13761	1526	287	924.3
B-4H-6W	90	91	31.08	15	5.5	3.3	2	13761	858	665	3878.4
B-4H-6W	114.5	115.5	31.33	16	5.5	3.5	2	13761	699	204.5	1464.0
C-4H-6W	125	127	33.75	15	5.5	3.4	2	13761	742	252	1699.5
B-5H-2W	83	84	34.33	16	5.5	3.5	2	13761	1260	322.75	1281.8
C-5H-2A	1	2	35.91	11	5.4	3.1	2	13761	572.0	269.5	2401.3
C-5H-3A	62	63	38.02	11	5.4	3.5	2	13761	692.0	178.5	1314.7
C-5H-4A	118	119	40.08	15	4.7	3.2	2	13761	1271	366.5	1688.5
C-5H-5A	56	57	40.96	11	5.6	3.4	2	13761	452	359.5	3908.9
C-5H-5A	94	95	41.34	11	3	2.4	2	13761	696	384	5061.5
C-5H-6A	134	135	43.24	8	4.4	2.9	2	13761	716	358.5	3131.9
C-5H-7A	56	57	43.96	8	4.6	3.1	2	13761	2333	318.5	816.8
C-5H-CCA	8	9	44.12	8	4.8	3.7	2	13761	1534	364	1360.6
C-5H-CCA	24	25	44.28	11	5.5	3.2	2	13761	359	307	4279.2

B-6H-2W	141.5	143	44.52	9	4.2	2.8	2	13761	1166	315.25	1771.7
C-6H-1A	18	19	44.81	1	5	3.5	2	13761	400	300	4128.3
C-6H-1A	28	29	44.91	2	3.9	2.8	2	13761	770	329	3015.2
B-6H-3W	66	67	45.26	16	5.5	3.5	2	13761	560	349.5	3123.0
B-6H-3W	139	141	45.99	9	5.5	3.3	2	13761	1372	316.5	1154.3
B-6H-3W	146	147	46.06	15	5.5	3.3	2	13761	1022	302	1478.7
B-6H-4W	3	5	46.13	5	3.8	3	2	13761	2321	449	1401.1
B-6H-4W	11	13	46.21	4	3.6	2.6	2	13761	884	304	2629.0
B-6H-4W	18	20	46.28	1	5.3	3.3	2	13761	543	317	3031.5
B-6H-4W	25	26	46.35	16	5.6	3.3	2	13761	615	430.5	3440.3
B-6H-4W	30	32	46.40	2	3.9	3	2	13761	670	303	3191.4
B-6H-4W	40	42	46.50	3	3.3	2.4	2	13761	1373	469.5	2851.9
B-6H-4W	50	52	46.60	4	3.7	2.5	2	13761	1456	418	2135.5
B-6H-4W	58	60	46.68	1	5	3.3	2	13761	828	313.5	2084.1
B-6H-4W	70	72	46.80	2	3.5	2.1	2	13761	1463	445	2391.8
B-6H-4W	80	82	46.90	3	3.4	2.3	2	13761	1299	418	2604.8
B-6H-4W	90	92	47.00	4	3.5	2.4	2	13761	601	365.5	4782.2
B-6H-4W	98	100	47.08	1	5.2	3.4	2	13761	1048	346	1747.4
B-6H-4W	107.5	109.5	47.18	2	3.5	2.6	2	13761	884	329	2926.5
B-6H-4W	114	115	47.24	15	5.5	3.6	2	13761	979	451.75	2309.0
B-6H-4W	120	122	47.30	3	3.9	2.8	2	13761	1779	401	1590.7
B-6H-4W	130	132	47.40	4	3.9	2.5	2	13761	972	496.5	3604.7
B-6H-4W	138	140	47.48	1	5.1	3.1	2	13761	1179	361	1652.4
B-6H-4W	146	147	47.56	16	5.5	3.5	2	13761	1141	352	1543.7
B-6H-5W	3	5	47.63	2	5.3	3.6	2	13761	NA	NA	NA
B-6H-5W	8	10	47.68	4	3.6	2.3	2	13761	1477	392.5	2031.6
B-6H-5W	15	17	47.75	3	3.9	2.5	2	13761	1100	266	1706.5
B-6H-5W	24	26	47.84	5	4	2.6	2	13761	2005	366	1256.0
B-6H-5W	34	36	47.94	1	3.7	2.7	2	13761	900	338	2793.5
B-6H-5W	41	42	48.01	15	5.5	3.3	2	13761	1267	321	1267.8
B-6H-5W	46	48	48.06	2	3.7	2.2	2	13761	1769	288.5	1213.1
B-6H-5W	54	56	48.14	3	3.8	2.8	2	13761	1007	305	2193.6
B-6H-5W	59	61	48.19	4	6.4	3.4	2	13761	624	408.5	2815.2
B-6H-5W	68	70	48.28	1	3.6	2.4	2	13761	800	305	2914.7
B-6H-5W	76	77	48.36	16	4.6	2.8	2	13761	863	342.75	2376.2
B-6H-5W	80	82	48.40	2	3.7	2.5	2	13761	1350	384	2115.8
C-6H-3W	87	89	48.50	3	3.6	2.2	2	13761	1096	312.5	2179.8
C-6H-3W	97	99	48.60	4	3.7	2.2	2	13761	767	344	3336.1
C-6H-3W	108.5	110.5	48.72	1	3.7	2.4	2	13761	413	356	6411.8
C-6H-3W	118.5	120.5	48.82	5	3.8	2.3	2	13761	816	300.5	2667.2
C-6H-3W	128	130	48.91	6	5.4	3.4	2	13761	1667	357.5	1093.0
C-6H-3W	147	149	49.10	2	4.6	3	2	13761	2046	373.5	1092.2
C-6H-4W	7	9	49.20	9	3.2	2.7	2	13761	1455	384	2269.9
C-6H-4W	17	19	49.30	4	3.7	2.4	2	13761	784	315	2988.6
C-6H-4W	27	29	49.40	5	4.4	2.5	2	13761	1057	309.5	1831.5
C-6H-4W	37	39	49.50	6	3.3	2.2	2	13761	2415	330.5	1141.4
C-6H-4W	47	49	49.60	5	4	2.9	2	13761	826	402	3348.6
C-6H-4W	57	59	49.70	7	3.45	2.7	2	13761	1309	321	1956.3

C-6H-4W	67	69	49.80	8	3.5	2.6	2	13761	2185	397.5	1430.5
C-6H-4W	75	77	49.88	4	4.3	3.2	2	13761	1237	353	1826.5
C-6H-4W	85	87	49.98	6	3.5	2.5	2	13761	1989	376.5	1488.5
C-6H-4W	95	97	50.08	5	3.4	2.8	2	13761	1325	355	2168.8
C-6H-4W	103	105	50.16	7	2.9	2.5	2	13761	1757	450	2430.7
C-4H-6W	109	110	50.22	15	5.5	3.4	2	13761	1063	450.25	2119.5
C-6H-4W	115	117	50.28	6	3.1	2.4	2	13761	2083	639	2723.5
C-6H-4W	125	127	50.38	8	3.1	2.3	2	13761	1311	315	2133.2
C-6H-4W	134.5	136.5	50.48	7	3	1.7	2	13761	1062	476	4111.9
C-6H-4W	140	142	50.53	5	2.8	1.9	2	13761	1670	706	4155.4
C-6H-5W	4	6	50.67	6	3.8	2.4	2	13761	1274	386	2194.4
C-6H-5W	15	17	50.78	7	3.1	2.5	2	13761	1503	499.5	2950.5
C-6H-5W	25	27	50.88	8	5	3.6	2	13761	1542	457	1631.3
C-6H-5W	35	37	50.98	8	3.7	2.7	2	13761	1209	462.5	2845.5
C-6H-5W	45	47	51.08	5	2.7	1.8	2	13761	972	395	4142.4
C-6H-5W	55	57	51.18	6	3.5	2.7	2	13761	1284	457	2798.7
C-6H-5W	65	67	51.28	7	3.7	2.2	2	13761	1943	440.25	1685.4
C-6H-5W	74	76	51.37	8	3.6	2.8	2	13761	2110	441.5	1599.7
C-6H-5W	85	87	51.48	6	3.7	2.7	2	13761	2020	541.75	1994.9
C-6H-5W	95	97	51.58	7	3.6	2	2	13761	1716	486	2165.2
C-6H-5W	105	107	51.68	11	3.6	2.8	2	13761	1303	353.5	2074.1
C-6H-5W	115	117	51.78	7	3.8	2.1	2	13761	2797	563.5	1459.1
C-6H-5W	125	127	51.88	5	4.4	2.9	2	13761	1438	310	1348.4
C-6H-5W	135	137	51.98	6	3.9	2.7	2	13761	7476	356.5	336.5
C-6H-5W	145	147	52.08	8	3.5	2.4	2	13761	4039	495.25	964.2
C-6H-6W	5	7	52.20	7	3.1	2.2	2	13761	1715	454	2350.2
C-6H-6W	15	17	52.30	5	3.6	2.6	2	13761	250	381	11651.0
C-6H-6W	25	27	52.40	11	4.1	2.6	2	13761	543	405	5006.7
C-6H-6W	35	37	52.50	6	4	2.4	2	13761	921	447.25	3341.3
C-6H-6W	45	47	52.60	7	4	2.5	2	13761	956	388	2792.5
C-6H-6W	55	57	52.70	8	4	2.7	2	13761	1128	354.5	2162.4
C-6H-6W	65	67	52.80	6	3.9	3.2	2	13761	1100	416	2668.8
C-6H-6W	75	77	52.90	5	4.6	3.4	2	13761	498	416.5	5003.9
C-6H-6W	85	87	53.00	8	3.9	2.5	2	13761	978	347	2503.8
C-6H-6W	95	97	53.10	7	3.4	2.4	2	13761	1329	358	2180.5
C-6H-6W	105	107	53.20	6	3.7	2.6	2	13761	1027	342.5	2480.7
C-6H-6W	115	117	53.30	5	3.9	3.1	2	13761	902	319	2495.7
C-6H-6W	125	127	53.40	7	3.9	2.5	2	13761	764	353.5	3265.2
C-6H-6W	135	137	53.50	8	3.2	2.4	2	13761	839	378	3874.9
C-6H-6W	143	145	53.58	7	4.2	2.7	2	13761	721	387.5	3521.8
B-7H-2W	98	100	53.66	6	4.9	3.5	4	13761	1080	334	3474.1

NA : non analysé

Inconnu : volume de l'échantillon inconnu dû à une erreur de manipulation.

Suppléments de l'Article 1 (QSR)

Tableau S4: Liste des datations de sites archéologiques du Paléolithique moyen et supérieur initial entre 50 et 30 ka BP. Les datations radiocarbones ont été recalibrées avec la courbe IntCal20.

Site name	Country	Lat.	Long.	Stratigraphic level	Method	date (14C uncalibrated)	uncertainty	Median_date (cal BP)	Lower_bound 95% (cal BP)	Upper_bound 95% (cal BP)	Condifence	Industry typology	Biological attribution	References
Abauntz	Spain	43.02	-1.64	h	AAR	47000	7000	47000	54000	40000	2	Middle Paleolithic	Neanderthal	Utrilla et al, 2015
Abric del Pastor	Spain	38.69	-0.45	level Ivb	U/Th	48000	5000	48000	53000	43000	2	Middle Palaeolithic	Neanderthal	Mallol et al. 2019 ; Sossa-Ríos et al. 2022
Abric Romani	Spain	41.53	1.69	B	Radiocarbon	39060	350	42730	43248.7	42211.3	2	Middle Palaeolithic	Neanderthal	Vaquero et al, 2013 ; Higham et al, 2014 ; Sharp et al, 2019
Abric Romani	Spain	41.53	1.69	D	Radiocarbon	40680	940	44051.5	45759.125	42343.875	2	Middle Palaeolithic	Neanderthal	Vaquero et al, 2013 ; Higham et al, 2014 ; Sharp et al, 2019
Abric Romani	Spain	41.53	1.69	E	Radiocarbon	43200	1100	45871	48503.45	43238.55	2	Middle Palaeolithic	Neanderthal	Vaquero et al, 2013 ; Higham et al, 2014 ; Sharp et al, 2019
Abric Romani	Spain	41.53	1.69	B (layer 4)	Radiocarbon	43500	1200	46115	48932.7	43297.3	2	Middle Palaeolithic	Neanderthal	Vaquero et al, 2013 ; Higham et al, 2014 ; Sharp et al, 2019
Abric Romani	Spain	41.53	1.69	H	Radiocarbon	44500	1200	47301	50128.2	44473.8	2	Middle Palaeolithic	Neanderthal	Vaquero et al, 2013 ; Higham et al, 2014 ; Sharp et al, 2019
Abric Romani	Spain	41.53	1.69	J	Radiocarbon	47100	2100	49865.5	54743.275	44987.725	2	Middle Palaeolithic	Neanderthal	Vaquero et al, 2013 ; Higham et al, 2014 ; Sharp et al, 2019
Abric Romani	Spain	41.53	1.69	B	Radiocarbon	39060	350	42730	43248.7	42211.3	2	Mousterian	Neanderthal	Camps and Higham, 2012
Abric Romani	Spain	41.53	1.69	D	Radiocarbon	40680	940	44051.5	45759.125	42343.875	2	Mousterian	Neanderthal	Vaquero et al, 2013
Abric Romani	Spain	41.53	1.69	E	Radiocarbon	43200	1100	45871	48503.45	43238.55	2	Mousterian	Neanderthal	Vaquero et al, 2013
Abric Romani	Spain	41.53	1.69	B	Radiocarbon	43500	1200	46115	48932.7	43297.3	2	Mousterian	Neanderthal	Carbonell et al, 1994
Abric Romani	Spain	41.53	1.69	H	Radiocarbon	44500	1200	47301	50128.2	44473.8	2	Mousterian	Neanderthal	Vaquero et al, 2013
Abric Romani	Spain	41.53	1.69	A	Radiocarbon	35400	810	39860	42082.05	37637.95	2	Proto-Aurignacian	Sapiens	Bischoff et al, 1994 ; Vaquero et al, 2013 ; Higham et al, 2014 ; Sharp et al, 2016
Abric Romani	Spain	41.53	1.69	A	Radiocarbon	35400	800	39866	42074.75	37657.25	2	Proto-Aurignacian	Sapiens	Carbonell et al, 1994
Abric Romani	Spain	41.53	1.69	A	Radiocarbon	35900	600	40736.5	42129.675	39343.325	2	Proto-Aurignacian	Sapiens	Camps and Higham, 2012
Abric Romani	Spain	41.53	1.69	A	Radiocarbon	36490	230	41452	42053.35	40850.65	2	Proto-Aurignacian	Sapiens	Camps and Higham, 2012

Abric Romani	Spain	41.53	1.69	A	Radiocarbon	36590	640	41083.5	42390.225	39776.775	2	Proto-Aurignacian	Sapiens	Bischoff et al, 1994
Abric Romani	Spain	41.53	1.69	A	Radiocarbon	36740	920	41035.5	42738.375	39332.625	2	Proto-Aurignacian	Sapiens	Bischoff et al, 1994
Abric Romani	Spain	41.53	1.69	A	Radiocarbon	37200	900	41307	42935.3	39678.7	2	Proto-Aurignacian	Sapiens	Carbonell et al, 1994
Abric Romani	Spain	41.53	1.69	A	Radiocarbon	37290	990	41331	43110.35	39551.65	2	Proto-Aurignacian	Sapiens	Bischoff et al, 1994 ; Vaquero et al, 2013 ; Higham et al, 2014 ; Sharp et al, 2016
Abric Romani	Spain	41.53	1.69	A	Radiocarbon	37900	1000	42055.5	44074.725	40036.275	2	Proto-Aurignacian	Sapiens	Bischoff et al, 1994
Abric Romani	Spain	41.53	1.69	A	Radiocarbon	37900	1000	42055.5	44074.725	40036.275	2	Proto-Aurignacian	Sapiens	Vaquero et al, 2013 ; Higham et al, 2014 ; Sharp et al, 2018
Abric Romani	Spain	41.53	1.69	A	Radiocarbon	37900	1000	42055.5	44074.725	40036.275	2	Proto-Aurignacian	Sapiens	Carbonell et al, 1994
Abric Romani	Spain	41.53	1.69	1.20 m above base of layer P at drill site	U/Th	54798	86	54798	54884	54712	2	Middle Palaeolithic	Neanderthal	Vaquero et al, 2013 ; Higham et al, 2014 ; Sharp et al, 2025
Abric Romani	Spain	41.53	1.69	1.20 m above base of layer P at drill site	U/Th	55033	69	55033	55102	54964	2	Middle Palaeolithic	Neanderthal	Vaquero et al, 2013 ; Higham et al, 2014 ; Sharp et al, 2026
Abric Romani	Spain	41.53	1.69	4.39 m below base of layer P at drill site	U/Th	57380	240	57380	57620	57140	2	Middle Palaeolithic	Neanderthal	Vaquero et al, 2013 ; Higham et al, 2014 ; Sharp et al, 2027
Abric Romani	Spain	41.53	1.69	4.39 m below base of layer P at drill site	U/Th	57470	290	57470	57760	57180	2	Middle Palaeolithic	Neanderthal	Vaquero et al, 2013 ; Higham et al, 2014 ; Sharp et al, 2028
Abric Romani	Spain	41.53	1.69	4.39 m below base of layer P at drill site	U/Th	57530	270	57530	57800	57260	2	Middle Palaeolithic	Neanderthal	Vaquero et al, 2013 ; Higham et al, 2014 ; Sharp et al, 2029
Abrigo de la Malia	Spain	41.00	-3.25	LU-V	OSL / IRSL/ TL	35000	2100	35000	37100	32900	2	Aurignacian	Sapiens	Sala et al, 2024
Abrigo de la Malia	Spain	41.00	-3.25	LU-V	Radiocarbon	27670	310	32056.5	33068.725	31044.275	2	Aurignacian	Sapiens	Sala et al, 2024
Abrigo de la Malia	Spain	41.00	-3.25	LU-V	Radiocarbon	28680	290	32966	34187.7	31744.3	2	Aurignacian	Sapiens	Sala et al, 2024
Abrigo de la Malia	Spain	41.00	-3.25	LU-V	Radiocarbon	28750	310	33007	34257.2	31756.8	2	Aurignacian	Sapiens	Sala et al, 2024

Abrigo de la Malia	Spain	41.00	-3.25	LU-V	Radiocarbon	28790	310	33031.5	34280.275	31782.725	2	Aurignacian	Sapiens	Sala et al, 2024
Abrigo de la Malia	Spain	41.00	-3.25	LU-V	Radiocarbon	28950	300	33141.5	34360.825	31922.175	2	Aurignacian	Sapiens	Sala et al, 2024
Abrigo de la Malia	Spain	41.00	-3.25	LU-V	Radiocarbon	29800	1000	34022	36764.65	31279.35	2	Aurignacian	Sapiens	Sala et al, 2024
Abrigo de la Malia	Spain	41.00	-3.25	LU-V	Radiocarbon	31060	410	35465	36581.25	34348.75	2	Aurignacian	Sapiens	Sala et al, 2024
Abrigo de la Malia	Spain	41.00	-3.25	LU-V	Radiocarbon	31100	400	35496.5	36606.575	34386.425	2	Aurignacian	Sapiens	Sala et al, 2024
Abrigo de la Quebrada	Spain	39.75	-0.99	III	Radiocarbon	40500	530	43673	44738.9	42607.1	2	Middle Palaeolithic	Neanderthal	Villaverde et al, 2008 ; Esteban et al, 2017
Abrigo de la Quebrada	Spain	39.75	-0.99	IV	Radiocarbon	43930	750	46532	48426.3	44637.7	2	Middle Palaeolithic	Neanderthal	Villaverde et al, 2008 ; Esteban et al, 2017
Abrigo del molino	Spain	40.95	-4.14	E/G	OSL / IRSL/ TL	43400	2700	43400	46100	40700	2	Middle Paleolithic	Neanderthal	Kehl et al., 2018
Abrigo del molino	Spain	40.95	-4.14	M	OSL / IRSL/ TL	44800	3300	44800	48100	41500	2	Middle Paleolithic	Neanderthal	Kehl et al., 2018
Abrigo del molino	Spain	40.95	-4.14	O	OSL / IRSL/ TL	45300	2900	45300	48200	42400	2	Middle Paleolithic	Neanderthal	Kehl et al., 2018
Abrigo del molino	Spain	40.95	-4.14	M	OSL / IRSL/ TL	56000	4500	56000	60500	51500	2	Middle Paleolithic	Neanderthal	Álvarez-Alonso et al, 2016
Abrigo del molino	Spain	40.95	-4.14	K	Radiocarbon	33300	200	38105.5	39188.025	37022.975	1	Middle Paleolithic	Neanderthal	Kehl et al., 2018
Abrigo del molino	Spain	40.95	-4.14	G	Radiocarbon	37200	300	41775	42352.6	41197.4	1	Middle Paleolithic	Neanderthal	Kehl et al., 2018
Abrigo del molino	Spain	40.95	-4.14	D	Radiocarbon	38600	500	42535.5	43223.775	41847.225	2	Middle Paleolithic	Neanderthal	Kehl et al., 2018

Abrigo del molino	Spain	40.95	-4.14	C	Radiocarbon	39500	600	43283	44394.5	42171.5	2	Middle Paleolithic	Neanderthal	Kehl et al., 2018
Abrigo del molino	Spain	40.95	-4.14	G	Radiocarbon	39900	400	43405.5	44331.275	42479.725	2	Middle Paleolithic	Neanderthal	Kehl et al., 2018
Abrigo del molino	Spain	40.95	-4.14	D	Radiocarbon	40000	500	43455.5	44472.475	42438.525	2	Middle Paleolithic	Neanderthal	Kehl et al., 2018
Abrigo del molino	Spain	40.95	-4.14	D	Radiocarbon	40100	600	43513	44627.35	42398.65	2	Middle Paleolithic	Neanderthal	Kehl et al., 2018
Abrigo del molino	Spain	40.95	-4.14	G	Radiocarbon	40200	400	43526	44445.6	42606.4	2	Middle Paleolithic	Neanderthal	Kehl et al., 2018
Abrigo del molino	Spain	40.95	-4.14	D	Radiocarbon	40700	600	43815	45011.05	42618.95	2	Middle Paleolithic	Neanderthal	Kehl et al., 2018
Aguilon P5	Spain	41.31	-1.05	e	Radiocarbon	41510	510	44299.5	45568.225	43030.775	2	Middle Palaeolithic	Neanderthal	Mazo & Alcolea, 2020
Aguilon P5	Spain	41.31	-1.05	e	Radiocarbon	44560	480	46976.5	48436.175	45516.825	2	Middle Palaeolithic	Neanderthal	Mazo & Alcolea, 2020
Aguilon P7	Spain	41.31	-1.05	top	Radiocarbon	34860	480	39737	41238	38236	1	Middle Palaeolithic	Neanderthal	Galán et al, 2016
Amalda I cave	Spain	43.23	-2.20	VII	Radiocarbon	42600	1600	45746.5	48947.525	42545.475	2	Mousterian	Neanderthal	Sánchez-Romero et al., 2020
Amalda I cave	Spain	43.23	-2.20	VII	Radiocarbon	44500	2100	48385.5	54718.875	43044.125	2	Mousterian	Neanderthal	Sánchez-Romero et al., 2020
Amalda III cave	Spain	43.23	-2.20	IV top	Radiocarbon	57700	3800	51194	54809.7	47578.3	2	Mousterian Vasconian	Neanderthal	Rios-Garaizar 2010
Ardales	Spain	36.87	-4.83	4	Radiocarbon	40180	634	43558	44716.05	42399.95	2	Middle Palaeolithic	Neanderthal	Ramos Muñoz et al, 2022
Ardales	Spain	36.87	-4.83	4	Radiocarbon	40514	664	43742.5	44993.175	42491.825	2	Middle Palaeolithic	Neanderthal	Ramos Muñoz et al, 2022
Ardales	Spain	36.87	-4.83	4	Radiocarbon	43697	945	46449	48623.55	44274.45	2	Middle Palaeolithic	Neanderthal	Ramos Muñoz et al, 2022
Ardales	Spain	36.87	-4.83	k	Radiocarbon	50041	1103	52084.5	54854.225	49314.775	2	Middle Palaeolithic	Neanderthal	Ramos Muñoz et al, 2023
Ardales	Spain	36.87	-4.83	3	Radiocarbon	51914	2324	51461	54823.05	48098.95	2	Middle Palaeolithic	Neanderthal	Ramos Muñoz et al, 2023
Ardales	Spain	36.87	-4.83	3	Radiocarbon	53071	2676	51414.5	54820.725	48008.275	2	Middle Palaeolithic	Neanderthal	Ramos Muñoz et al, 2023
Arrillor	Spain	43.01	-2.74	Lm	Radiocarbon	44900	2100	48968.5	54698.425	43238.575	2	Middle Palaeolithic	Neanderthal	Higham et al, 2014

Arrillor	Spain	43.01	-2.74	Lm	Radiocarbon	45600	2300	49056	54702.8	43409.2	2	Middle Palaeolithic	Neanderthal	Higham et al, 2014
Arrillor	Spain	43.01	-2.74	Smk-l	Radiocarbon	45600	2300	49056	54702.8	43409.2	2	Middle Palaeolithic	Neanderthal	Higham et al, 2014
Arrillor	Spain	43.01	-2.74	Amk	Radiocarbon	48500	3200	49658	54732.9	44583.1	2	Middle Palaeolithic	Neanderthal	Higham et al, 2014
Cueva de los aviones	Spain	37.59	-0.99	IV	Radiocarbon	38150	350	42313.5	42806.075	41820.925	2	Middle Palaeolithic	Neanderthal	Zilhao et al, 2016
Cueva de los aviones	Spain	37.59	-0.99	IV	Radiocarbon	42200	360	44995.5	45874.725	44116.275	2	Middle Palaeolithic	Neanderthal	Zilhao et al, 2016
Cueva de los aviones	Spain	37.59	-0.99	I	Radiocarbon	43290	390	45791	46894.9	44687.1	2	Middle Palaeolithic	Neanderthal	Zilhao et al, 2016
Cueva de los aviones	Spain	37.59	-0.99	II	Radiocarbon	45000	450	47380	48797.4	45962.6	2	Middle Palaeolithic	Neanderthal	Zilhao et al, 2016
Cueva de los aviones	Spain	37.59	-0.99	III	Radiocarbon	45150	650	47687	49695.3	45678.7	2	Middle Palaeolithic	Neanderthal	Zilhao et al, 2016
Axlor	Spain	43.12	-2.72	B	OSL / IRSL/ TL	50700	3500	50700	54200	47200	2	Middle Palaeolithic	Neanderthal	Demuro et al, 2023
Axlor	Spain	43.12	-2.72	B	Radiocarbon	42010	1280	45225	47898.3	42551.7	2	Middle Palaeolithic	Neanderthal	González Urquijo et al, 2005
Axlor	Spain	43.12	-2.72	B	Radiocarbon	42700	90	45265	45854	44676	2	Middle Palaeolithic	Neanderthal	González Urquijo et al, 2021
Bajondillo	Spain	36.62	-4.50	Bj13	Radiocarbon	36890	200	41684.5	42180.875	41188.125	2	Early Aurignacian	Sapiens	Cortés-Sánchez et al, 2019
Bajondillo	Spain	36.62	-4.50	Bj13	Radiocarbon	36890	210	41681	42188.3	41173.7	2	Early Aurignacian	Sapiens	Cortés-Sánchez et al, 2019
Bajondillo	Spain	36.62	-4.50	Bj13	Radiocarbon	37430	570	41752.5	42715.325	40789.675	2	Early Aurignacian	Sapiens	Cortés-Sánchez et al, 2019
Bajondillo	Spain	36.62	-4.50	Bj13	Radiocarbon	38160	230	42322	42669.7	41974.3	2	Early Aurignacian	Sapiens	Cortés-Sánchez et al, 2019
Bajondillo	Spain	36.62	-4.50	Bj13	Radiocarbon	39270	870	43082.5	44589.675	41575.325	2	Early Aurignacian	Sapiens	Cortés-Sánchez et al, 2019
Bajondillo	Spain	36.62	-4.50	Bj14	Radiocarbon	42710	1120	45562	48136.5	42987.5	2	Middle Palaeolithic	Neanderthal	Higham et al, 2014
Bajondillo	Spain	36.62	-4.50	Bj14	Radiocarbon	43840	490	46427.5	47977.425	44877.575	2	Middle Palaeolithic	Neanderthal	Higham et al, 2014
Bajondillo	Spain	36.62	-4.50	Bj14	Radiocarbon	44020	1290	46720.5	49887.325	43553.675	2	Middle Palaeolithic	Neanderthal	Higham et al, 2014
Bajondillo	Spain	36.62	-4.50	Bj14	Radiocarbon	46610	1740	49934	54746.7	45121.3	2	Middle Palaeolithic	Neanderthal	Higham et al, 2014

Bajondillo	Spain	36.62	-4.50	Bj14	Radiocarbon	46890	1810	49993	54749.65	45236.35	2	Middle Palaeolithic	Neanderthal	Higham et al, 2014
Bajondillo	Spain	36.62	-4.50	Bj14	Radiocarbon	48410	2420	50111.5	54755.575	45467.425	2	Middle Palaeolithic	Neanderthal	Higham et al, 2014
Banyoles	Spain	42.11	2.77	4	U/Th	45000	4000	45000	49000	41000	2	_	?	Julià & Bischoff, 1991 ; Keeling et al, 2023
Buraca Escura	Portugal	39.98	-8.55		U/Th	50000	30000	50000	80000	20000	1	Middle Palaeolithic	Neanderthal	Aubry et al, 2011
Carihuela	Spain	37.44	-3.43	V-IV	OSL / IRSL/ TL	21100	1300	21100	22400	19800	1	Middle Paleolithic	Neanderthal	Fernandez et al, 2007 ; Carrion et al, 2019
Carihuela	Spain	37.44	-3.43	V	OSL / IRSL/ TL	27400	1000	27400	28400	26400	1	Middle Paleolithic	Neanderthal	Fernandez et al, 2007 ; Carrion et al, 2019
Carihuela	Spain	37.44	-3.43	V	OSL / IRSL/ TL	28000	1000	28000	29000	27000	1	Middle Paleolithic	Neanderthal	Fernandez et al, 2007 ; Carrion et al, 2019
Carihuela	Spain	37.44	-3.43	V	OSL / IRSL/ TL	33000	1200	33000	34200	31800	2	Middle Paleolithic	Neanderthal	Fernandez et al, 2007 ; Carrion et al, 2019
Carihuela	Spain	37.44	-3.43	VI-V	OSL / IRSL/ TL	37350	2200	37350	39550	35150	2	Middle Paleolithic	Neanderthal	Fernandez et al, 2007 ; Carrion et al, 2019
Carihuela	Spain	37.44	-3.43	VI-V	OSL / IRSL/ TL	39400	2000	39400	41400	37400	2	Middle Paleolithic	Neanderthal	Fernandez et al, 2007 ; Carrion et al, 2019
Carihuela	Spain	37.44	-3.43	VI	OSL / IRSL/ TL	42400	1500	42400	43900	40900	2	Middle Paleolithic	Neanderthal	Fernandez et al, 2007 ; Carrion et al, 2019
Carihuela	Spain	37.44	-3.43	VI	OSL / IRSL/ TL	49200	2500	49200	51700	46700	2	Middle Paleolithic	Neanderthal	Fernandez et al, 2007 ; Carrion et al, 2019
Carihuela	Spain	37.44	-3.43	VI	OSL / IRSL/ TL	57700	2500	57700	60200	55200	2	Middle Paleolithic	Neanderthal	Fernandez et al, 2007 ; Carrion et al, 2019
Carihuela	Spain	37.44	-3.43	VI	OSL / IRSL/ TL	58800	2500	58800	61300	56300	2	Middle Paleolithic	Neanderthal	Fernandez et al, 2007 ; Carrion et al, 2019
Carihuela	Spain	37.44	-3.43	III-V (coprolithe)	Radiocarbon	16139	48	19492	19802.65	19181.35	1	Middle Paleolithic	Neanderthal/Sapiens	Fernandez et al, 2007 ; Carrion et al, 2019
Carihuela	Spain	37.44	-3.43	IV-V(coprolithe)	Radiocarbon	17691	50	21433.5	21857.675	21009.325	1	Middle Paleolithic	Neanderthal/Sapiens	Fernandez et al, 2007 ; Carrion et al, 2019
Carihuela	Spain	37.44	-3.43	V	Radiocarbon	20530	140	24681	25264.3	24097.7	1	Middle Paleolithic	Neanderthal	Fernandez et al, 2007 ; Carrion et al, 2019
Carihuela	Spain	37.44	-3.43	III-V(coprolithe)	Radiocarbon	20551	247	24763	25680.7	23845.3	1	Middle Paleolithic	Neanderthal/Sapiens	Fernandez et al, 2007 ; Carrion et al, 2019
Carihuela	Spain	37.44	-3.43	V	Radiocarbon	21430	130	25636	26040.7	25231.3	1	Middle Paleolithic	Neanderthal	Fernandez et al, 2007 ; Carrion et al, 2019
Carihuela	Spain	37.44	-3.43	V	Radiocarbon	22350	140	26595.5	27196.375	25994.625	1	Middle Paleolithic	Neanderthal	Fernandez et al, 2007 ; Carrion et al, 2019
Carihuela	Spain	37.44	-3.43	VI	Radiocarbon	22830	180	27062	27714.65	26409.35	1	Middle Paleolithic	Neanderthal	Fernandez et al, 2007 ; Carrion et al, 2019
Carihuela	Spain	37.44	-3.43	V-VI	Radiocarbon	25590	230	29938.5	30740.775	29136.225	1	Middle Paleolithic	Neanderthal	Fernandez et al, 2007 ; Carrion et al, 2019

Carihuela	Spain	37.44	-3.43	V	Radiocarbon	25850	180	30071.5	30841.475	29301.525	1	Middle Paleolithic	Neanderthal	Fernandez et al, 2007 ; Carrion et al, 2019
Carihuela	Spain	37.44	-3.43	VI	Radiocarbon	25970	250	30159.5	31041.575	29277.425	1	Middle Paleolithic	Neanderthal	Fernandez et al, 2007 ; Carrion et al, 2019
Carihuela	Spain	37.44	-3.43	VI	Radiocarbon	26060	260	30195.5	31075.675	29315.325	1	Middle Paleolithic	Neanderthal	Fernandez et al, 2007 ; Carrion et al, 2019
Carihuela	Spain	37.44	-3.43	IV-VI(coprolithe)	Radiocarbon	26158	188	30504	31061.65	29946.35	1	Middle Paleolithic	Neanderthal/Sapiens	Fernandez et al, 2007 ; Carrion et al, 2019
Carihuela	Spain	37.44	-3.43	V	Radiocarbon	28060	310	32397	33598.75	31195.25	1	Middle Paleolithic	Neanderthal	Fernandez et al, 2007 ; Carrion et al, 2019
Carihuela	Spain	37.44	-3.43	V	Radiocarbon	28440	240	32718.5	33777.275	31659.725	1	Middle Paleolithic	Neanderthal	Fernandez et al, 2007 ; Carrion et al, 2019
Carihuela	Spain	37.44	-3.43	V	Radiocarbon	28460	370	32737	34158.2	31315.8	1	Middle Paleolithic	Neanderthal	Fernandez et al, 2007 ; Carrion et al, 2019
Carihuela	Spain	37.44	-3.43	V	Radiocarbon	28490	330	32772.5	34113.425	31431.575	1	Middle Paleolithic	Neanderthal	Fernandez et al, 2007 ; Carrion et al, 2019
Carihuela	Spain	37.44	-3.43	IV	Radiocarbon	29490	360	33678.5	35092.575	32264.425	1	Middle Paleolithic	Neanderthal/Sapiens	Fernandez et al, 2007 ; Carrion et al, 2019
Carihuela	Spain	37.44	-3.43	V	Radiocarbon	32750	520	37469.5	39330.075	35608.925	1	Middle Paleolithic	Neanderthal	Fernandez et al, 2007 ; Carrion et al, 2019
Carihuela	Spain	37.44	-3.43	IV	Radiocarbon	37100	860	41266.5	42843.975	39689.025	2	Middle Paleolithic	Neanderthal/Sapiens	Fernandez et al, 2007 ; Carrion et al, 2019
Carihuela	Spain	37.44	-3.43	V	Radiocarbon	39300	1100	43105	44976.5	41233.5	2	Middle Paleolithic	Neanderthal	Fernandez et al, 2007 ; Carrion et al, 2019
Carihuela	Spain	37.44	-3.43	IV	Radiocarbon	39800	1200	43498.5	45569.975	41427.025	2	Middle Paleolithic	Neanderthal/Sapiens	Fernandez et al, 2007 ; Carrion et al, 2019
Carihuela	Spain	37.44	-3.43	VI	Radiocarbon	45200	1270	48321	51869.25	44772.75	2	Middle Paleolithic	Neanderthal	Fernandez et al, 2007 ; Carrion et al, 2019
Carihuela	Spain	37.44	-3.43	VI	U/Th	27960	1210	27960	29170	26750	2	Middle Paleolithic	Neanderthal	Fernandez et al, 2007 ; Carrion et al, 2019
Carihuela	Spain	37.44	-3.43	VI	U/Th	29470	1640	29470	31110	27830	2	Middle Paleolithic	Neanderthal	Fernandez et al, 2007 ; Carrion et al, 2019
Carihuela	Spain	37.44	-3.43	VI	U/Th	38780	4640	38780	43420	34140	2	Middle Paleolithic	Neanderthal	Fernandez et al, 2007 ; Carrion et al, 2019
Carihuela	Spain	37.44	-3.43	VI	U/Th	57970	3550	57970	61520	54420	2	Middle Paleolithic	Neanderthal	Fernandez et al, 2007 ; Carrion et al, 2019
Castelejo	Portugal	39.64	-7.69	C3	OSL / IRSL/ TL	32400	2400	32400	34800	30000	2	Upper Palaeolithic	Sapiens	Cunha et al, 2012
Coll Verdaguer	Spain	41.39	1.91	3	ESR	43900	3000	43900	46900	40900	2	Middle Palaeolithic	Neanderthal	Duara et al, 2017
Coll Verdaguer	Spain	41.39	1.91	1	ESR	46100	7400	46100	53500	38700	2	Middle Palaeolithic	Neanderthal	Duara et al, 2017

Coll Verdaguer	Spain	41.39	1.91	3	ESR	46400	2600	46400	49000	43800	2	Middle Palaeolithic	Neanderthal	Duara et al, 2017
Coll Verdaguer	Spain	41.39	1.91	2	OSL / IRSL/ TL	46600	4200	46600	50800	42400	2	Middle Palaeolithic	Neanderthal	Duara et al, 2017
Coll Verdaguer	Spain	41.39	1.91	1	Radiocarbon	37600	550	41882	42775	40989	2	Middle Palaeolithic	Neanderthal	Duara et al, 2017
Coll Verdaguer	Spain	41.39	1.91	2	Radiocarbon	38000	550	42093.5	42955.625	41231.375	2	Middle Palaeolithic	Neanderthal	Duara et al, 2017
Coll Verdaguer	Spain	41.39	1.91	1	Radiocarbon	39950	650	43464.5	44623.025	42305.975	2	Middle Palaeolithic	Neanderthal	Duara et al, 2017
Coll Verdaguer	Spain	41.39	1.91	1	U/Th	50055	4359	50055	54414	45696	2	Middle Palaeolithic	Neanderthal	Duara et al, 2017
Coll Verdaguer	Spain	41.39	1.91	1	U/Th	52950	9041	52950	61991	43909	2	Middle Palaeolithic	Neanderthal	Duara et al, 2017
Coll Verdaguer	Spain	41.39	1.91	2	U/Th	55175	13343	55175	68518	41832	2	Middle Palaeolithic	Neanderthal	Duara et al, 2017
Coll Verdaguer	Spain	41.39	1.91	2	U/Th	56137	6115	56137	62252	50022	2	Middle Palaeolithic	Neanderthal	Duara et al, 2017
Cova del Gegant	Spain	41.22	1.77	V	OSL / IRSL/ TL	55700	4800	55700	60500	50900	2	Middle Palaeolithic	Neanderthal	Daura et al, 2021
Cova del Gegant	Spain	41.22	1.77	II (Upper Palaeolithic 3b)	OSL / IRSL/ TL	32400	1900	32400	34300	30500	2	Upper Palaeolithic	Sapiens	Daura et al, 2021
Cova del Gegant	Spain	41.22	1.77	II/III (Upper Palaeolithic 3b)	OSL / IRSL/ TL	35300	2400	35300	37700	32900	2	Upper Palaeolithic	Sapiens	Daura et al, 2021
Cova del Gegant	Spain	41.22	1.77	XXIV (Upper Palaeolithic 3a)	OSL / IRSL/ TL	36000	2500	36000	38500	33500	2	Upper Palaeolithic	Sapiens	Daura et al, 2021
Cova del Gegant	Spain	41.22	1.77	XXIV (Upper Palaeolithic 3a)	OSL / IRSL/ TL	39700	2700	39700	42400	37000	2	Upper Palaeolithic	Sapiens	Daura et al, 2021
Cova del Gegant	Spain	41.22	1.77	IV	OSL / IRSL/ TL	44400	3100	44400	47500	41300	2	Upper Palaeolithic	Sapiens	Daura et al, 2021
Cova del Gegant	Spain	41.22	1.77	IV	Radiocarbon	34590	340	39663.5	40846.725	38480.275	2	Upper Palaeolithic	Sapiens	Daura et al, 2021
Cova del Gegant	Spain	41.22	1.77	IV	Radiocarbon	34800	1000	39226.5	41983.875	36469.125	2	Upper Palaeolithic	Sapiens	Daura et al, 2021
Cova del Gegant	Spain	41.22	1.77	IV	Radiocarbon	36060	390	40957.5	42017.225	39897.775	2	Upper Palaeolithic	Sapiens	Daura et al, 2021

Cova del Gegant	Spain	41.22	1.77	V	U/Th	52300	2300	52300	54600	50000	2	Middle Palaeolithic	Neanderthal	Daura et al, 2021
Cova del Gegant	Spain	41.22	1.77	V	U/Th	55800	240	55800	56040	55560	2	Middle Palaeolithic	Neanderthal	Daura et al, 2021
Cova del Gegant	Spain	41.22	1.77	V	U/Th	56850	1720	56850	58570	55130	2	Middle Palaeolithic	Neanderthal	Daura et al, 2021
Cova del Gegant	Spain	41.22	1.77	V	U/Th	56980	270	56980	57250	56710	2	Middle Palaeolithic	Neanderthal	Daura et al, 2021
Cova del Gegant	Spain	41.22	1.77	V	U/Th	57450	1500	57450	58950	55950	2	Middle Palaeolithic	Neanderthal	Daura et al, 2021
Cova Eiros	Spain	42.75	-7.21	2	OSL / IRSL/ TL	32787	2478	32787	35265	30309	2	Aurignacian	Sapiens	Lombera-Hermida et al, 2021
Cova Eiros	Spain	42.75	-7.21	2	Radiocarbon	31690	240	36073	36866.25	35279.75	2	Aurignacian	Sapiens	Lombera-Hermida et al, 2021
Cova Eiros	Spain	42.75	-7.21	3	Radiocarbon	35100	700	39742	41861.45	37622.55	2	Mousterian	Neanderthal	Lombera-Hermida et al, 2021
Cova Foradada	Spain	41.20	1.58	IV	Radiocarbon	31900	200	36199	36952.35	35445.65	0	Chatelperronian	Neanderthal	Morales et al, 2019
Cova Foradada	Spain	41.20	1.58	IV	Radiocarbon	34300	1000	38977.5	41750.075	36204.925	1	Chatelperronian	Neanderthal	Morales et al, 2019
Cova Foradada	Spain	41.20	1.58	IV	Radiocarbon	34490	320	39523	40697.2	38348.8	2	Chatelperronian	Neanderthal	Morales et al, 2019
Cova Foradada	Spain	41.20	1.58	IV	Radiocarbon	34570	240	39841	40600.05	39081.95	2	Chatelperronian	Neanderthal	Morales et al, 2019
Cova Foradada	Spain	41.20	1.58	IIIc	Radiocarbon	30220	180	34733	35319.15	34146.85	2	Early Aurignacian	Sapiens	Morales et al, 2019
Cova Foradada	Spain	41.20	1.58	IIIc	Radiocarbon	30760	150	35100.5	35660.525	34540.475	2	Early Aurignacian	Sapiens	Morales et al, 2019
Cova Foradada	Spain	41.20	1.58	IIIc	Radiocarbon	30770	180	35198	35891.5	34504.5	2	Early Aurignacian	Sapiens	Morales et al, 2019
Cova Foradada	Spain	41.20	1.58	IIIc	Radiocarbon	31690	180	36012	36679.85	35344.15	2	Early Aurignacian	Sapiens	Morales et al, 2019
Cova Foradada	Spain	41.20	1.58	IIIc	Radiocarbon	32050	550	36865	38944.55	34785.45	2	Early Aurignacian	Sapiens	Morales et al, 2019
Cova Foradada	Spain	41.20	1.58	IIIc	Radiocarbon	33170	370	37875	39359.85	36390.15	2	Early Aurignacian	Sapiens	Morales et al, 2019
Cova Gran	Spain	42.06	1.09	497D	OSL / IRSL/ TL	36610	4056	36610	40666	32554	2	Early Upper Palaeolithic	Sapiens	Mora et al., 2018
Cova Gran	Spain	42.06	1.09	497D	Radiocarbon	26340	130	30585	31079	30091	2	Early Upper Palaeolithic	Sapiens	Mora et al., 2018
Cova Gran	Spain	42.06	1.09	497D	Radiocarbon	32630	450	37401	39151.85	35650.15	2	Early Upper Palaeolithic	Sapiens	Mora et al., 2018
Cova Gran	Spain	42.06	1.09	497D	Radiocarbon	32368	241	36805.5	37584.025	36026.975	2	Early Upper Palaeolithic	Sapiens	Mora et al., 2018

Cova Gran	Spain	42.06	1.09	497D	Radiocarbon	33068	261	37825.5	39138.875	36512.125	2	Early Upper Palaeolithic	Sapiens	Mora et al., 2018
Cova Gran	Spain	42.06	1.09	497D	Radiocarbon	34179	247	39027.5	40275.325	37779.675	2	Early Upper Palaeolithic	Sapiens	Mora et al., 2018
Cova Gran	Spain	42.06	1.09	S1B	OSL / IRSL/ TL	35820	2237	35820	38057	33583	1	Middle Palaeolithic	Neanderthal	Mora et al., 2018
Cova Gran	Spain	42.06	1.09	S1B	Radiocarbon	38640	440	42548	43147.45	41948.55	2	Middle Palaeolithic	Neanderthal	Mora et al., 2018
Cova Gran	Spain	42.06	1.09	S1C	OSL / IRSL/ TL	40288	3389	40288	43677	36899	1	Middle Palaeolithic	Neanderthal	Mora et al., 2018
Cova Gran	Spain	42.06	1.09	S1C	Radiocarbon	32000	300	36396	37422	35370	1	Middle Palaeolithic	Neanderthal	Mora et al., 2018
Cova Gran	Spain	42.06	1.09	S1D	OSL / IRSL/ TL	41308	3979	41308	45287	37329	1	Middle Palaeolithic	Neanderthal	Mora et al., 2018
Cova Gran	Spain	42.06	1.09	S1D	Radiocarbon	33090	350	37817.5	39274.325	36360.675	1	Middle Palaeolithic	Neanderthal	Mora et al., 2018
Cova Gran	Spain	42.06	1.09	S1D	Radiocarbon	32180	430	36918	38507.35	35328.65	1	Middle Palaeolithic	Neanderthal	Mora et al., 2018
Cova Gran	Spain	42.06	1.09	S1D	Radiocarbon	32260	490	37152.5	38997.875	35307.125	1	Middle Palaeolithic	Neanderthal	Mora et al., 2018
Covalejos	Spain	43.39	-3.93	D/4	Radiocarbon	40650	2300	44313.5	48573.775	40053.225	2	discoid Mousterian	Neanderthal	Sanguino and Montes, 2005
Covalejos	Spain	43.39	-3.93	D/4	Radiocarbon	41640	650	44437	45920.9	42953.1	2	discoid Mousterian	Neanderthal	Sanguino and Montes, 2005
Covalejos	Spain	43.39	-3.93	D/4	Radiocarbon	43050	650	45917	47564.3	44269.7	2	discoid Mousterian	Neanderthal	Maroto et al, 2012
Covalejos	Spain	43.39	-3.93	D/4	Radiocarbon	39900	430	43410	44363.8	42456.2	2	Mousterian	Neanderthal	Maroto, Montes & Rasines del Rio, 2021
Covalejos	Spain	43.39	-3.93	C/3	Radiocarbon	32840	265	37659	39007.05	36310.95	2	Proto-Aurignacian	Sapiens	Sanguino and Montes, 2005
Covalejos	Spain	43.39	-3.93	C/3	Radiocarbon	34850	600	39537	41455.05	37618.95	2	Proto-Aurignacian	Sapiens	Marín-Arroyo et al., 2018
Covalejos	Spain	43.39	-3.93	C/3	Radiocarbon	35250	700	39830	41930.45	37729.55	2	Proto-Aurignacian	Sapiens	Marín-Arroyo et al., 2018
Covalejos	Spain	43.39	-3.93	C/3	Radiocarbon	37940	700	42020	43126.75	40913.25	2	Proto-Aurignacian	Sapiens	Maroto et al, 2012
Cueva Anton	Spain	38.06	-1.50	AS1 (I-k)	Radiocarbon	31790	270	36145.5	36998.125	35292.875	1	?	Neanderthal/Sapiens	Zilhão et al, 2016, 2017
Cueva Anton	Spain	38.06	-1.50	AS1 (I-k)	Radiocarbon	32330	250	36759.5	37573.175	35945.825	1	?	Neanderthal/Sapiens	Zilhão et al, 2016, 2017
Cueva Anton	Spain	38.06	-1.50	AS1 (II-a)	Radiocarbon	32390	280	36809.5	37698.225	35920.775	1	Middle Palaeolithic	Neanderthal	Zilhão et al, 2016, 2017
Cueva Anton	Spain	38.06	-1.50	AS1 (II-b)	Radiocarbon	32890	200	37667.5	38877.325	36457.675	1	Middle Palaeolithic	Neanderthal	Zilhão et al, 2016, 2017

Cueva Millan	Spain	42.06	-3.45	1b	Radiocarbon	37450	650	41714.5	42806.525	40622.475	1	Middle Paleolithic	Neanderthal	Moure and Garcia Soto, 1982 ; Diez et al, 2008
Cueva Millan	Spain	42.06	-3.45	1a	Radiocarbon	37600	700	41775	42926.4	40623.6	1	Middle Paleolithic	Neanderthal	Moure and Garcia Soto, 1982 ; Diez et al, 2008
Cueva Morin	Spain	43.36	-3.86	11	Radiocarbon	39770	730	43406.5	44644.825	42168.175	2	Middle Palaeolithic	Neanderthal	Maillo-Fernández et al, 2001
Cueva Morin	Spain	43.36	-3.86	11	Radiocarbon	43600	600	46301	47969.2	44632.8	2	Middle Palaeolithic	Neanderthal	Higham et al, 2014
Cueva Morin	Spain	43.36	-3.86	8	Radiocarbon	36590	770	40998	42505.65	39490.35	2	Proto-Aurignacian	Sapiens	Maillo-Fernández et al, 2001
El Canaveral	Spain	40.40	-3.55	Area 3	OSL / IRSL/ TL	33000	4000	33000	37000	29000	2	Middle Palaeolithic	Neanderthal	Nieto-Márquez & Baena Preysler, 2017
El Castillo	Spain	43.29	-3.97	XX (mean)	ESR	42700	9900	42700	52600	32800	2	Middle Palaeolithic	Neanderthal	Liberda et al, 2010
El Castillo	Spain	43.29	-3.97	18C	ESR	39900	4600	39900	44500	35300	1	Transitional	Neanderthal ?	Rink et al, 1996 ; Wood et al, 2018, Garralda et al, 2022
El Castillo	Spain	43.29	-3.97	16	Radiocarbon	34300	1000	38977.5	41750.075	36204.925	2	Archaic Aurignacian	Sapiens	Cabrera Valdes et al, 1996 ; Wood et al, 2018
El Castillo	Spain	43.29	-3.97	16	Radiocarbon	38600	1000	42627.5	44442.475	40812.525	2	Archaic Aurignacian	Sapiens	Wood et al, 2018
El Castillo	Spain	43.29	-3.97	20B2	Radiocarbon	39300	1900	43042.5	46555.125	39529.875	2	Middle Palaeolithic	Neanderthal	Cabrera Valdes et al, 1996 ; Wood et al, 2018
El Castillo	Spain	43.29	-3.97	Mousterian alpha	Radiocarbon	42100	1500	45386	48332.9	42439.1	2	Middle Palaeolithic	Neanderthal	Cabrera Valdes et al, 1996 ; Wood et al, 2018
El Castillo	Spain	43.29	-3.97	Mousterian alpha	Radiocarbon	42900	1400	45805	48791.8	42818.2	2	Middle Palaeolithic	Neanderthal	Bernaldo de Quiros et al, 2006 ; Wood et al, 2018
El Castillo	Spain	43.29	-3.97	20B2	Radiocarbon	43300	2900	48187.5	54659.375	41715.625	2	Middle Palaeolithic	Neanderthal	Cabrera Valdes et al, 1996 ; Wood et al, 2018
El Castillo	Spain	43.29	-3.97	Mousterian alpha	Radiocarbon	45700	1700	49584.5	54741.825	44679.175	2	Middle Palaeolithic	Neanderthal	Bernaldo de Quiros et al, 2006 ; Wood et al, 2018
El Castillo	Spain	43.29	-3.97	20C	Radiocarbon	48700	3400	49582.5	54729.125	44435.875	2	Middle Palaeolithic	Neanderthal	Wood et al, 2018
El Castillo	Spain	43.29	-3.97	20C	Radiocarbon	49400	3700	49572.5	54728.625	44416.375	2	Middle Palaeolithic	Neanderthal	Wood et al, 2018

El Castillo	Spain	43.29	-3.97	18B2	Radiocarbon	37100	2200	40564.5	45016.675	36112.325	2	Transitional	Neanderthal ?	Cabrera Valdes et al, 1996 ; Wood et al, 2018
El Castillo	Spain	43.29	-3.97	18B2	Radiocarbon	37700	1800	41109	44892.85	37325.15	1	Transitional	Neanderthal ?	Cabrera Valdés and Bischoff, 1989 ; Wood et al, 2018
El Castillo	Spain	43.29	-3.97	18B1	Radiocarbon	38500	1800	42286.5	45667.075	38905.925	1	Transitional	Neanderthal ?	Cabrera Valdés and Bischoff, 1989 ; Wood et al, 2018
El Castillo	Spain	43.29	-3.97	18B2	Radiocarbon	38500	1300	42334.5	44748.925	39920.075	2	Transitional	Neanderthal ?	Cabrera Valdes et al, 1996 ; Wood et al, 2018
El Castillo	Spain	43.29	-3.97	18C	Radiocarbon	39500	2000	43198.5	46865.025	39531.975	2	Transitional	Neanderthal ?	Cabrera Valdes et al, 1996 ; Wood et al, 2018
El Castillo	Spain	43.29	-3.97	18C	Radiocarbon	39800	1400	43514	45889.95	41138.05	2	Transitional	Neanderthal ?	Cabrera Valdes et al, 1996 ; Wood et al, 2018
El Castillo	Spain	43.29	-3.97	18C	Radiocarbon	40000	2100	43779.5	47754.775	39804.225	1	Transitional	Neanderthal ?	Cabrera Valdés and Bischoff, 1989 ; Wood et al, 2018
El Castillo	Spain	43.29	-3.97	18B2	Radiocarbon	40700	1600	44410	47350.25	41469.75	2	Transitional	Neanderthal ?	Cabrera Valdes et al, 1996 ; Wood et al, 2018
El Castillo	Spain	43.29	-3.97	18C	Radiocarbon	40700	1500	44269.5	46914.775	41624.225	2	Transitional	Neanderthal ?	Cabrera Valdes et al, 1996 ; Wood et al, 2018
El Castillo	Spain	43.29	-3.97	18C	Radiocarbon	41100	1700	44765	47918.05	41611.95	2	Transitional	Neanderthal ?	Cabrera Valdes et al, 1996 ; Wood et al, 2018
El Castillo	Spain	43.29	-3.97	18C	Radiocarbon	42000	1500	45329	48252.15	42405.85	2	Transitional	Neanderthal ?	Wood et al, 2018
El Castillo	Spain	43.29	-3.97	18C	Radiocarbon	42700	1600	45974	49360.75	42587.25	2	Transitional	Neanderthal ?	Wood et al, 2018
El Castillo	Spain	43.29	-3.97	18C	Radiocarbon	43100	1700	46274.5	49881.175	42667.825	2	Transitional	Neanderthal ?	Wood et al, 2018
El Castillo	Spain	43.29	-3.97	18B	Radiocarbon	45800	2300	49120.5	54706.025	43534.975	2	Transitional	Neanderthal ?	Wood et al, 2018
El Castillo	Spain	43.29	-3.97	18B	Radiocarbon	46000	2400	49126.5	54706.325	43546.675	2	Transitional	Neanderthal ?	Wood et al, 2018
El Conde	Spain	43.29	-5.98	N20b	Radiocarbon	34730	500	39445.5	41179.725	37711.275	2	Autignacian	Sapiens	Arbizou et al, 2010 ; López-García et al, 2011

El Conde	Spain	43.29	-5.98	N20A	Radiocarbon	37710	470	41970	42741.4	41198.6	2	Middle Palaeolithic	Neanderthal	Arbizou et al, 2010 ; López-Garcíaet al, 2011
El Conde	Spain	43.29	-5.98	N20A	Radiocarbon	38250	390	42351.5	42889.675	41813.325	2	Middle Palaeolithic	Neanderthal	Arbizou et al, 2010 ; López-García et al, 2011
El Conde	Spain	43.29	-5.98	N104	Radiocarbon	39110	520	43091.5	44098.975	42084.025	2	Middle Palaeolithic	Neanderthal	Arbizou et al, 2010 ; López-García et al, 2011
El Cuco	Spain	43.39	-3.23	X	Radiocarbon	42350	700	44987	46734.05	43239.95	2	Mousterian microlithic	Neanderthal	Gutiérrez-Zugasti et al, 2018 ; Rios-Garaizar et al, 2020
El Cuco	Spain	43.39	-3.23	X	Radiocarbon	46200	650	49019.5	51577.375	46461.625	2	Mousterian microlithic	Neanderthal	Gutiérrez-Zugasti et al, 2018 ; Rios-Garaizar et al, 2020
El Cuco	Spain	43.39	-3.23	XIII	Radiocarbon	46400	800	49185.5	52040.725	46330.275	2	Mousterian microlithic	Neanderthal	Gutiérrez-Zugasti et al, 2018 ; Rios-Garaizar et al, 2020
El Miron	Spain	43.27	-3.33	130	Radiocarbon	41280	1120	44539	46665.1	42412.9	2	Middle Palaeolithic	Neanderthal	Marín-Arroyo et al., 2020
El Miron	Spain	43.27	-3.33	130	Radiocarbon	48200	3300	49495	54724.75	44265.25	2	Middle Palaeolithic	Neanderthal	Marín-Arroyo et al., 2020
El Niño	Spain	38.57	-2.09	III	Radiocarbon	28270	80	32414	33060	31768	1	Middle Palaeolithic		García-Moreno et al., 2016
El Niño	Spain	38.57	-2.09	IV	Radiocarbon	28660	90	32902.5	33684.825	32120.175	1	Middle Palaeolithic		García-Moreno et al., 2016
El Niño	Spain	38.57	-2.09	XI	U/Th	55550	0	55550	55550	55550	2	Middle Palaeolithic		García-Moreno et al., 2016
El Salt	Spain	38.69	-0.51	XI	OSL / IRSL/ TL	44000	3300	44000	47300	40700	2	Middle Palaeolithic	Neanderthal	Galván et al. 2014
El Salt	Spain	38.69	-0.51	V	OSL / IRSL/ TL	44700	3200	44700	47900	41500	2	Middle Palaeolithic	Neanderthal (human remains level V)	Galván et al. 2014
El Salt	Spain	38.69	-0.51	V-VI	OSL / IRSL/ TL	45200	3400	45200	48600	41800	2	Middle Palaeolithic	Neanderthal (human remains level V)	Galván et al. 2014
El Salt	Spain	38.69	-0.51	VI-VII	OSL / IRSL/ TL	45800	4500	45800	50300	41300	2	Middle Palaeolithic	Neanderthal	Galván et al. 2014
El Salt	Spain	38.69	-0.51	V-VI	OSL / IRSL/ TL	47200	4400	47200	51600	42800	2	Middle Palaeolithic	Neanderthal (human remains level V)	Galván et al. 2014
El Salt	Spain	38.69	-0.51	IX	OSL / IRSL/ TL	47500	4300	47500	51800	43200	2	Middle Palaeolithic	Neanderthal	Galván et al. 2014
El Salt	Spain	38.69	-0.51	XI	OSL / IRSL/ TL	48200	4800	48200	53000	43400	2	Middle Palaeolithic	Neanderthal	Galván et al. 2014

El Salt	Spain	38.69	-0.51	XII	OSL / IRSL/ TL	49000	3700	49000	52700	45300	2	Middle Palaeolithic	Neanderthal	Galván et al. 2014
El Salt	Spain	38.69	-0.51	IX	OSL / IRSL/ TL	52200	320	52200	52520	51880	2	Middle Palaeolithic	Neanderthal	Galván et al. 2014
El Salt	Spain	38.69	-0.51	VI-VII	OSL / IRSL/ TL	52600	6800	52600	59400	45800	2	Middle Palaeolithic	Neanderthal	Galván et al. 2014
El Salt	Spain	38.69	-0.51	IX	OSL / IRSL/ TL	53900	3300	53900	57200	50600	2	Middle Palaeolithic	Neanderthal	Galván et al. 2014
El Salt	Spain	38.69	-0.51	XII	OSL / IRSL/ TL	55500	3100	55500	58600	52400	2	Middle Palaeolithic	Neanderthal	Galván et al. 2014
El Salt	Spain	38.69	-0.51	XI	OSL / IRSL/ TL	56500	3100	56500	59600	53400	2	Middle Palaeolithic	Neanderthal	Galván et al. 2014
El Salt	Spain	38.69	-0.51	IX	OSL / IRSL/ TL	57400	3700	57400	61100	53700	2	Middle Palaeolithic	Neanderthal	Galván et al. 2014
El Sidron	Spain	43.38	-5.32	Galeria del Osario III (Neanderthal bone)	Radiocarb on	48400	3200	49632	54731.6	44532.4	2	Middle Palaeolithic	Neanderthal	Wood et al., 2013
Els Canyars	Spain	41.30	1.98	Layer 1	Radiocarb on	34900	340	40112	41068.65	39155.35	2	Aurignacian	Sapiens	Daura et al, 2013
Els Canyars	Spain	41.30	1.98	Layer 1	Radiocarb on	34980	350	40162	41133.85	39190.15	2	Aurignacian	Sapiens	Daura et al, 2013
Els Canyars	Spain	41.30	1.98	Layer 1	Radiocarb on	33800	350	38512	39917.05	37106.95	2	Aurignacian	Sapiens	Daura et al, 2013
Els Pinyons	Spain	41.53	1.69	7	Radiocarb on	37900	500	42055.5	42855.875	41255.125	2	Middle Palaeolithic	Neanderthal	Vaquero, 2010
Els Pinyons	Spain	41.53	1.69	9	U/Th	48100	1300	48100	49400	46800	2	Middle Palaeolithic	Neanderthal	Vaquero, 2010
Els Pinyons	Spain	41.53	1.69	9	U/Th	52700	1900	52700	54600	50800	2	Middle Palaeolithic	Neanderthal	Vaquero, 2010
Ermitons	Spain	42.28	2.59	IV	Radiocarb on	40580	550	43728	44835.7	42620.3	2	Middle Palaeolithic	Neanderthal	Maroto et al, 2012
Escoural	Portugal	38.54	-8.14	test 3a	U/Th	48900	5650	48900	54550	43250	2	Middle Palaeolithic	Neanderthal	Zilhao, 2001
Esquilleu	Spain	43.23	-4.60	VI (F12)	Radiocarb on	43700	1400	46514	49834.25	43193.75	2	Middle Palaeolithic	Neanderthal	Higham et al, 2014
Esquilleu	Spain	43.23	-4.60	VI (F12)	Radiocarb on	44100	1300	46927.5	49967.975	43887.025	2	Middle Palaeolithic	Neanderthal	Higham et al, 2014
Estret de Trago	Spain	41.87	0.72	S6	OSL / IRSL/ TL	43000	4600	43000	47600	38400	2	Middle Palaeolithic	Neanderthal	Casanova et al, 2009, 2014
Estret de Trago	Spain	41.87	0.72	S5	OSL / IRSL/ TL	46100	4600	46100	50700	41500	2	Middle Palaeolithic	Neanderthal	Casanova et al, 2009, 2014
Estret de Trago	Spain	41.87	0.72	S7	OSL / IRSL/ TL	47800	4900	47800	52700	42900	2	Middle Palaeolithic	Neanderthal	Casanova et al, 2009, 2014

Estret de Trago	Spain	41.87	0.72	S7	OSL / IRSL/ TL	52100	6700	52100	58800	45400	2	Middle Palaeolithic	Neanderthal	Casanova et al, 2009, 2014
Foz do Enxarriq ue	Portugal	39.65	-7.67	T6 lower middle part	OSL / IRSL/ TL	43000	4000	43000	47000	39000	2	Middle Palaeolithic	Neanderthal	Cunha et al, 2019
Foz do Enxarriq ue	Portugal	39.65	-7.67	T6, base middle part	OSL / IRSL/ TL	44000	3000	44000	47000	41000	2	Middle Palaeolithic	Neanderthal	Cunha et al, 2019
Fuente Mudarra	Spain	42.35	-3.54	Layer 4	OSL / IRSL/ TL	56831	3310	56831	60141	53521	2	Middle Paleolithic	Neanderthal	Santamaría et al, 2021
Fuentes de San Cristobal	Spain	42.14	-0.41	G	Radiocarb on	36200	350	41099	42040.45	40157.55	2	Middle Palaeolithic	Neanderthal	Maroto et al, 2012
Fuentes de San Cristobal	Spain	42.14	-0.41	F	Radiocarb on	37330	490	41747.5	42570.675	40924.325	2	Middle Palaeolithic	Neanderthal	Maroto et al, 2012
Fuentes de San Cristobal	Spain	42.14	-0.41	G	Radiocarb on	38550	450	42502.5	43111.925	41893.075	2	Middle Palaeolithic	Neanderthal	Maroto et al, 2012
Fuentes de San Cristobal	Spain	42.14	-0.41	E	Radiocarb on	38650	600	42771	43922.4	41619.6	2	Middle Palaeolithic	Neanderthal	Maroto et al, 2012
Fuentes de San Cristobal	Spain	42.14	-0.41	F	Radiocarb on	39290	490	43172	44159.05	42184.95	2	Middle Palaeolithic	Neanderthal	Maroto et al, 2012
Gabasa	Spain	42.01	0.42	e	Radiocarb on	46500	4400	48444	54672.2	42215.8	1	Mousterian of Acheulean Tradition	Neanderthal	Blasco, 1997
Galeria de las Estatuas	Spain	42.35	-3.52	GE-I 1	Radiocarb on	43500	1800	46926	51076.55	42775.45	1	Middle Palaeolithic	Neanderthal	Arsuaga et al, 2017
Galeria de las Estatuas	Spain	42.35	-3.52	GE-I 3	Radiocarb on	44000	1900	47430	51920.65	42939.35	1	Middle Palaeolithic	Neanderthal	Arsuaga et al, 2017
Galeria de las Estatuas	Spain	42.35	-3.52	GE-II 1b	Radiocarb on	44200	2000	47535.5	52121.625	42949.375	1	Middle Palaeolithic	Neanderthal	Arsuaga et al, 2017
Gato Preto	Portugal	39.33	-8.93	C (average of 2 dates TL)	OSL / IRSL/ TL	38100.0	3900.0	38100.0	42000	34200	2	Aurignacian	Sapiens	Zilhão, 2006
Gatzarria	Spain	43.14	-0.92	Cj Mousterian	Radiocarb on	44300	1900	47574.5	52071.325	43077.675	1	Middle Palaeolithic	Neanderthal	Deschamps, 2019
Gatzarria	Spain	43.14	-0.92	cjn2	Radiocarb on	33800	550	38523.5	40498.075	36548.925	1	Proto-Aurignacian	Sapiens	Barshay-Szmidt et al, 2012
Gatzarria	Spain	43.14	-0.92	cjn2	Radiocarb on	36300	700	40878.5	42332.475	39424.525	2	Proto-Aurignacian	Sapiens	Barshay-Szmidt et al, 2012

Gatzarria	Spain	43.14	-0.92	Cj Mousterian	Radiocarbon	44200	2000	47535.5	52121.625	42949.375	1	Middle Palaeolithic	Neanderthal	Deschamps, 2019
Gatzarria	Spain	43.14	-0.92	Cj Mousterian	Radiocarbon	45600	2400	49005	54700.25	43309.75	1	Middle Palaeolithic	Neanderthal	Deschamps, 2019
Gatzarria	Spain	43.14	-0.92	Cj Mousterian	Radiocarbon	47200	2800	49518.5	54725.925	44311.075	1	Middle Palaeolithic	Neanderthal	Deschamps, 2019
Gorham	Spain	36.12	-5.34	III	Radiocarbon	32560	780	37252.5	39697.325	34807.675	1	Middle Palaeolithic	Neanderthal	Finlayson et al, 2006
Gorham	Spain	36.12	-5.34	context 18	Radiocarbon	42200	1100	45251.5	47728.625	42774.375	2	Middle Palaeolithic	Neanderthal	Schmidt et al., 2012
Gorham	Spain	36.12	-5.34	context 19	Radiocarbon	42800	2100	46495	50675.95	42314.05	2	Middle Palaeolithic	Neanderthal	Carrión et al., 2008
Gorham	Spain	36.12	-5.34	context 19	Radiocarbon	43800	1300	46560.5	49751.075	43369.925	2	Middle Palaeolithic	Neanderthal	Schmidt et al., 2012
Gorham	Spain	36.12	-5.34	IV	Radiocarbon	44090	2200	48054	54638.65	42765.35	2	Middle Palaeolithic	Neanderthal	Carrión et al., 2008
Gorham	Spain	36.12	-5.34	context 22	Radiocarbon	45300	1700	49051	54756.2	44418.8	2	Middle Palaeolithic	Neanderthal	Schmidt et al., 2012
Gorham	Spain	36.12	-5.34	IV	Radiocarbon	46540	1800	49870.5	54743.525	44997.475	2	Middle Palaeolithic	Neanderthal	Schmidt et al., 2012
Gorham	Spain	36.12	-5.34	context 19	Radiocarbon	46700	1900	49861.5	54743.075	44979.925	2	Middle Palaeolithic	Neanderthal	Schmidt et al., 2012
Gorham	Spain	36.12	-5.34	context 18	Radiocarbon	47900	2100	50188.5	54759.425	45617.575	2	Middle Palaeolithic	Neanderthal	Schmidt et al., 2012
Gorham	Spain	36.12	-5.34	context 22D	Radiocarbon	51700	3300	50406	54770.3	46041.7	2	Middle Palaeolithic	Neanderthal	Schmidt et al., 2012
Gruta do Caldeirao	Portugal	39.65	-8.42	K	OSL / IRSL/ TL	37700.0	2800.0	37700.0	40500	34900	2	Early Upper Palaeolithic	Sapiens	Zilhao 2021
Gruta do Caldeirao	Portugal	39.65	-8.42	M	OSL / IRSL/ TL	37900.0	2300.0	37900.0	40200	35600	2	Middle Palaeolithic	Neanderthal	Zilhao 2021
Gruta do Caldeirao	Portugal	39.65	-8.42	L	OSL / IRSL/ TL	39600.0	2300.0	39600.0	41900	37300	2	Middle Palaeolithic	Neanderthal	Zilhao 2021
Gruta do Caldeirao	Portugal	39.65	-8.42	N	OSL / IRSL/ TL	42000.0	2500.0	42000.0	44500	39500	2	Middle Palaeolithic	Neanderthal	Zilhao 2021
Gruta do Caldeirao	Portugal	39.65	-8.42	K	Radiocarbon	26790	260	30884	31645.9	30122.1	2	Early Upper Palaeolithic	Sapiens	Zilhao 2021
Gruta do Caldeirao	Portugal	39.65	-8.42	K	Radiocarbon	27600	600	32057	33953.2	30160.8	2	Early Upper Palaeolithic	Sapiens	Zilhao 2021
Gruta do Caldeirao	Portugal	39.65	-8.42	K	Radiocarbon	28000	210	32177	33111.8	31242.2	2	Early Upper Palaeolithic	Sapiens	Zilhao 2021
Gruta do Caldeirao	Portugal	39.65	-8.42	L	Radiocarbon	36490	390	41457	42028	40886	2	Middle Palaeolithic	Neanderthal	Zilhao 2021
Gruta do Caldeirao	Portugal	39.65	-8.42	L	Radiocarbon	28150	160	32337	33121.7	31552.3	0	Middle Palaeolithic	Neanderthal	Zilhao 2021

Gruta do Caldeirao	Portugal	39.65	-8.42	M	Radiocarbon	31900	170	36201	36904	35498	1	Middle Palaeolithic	Neanderthal	Zilhao 2021
Gruta do Caldeirao	Portugal	39.65	-8.42	Unit 6	Radiocarbon	32890	260	37691.5	39033.375	36349.625	1	Middle Palaeolithic	Neanderthal	Zilhao 2021
Gruta do Caldeirao	Portugal	39.65	-8.42	Unit 5	Radiocarbon	33810	290	38531.5	39797.375	37265.625	1	Middle Palaeolithic	Neanderthal	Zilhao 2021
Gruta do Caldeirao	Portugal	39.65	-8.42	L	Radiocarbon	36490	390	41329.5	42182.125	40476.875	1	Middle Palaeolithic	Neanderthal	Zilhao 2021
Higueral la Valleja	Spain	36.75	-5.81	VI	OSL / IRSL/ TL	54400	9700	54400	64100	44700	2	Middle Palaeolithic	Neanderthal	Jennings et al, 2009
Higueral la Valleja	Spain	36.75	-5.81	VI	OSL / IRSL/ TL	54900	5600	54900	60500	49300	2	Middle Palaeolithic	Neanderthal	Jennings et al, 2009
Higueral la Valleja	Spain	36.75	-5.81	V	Radiocarbon	20780	80	25067.5	25524.925	24610.075	0	Middle Palaeolithic	Neanderthal	Jennings et al, 2009
Higueral la Valleja	Spain	36.75	-5.81	VI	Radiocarbon	32840	210	37606.5	38822.025	36390.975	1	Middle Palaeolithic	Neanderthal	Jennings et al, 2009
Higueral la Valleja	Spain	36.75	-5.81	VII	Radiocarbon	33950	200	38724.5	39769.975	37679.025	1	Middle Palaeolithic	Neanderthal	Jennings et al, 2009
Higueral la Valleja	Spain	36.75	-5.81	VII	Radiocarbon	37220	290	41788	42352.3	41223.7	1	Middle Palaeolithic	Neanderthal	Jennings et al, 2009
Higueral la Valleja	Spain	36.75	-5.81	VIII	Radiocarbon	52400	2100	51774.5	54838.725	48710.275	0	Middle Palaeolithic	Neanderthal	Jennings et al, 2009
Higueral la Valleja	Spain	36.75	-5.81	VIII	Radiocarbon	56800	2900	51809	54840.45	48777.55	0	Middle Palaeolithic	Neanderthal	Jennings et al, 2009
Hotel California	Spain	42.35	-3.53	V	OSL / IRSL/ TL	48200	3900	48200	52100	44300	2	Middle Palaeolithic	Neanderthal	Arnold et al, 2013
Hotel California	Spain	42.35	-3.53	V	OSL / IRSL/ TL	48200	3300	48200	51500	44900	2	Middle Palaeolithic	Neanderthal	Arnold et al, 2013
Hotel California	Spain	42.35	-3.53	II	OSL / IRSL/ TL	57600	5700	57600	63300	51900	2	Middle Palaeolithic	Neanderthal	Arnold et al, 2013
Ibex cave	Spain	36.14	-5.35	Unit 319	ESR	49400	3200	49400	52600	46200	2	Middle Palaeolithic	Neanderthal	Rhodes et al, 2000; Vidal et al, 2004
Jarama VI	Spain	40.97	-3.33	2.2	Radiocarbon	49400	3700	49572.5	54728.625	44416.375	2	Middle Palaeolithic	Neanderthal	Wood et al., 2013
Jarama VI	Spain	40.97	-3.33	2.3	OSL / IRSL/ TL	53000	5200	53000	58200	47800	2	Middle Paleolithic	Neanderthal	Kehl et al., 2013; Wood et al., 2013
Jarama VI	Spain	40.97	-3.33	2.3	OSL / IRSL/ TL	58600	5100	58600	63700	53500	2	Middle Paleolithic	Neanderthal	Kehl et al., 2013; Wood et al., 2013
Jarama VI	Spain	40.97	-3.33	2.3	OSL / IRSL/ TL	57200	4900	57200	62100	52300	2	Middle Paleolithic	Neanderthal	Kehl et al., 2013; Wood et al., 2013
Jarama VI	Spain	40.97	-3.33	2.2	OSL / IRSL/ TL	52500	4900	52500	57400	47600	2	Middle Paleolithic	Neanderthal	Kehl et al, 2013

Jarama VI	Spain	40.97	-3.33	2.2	OSL / IRSL/ TL	58800	6800	58800	65600	52000	2	Middle Paleolithic	Neanderthal	Kehl et al, 2013
La Boja	Spain	38.07	-1.49	OH17	OSL / IRSL/ TL	32600	1900	32600	34500	30700	2	Aurignacian	Sapiens	Zilhao et al, 2017
La Boja	Spain	38.07	-1.49	OH18	OSL / IRSL/ TL	33700	4000	33700	37700	29700	2	Aurignacian	Sapiens	Zilhao et al, 2017
La Boja	Spain	38.07	-1.49	OH18	OSL / IRSL/ TL	35800	2800	35800	38600	33000	2	Aurignacian	Sapiens	Zilhao et al, 2017
La Boja	Spain	38.07	-1.49	OH18	OSL / IRSL/ TL	37400	5300	37400	42700	32100	2	Aurignacian	Sapiens	Zilhao et al, 2017
La Boja	Spain	38.07	-1.49	OH22	OSL / IRSL/ TL	36000	3900	36000	39900	32100	2	Middle Paleolithic	Neanderthal	Zilhao et al, 2017
La Boja	Spain	38.07	-1.49	OH21	OSL / IRSL/ TL	40900	5700	40900	46600	35200	2	Middle Paleolithic	Neanderthal	Zilhao et al, 2017
La Boja	Spain	38.07	-1.49	OH23	OSL / IRSL/ TL	41400	6100	41400	47500	35300	2	Middle Paleolithic	Neanderthal	Zilhao et al, 2017
La Boja	Spain	38.07	-1.49	OH23	OSL / IRSL/ TL	49300	3700	49300	53000	45600	2	Middle Paleolithic	Neanderthal	Zilhao et al, 2017
La Boja	Spain	38.07	-1.49	OH21	OSL / IRSL/ TL	51500	4500	51500	56000	47000	2	Middle Paleolithic	Neanderthal	Zilhao et al, 2017
La Boja	Spain	38.07	-1.49	OH18	Radiocarbon	30090	320	34542	35455.9	33628.1	2	Aurignacian	Sapiens	Zilhao et al, 2017
La Boja	Spain	38.07	-1.49	OH19	Radiocarbon	32331	439	37179	38947.9	35410.1	2	Aurignacian	Sapiens	Zilhao et al, 2017
La Boja	Spain	38.07	-1.49	OH20	Radiocarbon	33017	310	37771.5	39175.125	36367.875	2	Aurignacian	Sapiens	Zilhao et al, 2017
La Boja	Spain	38.07	-1.49	OH19	Radiocarbon	33233	335	37929.5	39341.675	36517.325	2	Aurignacian	Sapiens	Zilhao et al, 2017
La Boja	Spain	38.07	-1.49	OH22	Radiocarbon	40820	1090	44145	46016.5	42273.5	2	Middle Paleolithic	Neanderthal	Zilhao et al, 2017
La Boja	Spain	38.07	-1.49	horizon OH23	Radiocarbon	42800	1400	45738.5	48707.725	42769.275	2	Middle Paleolithic	Neanderthal	Zilhao et al, 2017
La Boja	Spain	38.07	-1.49	horizon OH22	Radiocarbon	45700	2100	49438	54721.9	44154.1	2	Middle Paleolithic	Neanderthal	Zilhao et al, 2017
La Boja	Spain	38.07	-1.49	horizon OH23	Radiocarbon	46200	2200	49575	54728.75	44421.25	2	Middle Paleolithic	Neanderthal	Zilhao et al, 2017
La Guelga	Spain	43.37	-5.10	D_2	Radiocarbon	37429	302	41875	42432.65	41317.35	2	Chatelperronian	Neanderthal ?	Menéndez et al, 2018
La Guelga	Spain	43.37	-5.10	D_2	Radiocarbon	40300	1200	43914.5	45897.625	41931.375	2	Chatelperronian	Neanderthal ?	Menéndez et al, 2018
La Guelga	Spain	43.37	-5.10	D_5	Radiocarbon	33610	220	38354	39437.95	37270.05	2	Early Aurignacian	Sapiens	Menéndez et al, 2018
La Guelga	Spain	43.37	-5.10	D_5	Radiocarbon	33900	550	38619	40588.35	36649.65	2	Early Aurignacian	Sapiens	Menéndez et al, 2018

La Guelga	Spain	43.37	-5.10	D_5	Radiocarbon	34121	266	38961.5	40241.625	37681.375	2	Early Aurignacian	Sapiens	Menéndez et al, 2018
La Guelga	Spain	43.37	-5.10	D_5	Radiocarbon	34164	273	39015	40328.85	37701.15	2	Early Aurignacian	Sapiens	Menéndez et al, 2018
La Guelga	Spain	43.37	-5.10	D_5	Radiocarbon	34355	751	38935.5	41279.625	36591.375	2	Early Aurignacian	Sapiens	Menéndez et al, 2018
La Guelga	Spain	43.37	-5.10	D_5	Radiocarbon	34500	763	39098.5	41473.975	36723.025	2	Early Aurignacian	Sapiens	Menéndez et al, 2018
La Guelga	Spain	43.37	-5.10	D_5	Radiocarbon	34750	600	39418.5	41344.625	37492.375	2	Early Aurignacian	Sapiens	Menéndez et al, 2018
La Guelga	Spain	43.37	-5.10	D_9	Radiocarbon	43700	800	46406.5	48335.475	44477.525	2	Middle Paleolithic	Neanderthal	Menéndez et al, 2018
La Guelga	Spain	43.37	-5.10	D_9	Radiocarbon	44330	1200	47170	49977.25	44362.75	2	Middle Paleolithic	Neanderthal	Menéndez et al, 2018
La Guelga	Spain	43.37	-5.10	D_4B	Radiocarbon	47400	2700	49654	54732.7	44575.3	2	Middle Paleolithic	Neanderthal	Menéndez et al, 2018
La Guelga	Spain	43.37	-5.10	D_4B	Radiocarbon	48500	3500	49405.5	54720.275	44090.725	2	Middle Paleolithic	Neanderthal	Menéndez et al, 2018
La Mina	Spain	42.09	-3.42	_	AAR	52500	0	52500	52500	52500	2	Middle Paleolithic	Neanderthal	Diez et al, 2008
Labeko Koba	Spain	43.06	-2.48	IX lower	Radiocarbon	37400	800	41499	42929.7	40068.3	2	Chatelperronian	Neanderthal ?	Higham et al, 2014
Labeko Koba	Spain	43.06	-2.48	IX lower	Radiocarbon	37800	900	41990	43791.95	40203.05	2	Chatelperronian	Neanderthal ?	Higham et al, 2014
Labeko Koba	Spain	43.06	-2.48	IX lower	Radiocarbon	37900	900	42165.5	43906.375	40424.625	2	Chatelperronian	Neanderthal ?	Higham et al, 2014
Labeko Koba	Spain	43.06	-2.48	IX lower	Radiocarbon	38000	900	42259	43988.95	40529.05	2	Chatelperronian	Neanderthal ?	Higham et al, 2014
Labeko Koba	Spain	43.06	-2.48	IX lower	Radiocarbon	38100	900	42336	44065	40607	2	Chatelperronian	Neanderthal ?	Higham et al, 2014
Labeko Koba	Spain	43.06	-2.48	VI	Radiocarbon	32200	450	37059.5	38797.525	35321.475	2	Early Aurignacian	Sapiens	Wood et al, 2014
Labeko Koba	Spain	43.06	-2.48	VI	Radiocarbon	33550	550	38325	40280.1	36369.9	2	Early Aurignacian	Sapiens	Wood et al, 2014
Labeko Koba	Spain	43.06	-2.48	VI	Radiocarbon	33600	500	38316.5	40144.775	36488.225	2	Early Aurignacian	Sapiens	Wood et al, 2014
Labeko Koba	Spain	43.06	-2.48	VI	Radiocarbon	34650	600	39284.5	41268.575	37300.425	2	Early Aurignacian	Sapiens	Wood et al, 2014
Labeko Koba	Spain	43.06	-2.48	VI	Radiocarbon	34750	600	39418.5	41344.625	37492.375	2	Early Aurignacian	Sapiens	Wood et al, 2014
Labeko Koba	Spain	43.06	-2.48	VI	Radiocarbon	35100	600	39783	41740	37826	2	Early Aurignacian	Sapiens	Wood et al, 2014
Labeko Koba	Spain	43.06	-2.48	VII	Radiocarbon	35400	650	40234	41963	38505	2	Proto-Aurignacian	Sapiens	Wood et al, 2014

Labeko Koba	Spain	43.06	-2.48	VII	Radiocarbon	36500	750	40956	42446.55	39465.45	2	Proto-Aurignacian	Sapiens	Wood et al, 2014
Labeko Koba	Spain	43.06	-2.48	VII	Radiocarbon	36850	800	41149	42669.95	39628.05	2	Proto-Aurignacian	Sapiens	Wood et al, 2014
Lapa do Picareiro	Portugal	39.53	-8.65	GG-II	Radiocarbon	33790	190	38586.5	39575.925	37597.075	2	Early Aurignacian	Sapiens	Haws et al, 2020
Lapa do Picareiro	Portugal	39.53	-8.65	GG-II	Radiocarbon	33880	160	38663.5	39615.875	37711.125	2	Early Aurignacian	Sapiens	Haws et al, 2020
Lapa do Picareiro	Portugal	39.53	-8.65	GG-II	Radiocarbon	33910	160	38692.5	39649.625	37735.375	2	Early Aurignacian	Sapiens	Haws et al, 2020
Lapa do Picareiro	Portugal	39.53	-8.65	GG-II	Radiocarbon	36390	210	41391	41993.3	40788.7	2	Early Aurignacian	Sapiens	Haws et al, 2020
Lapa do Picareiro	Portugal	39.53	-8.65	GG-II	Radiocarbon	36670	220	41569	42114.3	41023.7	2	Early Aurignacian	Sapiens	Haws et al, 2020
Lapa do Picareiro	Portugal	39.53	-8.65	JJ	Radiocarbon	40078	1239	43706.5	45838.775	41574.225	2	Middle Palaeolithic	Neanderthal	Haws et al, 2020
Lapa do Picareiro	Portugal	39.53	-8.65	JJ	Radiocarbon	41360	370	44135	45151.5	43118.5	2	Middle Palaeolithic	Neanderthal	Haws et al, 2020
Lapa do Picareiro	Portugal	39.53	-8.65	JJ	Radiocarbon	41480	220	44204.5	44983.975	43425.025	2	Middle Palaeolithic	Neanderthal	Haws et al, 2020
Lapa do Picareiro	Portugal	39.53	-8.65	JJ	Radiocarbon	41980	400	44722.5	45798.375	43494.625	2	Middle Palaeolithic	Neanderthal	Haws et al, 2020
Lapa do Picareiro	Portugal	39.53	-8.65	JJ	Radiocarbon	47510	760	50988.5	54835.325	47859.675	2	Middle Palaeolithic	Neanderthal	Haws et al, 2020
Lapa do Picareiro	Portugal	39.53	-8.65	JJ	Radiocarbon	48000	820	51494	54824.7	48163.3	2	Middle Palaeolithic	Neanderthal	Haws et al, 2020
Llonín	Spain	43.36	-4.58	VIII	Radiocarbon	43539	2419	47706.5	54440.325	42430.675	2	Middle Palaeolithic	Neanderthal	Sanchis et al., 2019
L'Arbreda	Spain	42.16	2.75	Level H	Radiocarbon	35900	650	40719.5	42167.775	39271.225	2	archaic Aurignacien	Sapiens	Wood et al, 2014
L'Arbreda	Spain	42.16	2.75	Level H	Radiocarbon	31900	530	36575	38441.75	34708.25	2	Proto-Aurignacian	Sapiens	Wood et al, 2014
L'Arbreda	Spain	42.16	2.75	Level H	Radiocarbon	32100	540	36901	38965.35	34836.65	2	Proto-Aurignacian	Sapiens	Wood et al, 2014
L'Arbreda	Spain	42.16	2.75	Level H	Radiocarbon	33800	550	38523.5	40498.075	36548.925	2	Proto-Aurignacian	Sapiens	Wood et al, 2014
L'Arbreda	Spain	42.16	2.75	Level H	Radiocarbon	34800	760	39428.5	41765.025	37091.975	2	Proto-Aurignacian	Sapiens	Wood et al, 2014
L'Arbreda	Spain	42.16	2.75	Level H	Radiocarbon	35700	830	40013	42199.9	37826.1	2	Proto-Aurignacian	Sapiens	Wood et al, 2014
L'Arbreda	Spain	42.16	2.75	Level H	Radiocarbon	35850	700	40678	42186.6	39169.4	2	Proto-Aurignacian	Sapiens	Wood et al, 2014
L'Arbreda	Spain	42.16	2.75	Level H	Radiocarbon	35900	860	40327	42297.3	38356.7	2	Proto-Aurignacian	Sapiens	Wood et al, 2014

L'Arbreda	Spain	42.16	2.75	Level H	Radiocarbon	36000	700	40746	42236.55	39255.45	2	Proto-Aurignacian	Sapiens	Wood et al, 2014
L'Arbreda	Spain	42.16	2.75	level I	Radiocarbon	37300	800	41430	42878.75	39981.25	2	Typical Mousterian	Neanderthal	Higham et al, 2014
L'Arbreda	Spain	42.16	2.75	level I	Radiocarbon	38350	400	42400	42942.45	41857.55	2	Typical Mousterian	Neanderthal	Higham et al, 2014
L'Arbreda	Spain	42.16	2.75	level I	Radiocarbon	39200	1000	43022	44735.8	41308.2	2	Typical Mousterian	Neanderthal	Higham et al, 2014
L'Arbreda	Spain	42.16	2.75	level I	Radiocarbon	44400	1900	47619	52118.2	43119.8	2	Typical Mousterian	Neanderthal	Higham et al, 2014
Las Palomas de Teba	Spain	36.98	-4.88	10	OSL / IRSL/ TL	39400	2600	39400	42000	36800	2	Middle Palaeolithic	Neanderthal	Kehl et al., 2016
Las Palomas de Teba	Spain	36.98	-4.88	9	OSL / IRSL/ TL	44900	4100	44900	49000	40800	2	Middle Palaeolithic	Neanderthal	Kehl et al., 2016
Las Palomas de Teba	Spain	36.98	-4.88	10	OSL / IRSL/ TL	45900	3400	45900	49300	42500	2	Middle Palaeolithic	Neanderthal	Kehl et al., 2016
Las Palomas de Teba	Spain	36.98	-4.88	9	OSL / IRSL/ TL	46600	4200	46600	50800	42400	2	Middle Palaeolithic	Neanderthal	Kehl et al., 2016
Las Palomas de Teba	Spain	36.98	-4.88	10	OSL / IRSL/ TL	47900	4300	47900	52200	43600	2	Middle Palaeolithic	Neanderthal	Kehl et al., 2016
Las Palomas de Teba	Spain	36.98	-4.88	10	OSL / IRSL/ TL	48400	6300	48400	54700	42100	2	Middle Palaeolithic	Neanderthal	Kehl et al., 2016
Las Palomas de Teba	Spain	36.98	-4.88	10	OSL / IRSL/ TL	48700	8400	48700	57100	40300	2	Middle Palaeolithic	Neanderthal	Kehl et al., 2016
Las Palomas de Teba	Spain	36.98	-4.88	10	OSL / IRSL/ TL	55000	6800	55000	61800	48200	2	Middle Palaeolithic	Neanderthal	Kehl et al., 2016
Los Casares	Spain	40.94	-2.29	c	Radiocarbon	39494	850	43288.5	44675.025	41901.975	2	Middle Palaeolithic	Neanderthal	Alcaraz-Castaño et al, 2017
Los Toros	Spain	40.51	-0.55	nivel d	Radiocarbon	35250	490	40408.5	41681.025	39135.975	2	Middle Paleolithic	Neanderthal	Montes et al, 2006
Los Toros	Spain	40.51	-0.55	a2	Radiocarbon	30920	230	35324.5	36124.875	34524.125	2	Upper Palaeolithic	Sapiens	Montes et al, 2006
Malladetes	Spain	39.02	-0.30	XII	Radiocarbon	29690	560	33799.5	35643.925	31955.075	2	Upper Palaeolithic	Sapiens	Villaverde et al., 2021
Malladetes	Spain	39.02	-0.30	XII	Radiocarbon	30100	280	34575	35392	33758	2	Upper Palaeolithic	Sapiens	Villaverde et al., 2021

Malladetes	Spain	39.02	-0.30	XIII	Radiocarbon	29520	270	33880	34697.95	33062.05	2	Upper Palaeolithic	Sapiens	Villaverde et al., 2021
Malladetes	Spain	39.02	-0.30	XIII	Radiocarbon	32120	360	36499	37635.2	35362.8	2	Upper Palaeolithic	Sapiens	Villaverde et al., 2021
Malladetes	Spain	39.02	-0.30	XIII	Radiocarbon	32080	350	36466.5	37580.375	35352.625	2	Upper Palaeolithic	Sapiens	Villaverde et al., 2021
Malladetes	Spain	39.02	-0.30	XIII	Radiocarbon	32160	360	36533	37679.65	35386.35	2	Upper Palaeolithic	Sapiens	Villaverde et al., 2021
Malladetes	Spain	39.02	-0.30	XIII	Radiocarbon	32400	360	37102	38597.3	35606.7	2	Upper Palaeolithic	Sapiens	Villaverde et al., 2021
Malladetes	Spain	39.02	-0.30	XIII	Radiocarbon	31880	350	36336.5	37431.375	35241.625	2	Upper Palaeolithic	Sapiens	Villaverde et al., 2021
Malladetes	Spain	39.02	-0.30	XIVa	Radiocarbon	32560	370	37413.5	38993.825	35833.175	2	Upper Palaeolithic	Sapiens	Villaverde et al., 2021
Malladetes	Spain	39.02	-0.30	XIVa	Radiocarbon	32860	380	37686	39187	36185	2	Upper Palaeolithic	Sapiens	Villaverde et al., 2021
Malladetes	Spain	39.02	-0.30	XIVa	Radiocarbon	33330	450	38021	39666.4	36375.6	2	Upper Palaeolithic	Sapiens	Villaverde et al., 2021
Malladetes	Spain	39.02	-0.30	XIVa	Radiocarbon	33370	400	38047.5	39593.625	36501.375	2	Upper Palaeolithic	Sapiens	Villaverde et al., 2021
Malladetes	Spain	39.02	-0.30	XV	Radiocarbon	35110	495	40167.5	41479.925	38855.075	2	Uncertain	Sapiens	Villaverde et al., 2021
Malladetes	Spain	39.02	-0.30	XV	Radiocarbon	36180	550	40918.5	42190.075	39646.925	2	Uncertain	?	Villaverde et al., 2021
Malladetes	Spain	39.02	-0.30	XVI	Radiocarbon	39310	810	43184	44539.65	41828.35	2	Uncertain	?	Villaverde et al., 2021
Mira Nascente	Portugal	39.71	-9.05	2	OSL / IRSL/ TL	33905	2690	33905	36595	31215	2	Middle Palaeolithic	Neanderthal	Bicho et al, 2015 ; Haws et al, 2010
Mira Nascente	Portugal	39.71	-9.05	3c	OSL / IRSL/ TL	34300	2630	34300	36930	31670	2	Middle Palaeolithic	Neanderthal	Bicho et al, 2015 ; Haws et al, 2010
Mira Nascente	Portugal	39.71	-9.05	2	OSL / IRSL/ TL	36035	2750	36035	38785	33285	2	Middle Palaeolithic	Neanderthal	Bicho et al, 2015 ; Hawset al, 2010
Mira Nascente	Portugal	39.71	-9.05	3b	OSL / IRSL/ TL	40450	2980	40450	43430	37470	2	Middle Palaeolithic	Neanderthal	Bicho et al, 2015 ; Haws et al, 2010
Mira Nascente	Portugal	39.71	-9.05	3c	Radiocarbon	36030	710	40754.5	42252.175	39256.825	2	Middle Palaeolithic	Neanderthal	Bicho et al, 2015 ; Haws et al, 2010
Mira Nascente	Portugal	39.71	-9.05	3c	Radiocarbon	36720	270	41567	42170.25	40963.75	2	Middle Palaeolithic	Neanderthal	Bicho et al, 2015 ; Haws et al, 2010
Mira Nascente	Portugal	39.71	-9.05	3a	Radiocarbon	37540	600	41803	42798.6	40807.4	2	Middle Palaeolithic	Neanderthal	Bicho et al, 2015 ; Haws et al, 2010
Mollet 1	Spain	42.16	2.75	2 & 3	Radiocarbon	33780	730	38563.5	40858.225	36268.775	2	Aurignacian	Sapiens	Maroto et al, 2012
Pego do Diabo	Portugal	38.83	-9.17	2/3	Radiocarbon	34900	1000	39280.5	42022.675	36538.325	2	Aurignacian	Sapiens	Zilhão et al, 2010

Pego do Diabo	Portugal	38.83	-9.17	2/3	Radiocarbon	38750	650	42835	44090.9	41579.1	2	Mousterian	Neanderthal	Zilhão et al, 2010
Pena Miel 1	Portugal	42.21	-2.62	c	Radiocarbon	37300	1300	41466	44083.25	38848.75	2	Aurignacian	Sapiens	Montes et al, 2001 ; Rios-Garaizar and Eixea, 2021
Pena Miel 1	Portugal	42.21	-2.62	e	Radiocarbon	40300	1600	43987.5	46774.325	41200.675	2	Middle Palaeolithic	Neanderthal	Montes et al, 2001 ; Rios-Garaizar and Eixea, 2021
Pena Miel 1	Portugal	42.21	-2.62	e	Radiocarbon	45500	1400	48762	54520.9	44808.1	2	Middle Palaeolithic	Neanderthal	Montes et al, 2001 ; Rios-Garaizar and Eixea, 2021
Prado Vargas	Spain	43.03	-3.63	N4	OSL / IRSL/ TL	46200	3200	46200	49400	43000	2	Middle Paleolithic	Neanderthal	Ruiz et al, 2021
Prado Vargas	Spain	43.03	-3.63	N4	OSL / IRSL/ TL	48300	3200	48300	51500	45100	2	Middle Paleolithic	Neanderthal	Ruiz et al, 2021
Prado Vargas	Spain	43.03	-3.63	N4	Radiocarbon	36820	330	41577.5	42249.625	40905.375	1	Middle Paleolithic	Neanderthal	Ruiz et al, 2021
Prado Vargas	Spain	43.03	-3.63	N4	Radiocarbon	38880	380	42653.5	43190.725	42116.275	1	Middle Paleolithic	Neanderthal	Ruiz et al, 2021
Praia Rei Cortico	Portugal	39.42	-9.24	PC5	OSL / IRSL/ TL	50356	1854	50356	52210	48502	2	Middle Palaeolithic	Neanderthal	Haws et al, 2010
Praia Rei Cortico	Portugal	39.42	-9.24	PC3	OSL / IRSL/ TL	51165	3865	51165	55030	47300	2	Middle Palaeolithic	Neanderthal	Haws et al, 2022
Praia Rei Cortico	Portugal	39.42	-9.24	PC5	OSL / IRSL/ TL	53781	2055	53781	55836	51726	2	Middle Palaeolithic	Neanderthal	Haws et al, 2010
Roca dels Bous	Spain	41.87	0.84	RB-N	OSL / IRSL/ TL	48400	4700	48400	53100	43700	2	Middle Palaeolithic	Neanderthal	Benito-Calvo et al, 2020
Roca dels Bous	Spain	41.87	0.84	RB-M	OSL / IRSL/ TL	48800	4400	48800	53200	44400	2	Middle Palaeolithic	Neanderthal	Benito-Calvo et al, 2020
Roca dels Bous	Spain	41.87	0.84	RB-G	OSL / IRSL/ TL	55200	5500	55200	60700	49700	2	Middle Palaeolithic	Neanderthal	Benito-Calvo et al, 2020
Roca dels Bous	Spain	41.87	0.84	R3	Radiocarbon	38800	1200	42704	44805.4	40602.6	1	Middle Palaeolithic	Neanderthal	Terradas et al, 1993
Salto do Boi	Portugal	40.98	-7.10	GFU5/UA10	OSL / IRSL/ TL	33600.0	2000.0	33600.0	35600	31600	2	Aurignacian	Sapiens	Aubry et al, 2020
Salto do Boi	Portugal	40.98	-7.10	GFU5/UA12	OSL / IRSL/ TL	39500.0	1800.0	39500.0	41300	37700	2	Middle Palaeolithic	Neanderthal	Aubry et al, 2020
Salto do Boi	Portugal	40.98	-7.10	GFU5/UA13	OSL / IRSL/ TL	42900.0	1900.0	42900.0	44800	41000	2	Middle Palaeolithic	Neanderthal	Aubry et al, 2020
Salto do Boi	Portugal	40.98	-7.10	GFU5/UA14	OSL / IRSL/ TL	43900.0	2100.0	43900.0	46000	41800	2	Middle Palaeolithic	Neanderthal	Aubry et al, 2020
Salto do Boi	Portugal	40.98	-7.10	GFU5/UA16	OSL / IRSL/ TL	49900.0	2700.0	49900.0	52600	47200	2	Middle Palaeolithic	Neanderthal	Aubry et al, 2020
Salto do Boi	Portugal	40.98	-7.10	GFU5/UA17	OSL / IRSL/ TL	51000.0	2400.0	51000.0	53400	48600	2	Middle Palaeolithic	Neanderthal	Aubry et al, 2020

Sima de la Palomas de Teba	Spain	36.98	-4.88	Unit 10 (CP1)	OSL / IRSL/ TL	39400	2600	39400	42000	36800	2	Mousterian	Neanderthal	Kehl et al, 2016
Sima de la Palomas de Teba	Spain	36.98	-4.88	Unit 7 (CP3)	OSL / IRSL/ TL	39800	2400	39800	42200	37400	2	Mousterian	Neanderthal	Kehl et al, 2016
Sima de la Palomas de Teba	Spain	36.98	-4.88	Unit 7(CP3)	OSL / IRSL/ TL	40500	3400	40500	43900	37100	2	Mousterian	Neanderthal	Kehl et al, 2016
Sima de la Palomas de Teba	Spain	36.98	-4.88	Unit 9 (CP2)	OSL / IRSL/ TL	44900	4100	44900	49000	40800	2	Mousterian	Neanderthal	Kehl et al, 2016
Sima de la Palomas de Teba	Spain	36.98	-4.88	Unit 10 (CP1, mean)	OSL / IRSL/ TL	45900	3400	45900	49300	42500	2	Mousterian	Neanderthal	Kehl et al, 2016
Sima de la Palomas de Teba	Spain	36.98	-4.88	Unit 9 (CP2)	OSL / IRSL/ TL	46600	4200	46600	50800	42400	2	Mousterian	Neanderthal	Kehl et al, 2016
Sima de la Palomas de Teba	Spain	36.98	-4.88	Unit 10 (CP1, mean)	OSL / IRSL/ TL	47900	4300	47900	52200	43600	2	Mousterian	Neanderthal	Kehl et al, 2016
Sima de la Palomas de Teba	Spain	36.98	-4.88	Unit 10 (CP1, mean)	OSL / IRSL/ TL	48400	6300	48400	54700	42100	2	Mousterian	Neanderthal	Kehl et al, 2016
Sima de la Palomas de Teba	Spain	36.98	-4.88	Unit 10/11	OSL / IRSL/ TL	48700	8400	48700	57100	40300	2	Mousterian	Neanderthal	Kehl et al, 2016
Sima de la Palomas de Teba	Spain	36.98	-4.88	Unit 10/11	OSL / IRSL/ TL	50800	6800	50800	57600	44000	2	Mousterian	Neanderthal	Kehl et al, 2016
Sima de la Palomas de Teba	Spain	36.98	-4.88	Unit 10/11	OSL / IRSL/ TL	55000	6800	55000	61800	48200	2	Mousterian	Neanderthal	Kehl et al, 2016

Sima de la Palomas de Teba	Spain	36.98	-4.88	Unit 6	Radiocarbon	38406	365	42428.5	42926.775	41930.225	1	Mousterian	Neanderthal	Weniger et al, 2023
Sima de la Palomas de Teba	Spain	36.98	-4.88	Unit 6	Radiocarbon	38755	365	42588	43094.35	42081.65	1	Mousterian	Neanderthal	Weniger et al, 2023
Sima de la Palomas de Teba	Spain	36.98	-4.88	Unit 11	Radiocarbon	41682	866	44611	46458.75	42763.25	1	Mousterian	Neanderthal	Weniger et al, 2023
Sima de la Palomas de Teba	Spain	36.98	-4.88	Unit 10	Radiocarbon	45804	1119	48736	52047.7	45424.3	1	Mousterian	Neanderthal	Weniger et al, 2023
Sima de la Palomas de Teba	Spain	36.98	-4.88	Unit 11	Radiocarbon	46433	865	49577.5	54813.625	46283.375	1	Mousterian	Neanderthal	Weniger et al, 2023
Sima de las Palomas	Spain	37.80	-0.90	2 k grey layer of AP-96	OSL / IRSL/ TL	54700	4700	54700	59400	50000	2	Middle Palaeolithic	Neanderthal	Walker et al, 2012
Sima de las Palomas	Spain	37.80	-0.90	2 f grey layer of SP-96	Radiocarbon	34450	600	39127.5	41140.075	37114.925	0	Middle Palaeolithic	Neanderthal	Walker et al, 2012
Sima de las Palomas	Spain	37.80	-0.90	2 l grey layer of SP-96	Radiocarbon	35030	270	40186.5	41039.125	39333.875	0	Middle Palaeolithic	Neanderthal	Walker et al, 2012
Sima de las Palomas	Spain	37.80	-0.90	2 i grey layer of SP-96	U/Th	43800	750	43800	44550	43050	1	Middle Palaeolithic	Neanderthal	Walker et al, 2012
Sima de las Palomas	Spain	37.80	-0.90	2 e grey layer of SP-96	U/Th	51000	1250	51000	52250	49750	2	Middle Palaeolithic	Neanderthal	Walker et al, 2012
Sima de las Palomas	Spain	37.80	-0.90	2 e grey layer of SP-96	U/Th	54100	3850	54100	57950	50250	2	Middle Palaeolithic	Neanderthal	Walker et al, 2012
Sopena	Spain	43.32	-4.95	XII	ESR	49300	5300	49300	54600	44000	2	Middle Paleolithic	Neanderthal	Pinto-Llona et al, 2012
Sopena	Spain	43.32	-4.95	XIV	ESR	50400	8700	50400	59100	41700	2	Middle Paleolithic	Neanderthal	Pinto-Llona et al, 2012
Sopena	Spain	43.32	-4.95	XIII	ESR	57100	12500	57100	69600	44600	2	Middle Paleolithic	Neanderthal	Pinto-Llona et al, 2012

Sopena	Spain	43.32	-4.95	XV	ESR	57200	12300	57200	69500	44900	2	Middle Paleolithic	Neanderthal	Pinto-Llona et al, 2012
Sopena	Spain	43.32	-4.95	XI	ESR	40300	4800	40300	45100	35500	2	Upper Palaeolithic	Sapiens	Pinto-Llona et al, 2012
Sopena	Spain	43.32	-4.95	XII	Radiocarbon	33100	150	37957.5	38992.525	36922.475	1	Middle Paleolithic	Neanderthal	Soressi, 2002 ; Guibert et al, 2009
Sopena	Spain	43.32	-4.95	XIII	Radiocarbon	39150	420	43063.5	43932.275	42194.725	2	Middle Paleolithic	Neanderthal	Pinto-Llona & Grandal-d'Anglade, 2022
Sopena	Spain	43.32	-4.95	XII	Radiocarbon	39390	280	42862.5	43345.575	42379.425	1	Middle Paleolithic	Neanderthal	Pinto-Llona & Grandal-d'Anglade, 2019
Sopena	Spain	43.32	-4.95	XIII	Radiocarbon	39530	420	43259.5	44188.125	42330.875	2	Middle Paleolithic	Neanderthal	Pinto-Llona & Grandal-d'Anglade, 2022
Sopena	Spain	43.32	-4.95	XIII	Radiocarbon	40350	460	43588.5	44563.675	42613.325	2	Middle Paleolithic	Neanderthal	Pinto-Llona & Grandal-d'Anglade, 2022
Sopena	Spain	43.32	-4.95	XII	Radiocarbon	41060	420	43958.5	44966.925	42950.075	2	Middle Paleolithic	Neanderthal	Pinto-Llona & Grandal-d'Anglade, 2022
Sopena	Spain	43.32	-4.95	XIV	Radiocarbon	42630	600	45398	46768.85	44027.15	2	Middle Paleolithic	Neanderthal	Pinto-Llona & Grandal-d'Anglade, 2022
Sopena	Spain	43.32	-4.95	XII	Radiocarbon	43830	480	46421	47957.15	44884.85	2	Middle Paleolithic	Neanderthal	Pinto-Llona & Grandal-d'Anglade, 2019
Sopena	Spain	43.32	-4.95	XII	Radiocarbon	45040	550	47439.5	49074.925	45804.075	2	Middle Paleolithic	Neanderthal	Pinto-Llona & Grandal-d'Anglade, 2019
Sopena	Spain	43.32	-4.95	XI	Radiocarbon	32870	530	37598	39443.85	35752.15	2	Upper Palaeolithic	Sapiens	Pinto-Llona et al, 2005
Sopena	Spain	43.32	-4.95	XI	Radiocarbon	34470	540	39167	41072.7	37261.3	2	Upper Palaeolithic	Sapiens	Maroto et al, 2012
Sopena	Spain	43.32	-4.95	XI	Radiocarbon	38445	250	42445	42819.3	42070.7	2	Upper Palaeolithic	Sapiens	Pinto-Llonaand & Grandal-d'Anglade, 2019
Sopena	Spain	43.32	-4.95	XI	Radiocarbon	40215	310	43534	44357.65	42710.35	2	Upper Palaeolithic	Sapiens	Pinto-Llonaand & Grandal-d'Anglade, 2019
Teixoneres	Spain	41.81	2.10	chamber X (unit II)	Radiocarbon	30780	110	35094	35588	34600	2	Not diagnostic	Neanderthal	Talamo et al, 2016
Teixoneres	Spain	41.81	2.10	chamber X (unit II)	Radiocarbon	34900	175	40067.5	40739.625	39395.375	2	Not diagnostic	Neanderthal	Talamo et al, 2016
Teixoneres	Spain	41.81	2.10	chamber X (unit II)	Radiocarbon	34940	173	40103	40777.5	39428.5	2	Not diagnostic	Neanderthal	Talamo et al, 2016
Teixoneres	Spain	41.81	2.10	chamber X (unit II)	Radiocarbon	36850	211	41662.5	42174.075	41150.925	2	Not diagnostic	Neanderthal	Talamo et al, 2016
Teixoneres	Spain	41.81	2.10	chamber X (unit II)	Radiocarbon	39000	260	42669.5	43073.725	42265.275	2	Not diagnostic	Neanderthal	Talamo et al, 2016
Teixoneres	Spain	41.81	2.10	chamber X (unit II)	Radiocarbon	39320	263	42819	43268.35	42369.65	2	Not diagnostic	Neanderthal	Talamo et al, 2016

Teixoneres	Spain	41.81	2.10	chamber X (unit III)	Radiocarbon	40610	340	43703.5	44543.775	42863.225	2	Middle Palaeolithic	Neanderthal	Talamo et al, 2016
Teixoneres	Spain	41.81	2.10	chamber X (unit II)	Radiocarbon	40800	320	43786	44621.05	42950.95	2	Middle Palaeolithic	Neanderthal	Talamo et al, 2016
Teixoneres	Spain	41.81	2.10	chamber X (unit III)	Radiocarbon	41270	327	44056.5	44985.125	43127.875	2	Middle Palaeolithic	Neanderthal	Talamo et al, 2016
Teixoneres	Spain	41.81	2.10	chamber X (unit III)	Radiocarbon	41560	337	44283	45294.75	43271.25	2	Middle Palaeolithic	Neanderthal	Talamo et al, 2016
Teixoneres	Spain	41.81	2.10	chamber X (unit III)	Radiocarbon	42020	370	44867	45779	43955	2	Middle Palaeolithic	Neanderthal	Talamo et al, 2016
Teixoneres	Spain	41.81	2.10	chamber X (unit III)	Radiocarbon	42250	359	45024.5	45896.125	44152.875	2	Middle Palaeolithic	Neanderthal	Talamo et al, 2016
Teixoneres	Spain	41.81	2.10	chamber X (unit III)	Radiocarbon	47200	670	50567.5	54847.275	47665.725	2	Middle Palaeolithic	Neanderthal	Talamo et al, 2016
Valdegoba	Spain	42.52	-3.77	VB1 (Level 5)	Radiocarbon	48400	3300	49562	54728.1	44395.9	2	Middle Paleolithic	Neanderthal	Dalén et al, 2012
Valongo Quarry	Portugal	41.17	-8.48	VQ3	OSL / IRSL/ TL	49520	3690	49520	53210	45830	2	Middle Palaeolithic	Neanderthal	Haws et al, 2020
Vanguard	Spain	36.12	-5.34	5a	OSL / IRSL/ TL	43000	3000	43000	46000	40000	2	Middle Palaeolithic	Neanderthal	Doerschner et al. 2019
Vanguard	Spain	36.12	-5.34	1c	OSL / IRSL/ TL	43000	2700	43000	45700	40300	2	Middle Palaeolithic	Neanderthal	Doerschner et al. 2019
Vanguard	Spain	36.12	-5.34	B50	OSL / IRSL/ TL	46300	3300	46300	49600	43000	1	Middle Palaeolithic	Neanderthal	**Pettitt and Bailey, 2000**
Vanguard	Spain	36.12	-5.34	5c	OSL / IRSL/ TL	50200	5400	50200	55600	44800	2	Middle Palaeolithic	Neanderthal	Doerschner et al. 2019
Vanguard	Spain	36.12	-5.34	10a-c	OSL / IRSL/ TL	52700	5300	52700	58000	47400	2	Middle Palaeolithic	Neanderthal	Doerschner et al. 2019
Vanguard	Spain	36.12	-5.34	4	OSL / IRSL/ TL	54600	4200	54600	58800	50400	2	Middle Palaeolithic	Neanderthal	Doerschner et al. 2019
Vanguard	Spain	36.12	-5.34	a1-49? LAYER1	OSL / IRSL/ TL	55600	4200	55600	59800	51400	2	Middle Palaeolithic	Neanderthal	Doerschner et al. 2019
Vanguard	Spain	36.12	-5.34	15	OSL / IRSL/ TL	57100	3900	57100	61000	53200	2	Middle Palaeolithic	Neanderthal	Doerschner et al. 2019
Vanguard	Spain	36.12	-5.34	B 52/Layer 22	Radiocarbon	41800	1400	45171	47938.35	42403.65	1	Middle Palaeolithic	Neanderthal	**Pettitt and Bailey, 2000**
Vanguard	Spain	36.12	-5.34	A upper part/Layer 6	Radiocarbon	45200	2400	48916.5	54695.825	43137.175	1	Middle Palaeolithic	Neanderthal	**Pettitt and Bailey, 2000**
Vanguard	Spain	36.12	-5.34	B hearth	Radiocarbon	46900	1500	50262.5	54763.125	45761.875	1	Middle Palaeolithic	Neanderthal	**Pettitt and Bailey, 2000**
Vanguard	Spain	36.12	-5.34	B hearth	Radiocarbon	54000	3300	50931	54796.55	47065.45	1	Middle Palaeolithic	Neanderthal	**Pettitt and Bailey, 2000**
Zafarraya	Spain	36.95	-4.13	Q15	Radiocarbon	46300	2500	49170	54708.5	43631.5	2	Middle Palaeolithic	Neanderthal	Higham et al, 2014

Zafarraya	Spain	36.95	-4.13	I (3-7)	Radiocarbon	29800	600	33967.5	35967.725	31967.275	0	Middle Palaeolithic	Neanderthal	Hublin et al, 1995
Zafarraya	Spain	36.95	-4.13	I (8)	Radiocarbon	31800	550	36466	38315.65	34616.35	0	Middle Palaeolithic	Neanderthal	Hublin et al, 1995
Zafarraya	Spain	36.95	-4.13	D	Radiocarbon	36900	3000	40238.5	45900.975	34576.025	1	Middle Palaeolithic	Neanderthal	Michel et al, 2013
Zafarraya	Spain	36.95	-4.13	E1	Radiocarbon	30900	1300	35403	39269.5	31536.5	0	Middle Palaeolithic	Neanderthal	Michel et al, 2013
Zafarraya	Spain	36.95	-4.13	Q14	Radiocarbon	36700	1400	40432	43688	37297	1	Middle Palaeolithic	Neanderthal	Michel et al, 2013
Zafarraya	Spain	36.95	-4.13	R16	Radiocarbon	34600	800	39212	41686.75	36737.25	1	Middle Palaeolithic	Neanderthal	Michel et al, 2013
Zafarraya	Spain	36.95	-4.13	mousterian level	Radiocarbon	30200	460	34639	36035.5	33242.5	0	Middle Palaeolithic	Neanderthal	Michel et al, 2013
Zafarraya	Spain	36.95	-4.13	mousterian level	Radiocarbon	33300	1200	37957.5	41187.975	34727.025	0	Middle Palaeolithic	Neanderthal	Michel et al, 2013
Zafarraya	Spain	36.95	-4.13	mousterian level	Radiocarbon	30650	650	35040	36840.25	33239.75	0	Middle Palaeolithic	Neanderthal	Michel et al, 2013
Zafarraya	Spain	36.95	-4.13	mousterian level	U/Th	32800	2100	32800	34900	30700	2	Middle Palaeolithic	Neanderthal	Michel et al, 2013
Zafarraya	Spain	36.95	-4.13	mousterian level	U/Th	47200	3700	47200	50900	43500	2	Middle Palaeolithic	Neanderthal	Michel et al, 2013
Zafarraya	Spain	36.95	-4.13	mousterian level	U/Th	56700	3900	56700	60600	52800	2	Middle Palaeolithic	Neanderthal	Michel et al, 2013
Zafarraya	Spain	36.95	-4.13	mousterian level	U/Th	30000	2500	30000	32500	27500	2	Middle Palaeolithic	Neanderthal	Michel et al, 2013
Zafarraya	Spain	36.95	-4.13	mousterian level	U/Th	39700	2200	39700	41900	37500	2	Middle Palaeolithic	Neanderthal	Michel et al, 2013
Zafarraya	Spain	36.95	-4.13	mousterian level	U/Th	48600	5400	48600	54000	43200	2	Middle Palaeolithic	Neanderthal	Michel et al, 2013
Zafarraya	Spain	36.95	-4.13	mousterian level	U/Th	45300	2100	45300	47400	43200	2	Middle Palaeolithic	Neanderthal	Michel et al, 2013
Zafarraya	Spain	36.95	-4.13	mousterian level	U/Th	40900	1300	40900	42200	39600	2	Middle Palaeolithic	Neanderthal	Michel et al, 2013
Zafarraya	Spain	36.95	-4.13	mousterian level	U/Th	47500	1700	47500	49200	45800	2	Middle Palaeolithic	Neanderthal	Michel et al, 2013
Zafarraya	Spain	36.95	-4.13	mousterian level	U/Th	46500	3200	46500	49700	43300	2	Middle Palaeolithic	Neanderthal	Michel et al, 2013
Zafarraya	Spain	36.95	-4.13	mousterian level	U/Th	38600	2700	38600	41300	35900	2	Middle Palaeolithic	Neanderthal	Michel et al, 2013
Zafarraya	Spain	36.95	-4.13	mousterian level	U/Th	60000	3700	60000	63700	56300	2	Middle Palaeolithic	Neanderthal	Michel et al, 2013
Zafarraya	Spain	36.95	-4.13	mousterian level	U/Th	31600	2300	31600	33900	29300	2	Middle Palaeolithic	Neanderthal	Michel et al, 2013

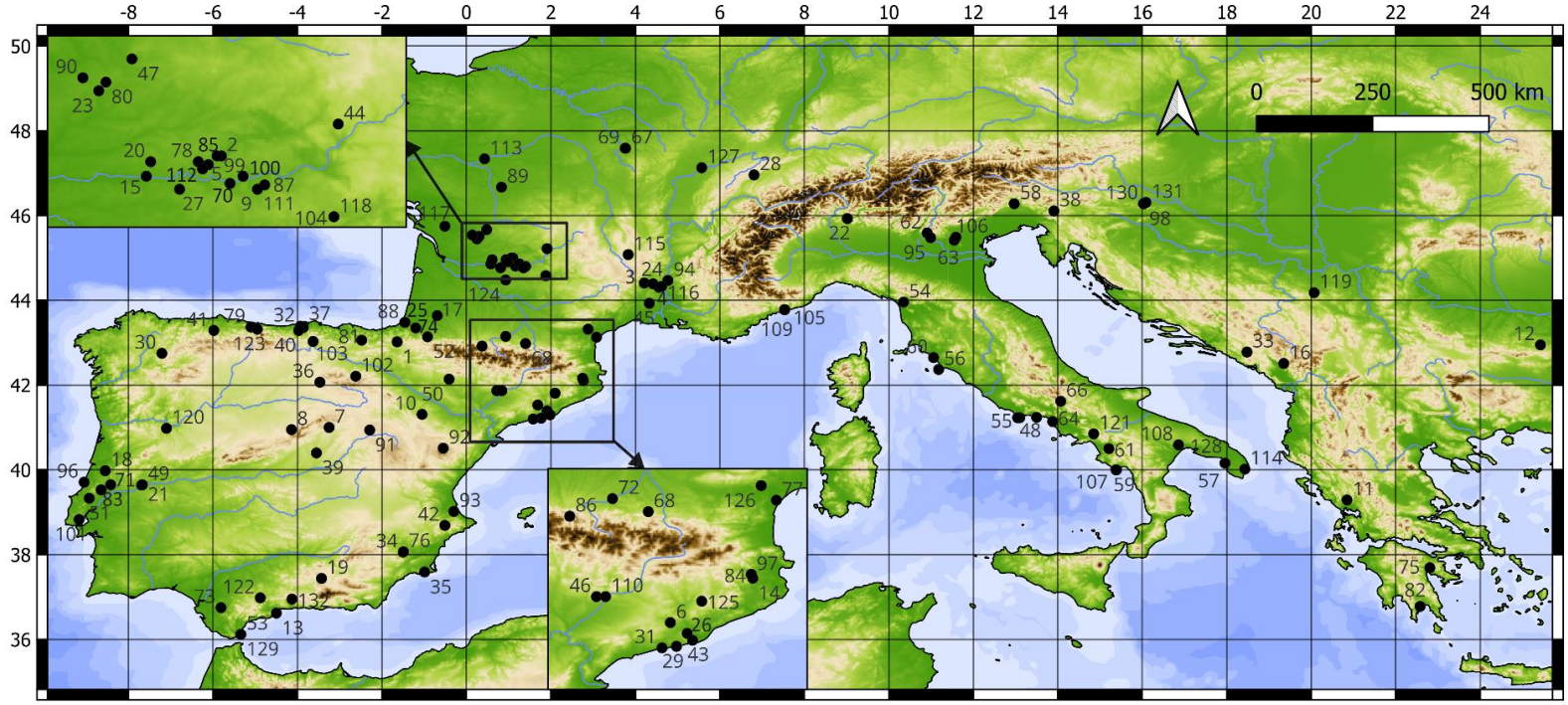


Fig. S1. Map of archaeological sites used in the dataset. **1**, Abauntz ; **2**, Abri Castanet ; **3**, Abri des Pêcheurs ; **4**, Abri du Maras ; **5**, Abri Pataud ; **6**, Abric Romaní ; **7**, Abrigo de la Malia ; **8**, Abrigo del molino ; **9**, Abris Peyroni ; **10**, Aguilón P7 ; **11**, Asprochaliko ; **12**, Bacho Kiro ; **13**, Bajondillo; **14**, Banyoles; **15**, Barbas III; **16**, Bioče ; **17**, Brassempouy ; **18**, Buraca Escura ; **19**, Carihuela ; **20**, Cassenade ; **21** Castelejo ; **22**, Caverna Generosa ; **23**, Chauverie ; **24**, Chauvet ; **25**, Chemin de Jupiter ; **26**, Coll Verdaguer ; **27**, Combe Capelle Bas ; **28**, Cotencher ; **29**, Cova del Gegant; **30**, Cova Eiros ; **31**, Cova Foradada ; **32**,Covalejos ; **33**, Crvena Stijena ; **34**, Cueva Antón ; **35**, Cueva de los aviones ; 36, Cueva Millán ; **37**, Cueva Morin; **38**, Divjie Babe; **39**, El Canaveral ; **40**, El Castillo ; **41**, El Conde ; **42**, El Salt ; **43**, Els Canyars ; **44**, Espagnac ; **45**, Esquicho-Grapaou ; 46, Estret de Tragó ; 47, Fontechevade ; 48, Fosselone ; 49, Foz do Enxarrique ; **50**, Fuentes de San Cristobal ; **51**, Gato Preto ; **52**, Gatzarria ; **53**, Gorham ; **54**, Grotta all'Onda ; **55**, Grotta Breuil ; **56**, Grotta dei santi ; **57**, Grotta del Cavallo ; **58**, Grotta del Rio Secco ; **59**, Grotta della Cala ; **60**, Grotta della Fabbrica ; **61**, Grotta di Castelcività ; **62**, Grotta di Fumane ; **63**, Grotta di San Bernardino ; **64**, Grotta di San Sebastiano ; **65**, Grotta di Sant' Agostino ; **66**, Grotta Reali ; **67**, Grotte du Bison ; **68**, Grotte du Portel Ouest ; **69**, Grotte du Renne ; **70**, Grotte XVI ; **71**, Gruta do Caldeirao ; **72**, Harregi ; **73**, Higueral la Valleja ; **74**, Isturitz ; **75**, Klisoura ; **76**, La Boja ; 77, La Crouzade ; 78, La Ferrassie ; 79, La Güelga ; **80**, La Quina ; **81**, Labeko Koba ; **82**, Lakonis cave I ; **83**, Lapa do Picareiro ; **84**, L'Arbreda ; **85**, Le Moustier ; **86**, Le Noisetier ; **87**, Le Piage ; **88**, Le Prissé ; **89**, Les Cottés ; **90**, Les Rois ; **91**, Los Casares ; **92**, Los Toros ; **93**, Malladetes ; **94**, Mandrin ; **95**, Mezzena ; **96**, Mira Nascente ; **97**, Mollet 1 ; **98**; Mujina Pećina ; **99**, Pech-de-l'Azé I ; **100**, Pech-de-l' Azé IV ; **101**, Pego do Diablo ; **102**, Peña Miel 1 ; **103**, Prado Vargas ; **104**, Ranc de l'Arc ; **105**, Riparo Bombrini ; **106**, Riparo del Broion ; **107**, Riparo del Poggio ; **108**, Riparo dell'Oscurusciuto ; **109**, Riparo Mochi ; **110**, Roca dels Bous ; **111**, Roc-de-Combe ; **112**, Roc-de-Marsal ; **113**, Roche cotard ; **114**, Romanelli ; **115**, Rond du Barry ; **116**, Saint-Marcel ; **117**, Saint-Césaire ; **118**, Sainte-Eulalie ; **119**, Šalitrena Pećina; **120**, Salto do Boi ; **121**, Serino ; **122**, Sima de la Palomas de Teba ; **123**, Sopeña ; **124**, Sous-les-Vignes ; **125**, Teixoneres ; 126, Tournal ; **127**, Trou de la mère Clochette ; **128**, Uluzzo ; **129**, Vanguard ; **130**, Velika Pećina ; **131**, Vindija ; **132**, Zafarraya.

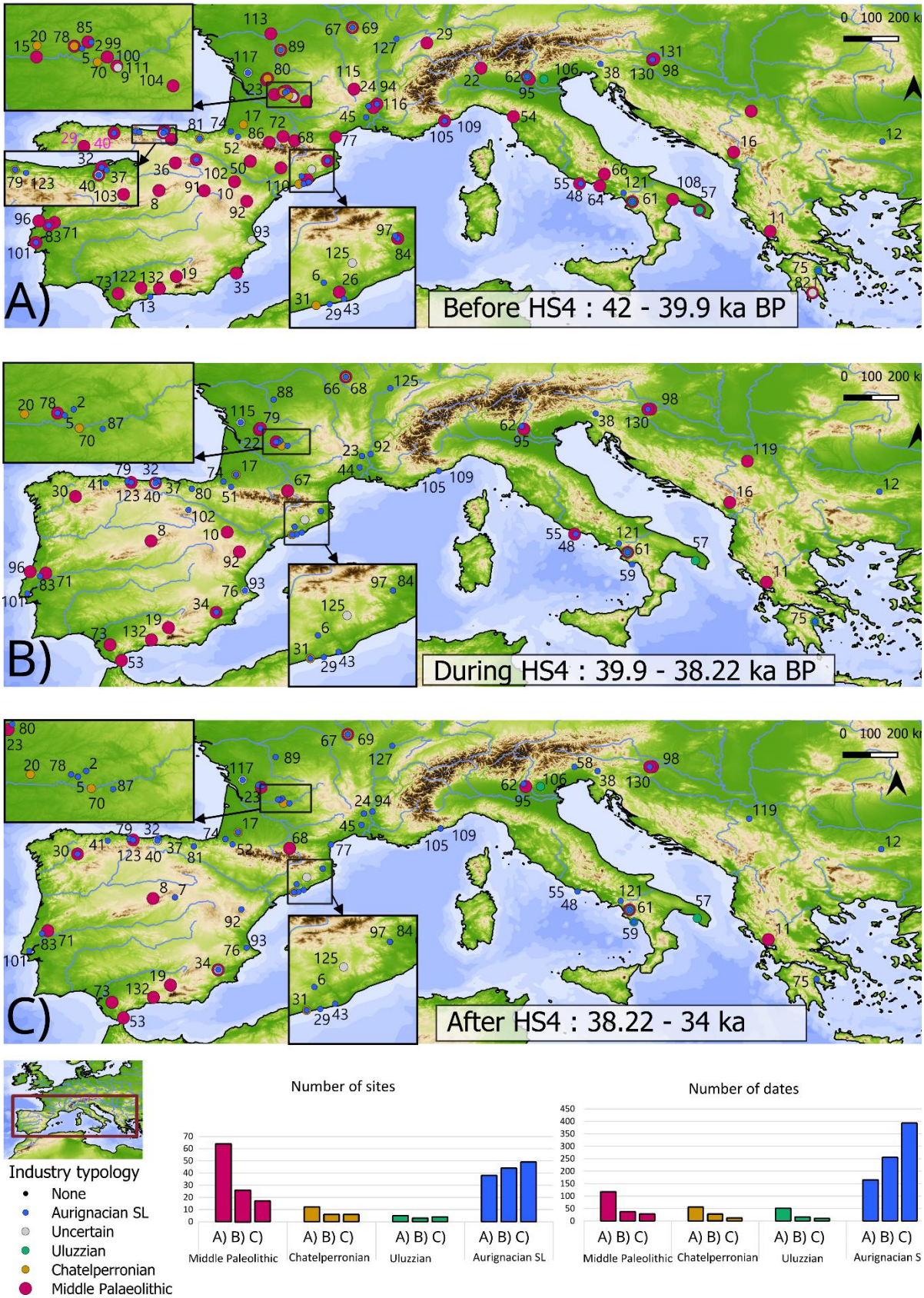


Fig. S2. Maps of archaeological sites and their associated technocomplexes with dates ranges falling before (A), during (B) and after (C) the HS4. Only radiocarbon dates with confidence index 1 and 2 were included (Table 6-D in results). The bar charts represent the number of sites (left) and dates (right) associated to each technocomplex for the three maps. See

Tableau S5: Sites archéologiques datés du Paléolithique moyen pendant le dernier cycle climatique dans la péninsule Ibérique

The radiometric age range indicated for the archaeological layers includes dating errors. When radiocarbon dates are included, they were recalibrated using Intcal20 curve on R package *Bchron* (Haslett and Parnell, 2008).

N°	Site name	Type of site	x	y	Layers	MIS attribution	Cultural attribution	Climate information ?	Single date	radiometric age range	Method	Ref	Note
1	Abauntz	Cave	43.016	-1.641	h	MIS 3	Middle Palaeolithic (Mousterian)			54-40	AAR	Utrilla et al., 2015	
2	Abric del Pastor	Rock shelter	38.687	-0.451	VI-IVb	MIS 4-3	Middle Palaeolithic (Mousterian)			72-43	OSL/ESR/U-series	Mallol et al., 2019	
3	Abric Romani	Rock shelter	41.533	1.688	P-A	MIS 4-3	Middle Palaeolithic (Mousterian)			72-42.2	U/Th and radiocarbon	Vaquero et al., 2013	
4	Abrigo de la Quebrada	Cave	39.744	-0.998	IX-VII	MIS 5	Middle Palaeolithic (Mousterian)			> 87	TL	Real et al., 2020	Age min
4	Abrigo de la Quebrada	Cave	39.744	-0.998	V-III	MIS 4-3	Middle Palaeolithic (Mousterian)	Warm and humid fauna		< 74-42.6	Radiocarbon and TL	Real et al., 2020	Age max
5	Abrigo del Molino	Rock shelter	40.952	-4.141	3-2 (G-C)	MIS 4-3	Middle Palaeolithic (Mousterian)			<60.5-41.8	TL and Radiocarbon	Álvarez-Alonso et al., 2018; Kehl et al., 2018	
6	Aguilon P5	Cave	41.309	-1.053	e	MIS 3	Middle Palaeolithic (Mousterian)			48.4-43	Radiocarbon	Mazo & Alcolea, 2020	
7	Amalda I	Cave	43.231	-2.202	VII	MIS 4	Middle Palaeolithic (Mousterian)			54.7-42.5	Radiocarbon	Sánchez-Romero et al., 2020	
8	Amalda III	Cave	43.231	-2.202	VI	MIS 5b-5a	Middle Palaeolithic (Mousterian)		91.3 ± 6.5		OSL	Rios-Garaizar et alo., 2024	
8	Amalda III	Cave	43.231	-2.202	V-IV (base)	MIS 5-4	Middle Palaeolithic (Mousterian)	climatic deterioration		90-77.3	OSL	Rios-Garaizar et alo., 2024	
8	Amalda III	Cave	43.231	-2.202	IV	MIS 3	Middle Palaeolithic (Mousterian with Vasconian)	warmer	57.7 ± 3.8		OSL	Rios-Garaizar et alo., 2024	

9	Arlanpe	Cave	43.140	-2.750	SQ3	MIS 5	Late Acheulean / EMP	Temperate / Humid		> 70.6	AAR	Rios-Garaizar et al., 2015	minimum age
10	Arrillor	Cave	43.006	-2.741	Lm-Smk-l-Amk	MIS 3	Middle Palaeolithic (Mousterian)			54.7-43.2	Radiocarbon	Higham et al., 2014; Iriarte-Chiapusso et al., 2019	
10	Arrillor	Cave	43.006	-2.741	Lm, SMk-l, Amk	MIS 3	Middle Palaeolithic (Mousterian)			54.7-43.2	Radicoarbon	Higham et al., 2014; Iriarte-Chiapusso et al., 2019	
11	Askondo	Cave	43.131	-2.664	11-12	MIS 4	Middle Palaeolithic (Mousterian)	mild and temperate phase		68.4-64	AAR	Torres Pérez-Hidalgo & Ortiz Menéndez, 2012	
12	Aviones	Cave	37.585	-0.986	I-IV	MIS 3	Middle Palaeolithic (Mousterian)			49.7-41.8	Radicoarbon	Zilhao et al, 2016	
13	Axlor	Cave	43.118	-2.719	N,M,F	MIS 5d-5a	Middle Palaeolithic (Mousterian)			107.2-74.2	OSL	Demuro et al., 2023	
13	Axlor	Cave	43.118	-2.719	B	MIS 3	Middle Palaeolithic (Mousterian with Vasconian)		70.4 ± 5.3		OSL	Demuro et al., 2023	
13	Axlor	Cave	43.118	-2.719	D	MIS 4	Middle Palaeolithic (Mousterian ith Quina)		50.7 ± 3.5	54.2->42.6	OSL and Radiocarbon	Demuro et al., 2023	Radiocarbon should be considered a minimum age
14	Bajondillo	Cave	36.621	-4.500	Bj19	MIS 6-5	Middle Palaeolithic (Mousterian)			172.9-113.9	U/Th and TL	Sánchez et al., 2011	
14	Bajondillo	Cave	36.621	-4.500	Bj18	MIS 5	Middle Palaeolithic (Mousterian)	warm humid phase		_	U/Th and TL	Sánchez et al., 2011	not directly dated

14	Bajondillo	Cave	36.621	-4.500	Bj17	MIS 4-3	Middle Palaeolithic (Mousterian)			76.9-58.1	U/Th and TL	Sánchez et al., 2011	
14	Bajondillo	Cave	36.621	-4.500	Bj16-14	MIS 3	Middle Palaeolithic (Mousterian)			54.7-42.3	Radiocarbon, U/Th and TL	Sánchez et al., 2011; Higham et al., 2014	
15	Bolomor	Cave	39.060	-0.250	IV	MIS 5e	Middle Palaeolithic (Mousterian)	Temperate humid	121 ± 18	103-140	TL	Arsuaga et al., 2012; Ochando et al., 2019	
16	Buena Pinta Cave	Cave	40.923	-3.807	3	MIS 4-3	Middle Palaeolithic (Mousterian)		63.4 ± 5.5		TL	Pérez-González et al., 2010	
17	Camino Cave	Cave	40.924	-3.808	8, 5	MIS 5	Middle Palaeolithic (Mousterian)			99.7-83.1	TL	Arsuaga et al., 2012	
17	Camino Cave	Cave	40.924	-3.808	South sector	MIS 5	Middle Palaeolithic (Mousterian)		74.5 ± 6.3	80.8- 68.2	TL	Arsuaga et al., 2012	
18	Can Garriga	Open air	42.034	2.838	2 & 3	MIS 5	Middle Palaeolithic (Mousterian)			85.2-107.6	U/Th	Daffara et al., 2018	
19	Carihuela	Cave	37.444	-3.433	XII	MIS 5	Middle Palaeolithic (Mousterian)	Interglacial Mediterranean forest	117 ± 41	158-76	U/Th	Carrión et al., 2019b	Very large uncertainty
19	Carihuela	Cave	37.444	-3.433	XI-X	MIS 5	Middle Palaeolithic (Mousterian)	Xerophytic vegetation maximum, cold stage MIS 5b		136-77.6	U/Th and ESR	Carrión et al., 2019b	
19	Carihuela	Cave	37.444	-3.433	IX-VIII	MIS 4	Middle Palaeolithic (Mousterian)	Cold stage (pollen and fauna)		67.2 - 54.4	U/Th and ESR	Carrión et al., 2019b	
19	Carihuela	Cave	37.444	-3.433	VIIb	MIS 4	Middle Palaeolithic (Mousterian)	Cold stage (pollen and fauna)		78-60.7	U/Th and ESR	Carrión et al., 2019b	
19	Carihuela	Cave	37.444	-3.433	VI-V	MIS 4-3	Middle Palaeolithic (Mousterian)	Cold stage (pollen and fauna)		74.7 – 30 (?)	ESR, Radiocarbon and TL	Carrión et al., 2019b	

20	Cova 120	Cave	42.280	2.608	VII-IV	MIS 5-3 ?	Middle Palaeolithic (Mousterian)		57.9 + 6.8/ -6.5	>51.4	U/Th	Agusti et al., 1991	Terminus ante-quem
21	Cova del Coll Verdaguer	Cave	41.393	1.911	1-3	MIS 4-3	Middle Palaeolithic (Mousterian)			62.2-40.9	Radiocarbon and U/Th	Daura et al., 2017	
22	Cova del Gegant	Cave	41.222	1.773	V	MIS 5-4	Middle Palaeolithic (Mousterian)			83.3- > 57	U/Th and OSL	Daura et al., 2021	Age min
23	Cova del Rinoceront	Cave	41.274	1.961	Unit 1 (III-II)	MIS 5	Middle Palaeolithic (Mousterian)			111-81.7	TL, U/Th, ESR, AAR	Daura et al., 2015	
23	Cova del Rinoceront	Cave	41.274	1.961	UNIT 1 (III)	MIS 5	Middle Palaeolithic (Mousterian)			139-119	TL, U/Th, ESR, AAR	Daura et al., 2015	
24	Cova del Tossal de la Font	Cave	40.113	-0.050	IIa	MIS 4-3	Middle Palaeolithic (Mousterian)			62.43-55.53	U/Th	Ollé et al., 2014	Age max
25	Cova Eirós	Cave	42.752	-7.210	3	MIS 3	Middle Palaeolithic (Mousterian)		35.1 ± 700	41.8-37.6	Radicoarbon	Lombera-Hermida et al., 2021	
26	Cova Gran	Cave	42.056	1.086	S1B	MIS 3	Middle Palaeolithic (Mousterian)		38.64 ± 440	43.1-41.9	Radicoarbon	Mora et al., 2018	Other radiocarbon ages older and younger discarted
27	Covalejos	Cave	43.395	-3.928	11(M)	MIS 5c	Archaic Mousterian	humid template climate		110.1-76.7	OSL	Maroto et al., 2021	
27	Covalejos	Cave	43.395	-3.928	9(K)-7(I)	MIS 4	Mousterian (+Quina)	humid template climate		72.5-55.9	OSL and AAR	Maroto et al., 2021	
27	Covalejos	Cave	43.395	-3.928	6-4 (H-D)	MIS 3	Mousterian (+Quina)			59.5-40	OSL and radiocarbon	Maroto et al., 2021; Jones et al., 2019	
28	Cueva Anton	Cave	38.064	-1.497	AS5-AS2	MIS 5a	Middle Palaeolithic (Mousterian)	warm humid (GI21) and then cold stadials	88.2 ± 8.9 ka (terminus ante	85-72	TL and paleoenvironmental correlation	Zilhão et al., 2016, 2017	

								quem for AS5)					
28	Cueva Anton	Cave	38.064	-1.497	AS1	MIS 3	Middle Palaeolithic (Mousterian)		38.9-35.3	Radiocarbon	Zilhão et al., 2016, 2017	few lit
29	Cueva Corazon	Cave	42.749	-4.275	2	MIS 5c	Middle Palaeolithic (Mousterian)		104.4-88.3	TL	Diez Martín et al., 2011; Yravedra et al., 2013	
30	Cueva de Ardales	Cave	36.873	-4.826	3-4	MIS 3	Middle Palaeolithic (Mousterian)		54.8-42.4	Radiocarbon	Ramos Muñoz et al., 2022	
31	Cueva Millan	Cave	42.059	-3.448	1a-1b	MIS 3	Middle Palaeolithic (Mousterian)		42.8-40.6	Radiocarbon	Moure and Garcia Soto, 1982 ; Diez et al, 2008	
32	Cueva Morin	Cave	43.359	-3.858	XI	MIS 3	Middle Palaeolithic (Mousterian)		48-42	Radiocarbon	Maillo-Fernández et al, 2001; Higham et al., 2014	
33	El Castillo	Cave	43.292	-3.966	XXII-XXI	MIS 5	Middle Palaeolithic (Mousterian)	_	100-80	U/Th and ESR	Martín-Perea et al., 2023	not directly dated, min/max date
33	El Castillo	Cave	43.292	-3.966	XX	MIS 4	Middle Palaeolithic (Mousterian)		80-43.26	Radiocarbon and ESR	Martín-Perea et al., 2023	
34	El Conde	Cave	43.288	-5.983	N20A	MIS 3	Middle Palaeolithic (Mousterian)		44-41.2	Radiocarbon and U/Th	López-García et al., 2011	
35	El Cuco	Rock shelter	43.392	-3.229	XIII-X	MIS 3	Middle Palaeolithic (Mousterian)		52-43.2	Radiocarbon	Gutiérrez-Zugasti et al, 2018	
36	El Esquilleu	Rock shelter	43.229	-4.598	ESQ-21-ESQ-3	MIS 4-3	Middle Palaeolithic (Mousterian)		> 50 to 40	Radiocarbon and TL	Maroto et al., 2012; Jordá et al., 2008; Baena et al., 2021	

37	El Pinar	Open-air	39.891	-0.255	?	MIS 5	Middle Palaeolithic (Mousterian)			101-74	TL	Casabo & Gomar, 2002	
38	El Salt	Rock shelter	38.687	-0.509	XII-V	MIS 4-3	Middle Palaeolithic (Mousterian)	Aridity in layer V		61.1-40.7	OSL/TL	Galván et al., 2014	
39	El Sidrón	Cave	43.383	-5.323	Galeria del Osario III (Neanderthal bone)	MIS 3	Middle Palaeolithic (Mousterian)		48.4 ± 3.2	54.7-44.5	Radicoarbon	Wood et al., 2013	
40	El Miron	Cave	43.282	-3.231	130	MIS 3	Middle Palaeolithic (Mousterian)			54.7-42.4	Radicoarbon	Marín-Arroyo et al., 2018	
41	El Niño	Cave	38.571	-2.091	XI-IV/III	MIS 3	Middle Palaeolithic (Mousterian)			< 55.55	U/Th and Radiocarbon	García-Moreno et al., 2016	age max, and very late radiocarbon dates up to 31 calka BP
42	Els Pinyons	Cave	41.530	1.691	9-7	MIS 2	Middle Palaeolithic (Mousterian)			54.6-41.2	U/Th and Radiocarbon	Vaquero, 2010	
43	Ermitons	Cave	42.280	2.590	IV	MIS 3	Middle Palaeolithic (Mousterian)		40.58 ± 0.55	44.8-42.6	Radicoarbon	Maroto et al., 2012	
44	Escoural	Cave	38.544	-8.138	test 3a	MIS 3	Middle Palaeolithic (Mousterian)		48.9 ± 56.5	54.5-43.2	U/Th	Zilhão, 2001	
45	Estret de Tragó	Cave	41.925	0.609	UA3-UA2	MIS 6-5	Middle Palaeolithic (Mousterian)			141-67.5	TL	Martínez-Moreno et al., 2004; Casanova et al., 2014	
45	Estret de Tragó	Cave	41.925	0.609	S7-S5	MIS 4-3	Middle Palaeolithic (Mousterian)			58.5-38.4	TL	Martínez-Moreno et al., 2004; Casanova et al., 2014	
46	Foz do Enxarrique	Open air	39.653	-7.674	T6, base middle part	MIS 3	Middle Palaeolithic (Mousterian)		44 ± 3	47- >35	OSL	Cunha et al., 2019; Zilhão, 2021	

47	Fuente Mudarra	Open-air	42.352	-3.538	8-4	MIS 5-3	Middle Palaeolithic (Mousterian)		132.6-53.5	OSL	Santamaría et al., 2021	
48	Galeria de la Estatuas	Cave	42.348	-3.519	4-1	MIS 5-4	Middle Palaeolithic (Mousterian)		119-65	OSL/U-series/ESR	Moreno et al., 2022; Demuro et al.,2019	
49	Gatzarria	Cave	43.139	-0.916	Cj	MIS 3	Middle Palaeolithic (Mousterian)		54.7-42.9	Radiocarbon	Deschamps, 2019	
50	Gorham	Cave	36.120	-5.342	IV	MIS 3	Middle Palaeolithic (Mousterian)		54.7-42.7	Radiocarbon	Finalyson et al., 2006	Persistence until 24 ka according to Finalyson et al., 2006
51	Gruta da Oliveira	Cave	39.507	-8.613	25-8	MIS 5d-5a	Middle Palaeolithic (Mousterian)		107.1-67.1	TL and U/Th	Zilhão et al., 2018	
52	Gruta do Caldeirao	Cave	39.648	-8.415	L-M-N	MIS 3	Middle Palaeolithic (Mousterian)		44.5- < 38.5	Radiocarbon and OSL	Zilhão, 2021	terminus post quem according to Zilhão, 2021
53	Gruta Nova do Columbeira	Cave	39.301	-9.181	8-3	MIS 5-3 ?	Middle Palaeolithic (Mousterian)		101-36	Radiocarbon and U/Th	Zilhão et al., 2011; Figueiredo et al., 2018	Very problematic dates with large uncertainties
54	HAT	Open-air	40.265	-3.529	Arganda IV	MIS 5	Middle Palaeolithic (Mousterian)	74 + 16/-12.1	_	TL	Panera et al., 2011	Age min
55	Higueral la Valleja	Cave	36.750	-5.810	VIII-V	MIS 4-3	Middle Palaeolithic (Mousterian)		64.1-44.7	OSL and radiocarbon	Jennings et al., 2009	
56	Hotel California	Open air	42.354	-3.532	I	MIS 5-4	Middle Palaeolithic (Mousterian)	71±5.6	76.6-65.4	OSL	Arnold et al, 2013	
56	Hotel California	Open air	42.354	-3.532	II	MIS 4-3	Middle Palaeolithic (Mousterian)	57.6 ± 5.7	63.3-51.9	OSL	Arnold et al, 2013	

56	Hotel California	Open air	42.354	-3.532	V	MIS 3	Middle Palaeolithic (Mousterian)		48.2 ± 3.3	51.5-43.3	OSL	Arnold et al, 2013	
57	Hundidero	Open air	42.352	-3.539	4-2	MIS 5-3	Middle Palaeolithic (Mousterian)			81.6-51.7	OSL/TL	Navazo et al., 2011	
58	Ibex Cave	Cave	36.135	-5.346	Unit 319	MIS 3	Middle Palaeolithic (Mousterian)		49.4 ± 3.2	52.6-46.2	ESR	Vidal et al., 2001	
59	Jarama VI	Rock shelter	40.974	-3.325	3-2	MIS 4-3	Middle Palaeolithic (Mousterian)			65.6-44.4	TL and Radiocarbon	Kehl et al., 2013; Wood et al., 2013	
60	La Boja	Rock shelter	38.072	-1.490	OH 23-21	MIS 3	Middle Palaeolithic (Mousterian)			56-42.3	OSL and radiocarbon	Zilhão, 2017	
61	La Ermita	Cave	43.231	-2.202	5a & 5b	MIS 5c	Middle Palaeolithic (Mousterian)			89-105.8	U/Th	Sánchez-Yustos & Diez-Martín, 2015	Age min and age max
62	La Guelga	Cave	43.365	-5.096	D 9-4B	MIS 3	Middle Palaeolithic (Mousterian)			54.5-44.5	Radiocarbon	Menéndez et al., 2018	
63	La Mina	Cave	42.088	-3.419	_	MIS 3	Middle Palaeolithic (Mousterian)			52.5	AAR	Diez et al, 2008	
64	Lapa do Picareiro	Cave	39.531	-8.652	JJ	MIS 3	Middle Palaeolithic (Mousterian)			54.8-41.6	Radiocarbon	Haws et al, 2020	
65	L'Arbreda	Cave	42.161	2.747	I	MIS 3	Middle Palaeolithic (Mousterian)			52.1-40	Radiocarbon	Higham et al., 2014	
66	Las Callejuelas	Open-air	40.457	-0.817	4-1	MIS 5e	Middle Palaeolithic (Mousterian)	Warm humid		135-116	AAR	Domingo et al., 2017	
67	Las Fuentes de San Cristobal	Cave	42.365	0.595	F-G	MIS 3	Middle Palaeolithic (Mousterian)			44.2-40.2	Radiocarbon	Maroto et al., 2012	
68	Lezetxiki	Cave	43.080	-2.530	VII-V ? (Layer H-G ?)	MIS 6-3 ? Includig	Middle Palaeolithic (Mousterian)	warm humid phase		147-55	ESR and U/Th	Falguères et al., 2005;	Problematic old dates, and layer D

						MIS 5e phase						Arriolabengoa et al., 2018	attributed to MIS 5e not directly dated in the new study
69	Llonin	Cave	43.332	-4.645	VIII	MIS 3	Middle Palaeolithic (Mousterian)	43.54± 2.42	54.4-42.4	Radiocarbon	Sanchis et al., 2019		
70	Los Casares	Cave	40.939	-2.292	Cj	MIS 3	Middle Palaeolithic (Mousterian)	39.49 ± 850	44.6-41.9	Radiocarbon	Alcaraz-Castaño et al, 2017		
71	Los Toros	Cave	40.513	-0.555	d	MIS 3	Middle Palaeolithic (Mousterian)	35.25 ± 490	41.7-39.1	Radiocarbon	Montes et al, 2006		
72	Maltravieso	Cave	39.460	-6.370	PE1	MIS 6-5	Middle Palaeolithic (Mousterian)	117 +17/-14	_	U/Th	Flores, 2011		
73	Mira Nascente	Open air	39.706	-9.050		MIS 3	Middle Palaeolithic (Mousterian)		43.4-39.2	Radiocarbon and OSL	Bicho et al, 2015 ; Haws et al, 2010		
74	Navalmaíllo	Rock shelter	40.925	-3.795	F-D	MIS 5a-MIS 4	Middle Palaeolithic (Mousterian)		83.25-66.6	TL	Blain et al., 2022		
75	Pedra Dreta	Open air	42.034	2.838		MIS 5	Middle Palaeolithic (Mousterian)		96 – 84.2	U/Th	Daffara et al., 2018	Age min / age max	
76	Pego do Diabo	Cave	38.830	-9.170	2/3	MIS 3	Middle Palaeolithic (Mousterian)	38.75 ± 650	44.1-41.6	Radiocarbon	Zilhão et al, 2010		
77	Peña Cabra	Rock shelter	40.969	-3.200	N7	MIS 5	Middle Palaeolithic (Mousterian)	92.7 ± 6.9	99.6-85.8	OSL	Luque et al., 2025		
78	Peña Miel	Cave	42.209	-2.620	e	MIS 3	Middle Palaeolithic (Mousterian)		54.5-41.2	Radiocarbon	Montes et al, 2001 ; Rios-Garaizar and Eixea, 2021		
79	Prado Vargas	Cave	43.032	-3.630	N4	MIS 3	Middle Palaeolithic (Mousterian)		51.5-40.9	Radiocarbon and OSL/IRSL/TL	Ruiz et al, 2021		

80	Praia Rei Cortico	Open air	39.424	-9.241	PC5-3	MIS 3	Middle Palaeolithic (Mousterian)			55.8-48.5	OSL	Haws et al, 2010, 2022	
81	Roca dels Bous	Rock shelter	41.873	0.844	N, M, G	MIS 3	Middle Palaeolithic (Mousterian)			60.7-43.7	Radiocarbon	Benito-Calvo et al, 2020	
81	Roca dels Bous	Rock shelter	41.873	0.844	R3	MIS 3	Middle Palaeolithic (Mousterian)		38.8±1.2	44.8-40.6	Radiocarbon	Benito-Calvo et al, 2020	
82	Salto do Boi	Open air	40.979	-7.099	UA17-12	MIS 3	Middle Palaeolithic (Mousterian)			53.4-37.7	OSL	Aubry et al, 2020	
83	Sima de las Palomas de Teba	Cave	36.983	-4.879	10-9	MIS 4-3	Middle Palaeolithic (Mousterian)			61.8-36.8	OSL	Kehl et al., 2016	
84	Sima de las Palomas del cabezo gordo	Cave	37.800	-0.897	2	MIS 3	Middle Palaeolithic (Mousterian)			57.9-37.1	Radiocarbon and OSL	Walker et al., 2012	
85	Sopeña	Rock shelter	43.321	-4.947	XVI-XII	MIS 4-3	Middle Palaeolithic (Mousterian)			69.5-39	Radiocarbon and ESR	Pinto-Llona et al., 2012; 2022	
86	Tarrazona	Open air	37.430	-5.830	E2	MIS 5e-5d	Mode 2 and Mode 3 industry			129-110	OSL	Caro Gómez et al., 2011	
86	Tarrazona	Open air	37.430	-5.830	E3	MIS 5c	Middle Palaeolithic (Mousterian)			110-105	OSL	Caro Gómez et al., 2011	
86	Tarrazona	Open air	37.430	-5.830	E4	< MIS 5c	Middle Palaeolithic (Mousterian)			<105	OSL	Caro Gómez et al., 2011	Age max
87	Teixoneres	Cave	41.810	2.097	Unit IIIb	MIS 5-4	Middle Palaeolithic (Mousterian)	Cold-humid		< 91.4-60	U-series and biostratigraphy	Talamo et al., 2016; Tissoux et al., 2006	Age max and age min
87	Teixoneres	Cave	41.810	2.097	Unit IIIa	MIS 4-3	Middle Palaeolithic (Mousterian)	Arid		< 60-42.8	biostratigraphy and Radiocarbon	Talamo et al., 2016; Tissoux et al., 2006	Age max

88	Toll Cave	Cave	41.865	2.711	Unit 4-3	MIS 4-3	Middle Palaeolithic (Mousterian)		69.8-43	AAR and radiocarbon	Ochando et al., 2022	
89	Valdegoba	Cave	42.517	-3.767	7-5	MIS 3	Middle Palaeolithic (Mousterian)	49.6 ± 5.2	54.7-44.4, <73 ka	Radiocarbon and U/Th	Dalén et al, 2012; Quam et al., 2001	
90	Valongo Quarry	Open air	41.172	-8.485	VQ3	MIS 3	Middle Palaeolithic (Mousterian)	49.5 ± 3.69		OSL	Haws et al, 2020	
91	Vanguard Cave	Cave	36.125	-5.341	22-1	MIS 5-3	Middle Palaeolithic (Mousterian)		78-40	OSL	Doerschner et al., 2019	
92	Zafarraya	Cave	36.951	-4.127	mousterian level	MIS 3	Middle Palaeolithic (Mousterian)		55-43.6	U/Th and radiocarbon	Higham et al., 2014; Michel et al., 2013	Radiocarbon dates extending until ~30 ka ?

Suppléments de l'article 2 (CP)

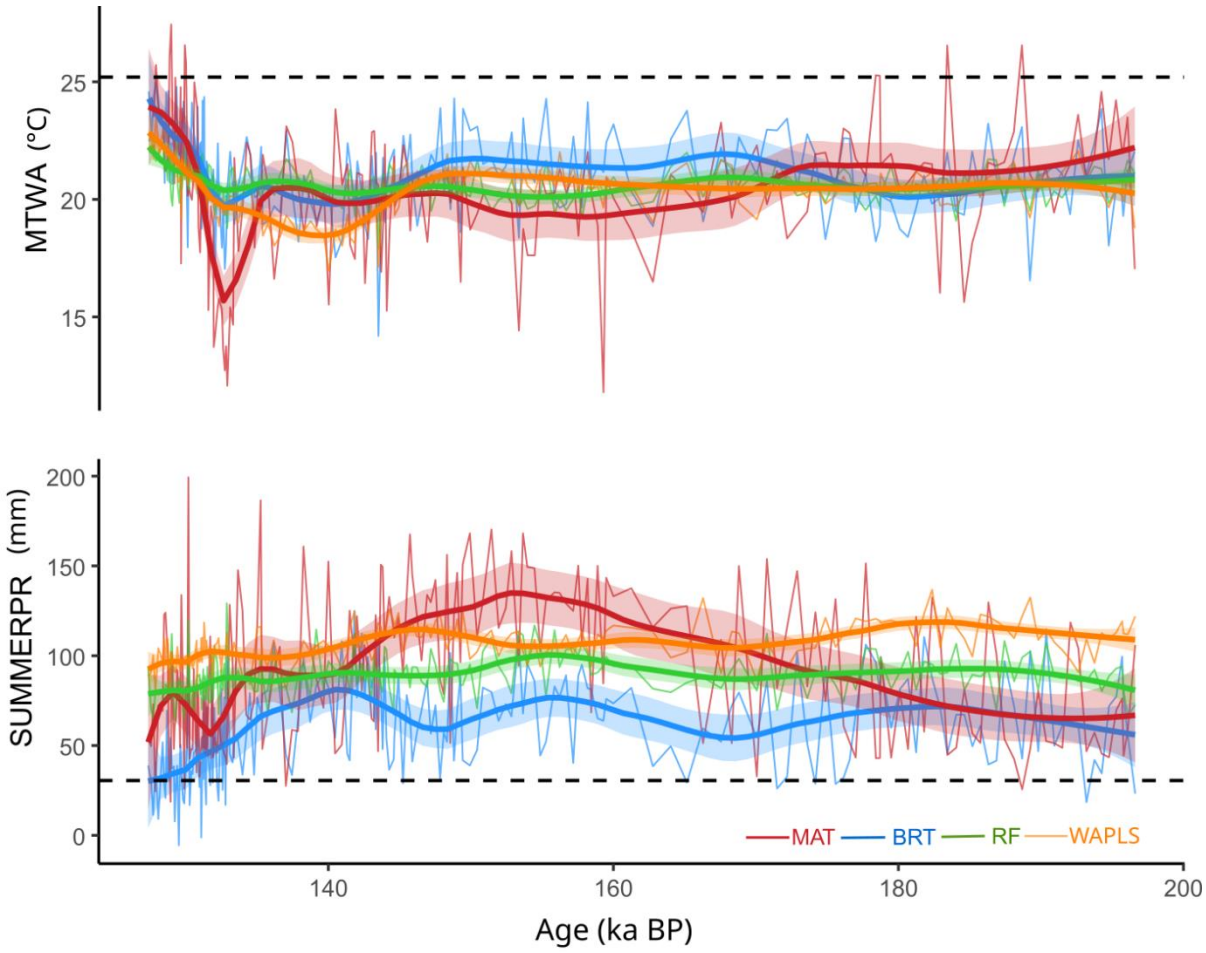


Fig. S3. Reconstructions climatiques à partir du pollen des paramètres d'été pour le MIS 6. Température moyenne du mois le plus chaud (MTWA) et précipitations d'hivers (SUMMERPR) reconstruites à partir des quatre méthodes appliquées dans cette étude : MAT (Modern Analogue Technique), WA-PLS (Weighted Averaging Partial Least Square), BRT (Boosted Regression Trees) and RF (Random Forest).

Tableau S6. Sites archéologiques attribués au MIS 6 en Méditerranée occidentale (page suivante).

N°	Site name	Lat	Long	Country	Context	Layer	Material	Method	Limite Sup	error	Limite Inf	error	Type of industry	Reference	Note
1	Matalascañas	37.02	-6.58	Spain	Open air	Ps2/AU1	sediment samples	OSL	132	10	151	11	Middle Paleolithic	Neto de Carvalho et al., 2023	Human footprints
2	Cueva del Angel	37.41	-4.42	Spain	Karst	XV level 7	Horse teeth	ESR/U-series	183	13	350	29	Acheulean	Falguères et al., 2019	Min age
3	Tarrazona	37.43	-5.83	Spain	Open air	E1/Layer 9		OSL	138.4	11.7			Acheulean	Caro Gómez et al., 2011	Min age
4	Los Aljezares	38.33	-0.73	Spain	Open air	Carbonate layer	sediment	U/Th	132	10		_	Middle Palaeolithic	Eixea et al., 2022	age min
5	Bolomor	39.06	-0.25	Spain	Karst	Phase III	burnt flint	TL and AAR	_		180	_	Early Middle Palaeolithic	Fernández Peris et al., 2008; Ochando et al., 2019	age max
6	Vale do Forno	39.25	-8.58	Portugal	Open air	T4 terrace	Sediment	quartz-OSL and K-feldspar post-IRIR29	155	_	200	_	Typical Mousterian	Cunha et al., 2017	
7	VF3 (Milharos)	39.25	-8.58	Portugal	Open air	Above T4 terrace	Sediment	quartz-OSL and K-feldspar post-IRIR29	32	_	155	_	Acheulean	Cunha et al., 2017	age min/max
8	El Provencio	39.38	-2.57	Spain	Open air	Layer 2 - 2/3	sediment	ESR / OSL	41	_	836	_	Mousterian	Domínguez-Solera et al., 2020	no age/ age min/max
9	Cueva de Maltravieso	39.46	-6.37	Spain	Karst	PE1/PE2	Speleothem	U/Th	117	-1.214285714	183	-1.166666667	Middle Palaeolithic	Standish et al., 2025; Eva Mancha, 2011	
10	Almonda	39.51	-8.62	Portugal	Karst	EVS zone	Horse teeth	U/Th	136	_	170	_	Acheulean	Zilhão & McKinney, 1995	Probably secondary position
11	Pegos do Tejo	39.64	-7.69	Portugal	Open air	T4 terrace	Quartz	OSL	135	21		_	Early Middle Palaeolithic	Cunha ert al., 2012	age min
12	Cobrinhos	39.67	-7.68	Portugal	Open air	T4 terrace	Sediment	quartz-OSL and K-feldspar post-IRIR29	155	_	165	_	Typical Mousterian	Pereira et al., 2019	Most probable range of T4 (but untill 200 ka BP)
13	Puente Pino	39.78	-5.09	Spain	Open air	PNA layer	Sediment	OSL	136.98	_	148.4	_	Acheulean	Rodríguez de Tembleque Moreno et al., 2011	
14	Preresa	40.31	-3.59	Spain	Open air	Archaeological layer	Teeth and sediment samples	ESR	169		270	_	Middle Paleolithic	Moreno et al., 2019; Yravedra et al., 2019	
15	EDAR-Culebro	40.31	-3.59	Spain	Open air	Unit 2	Equus bones	AAR	133	28			Middle Palaeolithic	Silva et al., 2013; Yravedra et all., 2014	
16	Arriaga II/III	40.32	-3.54	Spain	Open air	_	_	_	134				Evolved Acheulean	Silva et al., 2013	Min age
17	Arganda II (Valdocarros)	40.33	-3.46	Spain	Open air	_	_	_	174	20	262	7	Evolved Acheulean	Panera et al., 2011	Probably MIS 7, younger date discarted
18	Villacastin	40.8	-4.37	Spain	Karst	_	_	_	_	_	_	_	Middle Paleolithic	Carrion et al., 2007	

19	Valdecampana	41.54	-5.46	Spain	Open air	Various fluvial terraces	burnt flint	TL	148	11		_	Early Middle Palaeolithic	Diez Martín et al., 2008, 2010; Sánchez Yustos, 2009	One reliable date
20	Porto Maior	42.07	-8.56	Spain	Open air	PM4	Quartz / feldspars	Modelled ESR/TT-OSL	179		223		Acheulean	Demuro et al., 2020	
21	Arbo	42.08	-8.44	Spain	Open air		_	_	_	_	_	_	Acheulean	Méndez-Quintas et al., 2022	
22	Lezetxiki	43.08	-2.53	Spain	Karst	Level VIII	Human femur	U-serie	164	9		_	Early Middle Palaeolithic	de la Rua et al., 2016	minimum age
23	Arlanpe	43.14	-2.75	Spain	Karst	SQ1, SQ2, SQ3	Flowstone and Ursus bones	U/Th and AAR	>70.6		>184.271	+ 34,3/– 26,6	Early Middle Palaeolithic	Rios Garaizar et al., 2015	
24	Ventalaperra	43.26	-3.38	Spain	Karst	III	_	_	_	_	_	_	Early Middle Palaeolithic	Rios-Garaizar, 2016	
25	Aldènes	43.36	2.7	France	Karst	_	_	_	_	_	_	_	Acheulean	Rossoni-Notter et al., 2016	
26	Lazaret	43.69	7.3	France	Karst	Couche C	cervus teeth & stalagmite	17 ESR dates + U/Th	203	25	119.7	2.4	final Acheulean	Michel et al., 2018, 2022	
27	Baume Bonne	43.7	6.04	France	Karst	_	_	_	_	_	_	_	Early Middle Palaeolithic	Gagnepain & Gaillard, 2003	
28	Duclos	43.78	-0.23	France	Open air	Limons moyens	Sediment / burnt flint	OSL/TL	169	19	189	13	Acheulean	Hernandez et al., 2012	2 dates for MIS 6 range
29	Romenteres	43.78	-0.23	France	Open air	Limons moyens	Sediment / burnt flint	OSL/TL	168	12	172	9	Middle Paleolithic	Hernandez et al., 2012	
30	Grotte du Prince	43.79	7.53	Italy	Karst	_	_	_	_	_	_	_	Acheulean	Rossoni-Notter et al., 2016	
31	Bau de l'Aubesier	44.14	5.34	France	Karst	Layer H	Sediments	TL/ESR/U/TH	169	17	191	15	Middle Paleolithic	Carmignani and Soressi, 2023	
32	Coudoulous I	44.48	1.66	France	Karst	Layer 4	Sediments / bones / teeth	ESR/U-series, TT-OSL	157	14	144	11	Early Middle Palaeolithic	Hernandez et al., 2015, 2021	
32	Coudoulous I	44.48	1.66	France	Karst	Layer 7	Sediments / bones / teeth	ESR/U-series, TT-OSL	174	14	209	14	Acheulean	Hernandez et al., 2015, 2021	
33	Payre	44.71	4.66	France	Open air	Layers D-E	teeth, bones, burnt flint, stalagmitic	ESR/U-series, TL	139	16	186	-1.363636364	Early Middle Palaeolithic	Valladas et al., 2008; Moncel et al., 2003; Richard et al., 2021	
34	Grotte Vaufrey	44.8	1.2	France	Karst	Layer IV-VII	sediment samples	TT-OSL	131	9	205	20	Typical Mousterian	Hernandez et al., 2014	
35	Pech de l'Aze II	44.85	1.25	France	Karst	Layers 5-9	Teeth	ESR	128	_	162	_	Acheulean	Grün et al., 1991	
36	Barbas III	44.85	0.57	France	Open air	C'3	Burnt flint	TL	146	29	147	28	Acheulean	Boëda, 1995	
37	Combe Brune 3	44.87	0.5	France	Open air	Unit 7	Burnt flint	TL	183	20	195	16	Early Middle Palaeolithic	Frouin et al., 2014	
38	Combe Brune 2	44.87	0.5	France	Open air	_	Burnt flint	TL	156.4	11.7			Early Middle Palaeolithic	Brenet et al., 2008	Single date

39	Sainte -Anne	45.08	3.85	France	Karst	J1	tooth ennamel	ESR	193	22			Acheulean	Rhodes et al., 2007	
40	La Chaise	45.67	0.47	France	Karst	Bed 11	Travertine	U/Th	151	15			Early Middle Palaeolithic	Blackwell et al., 1983	Single date
41	Riparo del Poggio	40	15.38	Italy	Karst	Layer 18	_	_	_	_	_	_	Acheulean	Boscato et al., 2009	
42	Rosaneto	40.03	16.13	Italy	Open-air	Layer 4	_	_	_	_	_	_	Acheulean	Palma di Cesnola, 2004	
43	Altamura	40.87	16.59	Italy	Karst	Carstic concretion	Speleothem	U/Th	130	2	172	15	None	Lari et al., 2015	
44	Riparo Paglicci	41.65	15.62	Italy	Karst	Layers 3-4	_	_	_	_	_	_	Acheulean	Galiberti et al., 2008	
45	Poggetti Vecchi	42.82	11.07	Italy	Open air	U4	Pisoliths	U/Th	170	3		_	Middle Palaeolithic	Benvenuti et al., 2017; Aranguren et al., 2019	age min
46	Monte Conero	43.55	13.6	Italy	Karst	G-F	_	_	_	_	_	_	Early Middle Palaeolithic	Peretto and Scarpante, 1982	
47	Grotta del Colombo	44.18	8.31	Italy	Karst	Layers 5-12	_	_	_	_	_	_	Early Middle Palaeolithic	Arobba et al., 2008	
48	Due Pozzi / Scornetta	44.47	11.47	Italy	Open-air	_	_	_	_	_	_	_	Early Middle Palaeolithic	Fontana et al., 2010	
49	San Bernardino	45.42	11.55	Italy	Karst	VII-VIII	Bones	ESR	154	_	213	_	Middle Palaeolithic	Picin et al., 2013	

Planches microscopiques: pollen et spores (Ptéridophytes)

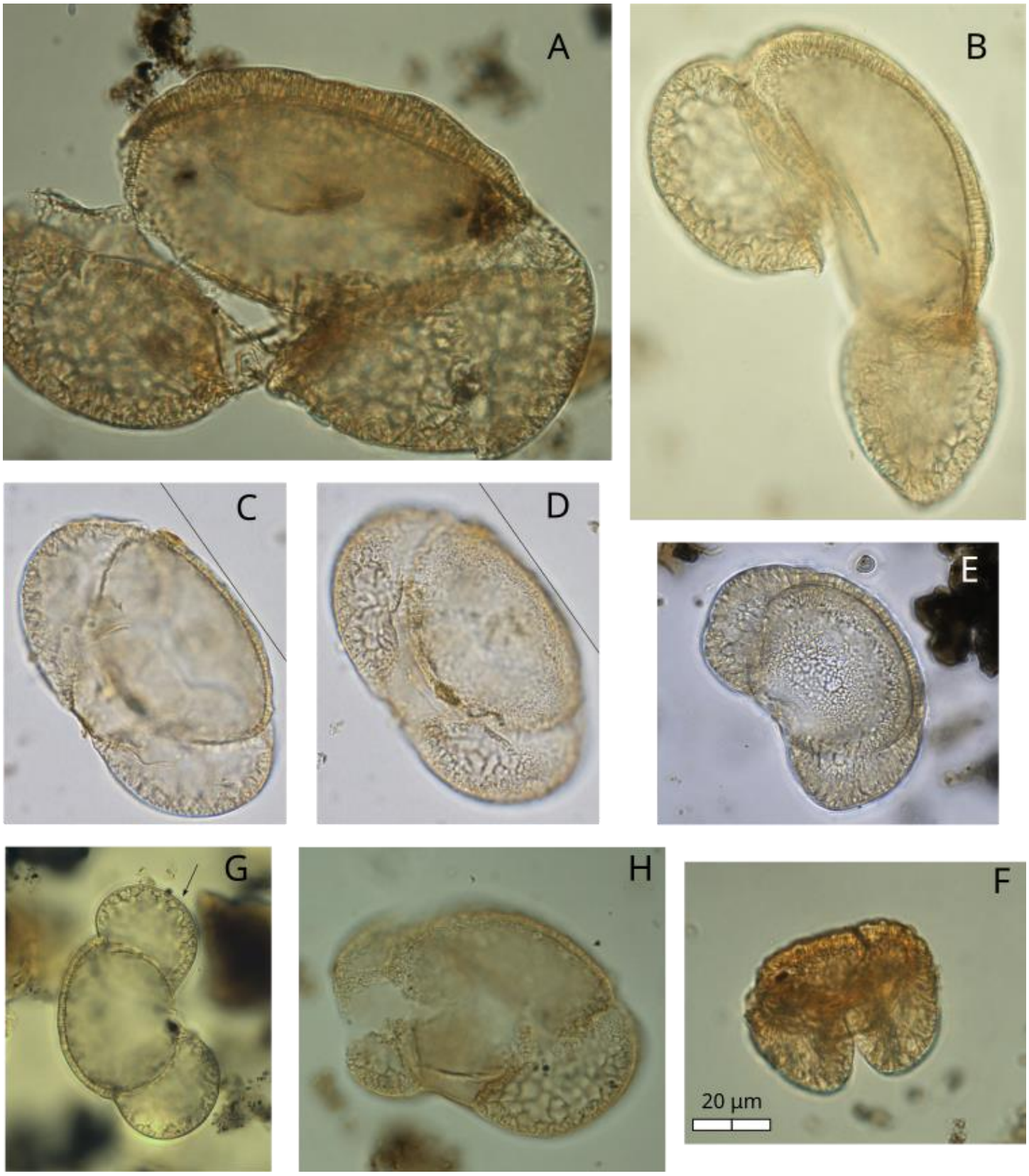


Planche 1 : Pinacées. A-B : *Abies* ; C-D : *Picea* ; E-F : *Cedrus* ; G-H : *Pinus.*

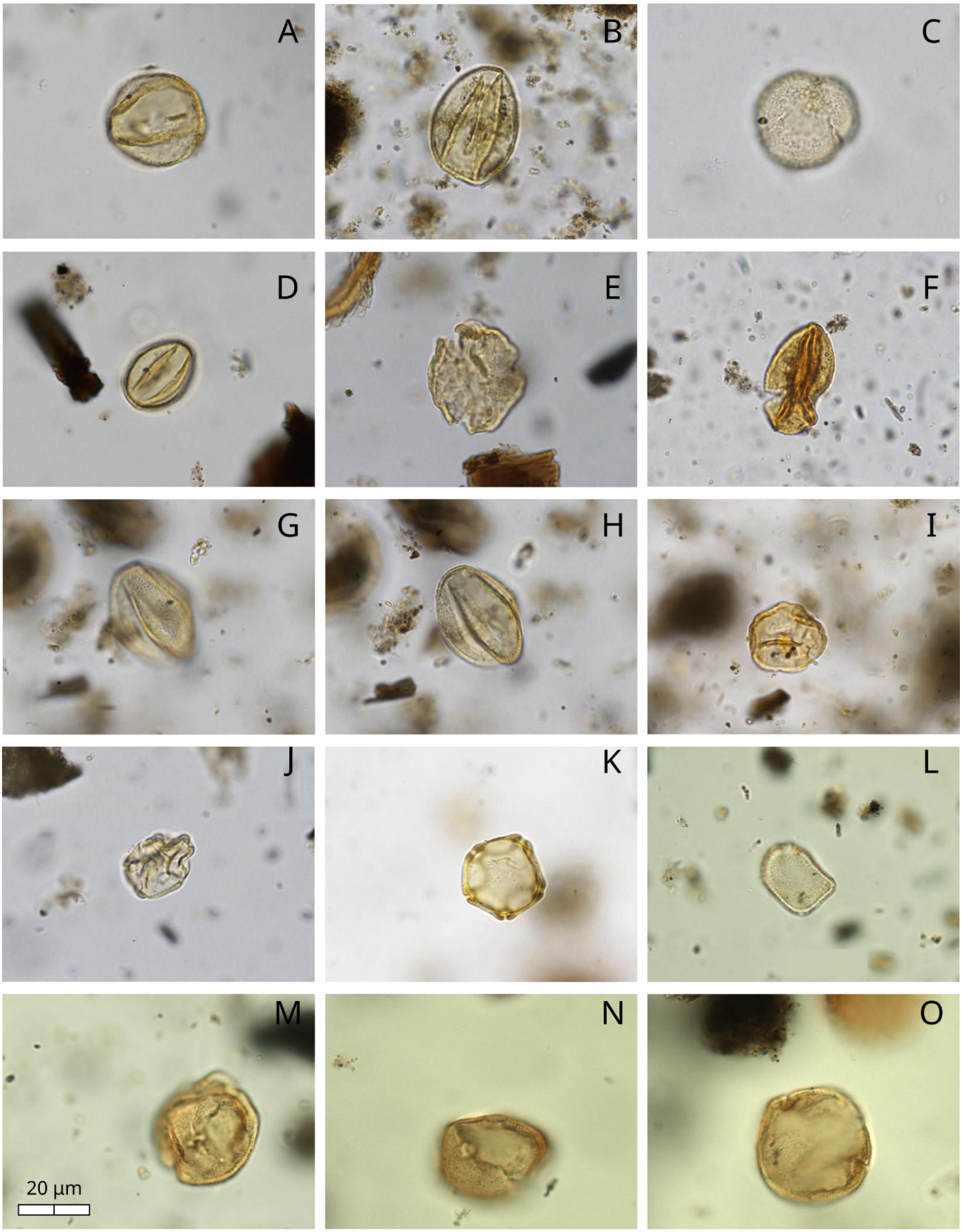


Planche 2 : Taxons de la forêt tempérée décidue (1). A-F : *Quercus* type décidu (E-F : grains très altérés/remaniés) ; G-H : *Acer* ; I : *Ulmus* ; J-K : *Alnus* (J : grain très altéré) ; L : *Taxus* ; M-O : *Fagus*

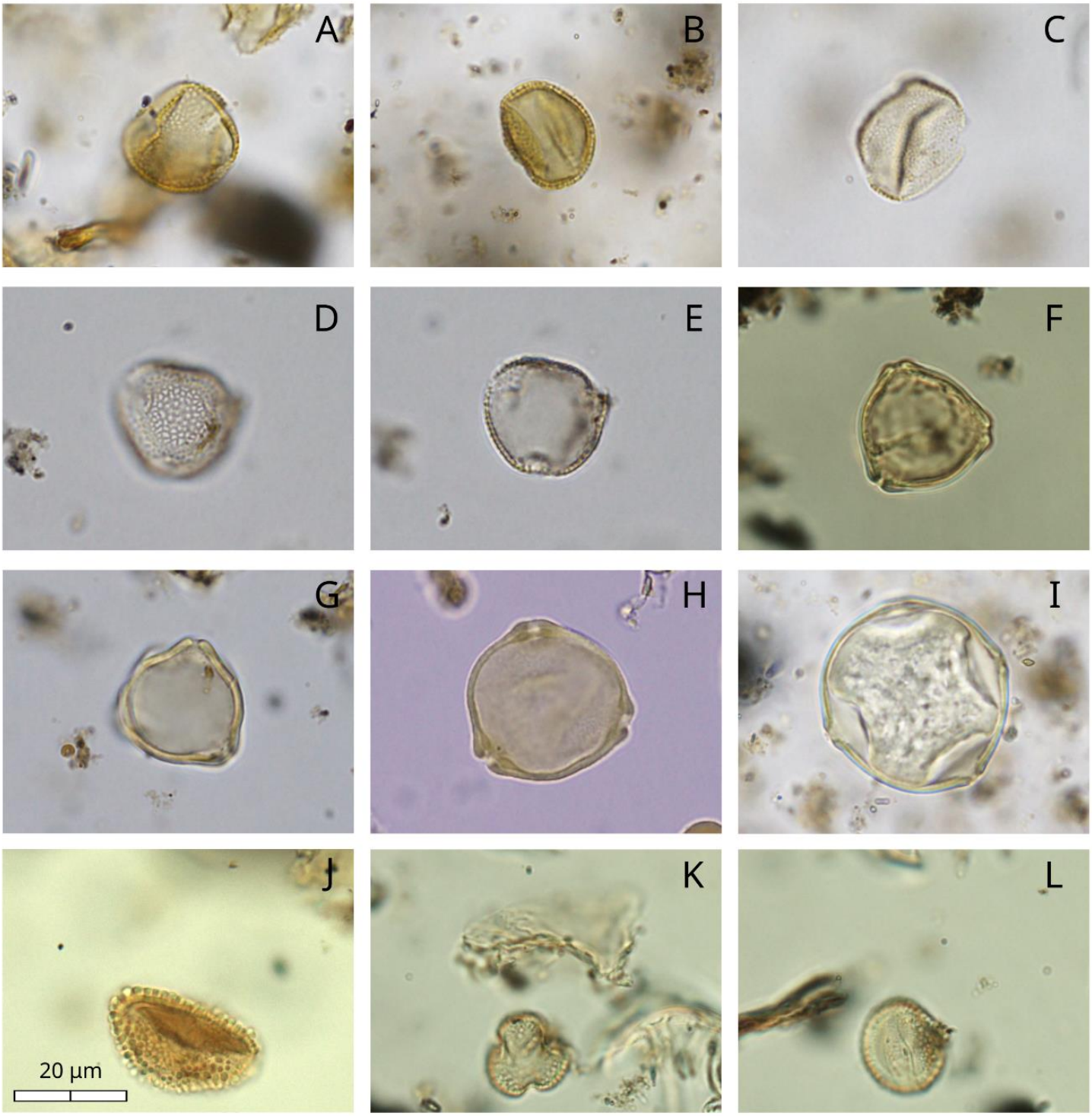


Planche 3 : Taxons de la forêt tempérée décidue (2). A-E : *Fraxinus* ; F-G: *Corylus* ; H: *Betula* ; I : *Carpinus* (grain moderne contaminant) ; J: *Ilex* ; K-L: *Salix*

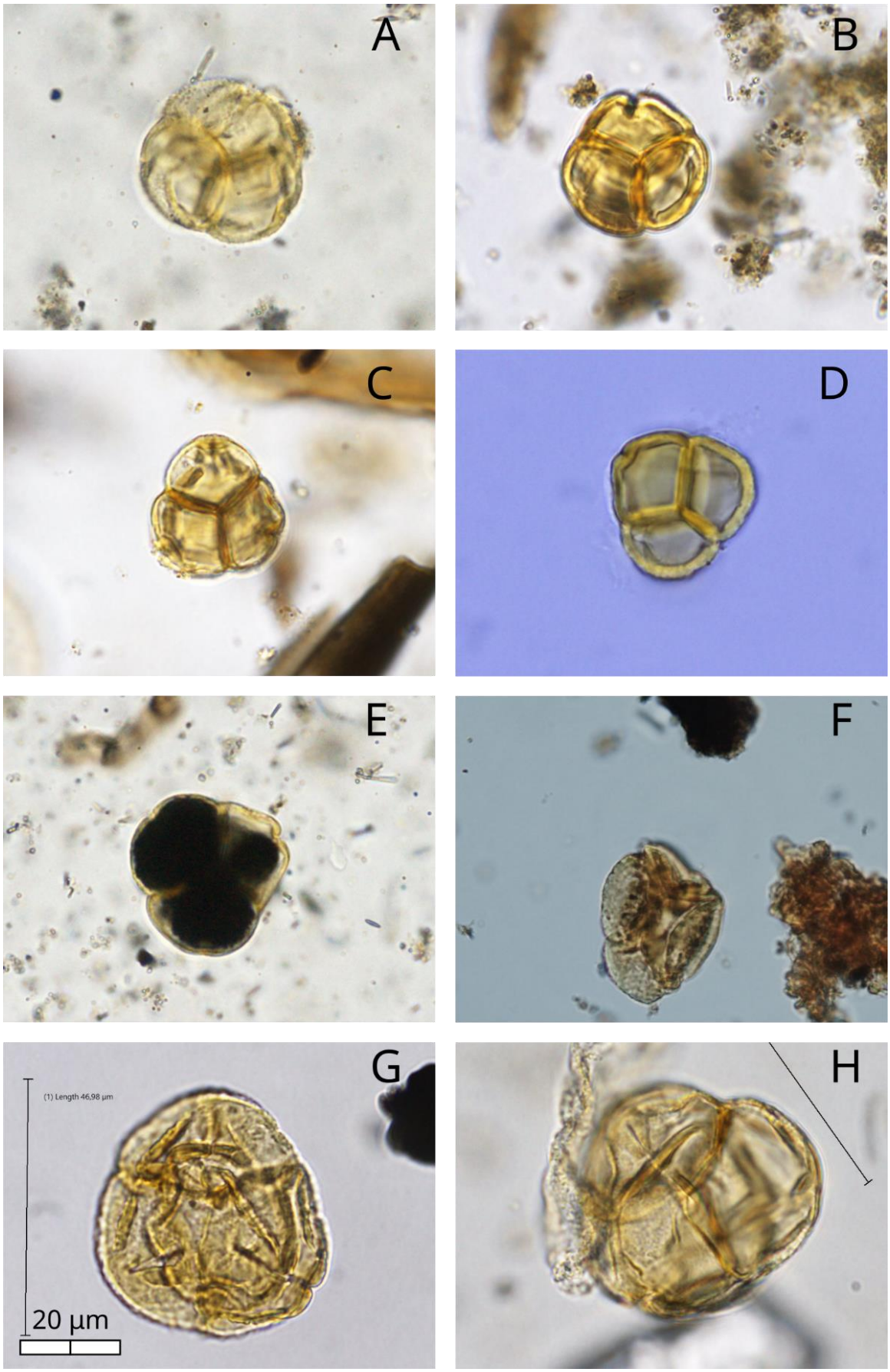


Planche 4: Ericaceae. A-E: type *Erica*. F: type *Calluna* ; G-H : larges grains, types *Arbutus* ou *Rhododendron*

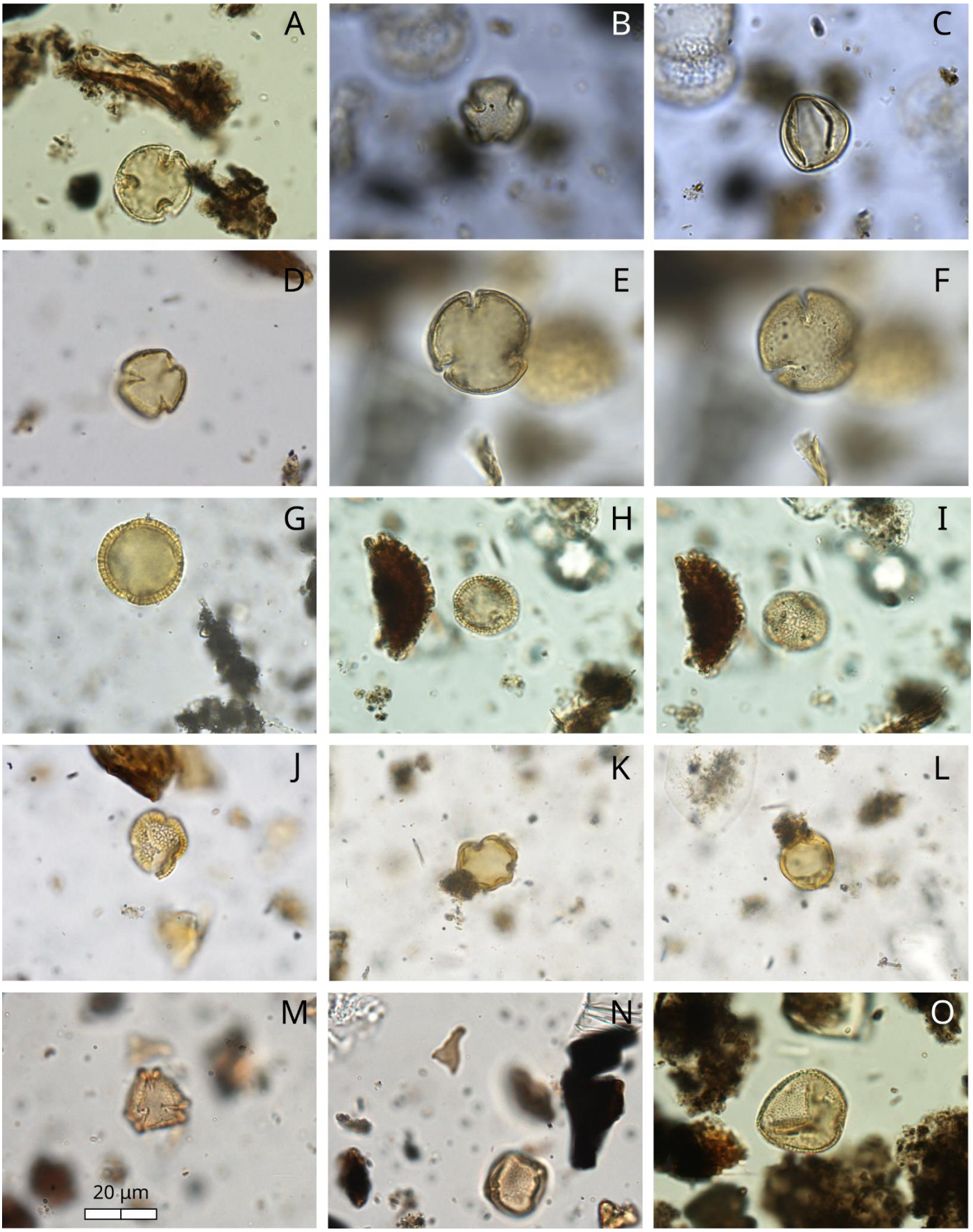


Planche 5 : Taxons à affinité Méditerranéenne. A-D : *Quercus* type *ilex-coccifera* ; E-F : *Quercus* type *suber* ; G-J : *Olea* ; K-L : *Vitis* ; M-N : *Rhamnus*, O : *Pistacia*.

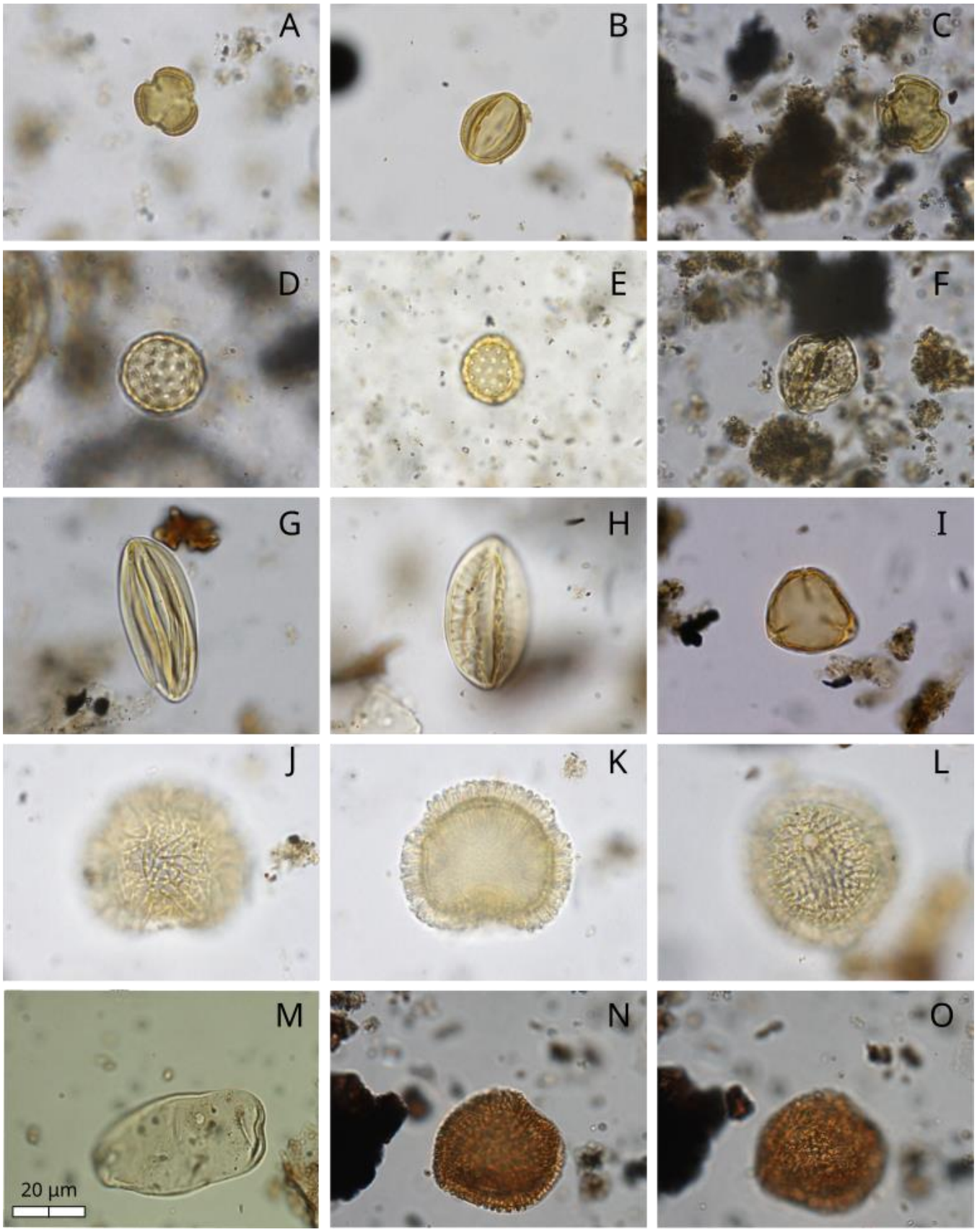


Planche 6 : Taxons à affinité de milieux steppiques à semi-désertiques. A-C : *Artemisia* (C: grain très altéré) ; D-F : Amaranthaceae (F : grain très altéré) ; G : *Ephedra fragilis*-type ; H : *Ephedra distachya*-type ; I : *Hippophae* ; J-L : *Erodium* ; **Taxons d'origine typiquement nord-africaine** : M : *Lygeum* ; N-O : *Cistus ladaniferus* (grain remanié)

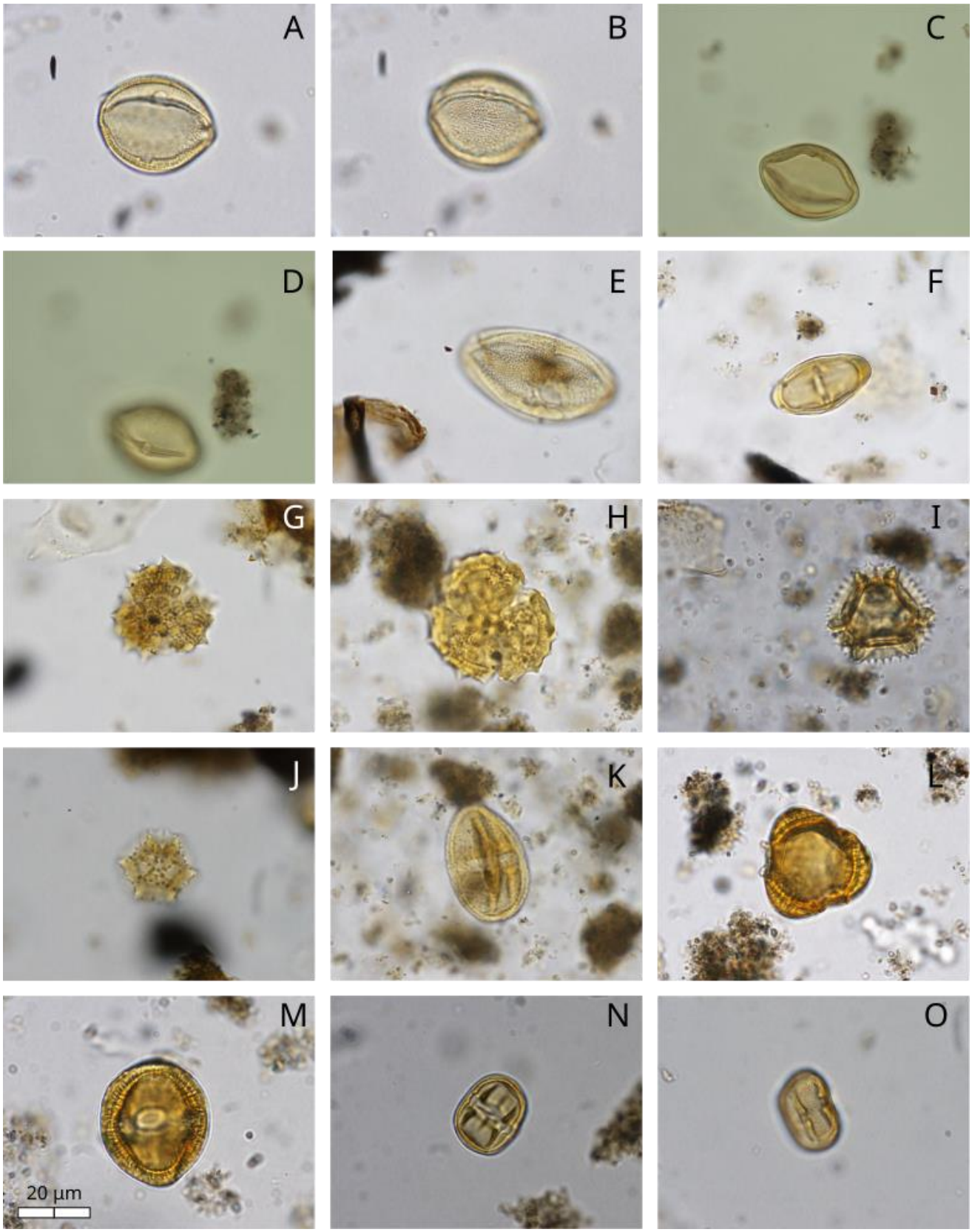


Planche 7: Herbacées, types tricoloporés (1). A-B: *Cistus* ; C-E: *Helianthemum* ; F: Apiaceae ; G-H Asteraceae type Asteroideae ; I-J: Asteraceae type Cichorioideae ; K-M: *Centaurea* type *cyanus* ; L-M: *Centaurea* type *jacea* ; N-O: *Polygonum*

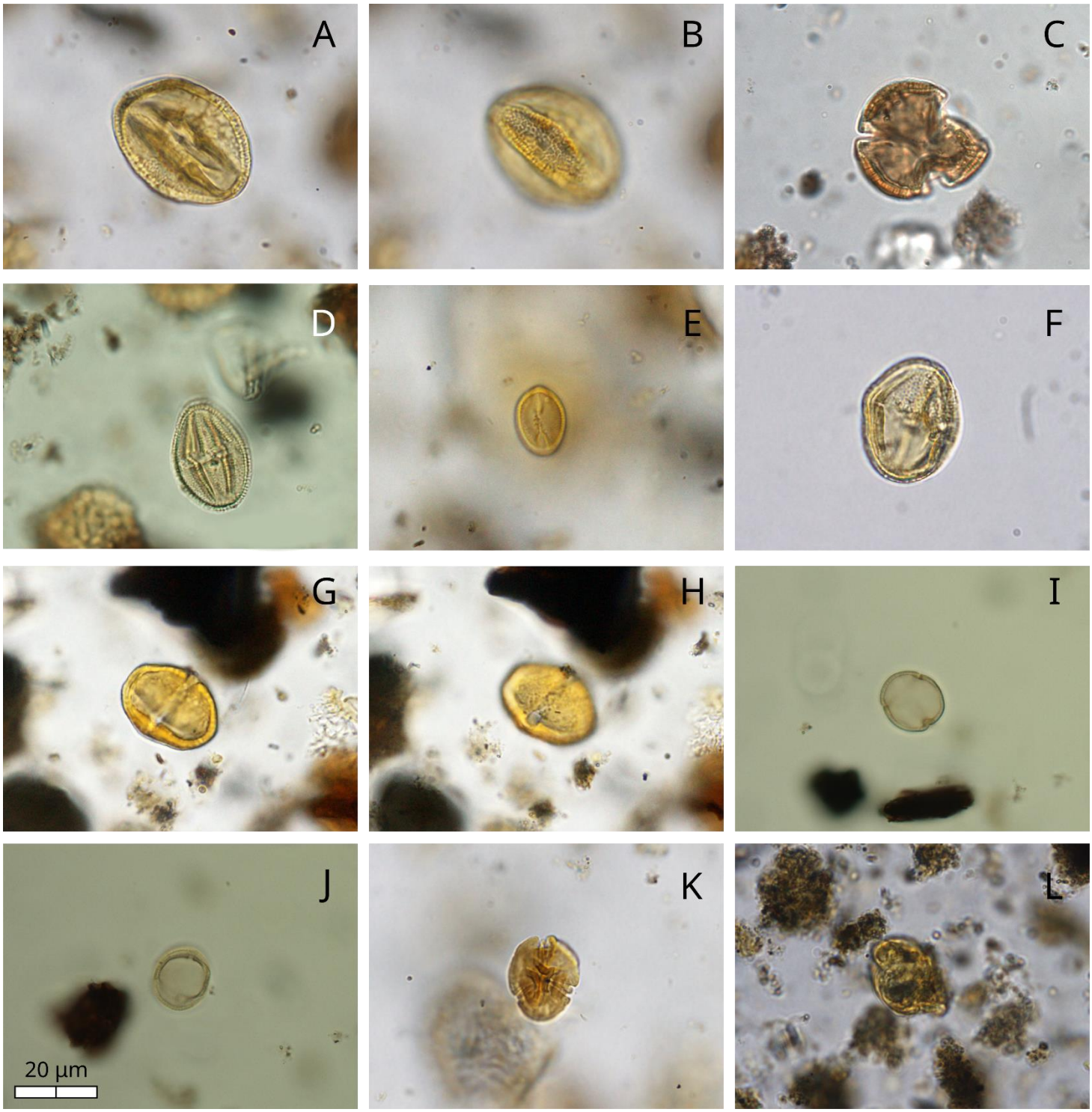


Planche 8: Herbacées, types tricoloporés (2). A-C : Euphobiaceae type *Euphorbia* ; D-E : Euphorbiaceae type *Mercurialis* ; F-H: Fabaceae ; I-J: *Rumex* ; K-L: Rosaceae.

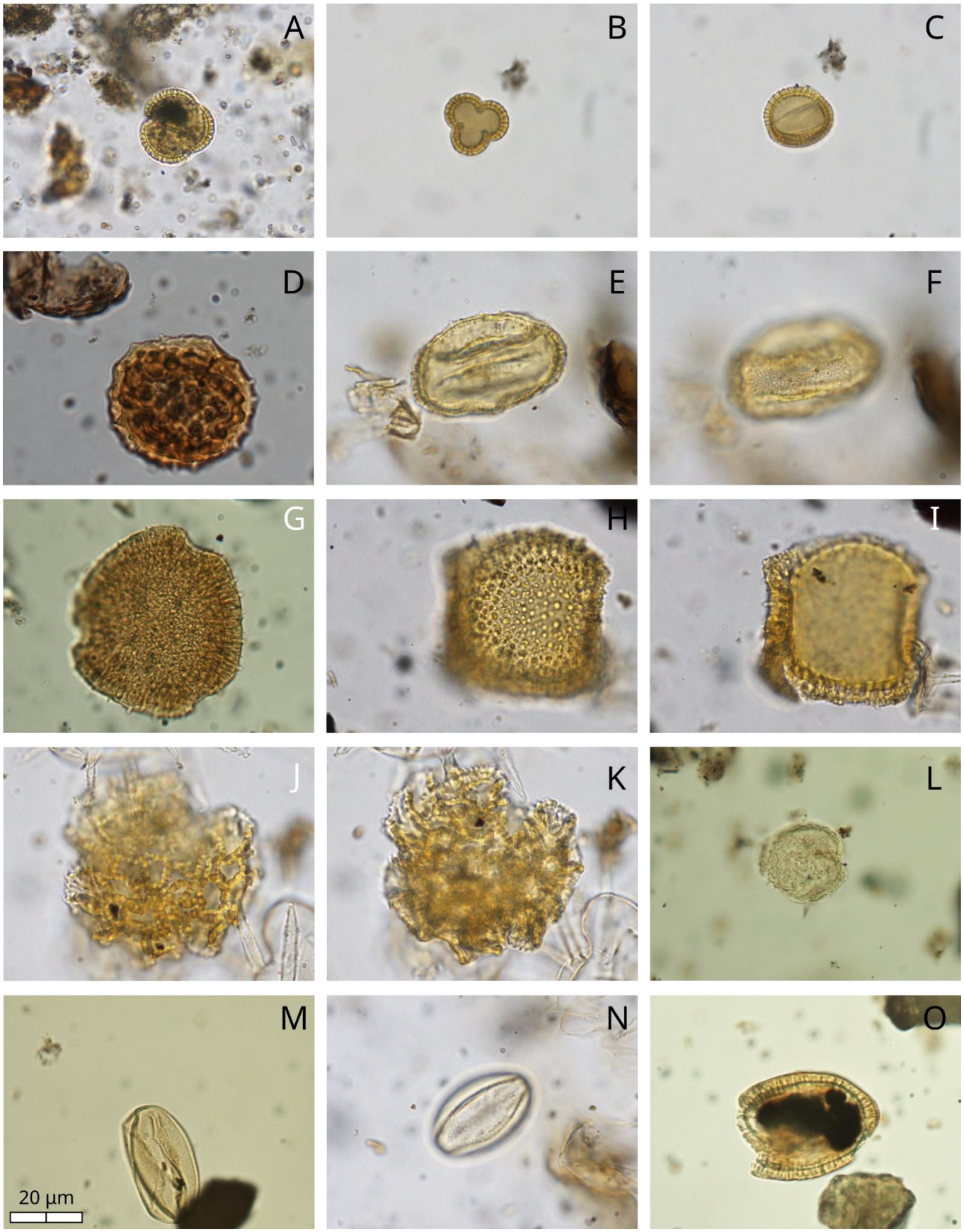


Planche 9: Herbacées types tricolpés. A-C: Brassicaceae ; D-F: Valerianaceae ; G: Dipsacaceae type *Scabiosa* ; H-I: Dipsacaceae type *Cephalaria* ; J-K: Plumbaginaceae ; L: Ranunculaceae ; M-N: Lamiaceae types tricolpés ; O: Convolvulaceae

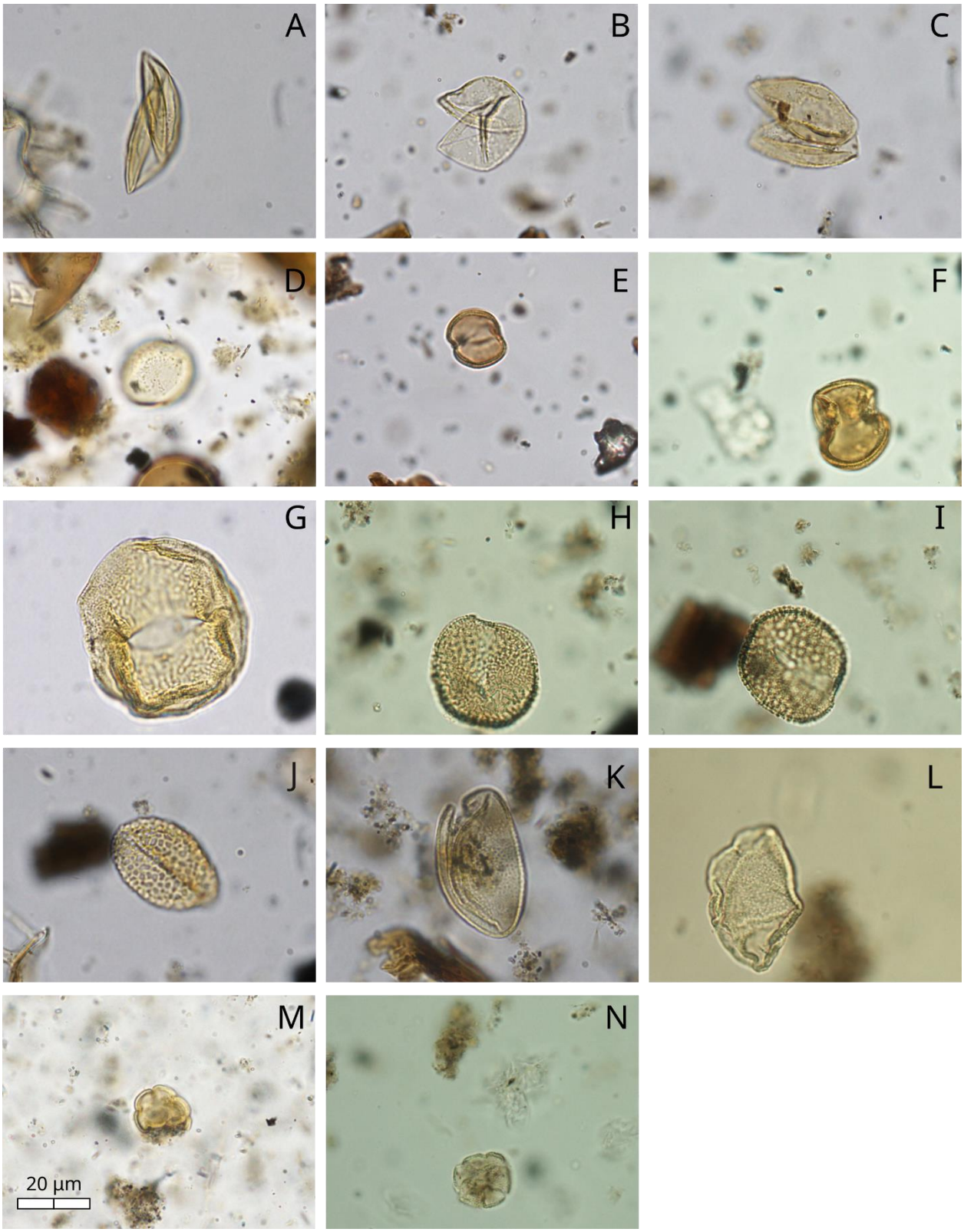


Planche 10: Grains inaperturés, dicolpés, monocolpés et stéphanocolpés. A-C: Cupressoideae type *Juniperus* ; D: Cupressoideae indifférenciée ; E-F: *Hypecoum* ; G: *Asphodelus* ; H-I: Liliaceae ; J: Asparagaceae ; K-L: Iridaceae ; M: Rubiaceae type *Galium* ; N: Lamiaceae type stéphanocolpé.

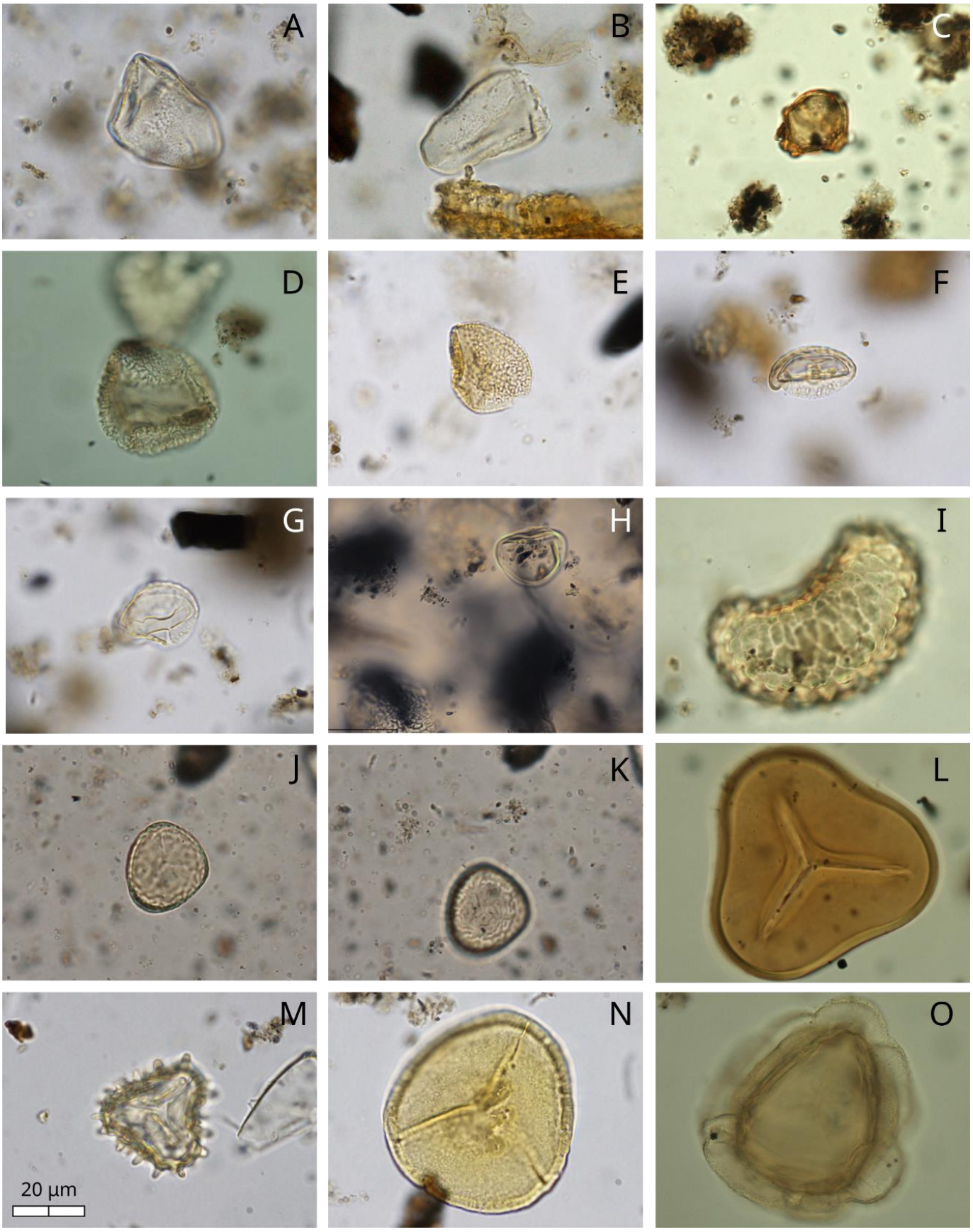


Planche 11: Plantes d'eau et Ptéridophytes. A-B: Cyperaceae ; C: *Myriophyllum* ; D: *Butomus* ; E: *Potamogeton* ; F-G: *Isoetes* ; H: Spore monolète ; I: Polypodium ; J-0: Spores trilètes

Planches microscopiques: spores de champignons, d'algues, restes de foraminifères et autres palynomorphes non-identifiés

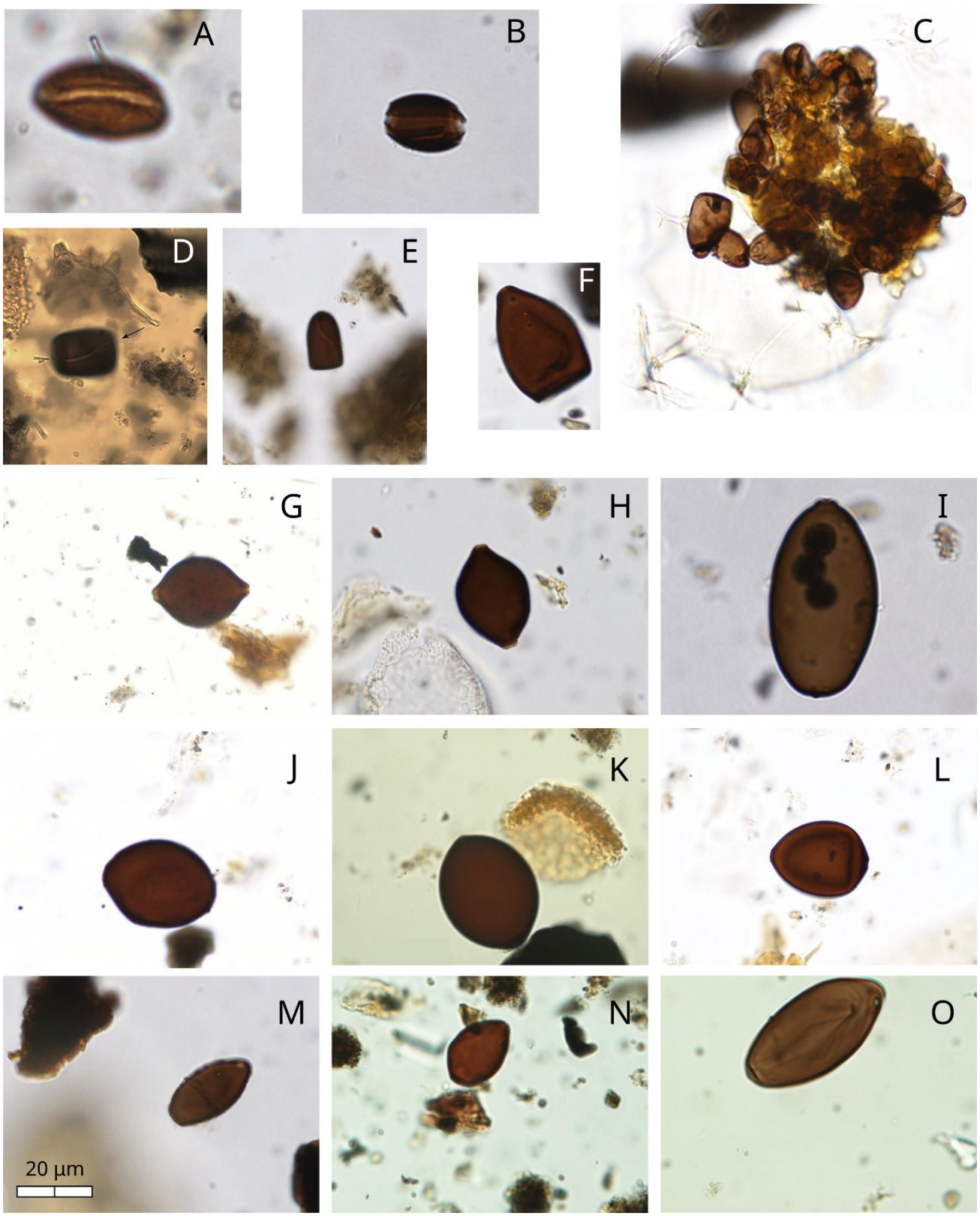


Planche 12: Spores de champignons lignicoles, carbonicoles et/ou coprophiles (1). A-B: Coniochaetaceae ; C: mycellium avec agglomérat de spores (*Apiosordaria* ?) ; D-E: *Sporormiella* ; F: HdV-169 (*Apiosordaria*) ; G-H: UAB-4 ; I-K: HdV-55A (*Sordaria*) ; L: cf. HdV-205 (*Sordaria* ?) ; M-N : HdV-112 (*Cercophora*) ; O : HdV-368 (*Podospora*)

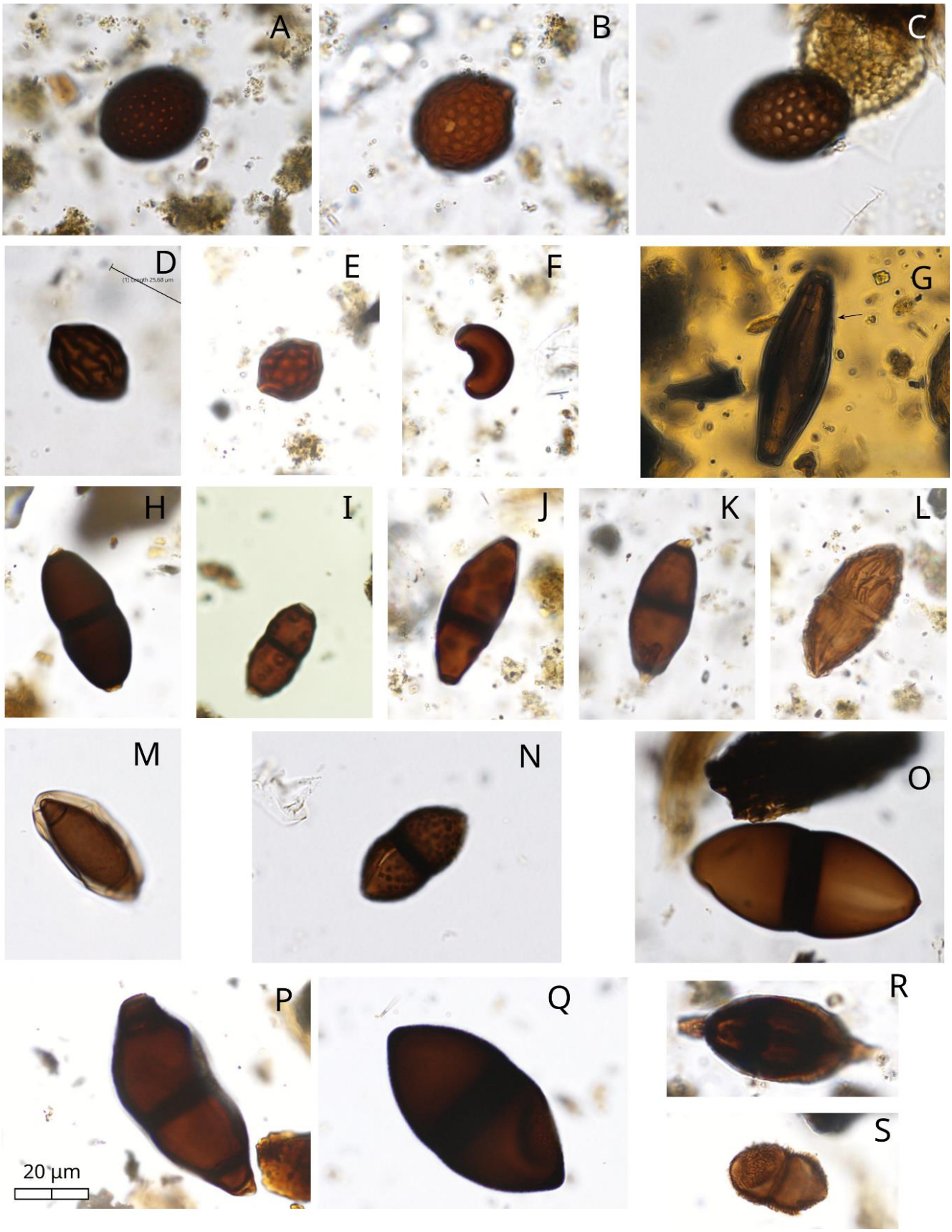


Planche 13: Spores de champignons lignicoles, carbonicoles et/ou coprophiles (2). A-C: *Gelasinospora* (A : HdV-1093 cf. *cratophora* ; B-C HdV-2 cf. *reticulispora*) ; D-E: *Sphaerodes*; F: TM-111 ; G: HdV-143 (*Diporotheca*) ; H: UAB-35 ; I-K: T-118 (*Savoryella* ?) ; L: HdV-263 (*Valsaria* ?) ; M: HdV-1048 ; N: cf. *Delitschia* ; O: *Delitschia* ; P: HdV-1001 (*Caryospora callicarpa*) ; Q-S: Didymosphores indéterminées.

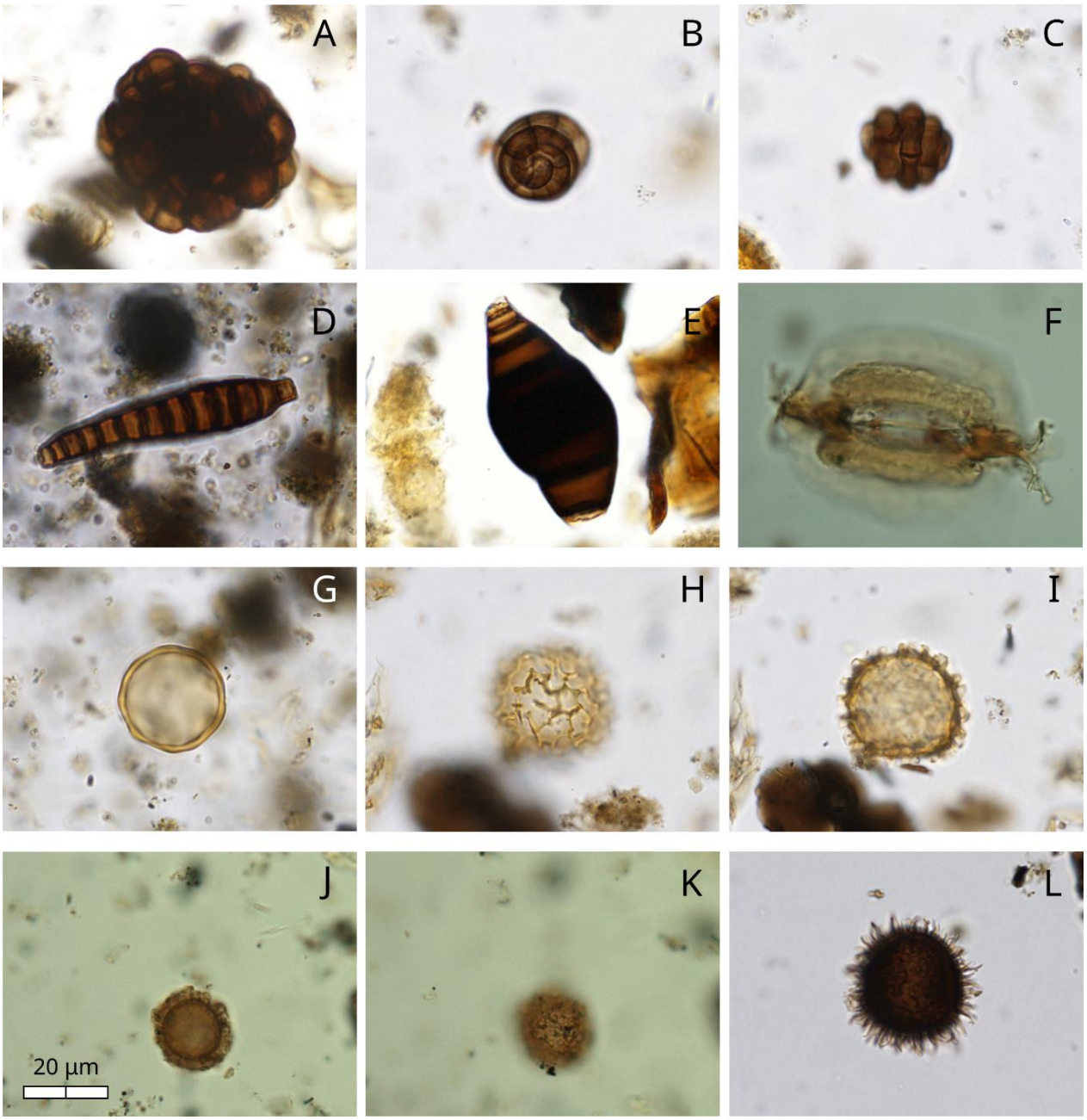


Planche 14: Conidia, stomate, et spores non-identifiées. A : UAB-20 ; B-C : HdV-30 (*Helicoon pluriseptatum*) ; D-E : Phragmoconidia indeterminés (E : cf. TM-4110) ; F: stomate de conifère; G: HdV-988 ; H : HdV-59 ; J-K : Amérospore indéterminée ; L : cf. S*cleroderma*.

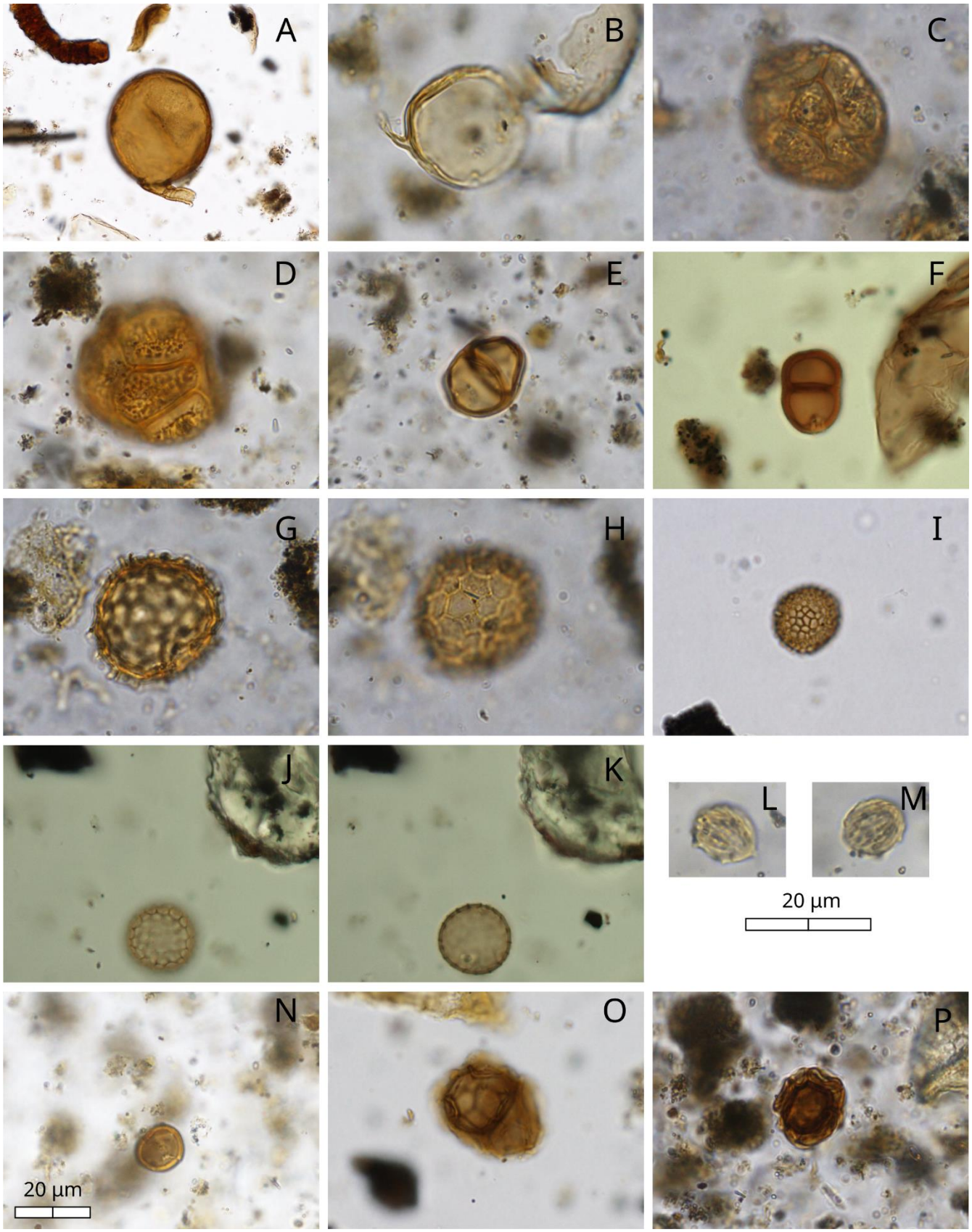


Planche 15: Spores de champignons mycorhiziens et phytopathogènes. A-B: HdV-207 (*Glomus*) ; C-D: *Tecaphora* ; E-F: HdV-357 (*Puccinia*) ; G-H : HdV-1055 (*Ustilago*) ; I-K : *Tilletia* ; L-M: *Entorhiza* ; N : Uredospore de champignon de rouille ; O-P : *Urocystis*.

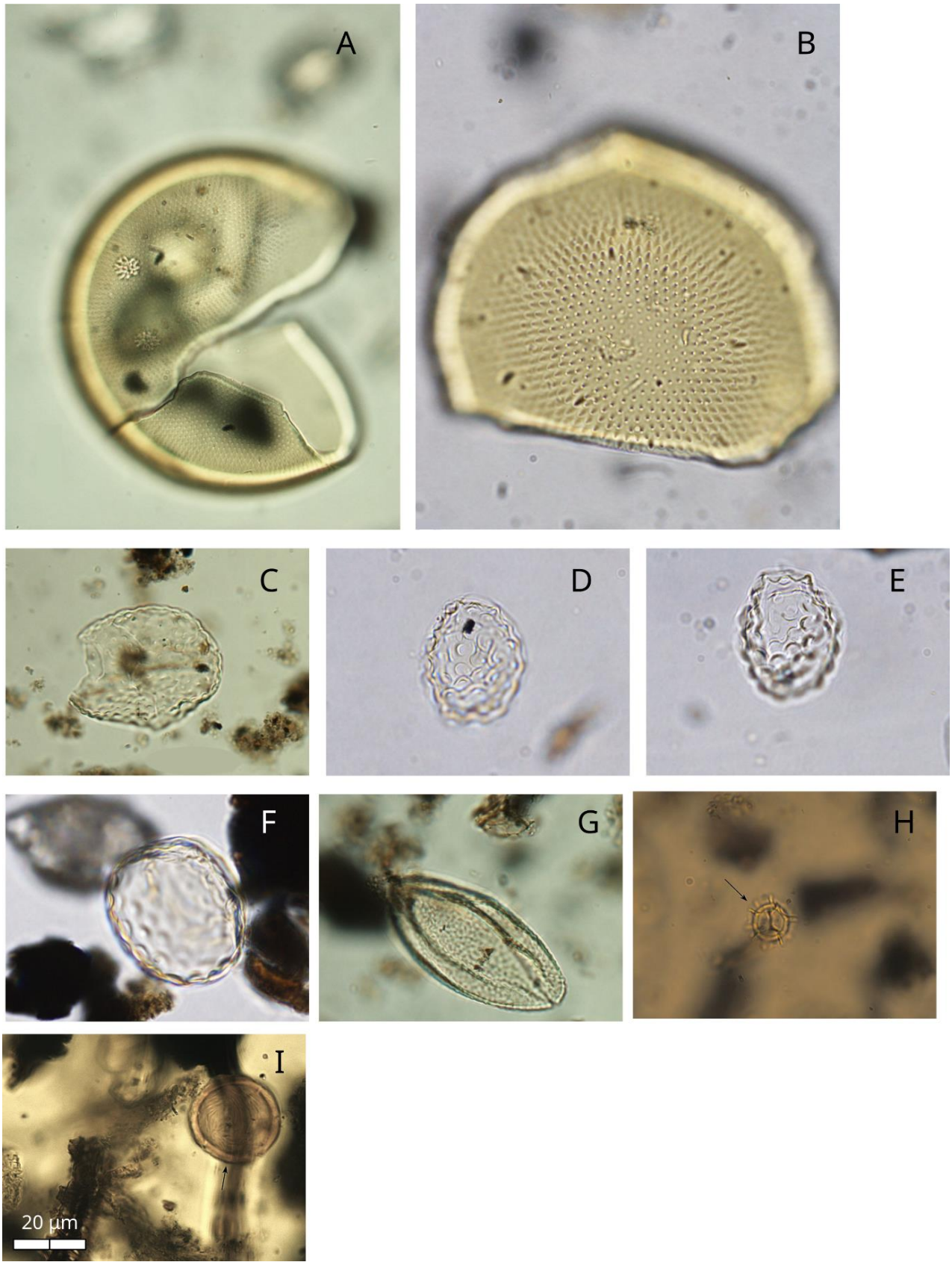


Planche 16: Spores d'algues. A-B : *Tasmanites ;* C *:* HdV-213 (*Zygnema*) ; D-F *:* HdV-314 (*Zygnema*) ; *G :* HdV-342 (*Spirogyra* cf *scrobiculata*) ; H: HdV-116 (*Cymatiosphaera* ?) ; I : Pseudoschizeae.

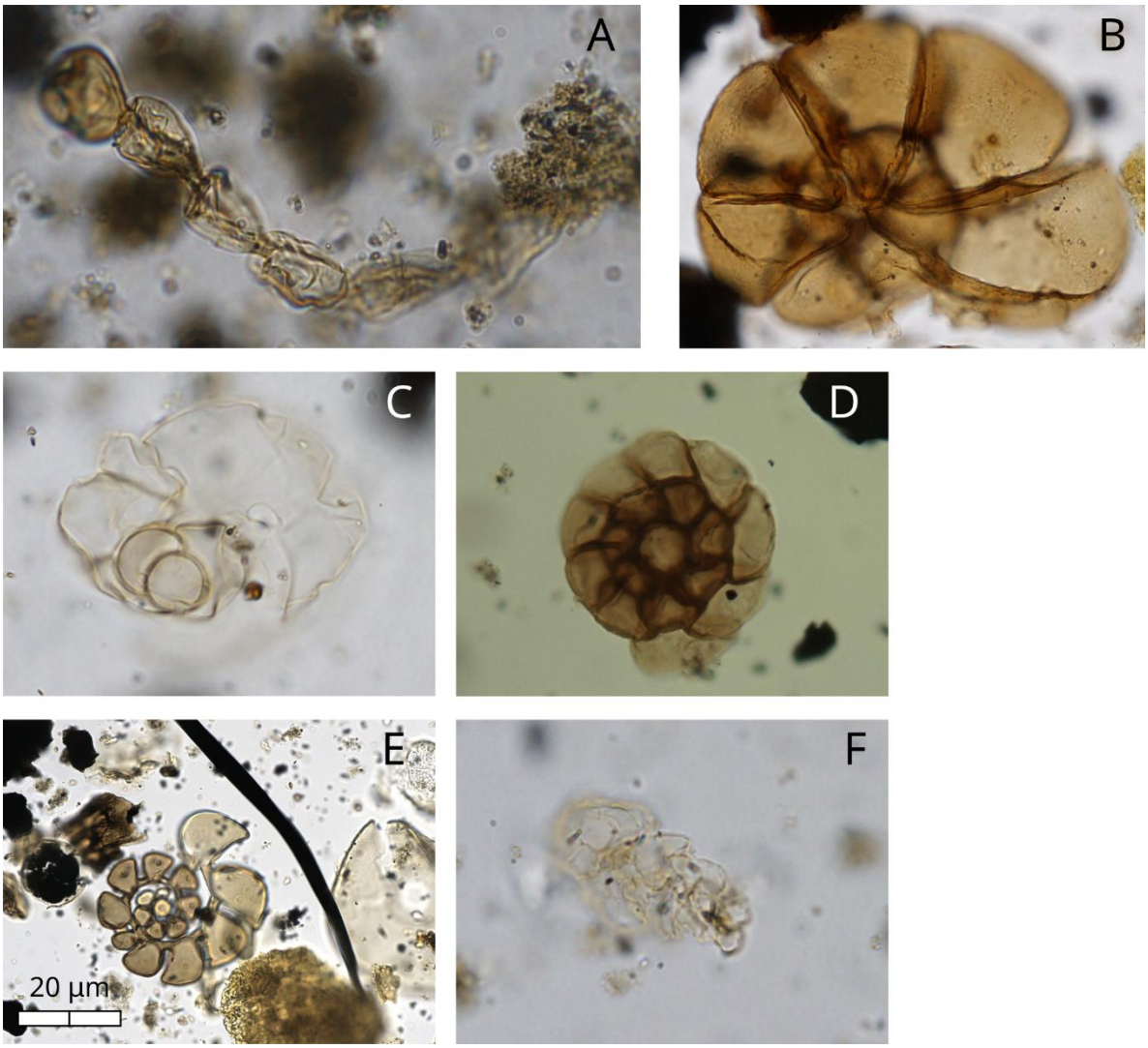


Planche 17: Restes organiques de foraminifères (« *foraminifera organic linings* »). A : type unisérié ; B-C : types enroulés en trochospirale : D-E : types enroulés en planispirale ; F : type bisérié.